Proton-Coupled Electron Transfer at Nickel Pincer Complexes

Dissertation

zur Erlangung des mathematisch-naturwissenschaftlichen Doktorgrades

“Doctor rerum naturalium“

der Georg-August-Universität Göttingen

Im Promotionsprogramm der Georg-August University School of Science (GAUSS)

vorgelegt von

Felix Schneck, M. Sc.

aus Wittingen

Göttingen, 2019

Betreuungsausschuss

Prof. Dr. Sven Schneider

Institut für Anorganische Chemie, Georg-August-Universität Göttingen

Prof. Dr. Franc Meyer

Institut für Anorganische Chemie, Georg-August-Universität Göttingen

Mitglieder der Prüfungskommission

Referent: **Prof. Dr. Sven Schneider**

Institut für Anorganische Chemie, Georg-August-Universität Göttingen

Korreferent: **Prof. Dr. Franc Meyer**

Institut für Anorganische Chemie, Georg-August-Universität Göttingen

Weitere Mitglieder der Prüfungskommission:

Prof. Dr. Dirk Schwarzer

Max-Planck-Institut für Biophysikalische Chemie

Prof. Dr. Inke Siewert

Institut für Anorganische Chemie, Georg-August-Universität Göttingen

Jun.-Prof. Dr. Nathalie Kunkel

Institut für Anorganische Chemie, Georg-August-Universität Göttingen

Prof. Dr. Manuel Alcarazo

Institut für Organische und Biomolekulare Chemie, Georg-August-Universität Göttingen

Tag der mündlichen Prüfung: 26.04.2019

Danksagung

An erster Stelle möchte ich Prof. Dr. Sven Schneider für die Möglichkeit danken, in seiner Arbeitsgruppe meine Doktorarbeit anzufertigen. Ich bedanke mich für die interessanten wissenschaftlichen Fragestellungen, die unzähligen Diskussionen, die ständige Hilfsbereitschaft, die unerschöpfliche Motivation sowie die Möglichkeit meine Forschung auf nationalen und internationalen Tagungen zu präsentieren.

Außerdem danke ich Prof. Dr. Franc Meyer für die Übernahme der Zweitkorrektur sowie Prof. Dr. Dirk Schwarzer, Prof. Dr. Inke Siewert, Jun.-Prof. Dr. Nathalie Kunkel sowie Prof. Dr. Manuel Alcarazo für Ihre Beteiligung an der Prüfungskommission.

Josh Abbenseth, Florian Wätjen und Dr. Arne Glüer danke ich für ihre Hilfe während der Korrektur dieser Arbeit.

Für die bereitwillige Durchführung von Messungen danke ich den Mitarbeitern des analytischen Labors, sowie der massenspektrometrischen Abteilung und der NMR-Abteilung der Georg-August-Universität.

Weiterhin danke ich Dr. A. Claudia Stueckl für EPR-spektroskopische Analysen und Dr. Christian Würtele für die Hilfsbereitschaft beim Durchführen röntgenkristallografischen Messungen. Der Arbeitsgruppe Siewert danke ich für die Durchführung von GC Messungen sowie die Bereitstellung des Gaschromatographen.

Dr. Markus Finger danke ich für die quantenchemischen Experimente und die hilfreichen wissenschaftlichen Diskussionen. Prof. Dr. Dirk Schwarzer, Dr. Jennifer Ahrens und Jan-Hendrik Borter danke ich für ihre Beiträge in den durchgeführten Pump-Probe Experimenten.

Dalila Griffin danke ich für die Unterstützung bei bürokratischen Fragestellungen.

Daniel Delony, Nareh Hatami, Rahel Ziemer, Xuan Thúy Nguyen, Sier Sang und Matthieu Haake danke ich für das Engagement während der Durchführung von Abteilungspraktika oder der Anfertigung von Abschlussarbeiten.

Der gesamten Arbeitsgruppe Schneider danke ich für die tolle Arbeitsatmosphäre in den vergangenen Jahren. Besonders Jan Gerkens und Josh Abbenseth danke ich für die freundliche Aufnahme in die Gruppe.

Thúy danke ich für die gemeinsame Zeit.

Mein besonderer Dank gilt meinen Eltern Gudrun und Heinrich Schneck für ihre Unterstützung.

Table of Contents

Part I: Carbon-Centered Proton-Coupled Electron Transfer at Nickel Pincer Complexes

Part of the research presented in this part has been published and citation of the original work is permitted by the publishers.

F. Schneck, M. Finger, M. Tromp, S. Schneider, *Chem. Eur. J.* **2017**, *23*, 33−37.

F. Schneck, J. Ahrens, M. Finger, A. C. Stückl, C. Würtele, D. Schwarzer, S. Schneider, *Nat. Commun.* **2018**, *9*, 1161−1169.

F. Schneck, F. Schendzielorz, N. Hatami, M. Finger, C. Würtele, S. Schneider, *Angew. Chem. Int. Ed.* **2018**, *57*, 14482−14487.

1.1 Introduction

1.1.1. Proton-Coupled Electron Transfer

Transfer of electrons and protons is among the most prominent reactions encountered in chemistry. Combining both is described as proton-coupled electron transfer (PCET). This term was initially introduced by *Meyer* to describe a concerted $1e^-/1H^+$ process, however lost its mechanistic denotation and is now used to entitle a broad area of reactions involving the combination of proton and electron transfer in varying stoichiometry without giving information on mechanistic details.[1] Aside from net hydrogen atom transfer processes, hydride transfer (HT) as $2e^-/1H^+$ process is also regarded as PCET.[2] Several more precise classifications exist to narrow down the vast field of PCET. As such, the original meaning of PCET is now best categorized as concerted proton-electron transfer (CPET) as introduced by *Savéant*.[3] Hydrogen atom transfer (HAT) is a popular concept in organic chemistry since decades and describes CPET which occurs by transfer of the electron and proton from the same site of a donor to the same site of an acceptor.[4] In contrast, multiple-site concerted proton-electron transfer (MS-CPET) is distinguished by transfer of the electron and proton to different acceptor sites or from different donor sites.[5] Net hydrogen atom transfer[1] between organic reactants often proceeds *via* HAT, explaining the frequent use of this term prior to investigation of transition metal complex based reactivity. Similarly, electrochemical CPET can be unambiguously assigned as MS-CPET. Assuming substrate oxidation, the electrode represents the electron acceptor site while a base acts as proton acceptor. While these examples illustrate the mechanistic scope of PCET, assignment of specific reactions is not trivial in most cases. Taking the oxidation of hydrocarbons by metal oxo complexes as example, homolytic C-H bond activation means electron and proton transfer from the same donor site as is observed in HAT. However, $1e^-/1H^+$ reduction of metal oxo complexes commonly results in transfer of the proton to the oxygen atom while electron transfer results in metal centered reduction. Therefore, the electron and proton are abstracted from the same donor site, but end up at different acceptor sites of the same molecule. Extensive explanation and discussion of the classification of reactions falling into the broad concept of PCET can be found in reviews by *Meyer*[5,6], *Mayer*[4,7], *Costentin*[8] and *Miller* and *Appel*[2].

$$E^{1/2} = E^0 - \frac{RT}{nF}\ln\left(\frac{[\mathrm{Red}]}{[\mathrm{Ox}]}\right) - \frac{RT}{F}\frac{m}{n}\mathrm{pH} \qquad (1)$$

The impact of proton coupling on the thermochemistry of electron transfer is long known. The *Nernst* eq. (1) for reversible redox processes involving proton transfer in aqueous media predicts a variation of the

[1] Meaning a $1e^-/1H^+$ process without making any mechanistic implications.

observed redox potential $E^{1/2}$ upon changing pH with a potential shift of $\Delta E = \frac{m}{n} 0.059$ V per magnitude of proton activity (m: number of involved protons; n: number of involved electrons). The plot of the observed redox potential $E^{1/2}$ over the pH of the solution, a so-called *Pourbaix* diagram, is useful for identification of regimes of existence of species involved in the PCET process. Coupling proton to electron transfer is particularly important in multielectron processes to avoid charge built-up and allow for more facile electron transfer. A prominent example found in nature is the enzyme photosystem II (PSII), which mediates photochemical water oxidation (Figure 1).

In PSII, light absorption by chlorophyll P_{680} (ChI_{D2} in Figure 1) is followed by pheophytin $Pheo_{D1}$ mediated electron transfer to bound plastoquinone Q_A giving a charge separated pair.[9] Oxidation of tyrosine TyrH161 (Tyr_Z) by PCET results in reduction of P_{680}^+, increasing the distance between oxidant and reductant. The reducing equivalents stored in Q_A^- undergo transfer to photosystem I (PSI) *via* multiple stages and are used in the *Calvin* cycle giving an overall Z scheme for photochemical CO_2 reduction.[10] The product of net hydrogen atom transfer from Tyr161 is a phenoxyl radical, located in close proximity to the oxygen evolving complex (OEC) consisting of a Mn_4 cluster and a Ca^{2+} cofactor. While the details of the *Kok* cycle involving the states S_0–S_4 of the OEC are reviewed elsewhere, fourfold oxidation of the OEC *via* PCET by the phenoxyl radical results in oxidation of water to dioxygen and the liberation of four protons and reducing equivalents.[5,9]

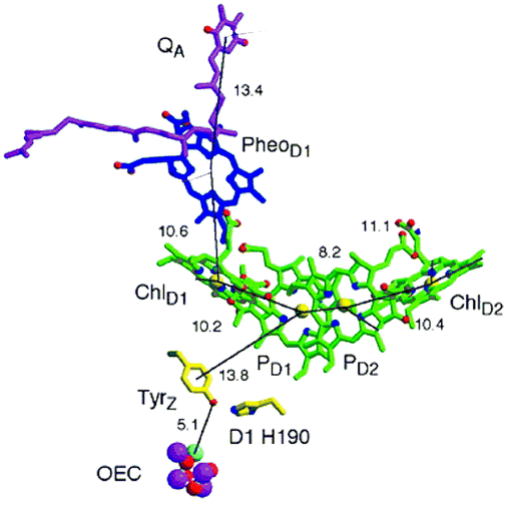

Figure 1: Molecular structure of the reaction center of PSII involved in water oxidation (figure reprinted with permission from ref. [11]).

The tyrosyl radical not only plays a role in water oxidation by PSII, but is further relevant for alcohol oxidation in galactose oxidase and other enzymatic reactions involving PCET.[4,12] Considering the

thermodynamics of electron transfer from tyrosine exemplifies the importance of proton coupling in its reactivity. The redox potential for tyrosine oxidation $E^0(\text{TyrH})^{aq}$ = 1.34 V *vs.* NHE is uphill compared to $E^0(P_{680})^{aq}$ = 1.26 V *vs.* NHE which is considered one of the strongest oxidants in biochemistry.[4,13] The high acidity of oxidized tyrosine $pK_a(\text{TyrH}^+)^{aq}$ = -2 and the cathodic shift of 0.059 V per pH unit observed in the *Pourbaix* diagram of tyrosine suggests PCET upon oxidation.[14]

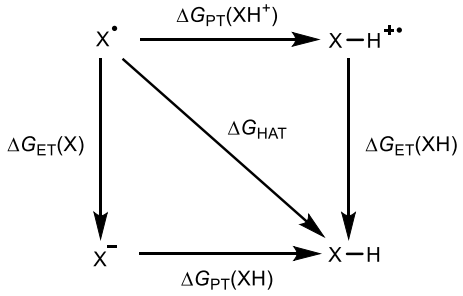

Figure 2: Thermodynamic square scheme for interconversion of X-H and X• *via* ET, PT and CPET.

From a thermodynamic point of view, subsequent electron and proton transfer can be expressed as net hydrogen atom transfer according to *Hess*' law. A popular way of illustrating the driving force of the individual steps connecting the oxidized (X•) and reduced form (XH) of a PCET reagent is a thermodynamic square scheme (Figure 2). Here, electron transfer (ET) steps are shown as vertical lines, whereas proton transfer (PT) is represented by horizontal lines and CPET is represented by the direct diagonal connection between X• and XH. The standard potential E^0 of an electrochemical process and the pK_a describe the free energy of an ET and PT process, respectively. Conversion into kcal·mol^{-1} can be performed according to eq. (2) and (3).

$$\Delta G_{PT} = -RT\ln(K_a) = 2.303\,RT\,pK_a = -1.37\ \text{kcal}\cdot\text{mol}^{-1}\cdot pK_a \qquad (2)$$

$$\Delta G_{ET} = -FE^0 = -23.06\ \text{kcal}\cdot\text{mol}^{-1}\cdot\text{V}^{-1}\cdot E^0 \qquad (3)$$

From *Hess*' law results an identical difference $\Delta\Delta G$ in the driving force for electron transfer ΔG_{ET} between protonated (XH/XH$^{+\bullet}$) and deprotonated species (X$^-$/X•) and the driving force for proton transfer ΔG_{PT} between oxidized (XH$^{+\bullet}$/X•) and reduced (XH/X$^-$) species. While the oxidized reactant will always be more acidic than its reduced form, the extent of $\Delta\Delta G_{ET}$ and $\Delta\Delta G_{PT}$ strongly varies between different compounds, rendering it a useful expression for quantifying the thermodynamic coupling of proton and electron transfer.[7] Comparison of the thermodynamics for subsequent ET/PT or PT/ET to the bond dissociation free energy (BDFE) of the bond involved in the concerted process is crucial to get mechanistic information on the PCET process.

$$\Delta G_{HAT} = 1.37\ \text{kcal·mol}^{-1}\cdot \text{p}K_a + 23.06\ \text{kcal·mol}^{-1}\cdot \text{V}^{-1}\cdot E^0 + C_G \quad (4)$$

The term BDFE is identical to ΔG_{HAT} and can be measured experimentally by calorimetry or by titration with a compound of similar bond strength. Alternately, ΔG_{HAT} can be expressed as the sum of ΔG_{ET} and ΔG_{PT} connecting XH and X along a path in the square scheme, giving eq. (4). In addition, C_G accounts for the reference electrode and the free energy of formation $\Delta G_f^0(\text{H}^\bullet)$ and solvation $\Delta G_{solv}^0(\text{H})$ of the hydrogen atom which is usually approximated by the free energy of solvation of H_2.[4] Since $\Delta G_f^0(\text{H})$ and $\Delta G_{solv}^0(\text{H})$ are solvent specific and E^0 is referenced to an internal standard, the same holds true for C_G. Based on the formation $S_f^0(\text{H})$ and solvation entropy $\Delta S_{solv}^0(\text{H})$ of the hydrogen atom, C_H can be determined according to eq. (5).[15]

$$C_H = C_G - T(S_f^0(\text{H}) + \Delta S_{solv}^0(\text{H})) \quad (5)$$

$$\Delta H_{HAT} = \Delta G_{HAT} + C_H - C_G \quad (6)$$

Assuming identical solvation entropies $\Delta S_{solv}^0(\text{XH})$ and $\Delta S_{solv}^0(\text{X}^\bullet)$, C_H can be used for conversion of BDFE to bond dissociation enthalpy (BDE) or ΔH_{HAT} according to eq. (6). While this assumption holds for most organic PCET reagents, transition metal complexes may undergo a significant change in solvation entropy upon PCET due to electronic rearrangement, requiring exact treatment and therefore consideration of free energies.[16,17]

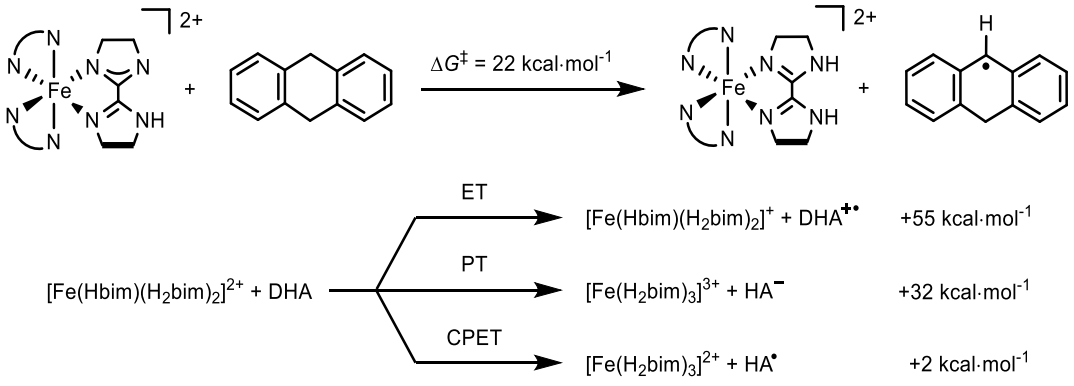

Figure 3: Thermodynamic and kinetic parameters for PCET from DHA to $[\text{Fe(Hbim)(H}_2\text{bim)}_2]^{2+}$.

Considering the ground state thermochemistry of CPET *vs.* stepwise ET/PT or PT/ET in a PCET reaction, the concerted process will always be favored. A popular approach to investigate if a stepwise process is a viable option to the concerted process is determination of the kinetic barrier according to transition state theory (TST, Chapter 1.1.2). Here, a concerted process is assumed as long as the experimentally determined $\Delta G^‡$ is smaller than ΔG for initial electron or proton transfer. Taking the oxidation of 1,10-dihydroantracene

(DHA) by Fe^{III} complex $[Fe(Hbim)(H_2bim)_2]^{2+}$ (H_2bim = 2,2'-biimidazolin) as example, CPET (ΔG_{HAT} = 2 kcal·mol^{-1}) is thermodynamically strongly favored over initial ET (ΔG_{ET} = 53 kcal·mol^{-1}) and PT (ΔG_{PT} = 30 kcal·mol^{-1}) (Figure 3). The kinetic barrier of $\Delta G^{\ddagger}$ = 22 kcal·mol^{-1} determined by kinetic analysis suggests CPET since it predicts the transition state for CPET at lower energy than simple ground state energy considerations for stepwise processes starting with either ET or PT.[18–21]

1.1.2. Linear Free Energy Relationships

Attempts to connect the thermodynamic driving force of a reaction to the kinetic barrier have been performed using linear free energy relationships (LFERs). The *Brønsted* catalysis law for proton transfer represents an early example and correlates the rate of an acid catalyzed reaction to the acidity of the *Brønsted* acid, representing a free energy.[22] *Hammett* correlations are still used frequently to correlate an substituent specific electronic parameter of benzene derivatives to a rate constant in a specific type of reaction.[23] In both cases, the correlation between rate *k* and free energy ΔG assumes a linear increase of the kinetic barrier with the driving force. This assumption holds only within a limited range of reactants or reactions which are considered *similar*. Consequently, additional empirical parameters are required and different LFERs are obtained for each class of compound or reaction.

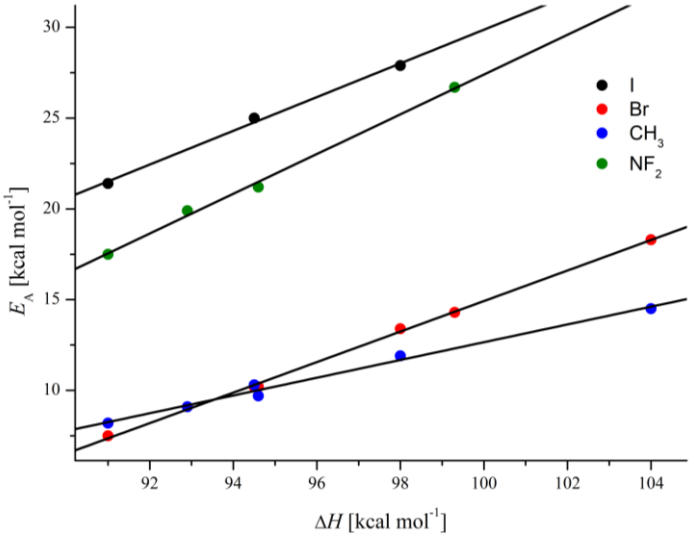

Figure 4: Linear energy relationships for hydrogen atom abstraction of different radicals from alkanes in the gas phase (thermodynamic and kinetic data are taken from ref. [24]).

A similar approach is followed in the *Bell-Evans-Polanyi* principle which states a linear relationship between the activation energy E_A and driving force of a reaction. Here, free radical substitution reactions are investigated and consequently the difference in bond strength, BDFE, is the driving force of the reaction (Figure 4). The activation energy E_A is determined from kinetic data by the *Arrhenius* equation (eq. (7)) assuming a temperature independent preexponential factor *A*.[25]

$$k = A \exp(-\frac{E_A}{RT}) \tag{7}$$

$$E_A = \alpha \Delta H + \beta \tag{8}$$

Importantly, the activation energy E_A is expressed by the difference in bond strength ΔH and the *Evans Polanyi* parameters α and β in the *Evans-Polanyi* equation (eq. (8)). Since E_A and ΔH are enthalpies, the *Bell Evans Polanyi* principle gives linear energy relationships rather than LFERs. However, the effect of entropy change on the driving force in HAT between organic substrates is negligible in most cases, as mentioned earlier. The experimental parameter α and β resemble the parameters used in the *Brønsted* catalysis law and *Hammett* correlations in a sense, that they vary between different substance classes and therefore allow for categorization. While *b* gives a lower limit of activation energy E_A within similar reactions, *a* is interpreted as the position of the transition state along the reaction coordinate.[25]

$$k = \kappa \frac{k_B T}{h} \exp(-\frac{\Delta G^{\ddagger}}{RT}) \tag{9}$$

The *Eyring-Polanyi* equation (eq. (9)) used in transition state theory (TST) has a theoretical basis which results in expression of the reaction barrier as the free energy $\Delta G^{\ddagger}$ of the transition state.[26] However, TST does not give a relationship between this barrier and the thermodynamic driving force ΔG of the reaction.

1.1.3. *Marcus* Theory of Outer-Sphere Electron Transfer

Turning to outer-sphere electron transfer, *Marcus* provides a basis for correlating a driving force and an energetic barrier.[27,28] Crucial in outer-sphere electron transfer is, that this chemical reaction does not include formation or scission of chemical bonds. While the potential energy surface in those reactions is usually regarded with respect to the atomic distances undergoing substantial change, the potential energy surface in *Marcus* theory is defined by all vibrational coordinates of the reactants and the dielectric polarization of the solvent. Importantly, the position of the electron is not represented in the reaction coordinate of outer-sphere electron transfer, since the Born-Oppenheimer approximation predicts rapid movement of the electron compared to inner-sphere and solvent reorganization. Assuming the simplest outer-sphere electron transfer which is a self-exchange reaction ($\Delta G = 0$), the parabolic potentials shown in Figure 5 result for the situation prior to (*R*) and after electron transfer (*P*). Electronic coupling results in adiabaticity, so potential splitting, at the former intersect of both diabatic (*e.g.* non-interacting) potentials and accordingly electron transfer proceeds at the transition state within a single electronic surface.[5] Following the *Franck-Condon* principle, electron transfer proceeds instantaneously compared to nuclei movement, giving rise to an activation barrier ΔG^{*} due to solvent and vibrational rearrangement.

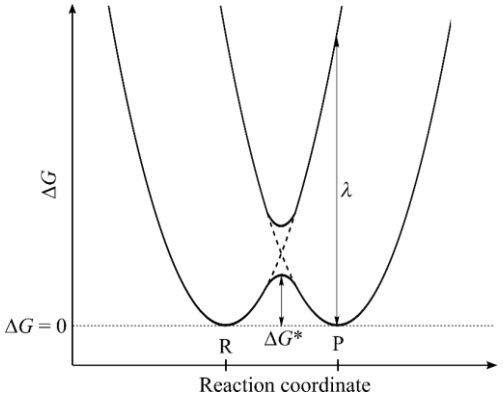

Figure 5: Free energy *vs*. reaction coordinate for self-exchange outer-sphere electron transfer according to *Marcus* theory (dotted lines correspond to the diabatic potential energy surfaces).

Eq. (10) is obtained for the rate k of electron transfer containing the preexponential factor $\kappa A\sigma^2$ accounting for the collision frequency and the average atomic distance of the reactants. Alternately, the kinetic barrier ΔG^* can be expressed by the driving force ΔG and the reorganization term λ giving the *Marcus* Equation eq. (11).[27]

$$k = \kappa A\sigma^2 \exp(-\frac{\Delta G^*}{RT}) \tag{10}$$

$$\Delta G^* = \frac{\lambda}{4}(1+\frac{\Delta G}{\mathrm{RT}})^2 \tag{11}$$

In contrast to LFERs discussed above, parameter λ is well-defined rather than empirical. It corresponds to rearrangement of the solvent and the vibrational coordinates of the reactants to the product geometry without the actual electron transfer (Figure 5). Accordingly, λ consists of a vibrational λ_o and solvational term λ_i which can be calculated based on properties of the solvent and the reactants.[28]

In case of an electron transfer cross reaction between reactants A and B, the reorganization term λ_{AB} is approximated based on the self-exchange reorganization λ_A and λ_B of the involved species (eq. (12)). As result, the *Marcus* cross relation (MCR) (eq. (13)) is obtained which correlates the rate constant of a cross reaction k_{AB} with the rate constants of self-exchange k_A and k_B of the reactants and the equilibrium constant K_{AB}. The frequency factor f_{AB} is usually taken as 1, assuming low driving force.

$$\lambda_{AB} = \frac{1}{2}(\lambda_A + \lambda_B) \tag{12}$$

$$k_{AB} = \sqrt{k_A k_B K_{AB} f_{AB}} \tag{13}$$

1.1.4. Application of *Marcus* Theory to PCET

The theoretical basis for the *Marcus* cross relation lies in outer-sphere electron transfer. However, self-exchange rates are readily determined experimentally for numerous reactions like electron transfer, proton transfer, net hydrogen atom and hydride transfer. As a result, the MCR is applied to reactions aside from outer-sphere electron transfer showing a good accuracy in predicting reaction rates even though, from a theoretical point of view, there is no justification for the use of the MCR in these reactions. [29–32]

As discussed, *Marcus* assumes adiabatic coupling of diabatic potential energy surfaces for the reactants of outer-sphere electron transfer. In case of weak electronic coupling, *e.g.* the nonadiabatic limit, the rate constants of electron transfer correlates to the electron tunneling frequency.[6] Adding proton transfer results in a two-dimensional energy surface consisting of four diabatic states in which the potential energy surface for proton transfer corresponds to a vibrational state of the proton. The proton is treated in the same way as the electron, so its movement does not contribute to the reaction coordinate and is considered much faster than vibrational and solvent reorganization. Accordingly, adiabatic and nonadiabatic behavior can result for both, electron and proton transfer and different combination of both are possible in PCET.[33] Notably, CPET reactions showing huge kinetic isotope effects (KIEs) are reported, indicating significant tunneling contribution in these reactions.[33] Since vibrationally excited states may be involved, interpretation is not trivial.[33]

Several assumptions are made in *Marcus* theory, which do not hold for proton-coupled electron transfer. Importantly, comparing BDFEs obtained by square schemes does not consider adduct formation. While, adduct formation in outer-sphere electron transfer is negligible, orientation of the reactants plays a role in PT and CPET. Accordingly, the driving force ΔG determined by a square scheme is an estimation of the driving force of the reaction. Oxidation of 2,2,6,6-tetramethylpiperidin-1-ol (TEMPO-H) by $[Co(Hbim)(H_2bim)_2]^{2+}$ in a PCET process shows a preequilibrium which is attributed to the formation of a H-bonded precursor complex. Comparison of the thermodynamics determined by a square scheme based on ΔG_{ET} and ΔG_{PT} with an extended version including precursor and successor complexes shows a change in driving force from ΔG_{HAT} = -3.0±0.4 kcal·mol^{-1} to $\Delta G'_{HAT}$ = -0.3±0.9 kcal·mol^{-1} upon considering the preequilibrium, showing that adduct formation can be significant in PCET.[34] The additivity postulate eq. (12) further results in equal contribution of the individual self-exchange rates to the kinetic barrier in the MCR eq. (13). Variation of observed rates for radical reactions of similar driving force are usually attributed to polar effects, meaning charge transfer from the reactants to the transition state, as reflected by parameter α in the *Evans-Polanyi* equation eq. (8).[25] Since these polar effects depend on matching radical philicity, they are not represented by the individual self-exchange rates and are unaccounted for by *Marcus* theory.[35]

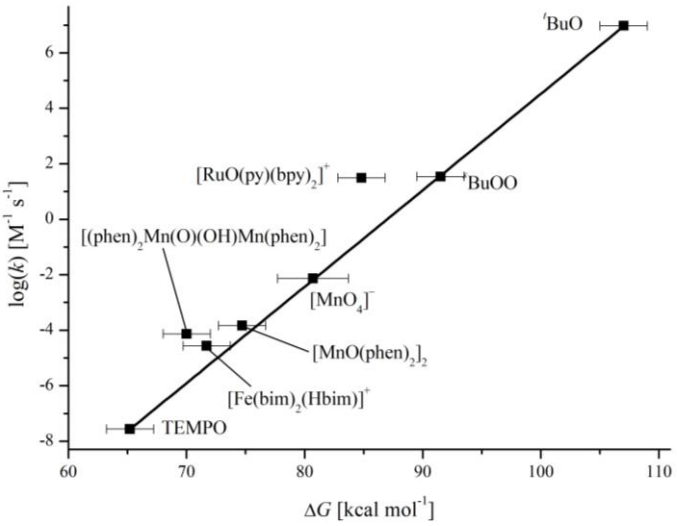

Figure 6: Plot of log(*k*) *vs*. Δ*G* for the oxidation of DHA by different organic and inorganic PCET reagents (assuming Δ*G*(ˢBuOO) = Δ*G*(ᵗBuOO); reported rate constants are statistically corrected for the number of identical donor and acceptor sites). The linear fit is based on the experimental data on DHA oxidation by ᵗBuO, ˢBuOO and TEMPO.[4,18,19,36–40]

Comparison of the MCR eq. (13) to the LFERs presented in Chapter 1.1.2 shows, that λ is related to the kinetic *Evans-Polanyi* parameter α, which is used to categorize reactants. Accordingly, log(*k*) *vs*. Δ*G* plots for CPET reactions give LFERs which can be classified by the self-exchange rates k_A of the reactants. Notably, in LFER plots over a large range of driving force a curvature is observed which is also present in the quadratic dependence of log(*k*) on Δ*G* in eq. (11).[7]

As starting point for ongoing research on PCET by coordination compounds, *Mayer* investigated the hydrocarbon oxidation by metal oxo complexes.[37] An extensive study featuring multiple complexes shows, that similar to organic oxyl radicals, metal oxo complexes show fast HAT self-exchange.[41] As consequence, organic and transition metal oxide complexes roughly share the same LFER in hydrocarbon oxidation (Figure 6).

The impact of the self-exchange rate on the rate constant of a CPET reaction can be seen in the oxidation of phenol and toluene by *tert*-butylperoxyl. While the difference in driving force $\Delta\Delta G$ = 1.9 kcal·mol[1] contributes to a change in the reaction rate by one order of magnitude according to eq. (13), the actually observed difference in rate is five orders of magnitude.[42] Considering the quadratic correlation between self-exchange and cross reaction rate given by the MCR, the slow HAT self-exchange of toluene compared to phenol agrees reasonably well with the experiment (Scheme 1). Based on organic HAT reactivity certain compound classes can be considered slow (hydrocarbons) or fast (amines, alcohols) HAT reagents which is reflected by slow or fast self-exchange, respectively.[43] As discussed, research by *Mayer* suggests a

conceptual similar behavior of organic molecules and transition metal complexes with respect to self-exchange rates.

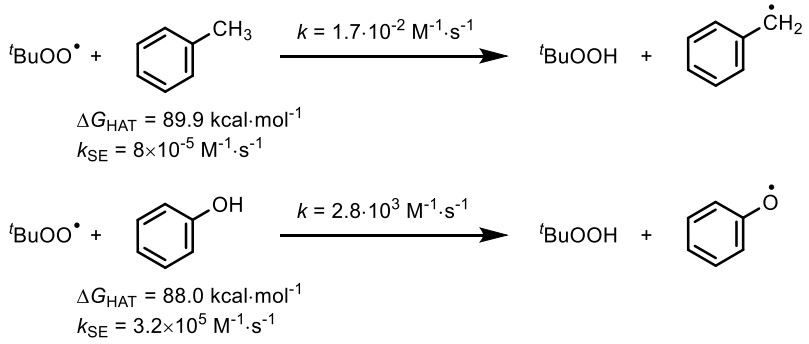

Scheme 1: Thermodynamic and kinetic data on oxidation of toluene and phenol by *tert*-butyl peroxyl.[42,43]

In contrast to previously discussed LFERs, application of *Marcus theory* to PCET reactivity provides an accurate prediction of cross-reaction rates based on self-exchange rates. Turning back to the example discussed in Chapter 1.1.2, CPET is considered favored over stepwise ET/PT or PT/ET based on ground state thermodynamics and transition-state theory. Since initial ET or PT is uphill compared to the experimentally determined barrier $\Delta G^{\ddagger}$ by simple ground state energy consideration, these stepwise reactions can be excluded. Accordingly, in case of a reaction which is characterized by $\Delta G^{\ddagger} > \Delta G_{ET}$ or $\Delta G^{\ddagger} > \Delta G_{PT}$, mechanistic assignment is not possibly. The MCR now allows for prediction of the individual ET, PT and CPET rates based on driving force and self-exchange rates. Comparison with the experimentally derived value then gives mechanistic insight. *Mayer* examined the accuracy of the MCR in predicting CPET rates by comparison with the experimentally measured rates.[44] Over a range of ca. 10^{18} in equilibrium constant and ca. 10^{9} in self-exchange rate constants, reproduction of the experimental value within two orders of magnitude is achieved by the MCR. Focusing on organic PCET reagents, additional correction by the *Ingold* kinetic solvent effect model and application of the *Abraham* model for hydrogen bonding further improves the accuracy of the MCR.[43,45,46]

1.1.5. Bond Activation by PCET in Transition Metal Complexes

One key accomplishment of investigation of PCET reactivity of metal complexes is that bond homolysis is driven by thermodynamic data rather than radical character. While organic HAT in most cases involves no change in overall spin, hydrocarbon oxidation by closed-shell $[MnO_4]^-$ or CrO_2Cl_2 means conversion of two diamagnetic reactants to paramagnetic products and can be rationalized simply by consideration of the driving force.[19] Molecular metal oxo complexes represent a popular class of transition metal based PCET reagents given their oxidizing nature. Initial investigation of the redox properties of $[RuO(bpy)_2(py)]^{2+}$

(bpy: 2,2'-bipyridine) was performed by *Meyer*.[47,48] This complex is among the best examined transition metal based PCET reagents and effectively oxidizes hydrocarbon based substrates.[36,49]

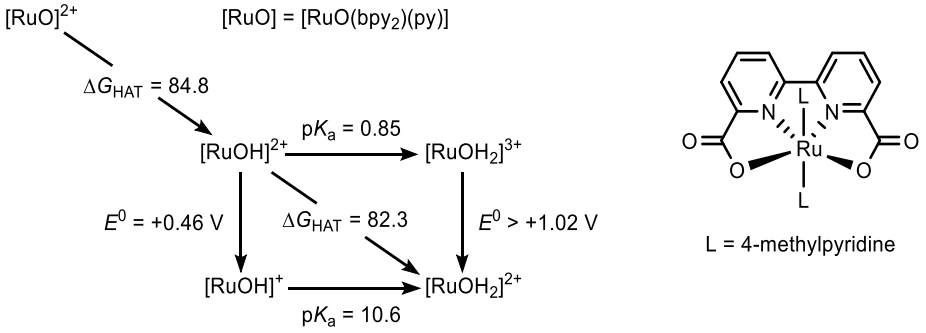

Scheme 2: Thermodynamic data for reduction of $[RuO(bpy)_2(py)]$ in aqueous solution and highly active water oxidation precatalyst [Ru(2,2'-bypridine-6,6'-dicarboxylate)(4-methylpyridine)$_2$].[4,50]

Oxidation of benzylic C-H bonds by the Ru^{IV} oxo can be understood based on thermodynamic data which suggest the formation of O-H bonds of comparable bond strength (Scheme 2). Comparison of the O-H bonds of the ruthenium coordinated hydroxo/aqua moiety to the BDFE of water ($\Delta G_{HAT}(H_2O)^{aq}$ = 122.7 kcal·mol^{-1}) and the hydroxyl radical ($\Delta G_{HAT}(HO)^{aq}$ = 106.9 kcal·mol^{-1}) shows a strong effect of metal coordination.[4] Making use of this finding, ruthenium polypyridyl complexes can be used as highly active catalysis in electrochemical water oxidation (Scheme 2).[50]

In light of the growing interest in ammonia synthesis by (photo-)electrochemical N_2 fixation, the effect of metal coordination on the thermodynamics of homo- and heterolytic ammonia bond activation is of great interest.[51] While metal oxo complexes are a class of well-examined transition metal based PCET reagents, *Chirik* reported on bond strength of a series of titanium and zirconium complexes bearing parent nitrogen based ligands.[52,53] The bond dissociation energies shown in Scheme 3 are obtained by computational analysis and supported by experiment. As for coordination of water to ruthenium complexes, the N-H bond of ammonia ($\Delta G_{HAT}(NH_3)^{gas}$ = 99.4 kcal·mol^{-1}) is weakened upon coordination to a metal center.[4,54]

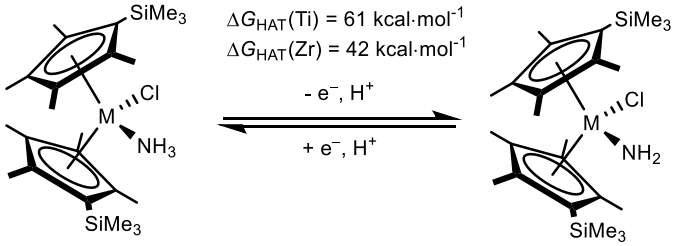

Scheme 3: Interconversion of titanium and zirconium coordinated amine and amido ligands by PCET.[52]

As shown in Figure 6, hydrocarbon oxidation by metal oxos and organic oxyl radicals share the same LFER for $\Delta G^{\ddagger}$ *vs.* ΔG. Accordingly, fast self-exchange rates ($k \approx 10^4$ M^{-1}s^{-1}) are observed in metal oxo/hydroxo

complexes.[41,43] Turning to nitrogen based monodentate ligands, bond strength are determined for several systems, including reports by *Peters* and *Schneider*.[52,55] Self-exchange measurement in contrast is limited to one report on an osmium anilido complexes by *Mayer*.[56] In [Os(NHPh)Cl_2Tp]/[Os(NH_2Ph)Cl_2Tp] (Tp = tris(pyrazolyl)borate) the PCET self-exchange rate $k = 3 \cdot 10^{-3}$ $M^{-1}s^{-1}$ is remarkably low, while proton and electron transfer shows much faster self-exchange. Similarly, surprisingly slow self-exchange ($k = 6.5 \cdot 10^{-3}$ $M^{-1}s^{-1}$) for PCET is observed in vanadium oxo [VO(^{t}Bu_2bpy)(py)]$^+$ (^{t}Bu_2bpy = (4,4'-di-*tert*-butyl-2,2'-bypridine). A low self-exchange rate for PCET suggests a high value for the reorganization term λ according to *Marcus* theory. Detailed analysis of [VO(^{t}Bu_2bpy)(py)]$^+$ attributes the observed slow self-exchange to major electronic rearrangement which gives rise to severe inner-sphere reorganization and is reflected by a significant change in the metal oxygen distance upon reduction.[41] In case of [Os(NHPh)Cl_2Tp], less inner-sphere reorganization is expected and the slow PCET self-exchange is rather attributed to formation of a precursor complex and nonadiabaticity of the reaction.[56]

The formation of strong O-H bonds enables hydrocarbon oxidation by metal oxo complexes. In several cases, oxygen atom transfer is reported as competing pathway, giving a mixture of products.[19,36,40,49,57] Group transfer can be prohibited by choosing a less reactive acceptor site for PCET. Upon $1e^-/1H^+$ reduction, imidazolin based [Fe(Hbim)(H_2bim)$_2$]$^{2+}$ undergoes metal centered electron transfer and protonation at a non-coordinating nitrogen atom. High selectivity in hydrocarbon oxidation is observed and the measured HAT self-exchange rate of $k = 9.7 \pm 1.0 \cdot 10^2$ $M^{-1}s^{-1}$ is orders of magnitude faster than what is observed for [Os(NHPh)Cl_2Tp].[20] Similarly, no oxygen atom transfer takes place in hydrocarbon oxidation by [Mn(facac)$_3$] (facac = hexafluoroacetylacetonate).[58]

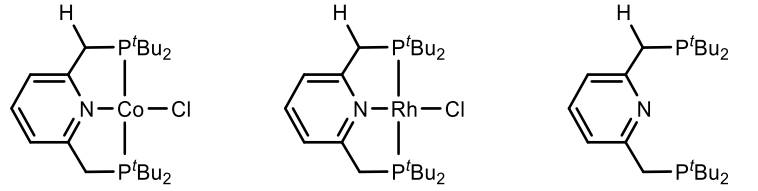

Scheme 4: Carbon centered PCET in a pyridyl diphosphine based pincer ligand and transition metal complexes.

Turning to carbon centered proton-coupled electron transfer on transition metal complexes, reports in the literature are rare. While research on organic HAT reagents shows slow PCET self-exchange rates, no such investigations of coordination compounds exists.[43] Bond strength are reported for a limited number of complexes, including a cobalt pincer complex reported by *Milstein* (Scheme 4).[59] According to computational analysis performed by *Chirik*, a low BDFE is present as reflected by stoichiometric reduction of diphenylacetylene by ligand chemical non-innocence (Scheme 4). Exchanging the coordinating metal to

rhodium greatly strengthens the C-H bond due to a anodically shifted Rh^{I}/Rh^{II} redox couple.[60] Notably, in both cases a weakening of the C-H bond strength results from metal coordination. Thermodynamic data on methylated metallocenes is available from *Peters* and *Astruc* and a niobium methoxide is reported by *Bruno*.[61–63] Recently, *Chirik* reported the conversion of a molybdenum ethylene to the ethyl complex by PCET (Scheme 5).[64] In most cases, weak C-H bond strength prohibit substrate oxidation and in general no kinetic data on the reactivity of these compounds is available.

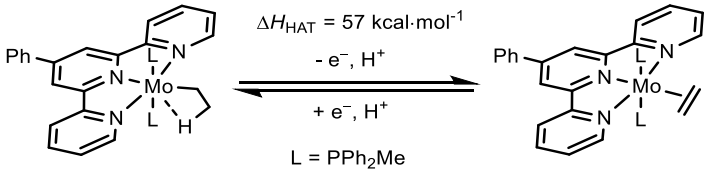

Scheme 5: Interconverison of molybdenum based ethylene and ethyl complexes by PCET.[2][64]

[2] The driving force of PCET in ref. [64] is given as ΔG, however it is calculated based on C_H^{THF} reported by *Morris*.[114] Accordingly, the driving force is reported herein as ΔH.

1.2 Outline

The influence of metal coordination on carbon-centered proton-coupled electron transfer processes is an undeveloped field of research. Reported literature is limited to thermodynamic investigations and substrate oxidation using C-H bond formation at metal complexes is not reported. Comparison of organic HAT processes with related processes in coordination compounds suggests similar linear free energy relationships for N-H and O-H bond dissociation/formation. Kinetic analysis of a carbon-centered process in a transition metal complex will allow for evaluation of the influence of metal coordination on carbon-centered PCET processes and therefore make a valuable contribution to understanding the generality of application of the *Marcus* theory on PCET processes.

Chirik and *Milstein* have investigated hydrogen atom abstraction from group 9 pyridyl diphosphine complexes.[59,60] Compared to the free ligand, metal coordination results in lowering of the reactive C-H bond. As a result of a metal centered redox process, the M^{II}/M^{I} redox potential is highly sensitive to the electronic situation of the complex which affects the C-H bond dissociation free energy. *Schneider* recently presented stabilization of square-planar Co^{III} by a related pincer ligand $^{tBu}P{=}N{=}P$ ($^{tBu}P{=}N{=}P$ = $N(CHCHP^tBu_2)_2$) including carbon-centered protonation on the Co^{II} oxidation state.[65] Introducing unsaturated vinylene moieties in the pincer backbone is crucial to provide sufficient stability of the Co^{III} complex, as proton coupled disproportionation is observed in case of saturated linkers, indicating the potential of such complexes in oxidative C-H bond activation by PCET.

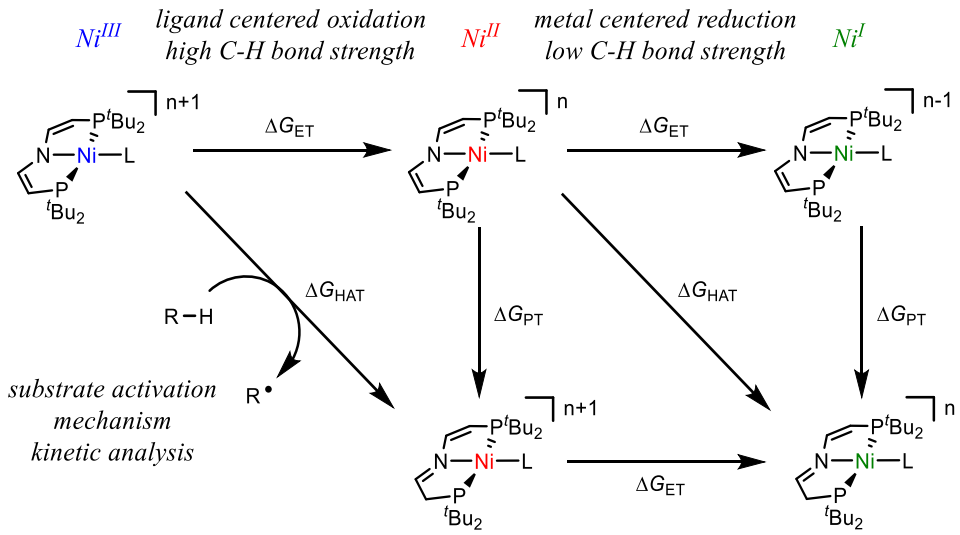

Scheme 6: Proton-coupled electron transfer on vinylene-based amido diphosphine ligated nickel complexes involving the Ni^{II}/Ni^{I} and Ni^{III}/Ni^{II} redox couple.

Based on the amido diphosphine ligand reported by *Schneider*, synthesis of a square-planar Ni^{II} complex is targeted and the oxidation and protonation of this compound is to be investigated. In case of sufficient stability of the square-planar Ni^{III} complex, analysis of the electronic structure is of interest regarding a ligand centered oxidation process. *Mindiola* showed ligand-centered oxidation of a related amido diphosphine ligated Ni^{II} complex.[66] Measurement of the free energies of proton and electron transfer for the Ni^{III}/Ni^{II} redox couple is planned by experimental determination of the acidity and redox potential. The free energy of carbon-centered proton-coupled electron transfer will be determined using a thermodynamic square scheme. If the bond dissociation free energy allows for activation of substrates, the reactivity of the oxidized compound is to be investigated. Kinetic analysis of proton-coupled electron transfer reactions is desirable to compare the experimental results to the values predicted by *Marcus* cross relation based on ground state thermodynamics and self-exchange rates. While low C-H bond strength is reported in metal pincer complexes involving the M^{II}/M^{I} oxidation states, a comparison of C-H bond strength involving two adjacent redox couples is not present in the literature. The thermodynamic square scheme based on the Ni^{III}/Ni^{II} redox couple is therefore planned to be extended to the Ni^{I} oxidation state. While the Ni^{III}/Ni^{II} redox couple is supposed to be mainly ligand based, the Ni^{II}/Ni^{I} most likely involved population of the $d_{x^2-y^2}$ orbital and accordingly is expected to be metal centered. To investigate the influence of electronic changes on C-H bond strength involving both redox couples, variation of the coordination sphere of the Ni complexes is of interest.

1.3 Activation of Benzylic C-H Bonds by Pincer Ligand Centered Chemical Non-Innocence

1.3.1. Synthesis, Protonation and Oxidation of [NiBr(^{tBu}P=N=P)] (3)

The synthesis of [NiBr(^{tBu}PN^{H}P)]Br (**1^{Br}**) (^{tBu}PN^{H}P = NH(CH$_2$CH$_2$P^{t}Bu$_2$)$_2$) was carried out following the procedure reported by *Lagaditis et al.* on preparation of [CoCl(^{tBu}PN^{H}P)].[65] Coordination of ^{tBu}PN^{H}P to a nickel precursor is achieved by stirring in THF (Scheme 7). [NiBr$_2$(dme)] (dme = 1,2-dimethoxyethane) shows faster complexation than NiCl$_2$ due to low solubility of NiCl$_2$ in THF. The resulting complex **1^{Br}** precipitates from solution as bright red powder. Compound **1^{Br}** was characterized by NMR spectroscopy and the NH proton resonates at δ = 6.95 ppm in the ^{1}H NMR spectrum in CD$_2$Cl$_2$. In agreement with protonation of the pincer amine **1^{Br}** features C_S symmetry on NMR timescale. No further characterization of **1^{Br}** was performed, but low solubility in THF suggests square-planar coordination of a cationic complex and an bromide anion as reported by *Arnold* for the *iso*-propyl substituted derivate.[67]

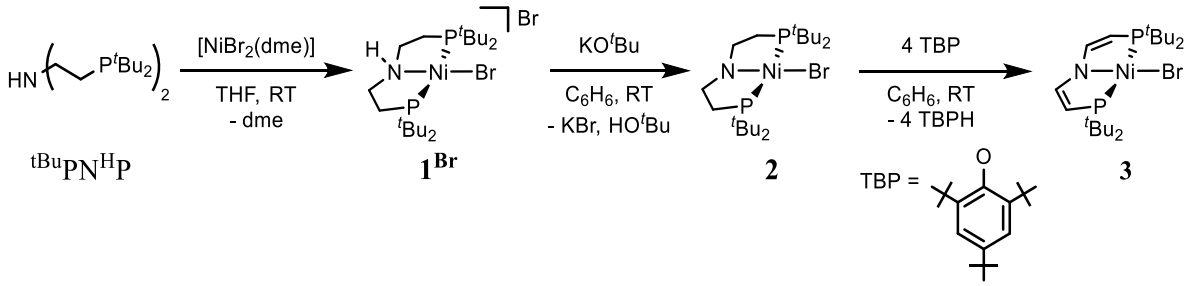

Scheme 7: Synthesis of nickel pincer bromide complexes.

Purification of **1^{Br}** can be achieved by evaporation of the solvent and washing with *n*-pentane to remove excess ^{tBu}PN^{H}P. Deprotonation of **1^{Br}** with KO^{t}Bu in benzene results in selective formation of amido [NiBr(^{tBu}PNP)] (**2**) (^{tBu}PNP = N(CH$_2$CH$_2$P^{t}Bu$_2$)$_2$). Complex **2** shows C_{2v} symmetry on NMR timescale. Reactions producing up to 570 mg of **2** can be carried out starting from ^{tBu}PN^{H}P and [NiBr$_2$(dme)] in 83% isolated yield. The reaction of **2** with 4.5 equivalents 2,4,6-tri-*tert*-butylphenoxyl (TBP) affords clean formation of [NiBr(^{tBu}P=N=P)] (**3**) accompanied by the formation of tris(2,4,6-*tert*-butyl)phenol. Separation of this byproduct by sublimation gives **3** in excellent yields of up to 94% on a 280 mg scale. Depending on the purity of starting materials, **2** and TBP, **3** may have to be recrystallized from *n*-pentane to obtain high purity product, resulting in lower yields of around 85%.

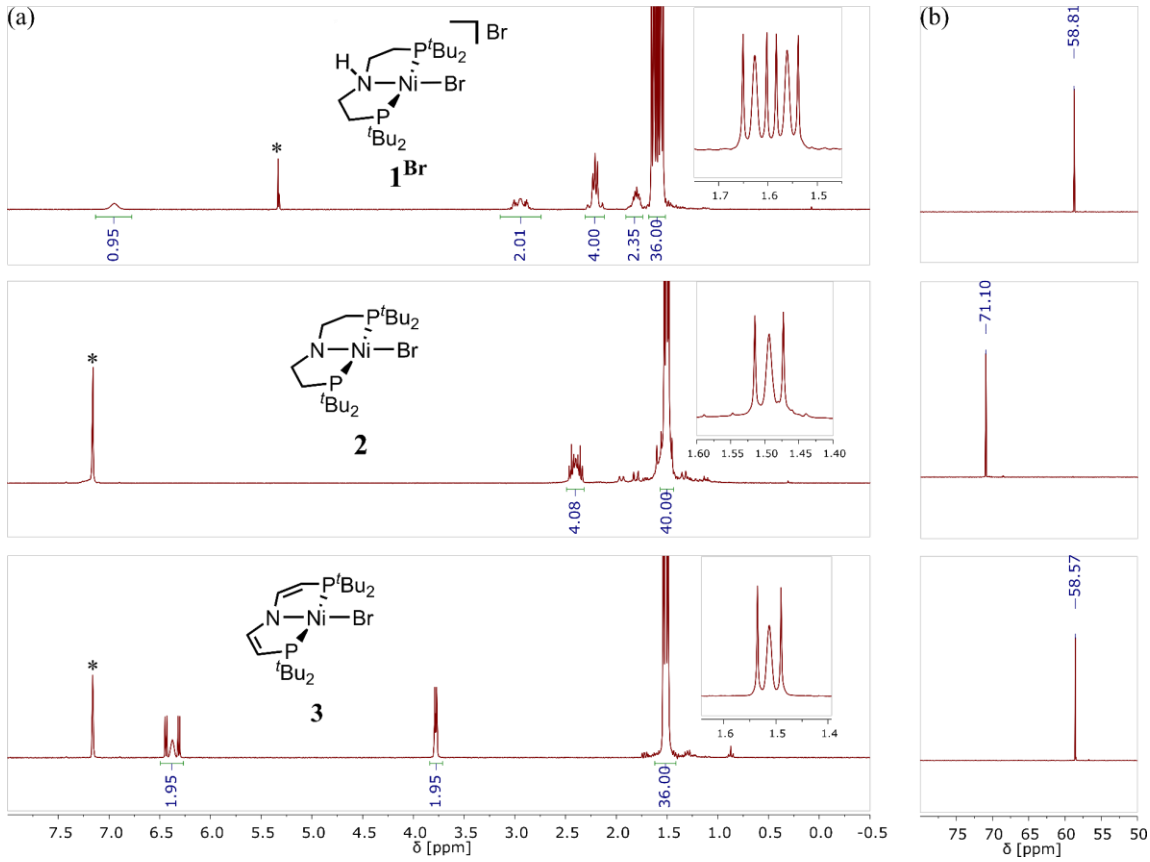

Figure 7: (a) ^{1}H NMR and (b) ^{31}P{^{1}H} NMR spectra of compound **1^{Br}** in CD_2Cl_2, **2** and **3** in C_6D_6 (*denotes the solvent signal).

By comparison of the ^{1}H NMR spectra of **1^{Br}**, **2** and **3** a significant downfield shift of the ligand's backbone hydrogen resonances can be observed upon oxidation (Figure 7). While the CH_2 groups of **1^{Br}** and **2** show multiplet resonances in the chemical shift range δ = 1.4–3.1 ppm, the phosphorus substituted CH proton in **3** resonates at δ = 3.78 ppm and the N-substituted CH group is observable at δ = 6.37 ppm. Peak separation of well above $\Delta\delta$ = 2 ppm is regularly observed for the α- and β-vinyl protons of vinylamines.[68]

Given the importance of the basicity of amido based ligands in cooperative substrate activation and catalytic processes, the basicity of compound **3** is of interest. Due to conjugation of the nitrogen with the unsaturated hydrocarbon ligand backbone, **3** undergoes protonation at the β-vinylene carbon upon reaction with strong acids giving enimine [NiBr(^{tBu}P=N=P^{H})]X (**4^{X}**) (^{tBu}P=N=P^{H} = N(CHCHP*t*Bu$_2$)(CHCH$_2$P*t*Bu$_2$)).[65,69] Isolation of the tetrafluoroborate salt **4^{BF4}** can be performed by reacting **3** with tetrafluoroboric acid etherate in diethyl ether, which results in precipitation of **4^{BF4}** as red powder. As a consequence of the molecules C_s symmetry, the ^{1}H NMR spectrum of the protonated species **4^{BF4}** shows two sets of ^{t}Bu resonances and the ^{31}P{^{1}H} NMR spectrum shows two phosphorus resonances (Figure 8). Since both phosphorus atoms are in comparable chemical environments, their resonances are observed at similar chemical shifts (δ = 65.2, 62.0 ppm). This gives rise to a strong roofing effect which can be observed in the doublet coupling pattern

($^2J_{PP}$ = 294.6 Hz). In agreement, four resonances for the aliphatic pincer backbone are observed in the ^{1}H NMR spectrum. The imine hydrogen is easily identified by its low field shift at δ = 8.48 ppm, and the CH_2 group resonates at δ = 3.25 ppm with twofold intensity. As in parent **3**, the nitrogen substituted CH position of the C-C double bond resonates at lower field. ^{1}H,^{1}H COSY NMR spectroscopic characterization confirms the structural assignment, showing appropriate $^3J_{HH}$ couplings for the pincer backbone (Figure 8).

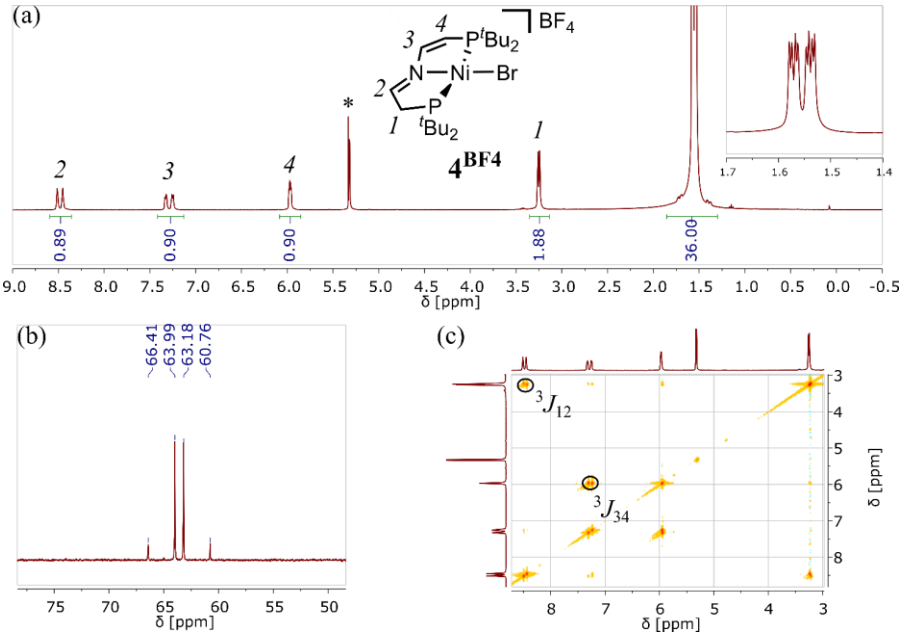

Figure 8: (a) ^{1}H NMR, (b) ^{31}P{^{1}H} NMR and (c) ^{1}H,^{1}H COSY NMR spectrum of compound **4**^{BF4} in CD_2Cl_2 (*denotes CD_2Cl_2).

Chemical oxidation of **3** with silver hexafluorophosphate in chlorobenzene gives clean formation of [NiBr(^{tBu}P=N=P)]PF_6 (**5**^{PF6}) which can be precipitated from solution by addition of *n*-pentane (Scheme 8). Complex **5**^{PF6} features a magnetic moment of μ = 1.9 μ_B, determined by *Evans*' method in CD_2Cl_2 at room temperature, indicative of a S = ½ ground state and therefore a low-spin d^7 configuration.[70]

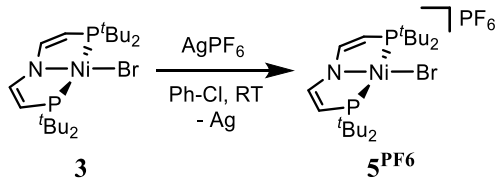

Scheme 8: Oxidation of parent bromide **3** to formal Ni^{III} **5**^{PF6}.

The solid state structure of compounds **2**, **3**, **4**^{OTf} and **5**^{PF6} was investigated by X-ray diffraction as shown in Figure 9, with **5**^{PF6} crystallizing as solvent adduct **5**^{PF6}·$(C_6H_5Cl)_{0.5}$. Selected crystallographic parameters are listed in Tables 1 and 2 and will be briefly discussed in the following. All four complexes clearly show square-planar coordination of the central nickel as is reflected by the low τ_4 values.[71] The Ni-N distance

increases in the order **2**, **3** and **4**$^{\mathbf{OTf}}$ as a result of lower donor strength of the N-donor in the pincer ligand. Accordingly, the Ni-Br bond length shortens in the opposite order due to a weaker *trans* donor ligand. Comparison of formal Ni^{III} **5**$^{\mathbf{PF6}}$ shows similar bond metrics at the nickel center as in parent Ni^{II} bromide **3**.

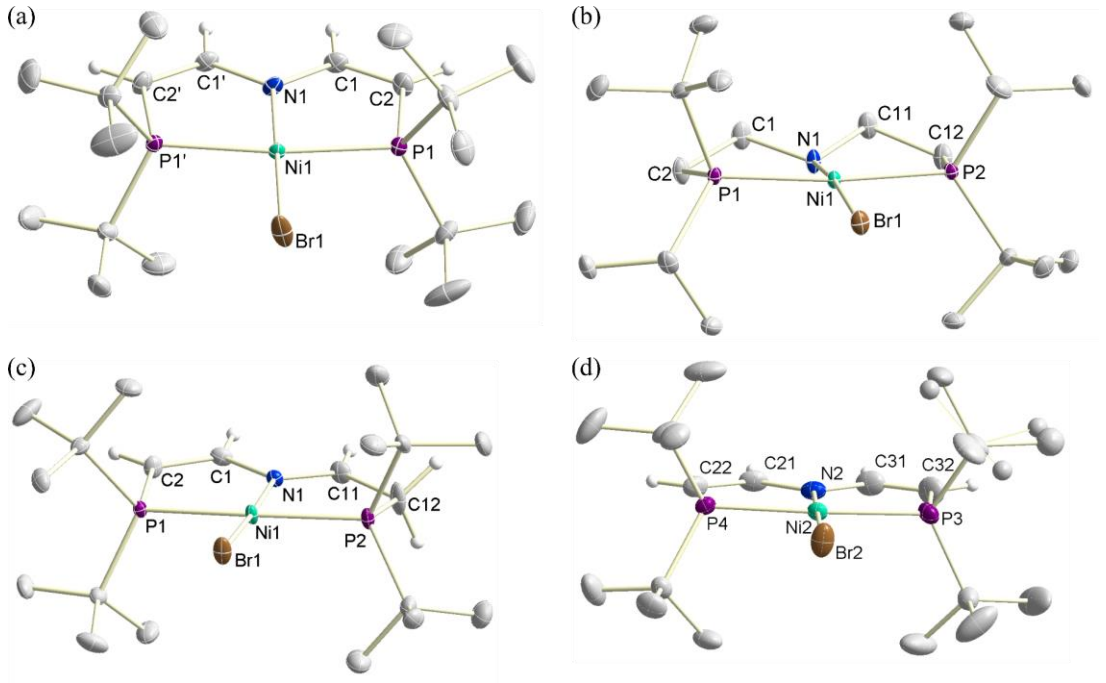

Figure 9: Solid state structures of (a) **2**, (b) **3**, (c) **4**$^{\mathbf{OTf}}$ and (d) **5**$^{\mathbf{PF6}}$ determined by X-ray diffraction. Thermal ellipsoids are drawn at the 50% probability level. Anions, solvent molecules, additional complex molecules of the asymmetric unit and selected hydrogen atoms are omitted for clarity. Minor occupation of disordered atoms is shown as spheres.

Table 1: Crystallographic parameters of the solid state structure of **2**, **3**, **4**$^{\mathbf{OTf}}$ and **5**$^{\mathbf{PF6}}$ determined by X-ray diffraction.

[Ni]	τ_4	*d*(Ni-Br) [Å]	*d*(Ni-N) [Å]	*d*(Ni-P) [Å]
2	0.12	2.3513(3)	1.8747(17)	2.2050(6)
				2.2139(6)
3	0.06	2.3094(3)	1.8814(15)	2.2368(4)
4$^{\mathbf{OTf}}$	0.08	2.2985(3)	1.9034(16)	2.2216(5)
				2.2295(6)
5$^{\mathbf{PF6}}$, [a]	0.06/	2.3031(4)/	1.878(2)/	2.2429(7)
				2.2408(7)/
	0.06	2.2922(4)	1.872(2)	2.2339(7)
				2.2366(7)

[a]The asymmetric unit contains two molecules.

Net dehydrogenation of the pincer backbone is clearly reflected by the C-C bond length, which shortens from *d*(C1-C2) = 1.523(3) Å in **2** to *d*(C1-C2) = 1.349(2) Å in **3**. Additionally, planarization of the amido coordination sphere results from conjugation with the vinylene backbone as is reflected by the sum of bond angles at the nitrogen atom $\sum(\alpha(N))$ and the torsion angle φ(N-C-C-P). In contrast, neither protonation nor oxidation has significant influence on the C=C double bond length or coordination geometry of the N donor. However, the position of the methylene group in $\mathbf{4^{OTf}}$ can be identified by a shortened C-N bond, an elongated C-C bond (*d*(N1-C11) =1.322(3) Å and *d*(C1-C2) = 1.434(3) Å) and comparison of the dihedral angles of the ligand backbone (φ(N1-C1-C2-P1) = 0.6(3)° *vs*. φ(N1-C11-C22-P2) = -13.4(4)°). Again, small deviation of bond parameters can be noticed upon comparison of **3** and $\mathbf{5^{PF6}}$.

Table 2: Crystallographic parameters of the solid state structure of **2**, **3**, $\mathbf{4^{OTf}}$ and $\mathbf{5^{PF6}}$ determined by X-ray diffraction.

[Ni]	*d*(C=C) [Å]	*d*(C-N) [Å]	*d*(C-C) [Å]	*d*(C=N) [Å]	$\sum(\alpha(N))$ [°]	φ(N-C-C-P) [°]
2	-	1.459(3)/	1.523(3)/	-	348.76	38.8(2)/
		1.460(3)	1.515(3)			-40.3(2)
3	1.349(2)	1.3718(16)	-	-	360.00	1.06(18)
$\mathbf{4^{OTf}}$	1.352(3)	1.395(2)	1.434(3)	1.322(3)	359.99	0.6(3)
						-13.4(4)
$\mathbf{5^{PF6}}$, [a]	1.354(4)	1.366(3)	-	-	360.00/	2.3(3)
	1.361(4)/	1.370(3)/				-4.1(4)/
	1.352(4)	1.369(4)			360.02	0.9(3)
	1.352(4)	1.372(3)				2.1(4)

[a]The asymmetric unit contains two molecules.

1.3.2. Electronic Structure of [NiBr(^{tBu}P=N=P)]PF_6 ($\mathbf{5^{PF6}}$)

Solid state metrics of **3** and $\mathbf{5^{PF6}}$ deviate insignificantly with respect to metal coordination and pincer ligand bond length, suggesting ligand centered oxidation from **3** to $\mathbf{5}^{PF6}$ and therefore motivate closer investigation of the electronic structure of $\mathbf{5^{PF6}}$. Computational analysis of $\mathbf{5}^{+}$ supports the assignment of $\mathbf{5^{PF6}}$ as Ni^{II} with an oxidized pincer ligand.[3] The MO scheme shown in Figure 10 results from structure optimization and single point calculation on D3BJ-PBE0/def2-TZVP level. For the sake of simplification, orbitals which are close in energy and spin density distribution for the α and β space are shown as doubly occupied orbitals. The individual orbitals of the α and β space are shown for orbitals which strongly differ in energy between α and β. As a result of exchange in the α space, the orbital which contributes mostly to the spin density plot shown in Figure 10b is located below the HOMO. In the restricted open shell picture this SOMO is the

[3] Computational analysis was performed by Dr. Markus Finger.

highest occupied orbital. Square-planar coordination in $\mathbf{5}^{+}$ gives rise to a high lying antibonding $d_{x^2-y^2}$ orbital. While the d_{z^2}, d_{xz} and d_{yz} are stabilized due to lack of coordination on the *z* axis, d_{xz} shows antibonding π interaction with the N- and Br-centered *p*-type orbitals (Figure 10a). The spin in $\mathbf{5}^{+}$ is mainly centered on the divinylamido moiety, confirming the assignment as closed-shell Ni^{II} coordinated by a divinylaminyl radical, as can be seen from the spin density distribution (Figure 10b). The contribution to the spin density by atom is Ni: 19.3%; C1: 79.4%; C2: -36.4%; N: 38.0%.

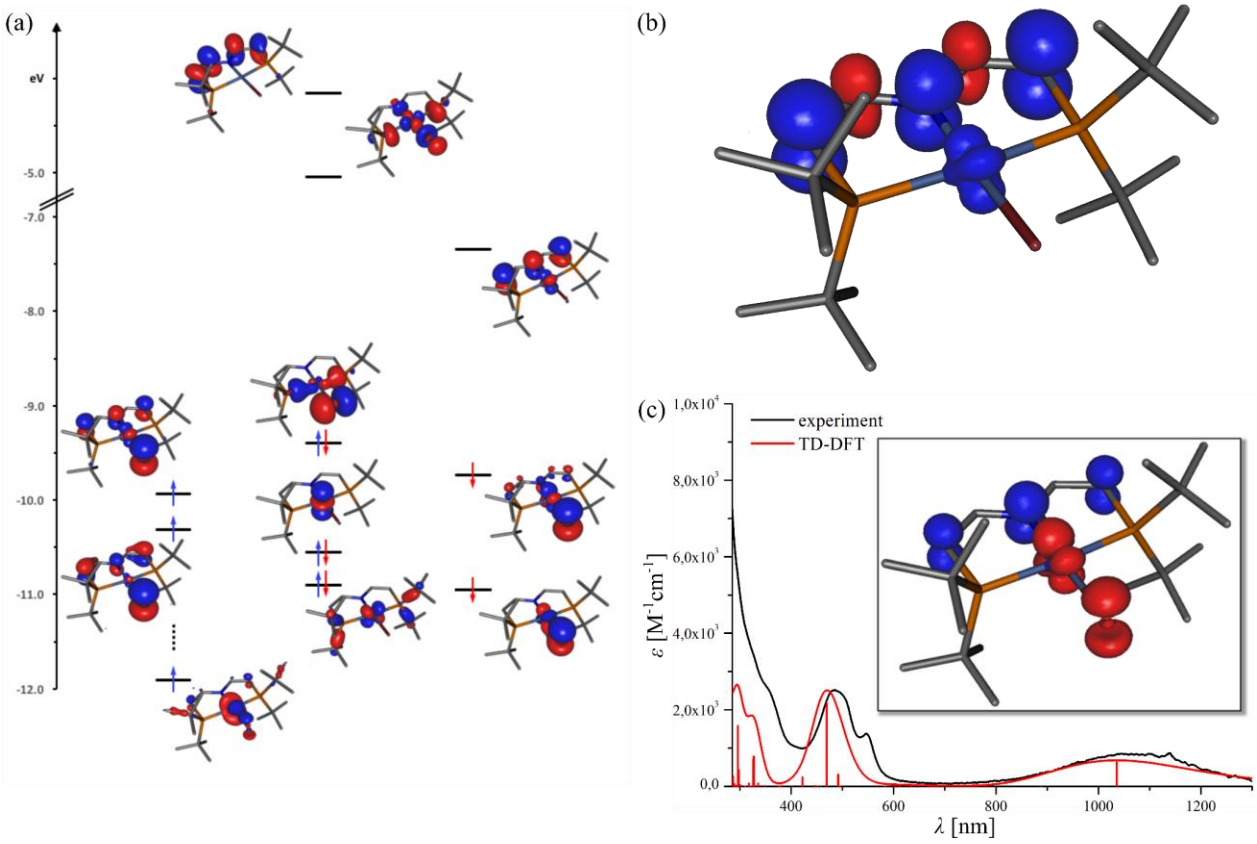

Figure 10: Computational analysis of $\mathbf{5}^{+}$ by DFT calculations: (a) MO scheme (blue: α spin, red: β spin) and (b) spin density plot of $\mathbf{5}^{+}$(blue color denotes positive and red color negative spin density); (c) experimental and computed UV-vis spectra of $\mathbf{5}^{+}$/$\mathbf{5}^{\mathbf{PF6}}$ with the calculated difference density of the transition at λ = 1036 nm shown in the insert (red color denotes decrease and blue color increase of electron density).

In agreement with the S = ½ ground state determined by Evan's method, $\mathbf{5}^{\mathbf{PF6}}$ can be characterized by EPR spectroscopy in frozen DCM solution (Figure 11).[4] The derived *g* value for the isotropic signal g_{iso} = 2.0441 is indicative of an organic radical. Significant broadening of the signal is attributed to the influence of the nickel center and prevents resolution of hyperfine coupling. Theory predicts a rhombic EPR resonance for

[4] EPR analysis was performed by Dr. A. Claudia Stueckl.

$\mathbf{5}^{+}$ on ZORA-D3(BJ)-RIJCOSX-DFT/def2-TZVPP level independent of the functional (B3LYP/PBE0). The isotropic g value as average of g_1, g_2 and g_3 lies close to the experiment in all cases (Table 3).

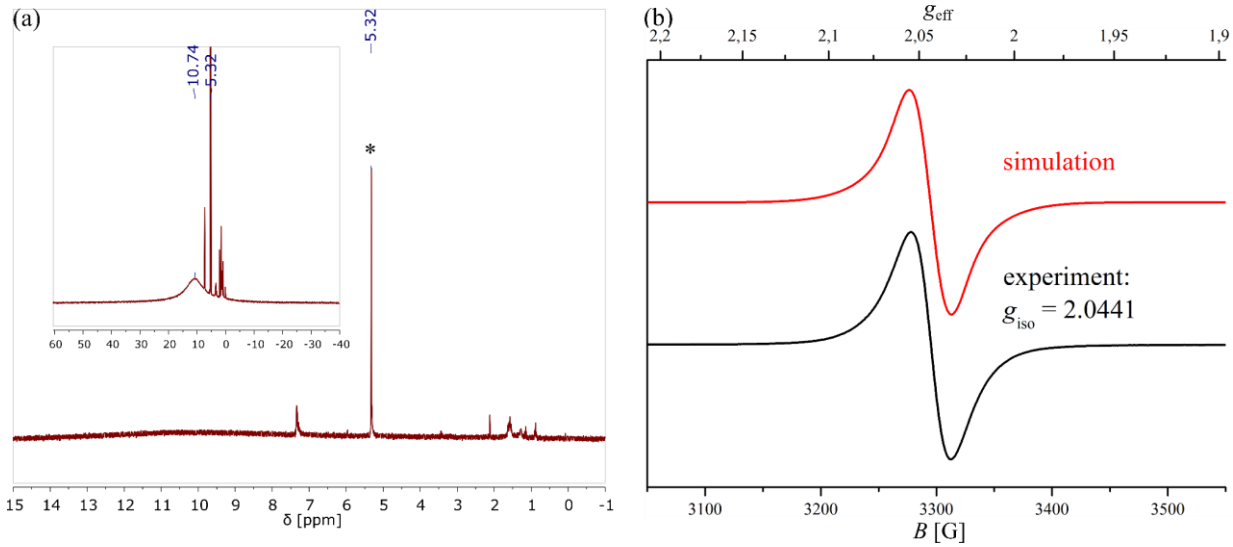

Figure 11: (a) ^{1}H NMR spectrum of $\mathbf{5}^{\mathbf{PF6}}$ in CD_2Cl_2 (*denotes the solvent signal) and (b) X-band EPR spectrum of $\mathbf{5}^{\mathbf{PF6}}$ in frozen DCM solution (T = 147 K, ν = 9.426710 GHz)

Table 3: g values obtained by DFT computation on $\mathbf{5}^{+}$ and EPR analysis of $\mathbf{5}^{\mathbf{PF6}}$.

	g_1	g_2	g_3	g_{iso}
B3LYP	2.035	2.064	2.133	2.077
PBE0	2.026	2.050	2.105	2.060
experiment	-	-	-	2.0441

Mindiola and *Meyer* report an isotropic EPR resonance for [NiCl{N(2-C_6H_3-5-CH_3-P*i*Pr_2)$_2$}]OTf in DCM solution at room temperature with g_{iso} = 2.0023, resembling the system reported here.[66] Hyperfine coupling to the nitrogen, two hydrogen atoms of the aromatic system as well as two phosphorus atoms is reported, which might be a result of a more narrow signal (ca. 70 G *vs.* 180 G). While *Heyduk* observes an isotropic resonance at room temperature for a THF solution of [NiPCy$_3$(SNS)] (SNS = bis(2-mercapto-4-methylphenylamine)), upon cooling to T = 10 K a rhombic signal (g_x = 1.99, g_y = 2.01, g_z = 2.03) is obtained.[72] EPR analysis of [NiX(NNN)] (NNN = *N*,*N*'-(2,6-dimethylphenyl)-2,6-pyridinedicarboxamidate; X = ONO_2, OAc, OCO_2H, Cl) by *McDonald* in frozen acetone solution at T = 77 K gives an axial (X = Cl) or rhombic (X = ONO_2, OAc, OCO_2H) resonance.[73,74]

Ray and *Neese* reported electronic structure analysis of metal *o*-dithiolene complexes, showing that $[Ni(S_2(o\text{-}C_6H_4))_2]^{1-}$ is best described as a Ni^{II} metal ion with one dianionic benzene dithiolato $(S_2(o\text{-}C_6H_4))^{2-}$ and one monoanionic dithiobenzosemiquinonato $(S_2(o\text{-}C_6H_4))^{-}$ ligand.[75] The redox non-innocent behavior

of the ligand gives rise to a high intensity ($\varepsilon \approx 1 \cdot 10^4$ $M^{-1}cm^{-1}$) absorption in the near infrared energy region which is best described as ligand-to-ligand charge transfer (LLCT) which the authors state as *'spectroscopic marker for the presence of ligand based radicals.'*.[75] *Mindiola* reports absorption at λ = 872 nm ($\varepsilon = 1.4 \cdot 10^3$ $M^{-1}cm^{-1}$) for [NiCl{N(2-C_6H_3-5-CH_3-P*i*Pr_2)$_2$}]OTf, showing much weaker oscillator strength. Electronic structure analysis by X-ray absorption spectroscopy and DFT computation nevertheless confirms the ligand centered redox process.[66]

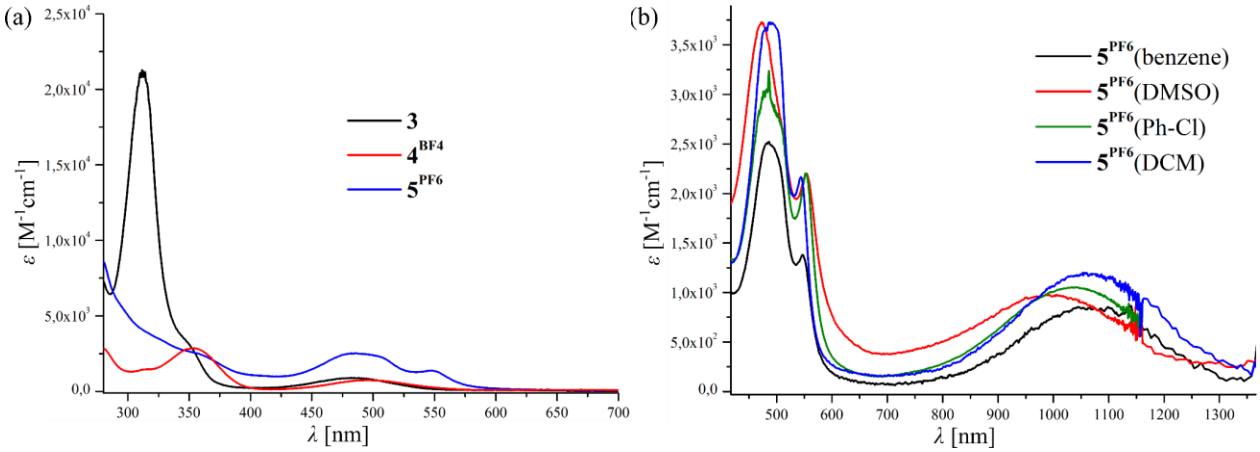

Figure 12: (a) UV-vis spectra of **3**, $\mathbf{4^{OTf}}$ and $\mathbf{5^{PF6}}$ in benzene. (b) Vis-NIR spectra of $\mathbf{5^{PF6}}$ in different solvents.

The UV-vis spectra of **3**, $\mathbf{4^{OTf}}$ and $\mathbf{5^{PF6}}$ in benzene are shown in Figure 12. Transitions centered at approximately λ = 500 nm are present in all compounds, giving rise to the intense red or orange color of the isolated compounds. While for **3** no transition can be observed at lower energy, $\mathbf{5^{PF6}}$ features an absorption at $\lambda \approx 1050$ cm^{-1} of comparable intensity as in *Mindiola's* system (Figure 12b). Since CT transitions result in a change in the dipole moment of the excited state with respect to the ground state, a solvatochromic shift of the absorption maximum is commonly observed in such transitions. To probe for solvent effects on the NIR transition in $\mathbf{5^{PF6}}$, UV-vis spectra were recorded in solvents of different polarity as shown in Table 4. A clear shift to higher energy is observed upon increasing the solvent polarity, confirming the assignment of the relevant transition as CT-type.

Table 4: Absorption maximum of the NIR transition of $\mathbf{5^{PF6}}$ in different solvents.

solvent	dipole moment [D]	λ_{max} [cm^{-1}]
benzene	0	1070
chlorobenzene	1.54	1035
dichloromethane	1.6	1057
dimethylsulfoxide	3.9	990

Time-dependent density functional theory (TD-DFT) computation on ZORA-D3(BJ)-RIJCOSX-DFT/def2-TZVPP(COSMO) nicely reproduce the experimental spectrum as shown in Figure 10c, giving a similar solvatochromic shift of $\Delta\lambda$ = -81 nm upon comparison of results with benzene and DMSO solvent approximation. Theory predicts the NIR feature mainly as population of the SOMO due to electron transfer from a MO representing an antibonding Ni(d_{xz})-Br(p_z) interaction. Therefore, DFT confirms the inter-ligand CT character of this transition with additional contribution of a MLCT type transition.

Maroney and coworkers have investigated the influence of oxidation state, coordination number and geometry on Ni K-edge X-ray absorption spectroscopy near-edge structure (XANES) of a variety of Nickel complexes.[76] By comparison of multiple isoleptic Ni^{III}/Ni^{II} pairs, they could show that upon ligand centered oxidation little influence in the spectra can be observed, while metal based oxidation has a much greater effect. Ni K-edge XANES and extended X-ray absorption fine structure (EXAFS) of solid **3**, $\mathbf{4^{BF4}}$ and $\mathbf{5^{PF6}}$ was measured (Figure 13).[5]

XANES of **3**, $\mathbf{4^{BF4}}$ and $\mathbf{5^{PF6}}$ gives nearly identical spectra, confirming the assignment of Ni^{II} oxidation state for $\mathbf{5^{PF6}}$ previously based on X-ray diffraction, EPR spectroscopy and DFT calculations (Figure 13). Square-planar coordination in all compounds is confirmed by a negligible 1*s* → 3*d* and a distinct 1s → 4p_z transition at E = 8336 eV prior to the E_0 threshold due to the spectroscopically allowed 1*s*→4*p* transition. The determined edge energies E_{edge} < 8341 eV are shifted to lower energy with respect to *McDonald'*s complexes (E_{edge} > 8345 eV) as expected for changing *N*- to softer *P*-donor atoms in the ligand framework.[73,74] Small deviations in the whiteline are attributed to minor differences in bond length. The simulated XANES fine structure is also present in the experimental spectrum of $\mathbf{5^{PF6}}$ albeit with lower resolution (Figure 13c). Simulation is done using FEFF9.0 and the density of states of $\mathbf{5^{+}}$ is shown in Figure 13d along the XANES simulation. The Fermi level E_f is positioned at E-E_0 = -8.2 eV, lying well above the SOMO as computed by DFT (Figure 10). Differences in intensity between the density of states of the Ni-4*p* level and the normalized XANES are due to orbital mixing, as can be seen in the pre-edge at E-E_0 = -6.4 eV which has main contribution of Ni-3*d* and further contribution of the Br-4*p* orbital.

Similar behavior for **3**, $\mathbf{4^{BF4}}$ and $\mathbf{5^{PF6}}$ is further observed in EXAFS, in agreement with little deviation in the metal coordination sphere determined by X-ray diffraction (Figure 13b). Detailed analysis using EFEFFIT within the Demeter package gives nickel donor atom distances close to bond length determined by X-ray diffraction (Table 5).

[5] XAS analysis was performed by Prof. Moniek Tromp, Van't Hoff Institute for Molecular Sciences.

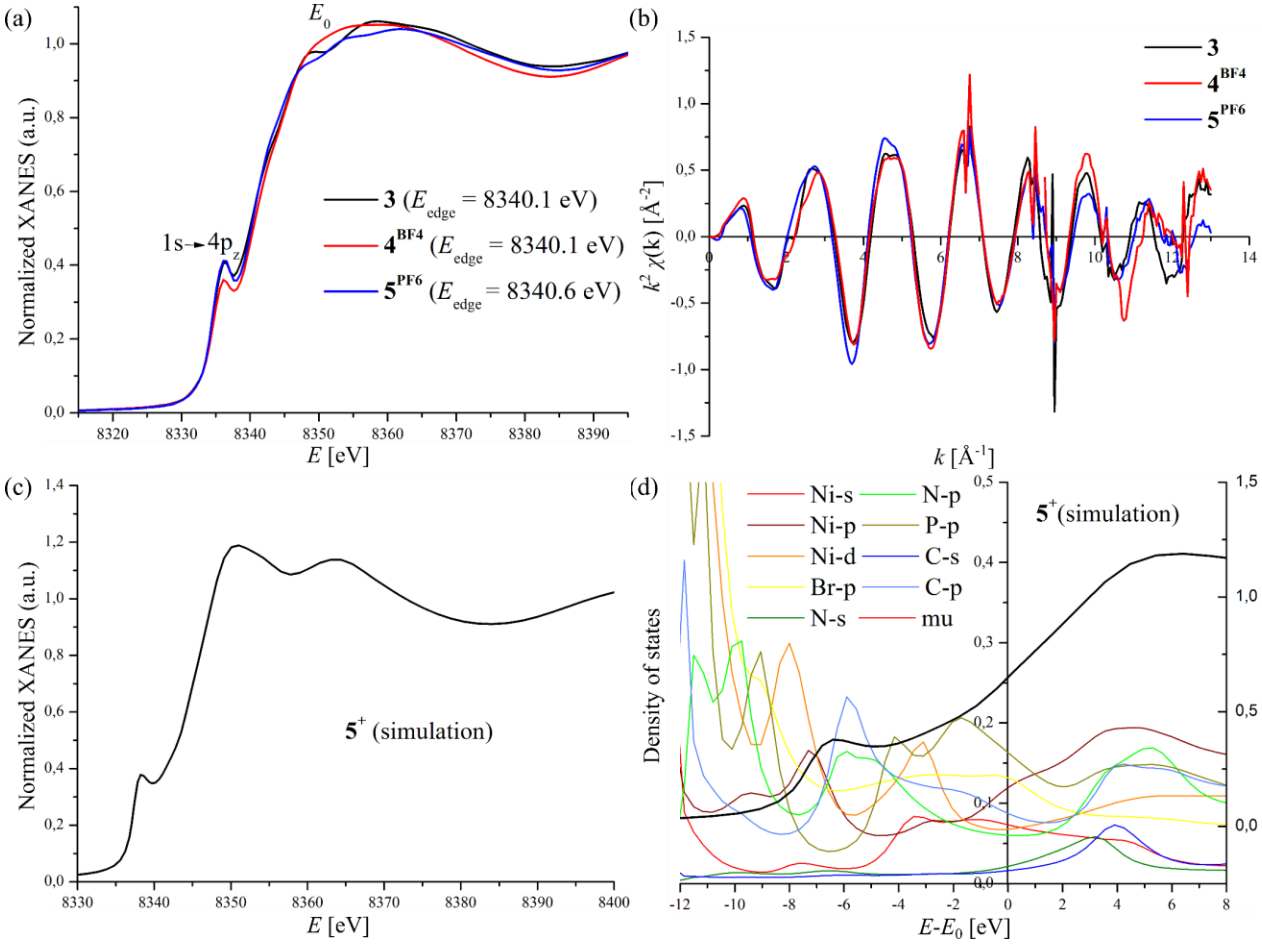

Figure 13: (a) Normalized Ni K-edge X-ray absorption spectroscopy near-edge structure (XANES) and (b) extended X-ray absorption fine structure (EXAFS) of **3**, $\mathbf{4^{BF4}}$ and $\mathbf{5^{PF6}}$; (c) normalized simulated XANES (FEFF9.0) and (d) simulated density of states of $\mathbf{5}^+$.

Table 5: Ni K-edge EXAFS analysis fitting results.

Abs-Sc[a]	C.N.[b]	*R* [Å][c]	*d* [Å][d]	*D.W.* [Å^{-2}][e]	Fit parameters
Ni-N (**3**)	1	1.90(4)	1.8814(15)	0.005(4)	*R* factor = 1.0%, E_0 = 8(1) eV
Ni-P (**3**)	2	2.22(3)	2.268(4)	0.008(2)	2 < *k* < 11, 1.0 < *R* < 3.0
Ni-Br (**3**)	1	2.28(251)	2.3094(3)	0.003(1)	k^1, k^2 and k^3 weighted fit
Ni-N ($\mathbf{4^{BF4}}$)	1	1.88(3)	1.9034(16)	0.002(2)	*R* factor = 0.9%, E_0 = 5(1) eV
Ni-P ($\mathbf{4^{BF4}}$)	2	2.22(2)	2.2256[f]	0.005(2)	2 < *k* < 11, 1.0 < *R* < 3.0
Ni-Br ($\mathbf{4^{BF4}}$)	1	2.29(2)	2.2985(3)	0.006(3)	k^1, k^2 and k^3 weighted fit
Ni-N ($\mathbf{5^{PF6}}$)	1	1.90(3)	1.875[f]	0.002(1)	*R* factor = 5.0%, E_0 = 8(1) eV
Ni-P ($\mathbf{5^{PF6}}$)	2	2.22(6)	2.2386[f]	0.010(7)	2 < *k* < 11, 1.0 < *R* < 3.0
Ni-Br ($\mathbf{5^{PF6}}$)	1	2.34(3)	2.2977[f]	0.001(3)	k^1, k^2 and k^3 weighted fit

[a]Abs = Absorber, Sc = Scatterer; [b]C.N. = coordination number; [c]*R* = distance; [d]*d* = bond length from X-ray diffraction; [e]*D.W.* = Debye Weller factor; [f]given as average of the asymmetric unit.

1.3.3. Benzylic C-H Activation by [NiBr(^{tBu}P=N=P)]PF$_6$ ($\mathbf{5^{PF6}}$)

The ability of the ^{tBu}P=N=P pincer ligand in **3** to act as electron and proton reservoir gives rise to the interest in examining PCET reactivity as combination of both. According to *Hess'* law, net hydrogen atom transfer can be formally separated into successive electron and proton transfer and the free energy ΔG_{HAT} can be expressed as sum of ΔG_{ET} and ΔG_{PT} for electron and proton transfer, respectively (Chapter 1.1.1).

Determination of pK_a for tridentate amido ligands in coordination compounds is limited to reports by *Schneider* and *Grützmacher*.[77–79] While the use of different metals results in limited comparability to enimine $\mathbf{4^{BF4}}$, metal coordination results in a significantly lower pK_a compared to dialkylamines (pK_a([PdPh{HN(CH$_2$CH$_2$P^{i}Pr$_2$)$_2$}])^{DMSO} = 23.2(1); pK_a(pyrrolidine)^{DMSO} ≈ 44).[80,81] In amines, exchanging alkyl for aryl rests has a strong influence on basicity as can be seen by comparison of the pK_a values of the conjugate acids of trimethylamine (pK_a(NMe$_3$)^{DMSO} = 8.4) and *N*,*N*-dimethylaniline pK_a(PhNMe$_2$)^{DMSO} = 2.4).[82,83] Since exchanging ethylene for vinylene linkers is shown to result in less strong electron donating properties of the tridentate ligand, enhanced acidity for $\mathbf{4^{BF4}}$ is expected.[65,84] The measurement of pK_a of $\mathbf{4^{X}}$ is conducted in DMSO-d_6 by titration of **3** with 1.00 eq of a reference acid (Scheme 9). Due to low basicity of **3** the use of trifluoromethansulfonic acid is necessary to reach a chemical equilibrium of **3** and protonated species $\mathbf{4^{OTf}}$.

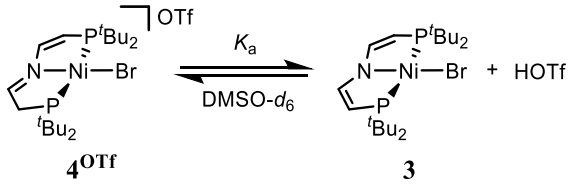

$\mathbf{4^{OTf}}$ **3**

Scheme 9: Acid base equilibrium involving conjugate base **3** and acid $\mathbf{4^{OTf}}$.

Analysis of the reaction mixture by ^{31}P{^{1}H} NMR spectroscopy gives the relative quantities of both species, whereas the presence of a chemical equilibrium is verified by ^{31}P,^{31}P NOESY (Figure 14). A side product resonates at δ = 58.1 ppm in the ^{31}P{^{1}H} NMR spectrum of the equilibrium mixture. Since NOESY suggests no exchange between this species and $\mathbf{3}$/$\mathbf{4^{OTf}}$, it is not considered during the pK_a determination. This side product only induces a small error in the determined equilibrium constant K_{eq} due to its low presence.

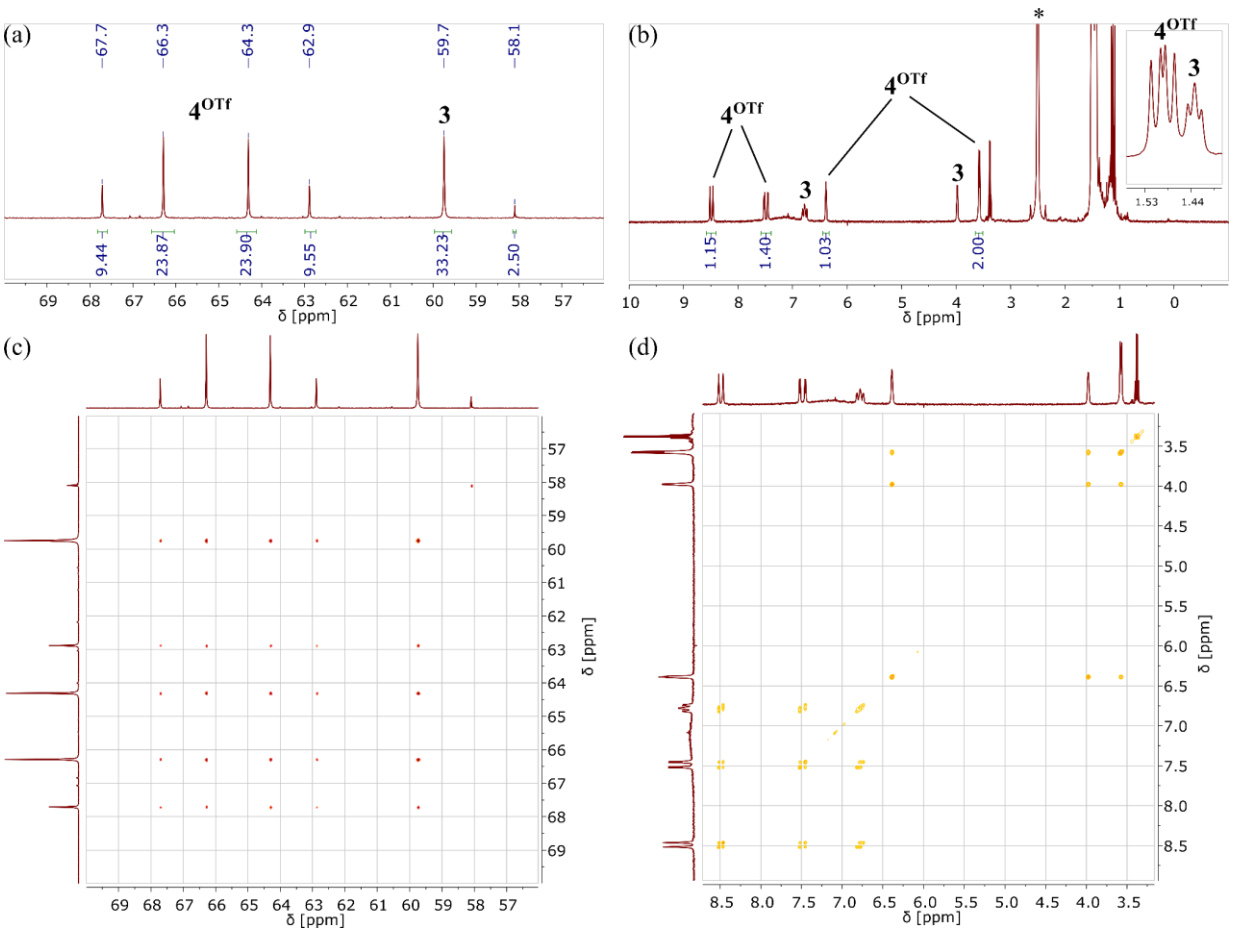

Figure 14: (a) $^{31}P\{^{1}H\}$, (b) ^{1}H, (c) $^{31}P,^{31}P$ NOESY and (d) $^{1}H,^{1}H$ NOESY NMR spectrum of titration of **3** with 1.00 eq trifluoromethansulfonic acid.

$pK_a(\mathbf{4^{OTf}})^{DMSO}$ is determined from the relative quantities of **3** and $\mathbf{4^{OTf}}$ in the mixture as follows:

$$K_{eq} = c(\mathbf{3})\cdot c(\text{HOTf})\cdot c(\mathbf{4}^{+})^{-1}\cdot c(\text{OTf}^{-})^{-1} = c(\mathbf{3})^{2}\cdot c(\mathbf{4^{OTf}})^{-2} \quad (14)$$

$$pK_a = -\log(K_a) = -\log(K_{a,ref}) - \log(K_{eq}) \quad (15)$$

$$pK_a(\mathbf{4^{OTf}})^{DMSO} = -\log(K_a(\text{HOTf})^{DMSO}) - \log(K_{eq}) \quad (16)$$

$$pK_a(\mathbf{4^{OTf}})^{DMSO} = pK_a(\text{HOTf})^{DMSO} - \log(c(\mathbf{3})^{2}\cdot c(\mathbf{4^{OTf}})^{-2}) \quad (17)$$

$$pK_a(\mathbf{4^{OTf}})^{DMSO} = 0.3 - \log(33.23^{2}\cdot 66.79^{-2}) = 0.91 \quad (18)$$

The determined pK_a($\mathbf{4}^{\mathbf{OTf}}$)^{DMSO} = 0.91 is exceptionally low, comparable to HBr in DMSO.[83] As mentioned, the comparability with reported pK_a values for metal coordinated polydentate amine ligands is limited, however $\mathbf{4}^{\mathbf{OTf}}$ is more acidic than related palladium and iridium complexes by multiple orders of magnitude.

With compounds **2** and **3** in hand, the ability of the saturated, ethylene bridged (^{tBu}PNP) and unsaturated, vinylene bridged pincer (^{tBu}P=N=P) to stabilize the formal Ni^{III} oxidation state was investigated by cyclic voltammetry (Figure 15, Figure 16)

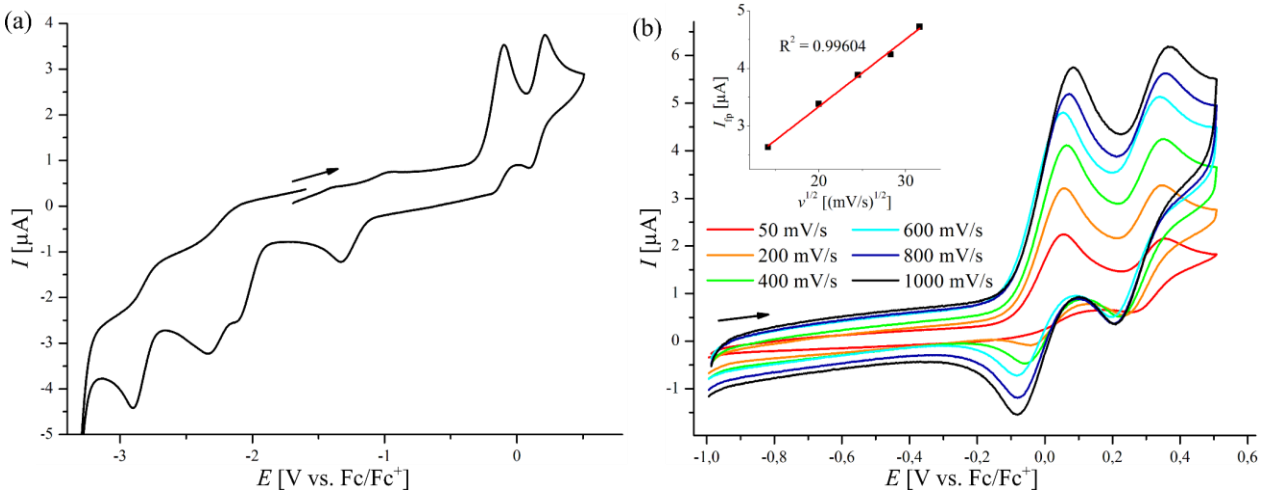

Figure 15: Cyclic voltammetry of a 1 mM solution of **2** in THF referenced to Fc^+/Fc (0.1 M [*n*-Bu_4N]PF_6, WE: GC, CE: Pt wire, RE: Ag/Ag^{+}[6]). (a) Full range scan at v = 100 mV/s and (b) scan of the initial oxidation event at different scan rates with the plot of I_{fp} *vs.* $v^{1/2}$ shown in the insert.

Complex **2** features a chemically irreversible oxidation process at $E^{1/2}$ = 0.0 V *vs.* Fc^+/Fc (Figure 15, Table 6). Complete irreversibility is observed at v = 50 mV/s, but the signal gains a significant return peak at v = 1 V/s. A second process is observed at $E^{1/2}$ = 0.31 V, overlapping with the initial oxidation. The presence of a return peak indicates chemical (quasi-)reversibility for the second electrochemical process whereas full characterization of this redox event is hampered by proximity of the peaks. Due to the initial irreversible oxidation, the second oxidation process is attributed to a species generated by a chemical process giving an overall *ECE* mechanism. Since the peak current ratio i_{rp} / i_{fp} of the initial redox event does not vary strongly over the scan rates investigated, no significant change in the ratio of the oxidative peak currents for the first and second electrochemical oxidation is observed (Table 6). Similar behavior is reported by *Lagaditis et al.* for related cobalt pincer complexes, showing disproportionation *via* formal hydrogen atom transfer (HAT) resulting in formation of imine and amino complexes.[65]

[6] 0.1 mM $AgNO_3$ in THF.

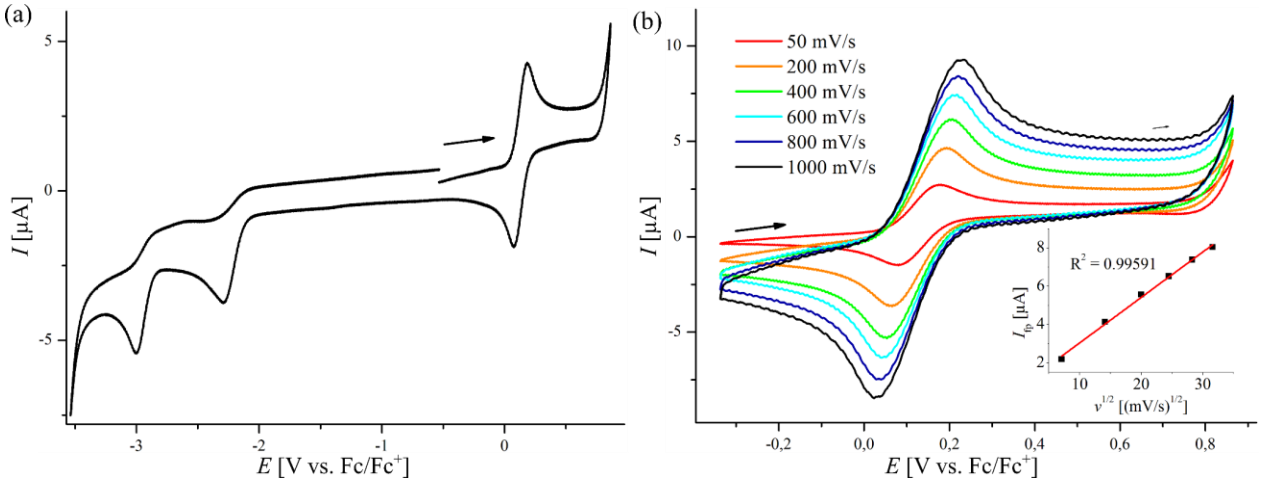

Figure 16: Cyclic voltammetry of a 1 mM solution of **3** in THF referenced to Fc^+/Fc (0.1 M [*n*-Bu_4N]PF_6, WE: GC, CE: Pt wire, RE: Ag/Ag^+[7]). (a) Full range scan at v = 100 mV/s and (b) scan of the initial oxidation event at different scan rates with the plot of I_{fp} *vs.* $v^{1/2}$ shown in the insert.

Table 6: Peak analysis of the initial oxidative responses of **2** and **3** in cyclic voltammetry.

2	v [mV/s]	$E^{1/2}$ [V]	i_{rp} / i_{fp}	ΔE^{P} [a]	**3**	v [mV/s]	$E^{1/2}$ [V]	i_{rp} / i_{fp}	ΔE^{P} [a]
	50[b]	-	-	-		50	0.127	1.10	1.14
	200	0.009	0.12	0.75		200	0.130	1.05	1.26
	400	0.002	0.22	0.80		400	0.130	1.05	1.24
	600	-0.016	0.23	0.78		600	0.130	1.04	1.27
	800	-0.004	0.26	0.80		800	0.128	1.03	1.28
	1000	0.002	0.24	0.78		1000	0.125	1.06	1.30

[a]Given as ratio between the analyte and the internal reference. [b]No detectable return peak.

Upon formal dehydrogenation of the pincer ligand's ethylene bridge, a reversible oxidation process is observed in compound **3** at a scan rate independent half wave potential of $E^{1/2}(\mathbf{3})^{THF}$ = 0.13 V *vs.* Fc^+/Fc. Electrochemically reversible electron transfer in the oxidation processes for **2** and **3** is verified by a linear increase of the forward peak current i_{fp} with $v^{1/2}$. The shift to higher potential with respect to **2** can be explained by the less strongly electron donating amido donor due to conjugation of the vinylene π system. The stabilization of high oxidation states by this unsaturated pincer ligand has also been observed for the related cobalt complexes and is assumed to originate in the lack of weak C-H bonds in **3** which most likely are responsible for the limited stability of **2** upon oxidation. The peak separation of the oxidation process of **3** clearly exceeds the theoretical value of ΔE^{p} = 59 mV/n and separation increases with scan rate v. This is attributed to the low polarity of the solvent. However, the values are close to the peak separation observed for decamethylferrocene, measured under identical conditions. The constant redox potential and i_{rp} / i_{fp} ≈ 1

[7] 0.1 mM $AgNO_3$ in THF.

indicate chemical reversibility for the oxidation of **3** (Table 6). Comparison of the M^{II}/M^{I} oxidation potential of **3** with other square-planar transition metal halide complexes featuring the same chelating ligand reported in the literature shows small variation of the redox potential with changing metal center suggesting ligand centered oxidation processes ([CoCl(^{tBu}P=N=P)]: E^0 = 0.01 V, [IrCl(^{tBu}P=N=P)]: E^0 = 0.02 V, [OsCl(^{tBu}P=N=P)]: E^0 = -0.04 V; all potentials are referenced to Fc^+/Fc).[65,85,86]

For both complexes **2** and **3** irreversible reduction processes are observable. Assignment of the reductive features in the voltammogram of **2** is non-trivial since the reduction processes might be connected to the irreversible oxidation. Cyclic voltammetry of **2** with initial application of a cathodic potential was not performed. Complex **3** exhibits two processes assigned to the Ni^{II}/Ni^{I} (E^p = -2.29 V, v = 100 mV) and subsequent Ni^{I}/Ni^{0} (E^p = -3.01 V, v = 100 mV) couple (chemical reduction of **3** will be discussed in Chapter 1.2.2).

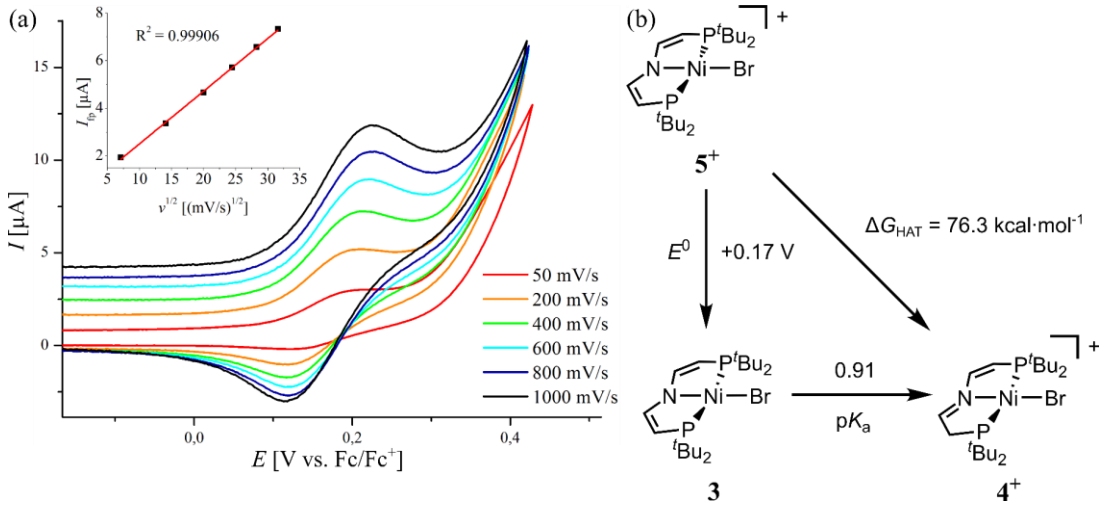

Figure 17: (a) Cyclic voltammetry of a 1 mM solution of **3** in DMSO referenced to Fc^+/Fc (0.1 M [*n*-Bu_4N]PF_6, WE: GC, CE: Pt wire, RE: Ag wire) with the plot of I_{fp} *vs.* $v^{1/2}$ shown in the insert. (b) Interconversion of **3**, **4**$^+$ and **5**$^+$ *via* proton, electron and proton-coupled electron transfer.

Turning to DMSO as solvent, the oxidation process of **3** shifts anodically to a small extend (Figure 17a). A constant i_{fp} *vs.* $v^{1/2}$, $E^{1/2}$ and a low peak separation indicate electrochemically reversible oxidation, but the peak current ratio is reduced with respect to the measurement in THF (Table 7). Given the strong overlap of the redox wave with solvent oxidation, graphical determination of the peak currents is prone to uncertainty and should be taken with care, allowing for determination of E^0(**3**)^{DMSO} = +0.17 V in good approximation.

Table 7: Peak analysis of the initial oxidative response of **3** in cyclic voltammetry in DMSO.

3	v [mV/s]	$E^{1/2}$ [V]	i_{rp} / i_{fp}	ΔE^{p} [a]
	50[b]	-	-	-
	200	0.164	0.27	0.88
	400	0.165	0.34	0.83
	600	0.171	0.41	0.88
	800	0.172	0.45	0.95
	1000	0.169	0.47	0.90

[a]Given as ratio between the analyte and the internal reference. [b]No detectable return peak.

Taking experimentally determined $pK_a(\mathbf{4^{OTf}})^{DMSO}$ = 0.91 and $E^0(\mathbf{3})^{DMSO}$ = +0.17 V, the bond dissociation free energy of the backbone methylene group in $\mathbf{4^{OTf}}$, BDFE($\mathbf{4^{OTf}}$), can be derived *via* combination of redox potential of the $\mathbf{5}^+/\mathbf{3}$ couple and the acidity of $\mathbf{4^{OTf}}$ as described by *Bordwell* (Figure 17b).[87] C_G accounts for redox potential, solvation and formation free energy of the $H^+/H^\bullet$ couple and therefore is solvent dependent. By determining $E^0(\mathbf{3})^{DMSO}$ and taking $C_G{}^{DMSO}$ from *Mayer*s review on proton-coupled electron transfer (PCET), $\Delta G_{HAT}(\mathbf{4^{OTf}})^{DMSO}$ = 76.3 kcal·mol^{-1} can be derived ($C_G{}^{DMSO}$ = 71.1 kcal·mol^{-1}), which is in excellent agreement with computation ($\Delta G_{HAT}(\mathbf{4}^+)^{DFT}$ = 77.2 kcal·mol^{-1}; D3BJ-PBE/def2-TZVP(COSMO: DMSO)).[8][4]

While HAT reactivity of 3d transition metal based pincer complexes is reported in literature, work by *Chirik* and *Heyduk* reports much lower values of $\Delta G_{HAT}(\text{C-H})^{DFT}$ = 49.9 kcal·mol^{-1} for [CoCl(NC_5H_3-2,6-(CH_2P*t*Bu_2)$_2$] and $\Delta G_{HAT}(\text{N-H})^{MeCN}$ = 63.9±0.8 kcal·mol^{-1} for [NiPCy$_3$(SNS)].[59,60,72] While the N-H bond strength in [NiPR$_3$(SNS)] changes little upon changing the substituents on the phosphine, ligand or metal exchange in *Chirik*'s system has a much greater effect on C-H bond strength, which is in agreement with a more metal based radical in case of the cobalt complexes. In both cases, the C-H bond strength is comparable to or even below hydroxylamine O-H bonds of low bond strength like TEMPO-H ($\Delta G_{HAT}(\text{TEMPO-H})^{MeCN}$ = 66.5 kcal·mol^{-1}), rendering these complexes unsuitable for C-H bond activation.

If $\mathbf{5^{PF6}}$ is synthesized in DCM or THF, significant amounts of $\mathbf{4^{PF6}}$ are obtained indicating that C-H activation is feasible on this platform. Accordingly, pure $\mathbf{5^{PF6}}$ converts to $\mathbf{4^{PF6}}$ in DCM or THF solution, however is stable over several days in more inert chlorobenzene. To examine hydrogen atom abstraction (HAA) from activated hydrocarbons, $\mathbf{5^{PF6}}$ was reacted with 100 eq of different substrates in DCM-d_2 solution, showing accelerated conversion to $\mathbf{4^{PF6}}$ in all cases (Figure 18a). The reaction progress is monitored $^1H\{^{31}P\}$ NMR

[8] Computational analysis was performed by Dr. Markus Finger.

spectroscopically by integration *vs.* hexamethylbenzene as internal standard. In case of 9,10-dihydroanthracene (DHA) and xanthene the reaction is nearly finished upon measurement of the first spectrum, whereas the rate of **4**$^{\mathbf{PF6}}$ production decreases with increasing ΔG_{HAT}(C-H) of the substrate. Statistic effects accounting for the number of C-H bonds of lowest energy have to be considered as can be seen upon comparison of the time traces (*e.g.* Ph_2CH_2 and Ph_3CH).

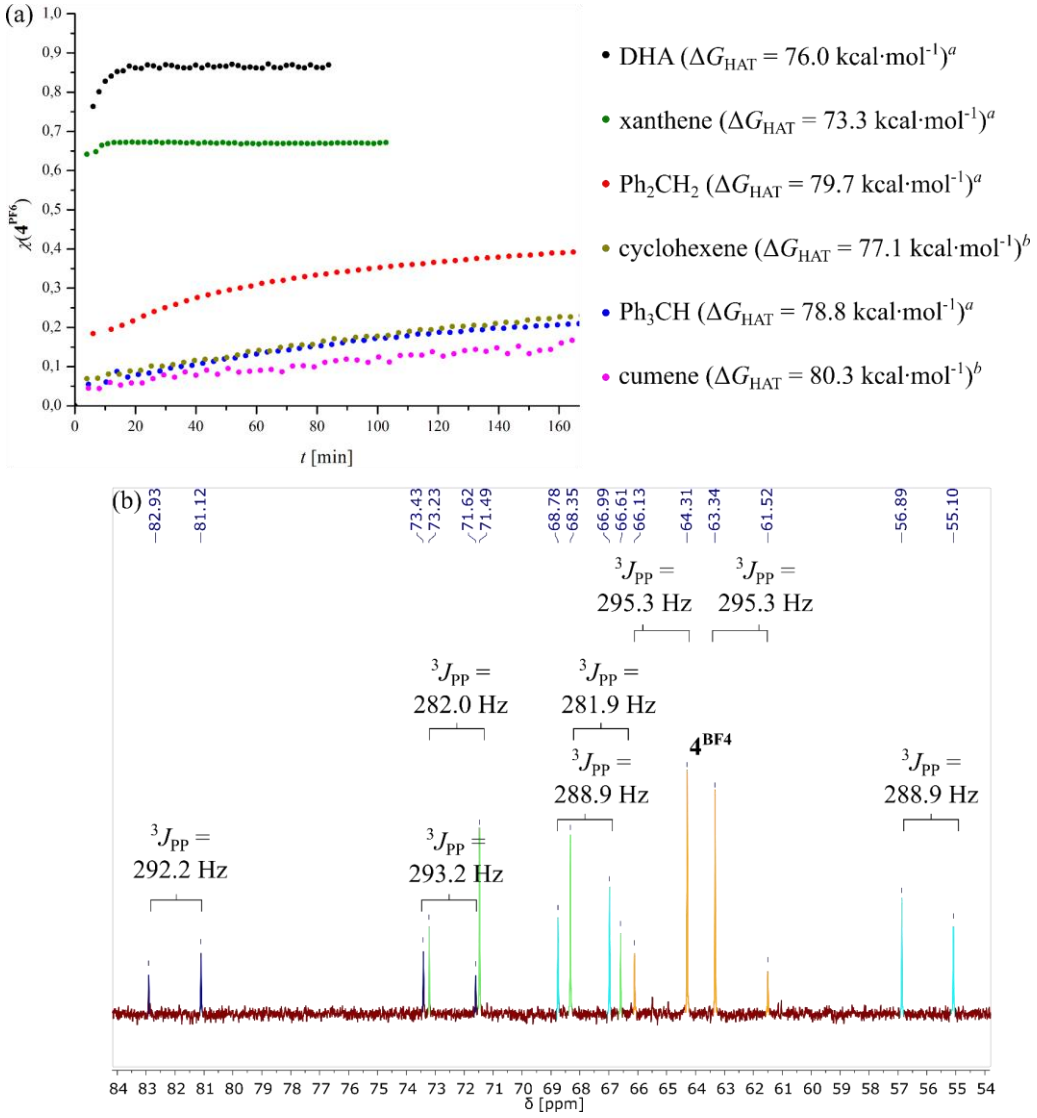

Figure 18: (a) Plot of molar fraction χ(**4**$^{\mathbf{PF6}}$) *vs.* *t* of reaction of **5**$^{\mathbf{PF6}}$ with 100 eq of substrate (ΔG_{HAT} given in MeCN; [a]taken from ref. [4]; [b]taken as ΔH_{HAT}^{MeCN} from ref. [88] and converted to ΔG_{HAT}^{MeCN} using C_G^{MeCN} as described in ref. [4]). (b) $^{31}P\{^1H\}$ NMR spectrum of the reaction of **5**$^{\mathbf{PF6}}$ with 100 eq of fluorene.

While **4**$^{\mathbf{PF6}}$ is the main product of all reactions, most substrates do not give clean conversion as can be seen by the final molar fraction of **4**$^{\mathbf{PF6}}$ being below 1 for xanthene. Pincer backbone functionalization as alternate pathway to HAA is indicated by doublet resonances for side products in $^{31}P\{^1H\}$ NMR spectroscopy, showing a larger difference in chemical shift $\Delta\delta$ for both phosphorus atoms compared to protonated **4**$^{\mathbf{PF6}}$. In

Figure 18b the $^{31}P\{^{1}H\}$ NMR spectrum of the reaction of $\mathbf{5}^{\mathbf{PF6}}$ with 100 eq of fluorene is depicted, showing formation of four species including $\mathbf{4}^{\mathbf{BF4}}$ which can be clearly assigned by comparison of the coupling constants. Structural identification based on ^{1}H NMR spectra is not possible due to overlap with the strong substrate signals. The reaction with fluorene as substrate is not included in Figure 18a due to low selectivity.

Since the conversion of $\mathbf{5}^{\mathbf{PF6}}$ to $\mathbf{4}^{\mathbf{PF6}}$ by C-H activation in CD_2Cl_2 shows highest selectivity with DHA as substrate, this reaction was examined in less reactive solvent Ph-Cl-d_5. Upon reacting $\mathbf{5}^{\mathbf{PF6}}$ with 100 eq DHA, clean conversion to $\mathbf{4}^{\mathbf{PF6}}$ can be observed by $^{31}P\{^{1}H\}$ and ^{1}H NMR spectroscopy within 30 minutes as shown in Figure 19.

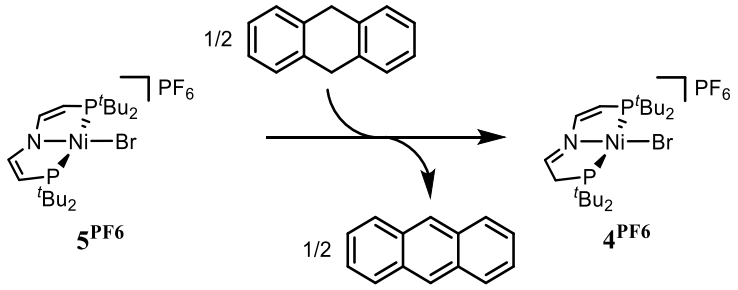

Scheme 10: Oxidation of 9,10-dihydroanthracene to anthracene *via* HAA by $\mathbf{5}^{\mathbf{PF6}}$.

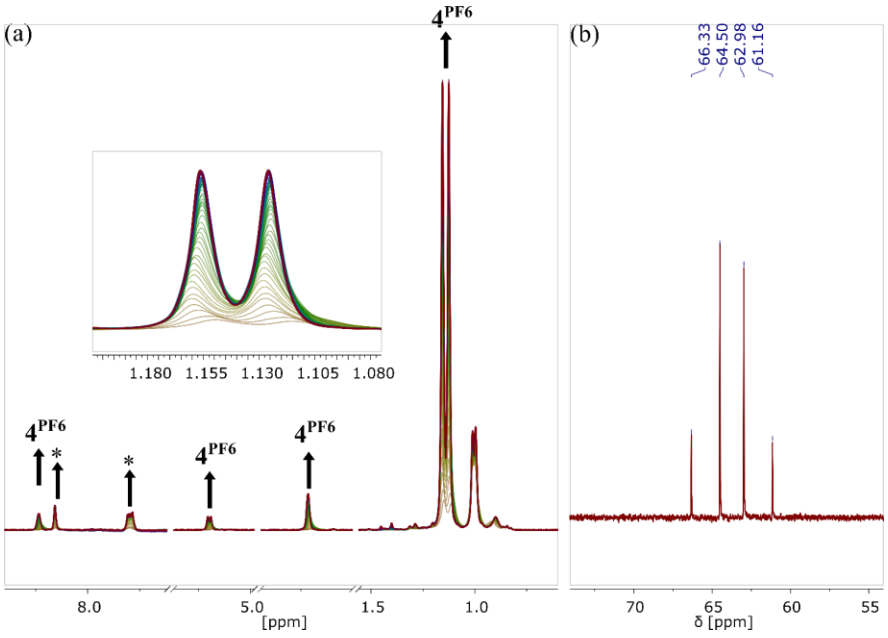

Figure 19: (a) $^{1}H\{^{31}P\}$NMR spectral evolution of the reaction of $\mathbf{5}^{\mathbf{PF6}}$ with 100 eq DHA in Ph-Cl-d_5 (*denotes anthracene). (b) $^{31}P\{^{1}H\}$ NMR spectrum after full conversion.

Formation of anthracene can be detected NMR spectroscopically without any observable byproducts. This stands in contrast to oxo complexes which are commonly utilized for benzylic C-H activation, giving oxidized products from oxygen atom transfer as side reaction.[36,40] Similar selectivity in DHA oxidation by

HAT is observed with $[nBu_4N][MnO_4]$, $[V(O)_2(tBu_2bpy)_2]BF_4$ (tBu_2bpy = 4,4'-di-*tert*-butyl-2,2'-bipyridin) and $[Mn(hfacac)_3]$ (hfacac = hexafluoroacetylacetonate) among others.[37,41,58]

Conversion of $\mathbf{5}^{\mathbf{PF6}}$ to $\mathbf{4}^{\mathbf{PF6}}$ can also be observed in the presence of hydrocarbons containing stronger C-H bonds like toluene (ΔG_{HAT} = 82.8 kcal·mol^{-1} in DMSO) and *p*-methylanisole ($\Delta G_{HAT} \approx$ 82 kcal·mol^{-1} in DMSO) in Ph-Cl-d_5.[58,89–92]

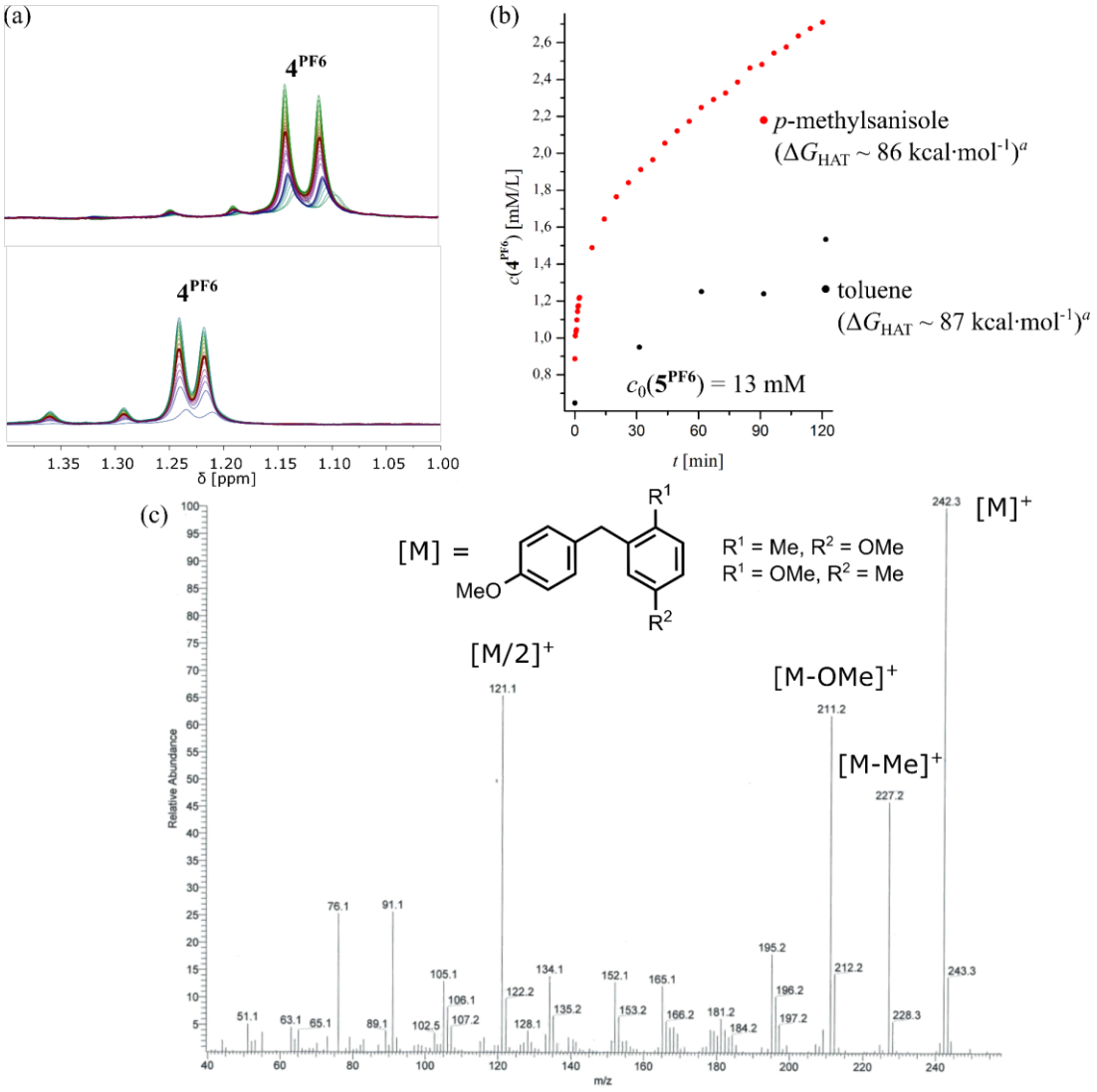

Figure 20: (a) ^{1}H NMR spectral evolution of the reaction of $\mathbf{5}^{\mathbf{PF6}}$ with 100 eq of *p*-methylanisole (top) and toluene (bottom) in Ph-Cl-d_5. (b) Plot of $c(\mathbf{4}^{\mathbf{PF6}})$ *vs. t* (ΔG_{HAT} given in MeCN; [a]taken from ref. [4] and ref. [58]). (c) GC-MS(EI+) of the organic phase of the reaction of $\mathbf{5}^{\mathbf{PF6}}$ with 100 eq of *p*-methylanisole after filtration over silica.

^{1}H NMR spectroscopy shows high selectivity in formation of $\mathbf{4}^{\mathbf{PF6}}$ with minor amounts of side products visible in both reactions (Figure 20a). While in both ^{1}H NMR spectra a difference in chemical shift δ of the ^{t}Bu resonance is present, the identity of $\mathbf{4}^{\mathbf{PF6}}$ is confirmed by ^{31}P{^{1}H} NMR spectroscopy. As expected, the reaction takes much longer compared to DHA as substrate and was not monitored until full conversion

(Figure 20b). While kinetic analysis was not performed, organic product distribution gives mechanistic insight (Scheme 11). By GC-MS(EI+), 2,4'-dimethoxy-5-methyldiphenylmethane or 3,4'-dimethoxy-6-methyldiphenylmethane can be identified as the product of *p*-methylanisole oxidation (Figure 20c).[93,94] Both isomers cannot be distinguished by mass spectroscopy and NMR spectroscopic characterization is impeded by overlap with the substrate resonances. Homo coupling to bis-4,4'-methoxydibenzyl can be excluded based on the fragmentation of the methoxy (*m/z* = 211.2) and the methyl substituent (*m/z* = 227.2) which is not observed in bis-4,4'-methoxybibenzyl.[95] Formation of biaryl species would give similar mass spectra, but is ruled out since it would be a result of initial hydrocarbon oxidation which is thermodynamically strongly uphill due to the high oxidation potential of toluene derivatives.[4,40] The formation of diphenylmethane derivatives and the absence of homo coupling products suggests oxidation of the initially formed benzyl radical and subsequent *Friedel-Crafts* type electrophilic aromatic substitution chemistry (Scheme 11).[40,58]

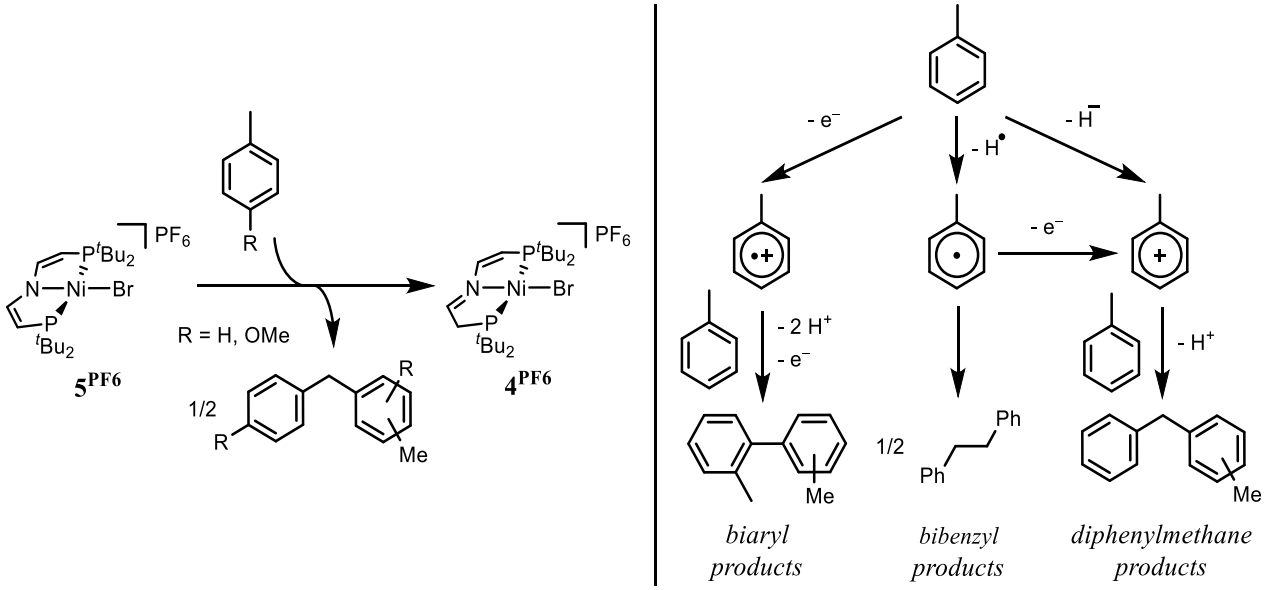

Scheme 11: (left) Oxidation of toluene derivatives by $\mathbf{5^{PF6}}$. (right) Product distribution in toluene oxidation.

While in DHA oxidation, thermochemistry basically renders stepwise PCET impossible due to the high oxidation potential and low acidity of DHA as well as the low ΔG_{HAT}(C-H) of the hydroanthracenyl radical (HA), the situation changes in toluene derivatives. The initially activated C-H bond has a much higher ΔG_{HAT} as compared to DHA (Scheme 13), but the formed benzyl radical does not readily lose another hydrogen atom as the hydroanthracenyl radical does. Therefore, oxidation of the benzyl radical to the benzyl cation can proceed at a mild potential of E^0 =-0.22 V *vs* Fc^+/Fc in DMSO. Combination of HAT and oxidation results in formal hydride transfer with the driving force ΔG_{HT}, considering the potential of hydrogen atom reduction in DMSO ($E^0(H^•/H^-)$ = -1.09 V):[4]

$$\Delta G_{HT} = \Delta G_{HAT} + 23.06\ \text{kcal·mol}^{-1}\cdot\text{V}^{-1}\cdot(E^0 - E^0(\text{H}^\bullet/\text{H}^-)) \quad (19)$$

To investigate whether benzyl cation formation from toluene proceeds *via* stepwise or concerted PCET, electrochemical behavior of $\mathbf{4}^{\mathbf{BF4}}$ in DMSO was investigated to determine the hydride affinity of $\mathbf{5}^{\mathbf{PF6}}$.

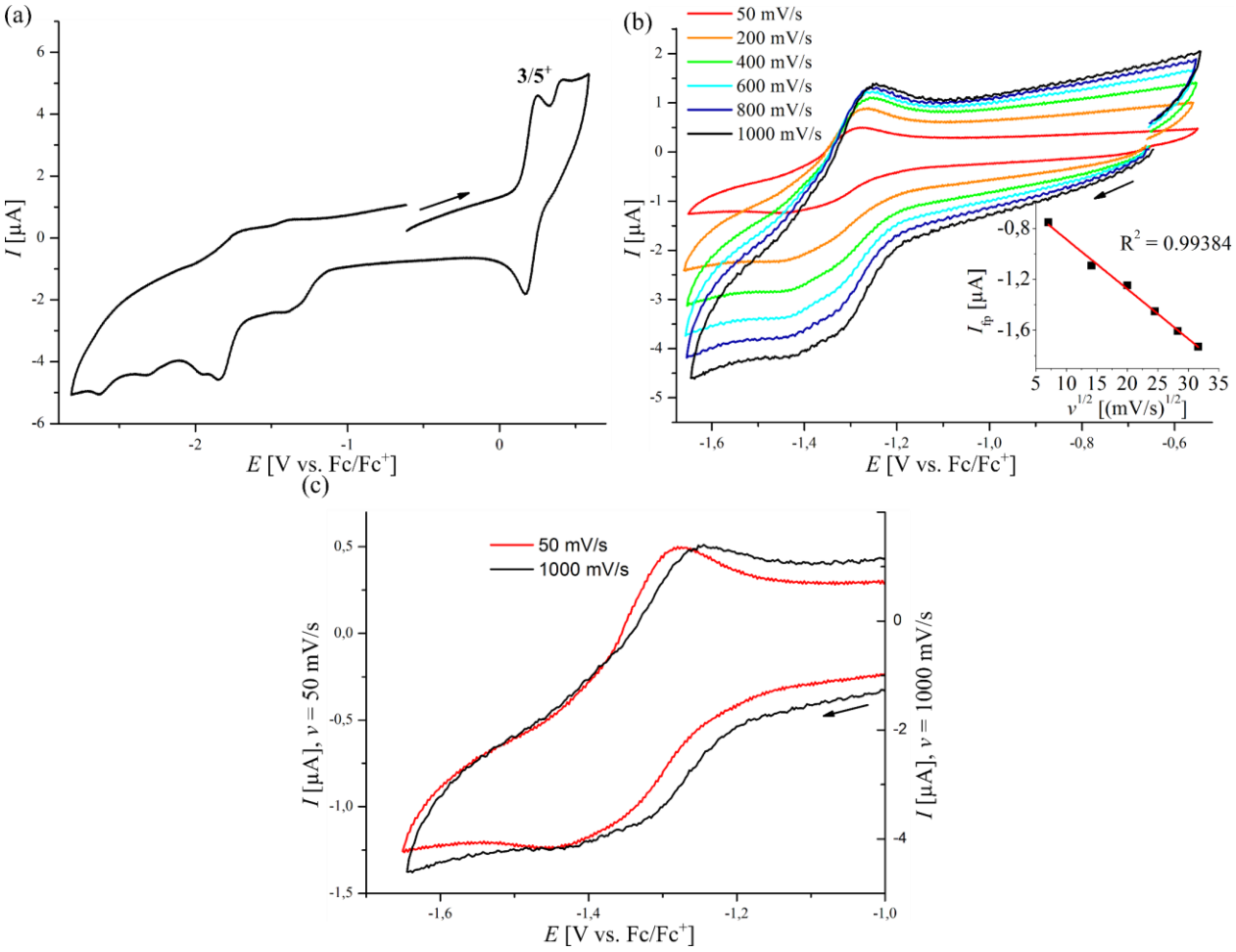

Figure 21: Cyclic voltammetry of $\mathbf{4}^{\mathbf{BF4}}$ in DMSO (0.1 M [*n*-Bu_4N]PF_6, WE: GC, CE: Pt, RE: Ag). (a) Full range scan at v = 100 mV/s, (b) scan of the initial reduction event at different scan rates with the plot of I_{fp} *vs.* $v^{1/2}$ shown in the insert and (c) comparison of the initial reduction event at v = 50 mV/s and v = 1000 mV/s.

Dissolving $\mathbf{4}^{\mathbf{BF4}}$ in DMSO results in partial solvent protonation as predicted by $pK_a(\mathbf{4}^{\mathbf{OTf}})^{DMSO}$ = 0.91 and consequently cyclic voltammetry of $\mathbf{4}^{\mathbf{BF4}}$ shows an Ni^{III}/Ni^{II} oxidation at $E^0(\mathbf{3})$ = 0.17 V vs. Fc^+/Fc corresponding to conjugate base **3** as shown in Figure 21a. Turning to cathodic potentials, an initial quasireversible reduction process can be monitored. Closer investigation of this redox feature reveals two overlapping reduction events at close potential and a single return peak (Figure 21b). Comparison of the forward peak currents of both redox events at v = 50 mV/s and v = 1000 mV/s shows a more pronounced initial reduction at high scan rate (Figure 21c). Further, an anodic shift of the initial electron transfer potential at a higher scan rate v is observed. Both experimental observations are in agreement with an *ECE*

mechanism. A high scan rate results in less efficient chemical conversion after the initial electron transfer. Accordingly, an anodic shift results for the first redox potential and a less intense peak current is observed for the second reduction. The assignment of the return peak to one of the forward peaks is not trivial given the low peak separation, however comparison of the second forward peak current to the return peak current gives a nearly constant ratio i_{fp} / i_{rp} upon changing *v*, suggesting that the oxidative feature is most likely corresponding to the second reduction event (Table 8). The anodic shift of the return peak at high scan rates *v* is attributed to an overlap with the return peak of the initial electron transfer process, which gains intensity at higher scan rates.

Table 8: Peak analysis of the cathodic response of **4**$^{\mathbf{BF4}}$ in cyclic voltammetry.

4$^{\mathbf{BF4}}$	*v* [mV/s]	*E*° [V]^{a}	i_{rp} / i_{fp} ^{a}	ΔE^{P} ^{b}
	50^{a}	-1.357	0.78	1.67
	200	-1.351	0.79	1.76
	400	-1.342	0.83	1.86
	600	-1.341	0.81	1.92
	800	-1.336	0.77	1.72
	1000	-1.331	0.79	1.81
+ 10 eq [(*n*-Hex)$_4$N]Br	50^{a}	-1.388	0.92	1.13
	100	-1.385	0.87	1.22
	200	-1.384	0.85	1.15

^{a}Determined for the second forward peak. ^{b}Given as ratio between the analyte and the internal reference.

The close potential for both observable reductive processes of the *ECE* mechanism can be interpreted as oxidation of the initially formed Ni^{I} *via* the chemical follow-up process, resulting in a close reduction potential for the subsequent second electrochemical event. Proton reduction would result in formation of Ni^{II} **3**, however cyclic voltammetry of isolated **3** does not show reduction at such high potential (Figure 16) and therefore does not serve as explanation of the observed mechanism. Upon addition of 10 eq of [(*n*-Hex)$_4$N]Br to a DMSO solution of **4**$^{\mathbf{BF4}}$ the *ECE* process simplifies to a chemically reversible reduction, suggesting bromide loss as chemical follow-up reaction after initial reduction of **4**$^{\mathbf{BF4}}$ (Figure 22a). A cathodic shift of the initial reduction process can be observed which is expected upon lowering the driving force for the chemical follow-up and no subsequent reduction event is present after addition of additional bromide source. In [(*n*-Hex)$_4$N]Br containing solution, the Ni^{II}/Ni^{I} reduction shows a constant potential and a peak current ratio i_{fp} / i_{pr} close to 1, enabling determination of $E^{1/2}$(**4**$^{\mathbf{BF4}}$)^{DMSO} = -1.39 V (Figure 22b) as good approximation of E^{0}(**4**$^{\mathbf{BF4}}$)^{DMSO}.

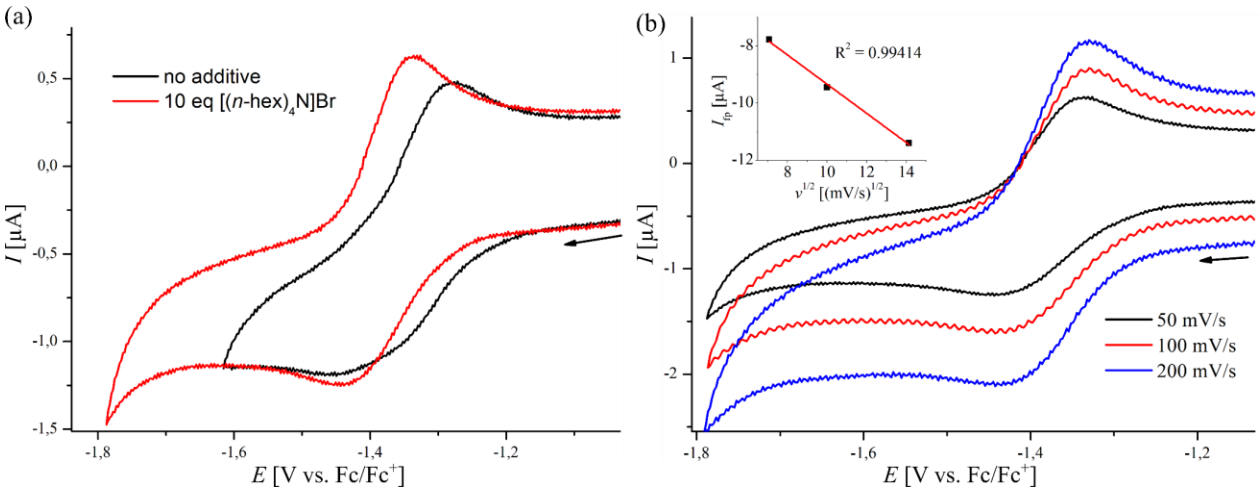

Figure 22: Cyclic voltammetry of **4**$^{\mathbf{BF4}}$ in DMSO (0.1 M [*n*-Bu$_4$N]PF$_6$, WE: GC, CE: Pt, RE: Ag). (a) Scan of the initial reduction event at v = 50 mv/s in the absence and presence of 10 eq [(*n*-Hex)$_4$N]Br and (b) scan of the initial reduction event in the presence of 10 eq [(*n*-Hex)$_4$N]Br at different scan rates with the plot of I_{fp} *vs.* $v^{1/2}$ shown in the insert.

With E^0(**4**$^{\mathbf{BF4}}$)^{DMSO} = -1.39 V in hand, the thermodynamic square-scheme shown in Figure 17b can be extended to include hydrogen atom transfer on two formal oxidation states of the {NiBr(^{tBu}P=N=P)} platform (Scheme 12). For convenience, the square schemes will be shown with electron transfer as horizontal and proton transfer as vertical transitions in the following. While the Ni^{III}/Ni^{II} oxidation potential allows for benzylic C-H activation, the low Ni^{II}/Ni^{I} potential of **4**$^{\mathbf{BF}}$ results in a dramatically weaker methylene C-H bond ΔG_{HAT}([NiBr(^{tBu}P=N=P^H]) = 40.3 kcal·mol^{-1} on the Ni^I oxidation state. Additionally, the hydride affinity of **5**$^+$ can be determined to be ΔG_{HT}([NiBr(^{tBu}P=N=P^H]) = 69.4 kcal·mol^{-1} (E^0(H$^•$/H$^-$)^{DMSO} = -1.09 V).[4]

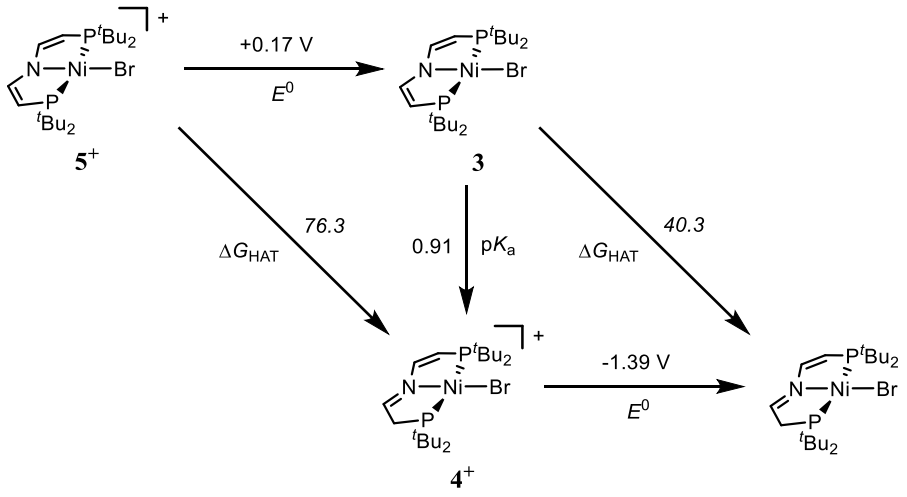

Scheme 12: Interconversion of nickel pincer bromide complexes *via* proton, electron and proton-coupled electron transfer in DMSO solvent. Values written in italics are calculated *via* a square scheme, whereas non-italic values are experimentally determined. Free energies are given in kcal·mol^{-1}.

Based on the thermodynamic data available on the investigated nickel complexes and toluene, the thermodynamic square scheme shown in Scheme 13 is constructed. Hydrogen atom transfer from DHA to $\mathbf{5^{PF6}}$ proceeds with ΔG = -0.3 kcal·mol^{-1}, while HAT from toluene gives ΔG = +6.5 kcal·mol^{-1}, which is in agreement with a much slower reaction. Once the benzyl radical is formed, oxidation by another equivalent of $\mathbf{5^{PF6}}$ is downhill by ΔG = -9.0 kcal·mol^{-1} as can be seen by the more negative oxidation potential of the benzyl radical. Concerted hydride transfer from the hydrocarbon is thermodynamically unfeasible with ΔG_{HT} = +43.6 for toluene, suggesting that both, toluene and DHA oxidation, proceeds *via* initial HAT as shown in Scheme 13.

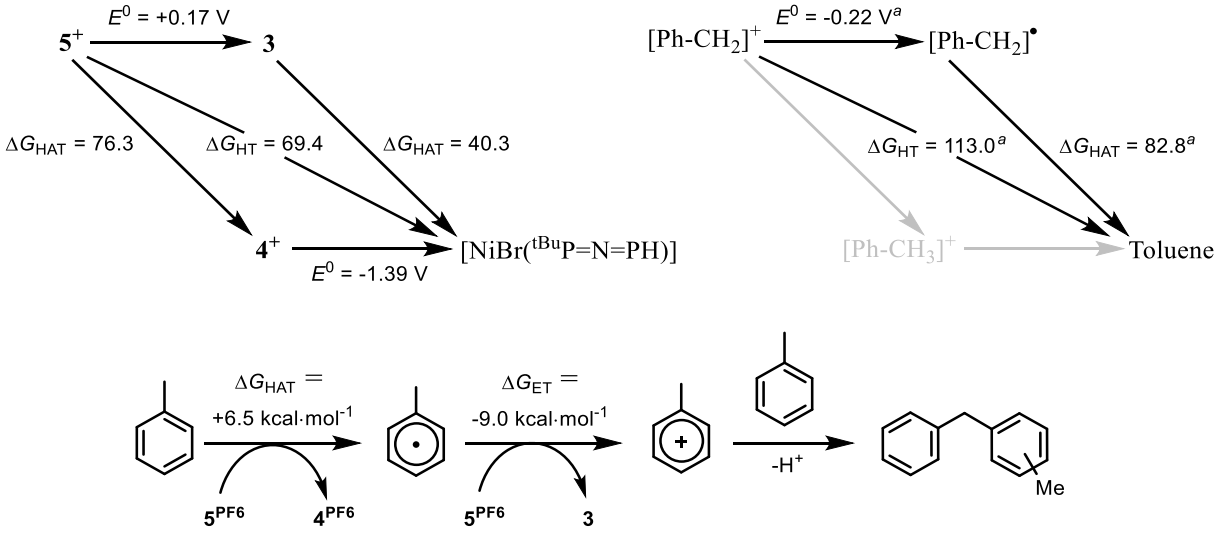

Scheme 13: Thermodynamic square scheme of investigated complexes and toluene in DMSO and mechanism for oxidation of toluene derivatives by $\mathbf{5^{PF6}}$ ([a]ref. [91], free energies are given in kcal·mol^{-1}).

1.3.4. Kinetic Analysis of DHA Oxidation by [NiBr(^{tBu}P=N=P)]PF_6 ($\mathbf{5^{PF6}}$)

To obtain kinetic data on the reaction of $\mathbf{5^{PF6}}$ with DHA the reaction progress was monitored by UV-vis spectroscopy using the distinct absorption of $\mathbf{5^{PF6}}$ in the NIR region. Initial experiments indicate that this absorption A_{1030} at λ = 1030 nm shows linear behavior with respect to the concentration of $\mathbf{5^{PF6}}$ and the relationship shown in Figure 23a is used to calculate $c(\mathbf{5^{PF6}})$ from the measured absorption.

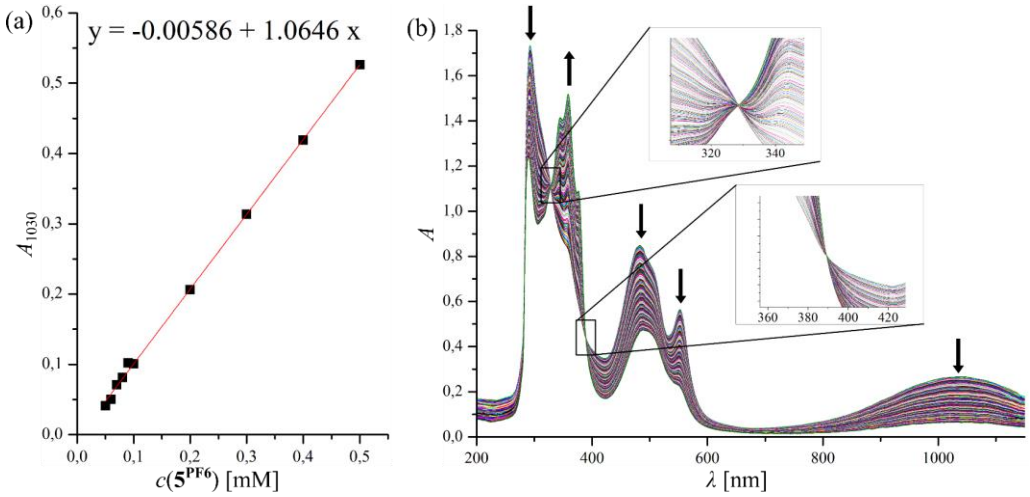

Figure 23: (a) Plot of the absorbance A_{1030} *vs.* $c(\mathbf{5^{PF6}})$ in Ph-Cl. (b) UV-vis spectra recorded during the reaction of $\mathbf{5^{PF6}}$ with 100 eq of DHA at T = 298.15 K.

Upon following the reaction progress by UV-vis spectroscopy, aside from the decrease in absorption in the NIR region, a decrease in intensity in the visible region of the spectra can be observed which is expected for conversion of $\mathbf{5^{PF6}}$ to $\mathbf{4^{PF6}}$ (see Figure 12a for authentic spectra of the isolated compounds). While the decreasing absorption at λ = 300 nm can be again attributed to the reduction of $\mathbf{5^{PF6}}$, there is an increase in absorption close to λ = 400 nm, which appears due to anthracene formation.[97] Two isosbestic points at λ = 328 nm and λ = 389 nm confirm clean conversion of $\mathbf{5^{PF6}}$ to $\mathbf{4^{PF6}}$ without long-lived intermediates, suggesting concerted proton-electron transfer (CPET).

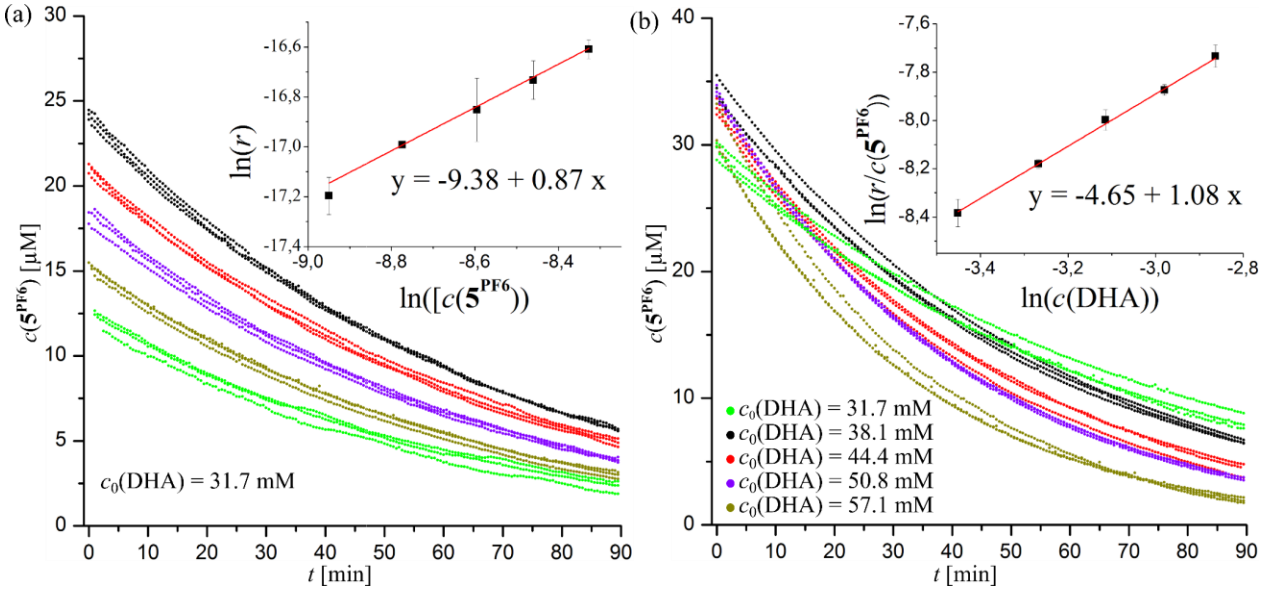

Figure 24: Results of kinetic investigation of DHA oxidation by $\mathbf{5^{PF6}}$ in Ph-Cl at 298.15 K. $c(\mathbf{5^{PF6}})$ is determined by monitoring A_{1030} by UV-Vis spectroscopy and using the relationship shown in Figure 23a. (a) $c(\mathbf{5^{PF6}})$ *vs.* t with different $c_0(\mathbf{5^{PF6}})$ (c(DHA) = 31.7 mM). (b) $c(\mathbf{5^{PF6}})$ *vs.* t with different c_0(DHA). Inserts: first-order plot from initial rate measurements (t = 0–420 s).

To determine the rate law for the reaction, initial rates were measured for variation of $c_0(\mathbf{5^{PF6}})$ and c_0(DHA) as shown in Figure 24. In both cases, the slope shows good agreement with a rate-determining step which is first-order in both, substrate and oxidant. Therefore, the following rate law arises for the reaction assuming steady state concentrations for the hydroanthracenyl radical and neglectable back reaction due to significant lower C-H bond strength as compared to DHA: [43]

$$-d(c(\mathbf{5^{PF6}}))/dt = k_{obs}\, c(\mathbf{5^{PF6}})\, c(\text{DHA}) = 2\, k\, c(\mathbf{5^{PF6}})\, c(\text{DHA}) \qquad (20)$$

$$k = (3.9\pm0.2)\cdot10^{-3}\ \text{M}^{-1}\cdot\text{s}^{-1} \qquad (21)$$

The second-order rate constant k_{obs} = (7.8±0.2)·10^{-3} M^{-1}·s^{-1} can be extracted from the kinetic data giving k = (3.9±0.2)·10^{-4} M^{-1}·s^{-1} upon considering the stoichiometry of the reaction. The rate constant k^{HAT} is commonly utilized to formulate linear free energy relationships for reacting one oxidant with different substrates. Therefore, k is corrected for the number of reactive H atoms in the substrate, giving k^{HAT} = 9.8·10^{-4} M^{-1}·s^{-1} (DHA contains 4 equivalent benzylic C-H atoms). When comparing rate constants of reactions containing both different oxidants and reductants, an additional correction for the reactive sites of the oxidant has to be made, giving k_{sym}^{HAT} = 4.9·10^{-4} M^{-1}·s^{-1} ($\mathbf{5^{PF6}}$ contains 2 equivalent H acceptor sites based on consideration of the rotational symmetry number as discussed by *Truhlar*[98]).[41]

Mayer has established the transfer of thermodynamic and kinetic formalism of outer-sphere electron transfer processes as described by *Marcus* to PCET involving metal complexes.[27,44] The reorganization energy λ in

electron-transfer corresponds to an energetic barrier and can be described by the self-exchange rates k_{sym}^{SE} of the oxidant and reductant in the *Marcus* cross relation (eq. (13), Chapter 1.1.3). Analogously, the rate of a PCET reaction can be predicted with decent precision (1–2 order of magnitude as stated in ref. [43]) based on the change in bond strength accounting for thermochemistry and self-exchange rates as measure for the barrier of the reaction (the frequency factor *f* is usually taken as 1, assuming reactions of low driving force):[42,43]

$$k_{sym}^{HAT} = \sqrt{k_{sym}^{SE1}\, k_{sym}^{SE2}\, K_{12} f_{12}} \tag{22}$$

The self-exchange rate k_{sym}^{SE} can be used to categorize compounds into different groups which show linear increase in log(*k*) upon variation of driving force over a limited range of $\Delta\Delta G$ due to similar self-exchange rates. A comparable categorization by 'nature' of substrate is done in the *Bell-Evans-Polanyi* relationship which interprets LFER using the Arrhenius equation (Chapter 1.1.2).[25]

Table 9: Thermodynamic data of DHA reduction by selected PCET reagents and self-exchange rates.

	k_{sym}^{HAT} [a,b]	ΔG_{HAT} [c]	k_{sym}^{SE} [a,b]
5^{PF6}	$4.9\cdot10^{-4}$	76.3	$5\cdot10^{2}$–$1.4\cdot10^{4}$ [d]
$[Mn(hfacac)_3]$ [58]	$2.8\cdot10^{-5}$	-	-
$[V(O)_2(t\text{Bu}_2\text{bpy})_2]^+$ [41]	$1.3\cdot10^{-7}$	70.6±1.2	$6.5\pm0.1\cdot10^{-3}$
$[RuO(pyr)(bpy)_2]^{2+}$ [4,36]	$3.1\cdot10^{1}$	84.8	$7.6\pm0.4\cdot10^{4}$
$[Fe(Hbim)_2(bim)]^+$ [4,18,99]	$2.75\cdot10^{-5}$	71.7	$9.7\pm1.0\cdot10^{2}$

[a] in $M^{-1}\cdot s^{-1}$; [b] T = 298.15 K; [c] in kcal·mol^{-1}; [d] predicted *via Marcus* cross relation.

Table 9 shows a comparison of DHA oxidation *via* initial HAT using different complexes reported by *Mayer* and **5^{PF6}**. While in the literature usually k_{obs} is given, k_{sym}^{SE} is calculated to give better comparability based on consideration of stoichiometry and number of reactive sites of the reactants. $[RuO(pyr)(bpy)_2]^{2+}$ clearly shows the highest k_{sym}^{HAT} for HAT from DHA, while the other complexes react several orders of magnitude slower. This is easily explained by the formation of a strong O-H bond in $[Ru(OH)(pyr)(bpy)_2]^{2+}$. Complex **5^{PF6}**, $[Mn(hfacac)_3]$ and $[Fe(Hbim)_2(bim)]^+$ show comparable rates k_{sym}^{HAT} for DHA oxidation. The low k_{sym}^{HAT} for DHA oxidation by $[V(O)_2(^t\text{Bu}_2\text{bpy})_2]^+$ results from a low O-H bond strength in combination with an unusually low self-exchange rate due to relatively large structural changes upon reduction.[41] In organic compounds, self-exchange rates for HAT processes involving O-H or N-H formation are significantly faster than C-H bond self-exchange rates by a factor of ca. 10^8.[42] The reported k_{sym}^{SE} rates for metal complexes

$[Fe(Hbim)_2(bim)]^+$ and $[RuO(pyr)(bpy)_2]^{2+}$ show similarly fast exchange as alcohols, suggesting related behavior as in organic compounds, with $[V(O)_2(^tBu_2bpy)_2]^+$ deviating as already discussed. Accordingly, the rate constant of HAA from DHA by $[Fe(Hbim)_2(bim)]^+$ and $[RuO(pyr)(bpy)_2]^{2+}$ shares a LFER with organic reagents and other molecular metal oxides (see Chapter 1.1.4).[42]

Since $\mathbf{5^{PF6}}$ is a rare example of HAA involving C-H bond formation at a metal complex, investigation of the self-exchange rate is of interest, to verify whether the rate follows a different LFER compared to other metal complexes. An estimate of $k_{sym}^{SE}(\mathbf{5^{PF6}})$ can be predicted by the *Marcus* cross relation, taking into account that an error arises from measurement of k_{sym}^{HAT} and ΔG_{HAT} in different solvent (k_{sym}^{HAT} for DHA oxidation by $\mathbf{5^{PF6}}$ is measured in Ph-Cl and thermodynamic data determination is performed in DMSO).

$$k_{sym}^{HAT} = \sqrt{k_{sym}^{SE}(\mathbf{5^{PF6}})\, k_{sym}^{SE}(\mathrm{DHA})\, K_{\mathbf{5PF6},\mathrm{DHA}}\, f} \tag{23}$$

The necessary self-exchange rate of DHA k_{sym}^{SE}(DHA) can be similarly derived from a system in which experimental values for k_{sym}^{HAT}, K, and k_{sym}^{SE} are reported. This is the case for the iron, vanadium and ruthenium based system shown in Table 9, giving a range of $k_{sym}^{SE}(\mathrm{DHA}) \approx 3\cdot10^{-10}$–$1\cdot10^{-11}$ l·mol^{-1}·s^{-1}.[9] Based on this estimation, $k_{sym}^{SE}(\mathbf{5^{PF6}}) \approx 5\cdot10^{2}$–$1.4\cdot10^{4}$ M^{-1}s^{-1} is predicted by eq. (23) using $K_{5,\mathrm{DHA}} = 1.660$ ($\Delta G_{HAT}(\mathrm{DHA})^{DMSO} = 76.0$ kcal·mol^{-1}, $T = 298.15$ K), showing a self-exchange rate in the same order of magnitude as O-H and N-H bonds and therefore dramatically faster compared to organic C-H bonds.[4]

To investigate the viability of the predicted rate $k_{sym}^{SE}(\mathbf{5^{PF6}})$, chemical exchange between $\mathbf{5^{PF6}}$ and $\mathbf{4^{BF4}}$ was examined NMR spectroscopically. Upon addition of $\mathbf{5^{PF6}}$ to a 5.7 mM solution of $\mathbf{4^{BF4}}$ in Ph-Cl-d_5, broadening of the ^{1}H NMR resonances of $\mathbf{4^{BF4}}$ is observed as shown in Figure 25b, while a neglectable change is observed in the solvent signals. Even though the effect can be observed in all 5 signals of $\mathbf{4^{BF4}}$, the extend differs strongly between the signals as will be discussed later on. Aside from the influence on the full width at half maximum (FWHM, W), the ^{1}H NMR resonances of $\mathbf{4^{BF4}}$ show a variation of shift $\Delta\delta$ upon addition of $\mathbf{5^{PF6}}$. This is important to note, since chemical exchange in NMR spectroscopy is commonly categorized by the ratio of the first-order exchange rate constant k_{obs}^{SE} and the difference in resonance frequency $\Delta\upsilon$ of the involved transitions. A broadened signal at the same shift as in an authentic sample indicates slow exchange ($k_{obs}^{SE} << |\Delta\upsilon|$), while an average signal according to the weighted chemical shifts of the exchanging substances indicates fast exchange ($k_{obs}^{SE} >> |\Delta\upsilon|$) and two broadened signals which are

[9] *Mayer* and coworkers repeatedly report a value of $k_{sym}^{SE}(\mathrm{DHA}) \approx 5\cdot10^{-11}$ M^{-1}·s^{-1}. This value considers only the reported data on DHA oxidation by $[Fe(Hbim)_2(bim)]^+$, further using the rate constant k_{sym}^{HAT} at $T = 303.15$ K instead of $T = 298.15$ K).[369]

shifted towards each other are observed in the intermediate exchange ($k_{obs}^{SE} \approx |\Delta\upsilon|$) which results in coalescence, ultimately.

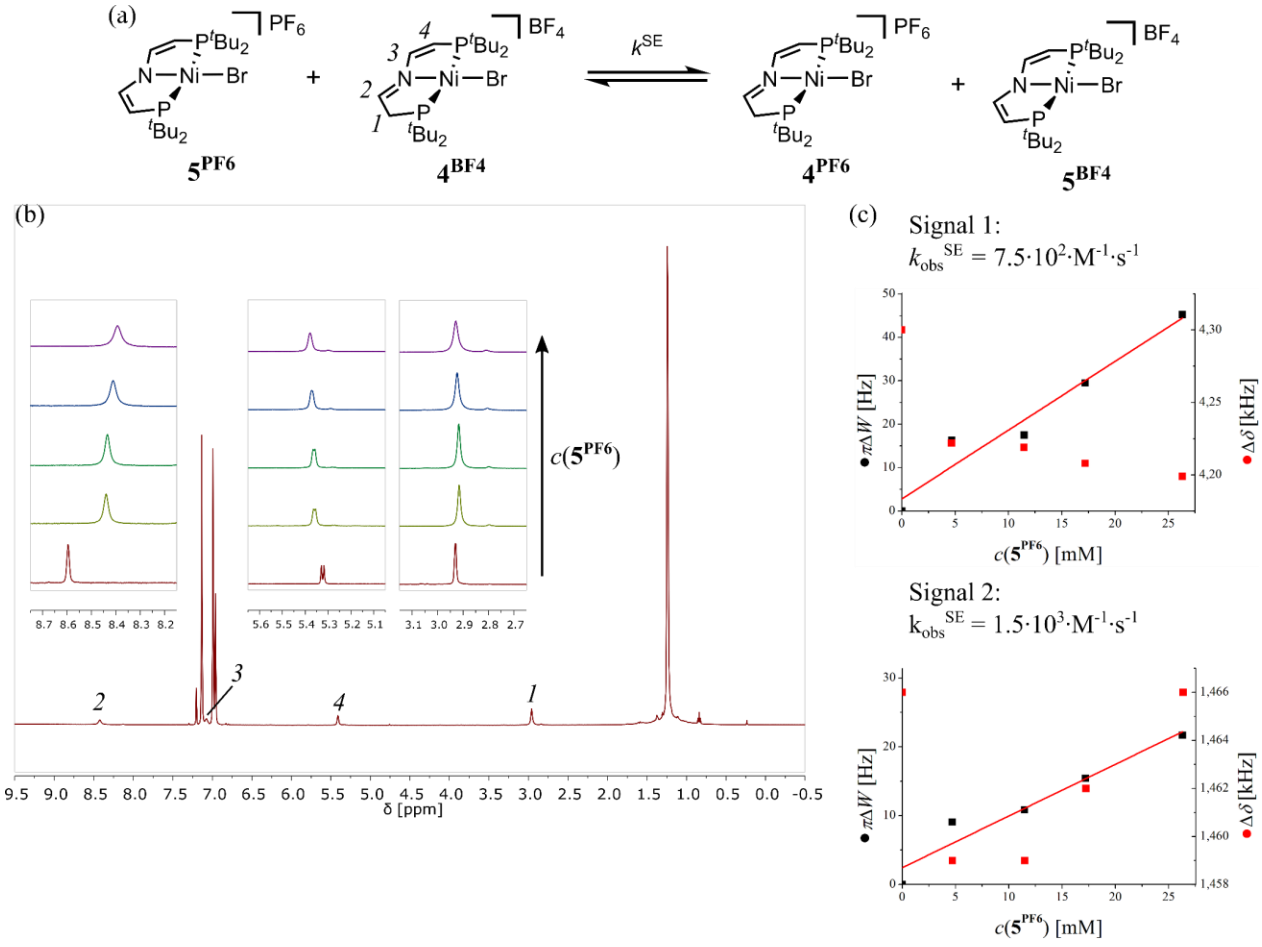

Figure 25: (a) Self-exchange reaction of $\mathbf{5}^{\mathbf{PF6}}$ and $\mathbf{4}^{\mathbf{BF4}}$. (b) ^{1}H NMR spectra of titration of $\mathbf{4}^{\mathbf{BF4}}$ with $\mathbf{5}^{\mathbf{PF6}}$ in Ph-Cl-d_5. (c) Plot of $\pi\Delta W$ *vs* $c(\mathbf{5}^{\mathbf{PF6}})$ for self-exchange rate determination.

In the ^{1}H NMR spectrum of $\mathbf{5}^{\mathbf{PF6}}$ only one peak is visible, most likely being the ^{t}Bu resonance due to its high intensity (see Figure 11a for authentic sample). Therefore, $\Delta\upsilon$ can only be determined for the ^{t}Bu resonances experimentally ($\Delta\upsilon_{tBu} \approx 4.5\cdot10^3$ Hz), showing that the observed change in the chemical shift $\Delta\delta \approx 2$ Hz is negligible in this case. Since interconversion of $\mathbf{5}^{\mathbf{PF6}}$ and $\mathbf{4}^{\mathbf{BF4}}$ further results in a change of symmetry from C_{2v} to C_S, coalescence would result in overlap of resonances *1* and *4* as well as *2* and *3*, respectively, referring to the annotation in Figure 25a. Since the change in shift of the measured ^{1}H NMR resonances over the course of titration is small compared to $\Delta\upsilon$, recorded spectra are measured at conditions far from $k_{obs}^{SE} = k_c$ (k_c: coalescence rate constant) for all resonances. Finally, line broadening increases linearly with $c(\mathbf{5}^{\mathbf{PF6}})$ for all signals, suggesting a self-exchange reaction as origin of this effect, while $\Delta\delta$ shows no uniform behavior (Figure 25c). *Mayer* contributed a similar effect in osmium anilides to cation anion interactions.[56]

Considering ion-pair formation in Ph-Cl and the different anions in $\mathbf{5}^{\mathbf{PF6}}$ and $\mathbf{4}^{\mathbf{BF4}}$, a similar effect might be present in this case.[100]

Line shape analysis of the spectra shown in Figure 25b gives ΔW for the individual resonances. Signal *3* is not analyzed due to strong overlap with the solvent signal. Plotting $\pi\Delta W$ over $c(\mathbf{5}^{\mathbf{PF6}})$ gives the second-order self-exchange rate constants $k^{SE}(\mathbf{5}^{\mathbf{PF6}})$ by eq. (24), assuming slow self-exchange as discussed earlier (Table 10).

$$k^{SE}(\mathbf{5}^{\mathbf{PF6}}) = \pi\Delta W \cdot c(\mathbf{5}^{\mathbf{PF6}})^{-1} \quad (24)$$

Table 10: Self-exchange rates k^{SE} in $M^{-1}\cdot s^{-1}$ for titration of $\mathbf{4}^{\mathbf{BF4}}$ with $\mathbf{5}^{\mathbf{PF6}}$ derived by NMR spectroscopic line shape analysis.

	1[a]	*2*[a]	*4*[a]	^{t}Bu	$\bar{x}$
$k^{SE}(\mathbf{5}^{\mathbf{PF6}})$ [b]	$(7.5\pm1.1)\cdot10^2$	$(1.5\pm0.4)\cdot10^3$	$(5.7\pm1.2)\cdot10^2$	$(2.1\pm0.4)\cdot10^2$/ $(2.7\pm0.5)\cdot10^2$	$(6.6\pm5.2)\cdot10^2$
$k^{SE}_{sym}(\mathbf{5}^{\mathbf{PF6}})$ [b]	$(1.9\pm0.3)\cdot10^2$	$(3.8\pm1.0)\cdot10^2$	$(1.4\pm0.3)\cdot10^2$	$(5.3\pm1.0)\cdot10^1$/ $(6.7\pm1.2)\cdot10^1$	$(1.7\pm1.3)\cdot10^2$

[a]referring to the annotation of Figure 25b. [b] in $M^{-1}\cdot s^{-1}$.

Again, consideration of statistic correction gives $k^{SE}_{sym}(\mathbf{5}^{\mathbf{PF6}}) = (1.7\pm1.3)\cdot10^2\ M^{-1}s^{-1}$. It is noteworthy that the values are much closer within the positions of $\mathbf{4}^{\mathbf{BF4}}$ which become equivalent upon PCET to $\mathbf{5}^{\mathbf{PF6}}$, so signals *1* and *4* as well as the two sets of ^{t}Bu signals.

Comparison of the experimentally derived $k^{SE}_{sym}(\mathbf{5}^{\mathbf{PF6}})$ and the value predicted by *Marcus* cross relation is difficult, since ill-defined k^{SE}_{sym}(DHA) gives rise to a huge error in the predicted value. Upon assuming $k^{SE}_{sym}(DHA) \approx 5\cdot10^{-11}\ M^{-1}s^{-1}$ which is commonly taken in the literature and lies in the middle of the range suggested earlier, the cross relation predicts $k^{SE}_{sym}(\mathbf{5}^{\mathbf{PF6}}) = 2.9\cdot10^3\ M^{-1}\cdot s^{-1}$ which deviates by one order of magnitude from the value derived by ^{1}H NMR spectroscopy. This error lies within the precision of the *Marcus* cross relation in predicting hydrogen transfer reactions, which is 1–2 orders of magnitude in k^{HAT}_{sym} and therefore 2–4 orders of magnitude in k^{SE}_{sym} following eq. (23).[44] Accordingly, the MCR predicts $k^{HAT}_{sym} = (1.2\pm1.0)\cdot10^{-4}\ M^{-1}\cdot s^{-1}$ for DHA oxidation by $\mathbf{5}^{\mathbf{PF6}}$ based on experimental $k^{SE}_{sym}(\mathbf{5}^{\mathbf{PF6}}) = (1.7\pm1.3)\cdot10^2\ M^{-1}\cdot s^{-1}$ and $k^{SE}_{sym}(DHA) \approx 5\cdot10^{-11}\ M^{-1}\cdot s^{-1}$. Correcting for solvent effects is not performed, however has been shown to improve the precision of the model.[43]

As discussed in Chapter 1.1.4, the formation of a preequilibrium of the reactants can alter the driving force of the CPET reaction. While support for the formation of a potential preequilibrium cannot be taken from

kinetic analysis of DHA oxidation by $\mathbf{5}^{\mathbf{PF6}}$ it cannot be ruled out in principle. The MCR further does not account for radical philicity of the reactants. Benzyl radicals are in general considered nucleophilic radicals whereas the oxidation potential E^0(**3**) suggests electrophilicity of $\mathbf{5}^{\mathbf{PF6}}$.[101] Accordingly, an acceleration of the reaction from philicity matching is expected which is not accounted for in the MCR and is in agreement with *underestimation* of the experimental rate by MCR. Further analysis by measurement of kinetic isotope effects for C-H deuteration was not performed.[102]

Summing up, both prediction by MCR and experimental derived rates show that the couple $\mathbf{5}^{\mathbf{X}}/\mathbf{4}^{\mathbf{X}}$ undergoes HAT self-exchange which is close to what is commonly observed for HAT involving N-H/O-H bonds, therefore being orders of magnitude faster than previously described C-H bond centered processes. Work on a slow O-H exchange in $[V(O)_2(t\mathrm{Bu}_2\mathrm{bpy})_2]^+$ has attributed the unusual rate on comparably large electronic reorganization derived by DFT computation, which gives rise to a higher barrier compared to $[Ru(O)(pyrr)(bpy)_2]^+$ as model for well-studied $[RuO(pyr)(bpy)_2]^{2+}$.[56] The change in the electronic situation can be visualized by comparison of the metal oxygen bond in the oxidized and reduced form, which undergoes stronger elongation in case of vanadium (Figure 26). As a result of the electronic structure of $\mathbf{5}^+$ (see Chapter 1.3.2 for detailed discussion), structural changes upon conversion to $\mathbf{4}^+$ are small as compared with these two examples. Therefore, the fast self-exchange rate $k_{\mathrm{sym}}^{\mathrm{SE}}(\mathbf{5}^{\mathbf{PF6}})$ is further attributed to small changes in the electronic and structural parameters upon reduction to $\mathbf{4}^{\mathbf{PF6}}$ by PCET.

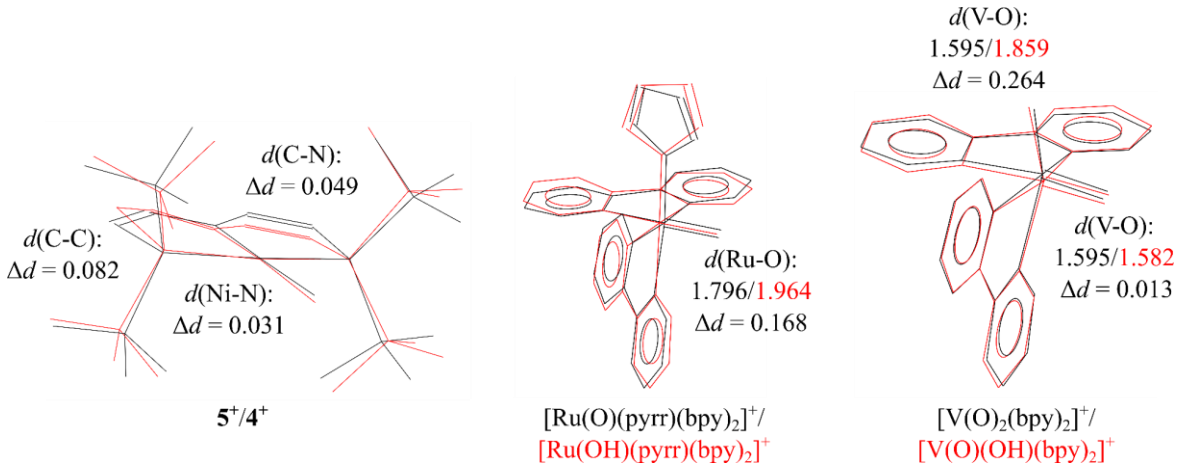

Figure 26: Comparison of bond metrics of oxidized and reduced form of PCET reagents (geometric parameters on $\mathbf{4}^+$ and $\mathbf{5}^+$ are obtained by X-ray crystallographic data as can be seen in Chapter 1.3.1. Data on V and Ru complexes is taken from ref. [41]).

1.4 Effect of Ligand Substitution on Pincer C-H Bond Strength

1.4.1. Effect of Substitution of Bromide for Acetonitrile on Pincer C-H Bond Strength

The reactivity of $\mathbf{5^{PF6}}$ shows that the ^{tBu}P=N=P pincer ligand can be utilized for benzylic C-H activation. However, a fast reaction can just be observed by working in the presence of a large excess of strongly activated substrate DHA. Increasing the C-H bond strength of the nickel pincer platform is necessary to activate strong benzylic C-H bonds in a more effective fashion. The effect of ligand substitution on the thermodynamics of pincer ligand centered PCET will be discussed in the following.

It is difficult to exchange the bromide ligand in ^{tBu}P=N=P coordinated complex **3**, but the reaction of **2** with $NaBF_4$ or NaBArF (BArF = $\{(3,5\text{-}(CF_3)_2C_6H_3)_4B\}^-$) in acetonitrile gives the cationic compounds [Ni(NCMe)(^{tBu}PNP)]X ($\mathbf{6^X}$, X = BF_4, BArF) (Scheme 14). The higher reactivity of the bromide ligand in **2** compared to **3** is attributed to the stronger amido donor in *trans* position.

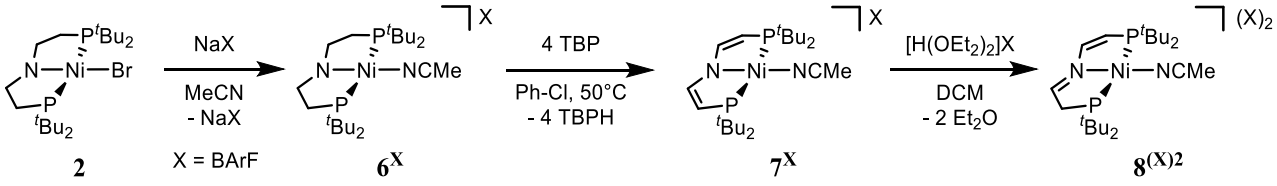

Scheme 14: Synthesis of nickel pincer acetonitrile complexes.

Oxidation of the ethylene backbone in $\mathbf{6^X}$ can again be accomplished using 2,4,6-tri-*tert*-butylphenoxyl giving [Ni(NCMe)(^{tBu}P=N=P)]X ($\mathbf{7^X}$, X = BF_4, BArF). However, the reaction takes two days at T = 50°C to give complete conversion. To provide sufficient stability of the phenoxyl radical under these conditions, chlorobenzene has to be used as solvent.

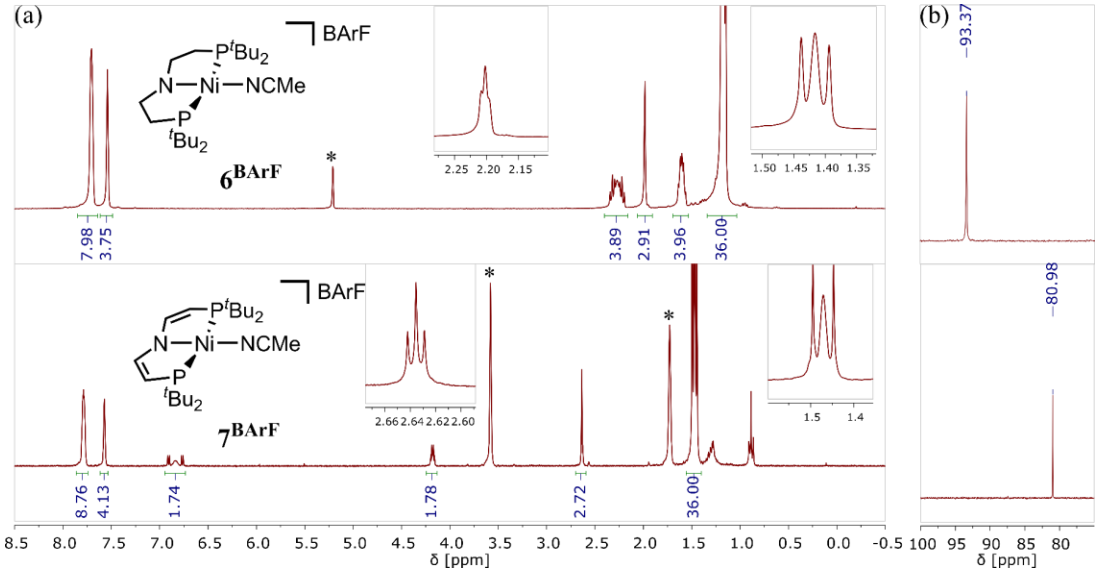

Figure 27: (a) ^{1}H NMR and (b) ^{31}P{^{1}H} NMR spectra of compounds $\mathbf{6}^{\mathbf{BArF}}$ and $\mathbf{7}^{\mathbf{BArF}}$ (*denotes the solvent signal).

The proposed structure of both compounds $\mathbf{6}^{\mathbf{BArF}}$ and $\mathbf{7}^{\mathbf{BArF}}$ can be clearly assigned by NMR spectroscopy (Figure 27). The MeCN ligand in $\mathbf{6}^{\mathbf{BArF}}$ resonates at δ = 2.20 ppm in the ^{1}H NMR spectrum with a $^{5}J_{HP}$ coupling of 2.0 Hz and at δ = 2.64 ppm with $^{5}J_{HP}$ = 2.0 Hz in $\mathbf{7}^{\mathbf{BArF}}$. Furthermore, the BArF anion can be identified by two signals in the aromatic region.

X-ray diffraction analysis of $\mathbf{6}^{\mathbf{BArF}}$ shows two complete molecules in the asymmetric unit containing strongly disordered CF_3 group in the BArF anion (Figure 28). Therefore, refinement of three domains with EADP and SADI constrains is necessary to give acceptable ellipsoids. The structural parameters of $\mathbf{6}^{\mathbf{BArF}}$ will be discussed as average of both molecules in the asymmetric unit, since they are almost identical. Comparison of the bond metrics with crystallographic data of **2** shows a nearly identical {Ni($^{t\mathrm{Bu}}$PNP)} fragment with a shortened Ni-amido distance ($\mathbf{6}^{\mathbf{BArF}}$: d(Ni-N_{amido}) = 1.8535 Å; **2**: d(Ni-N_{amido}) = 1.8747(17) Å) due to a less strongly donating ligand in *trans* position. Similar behaviour is observed upon comparing structural details of $\mathbf{7}^{\mathbf{BF4}}$ with **3** ($\mathbf{7}^{\mathbf{BF4}}$: d(Ni-N_{amido}) = 1.8709(13) Å; **3**: d(Ni-N_{amido}) = 1.8814(15) Å). The metal nitrile distance in both compounds is nearly identical to the metal amido distance ($\mathbf{6}^{\mathbf{BArF}}$: d(Ni-N_{MeCN}) = 1.863 Å, $\mathbf{7}^{\mathbf{BF4}}$: d(Ni-N_{MeCN}) = 1.8456(14) Å), indicating no significant π donation from the pincer ligand. Minor differences in π backbonding between both complexes is suggested by similar structural paramters of the MeCN moiety and identical IR frequencies of $\tilde{\nu}$(C-N) = 2360 cm^{-1} ($\mathbf{6}^{\mathbf{BArF}}$: d(C-N_{MeCN}) = 1.141 Å, α(Ni-N-C) = 177.0°; $\mathbf{7}^{\mathbf{BF4}}$: d(C-N_{MeCN}) = 1.138(2) Å, α(Ni-N-C) = 178.80°).

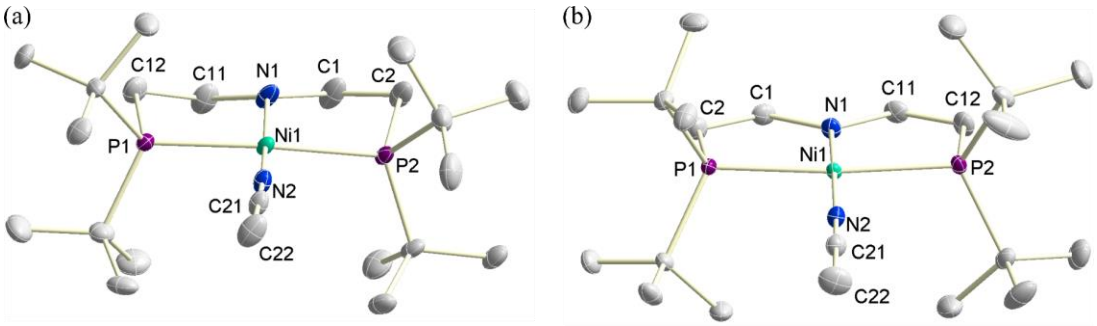

Figure 28: Solid state structure of $\mathbf{6}^{\mathbf{BF4}}$ and $\mathbf{7}^{\mathbf{BArF}}$ determined by X-ray diffraction. Thermal ellipsoids are drawn at the 50% probability level. Anions, additional complex molecules of the asymmetric unit and hydrogen atoms are omitted for clarity.

Compound $\mathbf{7}^{\mathbf{BArF}}$ can be selectively protonated using $[H(OEt_2)_2]BArF$ in dichloromethane to yield dicationic $[Ni(NCMe)(^{tBu}P{=}N{=}P^{H})](BArF)_2$ ($\mathbf{8}^{\mathbf{(BArF)2}}$). The NMR spectroscopic signature of $\mathbf{8}^{\mathbf{(BArF)2}}$ qualitatively resembles the data obtained for $\mathbf{4}^{\mathbf{BF4}}$ with two downfield shifted resonances in the $^{31}P\{^1H\}$ NMR spectrum at δ = 87.3 ppm and δ = 84.7 ppm and a smaller *trans* $^2J_{PP}$ coupling constant of 215.8 Hz (Figure 29b). The presence of two BArF anions is confirmed by integration in the ^1H NMR spectrum (Figure 29a).

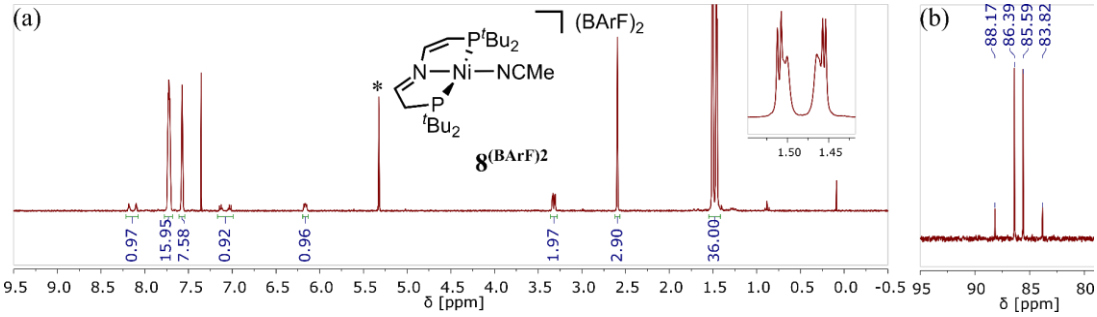

Figure 29: (a) ^1H NMR and (b) $^{31}P\{^1H\}$ NMR spectra of compound $\mathbf{8}^{\mathbf{(BArF)2}}$ (*denotes CD_2Cl_2).

Turning to MeCN-d_3 as solvent, the $^{31}P\{^1H\}$ NMR spectroscopic resonance of $\mathbf{8}^{\mathbf{(BArF)2}}$ simplifies to a singlet at δ = 83.4 ppm indicating fast solvent mediated proton exchange. The ^1H NMR spectrum of $\mathbf{8}^{\mathbf{(BArF)2}}$ in MeCN-d_3 shows four resonances corresponding to the pincer ligand's backbone. However, the multiplicity of the signals shows the higher order coupling pattern typically observed for C_{2v} symmetric complexes due to coupling to two chemically identical, however magnetically inequivalent phosphorus atoms (Figure 30). Furthermore, a signal corresponding to non-coordinated MeCN is observed in ^1H NMR spectroscopy, suggesting exchange of the acetonitrile ligand in MeCN-d_3 solvent. While the fast proton exchange present in MeCN solution indicates high acidity of $\mathbf{8}^{\mathbf{(BArF)2}}$, the integral ratio in ^1H NMR clearly confirms protonation of the nickel complex. Additionally, no change of the chemical shift δ in $^{31}P\{^1H\}$ NMR spectroscopy can be observed upon variation of $c(\mathbf{8}^{\mathbf{(BArF)2}})$ which would be expected for solvent protonation.

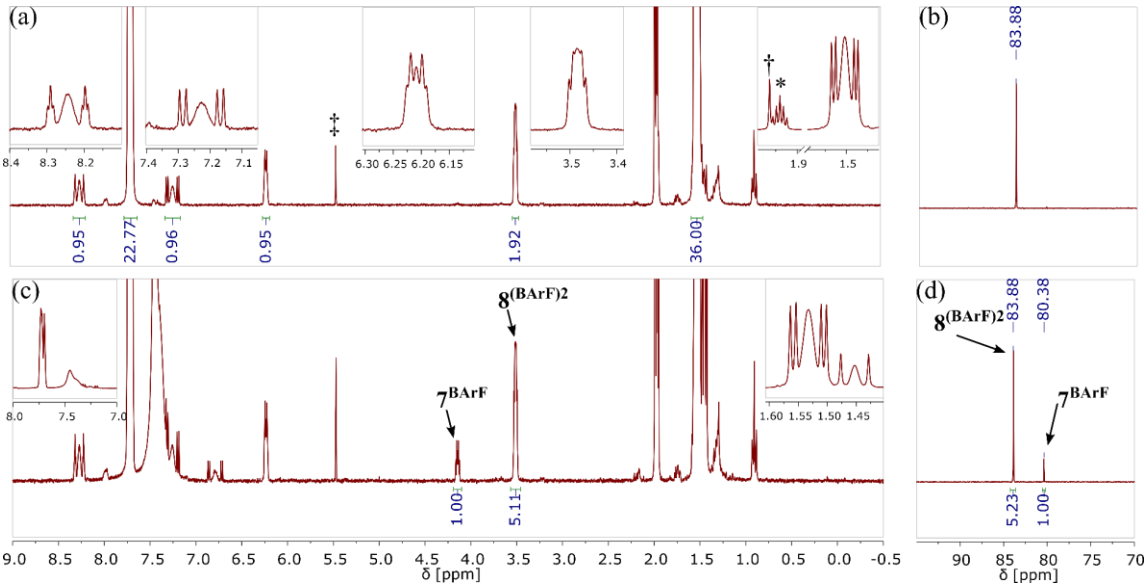

Figure 30: (a) ^{1}H NMR and (b) ^{31}P{^{1}H} NMR spectra of a MeCN-d_3 solution of **8**$^{(BArF)2}$. (c) ^{1}H NMR and (d) ^{31}P{^{1}H} NMR spectra of a MeCN-d_3 solution of **8**$^{(BArF)2}$ in the presence of 1 eq triphenylphosphine (*denotes MeCN-d_3, †denotes MeCN and ‡denotes CH_2Cl_2).

pK_a measurement for **8**$^{(BArF)2}$ in MeCN-d_3 can be performed by titration with a suitable base, as it was performed for **4**^{OTf} in DMSO-d_6 solvent. Addition of equimolar quantities of triphenylphosphine result in partial deprotonation of the complex and the ratio of conjugate acid **8**$^{(BArF)2}$ and base **7**^{BArF} is determined NMR spectroscopically (Figure 30). While the ^{31}P{^{1}H} and ^{1}H NMR spectra are in good agreement, the ratio determined by ^{1}H NMR spectroscopy is taken for determination of pK_a(**8**$^{(BArF)2}$)^{MeCN} according to eq. (25) using literature known pK_a(PPh$_3$)^{MeCN} = 7.61.[103]

$$pK_a(\mathbf{8}^{(BArF)2})^{MeCN} = pK_a(PPh_3)^{MeCN} - \log \frac{c(\mathbf{7}^{BArF})}{c(\mathbf{8}^{(BArF)2})} \quad (25)$$

$$pK_a(\mathbf{8}^{(BArF)2})^{MeCN} = 7.61 - \log \frac{1}{5.11} \quad (26)$$

$$pK_a(\mathbf{8}^{(BArF)2})^{MeCN} = 8.32 \quad (27)$$

Parker has shown that the pK_a of organic C-H acids in DMSO is about 11 units lower than in MeCN.[96] While this comparison does not include examples of different charge, it is utilized here for comparison of pK_a(**4**^{OTf})^{DMSO} and pK_a(**8**$^{(BArF)2}$)^{MeCN} since **4**^{X} is not a stable compound in acetonitrile solution and **8**$^{(BArF)2}$ is too acidic to allow for pK_a measurement in DMSO. The estimated pK_a(**4**^{OTf})$^{MeCN} \approx 12$ shows the strong effect of substitution of bromide by acetonitrile on the acidity which is lower by approximately 4 units in **8**$^{(BArF)2}$.

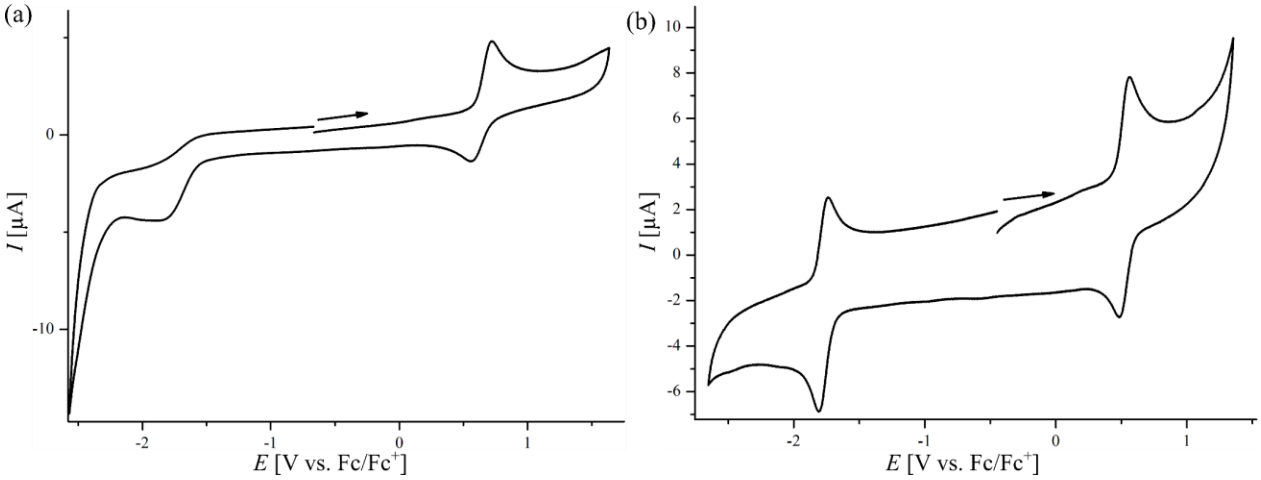

Figure 31: Cyclic voltammetry of 1 mM solutions of $\mathbf{7}^{\mathbf{BArF}}$ in (a) THF at v = 100 mV/s (0.1 M [n-Bu$_4$N]PF$_6$, WE: GC, CE: Pt wire, RE: Ag) and (b) MeCN at v = 100 mV/s (0.1 M [n-Bu$_4$N]PF$_6$, WE: GC, CE: Pt wire, RE: Ag wire). Both voltammograms are referenced to Fc$^+$/Fc.

To determine the methylene BDFE of $\mathbf{8}^{\mathbf{(BArF)2}}$, cyclic voltammetry of conjugate base $\mathbf{7}^{\mathbf{BArF}}$ was conducted (Figure 31). In THF, at fast scan rates a quasireversible oxidation process at $E^{1/2}(\mathbf{7}^{\mathbf{BArF}})^{\mathrm{THF}}$ = +0.66 V *vs.* Fc$^+$/Fc is observed which is shifted anodically by ΔE = 0.53 V as compared with the Ni$^{\mathrm{III}}$/Ni$^{\mathrm{II}}$ wave in the cyclic voltammetry of **3** measured under the same conditions. This big shift in potential is most likely mainly influenced by the cationic charge of $\mathbf{7}^{\mathbf{BArF}}$, while a small contribution from the different donor strength of acetonitrile and bromide is expected. Turning to MeCN solvent for BDFE determination, the oxidation process is observed at a more cathodic potential.

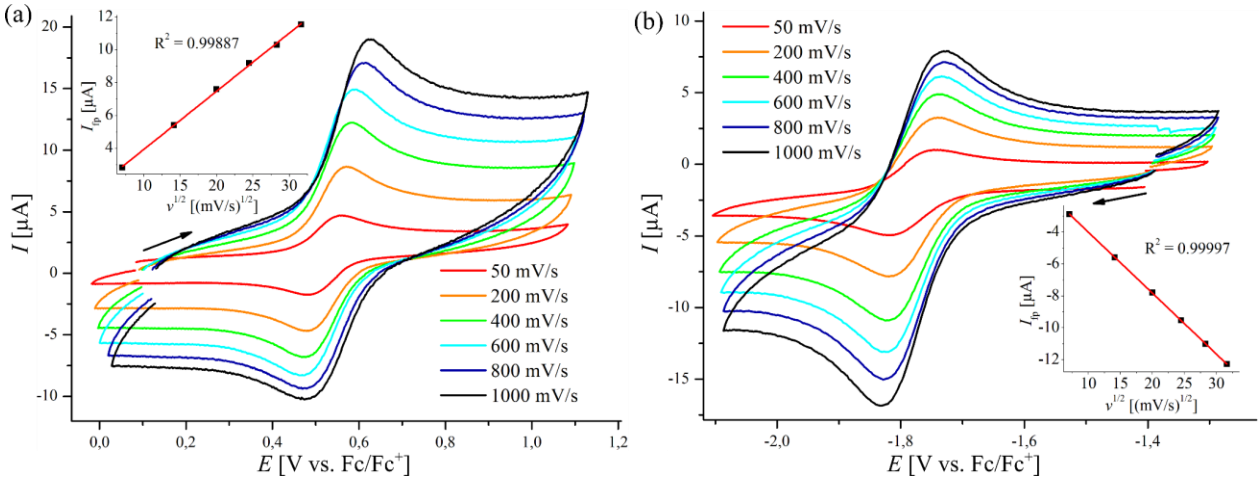

Figure 32: Cyclic voltammetry of a 1 mM solution of $\mathbf{7}^{\mathbf{BArF}}$ in MeCN referenced to Fc$^+$/Fc (0.1 M [n-Bu$_4$N]PF$_6$, WE: GC, CE: Pt wire, RE: Ag wire). Measurement of the initial (a) oxidative and (b) reductive redox process at different scan rates with the plot of I_{fp} *vs.* $v^{1/2}$ shown in the insert.

At negative potential in THF, a completely irreversible reduction process is observed at E^p =-1.9 V (v = 100 mV/s). In acetonitrile solvent this peak gains a significant return peak and accordingly this process

is attributed to loss of the MeCN ligand *via* an *EC* mechanism, since the large excess of MeCN shifts the equilibrium of the chemical reaction.

Table 11: Peak analysis of the initial oxidative and reductive responses of $\mathbf{7}^{\mathbf{BArF}}$ in cyclic voltammetry.

$\mathbf{7}^{\mathbf{BArF}}$	v [mV/s]	$E^{1/2}$ [V]	i_{rp} / i_{fp}	ΔE^{p} [a]	$\mathbf{7}^{\mathbf{BArF}}$	v [mV/s]	$E^{1/2}$ [V]	i_{rp} / i_{fp}	ΔE^{p} [a]
	50	0.522	0.88	0.86		50	-1.779	0.78	0.86
	200	0.525	0.81	1.12		200	-1.779	0.77	0.97
	400	0.529	0.74	1.21		400	-1.780	0.76	0.87
	600	0.530	0.70	1.35		600	-1.779	0.74	1.00
	800	0.542	0.66	1.35		800	-1.779	0.72	0.93
	1000	0.551	0.61	1.35		1000	-1.779	0.70	0.92

[a]Given as ratio between the analyte and the internal reference.

Closer investigation of the oxidation process reveals fast electron transfer at all scan rates investigated as indicated by a linear i_{fp} vs. $v^{1/2}$ plot (Figure 32a, Table 11). While the half wave potential shifts anodically upon increasing v, the peak current ratio i_{rp} / i_{fp} decreases. Both observed features are indicative of reversible electron transfer followed by a first-order reversible chemical reaction at intermediate kinetics as stated by *Zanello* (eq. (28), k_f: forward reaction rate, k_r: reverse reaction rate).[104]

$$k_f + k_r \approx \frac{n \cdot F \cdot v}{RT} \tag{28}$$

Here, upon increasing the scan rate the observed $E^{1/2}$ shifts towards E^0 due to less effective chemical follow-up reactivity, which at the same time leads to a lower return peak current as a consequence of less effective equilibration of the chemical reaction product. While determination of an exact $E^0(\mathbf{7}^{\mathbf{BArF}})^{MeCN}$ is not possible under these conditions, $E^{1/2}(\mathbf{7}^{\mathbf{BArF}})^{MeCN}$ = 0.55 V determined at the highest measured scan rate serves as lower limit for $E^0(\mathbf{7}^{\mathbf{BArF}})^{MeCN}$.

The Ni^{II}/Ni^{I} reduction process shows similar characteristics as the oxidation event (Figure 32b, Table 11). Again, i_{rp} / i_{fp} decreases upon increasing v, indicating a first-order reversible chemical reaction following a reversible electron transfer. However, the rate constant of the reversible chemical follow-up is smaller compared to the oxidation process, since i_{rp} / i_{fp} drops to a smaller extent and no variation of $E^{1/2}(\mathbf{7}^{\mathbf{BArF}})^{MeCN}$ = -1.78 V can be observed.

While no experimental investigation of the oxidation and reduction of $\mathbf{7}^{\mathbf{BArF}}$ was performed, reversible acetonitrile dissociation seems to be a likely chemical reaction upon reduction given the occupation of antibonding $d_{x^2-y^2}$ as discussed for reduction of bromide $\mathbf{4}^{\mathbf{BF4}}$ (see Chapter 1.3.3). Furthermore, *Lee* has shown reversible coordination of a T-shaped pincer Ni^{I} complex by weak π acceptor pyridine.[105] The

chemical reversible process following the Ni^{III}/Ni^{II} redox wave might be attributed to additional coordination of acetonitrile, as similar reactivity was recently reported for nickel pincer complexes upon oxidation by *Zargarian*.[106]

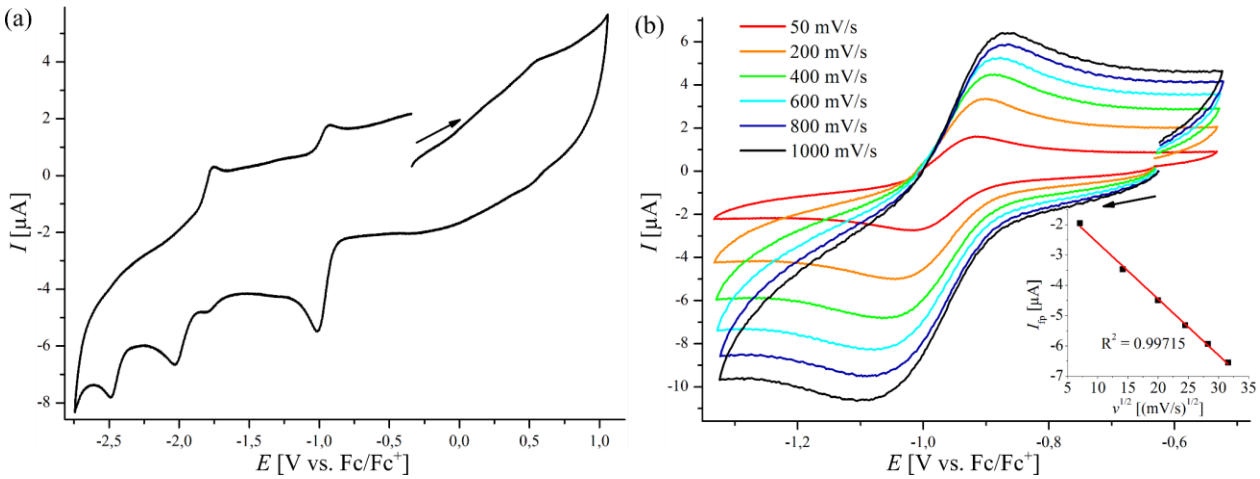

Figure 33: Cyclic voltammetry of a 1 mM solution of $\mathbf{8}^{(BArF)2}$ in MeCN referenced to Fc^+/Fc (0.1 M [*n*-Bu_4N]PF_6, WE: GC, CE: Pt wire, RE: Ag wire). (a) Full range scan at v = 100 mV/s and (b) scan of the initial oxidation event at different scan rates with the plot of I_{fp} *vs.* $v^{1/2}$ shown in the insert.

Table 12: Peak analysis of the initial reductive responses of $\mathbf{8}^{(BArF)2}$ in cyclic voltammetry.

$\mathbf{8}^{(BArF)2}$	v [mV/s]	$E^{1/2}$ [V]	i_{rp} / i_{fp}	$\Delta E^{p\,a}$
	50[a]	-0.966	0.97	1.36
	200	-0.972	0.90	1.44
	400	-0.973	0.83	1.54
	600	-0.979	0.75	1.39
	800	-0.979	0.70	1.47
	1000	-0.981	0.71	1.47

[a]Given as ratio between the analyte and the internal reference.

Turning to protonated $\mathbf{8}^{(BArF)2}$, cyclic voltammetry in acetonitrile solvent shows no Ni^{III}/Ni^{II} oxidation event, which is attributed to the twofold cationic charge of $\mathbf{8}^{(BArF)2}$ (Figure 33). Upon changing to cathodic potential, several reduction events are present and investigation of the initial reduction at different scan rates v reveals similar behavior as is observed for $\mathbf{7}^{BArF}$. A cathodic shift and a decrease in the peak current ratio i_{rp} / i_{fp} shows that a reversible electron transfer followed by a first-order reversible chemical reaction is present (Table 12). Loss of acetonitrile seems likely as chemical follow-up reaction after electron transfer, as suggested in case of $\mathbf{7}^{BArF}$. Again, the observed $E^{1/2}(\mathbf{8}^{(BArF)2})^{MeCN}$ = -0.98 V at the highest scan rate v = 1000 mV/s serves as approximation of $E^0(\mathbf{8}^{(BArF)2})^{MeCN}$.

Even though the approximation of $E^0(\mathbf{7}^{\mathbf{BArF}})^{MeCN}$ and $E^0(\mathbf{8}^{\mathbf{(BArF)2}})^{MeCN}$ will introduce an error in the determination of $\Delta G_{HAT}(\mathbf{8}^{\mathbf{(BArF)2}})^{MeCN}$, the extent of this error is small considering $\Delta\Delta G_{HAT}$= 0.23 kcal·mol^{-1} upon variation of ΔE^0 = 10 mV, and an observed variation of the half wave potential $\Delta E^{1/2}(\mathbf{7}^{\mathbf{BArF}})^{MeCN}$ = 29 mV and $\Delta E^{1/2}(\mathbf{8}^{\mathbf{(BArF)2}})^{MeCN}$ = 15 mV over the investigated scan rates. Importantly, the determined half wave potentials $E^{1/2}(\mathbf{7}^{\mathbf{BArF}})^{MeCN}$ = 0.55 V and $E^{1/2}(\mathbf{8}^{\mathbf{(BArF)2}})^{MeCN}$ = -0.98 V serve as lower and upper limit of E^0, respectively, since the chemical follow-up reaction lowers the driving force for electron transfer.[104] Overall, introduction of a cationic charge in the complex by substitution of a bromide for an acetonitrile ligand gives increased acidity and a strong anodic shift of the oxidation and reduction potentials. As a result, the methylene C-H bond $\Delta G_{HAT}(\mathbf{8}^{\mathbf{(BArF)2}})^{MeCN} \geq$ 79.0 kcal·mol^{-1} (C_G^{MeCN} = 54.9 kcal·mol^{-1}) is obtained, being stronger than $\Delta G_{HAT}(\mathbf{4}^{\mathbf{OTf}})^{DMSO}$ = 76.3 kcal·mol^{-1}.[4] Similarly, a strengthening of the C-H bond on the Ni^{I} oxidation state is present giving $\Delta G_{HAT}([Ni(NCMe)(^{tBu}P{=}N{=}P^{H})])^{MeCN} \leq$ 43.7 kcal·mol^{-1} ($\Delta G_{HAT}([NiBr(^{tBu}P{=}N{=}P^{H})])^{MeCN}$ = 40.3 kcal·mol^{-1}).

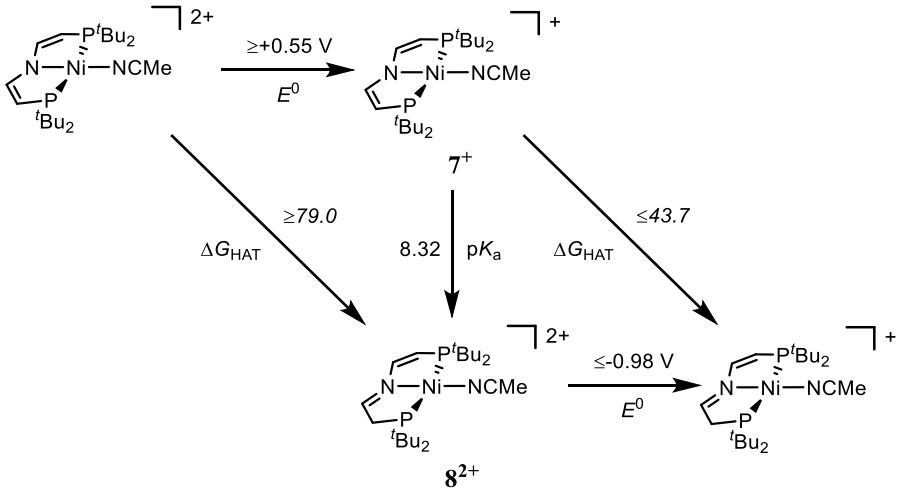

Scheme 15: Interconversion of nickel pincer acetonitrile complexes *via* proton, electron and proton-coupled electron transfer in MeCN solvent. Values written in italics are calculated *via* a square scheme, whereas non-italic values are experimentally determined. Free energies are given in kcal·mol^{-1}.

For closer comparison of the free energies of proton, electron and hydrogen atom transfer steps in the {NiBr(^{tBu}P=N=P)} and {Ni(NCMe)(^{tBu}P=N=P)} platform, the different solvents used for determination of experimental data have to be considered. While conversion of pK_a into different solvents was discussed earlier, ΔG_{HAT} can be converted into different solvents upon considering the difference in solvatization energy $\Delta\Delta G_{solv}$ of the involved species, being the oxidized and reduced compound and the hydrogen radical (eq. (29)).[43]

$$\Delta\Delta G_{HAT} = \Delta\Delta G_{solv}(H) + \Delta\Delta G_{solv}(Ox) - \Delta\Delta G_{solv}(Red) \quad (29)$$

When working in aprotic solvents, the term $\Delta\Delta G_{solv}(Ox)$ can be neglected, while $\Delta\Delta G_{solv}(Red)$ can be obtained by applying *Abraham*'s model for hydrogen bond interactions.[43,45] Here, the solvatization energy ΔG_{solv} of a compound is predicted by empirically determined parameters α_2^H and β_2^H with α_2^H describing the class of compound and β_2^H describing the solvent. Since α_2^H for C-H bonds is assumed to be 0 in general and only C-H bonds are discussed here, $\Delta\Delta G_{HAT}$ simplifies to the different in solvatization free energy of the hydrogen radical, which is $\Delta\Delta G_{solv}(H)$ = -1.1 kcal·mol^{-1} for interconversion of values between DMSO and MeCN solvent.[10][43]

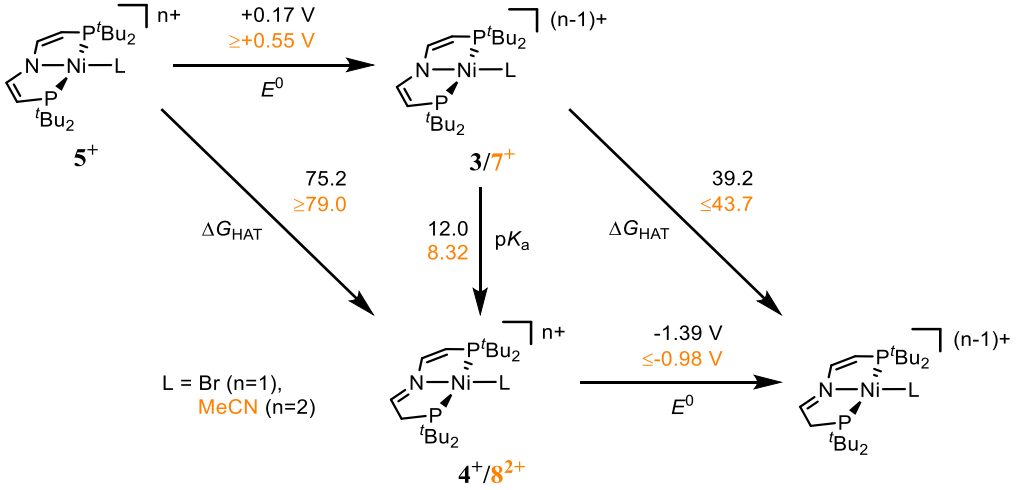

Scheme 16: Comparison of thermodynamic data on {NiBr(^{tBu}P=N=P)} and {Ni(NCMe)(^{tBu}P=N=P)} in MeCN solvent. Free energies are given in kcal·mol^{-1}.

For comparison of {NiBr(^{tBu}P=N=P)} and {Ni(NCMe)(^{tBu}P=N=P)}, MeCN is chosen as solvent, since in this solvent most thermodynamic data is available in the literature. Assuming $\Delta G_{HAT}(\mathbf{4^{OTf}})^{MeCN} = \Delta G_{HAT}(\mathbf{4^{OTf}})^{DMSO} - 1.1$ kcal·mol^{-1} and $pK_a(\mathbf{4^{OTf}})^{MeCN} = 12.0$, the square-schemes shown in Scheme 16 for both platforms can be determined in acetonitrile. While ΔG_{ET} for Ni^{III}/Ni^{II} increases by $\Delta\Delta G_{ET} \geq 8.8$ kcal·mol^{-1} upon changing the bromide to an acetonitrile ligand, ΔG_{PT} decreases by $\Delta\Delta G_{PT} = 5.0$ kcal·mol^{-1}. Both effects compensate each other to a large amount and in sum an increase of $\Delta\Delta G_{HAT} \geq 3.8$ kcal·mol^{-1} results which should result in more facile C-H bond activation by an acetonitrile coordinated formal Ni^{III} pincer complex. Investigation of such a species was not performed. Turning to Ni^{II}/Ni^{I}, the difference in free energy of electron transfer slightly increases to $\Delta\Delta G_{ET} \geq 9.5$ kcal·mol^{-1} with a constant $\Delta\Delta G_{PT} = 5.0$ kcal·mol^{-1} resulting in a similar difference in C-H bond strength $\Delta\Delta G_{HAT} \leq 4.5$ kcal·mol^{-1} compared to the Ni^{III}/Ni^{II} couple. Changing to acetonitrile solvent has a small impact on the hydricity $\Delta G_{HT}(\mathbf{5^{PF6}})^{MeCN} = 69.2$ kcal·mol^{-1} ($E^0(H/H^-)^{MeCN}$ = -1.13 V[4]). Due to the anodic

[10] While $pK_a(\mathbf{4^{BF}})^{DMSO}$ exceeds reports on the acidity of organic hydrocarbons, there is no general connection of the free energy of proton transfer and hydrogen bonding as stated by *Abraham*.[83,370]

Ni^{III}/Ni^{II} potential in {Ni(NCMe)(^{tBu}P=N=P)}, a higher hydride affinity of $\Delta G_{HT}([Ni(NCMe)(^{tBu}P=N=P)]^{2+})^{MeCN} \geq 82.5$ kcal·mol^{-1} results.

1.4.2. Ligand Induced Proton Reduction by [Ni(^{tBu}P=N=P^{H})]BArF (**10**^{BArF})

In the thermodynamic square scheme for the interconversion of nickel pincer species depicted in Scheme 16 is shown that the methylene C-H bond strength is highly sensitive to the electronic situation. While in the formal Ni^{II} oxidation state $\Delta G_{HAT}(C\text{-}H)^{MeCN}$ is comparably high, upon reduction to Ni^{I} the BDFE decreases. Interested in using the C-H bond for substrate reduction on the Ni^{I} oxidation state, chemical reduction of **4**^{BF4} was performed.

When isolated **4**^{BF4} is reacted with cobaltocene in THF solution, formation of neutral bromide **3** is observed (Scheme 17). Headspace analysis by thermal conductivity detector gas chromatography (TCD-GC) shows H_2 evolution which is in agreement with the homolytic bond strength of H_2 ($\Delta G_{HAT}(H_2)^{MeCN}$ = 102.3 kcal·mol^{-1}[4]) exceeding $2x\Delta G_{HAT}([NiBr(^{tBu}P=N=P^{H})])^{DMSO}$ = 80.3 kcal·mol^{-1}, therefore rendering H_2 formation thermodynamically favorable (Figure 34).

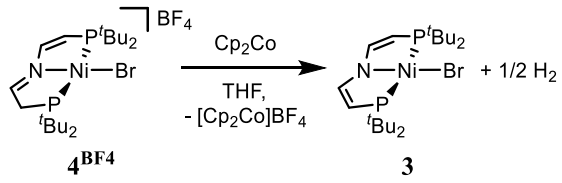

4^{BF4} **3**

Scheme 17: Reduction of **4**^{BF4} with cobaltocene.

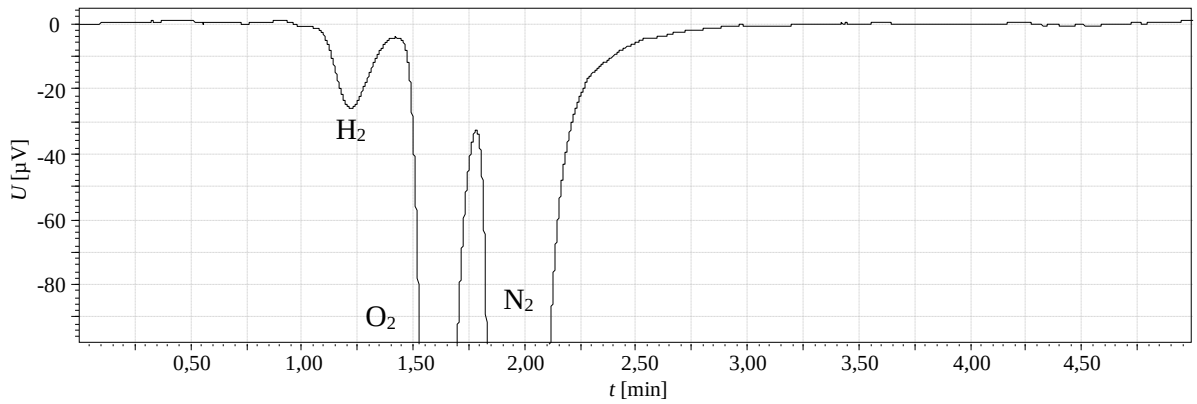

Figure 34: TCD-GC headspace analysis of the reaction of **4**^{BF4} with cobaltocene.

No Ni^{I} intermediates can be observed upon reduction of **4**^{BF4} but closer investigating of such a compound is of interest since electrochemical measurement suggests bromide loss upon reduction of **4**^{BF4} in DMSO rather than proton reduction (Chapter 1.3.3). As shown in Figure 16, parent bromide **3** shows an irreversible Ni^{II}/Ni^{I} reduction event at E^{p} = -2.29 V (v = 100 mV/s). The absence of acidic protons in **3** and the presence

of a halide ligand, suggest electrochemical irreversibility due to halide loss as present in the synthesis of three coordinate T-shaped PNP Ni^{I} complexes recently reported by *Lee* and coworkers.[105]

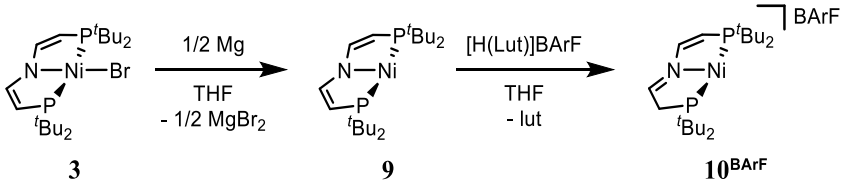

3 **9** **10^{BArF}**

Scheme 18: Synthesis of T-shaped nickel pincer complexes **9** and **10^{BArF}**.

Stirring a THF solution of **3** overnight in the presence of a large excess of magnesium powder results in brightening of the solution from brown to orange. Formation of [Ni(^{tBu}P=N=P)] (**9**) proceeds with high selectivity, the excess of reductant is necessary to provide complete conversion of the starting material, since separation of **3** and **9** is difficult due to similar solubility.

In agreement with the d^9 electronic configuration, **9** shows no resonance in the $^{31}P\{^1H\}$ NMR spectrum, while in the ^1H NMR spectrum a broad resonance centered at $\delta \approx 8$ ppm can be observed. Notably, protonation of **9** with [H(lut)]BArF (lut = 2,6-lutidine) results in clean formation of [Ni(^{tBu}P=N=P^H)]BArF (**10^{BArF}**) as result of pincer ligand protonation with no detectible proton reduction in contrast to the reactivity of **4^{BF4}** upon reduction. The NMR spectroscopic signature of both compounds is similar with additional resonances for the BArF anion in **10^{BArF}** as shown in Figure 35.

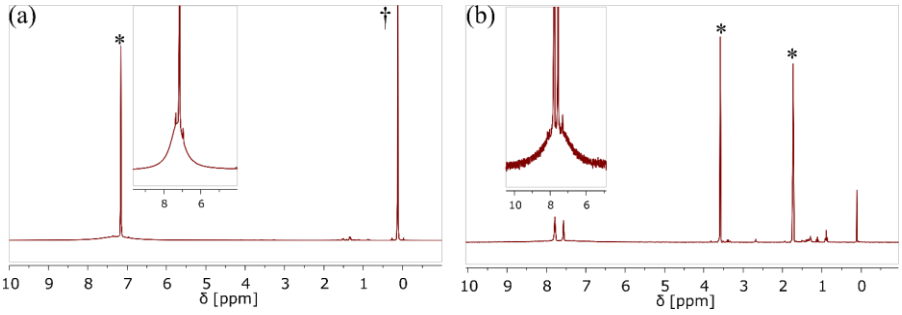

Figure 35: ^1H NMR spectra of (a) **9** in C_6D_6 and (b) **10^{BArF}** in THF-d_8 (*denotes the solvent resonance, †denotes TMS_2O).

The d^9 electronic configuration present in the Ni^{I} oxidation state gives rise to a strong EPR resonance in **9** and **10^{BArF}**.[11] In frozen THF solution at T = 152 K, a rhombic signal can be observed for **9** as shown in Figure 36a (the sample is prepared by photolysis of **12** as described in Chapter 2.4.5). Two g values are observed at similar field B, while the g_z resonance at higher field shows ^{14}N hyperfine coupling. The overall spectrum shows similar features as other T-shaped pincer Ni^{I} complexes reported by *Gade* and *Lee*.[105,107]

[11] EPR analysis was performed by Dr. A. Claudia Stueckl.

EPR analysis of *in situ* generated **10**$^{\mathbf{BArF}}$ by reacting **9** with [H(lut)]BArF in THF results in a rhombic resonance showing strong hyperfine coupling to two inequivalent phosphorus atoms (Figure 36b).

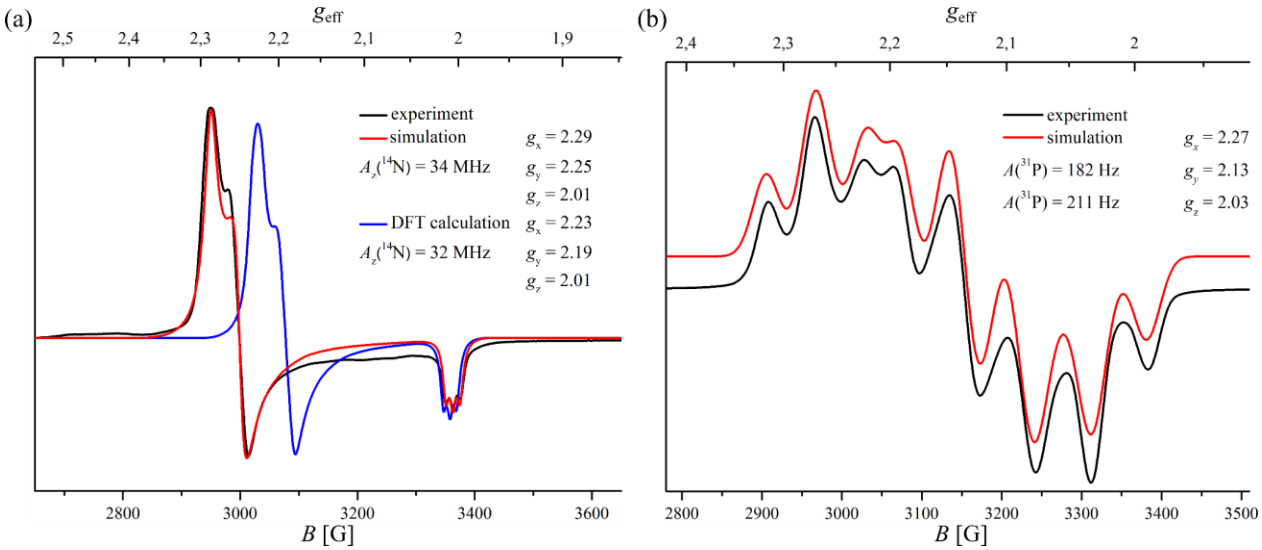

Figure 36: X-band EPR spectra of (a) **9** in frozen THF-d_8 solution (T = 152 K, c(**9**) = 12.1 mM, ν = 9.44016 GHz) and (b) **10**$^{\mathbf{BArF}}$ in frozen THF solution (T = 146 K, c(**10**$^{\mathbf{BArF}}$) = 16.2 mM, ν = 9.422594 GHz).[12]

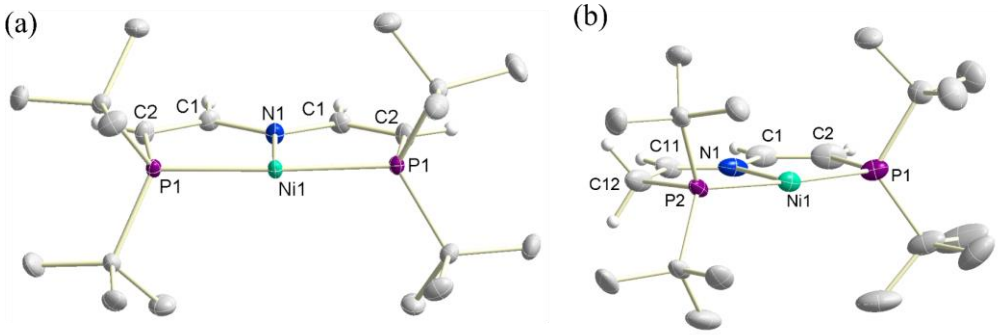

Figure 37: Solid state structure of (a) **9** and (b) **10**$^{\mathbf{BArF}}$ determined by X-ray diffraction. Thermal ellipsoids are drawn at the 50% probability level. The anion of **10**$^{\mathbf{BArF}}$ and selected hydrogen atoms are omitted for clarity.

Table 13: Crystallographic parameters of the solid state structure of **9** and **10**$^{\mathbf{BArF}}$ determined by X-ray diffraction.

[Ni]	d(Ni-N) [Å]	d(Ni-P) [Å]	α(P-Ni-N)	α(P-Ni-P)
9	1.9337(12)	2.2125(3)	86.783(8)	173.565(16)
10$^{\mathbf{BArF}}$	1.9604(18)	2.2107(7)	87.99(7)	174.71(3)
		2.2078(7)	87.16(7)	

[12] c(**9**) is calculated based on NMR spectroscopic determination of conversion of **12** by photolysis.

Crystallographic analysis of **9** and **10^{BArF}** shows the effect of reduction from Ni^{II} to Ni^{I} and the change in the coordination geometry from square-planar to T-shaped on the bond metrics (Table 13). The more electron rich metal center results in an elongated nickel nitrogen distance in both, **9** and **10^{BArF}**. In contrast, the Ni-P bond length in **9** and **10^{BArF}** are close to commonly observed Ni-P distancens in Ni^{II} complexes reported within this thesis. Both compounds clearly have a T-shaped coordinated Ni atom as can be seen in α(P-Ni-N) close to 90° and α(P-Ni-P) close to 180°.

Table 14: Crystallographic parameters of the solid state structure of **9** and **10^{BArF}** determined by X-ray diffraction.

[Ni]	*d*(C=C) [Å]	*d*(C-N) [Å]	*d*(C-C) [Å]	*d*(C=N) [Å]	φ(N-C-C-P) [°]
9	1.3588(15)	1.3586(12)	-	-	-0.91(14)
10^{BArF}	1.368(4)	1.367(3)	1.430(4)	1.327(3)	-1.4(3)
					5.5(3)

The effect in protonation of the pincer ligand results in the expected elongation of one C-C bond (Table 14). Concerning bond lengths, the crystallographic data of **9** and **10^{BArF}** are in good agreement with related complexes discussed earlier. The out-of-plane bending of the protonated pincer arm however is reduced with respect to protonated Ni^{II} bromide **4^{OTf}** (Table 2).

pK_a determination of **10^{BArF}** was performed NMR spectroscopically by titration as it was done for determination of pK_a(**4^{OTf}**) and pK_a(**8$^{(BArF)2}$**). Since **9** and **10^{BArF}** show limited stability in DMSO and MeCN, pK_α determination was performed in THF by measuring pK_{ip} and applying commonly used correction terms to account for ion parring.[108,109]

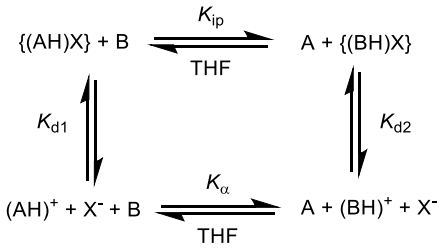

Scheme 19: Acid base equilibrium in THF including contact ion pairs and dissociation equilibria to solvated free ions. Contact ion pairs are denoted using braces.

Due to incomplete solvatization of ion pairs in unpolar solvents, the experimentally determined equilibrium constant K_{eq} describes the equilibrium between ion pairs therefore being denoted K_{ip} as shown in Scheme 19. *Antipin* and coworkers have shown for cryptated lithium salts of C-H acidic compounds, that in 0.01 M THF solution monomeric contact ion pairs account for 98% of the solvated species.[108,110] Therefore K_a can be estimated based on assuming coupled dissociation equilibria of the involved monomeric contact ion pairs

to the solvated ions with the dissociation constant K_d. To account for small deviations from an authentic K_a equilibrium constant, the obtained value is denoted K_α.

$$pK_\alpha(BH^+)^{THF} = pK_\alpha(AH^+)^{THF} - pK_{ip} - \log\frac{K_{d1}}{K_{d2}} \quad (30)$$

$$pK_\alpha(BH^+)^{THF} = pK_\alpha(AH^+)^{THF} - pK_{eq} + \Delta pK_d \quad (31)$$

Work by *Fuoss* shows, that K_d for contact ion pairs can be estimated based on an electrostatic model giving rise to the *Fuoss* eq. (32), where a is the inter-ion distance in centimeters as the sum of ion radii commonly obtained by X-ray diffraction and ε is the dielectric constant of the solvent.[111]

$$K_d = 3000e^b/(4\pi Na^3) \text{ with } b = -e^2/(a\varepsilon kT) \quad (32)$$

Simplification of eq. (32) gives eq. (33) with a given in angstroms.

$$\Delta pK_d = -33.5(1/a_{[(BH)X]} - 1/a_{[(AH)X]}) + 3\log(a_{[(AH)X]}/a_{[(BH)X]}) \quad (33)$$

Since **9** and **10**$^{\mathbf{BArF}}$ feature similar NMR spectroscopic resonances, the effect on the NMR signature of the titration agent triethylamine was monitored. Addition of 1.00 eq of NEt_3 to **10**$^{\mathbf{BArF}}$ in THF-d_8 gives rise to broadened CH_2 and CH_3 resonances of the NEt_3 in the ^{1}H NMR spectrum (Figure 38a).

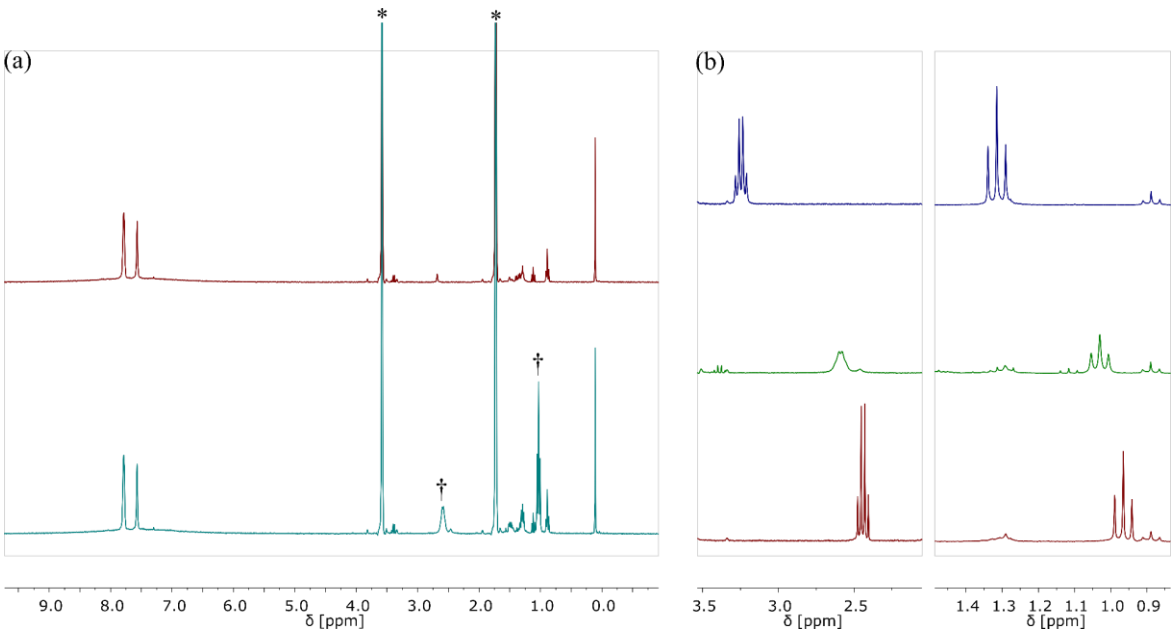

Figure 38: (a) ^{1}H NMR of a THF-d_8 solution of **10**$^{\mathbf{BArF}}$ before (top) and after addition of 1 eq NEt_3 (bottom) (*denotes THF-d_8, †denotes NEt_3). (b) ^{1}H NMR of a THF-d_8 solution of (top) [H(NEt_3)]BArF, (mid) **10**$^{\mathbf{BArF}}$ and 1 eq NEt_3 and (bottom) NEt_3.

Most importantly, the chemical shift of those resonances shows a deviation from the chemical shift for the resonances of pure NEt_3 and $[H(NEt_3)]BArF$ measured at the same concentration, therefore indicating fast equilibrium between the conjugate acid and base (Figure 38b). In fast equilibrium between two species, one resonance at a chemical shift according to the weighted average of the chemical shift of the involved species is observed:

$$\delta(\mathbf{10}^{\mathbf{BArF}}+NEt_3) = \chi(\mathbf{9})\delta([H(NEt_3)]X) + \chi(\mathbf{10}^{\mathbf{X}})\delta(NEt_3) \tag{34}$$

With $\chi(\mathbf{9}) = 0.173$ based on the CH_2 resonance and $\chi(\mathbf{9}) = 0.2$ based on the CH_3 resonance, an average value of $\chi(\mathbf{9}) = 0.187$ results, giving $K_{eq} = 18.9$ according to eq. (35).

$$K_{eq} = \frac{c(\mathbf{10}^{\mathbf{BArF}})^2}{c(\mathbf{9})^2} = \frac{\chi(\mathbf{10}^{\mathbf{BArF}})^2}{\chi(\mathbf{9})^2} = 18.9 \tag{35}$$

To determine ΔpK_d by eq. (33), the inter ion distances a are calculated as sums of the ion radii from X-ray crystallographic analysis. While $r(HNR_3^+) = 2.2$ Å is commonly assumed in literature, $r(\mathbf{10}^+) = 3.9$ Å and $r(BArF^-) = 6.2$ Å is determined based on structural data on $\mathbf{10}^{\mathbf{BArF}}$ taken from X-ray diffraction.[108]

$$\Delta pK_d = -33.5\left(\frac{1}{10.1} - \frac{1}{8.4}\right) + 3\log\left(\frac{8.4}{10.1}\right) = 0.43 \tag{36}$$

Taking $pK_\alpha(NEt_3)^{THF} = 12.5$ from literature, finally $pK_\alpha(\mathbf{10}^{\mathbf{BArF}})^{THF} = 14.4$ is determined:

$$pK_\alpha(\mathbf{10}^{\mathbf{BArF}})^{THF} = pK_\alpha(NEt_3)^{THF} + \log(K_{eq}) + \Delta pK_d \tag{37}$$

$$pK_\alpha(\mathbf{10}^{\mathbf{BArF}})^{THF} = 12.5 + 1.28 + 0.43 = 14.2 \tag{38}$$

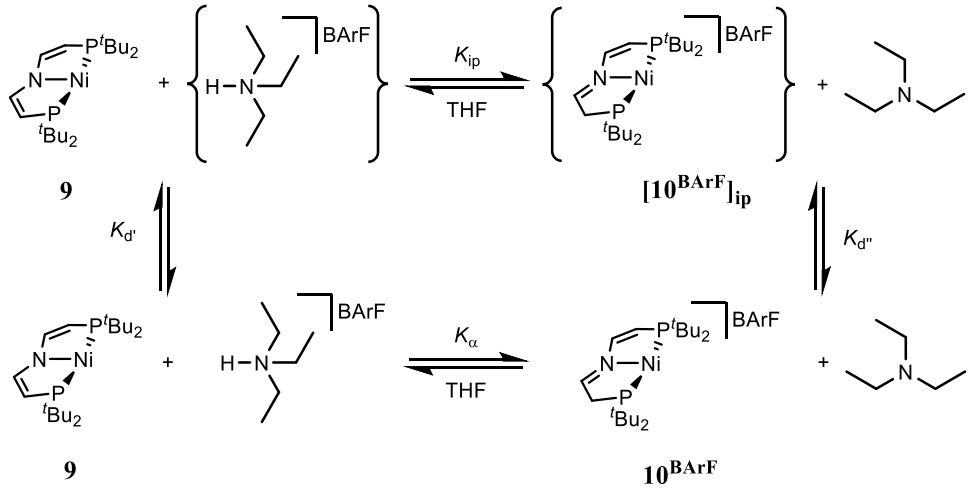

Scheme 20: Acid base equilibrium between **9** and $[H(NEt_3)]BArF$ involving formation of contact ion-pairs.

Using the correlation of pK_a scales in acetonitrile and THF for cationic acids as reported by *Morris* (eq. (39)), this pK_α(**10**$^{\mathbf{BArF}}$)^{THF} can be converted to pK_a(**10**$^{\mathbf{BArF}}$)^{MeCN} = 19.7 to give better comparability with the previously determined acidities of related compounds.[108]

$$pK_a(\mathbf{10}^{\mathbf{BArF}})^{MeCN} = 1.13\ pK_\alpha(\mathbf{10}^{\mathbf{BArF}})^{THF} + 3.7 \qquad (39)$$

In agreement with the reduced metal center, **10**$^{\mathbf{BArF}}$ is the most basic compound in the series of nickel pincer complexes showing pincer ligand centered protonation investigated with respect to their pK_a value.

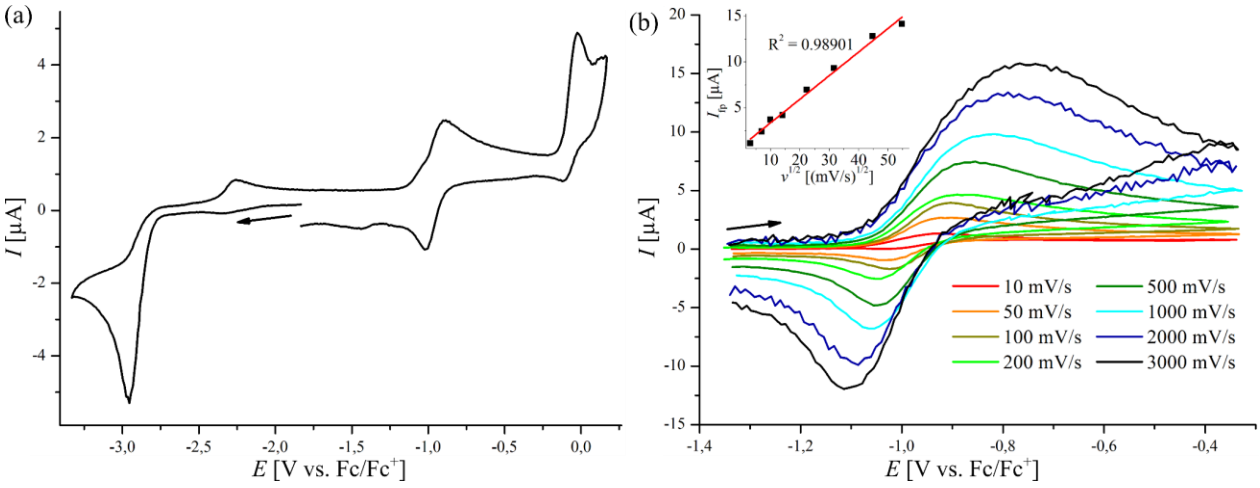

Figure 39: Cyclic voltammetry of a 1 mM solution of **9** in THF referenced to Fc^+/Fc (0.1 M [*n*-Bu_4N]PF_6, WE: GC, CE: Pt wire, RE: Ag wire). (a) Full range scan at v = 100 mV/s and (b) scan of the initial oxidation event at different scan rates with the plot of I_{fp} *vs.* $v^{1/2}$ shown in the insert.

Given the stability of protonated Ni^I **10**$^{\mathbf{BArF}}$, determination of ΔG_{HAT}(**10**$^{\mathbf{BArF}}$) is of interest and the oxidation of **9** was investigated by cyclic voltammetry (Figure 39). In THF, two oxidation events representing the Ni^{II}/Ni^I and Ni^{III}/Ni^{II} oxidation and one irreversible reduction Ni^I/Ni^0 can be observed (Figure 39a). Closer investigation of the initial oxidation reveals a quasireversible process which is characterized by a broad forward peak and a more defined return peak. The process shows a half wave potential $E^{1/2}$ which shifts anodically upon increasing the scan rate v, a peak current ratio i_{rp} / i_{fp} varying between approximately 0.7 and 0.9, therefore showing significant chemical reversibility of the redox process, and a peak separation which exceeds the internal reference ferrocene at high scan rates (Table 15). According to *Zanello* a chemical reaction preceeding an electron transfer can be excluded based on the absence of a limiting current i_L (for the limit of a fast chemical reaction) and i_{rp} / i_{fp} < 1 (for the limit of an intermediate chemical reaction).[104] The difference in shape of the forward and return peak as well as a large peak separation at high scan rate and deviation from linearity of the i_{fp} *vs.* $v^{1/2}$ plot is therefore best interpreted as an electrochemically quasireversible redox process. While the broad oxidation feature could be interpreted as the transfer coefficient α < 0.5, this would result in i_{rp} / i_{fp} > 1 which is not observed. Therefore, the cyclovoltammetric response of **9** is best described as an *EC*$_i$ mechanism consisting of an electrochemically

quasireversible oxidation giving rise to the unusual peak shape due to $\alpha < 0.5$, followed by a chemical reaction resulting in a scan rate dependent half wave potential and $i_{rp} / i_{fp} < 1$. While at low scan rates i_{rp} / i_{fp} increases due to less effective chemical follow-up, at high scan rates electron transfer becomes slow which results in a decrease of i_{rp} / i_{fp} and an increasing peak separation. The redox potential E^0 cannot be determined under these conditions, but $E^{1/2}(\mathbf{9})^{THF}$ = -0.94 V will be used as lower limit of $E^0(\mathbf{9})^{THF}$ for determination of $\Delta G_{HAT}(\mathbf{10}^{\mathbf{BArF}})$.

Table 15: Peak analysis of the initial oxidative responses of **9** and $\mathbf{10}^{\mathbf{BArF}}$ in cyclic voltammetry.

9	v [mV/s]	$E^{1/2}$ [V]	i_{rp} / i_{fp}	$\Delta E^{p\,a}$	$\mathbf{10}^{\mathbf{BArF}}$	v [mV/s]	$E^{1/2}$ [V]	i_{rp} / i_{fp}	$\Delta E^{p\,a}$
	10[a]	-0.979	0.72	1.17		50	-0.837	0.95	1.44
	50	-0.968	0.66	1.11		200	-0.839	1.02	1.71
	100	-0.964	0.70	0.90		400	-0.836	1.09	2.03
	200	-0.962	0.84	1.14		600	-0.842	1.02	2.00
	500	-0.949	0.87	1.10		800	-0.837	1.11	2.12
	1000	-0.935	0.85	1.18		1000	-0.837	1.05	2.23
	2000	-0.938	0.78	1.22					
	3000	-0.935	0.71	1.37					

[a]Given as ratio between the analyte and the internal reference.

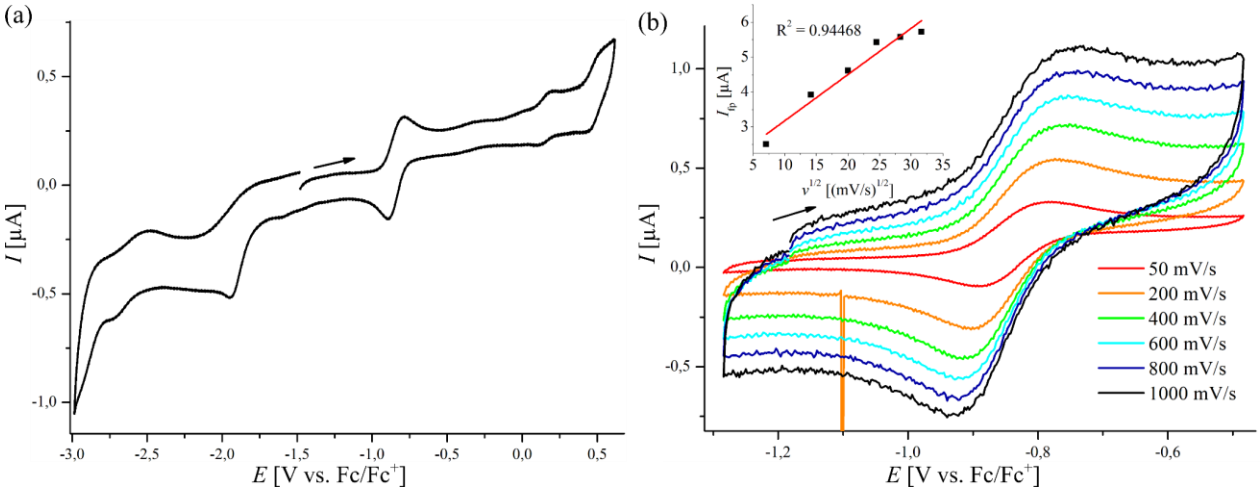

Figure 40: Cyclic voltammetry of 1 mM solutions of $\mathbf{10}^{\mathbf{BArF}}$ in THF (0.1 M [*n*-Bu$_4$N]PF$_6$, WE: GC, CE: Pt wire, RE: Ag wire). (a) Full range scan at v = 100 mV/s and (b) scan of the initial oxidation event at different scan rates with the plot of I_{fp} *vs.* $v^{1/2}$ shown in the insert.

Cyclic voltammetry of protonated Ni^{I} $\mathbf{10}^{\mathbf{BArF}}$ in THF reveals one oxidation and reduction wave (Figure 40). While the reduction process can be classified as chemically irreversible due to the absence of a return current up to v = 1000 mV/s, measurement of the oxidation at different scan rates reveals an electrochemically quasireversible oxidation. While a constant half wave potential $E^{1/2}$ and a peak current ratio i_{rp} / i_{fp} close to

1 is observed, the peak separation significantly exceeds the internal reference at all scan rates and importantly i_{fp} *vs.* $v^{1/2}$ does not show linear correlation (Table 15). Since the forward and return peak show a similar shape, a transfer coefficient α close to 0.5 can be assumed, allowing for determination of a redox potential $E^{1/2}(\mathbf{10}^{\mathbf{BArF}})^{THF}$ = -0.84 V as good approximation of $E^{0}(\mathbf{10}^{\mathbf{BArF}})^{THF}$.

Electrochemical quasireversibility is a consequence of slow electron transfer compared to mass transport and often results from structural reorganization due to oxidation/reduction.[104] While the pincer ligand in **9** and $\mathbf{10}^{\mathbf{BArF}}$ can be regarded as a rigid coordination framework, flexibility in coordination is reported within this thesis (Chapter 2.4.6) and observed upon oxidation of a related three-coordinate Ni^{I} pincer complex.[112] Furthermore, oxidation of d^9 paramagnetic **9** and $\mathbf{10}^{\mathbf{BArF}}$ without any structural rearrangement gives T-shaped d^8 complexes which are expected to show singlet and triplet ground states of similar energy.[112] Therefore, electronic rearrangement might result in an activation barrier for electron transfer, resulting in a quasireversible redox process.

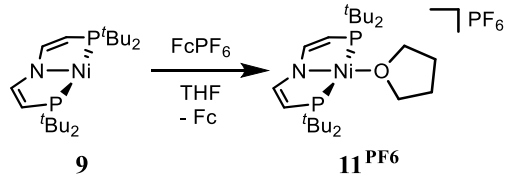

9 $\mathbf{11}^{\mathbf{PF6}}$

Scheme 21: Oxidation of **9** in the presence of THF.

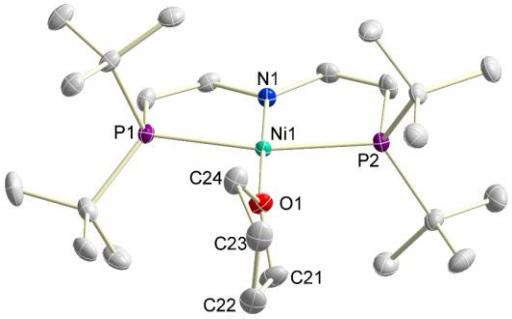

Figure 41: Solid state structure of $\mathbf{11}^{\mathbf{PF6}}$ determined by X-ray diffraction. Thermal ellipsoids are drawn at the 50% probability level. Anions and hydrogen atoms are omitted for clarity.

Chemical oxidation of **9** in THF confirms the assignment of the cyclovoltammetric oxidation event of **9** as *EC* since coordination of the Ni^{II} center by the solvent is observed. While full characterization of [Ni(κ*O*-THF)(^{tBu}P=N=P)]PF_6 ($\mathbf{11}^{\mathbf{PF6}}$) is impeded by decomposition of $\mathbf{11}^{\mathbf{PF6}}$ in solution which is accompanied by polymerization of the solvent, crystallographic characterization confirms the structural identity (Figure 41). No decomposition is reported on literature reported PCP Ni^{II} THF adducts, but no significant structural difference of the THF ligand can be taken from crystallographic data ($\mathbf{11}^{\mathbf{PF6}}$: *d*(Ni-O)

= 1.9255(14) Å, d(C-O) = 1.448(3)/1.465(2) Å; [Ni(κO-THF){CH(2-C_6H_4-P^{i}Pr$_2$)$_2$}]SbF_6: d(Ni-O) = 1.978(4) Å, d(C-O) = 1.448(7)/1.448(7) Å).[113]

Compound **9** does not feature a fully reversible oxidation event, but the experimentally determined $E^{1/2}$ for a quasireversible oxidation serves as a lower limit for $E^0(\mathbf{9})^{THF}$ since follow-up processes according to an *EC* mechanism will shift the oxidation peak potential anodically with respect to an reversible process.[104] With p$K_\alpha(\mathbf{10^{BArF}})^{THF}$ and a good estimate of $E^0(\mathbf{9})^{THF}$ in hand, determination of $\Delta G_{HAT}(\mathbf{10^{BArF}})^{THF}$ is of interest given the stability of this compound with respect to proton reduction. While C_G is reported for several solvents, $C_G{}^{THF}$ is not reported in the literature. Determination of $C_G{}^{THF}$ can be performed using the redox potential for the H^+/H couple, however $C_G{}^{THF}$ = 61 kcal·mol^{-1} based on *Morris*' report is used in the following for BDFE determination since it is commonly used in the literature (see Chapter 1.10 for detailed discussion).[114] $\Delta G_{HAT}(\mathbf{10^{BArF}}) \geq$ 59 kcal·mol^{-1} can be estimated based on $E^{1/2}(\mathbf{9})^{THF} \geq$ -0.94 V *vs.* Fc^+/Fc which is the redox potential determined in the measurement with the highest scan rate ν = 3000 mV s^{-1} (Scheme 22).

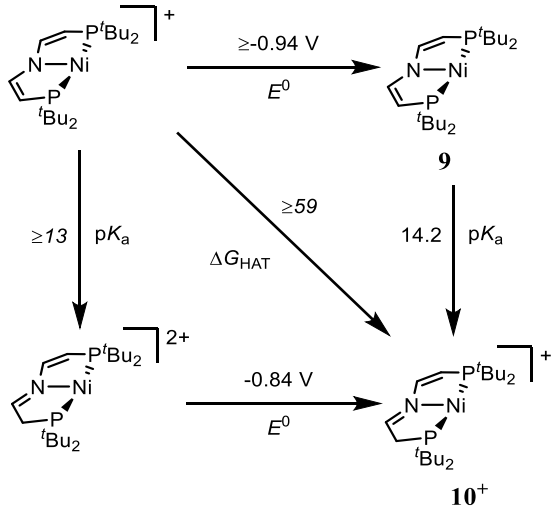

Scheme 22: Interconversion of T-shaped nickel pincer complexes *via* proton, electron and proton-coupled electron transfer. Values written in italics are calculated *via* a square scheme, whereas non-italic values are experimentally determined.

Comparison of $\Delta G_{HAT}(\mathbf{10^{BArF}})^{THF} \geq$ 59 kcal·mol^{-1} and $\Delta G_{HAT}([NiBr(^{tBu}P{=}N{=}P^H)])^{DMSO}$ = 40.3 kcal·mol^{-1}/$\Delta G_{HAT}([Ni(NCMe)(^{tBu}P{=}N{=}P^H)]^+)^{MeCN} \leq$ 43.7 kcal·mol^{-1} shows that introducing a fourth ligand at the Ni(I) oxidation state of the {Ni(^{tBu}P=N=P^H)} platform dramatically weakens the methylene C-H bond. Importantly, while $2\times\Delta G_{HAT}([NiBr(^{tBu}P{=}N{=}P^H)])^{DMSO}$ is below the reported value for H_2 bond homolysis ($\Delta G_{HAT}(H_2)^{MeCN}$ = 102.3 kcal·mol^{-1}[4]), $2\times\Delta G_{HAT}(\mathbf{10^{BArF}})^{THF}$ exceeds this value, therefore serving as explanation of the stability of $\mathbf{10^{BArF}}$ with respect to H_2 liberation. While the Ni^{III}/Ni^{II} redox couple features a ligand based oxidation process, the reduction from Ni^{II} to Ni^{I} is

metal centered and results in population of a high lying metal centered $d_{x^2-y^2}$ orbital. From a qualitative point of view, the stability of **10**$^{\mathbf{BArF}}$ can therefore be understood based on the stability of the Ni^{I} oxidation state in the T-shaped coordination geometry. Comparison of the difference in free energy of proton transfer ΔG_{PT} in the oxidized and reduced state or the difference in free energy of electron transfer ΔG_{ET} in the protonated and deprotonated state of {Ni(^{tBu}P=N=P)} reveals a low thermodynamic coupling of electron and proton transfer with $\Delta\Delta G_{ET/PT}$ = 2.3 kcal·mol^{-1}.

To gain further insight into the origin of the stabilization of the C-H bond in **10**$^{\mathbf{BArF}}$, careful analysis of the oxidation potential E^0 and the pK_a has to be performed. While ΔG_{HAT}(**10**$^{\mathbf{BArF}}$)^{THF} is an estimated lower limit as discussed earlier, this value will be assumed as exact for the following comparison with the {NiBr(^{tBu}P=N=P)} and {Ni(NCMe)(^{tBu}P=N=P)} platform. ΔG_{HAT}([NiBr(^{tBu}P=N=P^{H})])^{DMSO} and ΔG_{HAT}([Ni(NCMe)(^{tBu}P=N=P^{H})]$^{+}$)^{MeCN} are determined based on the Ni^{II}/Ni^{I} wave of the protonated species, whereas ΔG_{HAT}(**10**$^{\mathbf{BArF}}$)^{THF} is calculated based on the Ni^{II}/Ni^{I} redox potential of the deprotonated species. To allow for comparison of both systems, the same path along the square scheme has to be taken. Since the Ni^{II}/Ni^{I} redox potential of **10**$^{\mathbf{BArF}}$ is experimentally available as discussed earlier, the pK_{α} of [Ni(^{tBu}P=N=P^{H})]$^{2+}$ is calculated to be ≥13 in THF based on ΔG_{HAT}(**10**$^{\mathbf{BArF}}$)^{THF} = 59 kcal·mol^{-1} as can be seen in Scheme 22.

For transfer of the thermodynamic data shown in Scheme 22 to MeCN as solvent, a solvent independent ΔG_{HAT} is assumed, since the difference in solvation energy of the hydrogen atom $\Delta\Delta G_{solv}$(H) = 0.2 kcal·mol^{-1} for changing from THF to MeCN solvent is neglectable.[115]

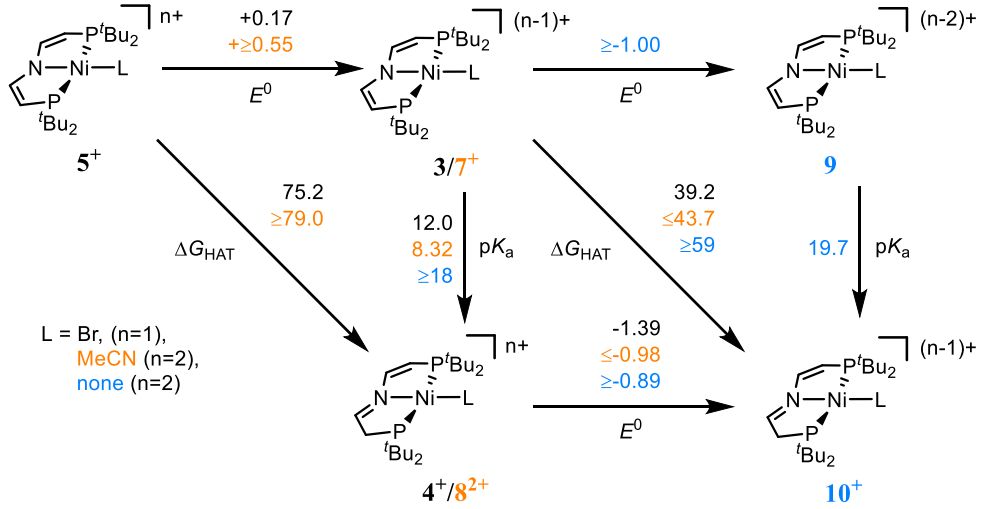

Scheme 23: Comparison of thermodynamic data on {NiBr(P=N=P)}, {Ni(NCMe)(P=N=P)} and {Ni(P=N=P)} in MeCN solvent. Free energies are given in kcal·mol^{-1}.

Comparison of the thermochemical data in MeCN shows that both ΔE^0 and ΔpK_a result in stabilization of the C-H bond in **10^{BArF}** compared to [NiBr(^{tBu}P=N=P^{H})] and [Ni(NCMe)(^{tBu}P=N=P^{H})]$^+$ (Scheme 23) . The ratio between both contributing factors varies strongly, with $\Delta\Delta G_{ET}$ = 11.5 kcal·mol^{-1} and $\Delta\Delta G_{PT} \geq 7.9$ kcal·mol^{-1} upon comparing {NiBr(^{tBu}P=N=P)} and {Ni(^{tBu}P=N=P)}. In contrast {Ni(^{tBu}P=N=P)} shows a strong stabilization of the Ni^{I} methylene bond due to increased basicity with respect to {Ni(NCMe)(^{tBu}P=N=P)} which makes up for $\Delta\Delta G_{PT} \geq$ 13.0 kcal·mol^{-1}, whereas $\Delta\Delta G_{ET} \geq$ 2.1 kcal·mol^{-1} is much smaller. This stands in contrast to the thermodynamic data on {NiBr(^{tBu}P=N=P)} and {Ni(NCMe)(^{tBu}P=N=P)} in the Ni^{III}/Ni^{II} oxidation state, which show that variation of the redox potential and pK_a by ligand variation compensate each other to a large extend (Chapter 1.4.1).

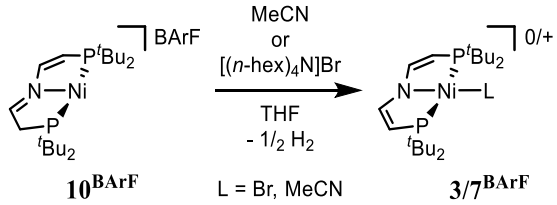

10^{BArF} **3/7^{BArF}**

Scheme 24: Hydrogen loss from **10^{BArF}** upon addition of coordinating substrates.

Interested in the stability of **10^{BArF}** upon addition of additional ligands, **10^{BArF}** was reacted with acetonitrile and [(*n*-Hex)$_4$N]Br, which results in clean formation of bromide coordinated **3** or acetonitrile ligated **7^{BArF}**, respectively. Attempts to use HAT reactivity at the Ni^{I} oxidation state for substrate reduction instead of H_2 formation did not succeed, neither by addition of styrene to **10^{BArF}** nor by addition of styrene and [(*n*-Hex)$_4$N]Br.

1.4.3. Synthesis and Oxidation of [NiH(^{tBu}P=N=P)] (12)

Since the methylene C-H bond strength on the Ni^{III}/Ni^{II} oxidation state is to a large extend defined the pincer ligand, there is little deviation in C-H bond strength upon variation of the fourth ligand, as confirmed by comparison of ΔG_{HAT}(**4^{OTf}**) and ΔG_{HAT}(**8$^{(BArF)2}$**). Since nickel hydrides usually have Ni-H bond strength of ΔG_{HAT} = 50–60 kcal·mol^{-1} the formation of a strong C-H bond could potentially be used to generate a low coordinate Ni^{II} fragment by Ni-H bond scission which then might be active in cooperative substrate activation.[116–119]

Reacting **3** with 1 eq of LiAlH$_4$ in THF results in a color change from brown to orange over 30 minutes and two products of this reaction can be detected ^{31}P{^{1}H} NMR spectroscopically (Figure 42). At δ = 85.64 ppm the desired [NiH(^{tBu}P=N=P)] (**12**) can be observed as the main species, however at δ = -11.51 ppm a side product resonates. The high field shifted ^{31}P{^{1}H} signal and the multiplicity in the ^{1}H NMR spectrum indicate that this side product does not contain metal coordinated phosphorus atoms. In ^{31}P{^{1}H} NMR

spectroscopy the observed negative chemical shift δ lacks the downfield shift due to 5-membered ring formation by metal coordination and non-coordinated phosphine ligands are typically observed at such high field.[120] In ^{1}H NMR spectroscopy the absence of higher order coupling pattern in the doublet resonance at δ = 1.25 ppm and δ = 4.36 ppm shows that this species is most likely a lithium amido species Li[^{tBu}P=N=P] based on the unsaturated ligand.

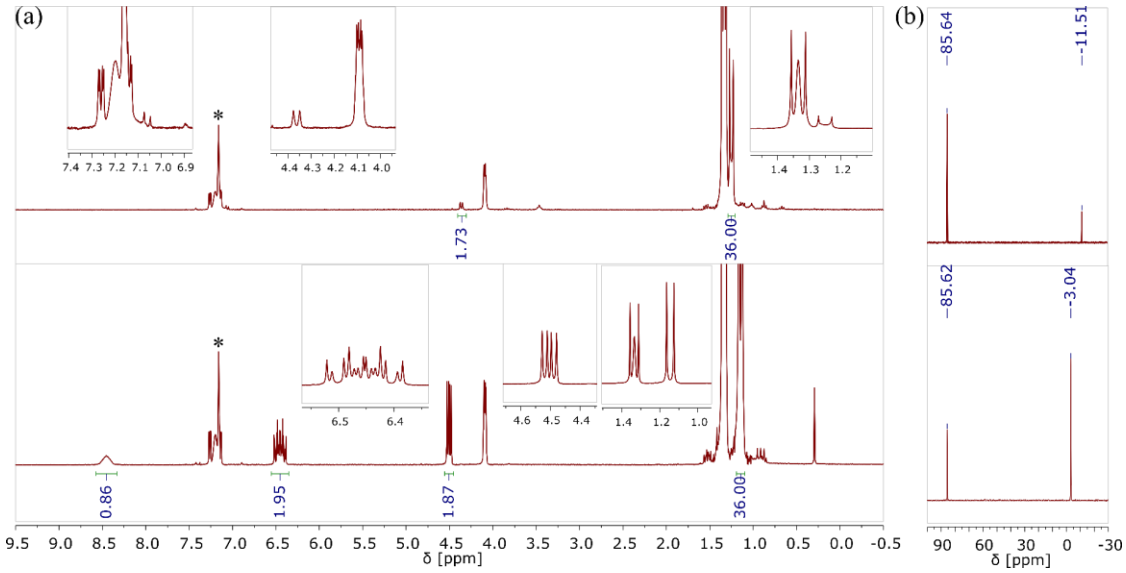

Figure 42: (a) ^{1}H and (b) ^{31}P{^{1}H}NMR spectra of (top) the reaction of **3** with 1 eq $LiAlH_4$ and (bottom) the mixture obtained by washing with methanol.

From this mixture of **12** and Li[^{tBu}P=N=P] the side product can be removed by extensive washing with methanol at 0°C due to low solubility of neutral {Ni(^{tBu}P=N=P)} complexes in polar solvents. Purity of the product after crystallization from *n*-pentane at -36°C can be verified NMR spectroscopically as shown in Figure 43. The hydride ligand resonates at δ = -17.52 ppm, which is the commonly observed region for Ni^{II} PNP hydride complexes.[121] Aside from the expected $^{2}J_{HP}$ coupling of 59.4 Hz, the hydride couples to all four CH positions of the backbone ($^{4}J_{HH}$ = 1.7), therefore giving a triplet of pentet multiplicity. Accordingly, the backbone resonances show an additional coupling in comparison to the spectrum of **3**. Due to incomplete decoupling of the hydride phosphorus coupling, the resonance of **12** in ^{31}P{^{1}H} NMR spectroscopy often appears as an unresolved multiplet.

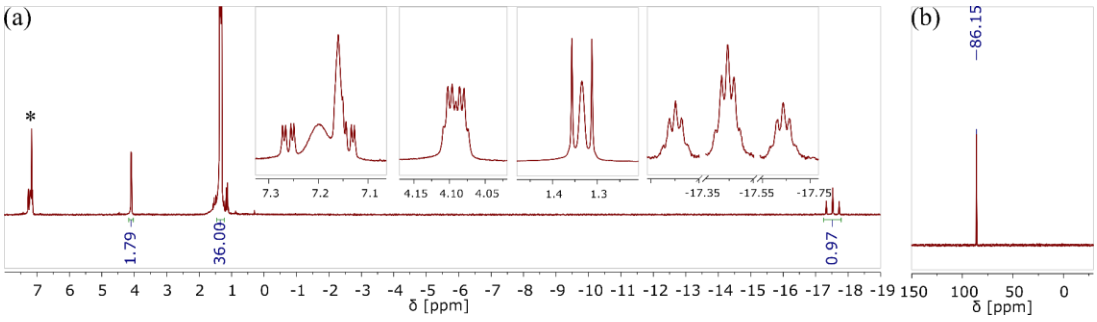

Figure 43: (a) ^{1}H and (b) ^{31}P{^{1}H}NMR spectra of **12** in C_6D_6.

When the methanol solution obtained by washing of **12** is dried by applying vacuum and investigated NMR spectroscopically, selective conversion of Li[^{tBu}P=N=P] to a new compound resonating at δ = -3.04 ppm in the ^{31}P{^{1}H} NMR spectrum can be observed (Figure 42). Aside from changes in the chemical shifts and multiplicities as compared to Li[^{tBu}P=N=P], this new compound features an additional broad peak at δ = 8.46 ppm in the ^{1}H NMR spectrum indicative of an amine proton suggesting formation of amino diphosphine HN(CHCHP*t*Bu$_2$)$_2$ **13** by protonation of Li[^{tBu}P=N=P] due to reaction with methanol. By analyzing the coupling pattern of the CH resonances of **13**, the $^{3}J_{HH}$ coupling constant can be determined to be 9.3 Hz, with is expected for a vicinal *cis* coupling in olefins. Apparently the *cis,cis* configuration of the PNP fragment stays rigid over the course of metal dissociation and protonation, yielding the dieneamine without isomerization to the enimine.

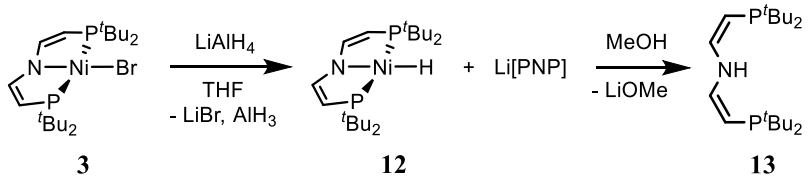

Scheme 25: Synthesis of nickel pincer hydride **12** and dieneamine **13**.

Isotopologue [NiD(^{tBu}P=N=P)] (**12-D**) can be synthesized by the same procedure as **12** using $LiAlD_4$. Ground state IR spectra of **12** in KBr matrix and THF-d_8 solution show a strong band at $\tilde{\upsilon}$ = 1834 (KBr) and $\tilde{\upsilon}$ = 1850 cm^{-1} (THF-d_8), respectively (Figure 44a). Prediction of $\tilde{\upsilon}_D$ based on assumption of similar force constants gives $\tilde{\upsilon}_D$ = 1297 cm^{-1} (KBr) according to eq. (40).

$$\tilde{\upsilon}_D = \tilde{\upsilon}_H / 2^{1/2} \qquad (40)$$

IR spectra of **12-D** show two overlapping bands close to the predicted value, indicating fermi resonance of the Ni-D stretch and a second vibration of similar energy (Figure 44b). Observation of a similar fermi doublet for the fundamental vibration at half energy confirms this assumption. The vibration overlapping with the Ni-D stretch can be identified as a low intensity band at $\tilde{\upsilon} \approx$ 1330 cm^{-1} in the IR spectrum of **12** in

THF-d_8. In agreement with interpretation of the two resonances in the IR spectra of **12-D** as a fermi doublet, the low intensity band at $\tilde{\upsilon} \approx 1330$ cm^{-1} in **12** gains intensity in the IR spectra of **12-D** and shifts to higher energy ($\tilde{\upsilon} = 1339$ cm^{-1} (THF-d_8), $\tilde{\upsilon} = 1333$ cm^{-1} (KBr)). In contrast, the Ni-D stretch gives rise to resonance of relatively low intensity as compared to the Ni-H stretch in the IR spectra of **12** and can be assigned to $\tilde{\upsilon}_D = 1327$ cm^{-1} (THF-d_8) and $\tilde{\upsilon}_D = 1318$ cm^{-1} (KBr), close to the value predicted by eq. (40).

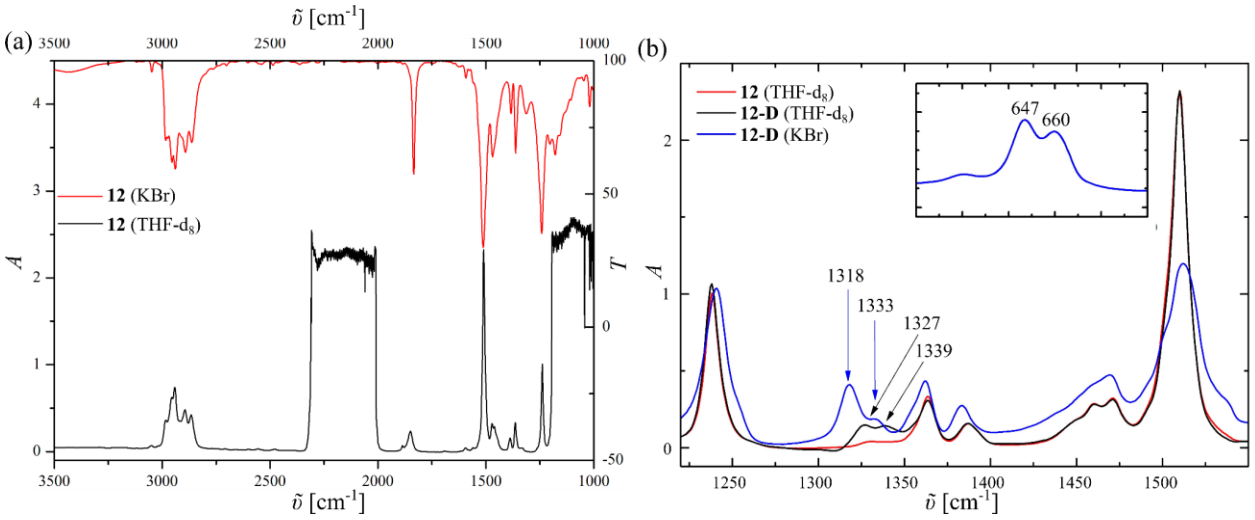

Figure 44: (a) Infrared spectra of **12** in KBr matrix and THF-d_8 solution. (b) Comparison of infrared spectra of **12** and **12-D**.

Protonation of **12** with 1 eq of $[H(OEt_2)_2]BArF$ or $[H(OEt_2)]BF_4$ in Et_2O at -36°C yields clean formation of enimine hydride $[NiH(^{tBu}P{=}N{=}P^{H})]X$ (**14^{X}**, X = BArF, BF_4), while performing the reaction with $[H(OEt_2)_2]BArF$ at room temperature gives an unidentified side product. Once isolated, **14^{X}** is a stable compound as solid and in solution at room temperature.

The NMR spectroscopic signature of **14^{X}** resembles the reported data on **4^{X}** and **8^{X}** with two doublet resonances in the $^{31}P\{^1H\}$ NMR spectrum slightly shifted downfield with respect to **12** and $^2J_{PP} = 215.5$ Hz (Figure 45d). The hydride ligand resonates at $\delta = -18.25$ ppm in the ^1H NMR spectrum close to the observed hydride peak for **12** with a similar $^2J_{HP}$ coupling constant of 59.7 Hz. The Ni-H stretching vibration of **14^{BArF}** can be observed at $\tilde{\upsilon}$(Ni-H) = 1884.2 cm^{-1} in KBr matrix, shifted to higher energy with respect to **12** ($\tilde{\upsilon}$(Ni-H) = 1834.3 cm^{-1}).

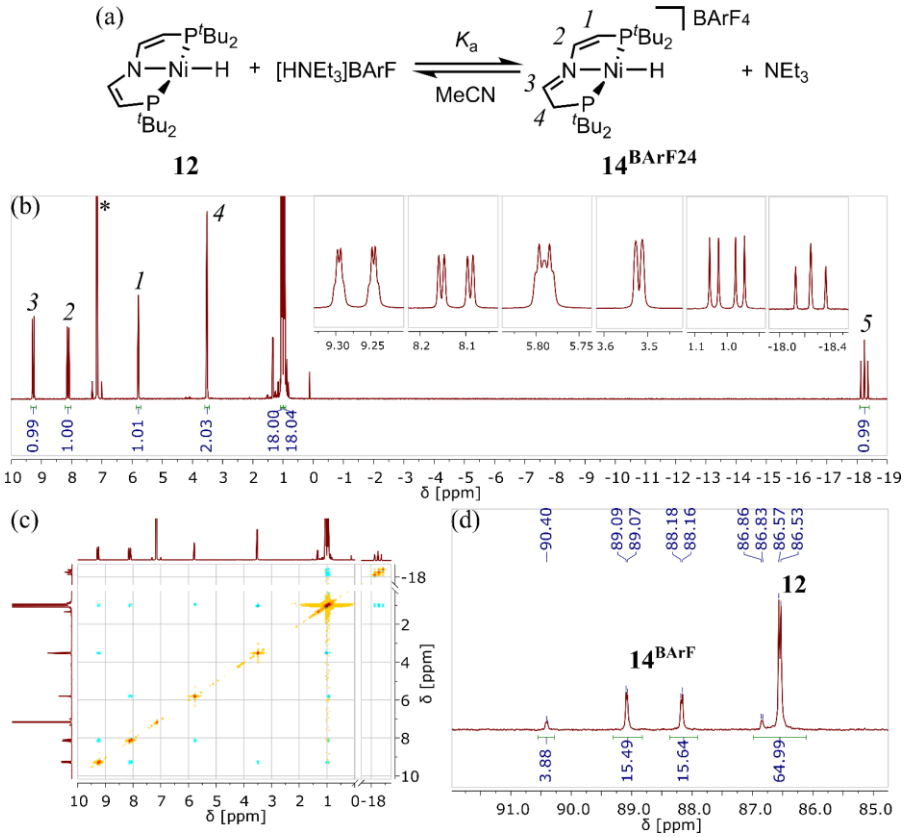

Figure 45: (a) Acid-base equilibrium of **12** and $\mathbf{14^{BArF}}$. (b) ^{1}H NMR and (c) ^{1}H,^{1}H NOE spectrum of compound $\mathbf{14^{BF4}}$ (*denotes C_6D_6). (d) ^{31}P{^{1}H} NMR spectrum of titration of **12** with 1 eq [HNEt$_3$]BArF in MeCN.

To examine, if the stronger hydride donor in $\mathbf{14^{X}}$ as compared to the bromide in $\mathbf{4^{X}}$ results in an enhanced basicity, pK_a determination was conducted by titration of **12** in MeCN with 1 eq of [H(NEt$_3$)]BArF (Figure 45) giving pK_a($\mathbf{14^{BArF}}$)^{MeCN} = 18.4, following the procedure described for determination of pK_a($\mathbf{8^{(BArF)2}}$)^{MeCN} (Chapter 1.4.1). Therefore, a strong influence of the *trans* ligand on the pK_a of the nickel pincer platform can be observed upon comparing compounds of identical charge (pK_a($\mathbf{4^{BArF}}$)^{MeCN} ≈ 12).[103] Notably, the effect of substituting the bromide for a hydride ligand on the acidity, is comparable to reduction to Ni^{I} (pK_a($\mathbf{10^{BArF}}$)^{MeCN} ≈ 19.7).

Compound **12** and $\mathbf{14^{O2CCF3}}$ can both be characterized crystallographically by X-ray diffraction. Hydride **12** crystallizes as half a complex molecule per asymmetric unit and $\mathbf{14^{O2CCF3}}$ cocrystallized with one additional molecule of trifluoroacetic acid. The structural parameters are shown in Table 16 and are in overall agreement with the trends observed for the structures of $\mathbf{3}$–$\mathbf{5^{PF6}}$ discussed earlier (Table 1, Table 2). Again, in $\mathbf{14^{O2CCF3}}$ the imine can be clearly localized by comparing the bond length of both C_2 bridges of the pincer backbone. The torsion angle φ(N-C-C-P) is identical in both pincer arms of $\mathbf{14^{O2CCF3}}$, contrasting the crystallographic data in $\mathbf{4^{OTf}}$, in which case the protonation results in significant deplanarization of this 5-membered chelate. An elongated ellipsoid for methylene position C2 in Figure 46b might hint at an

unresolved crystallographic disorder which gives rise to an average position for this atom. In both data sets the electron density of the hydride ligand can be clearly observed despite the proximity of the metal atom. Regardless, Ni-H bond length discussion will not be performed given the uncertainty in crystallographically determined metal hydrogen bond parameters.

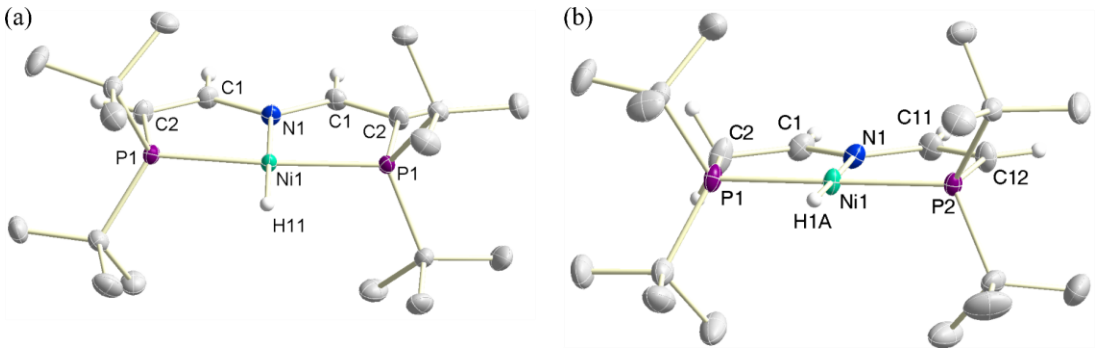

Figure 46: Solid state structure of **12** and **14**^{O2CCF3}·F_3CCO_2H determined by X-ray diffraction. Thermal ellipsoids are drawn at the 50% probability level. Anions, additional molecules of the asymmetric unit and selected hydrogen atoms are omitted for clarity.

Table 16: Crystallographic parameters of the solid state structure of **12** and **14**^{O2CCF3}·F_3CCO_2H determined by X-ray diffraction.

[Ni]	*d*(C=C) [Å]	*d*(C-N) [Å]	*d*(C-C) [Å]	*d*(C=N) [Å]	*φ*(N-C-C-P) [°]
12	1.3587(13)	1.3646(10)	-	-	0.8(1)
14^{O2CCF3}	1.346(2)	1.3718(16)	1.405(2)	1.3019(19)	1.4(2)/1.2(2)

While **3** and **7**^{BArF} feature (quasi-)reversible oxidation processes in the cyclic voltammetry, **12** shows an irreversible oxidation close to the Fc^+/Fc potential (Figure 47a). In a MeCN solution, the redox process remains completely irreversible up to scan rates of ν = 2.5 V/s. For **12** no reductive process is observable, but protonation to **14**^{BArF} results in an irreversible process at E^p = -1.39 V (ν = 100 mV/s) which is shifted cathodically by a small amount compared to **4**^{BF4} which is in agreement with a more electron rich metal center due to the strongly donating hydride ligand.

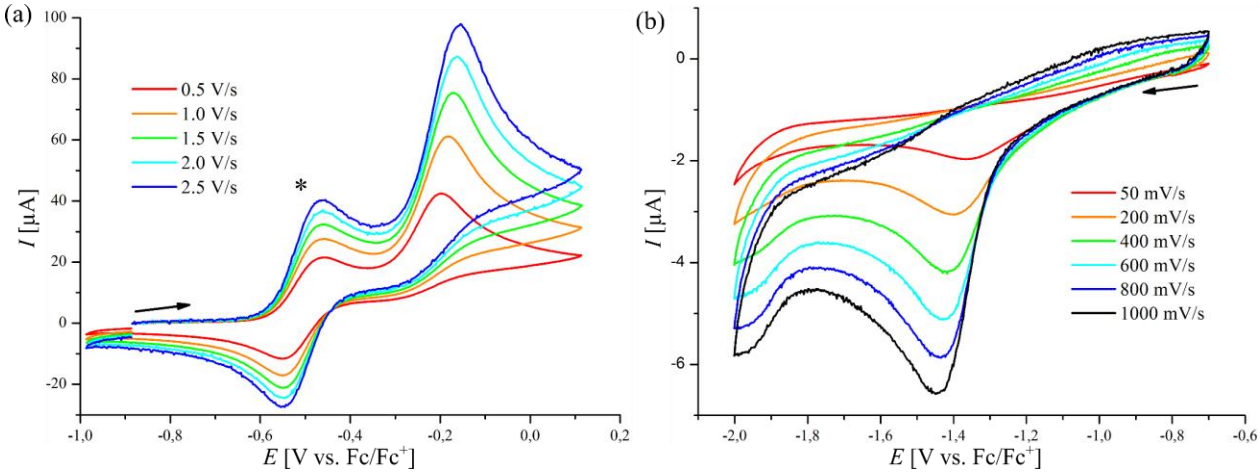

Figure 47: Cyclic voltammetry of 1 mM solutions of (a) **12** (0.1 M [*n*-Bu_4N]PF_6, WE: GC, CE: Pt wire, RE: Ag wire) and (b) **14**^{BArF} (0.1 M [*n*-Bu_4N]PF_6, WE: Pt wire, CE: Pt wire, RE: Ag wire) in MeCN (*denotes $(Cp^*_2Fe]$[13]). Both voltammograms are referenced to Fc^+/Fc.

To investigate the reactivity of **12** upon oxidation, **12** is reacted with 1 eq $AgPF_6$ as oxidant in acetonitrile. While the reaction does not proceed completely selective, **14**^{PF6} and **7**^{PF6} can be identified as major products by NMR spectroscopy (Figure 48). Integration in the ^{1}H NMR spectrum shows that the ratio of both compounds is close to 1, suggesting a disproportionation reaction as intended by introducing a weak Ni-H bond in **12**. Formation of **14**^{PF6} can therefore be explained by initial formation of a highly reactive formal Ni^{III} hydride which is experimentally not observed, in agreement with a strongly irreversible oxidation process as observed in cyclic voltammetry. Since paramagnetic, cationic hydride species are prone to hydride bond homolysis as discussed by *Norton*, PCET of the hydride ligand to the pincer backbone of another Ni^{III} hydride is a valid assumption, creating a low coordinate $[Ni(^{tBu}P{=}N{=}P)]^+$ fragment which readily coordinates acetonitrile to form **7**^{PF6}.[122]

[13] Cp* = pentamethylcyclopentadienyl

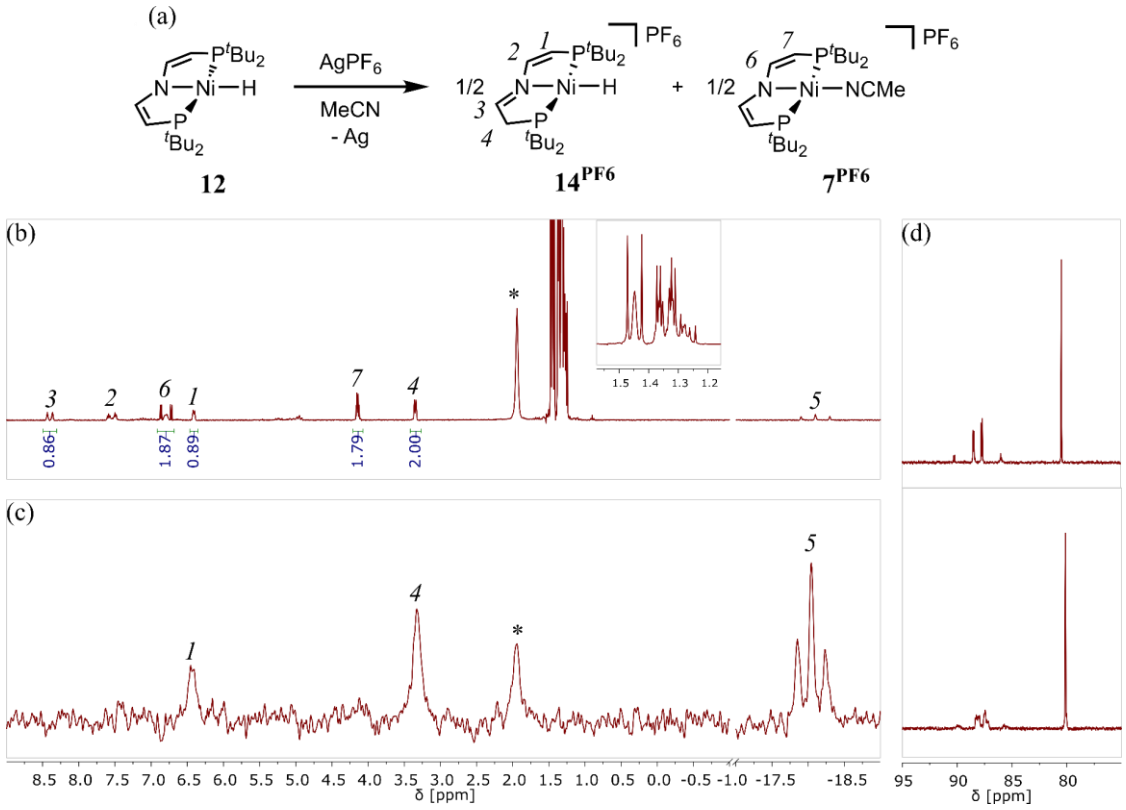

Figure 48: (a) Oxidation of **12** in MeCN results in formation of **14^{PF6}** and **7^{PF6}**.(b) ^{1}H NMR spectrum of the oxidation of **12** with 1 eq $AgPF_6$ in MeCN-d_3. (c) ^{2}H NMR spectrum of the oxidation of **12-D** with 1 eq $AgPF_6$ in MeCN. (d) $^{31}P\{^{1}H\}$ NMR spectrum of the oxidation of **12** (top) and **12-D** (bottom) with 1 eq $AgPF_6$ in MeCN.

To validate this mechanistic picture, the same reaction was performed using nickel deuteride **12-D**. The $^{31}P\{^{1}H\}$ NMR spectrum of the reaction mixture shows a similar product distribution as depicted in Figure 48d, with broader resonances for **14^{PF6}-D** in the $^{31}P\{^{1}H\}$ NMR spectrum due to the lack of decoupling of the $^{2}J_{PD}$ interaction with the deuteride ligand. ^{2}H NMR measurement clearly shows the deuteride and CHD resonance of **14^{PF6}** with no signal assignable to **7^{PF6}**, therefore confirming the proposed intermolecular HAT reaction (Figure 48c). Furthermore, deuterium incorporation in the PCH position in **14^{PF6}** can be detected which is most likely attributed to chemical exchange of the PCH and PCHD positions due to acidity of **14^{PF6}**. This exchange proceeds below NMR timescale, since it is not visible in ^{1}H,^{1}H NOE spectroscopy as shown in Figure 45c.

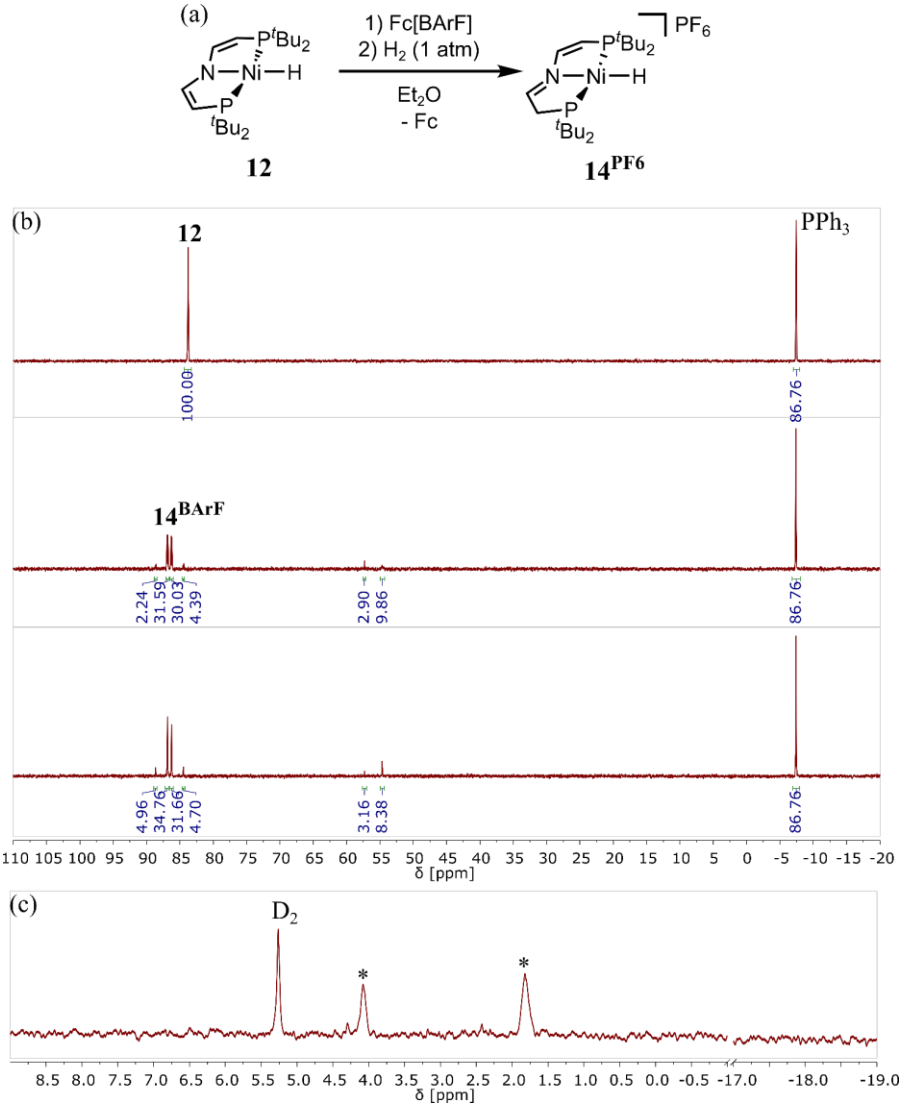

Figure 49: (a) Oxidation of **12** in Et_2O under H_2 atmosphere. (b) $^{31}P\{^1H\}$ NMR spectra of (top) **12** in Et_2O, (middle) after addition of 1 eq [Fc]BArF and (bottom) exchanging the atmosphere for H_2 (1 atm). (c) ^2H NMR spectrum of the oxidation of **12** with 1 eq [Fc]BArF in Et_2O under D_2 atmosphere (1 atm).

Since acetonitrile ligated complex $\mathbf{7^{BArF}}$ does not undergo H_2 activation ($p(H_2)$ = 1 atm), even in the presence of base DBU, substrate activation *via* metal-ligand cooperativity at a low coordinate Ni^{II} intermediate was attempted in non-coordinating solvents. After oxidation of **12** with [Fc]BArF in diethyl ether, H_2 (1 atm) was added to convert the postulated $[Ni^{II}(^{tBu}P{=}N{=}P)]^+$ fragment to $\mathbf{14^{BArF}}$ in the absence of a coordinating solvent. Compound $\mathbf{14^{BArF}}$ is formed in >65% yield with respect to **12** based on integration in $^{31}P\{^1H\}$ NMR against an internal standard (closed capillary of PPh_3 in toluene), exceeding the highest possible yield of 50% by a disproportion mechanism as discussed for the reaction in acetonitrile. However, this yield is already observed before exchanging the argon atmosphere for hydrogen excluding formation of $\mathbf{14^{BArF}}$ by H_2 activation. Closer examination using D_2 gas shows, that no deuterium is incorporated into $\mathbf{14^{BArF}}$, further showing that $\mathbf{14^{BArF}}$ does not undergo H/D exchange with D_2. The additionally formed $\mathbf{14^{BArF}}$ is therefore

attributed to HAA from the solvent as is observed for $\mathbf{5^{PF6}}$ in THF (D^0(Et_2O) = 81.7±0.4 kcal·mol^{-1}, D^0(THF) = 92.0±1 kcal·mol^{-1})[123]. Accordingly, thawing a frozen solution of **12** and oxidant in fluorobenzene[14] under H_2 atmosphere gives a lower yield of approximately 55% in $\mathbf{14^{PF6}}$ (Figure 49). Comparison of the reaction under Argon and H_2 atmosphere shows, that conversion of **12** to $\mathbf{14^{PF6}}$ proceeds faster and more selective in the presence of H_2. While H_2 activation does not seem to take place, the presence of additional ligands like acetonitrile, Et_2O and H_2 seems to be beneficial for formation of $\mathbf{14^{PF6}}$, suggesting a more complex associative mechanism for the disproportionation of **12** to $\mathbf{14^{X}}$ under oxidative conditions.

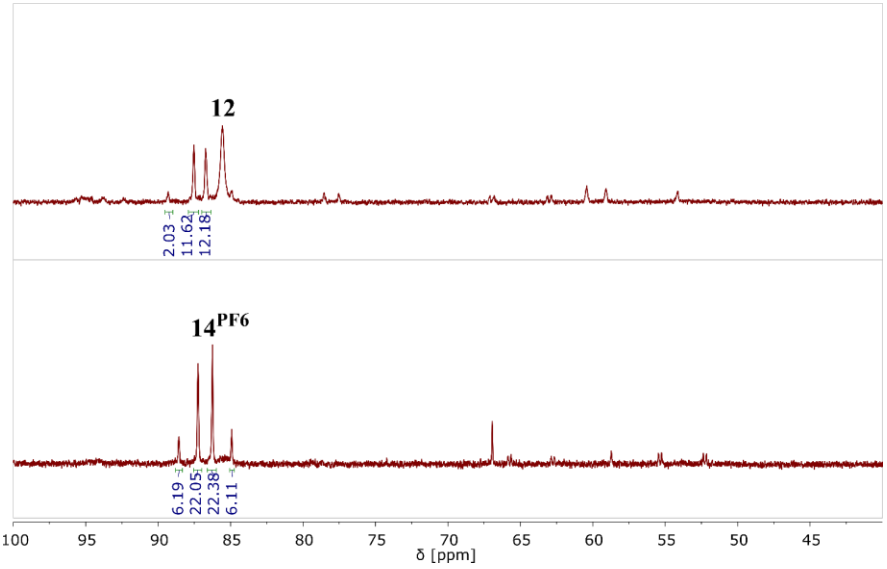

Figure 50: $^{31}P\{^1H\}$ NMR spectra of the oxidation of **12** in fluorobenzene under (top) argon atmosphere after 1 day and (bottom) under H_2 atmosphere after 30 minutes. Integrals are given as percentage of starting material **12** determined by integration against an internal standard.

[14] D^0(Ph-F) is not available in the literature, but is expected to be higher than D^0(Et_2O) and D^0(THF) based on reported D^0(Ph-Cl) = 107.10 kcal·mol^{-1}.[371]

1.5 Conclusion

The synthetic procedure for ^{tBu}P=N=P based cobalt complexes can successfully be transferred to nickel complexes, allowing for isolation of [NiBr(^{tBu}P=N=P)] **3** in 78% yield in a two-step synthesis starting from [$NiBr_2$(dme)] and ^{tBu}PN^{H}P. Compound **3** can be protonated to enimine [NiBr(^{tBu}P=N=P^{H})]BF_4 **4^{BF4}** and oxidized to formal Ni^{III} [NiBr(^{tBu}P=N=P)]PF_6 **5^{PF6}**. Electronic structure analysis of **5^{PF6}** by UV-vis, EPR, XANES and EXAFS spectroscopy, as well as cyclic voltammetry, crystallographic analysis and TD-DFT computation suggests a ligand centered oxidation. Experimental determination of the free energy of proton and electron transfer is performed by pK_a titration using a reference acid and cyclic voltammetry. The free energy of concerted proton-electron transfer ΔG_{HAT}(**4^{OTf}**)^{DMSO} = 76.3 kcal·mol^{-1} is in excellent agreement with theory and exceeds all reports on experimentally determined C-H bond strength of pincer based transition metal complexes allowing for unprecedented benzylic C-H activation by C-H bond formation *via* PCET to a coordination compound.

While hydrogen atom abstraction by **5^{PF6}** is observed with several substrates, the oxidation of 9,10-dihydroanthracene in chlorobenzene gives clean oxidation to anthracene by formation of **4^{PF6}**. Kinetic analysis by UV-vis spectroscopy reveals a stoichiometry corrected rate constant of k_{sym}^{HAT} = 4.9·10^{-4} M^{-1}s^{-1} rivaling reports on DHA oxidation by nitrogen and oxygen centered acceptor sites in coordination compounds. Applying the *Marcus* cross relation predicts a self-exchange rate constant k_{sym}^{SE}(**5^{PF6}**) = 2.9·10^{3} M^{-1}s^{-1} for concerted proton-electron transfer which is higher than reported carbon centered self-exchange rates by several orders of magnitude. NMR spectroscopic measurement gives k_{sym}^{SE}(**5^{PF6}**) = (1.7±1.3)·10^{2} M^{-1}s^{-1}, showing decent agreement with the value predicted by the *Marcus* cross relation. Substrate oxidation by **5^{PF6}** not only shows that C-H bond formation on transition metal complexes can be used for homolytic C-H bond activation in organic substrates. Tt further suggests a substantial difference in self-exchange rate constants between **5^{PF6}** and organic substrates containing reactive C-H bonds, resulting in a rate constant for C-H oxidation comparable to nitrogen and oxygen centered processes. A low reorganization energy as a result of minor inner-sphere reorganization upon reduction of **5^{PF6}** to **4^{PF6}** is suggested as explanation of the fast self-exchange.

Oxidation of *p*-methylanisol by **5^{PF6}** results in formation of diphenylmethane derivatives by intermediate formation of a benzyl radical cation. Determination of the hydricity ΔG_{HT}([NiBr(^{tBu}P=N=P^{H}])^{DMSO} = 69.4 kcal·mol^{-1} is performed by electrochemical measurement of the Ni^{II}/Ni^{I} redox couple for reduction of **4^{BF4}**. Comparison of ground-state thermodynamics for concerted and stepwise 2e^{-}/1H^{+} processes suggest initial concerted hydrogen atom abstraction followed by oxidation of the benzyl radical. The Ni^{II}/Ni^{I} redox potential further allows for determination of

$\Delta G_{HAT}([NiBr(^{tBu}P=N=P^{H})])^{DMSO}$ = 40.3 kcal·mol^{-1} showing a dramatic weakening of the C-H bond upon reduction.

Variation of the bromide ligand in **3** for acetonitrile gives complex [Ni(NCMe)(^{tBu}P=N=P)]BArF **7^{BArF}** which analogously allows for protonation to [Ni(NCMe)(^{tBu}P=N=P^{H})](BArF)$_2$ **8$^{(BArF)2}$**. Experimentally determination of ΔG_{HAT}(**8$^{(BArF)2}$**)^{MeCN} ≥79.0 kcal·mol^{-1} and $\Delta G_{HAT}([Ni(NCMe)(^{tBu}P=N=P^{H}]^{+})^{MeCN}$ ≤ 43.7 kcal·mol^{-1} for the Ni^{III}/Ni^{II} and Ni^{II}/Ni^{I} redox couple respectively, shows an increase of approximately 4 kcal·mol^{-1} for both C-H bonds upon ligand exchange on both oxidation states. Accordingly, both PCET processes involving the formal Ni^{II}/Ni^{I} and Ni^{III}/Ni^{II} oxidation states are affected to the same degree by ligand substitution.

T-shaped Ni^{I} [Ni(^{tBu}P=N=P)] **9** can be isolated upon reduction of **3** with magnesium and protonation gives enimine [Ni(^{tBu}P=N=P^{H})]BArF **10^{BArF}**. Cyclic voltammetry of both compounds reveals slow electron transfer upon oxidation which is attributed to a high kinetic barrier for formation of T-shaped d^8 Ni^{II} complexes. Based on the acidity of **10^{BArF}**, ΔG_{HAT}(**10^{BArF}**)^{THF} ≥ 59 kcal·mol^{-1} is determined, showing a huge impact of the coordination geometry of the C-H bond strength of the Ni^{II}/Ni^{I} redox couple. Upon addition of bromide or acetonitrile, formation of **3** or **7^{BArF}** accompanied by H_2 loss is observed due to weakening of the pincer C-H bond upon coordination. In agreement, reversible loss of bromide or acetonitrile in electrochemical reduction of **3** or **7^{BArF}** is observed in cyclic voltammetry.

Selective introduction of a weak Ni-H bond in Ni^{II} hydride [NiH(^{tBu}P=N=P)] **12** results in disproportionation by PCET upon oxidation in acetonitrile giving imine hydride [NiH(^{tBu}P=N=P^{H})]BArF **14^{BArF}** and solvent coordinated **7^{BArF}**. Incorporation of the former hydride in the ligand backbone is confirmed by labeling experiments. Due to a fast chemical process after electrochemical oxidation of **12**, determination of the Ni^{III}/Ni^{II} redox potential is not possible and accordingly the C-H bond strength of **14^{BArF}** is not accessible by a thermodynamic square scheme. Moving to unpolar solvents, disproportionation upon oxidation is sluggish, impeding H_2 activation at a low coordinate Ni^{II} complex.

Part I: Experimental Data

1.6 Materials and Methods

All experiments were performed under an argon atmosphere using standard Schlenk and glove box techniques. Toluene, benzene, *n*-pentane, dichloromethane, diethyl ether and THF were purchased in HPLC quality (Sigma Aldrich) and dried using an MBraun Solvent Purification System. Chlorobenzene (Sigma Aldrich) was dried over CaH_2 followed by distillation. Methanol (Sigma Aldrich) was degassed and stored over molecular sieves (3 Å). Acetonitrile (Sigma Aldrich) and H_2O was degassed and used without further purification. Deuterated solvents were obtained from Deutero GmbH and dried over Na/K (C_6D_6,, THF-d_8) or CaH_2 (CD_2Cl_2, PhCl-d_5). DMSO-d_6 was purified by fractional distillation twice and stored over molecular sieves (3 Å). MeCN-d_3 was degassed and stored over molecular sieves (3 Å).

[$NiBr_2$(dme)] (abcr), $AgPF_6$ (abcr), 1,8-bis(dimethylamino)naphthalene (Sigma Aldrich), Cp_2Co (Sigma Aldrich), 15-crown-5 (Sigma Aldrich), DBU (Acros), DBN (Sigma Aldrich), di-*iso*-propylethylamine (Roth), DHA (Sigma Aldrich), $K_3[Fe(C_2O_4)_3]$, KOH (Sigma Aldrich) $LiAlD_4$ (98% isotopic purity, Strem), $LiAlH_4$ (Sigma Aldrich), $LiHBEt_3$ solution (Sigma Aldrich), magnesium powder (Sigma Aldrich), MeMgCl solutution (Sigma Aldrich), $NaBF_4$ (Sigma Aldrich), $NaBH_4$ (Sigma Aldrich), NaHMDS (Sigma Aldrich), NaN_3 (Sigma Aldrich), [(*n*-hex)$_4$N]Br (Sigma Aldrich), phenol (Sigma Aldrich), phosphoric acid (Sigma Aldrich), piperidine (Sigma Aldrich), sodium (Sigma Aldrich), tetramethylsilane (Sigma Aldrich), triflic acid (abcr), trifluoroacetic acid (Sigma Aldrich), trifluoroboric acid diethylether adduct (Sigma Aldrich) and *Verkade*'s base (Sigma Aldrich) was used without further purification. DABCO (TCI), KO*t*Bu (Sigma Aldrich), napththalene (Sigma Aldrich) and PPh_3 (Sigma Aldrich) was purified by sublimation. TMS_2O (Sigma Aldrich) and TMG (abcr) was purified by distillation and stored over molecular sieves (3 Å). CO (≥99.997%) was purchased from Air Liquide. CO_2 (≥99.9993%, Linde) was purified as described in the experimental procedures. H_2 (≥99.9999%, Linde) was purified by a high capacity moisture filter (Pure Gas Products) prior to use. CH_4 (>99.995%, Messer), $^{13}CO_2$ (99 atom % isotopic purity, Sigma Aldrich) and D_2 (99.9 atom % isotopic purity, Sigma Aldrich) was used without further purification. NEt_3 (Sigma Aldrich) was dried over KOH. ^{t}BuOH (Sigma Aldrich) was purified by distillation prior to use. Styrene (Sigma Aldrich), 1-octene (Sigma Aldrich), 3,3-dimethylbuten (Sigma Aldrich), cyclooctene (TCI) and benzaldehyde (Sigma Aldrich) was degassed and stored over molecular sieves (3 Å). Molecular sieves and Celite® was dried by prolonged heating under vacuum. 2,4,6-Tri-*tert*-butylphenoxyl,[124] [H(OEt$_2$)]BArF,[125] [Fc]BArF[126], NaBArF[127], KC_8[128], [PPN]N_3[129], [NiH{N(2-C_6H_3-5-CH_3-P^{i}Pr$_2$)$_2$}][130] and $^{tBu}PN^HP$[131] was synthesized according to published procedures. [H(lut)]BArF, [H(NEt_3)]BArF and [H(piperidine)]BArF was prepared by reacting the conjugate base with an equimolar amount of

[$H(OEt_2)$]BArF in diethylether and crystallization of the product at -36°C. TEMPO-H was prepared according to literature, and TEMPO-D was prepared using deuterated acetone and water instead.[132] ^{t}BuOD was prepared by reacting KO^{t}Bu with an excess of D_2O followed by purification by distillation and stored over molecular sieves (3 Å).

NMR spectra were recorded on Bruker Avance III 300, Avance III 400 or Avance 500 spectrometers equipped with a Prodigy broadband CryoProbe. Spectra were calibrated to the residual solvent signals (C_6D_6: δ_H = 7.16 ppm, δ_C = 128.4 ppm; THF-d_8: δ_H = 3.58 ppm, δ_C = 67.21 ppm; CD_2Cl_2: δ_H = 5.32 ppm, δ_C = 54.0 ppm; MeCN-d_3: δ_H = 1.94 ppm, δ_C = 118.26 ppm, Ph-Cl-d_5: δ_H = 7.14 ppm, δ_C = 134.19 ppm). ^{31}P-NMR data was referenced externally to phosphoric acid (δ = 0.0 ppm). The following abbreviations were used for signal multiplicities: s (singlet), d (doublet), t (triplet), q (quartet), p (pentet), m (multiplet), br (broad), vt (virtual triplet). LIFDI (Linden CMS) mass spectra were measured by the Zentrale Massenabteilung, Fakultät für Chemie, Georg-August-Universität. Elemental analyses were obtained from the Analytisches Labor, Georg-August-Universität using an Elementar Vario EL 3 analyzer. IR spectra were obtained as KBr pellets or as KBr protected solutions on a Thermo Science Nicolet iZ10, or as powder or solution on a Bruker ALPHA FT-IR spectrometer with Platinum ATR module. UV-vis spectra were obtained on an Agilent Cary 300 spectrometer or an Avantes AvaLight-DH-S-BAL light source in combination with an AvaSpec-2048 fibre optic spectrometer and an AvaSpec-NIR-256-2.5-HSC detector. EPR spectra were measured using a Bruker ELEXSYS E500 spectrometer, equipped with the digital temperature control system ER 4131VT using nitrogen as coolant. All spectra at 150 K were recorded at about 9.4 GHz microwave frequency and 4 G field modulation amplitude, 100 kHz field modulation frequency, and around 10 mW microwave power. Gas phase analysis was performed by a Shimadzu GC-2014 equipped with a TCD detector and a molecular sieve 5 Å, 80/100 column. Photolysis experiments were performed using a 150 W Xe arc lamp with a lamp housing and arc lamp power supply from LOT-Quantum Design GmbH or a Kessil PR160-390 150 W monochromatic ($\lambda_{exc.}$ = 390 nm) LED light source. IR irradiation emitted by the arc lamp was cut off by a water filter. The photolyzed sample was kept at room temperature by cooling with a water bath if not stated otherwise. Kinetic data analysis was performed using the program package *COPASI*.[133]

1.7 Isolated Substances

1.7.1 [NiBr(^{tBu}PNP)] (2)

$^{tBu}PN^{H}P$ (500 mg, 1.38 mmol, 1.00 eq) and [$NiBr_2$(dme)] (429 mg, 1.38 mmol, 1.00 eq) is suspended in 10 mL of THF and stirred at room temperature overnight. The solvent is evaporated and the red residue is washed with 3×5 mL of *n*-pentane. The red powder is suspended in 10 mL of benzene and potassium *t*ert-butoxide (171 mg, 1.52 mmol, 1.10 eq) is added. After stirring for two hours at room temperature, the precipitate is removed by filtration and the solvent is evaporated. The residue is extracted and filtered with *n*-pentane. Evaporation of the solvent and drying *in vacuo* yields the product as a dark green solid. Yield: 570 mg (83%).

Crystals suitable for X-ray diffraction are obtained from a solution of **2** in *n*-pentane by slow evaporation of the solvent.

Anal. Calcd. for $C_{20}H_{44}NP_2NiBr$ (499.12): C, 48.13; H, 8.89; N, 2.81%. Found: C, 48.82; H, 9.42; N, 2.76%.

$^{31}P\{^1H\}$ NMR (121 MHz, C_6D_6) δ = 71.1 (s) ppm.

^{1}H NMR (300 MHz, C_6D_6) δ = 2.39 ($A_{18}B_2C_2XX'C'_2B'_2A'_{18}$, N = $|^3J_{CX}+^4J_{CX'}|$ = 25.5 Hz, $^3J_{CB}$ = 6.5 Hz, 4H, NCH_2), 1.50 ($A_{18}B_2C_2XX'C'_2B'_2A'_{18}$, N = $|^3J_{AX}+^5J_{AX'}|$ = 12.6 Hz, 36H, P^{t}Bu) ppm. *The PC*H_2 *resonance is superimposed by the* ^{t}*Bu resonance which is confirmed by* ^{1}*H,*^{1}*H COSY and* ^{1}*H,*^{13}*C HSQC.*

$^{13}C\{^1H\}$ NMR (75 MHz, C_6D_6): δ = 61.4 (vt, $^2J_{CP}$ = 5.6 Hz, N*C*H_2), 35.9 (vt, $^1J_{CP}$ = 6.9 Hz, P*C*H_2), 29.7 (vt, $^2J_{CP}$ = 2.1 Hz, PC*Me*$_3$), 24.0 (vt, $^1J_{CP}$ = 8.8 Hz, P*C*Me$_3$) ppm.

MS (LIFDI, toluene): *m/z* = 499.1 (100%, $[C_{20}H_{44}NP_2NiBr]^+$).

1.7.2 [NiBr(^{tBu}P=N=P)] (3)

[NiBr(^{tBu}PNP)] (**2**) (300 mg, 0.601 mmol, 1.00 eq) and 2,4,6-tri-*tert*-butylphenoxyl (707 mg, 2.70 mmol, 4.49 eq) is dissolved in 30 mL of benzene and stirred at room temperature for 2 h. After removal of the solvent, the solid is sublimed overnight at 70°C and the residue is collected. Yield: 280 mg (94%).

Crystals suitable for X-ray diffraction are obtained from a solution of **3** in *n*-pentane by crystallization at -36°C.

Anal. Calcd. for $C_{20}H_{40}NP_2NiBr$: C, 48.53; H, 8.14; N, 2.83%. Found: C, 49.07; H, 8.10, N, 2.74%.

$^{31}P\{^1H\}$ NMR (121 MHz, C_6D_6): δ = 58.6 (s) ppm.

^{1}H NMR (300 MHz, C_6D_6): δ = 6.38 (A_{18}BCXX'C'B'A'$_{18}$, N = $|^{3}J_{CX}+^{4}J_{CX'}|$ = 38.5 Hz, $^{3}J_{CB}$ = 5.4 Hz, 2H, NC*H*), 3.78 (A_{18}BCXX'C'B'A'$_{18}$, N = $|^{2}J_{BX}+^{4}J_{BX'}|$ = 3.8 Hz, $^{3}J_{BC}$ = 5.4 Hz, 2H, PC*H*), 1.51 (A_{18}BCXX'C'B'A'$_{18}$, N = $|^{3}J_{AX}+^{5}J_{AX'}|$ = 13.6 Hz, 36H, P^{t}Bu) ppm.

^{13}C{^{1}H} NMR (75 MHz, C_6D_6): δ = 162.0 (vt, $^{2}J_{CP}$ = 11.4 Hz, NC*H*), 83.1 (vt, $^{1}J_{CP}$ = 17.8 Hz, P*C*H$_2$), 36.2 (vt, $^{1}J_{CP}$ = 9.4 Hz, P*C*Me$_3$), 29.6 (vt, $^{2}J_{CP}$ = 2.5 Hz, PC*Me*$_3$) ppm.

MS (LIFDI, toluene): *m/z* = 495.1 (100%, $[C_{20}H_{40}NP_2NiBr]^{+}$).

1.7.3 [NiBr(^{tBu}P=N=P^{H})]BF$_4$ (4^{BF4})

[NiBr(^{tBu}P=N=P)] (**3**) (39 mg, 0.060 mmol, 1.00 eq) is dissolved in 1 mL of Et_2O and $HBF_4{\cdot}Et_2O$ (11 mg, 0.068 mmol, 1.1 eq) is added which results in precipitation of a red solid. After removal of the solvent, the red solid is washed with 2 mL of *n*-pentane and dried *in vacuo*. Yield: 29 mg (83%).

Anal. Calcd. for $C_{20}H_{41}BNF_4P_2NiBr$ (582.90): C, 41.21; H, 7.09; N, 2.40%. Found: C, 40.88 H, 7.30; N, 2.00%.

^{31}P{^{1}H} NMR (121 MHz, CD_2Cl_2) δ = 65.2 (d, $^{2}J_{PP}$ = 295 Hz), 62.0 (d, $^{2}J_{PP}$ = 295 Hz) ppm.

^{1}H NMR (300 MHz, CD_2Cl_2) δ = 8.48 (d, $^{3}J_{HP}$ = 22.7 Hz, 1H, NC*H*CH$_2$), 7.29 (ddd, $^{3}J_{HP}$ = 29.1 Hz, $^{3}J_{HH}$ = 6.0 Hz, $^{4}J_{HH}$ = 2.8 Hz, 1H, NC*H*), 5.97 (dd, $^{2}J_{HP}$ = 3.3 Hz, $^{3}J_{HH}$ = 6.1 Hz, 1H, PC*H*), 3.25 (dd, $^{2}J_{HP}$ = 7.5 Hz, $^{3}J_{HH}$ = 2.3 Hz, 2H, PC*H*$_2$), 1.56 (dd, $^{3}J_{HP}$ = 13.0 Hz, $^{5}J_{HP}$ = 2.1 Hz, 18H, P^{t}Bu), 1.55 (dd, $^{3}J_{HP}$ = 12.8 Hz, $^{5}J_{HP}$ = 2.1 Hz, 18H, P^{t}Bu) ppm.

^{13}C{^{1}H} NMR (75 MHz, CD_2Cl_2) δ = 186.8 (dd, $^{2}J_{CP}$ = 7.2 Hz, $^{4}J_{CP}$ = 3.5 Hz, N*C*HCH$_2$), 157.7 (dd, $^{2}J_{CP}$ = 10.6 Hz, $^{4}J_{CP}$ = 3.5 Hz, N*C*HCH), 122.0 (dd, $^{1}J_{CP}$ = 22.4 Hz, $^{3}J_{CP}$ = 2.1 Hz, P*C*H), 37.8 (dd, $^{1}J_{CP}$ = 14.2 Hz, $^{3}J_{CP}$ = 3.6 Hz, P*C*Me$_3$), 36.9 (dd, $^{1}J_{CP}$ = 11.8 Hz, $^{3}J_{CP}$ = 3.3 Hz, P*C*Me$_3$), 34.9 (d, $^{1}J_{CP}$ = 16.9 Hz, P*C*H$_2$), 29.6 (dd, $^{2}J_{CP}$ = 2.7 Hz, $^{4}J_{CP}$ = 1.2 Hz, PC*Me*$_3$), 29.1 (dd, $^{2}J_{CP}$ = 2.4 Hz, $^{4}J_{CP}$ = 1.4 Hz, PC*Me*$_3$) ppm.

MS (LIFDI, CH_2Cl_2): *m/z* = 496.1 (100, $[C_{20}H_{41}NP_2NiBr]^{+}$).

4^{OTf} is obtained by a similar procedure, using HOTf instead of $HBF_4{\cdot}OEt_2$. Crystals suitable for X-ray diffraction are obtained by layering a solution of 4^{OTf} in dichloromethane with* n*-pentane.

1.7.4 [NiBr(^{tBu}P=N=P)]PF$_6$ (5^{PF6})

[NiBr(^{tBu}P=N=P))] (**3**) (20 mg, 0.040 mmol, 1.0 eq) and $AgPF_6$ (10 mg, 0.040 mmol, 1.0 eq) is dissolved in 3 mL of chlorobenzene and stirred for 5 minutes at room temperature, which causes the solution to turn red and a black precipitate to form. After filtration, 5 mL of *n*-pentane are added to precipitate a red solid. After decantation, the solid is washed with 3×3 mL of *n*-pentane and the red solid is dried *in vacuo*. Yield: 20 mg (78%).

Crystals suitable for X-ray diffraction are obtained after one day by layering a solution of **5^{PF6}** in chlorobenzene with *n*-pentane.

Anal. Calcd. for $C_{20}H_{40}NF_6P_3NiBr$ (640.06): C, 37.53; H, 6.30; N, 2.19%. Found: C, 37.38 H, 6.18; N, 2.02%.

^{1}H NMR (300 MHz, CD_2Cl_2) δ = 10.7 (br, P^{t}Bu) ppm.

MS (LIFDI, CH_2Cl_2): *m/z* = 495.1 (100%, $[C_{20}H_{40}NP_2NiBr]^+$).

Evans' method: μ_{eff} = 1.9 ± 0.1 μ_B.

1.7.5 [Ni(NCMe)(^{tBu}PNP)]BArF (6^{BArF})

[NiBr(^{tBu}PNP)] (**2**) (50 mg, 0.10 mmol, 1.0 eq) and NaBArF (89 mg, 0.10 mmol, 1.0 eq) is dissolved in 5 mL of acetonitrile and stirred at room temperature overnight. After evaporation of the solvent the violet residue is dissolved in DCM and filtered. The volume of the solution is reduced to 1 mL and the product is precipitated by addition of *n*-pentane. Removal of the solvent and drying *in vacuo* gives the product as a violet powder. Yield: 114 mg (86%).

Crystals suitable for X-ray diffraction are obtained by layering a solution of **6^{BArF}** in chlorobenzene with *n*-pentane.

Anal. Calcd. for $C_{54}H_{59}BF_{24}N_2NiP_2$ (1323.49): C, 49.01; H, 4.49; N, 2.12%. Found: C, 49.04 H, 4.27; N, 2.03%.

^{31}P{^{1}H} NMR (122 MHz, CD_2Cl_2) δ = 93.4 ppm.

^{1}H NMR (300 MHz, CD_2Cl_2) δ = 7.73 (br, 8H, BArF), 7.57 (br, 4H, BArF), 2.48 ($A_{18}B_2C_2XX'C'_2B'_2A'_{18}$, $N = |{}^3J_{CX} + {}^4J_{CX'}| = 29.1$ Hz, $^3J_{CB}$ = 6.6 Hz, 4H, NCH_2), 2.20 (t, $^5J_{HP}$ = 2.0 Hz, 3H, NCCH_3), 1.83 ($A_{18}B_2C_2XX'C'_2B'_2A'_{18}$, $N = |{}^2J_{BX} + {}^4J_{BX'}| = 9.0$ Hz, $^3J_{BC}$ = 6.6 Hz, 4H, PCH_2), 1.42 ($A_{18}B_2C_2XX'C'_2B'_2A'_{18}$, $N = |{}^3J_{AX} + {}^5J_{AX'}| = 13.4$ Hz, 36H, P^{t}Bu) ppm.

^{13}C{^{1}H} NMR (75 MHz, CD_2Cl_2) δ = 162.2 (q, $^1J_{CB}$ = 49.81 Hz, BArF), 135.2 (s, BArF), 132.2 (s, N*C*Me), 129.4 (qq, $^2J_{CB}$ = 2.8 Hz, $^2J_{CF}$ = 30.11 Hz, BArF), 125.0 (q, $^1J_{CF}$ = 272.40 Hz, BArF), 117.9 (p, $^3J_{CF}$ = 4.2 Hz, BArF), 61.9 (vt, $^2J_{CP}$ = 4.2 Hz, N*C*H$_2$), 36.5 (vt, $^1J_{CP}$ = 7.3 Hz, P*C*Me$_3$), 29.2 (vt, $^2J_{CP}$ = 2.1 Hz, PC*Me*$_3$), 22.6 (vt, $^1J_{CP}$ = 11.1 Hz, P*C*H$_2$), 4.9 (s, NC*Me*) ppm.

IR (KBr): $\tilde{\upsilon}$ = 2360.3, 2340.0 cm^{-1}.

MS (LIFDI, CH_2Cl_2): *m/z* = 419.2 (100%, $[C_{20}H_{44}NP_2Ni]^+$).

1.7.6 [Ni(NCMe)(^{tBu}PNP)]BF_4 (6^{BF4})

[NiBr(^{tBu}PNP)] (**2**) (200 mg, 0.401 mmol, 1.00 eq) and $NaBF_4$ (44.0 mg, 0.401 mmol, 1.00 eq) is dissolved in 10 mL of acetonitrile and stirred at room temperature overnight. The solution is filtered. After evaporation of the solvent the violet residue is dissolved in DCM and filtered again. The volume of the solution is reduced to 1 mL and the product is precipitated by addition of *n*-pentane. Removal of the solvent and drying *in vacuo* gives the product as a violet powder. Yield: 197 mg (90%).

The NMR spectroscopic signature of the cation of ***6^{BArF}*** *and* ***6^{BF4}*** *is identical.*

Anal. Calcd. for $C_{22}H_{43}BF_4N_2P_2Ni$ (543.04): C, 48.66; H, 7.98; N, 5.16%. Found: C, 48.06 H, 7.97; N, 4.71%.

1.7.7 [Ni(NCMe)(^{tBu}P=N=P)]BArF (7^{BArF})

[Ni(NCMe)(^{tBu}PNP)]BArF (**6^{BArF}**) (74 mg, 0.056 mmol, 1.0 eq) and 2,4,6-tri-*tert*-butylphenoxyl (102 mg, 0.390 mmol, 7.0 eq) is dissolved in 5 mL of chlorobenzene and stirred at 50°C for 36 hours. After cooling to room temperature, the product is precipitated by addition of *n*-pentane to yield a pale green solid. After decantation of the solvent and drying *in vacuo*, the residue is dissolved in a minimum amount of dichloromethane and again precipitated by addition of *n*-pentane. After decantation of the solvent and drying *in vacuo*, the product is obtained as a pale green solid. Yield: 45 mg (61%).

Anal. Calcd. for $C_{54}H_{55}BF_{24}N_2NiP_2$ (1319.46): C, 49.16; H, 4.20; N, 2.12%. Found: C, 48.99 H, 4.22; N, 2.03%.

^{31}P{^{1}H} NMR (121 MHz, THF-d_8) δ = 81.0 ppm.

^{1}H NMR (300 MHz, THF-d_8) δ = 7.79 (m, 8H, BArF), 7.57 (br, 4H, BArF), 6.84 (A_{18}BCXX'C'B'A'$_{18}$, N = $|{}^3J_{CX} + {}^4J_{CX'}|$ = 42.93 Hz, $^3J_{CB}$ = 5.3 Hz, 2H, NC*H*), 2.64 (t, $^5J_{HP}$ = 2.0 Hz, 3H, NCCH_3), 1.83 (A_{18}BCXX'C'B'A'$_{18}$, N = $|{}^2J_{BX} + {}^4J_{BX'}|$ = 3.4 Hz, $^2J_{BC}$ = 5.2 Hz, 2H, PC*H*), 1.47 (A_{18}BCXX'C'B'A'$_{18}$, N = $|{}^3J_{AX} + {}^5J_{AX'}|$ = 14.4 Hz, 36H, P^{t}Bu) ppm.

^{13}C{^{1}H} NMR (75 MHz, THF-d_8) δ = 164.7 (vt, $^2J_{CP}$ = 9.6 Hz, NC*H*), 162.6 (q, $^1J_{BC}$ = 49.70 Hz, BArF), 140.3 *(detected by ^{13}C,^{1}H-HMBC*, NC*Me*), 135.4 (s, BArF), 129.8 (qq, $^2J_{CB}$ = 2.8 Hz, $^2J_{CF}$ = 30.11 Hz, BArF), 125.3 (q, $^1J_{CF}$ = 272.20 Hz, BArF), 118.0 (p, $^3J_{CF}$ = 4.0 Hz, BArF), 81.5 (vt, $^1J_{CP}$ = 21.0 Hz, P*C*H), 37.0 (vt, $^1J_{CP}$ = 9.7 Hz, P*C*Me$_3$), 29.1 (vt, $^2J_{CP}$ = 2.4 Hz, PC*Me*$_3$), 3.4 (s, NC*Me*) ppm.

IR (KBr): $\tilde{\upsilon}$ = 2360.5, 2338.1 cm^{-1}.

MS (LIFDI): *m/z* = 455.2 (100%, $[C_{22}H_{43}N_2P_2Ni]^+$).

1.7.8 [Ni(NCMe)(^{tBu}P=N=P)]BF_4 (7^{BF4})

[Ni(NCMe)(^{tBu}PNP)]BF_4 (**6^{BF4}**) (150 mg, 0.274 mmol, 1.00 eq) and 2,4,6-tris-*tert*-butylphenoxyl (502 mg, 1.92 mmol, 7.01 eq) is dissolved in 10 mL of chlorobenzene and stirred at 50°C for 36 hours. After cooling to room temperature, the product is precipitated by addition of *n*-pentane to yield a pale red solid. The reaction mixture is filtered and washed with 10×5 mL of *n*-pentane. The solid is dissolved in dichloromethane and again precipitated by addition of *n*-pentane. After removal of the solvent and drying *in vacuo*, the product is obtained as a pale red solid. Yield: 103 mg (69%).

Crystals suitable for X-ray diffraction are obtained by layering a solution of **7^{BF4}** in chlorobenzene with *n*-pentane.

*The NMR spectroscopic signature of the cation of **7^{BArF}** and **7^{BF4}** is identical.*

1.7.9 [Ni(NCMe)(^{tBu}P=N=P^H)]$(BArF)_2$ ($8^{(BArF)2}$)

[Ni(NCMe)(^{tBu}P=N=P)]BArF (**7^{BArF}**) (30 mg, 0.023 mmol, 1.0 eq) and [H(OEt_2)$_2$]BArF (23 mg, 0.023 mmol, 1.0 eq) is dissolved in 5 mL of dichloromethane. The solution is stirred for 30 min at room temperature and filtered. Evaporation of the solvent and washing with 2×1 mL of *n*-pentane, followed by drying *in vacuo* gives the product as a yellow solid. Yield: 43 mg (86%).

Anal. Calcd. for $C_{86}H_{67}B_2F_{48}N_2NiP_2$ (2182.68): C, 47.32; H, 3.09; N, 1.28%. Found: C, 47.23 H, 3.00; N, 1.29%.

$^{31}P\{^1H\}$ NMR (203 MHz, CD_2Cl_2) δ = 87.0 (d, $^2J_{PP}$ = 215.7 Hz), 84.8 (d, $^2J_{PP}$ = 215.8 Hz) ppm.

^1H NMR (126 MHz, CD_2Cl_2) δ = 8.14 (dt, $^3J_{HP}$ = 25.8 Hz, $^3J_{HH}$ = 2.4 Hz, 1H, NC*H*CH_2), 7.73 (m, 16H, BArF), 7.57 (br, 8H, BArF), 7.08 (dd, $^3J_{HP}$ = 33.0 Hz, $^3J_{HH}$ = 6.0 Hz, 1H, NC*H*), 6.16 (dd, $^2J_{HP}$ = 3.7 Hz, $^3J_{HH}$ = 5.9 Hz, 1H, PC*H*), 3.32 (dd, $^2J_{HP}$ = 8.2 Hz, $^3J_{HH}$ = 2.4 Hz, 2H, PCH_2), 2.60 (t, $^5J_{HP}$ = 2.0 Hz, 3H, NCCH_3), 1.48 (m, 18H. P^{t}Bu), 1.48 (m, 18H. P^{t}Bu) ppm.

$^{13}C\{^1H\}$ NMR (500 MHz, CD_2Cl_2) δ = 188.8 (dd, $^2J_{CP}$ = 2.7 Hz, $^3J_{CP}$ = 5.9 Hz, N*C*HCH_2), 162.6 (q, $^1J_{BC}$ = 49.80 Hz, BArF), 157.8 (dd, $^2J_{CP}$ = 2.8 Hz, $^3J_{CP}$ = 8.1 Hz, N*C*HCH), 135.2 (m, BArF), 129.3 (qq, $^2J_{CB}$ = 2.9 Hz, $^2J_{CF}$ = 31.6 Hz, BArF), 125.0 (q, $^1J_{CF}$ = 272.4 Hz, BArF), 122.1 (dd, $^1J_{CP}$ = 29.1 Hz, $^3J_{CP}$ = 1.5 Hz, NCH*C*H),117.9 (p, $^3J_{CF}$ = 4.0 Hz, BArF), 39.2 (dd, $^1J_{CP}$ = 13.2 Hz, $^3J_{CP}$ = 2.7 Hz, P*C*Me_3), 38.2 (dd, $^1J_{CP}$ = 11.4 Hz, $^3J_{CP}$ = 2.5 Hz, P*C*Me_3), 33.8 (d, $^1J_{CP}$ = 21.2 Hz, P*C*H_2), 29.3 (dd, $^2J_{CP}$ = 2.7 Hz, $^4J_{CP}$ = 1.1 Hz, P*C*Me_3), 28.9 (dd, $^2J_{CP}$ = 2.5 Hz, $^4J_{CP}$ = 1.0 Hz, P*C*Me_3), 5.5 (s, NC*Me*) ppm. *The quaternary carbon resonance of the NCMe moiety is not detected due to low signal intensity.*

IR (ATR): $\tilde{\upsilon}$ = 2324.9, 2294.1 cm^{-1}.

1.7.10 [Ni(^{tBu}P=N=P)] (9)

[NiBr(^{tBu}P=N=P)] (**3**) (80 mg, 0.16 mmol, 1.0 eq) and magnesium powder (78 mg, 3.2 mmol, 20 eq) is suspended in 5 mL of THF and stirred for 30 minutes at room temperature, upon which the solution turns orange. The solvent is evaporated, and the residue is dissolved in *n*-pentane and filtered over Celite®. The orange solution is dried *in vacuo* and the orange powder is dissolved in a minimum amount of *n*-pentane followed by recrystallization at -36°C. The supernatant solution is decanted, and again recrystallized at -36°C. This procedure is repeated afterwards. Yield: 42mg (62%).

Crystals suitable for X-ray diffraction are obtained from a solution of **9** in *n*-pentane by crystallization at -36°C.

Anal. Calcd. for $C_{20}H_{40}NP_2Ni$ (415.19): C, 57.86; H, 9.71; N, 3.37%. Found: C, 57.59 H, 9.48; N, 3.27%.

^{1}H NMR (400 MHz, C_6D_6) δ = 7.2 (br, P^{t}Bu), -62.0 (br, C*H*) ppm.

MS (LIFDI, toluene): *m/z* = 414.1 (100%, $[M]^+$).

1.7.11 [Ni(^{tBu}P=N=P^H)]BArF (10^{BArF})

[Ni(^{tBu}P=N=P)] (**9**) (20 mg, 0.048 mmol, 1.0 eq) and [H(lut)]BArF (47 mg, 0.048 mmol, 1.0 eq) is dissolved in 5 mL of THF and stirred for 45 min at room temperature. After evaporation of the solvent, the orange residue is washed with 3×2 mL of *n*-pentane, dissolved in diethyl ether and filtered. The product is precipitated by addition of *n*-pentane and dried *in vacuo*. Yield: 52 mg (84%).

Crystals suitable for X-ray diffraction are obtained from a solution of **10^{BArF}** in a THF/*n*-pentane mixture by crystallization at -36°C.

Anal. Calcd. for $C_{52}H_{53}BNF_{24}P_2Ni$ (1278.27): C, 48.82; H, 4.18; N, 1.09%. Found: C, 48.58; H, 4.16; N, 1.18%.

1.7.12 [Ni(*κO*-THF)(^{tBu}P=N=P)] PF_6 (11^{PF6})

[NiBr(^{tBu}P=N=P)] (**3**) (50 mg, 0.10 mmol, 1.0 eq) and magnesium powder (50 mg, 21 mmol, 21 eq) are suspended in 5 mL of THF and stirred at room temperature for 1 h. After evaporation of the solvent, the residue is extracted with *n*-pentane, filtered over Celite® and dried *in vacuo*. $FcPF_6$ (33 mg, 0.097 mmol, 1.0 eq) and 5 mL of THF is added and the mixture is stirred for 1 h at room temperature. After evaporation of the solvent, the red residue is dissolved in a small amount of THF and the product as precipitated by addition of *n*-pentane.

Crystals suitable for X-ray diffraction are obtained from a solution of **11^{PF6}** in a THF/ *n*-pentane mixture by crystallization at -36°C.

^{31}P{^{1}H} NMR (121 MHz, THF-d_8) δ = 61.9 ppm.

1.7.13 [NiH(^{tBu}P=N=P)] (12)

[NiBr(^{tBu}P=N=P)] (**3**) (208 mg, 0.420 mmol, 1.00 eq) and $LiAlH_4$ (16.0 mg, 0.422 mmol, 1.00 eq) is dissolved in 6 mL of THF. After stirring at room temperature for 30 minutes, the solvent of the orange solution is removed *in vacuo*. The orange residue is extracted with *n*-pentane and the resulting solution is filtered over Celite® to yield a yellow solution. The solvent is evaporated and the yellow solid is washed with 7×2 mL of methanol at 0°C. The residue is dissolved in 10 mL of *n*-pentane and filtered. After evaporation of the solvent, the yellow solid is dissolved in a minimal amount of *n*-pentane and recrystallized at -36°C. The supernatant solution is decanted, and again recrystallized at -36°C. The yellow crystalline material is dried *in vacuo*. Yield: 106 mg (61%).

Crystals suitable for X-ray diffraction are obtained from a solution of **12** in *n*-pentane by crystallization at -36°C.

Anal. Calcd. for $C_{40}H_{41}NNiP_2$ (416.20): C, 57.72; H, 9.93; N, 3.37%. Found: C, 57.48 H, 9.80; N, 3.41%.

^{31}P{^{1}H} NMR (121 MHz, C_6D_6) δ = 86.2 ppm.

^{1}H NMR (300 MHz, C_6D_6) δ = 7.20 (A_{18}BCXX'C'B'A'$_{18}$, N = $|{}^{3}J_{CX} + {}^{4}J_{CX'}|$ = 36.6 Hz, ${}^{3}J_{CB}$ = 5.0 Hz, ${}^{4}J_{HH}$ = 1.9 Hz, Hz, 2H, NC*H*), 4.09 (A_{18}BCXX'C'B'A'$_{18}$, N = $|{}^{2}J_{BX} + {}^{4}J_{BX'}|$ = 1.8 Hz, ${}^{3}J_{BC}$ = 5.1 Hz, ${}^{4}J_{HH}$ = 1.8 Hz, 2H, PC*H*), (A_{18}BCXX'C'B'A'$_{18}$, N = $|{}^{3}J_{AX} + {}^{5}J_{AX'}|$ = 13.4 Hz, 36H, P^{t}Bu), -18.52 (tp, ${}^{2}J_{HP}$ = 59.4 Hz, ${}^{4}J_{HH}$ = 2.0 Hz, 1H, Ni*H*) ppm.

^{13}C{^{1}H} NMR (75 MHz, C_6D_6) δ = 160.8 (vt, ${}^{2}J_{CP}$ = 11.8 Hz, NC*H*), 83.0 (vt, ${}^{1}J_{CP}$ = 15.8 Hz, P*C*H), 33.8 (vt, ${}^{1}J_{CP}$ = 11.1 Hz, P*C*Me$_3$), 29.8 (vt, ${}^{2}J_{CP}$ = 2.9 Hz, PC*Me*$_3$) ppm.

IR (KBr): $\tilde{\upsilon}$ = 1834.3 cm^{-1}.

MS (LIFDI, toluene): *m/z* = 415.1 (100%, $[M]^+$).

Spectroscopic data on HN(CHCHP^{t}Bu$_2$)$_2$ (**13**) can be obtained from analysis of the methanol washing solution after evaporation of the solvent.

^{31}P{^{1}H} NMR (121 MHz, C_6D_6) δ = -3.0 ppm.

^{1}H NMR (300 MHz, C_6D_6) δ = 8.45 (br, $^3J_{HH}$ = 12.0 Hz, 1H, N*H*), 6.45 (dddd, $^3J_{HP}$ = 16.9 Hz, $^3J_{HH}$ = 12.0 Hz, $^3J_{HH}$ = 9.2 Hz, $^5J_{HP}$ = 2.8 Hz, 2H, NC*H*), 4.50 (dd, $^3J_{HH}$ = 9.3 Hz, $^2J_{HP}$ = 5.3 Hz, 2H, PC*H*), 1.14 (d, $^3J_{HP}$ = 11.5 Hz, 36H, P^{t}Bu) ppm.

1.7.14 [NiD(^{tBu}P=N=P)] (12-D)

[NiBr(^{tBu}P=N=P)] (**3**) (150 mg, 0.303 mmol, 1.0 eq) and $LiAlD_4$ (13.0 mg, 0.310 mmol, 1.02 eq) is dissolved in 6 mL of THF. After stirring at room temperature for 30 minutes, the solvent of the orange solution is removed *in vacuo*. The orange residue is extracted with *n*-pentane and the resulting solution is filtered over Celite® to yield a yellow solution. The solvent is evaporated and the yellow solid is washed with 7×2 mL of methanol at 0°C. The residue is dissolved in 10 mL of *n*-pentane and filtered. After evaporation of the solvent, the yellow solid is dissolved in a minimal amount of *n*-pentane and recrystallized at -36°C. The supernatant solution is decanted, and again recrystallized at -36°C. The yellow crystalline material is dried *in vacuo*. Yield: 69 mg (55%).

^{2}H NMR (46 MHz, C_6H_6) δ = -17.50 (t, $^2J_{DP}$ = 9.0 Hz, Ni*D*) ppm.

IR (THF-d_8): $\tilde{\upsilon}$ = 1318, 1333 cm^{-1}.

1.7.15 [NiH(^{tBu}P=N=P^H)]BF_4 (14^{BF4})

[NiH(^{tBu}P=N=P)] (**12**) (20 mg, 0.048 mmol, 1.0 eq) is dissolved in 5 mL of Et_2O and cooled to -36°C. $HBF_4{\cdot}Et_2O$ (9.0 mg, 0.056 mmol, 1.2 eq) is added and the solution is warmed to room temperature over 30 minutes. The solvent is evaporated and the yellow solid is dissolved in benzene followed by filtration. After evaporation of the solvent and washing with 2×2 mL of *n*-pentane the yellow product is dried *in vacuo*. Yield: 22 mg (92%).

Anal. Calcd. for $C_{20}H_{42}BNF_4P_2Ni$ (504.01): C, 47.66; H, 8.40; N, 2.78%. Found: C, 48.18 H, 8.20; N, 2.61%.

^{31}P{^{1}H} NMR (203 MHz, C_6D_6) δ = 88.2 (d, $^2J_{PP}$ = 215 Hz), 85.5 (d, $^2J_{PP}$ = 215 Hz) ppm.

^{1}H NMR (500 MHz, C_6D_6) δ = 9.27 (ddt, $^3J_{HP}$ = 24.8 Hz, $^3J_{HH}$ = 2.2 Hz, $^4J_{HH}$ = 2.2 Hz, 1H, NC*H*CH$_2$), 8.12 (dd, $^3J_{HP}$ = 31.3 Hz, $^3J_{HH}$ = 6.0 Hz, 1H, NC*H*CH), 5.79 (ddd, $^3J_{HH}$ = 6.0 Hz, $^2J_{HP}$ = 2.2 Hz, $^5J_{HH}$ = 2.2 Hz, 1H, NCHC*H*), 3.52 (d, $^2J_{HP}$ = 7.5 Hz, 2H, PC*H*$_2$), 1.04 (d, $^3J_{HP}$ = 14.1 Hz, 18H, P^{t}Bu), 0.96 (d, $^3J_{HP}$ = 14.0 Hz, 18H, P^{t}Bu), -18.25 (t, $^2J_{HP}$ = 59.7 Hz, 1H, Ni*H*) ppm.

^{13}C{^{1}H} NMR (126 MHz, C_6D_6) δ = 182.6 (dd, $^2J_{CP}$ = 4.0 Hz, $^3J_{CP}$ = 6.6 Hz, N*C*HCH$_2$), 157.4 (dd, $^2J_{CP}$ = 3.3 Hz, $^3J_{CP}$ = 10.6 Hz, N*C*HCH), 121.9 (d, $^1J_{CP}$ = 21.2 Hz, NCH*C*H), 36.5 (d, $^1J_{CP}$ = 16.5 Hz, P*C*H$_2$),

33.8 (vt, $^{2}J_{CP}$ = 2.5 Hz, $^{3}J_{CP}$ = 10.3 Hz, P*C*Me$_3$), 33.7 (dd, $^{2}J_{CP}$ = 2.4 Hz, $^{3}J_{CP}$ = 12.5 Hz, P*C*Me$_3$), 29.2 (d, $^{2}J_{CP}$ = 5.1 Hz, PC*Me*$_3$), 28.9 (d, $^{2}J_{CP}$ = 4.9 Hz, PC*Me*$_3$) ppm.

IR (KBr): $\tilde{\upsilon}$ = 1884.2 cm^{-1}.

MS (LIFDI, toluene): *m/z* = 416.2 (100%, $[C_{20}H_{42}NP_2Ni]^+$).

1.7.16 [NiH(^{tBu}P=N=P^{H})]BArF (14^{BArF})

[NiH(^{tBu}P=N=P)] (**12**) (37 mg, 0.089 mmol, 1.0 eq) is dissolved in 5 mL of Et_2O and cooled to -36°C. $[H(OEt_2)_2]$BArF (90 mg, 0.089 mmol, 1.0 eq) is added and the solution is warmed to room temperature over 30 minutes. The solvent is evaporated and the yellow solid is washed with 3×2 mL of *n*-pentane and dissolved in diethyl ether followed by filtration. After evaporation of the solvent the yellow product is dried *in vacuo*. Yield: 100 mg (88%).

Anal. Calcd. for $C_{52}H_{54}BNF_{24}P_2Ni$ (1280.42): C, 48.78; H, 4.25; N, 1.09%. Found: C, 48.30 H, 4.05; N, 0.98%.

*The NMR spectroscopic signature of the cation of **14**^{BArF} and **14**^{BF4} is identical.*

1.7.17 [NiH(^{tBu}P=N=P^{H})]O_2CCF_3 (14^{O2CCF3})

[NiH(^{tBu}P=N=P)] (**12**) (10 mg, 0.024 mmol, 1.0 eq) and trifluoroacetic acid (14 mg, 0.123 mmol, 5.1 eq) is dissolved in 1 mL of Et_2O and cooled to -36°C yielding crystals suitable for X-ray diffraction overnight.

1.8 Activation of Benzylic C-H Bonds by Pincer Ligand Centered Chemical Non-Innocence

1.8.1 Determination of pK_a($\mathbf{4^{OTf}}$)^{DMSO} by Reaction of [NiBr(^{tBu}P=N=P)] (3) with Triflic Acid

[NiBr(^{tBu}P=N=P)] (**3**) (5.6 mg, 0.011 mmol, 1.0 eq) is dissolved in 2 mL of DMSO-d_6 and a solution of HOTf (0.113 M in DMSO-d_6, 100 µL, 0.0113 mmol, 1.0 eq) is added. 0.5 mL of the solution is filled into a J Young NMR tube.

1.8.2 Reaction of [NiBr(^{tBu}P=N=P)]PF_6 ($\mathbf{5^{PF6}}$) with Hydrocarbons

[NiBr(^{tBu}P=N=P)]PF_6 ($\mathbf{5^{PF6}}$) (5.0 mg, 7.9 µmol, 1.0 eq) and the substrate (0.79 mmol, 100 eq) is filled into a J Young NMR tube. A solution of tetramethylsilane (3 µL, 0.02 mmol, 3 eq) in 0.6 mL of deuterated solvent is condensed into the NMR tube at -196 °C. The sample is warmed to room temperature, immediately inserted into the NMR spectrometer and the formation of [NiBr(^{tBu}P=N=P^H)]PF_6 ($\mathbf{4^{PF6}}$) is monitored by NMR spectroscopy.

1.8.3 Determination of Kinetic Data for the Reaction of [NiBr(^{tBu}P=N=P)]PF_6 ($\mathbf{5^{PF6}}$) with 9,10-Dihydroanthracene

The decay of [NiBr(^{tBu}P=N=P)]PF_6 ($\mathbf{5^{PF6}}$) in the presence of 9,10-dihydroanthracene was monitored UV-vis-NIR spectroscopically. In a typical experiment, a stock solution of 9,10-dihydroanthracene (0.127 M in chlorobenzene, 0.50 mL, 64 µmol, 125 eq) is filled into a tempered cuvette inside of a glove box. The cuvette is filled with chlorobenzene to a total volume of 1.5 mL and the solution is stirred. A stock solution of $\mathbf{5^{PF6}}$ (1.01 mM in chlorobenzene, 0.50 mL, 0.51 µmol, 1.0 eq) is added and the experiment is monitored by measuring UV-vis-NIR spectra every 30 seconds**.** The absence of long-lived intermediates is evidenced by isosbestic points at λ = 328 nm and λ = 389 nm. The second-order rate constant was derived by following the NIR absorption of $\mathbf{5^{PF6}}$ at λ = 1040 nm and fitting the initial rates (t = 0 – 420 s) to the rate law shown in eq. (20).

1.8.4 Determination of Self-Exchange Rate

[NiBr(^{tBu}P=N=P^H)]BF_4 ($\mathbf{4^{BF4}}$) (2.0 mg, 3.4 µmol, 1.0 eq) is dissolved in 0.6 mL of Ph-Cl-d_5 and the sample is analyzed NMR spectroscopically. [NiBr(^{tBu}P=N=P)]PF_6 ($\mathbf{5^{PF6}}$) is added stepwise and after each addition, NMR spectra are recorded.

1.9 Effect of Ligand Substitution on Pincer C-H Bond Strength

1.9.1 Determination of pK_a($\mathbf{8^{BArF}}$)^{MeCN} by Reaction of [Ni(NCMe)(^{tBu}P=N=P^{H})](BArF)$_2$ ($\mathbf{8^{(BArF)2}}$) with Triphenyl Phosphine

[Ni(NCMe)(^{tBu}P=N=P^{H})](BArF)$_2$ (**8**$^{(BArF)2}$) (17 mg, 7.8 µmol, 1.0 eq) and PPh_3 (2.0 mg, 7.6 µmol, 1.0 eq) is filled into a J Young NMR tube and 0.5 mL of MeCN-d_3 is added. NMR spectroscopic measurement is performed to determine the ratio of [Ni(NCMe)(^{tBu}P=N=P^{H})](BArF)$_2$ (**8**$^{(BArF)2}$) and [Ni(NCMe)(^{tBu}P=N=P)]BArF (**7**^{BArF}). After stirring at room temperature for 4 hours, no change in the ratio is observed.

1.9.2 Reduction of [NiBr(^{tBu}P=N=P^{H})]BF$_4$ (**4**^{BF4}) with Cobaltocene

[NiBr(^{tBu}P=N=P^{H})]BF$_4$ (**4**^{BArF}) (5.0 mg, 9.9 µmol, 1.0 eq) and cobaltocene (2.0 mg, 0.011 mmol, 1.1 eq) is filled into a J Young NMR tube and 0.5 mL of THF-d_8 is condensed into the tube. After thawing to room temperature, a gradual color change from red to orange can be observed within the first 5 minutes. After 1 hour, the sample is analyzed NMR spectroscopically and the headspace is analyzed by TCD-GC.

1.9.3 Determination of pK_a($\mathbf{10^{BArF}}$)^{THF} by Reaction of [Ni(^{tBu}P=N=P^{H})]BArF (**10**^{BArF}) with Triethylamine

[Ni(^{tBu}P=N=P^{H})]BArF (**10**^{BArF}) (3.3 mg, 2.6 µmol, 1.0 eq) is dissolved in 0.4 mL of THF-d_8, filled into a J Young NMR tube and a solution of NEt_3 (0.26 M in THF-d_8, 10 µL, 2.6 µmol, 1.0 eq) is added. NMR spectroscopic measurement is performed to determine the ratio of NEt_3 and [H(NEt_3)]BArF. After stirring at room temperature overnight, no change in the ratio is observed.

1.9.4 Reaction of [Ni(^{tBu}P=N=P^{H})](BArF)$_2$ (**10**^{BArF}) with [(*n*-Hex)$_4$N]Br

[Ni(^{tBu}P=N=P^{H})]BArF (**10**^{BArF}) (3.0 mg, 2.3 µmol, 1.0 eq) is dissolved in 0.4 mL of THF-d_8, filled into a J Young NMR tube and [(*n*-Hex)$_4$]Br (1.0 mg, 2.6 µmol, 1.1 eq) is added giving an immediate intensification of the orange color indicating formation of [NiBr{N(CHCHP^{t}Bu$_2$)$_2$}] (**3**).

1.9.5 Reaction of [Ni(^{tBu}P=N=P^{H})]BArF (**10**^{BArF}) with Acetonitrile

[Ni(^{tBu}P=N=P^{H})]BArF (**10**^{BArF}) (3.0 mg, 2.3 µmol, 1.0 eq) is filled into a J Young NMR tube and 0.5 mL of MeCN is added. After stirring overnight, formation of [Ni(NCMe)(^{tBu}P=N=P)]BArF (**7**^{BArF}) can be observed NMR spectroscopically.

1.9.6 Reaction of [Ni(^{tBu}P=N=P)](10^{BArF}) with Styrene

[Ni(^{tBu}P=N=P^{H})]BArF (**10^{BArF}**) (3.0 mg, 2.3 µmol, 1.0 eq) is dissolved in 0.4 mL of THF-d_8, filled into a J Young NMR tube and styrene (1.3 µL, 12 µmol, 5.2 eq) is added. After NMR spectroscopic analysis, [(*n*-Hex)$_4$]Br (1.0 mg, 2.6 µmol, 1.0 eq) is added. No change in reactivity compared to the addition of [(*n*-Hex)$_4$]Br to **10^{BArF}** in the absence of styrene is observed.

1.9.7 Determination of pK_a(14^{BArF})^{MeCN} by Reaction of [NiH(^{tBu}P=N=P)] (12) with [H(NEt$_3$)]BArF

[NiH(^{tBu}P=N=P)] (**12**) (1.1 mg, 2.6 µmol, 1.0 eq) and [H(NEt$_3$)]BArF (2.5 mg, 2.6 µmol, 1.0 eq) is dissolved in 1.5 mL of MeCN, filled into a J Young NMR tube and the ratio of **12** and [NiH(^{tBu}P=N=P^{H})]BArF (**14^{BArF}**) is derived NMR spectroscopically.

1.9.8 Oxidation of [NiH(^{tBu}P=N=P)] (12) in Acetonitrile

[NiH(^{tBu}P=N=P)] (**12**) (6.7 mg, 0.016 mmol, 1.0 eq) and $AgPF_6$ (4.0 mg, 0.016 mmol, 1.0 eq) is filled into a J Young NMR tube and 0.5 mL of MeCN-d_3 is added.

1.9.9 Oxidation of [NiD(^{tBu}P=N=P)] (12-D) in Acetonitrile

[NiH(^{tBu}P=N=P)] (**12**) (5.0 mg, 0.012 mmol, 1.0 eq) and $AgPF_6$ (3.0 mg, 0.012 mmol, 1.0 eq) is filled into a J Young NMR tube and 0.5 mL of MeCN is added.

1.9.10 Oxidation of [NiH(^{tBu}P=N=P)] (12) in Diethyl Ether in the Presence of H_2

A solution of [NiH(^{tBu}P=N=P)] (**12**) (3.0 mg, 7.2 µmol, 1.0 eq) in 0.5 mL of Et_2O is filled into a J Young NMR tube and a capillary containing a solution of PPh_3 in toluene is added. After NMR spectroscopic determination of the ratio between internal standard and **12**, [Fc]BArF (8.0 mg, 7.6 µmol, 1.0 eq) is added and the sample is analyzed NMR spectroscopically. The sample is degassed by three freeze-pump-thaw cycles and H_2 atmosphere ($p(H_2)$ = 1 atm) is applied.

1.9.11 Oxidation of [NiH(^{tBu}P=N=P)] (12) in Diethyl Ether in the Presence of D_2

[NiH(^{tBu}P=N=P)] (**12**) (3.0 mg, 7.2 µmol, 1.0 eq) and [Fc]BArF (8.0 mg, 7.6 µmol, 1.0 eq) is filled into a J Young NMR tube. 0.5 mL of Et_2O is condensed into the tube and after thawing to room temperature, D_2 atmosphere ($p(D_2)$ = 1 atm) is applied.

1.9.12 Oxidation of [NiH(^{tBu}P=N=P)] (12) in Fluorobenzene

A solution of [NiH(^{tBu}P=N=P)] (**12**) (5.0 mg, 0.012 mmol, 1.0 eq) in 0.5 mL of PhF is filled into a J Young NMR tube and a capillary containing an aqueous solution of H_3PO_4 is added. After NMR spectroscopic determination of the ratio between internal standard and **12**, $AgPF_6$ (3.3 mg, 0.013 mmol, 1.1 eq) is added

and the sample is analyzed NMR spectroscopically. The sample is degassed by three freeze-pump-thaw cycles and H_2 atmosphere ($p(H_2)$ = 1 atm) is applied.

1.9.13 Oxidation of [NiH(^{tBu}P=N=P)] (12) in Fluorobenzene in the Presence of H_2

A solution of [NiH(^{tBu}P=N=P)] (**12**) (5.0 mg, 0.012 mmol, 1.0 eq) in 0.5 mL of PhF is filled into a J Young NMR tube and a capillary containing an aqueous solution of H_3PO_4 is added. After NMR spectroscopic determination of the ratio between internal standard and **12**, the solvent is condensed into a J Young flask. $AgPF_6$ (3.3 mg, 0.013 mmol, 1.1 eq) is added to the J Young NMR tube and the solvent is condensed from the J Young flask into the NMR tube. After thawing to room temperature, H_2 atmosphere ($p(H_2)$ = 1 atm) is applied.

1.10 Determination of C_G^{THF}

As discussed by *Mayer*, C_G sums up the free energy of formation $G^0_f(H)$ of the hydrogen atom, its solvatization energy $\Delta G^0_{solv}(H)$ and the reference potential E^0 (eq. (41)).[4,87]

$$C_G = G^0_f(H) + \Delta G^0_{solv}(H)^{THF} + 23.06\ \text{kcal·mol}^{-1}\text{·V}^{-1}\text{·}E^0 \quad (41)$$

The free energies $G^0_f(H) = 48.6\ \text{kcal·mol}^{-1}$ and $\Delta G^0_{solv}(H)^{THF} = 4.9\ \text{kcal·mol}^{-1}$ can be taken from the literature.[115,134] To obtain C_G referenced to the Fc^+/Fc couple in a certain solvent, the potential $E_{NHE(S)}(Fc^+/Fc)^S$ of the Fc^+/Fc couple referenced to the NHE potential in that particular solvent has to be known. *Bontempelli* provides electrochemical measurement of the H^+/H redox couple referenced to Fc^+/Fc in several solvents including THF.[135] Taking the reported potential $E^{1/2} = 0.44$ V as approximation of $E_{NHE(THF)}(Fc^+/Fc)^{THF}$ allows for determination of $C_G{}^{THF} = 63.6\ \text{kcal·mol}^{-1}$ according to eq. (41).

Alternatively, $E_{NHE(S)}(Fc^+/Fc)^S$ can be calculated based on the Fc^+/Fc potential referenced to the NHE(aq) reference, which is reported for many solvents.[136] The difference in the scale referenced to NHE(aq) and NHE(S) can be obtained by comparison of $E_{NHE(aq)}(H/H^+)^S$ and $E_{NHE(S)}(H/H^+)^S$ as reported by *Parker*.[137]

$$-23.06\ \text{kcal·mol}^{-1}\text{·V}^{-1}\text{·}E_{NHE(S)}(H/H^+)^S = G^0_f(H) + \Delta G^0_{solv}(H)^S \quad (42)$$

$$-23.06\ \text{kcal·mol}^{-1}\text{·V}^{-1}\text{·}E_{NHE(aq)}(H/H^+)^S = -23.06\ \text{kcal·mol}^{-1}\text{·V}^{-1}\text{·}E_{NHE(aq)}(H/H^+)^{aq} + \Delta\Delta G_{solv}(H) - \Delta G_{tr}{}^{aq\rightarrow S}(H^+) \quad (43)$$

While the potential $E_{NHE(S)}(H/H^+)^S$ is available from the free energy of formation $G^0_f(H)$ and the solvation free energy $\Delta G^0_{solv}(H)^S$ of the hydrogen atom according to eq. (42), $E_{NHE(aq)}(H/H^+)^S$ requires the free energy of transfer of the proton from water to the solvent of choice $\Delta G_{tr}{}^{aq\rightarrow S}(H^+)$, the change in solvation free energy $\Delta\Delta G_{solv}(H)$ and the potential $E_{NHE(aq)}(H/H^+)^{aq}$ (eq. (43).).

For THF, $E_{NHE(aq)}(Fc^+/Fc)^{THF} = +0.826$ V and $E_{NHE(THF)}(H/H^+)^{THF} = -2.32$ V is calculated based on available data in the literature.[115,134,136] While $E_{NHE(aq)}(H/H^+)^{aq} = -2.42$ V and $\Delta\Delta G_{solv}(H) = -2.2\ \text{kcal·mol}^{-1}$ can be taken from *Parker*, reported values of $\Delta G_{tr}{}^{aq\rightarrow THF}(H^+)$ in the literature are not reliable.[137] The free energy of transfer of the proton from water to THF $\Delta G_{tr}{}^{aq\rightarrow THF}(H^+)$ is reported by *Elsemongy*, *Kundu* and *Wells*.[138–141] While *Kundu*'s and *Wells*'s data is limited to water/THF mixtures of a maximum amount of 50% THF, *Elsemongy* includes values for pure THF. However, in case of *Elsemongy*'s report, determination of $\Delta G_{tr}{}^{aq\rightarrow THF}$ does not follow the tetraphenylarsonium tetraphenylborate (TATB) assumption and should

therefore not be used for calculation of C_G^{THF}.[15][141] However, *Bontempelli* provides an empirical correlation for the experimentally determined redox potential and $\Delta G_{tr}^{aq\rightarrow S}(H^+)$, which allows for determination of $\Delta G_{tr}^{aq\rightarrow THF}(H^+)$ = 5.71 kcal·mol^{-1} and therefore $E_{NHE(aq)}(H/H^+)^S$ = -2.08 V. Referencing the Fc^+/Fc couple to NHE(THF) results in $E_{NHE(THF)}(H/H^+)^{THF}$ = 0.59 V, which gives C_G^{THF} = 67.1 kcal·mol^{-1}.

In a third approach, C_G^{THF} can be determined based on C_H^{THF} = 66 kcal·mol^{-1} which is reported by *Morris* and found application in determination of BDEs in THF.[64,114,142] The C_H^{THF} reported by *Morris* is obtained by measurement of the acidity and redox potential of a ruthenium hydride of known bond strength, assuming a solvent independent BDE and identical solvation entropies $\Delta S_{solv}^0(XH)$ and $\Delta S_{solv}^0(X^{\bullet})$ as discussed in Chapter 1.1.1.[114,143] Accordingly, C_H^{THF} has to be treated as approximation based on experimental bond strength rather than an exactly determined parameter. C_H can be converted to C_G upon consideration of the entropy of hydrogen atom formation $S^0_f(H)$ and solvatization $\Delta S^0_{solv}(H)$ at a given temperature and solvent as described in eq. (5). While the formation entropy of the hydrogen atom in the gas phase is known with $S^0_f(H)$ = 27.419 cal·mol^{-1}·K^{-1}, the solvatization of the hydrogen atom $\Delta S^0_{solv}(H)$ is commonly estimated on the basis of the solvatization entropy of H_2.[4,134] Taking $\Delta S^0_{solv}(H_2)^{THF}$ = 10.8174 cal·mol^{-1}·K^{-1} determined by *Brunner* for the solvatization entropy of H in THF, C_G^{THF} = 61 kcal·mol^{-1} is determined eq. (44).[114,115]

$$C_G^{THF} = 66\ \text{kcal·mol}^{-1} - 298.15\ \text{K·(38.236 cal·mol}^{-1}\text{·K}^{-1}) = 61\text{·kcal·mol}^{-1} \quad (44)$$

[15] The TATB assumption states an equal contribution of the tetraphenylarsonium cation $\Delta G_{tr}^{aq\rightarrow S}(TA)$ and tetraphenylborate anion $\Delta G_{tr}^{aq\rightarrow S}(TB)$ to the overall transfer free energy of TATB $\Delta G_{tr}^{aq\rightarrow S}(TATB)$. Based on this assumption, the transfer energy of any ion is determined. Ref. [138] does not use the TATB assumption for calculation of the individual ion contribution.

Part II: Photochemical Reactivity of Nickel Pincer Complexes

Part of the research presented in this part has been published and citation of the original work is permitted by the publishers.

F. Schneck, M. Finger, M. Tromp, S. Schneider, *Chem. Eur. J.* **2017**, *23*, 33−37.

F. Schneck, J. Ahrens, M. Finger, A. C. Stückl, C. Würtele, D. Schwarzer, S. Schneider, *Nat. Commun.* **2018**, *9*, 1161−1169.

F. Schneck, F. Schendzielorz, N. Hatami, M. Finger, C. Würtele, S. Schneider, *Angew. Chem. Int. Ed.* **2018**, *57*, 14482−14487.

2.1 Introduction

2.1.1 Emission and Use of CO_2 as Key Factor in Future Global Energy Policy

The use of fossil fuels results in an enrichment of carbon dioxide in the terrestrial atmosphere and the 400 ppm level was crossed, recently.[144] The combustion of oil, gas and coal resulted in a global CO_2 emission of 33.4 $Gt \cdot a^{-1}$ ($Gt \cdot a^{-1}$: gigatons per year) in 2017, marking a 1.6% increase compared to 2016.[145] With an annual 90 $Gt \cdot a^{-1}$ natural CO_2 flux between the atmosphere and the oceans, biosequestration greatly impacts the terrestrial atmosphere and lowers the net anthropogenic emission to 15 $Gt \cdot a^{-1}$ by CO_2 uptake in land and ocean sinks.[146,147] While CO_2 acts as a greenhouse gas itself, the consequences of global warming and ocean acidification impact marine photosynthesis and therefore CO_2 absorption in the oceans.

Artificial CO_2 sequestration in underground rock formations is motivated by substantial CO_2 storage capacities. However, the annual operating CO_2 capture capacity of the global carbon capture and storage (CSS) institute did not exceed 40 $Mt \cdot a^{-1}$ in 2018.[148,149] Of the $9.8 \cdot 10^7$ barrels of crude oil consumed daily in 2017, approximately 10% are used for chemical application.[145,150] Assuming a density of 0.8 $g \cdot ml^{-1}$ and an average carbon content of 90% for crude oil, this corresponds to an annual consumption of 410 $Mt \cdot a^{-1}$ carbon for chemical synthesis. If all chemicals based on crude oil would be produced from CO_2 as carbon stock instead, a reduction in anthropogenic CO_2 emission by 1.5 $Gt \cdot a^{-1}$ would result, accounting for 4% of the global CO_2 emission. These examples are not meant to give a thorough review of global CO_2 economy, however they showcase that only the substitution of fossil fuels as primary energy source can result in a substantial reduction of anthropogenic CO_2 emission.[151]

Table 17: World energy consumption in 2017 by energy carrier (data taken from ref. [145]).

Energy carrier	Share of global energy consumption [Wh]	Share of global energy consumption [%]
Oil	$5.5 \cdot 10^{16}$	34
Natural gas	$3.8 \cdot 10^{16}$	23
Coal	$4.5 \cdot 10^{16}$	28
Nuclear energy	$7.2 \cdot 10^{15}$	4
Hydroelectricity	$1.1 \cdot 10^{16}$	7
Solar	$1.2 \cdot 10^{15}$	1
Wind	$3.0 \cdot 10^{15}$	2
Other renewables	$1.6 \cdot 10^{15}$	1

Comparing the global energy consumption of $1.6 \cdot 10^{17}$ Wh in 2017 by fuel, the fossil fuels oil, natural gas and coal make up for 85% of the consumed energy in the world (Table 17). The remaining energy is contributed by nuclear energy, hydroelectricity and renewable energy sources. While nuclear energy provides an alternative energy source to fossil fuels, it stagnates at a near constant share to the consumed energy since 2000 and suffers extensive waste management.[145] Most of the renewable energy sources nowadays are used for electricity generation. Solar energy currently contributes a small amount of 1% to the energy consumed globally. The sun however provides a, from a human perspective, near inexhaustible source of energy. Approximately 1500 times the annual world energy need is hitting the surface of the continents as sunlight every year.[152] For the Sahara desert an average annual insolation of 2300 $kWh \cdot m^2$ is reported.[153] Accordingly, covering $7 \cdot 10^5$ km^2, so less than 10%, of the Sahara desert with photovoltaics of 10% efficiency would provide the energy consumed in 2017 every year.

Given the energy potential of solar energy, it has to play a major role in substituting fossil fuels as energy carrier. However, conversion of solar energy to electricity is not sufficient to provide energy on demand. Since solar energy supply undergoes temporal variation, energy storage in chemical bonds is crucial to deliver the energy when it is needed by combustion. Several energy storage materials are being discussed, including hydrogen carriers, however most of them require the built up of new infrastructure. Assuming economic production of H_2 from renewable energy, hydrogenation of CO_2 to hydrocarbons is of high interest for solar fuel production.

2.1.2 Reduction of Carbon Dioxide with Molecular Hydrogen to C_1 Products

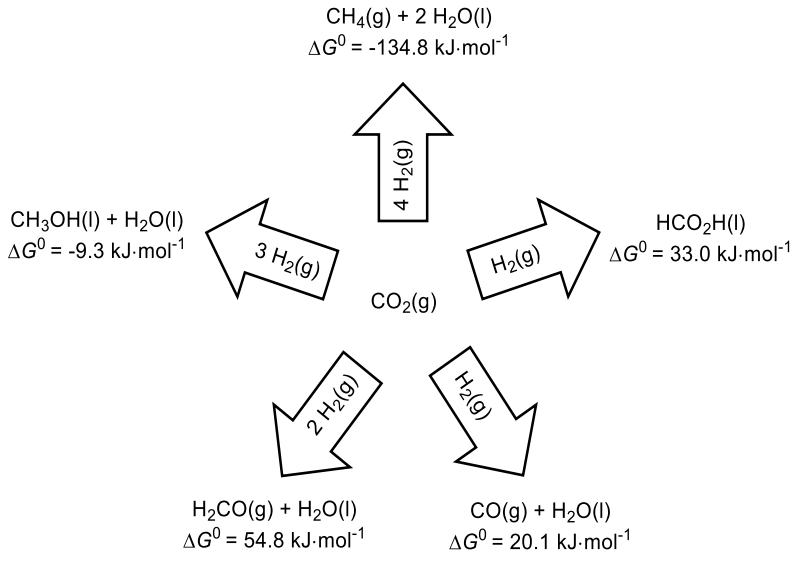

Figure 51: Products of the reduction of carbon dioxide with dihydrogen and reaction free energies (data taken from ref. [123]).

The hydrogenation of carbon dioxide can give several products depending on the number of reducing equivalents (Figure 51). Equimolar reduction with H_2 can give formic acid or carbon monoxide by formation of water as byproduct and both possible products can be interconverted by (de-)hydration.[154] Formic acid is produced industrially on a $6 \cdot 10^5$ t·a^{-1} scale for application in chemical industry and as silage additive, however not from carbon dioxide.[155] The thermodynamic bias for formic acid production from CO_2 can be tackled by choosing the right solvent or addition of base which adds driving force due to deprotonation to formate salts.[156] Formic acid is discussed as H_2 storage material with 4.4 wt% hydrogen content because of the facile, selective and reversible catalytic interconversion of CO_2 and H_2 to formic acid.[157]

The hydrogenation of CO_2 to carbon monoxide is called the reverse water-gas shift (rWGS) reaction. As formic acid production, it is thermodynamically unfavorable at room temperature. However, the equilibrium shifts upon increasing temperature and formation of carbon monoxide gets favorable at $T > 1052.6$ K (Figure 52).[158] The hydration of carbon monoxide, the water-gas shift (WGS) reaction, is used on large scale for production of hydrogen gas from water and carbon monoxide. Further, hydrogen gas obtained from steam reforming contains carbon monoxide which is a catalyst poison for many heterogeneous catalysts. The crude H_2 gas can be purified by WGS *via* addition of steam as is performed in *Haber-Bosch* ammonia synthesis. Similarly, in *Fischer-Tropsch* synthesis which uses CO from coal gasification as feedstock for synthesis of hydrocarbons, the WGS is used to adjust the CO/H_2 ratio of the synthesis gas.[158]

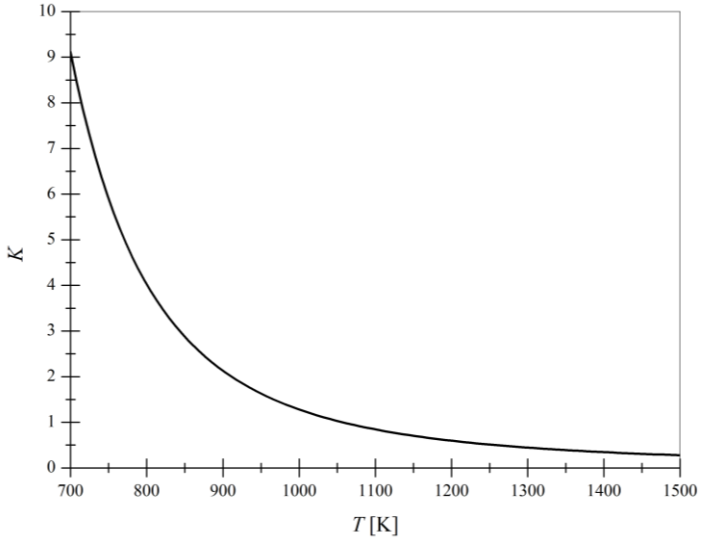

Figure 52: Temperature dependent equilibrium constant *K* of the water-gas shift (WGS) reaction (data taken from ref. [158]).

Turning to two equivalents of H_2, the products of CO_2 hydrogenation are formaldehyde and water. This reaction has a low driving force compared to formation of other hydrogenation products and its production from CO_2 is hampered by selectivity issues due to overreduction and decomposition.[155] Nevertheless,

formaldehyde has industrial relevance with an annual production volume of > $2 \cdot 10^7$ t·a^{-1} and is obtained by oxidation of methanol.[155] While homogeneous hydrogenation of CO_2 to formaldehyde is unprecedented in the literature, ruthenium catalyzed hydrogenation of CO_2 to methanol is postulated to proceed *via* a mechanism including formic acid and formaldehyde as $2e^-$ and $4e^-$ reduced intermediates, respectively.[155,159]

Methanol is obtained by carbon dioxide reduction with three equivalents of H_2 with concomitant formation of water in an exergonic reaction at standard conditions (Scheme 50). It is an important resource for chemical industry which is reflected by the massive annual consumption of $7.5 \cdot 10^7$ t·a^{-1}. However, the use of methanol as energy carrier gains significance and up to 40% of the consumed methanol today is used in this field, for example as fuel additive.[155,160] While methanol is discussed as future fuel itself, its high hydrogen content of 12 wt% further motivates consideration as hydrogen storage material.[155,161] Methanol production is performed starting from synthesis gas in a heterogeneously catalyzed reaction. CO_2 is added to the feed in case of H_2 rich synthesis gas, since it requires more equivalents of H_2 for reduction to methanol. Accordingly, CO_2 is used as carbon feedstock for methanol synthesis, which however results in hydrogenation to CO *via* rWGS as side reaction. Similarly, the direct CO_2 hydrogenation to methanol is possible on Cu based catalytic materials, but the initial formation of CO and subsequent CO reduction is discussed as an alternate mechanism.[162,163] The CAMERE process proceeds *via* feeding a CO_2/H_2 mixture into a rWGS reactor and subsequent methanol synthesis from the gas mixture obtained after water removal.[164] Notably, treatment of the feed mixture in the rWGS reactor before methanol synthesis increases the yield in methanol to 89%, compared to 69% obtained for direct injection of the feed into the methanol synthesis reactor.

Complete reduction of CO_2 yields methane in the strongly exergonic *Sabatier* reaction which gains driving force by formation of two equivalents of water. In combination with hydrogen generation by renewable energy driven electrolysis, CO_2 hydrogenation to methane is part of the *power-to-gas* concept for energy storage.[165] For synthesis of liquid fuels, methane is processed by steam reforming giving CO and H_2 followed by hydrogenation of carbon monoxide. Accordingly, direct reduction of CO_2 to methanol represents a more attractive approach to liquid fuel generation. As for CO_2 reduction to methanol, the catalytic methanation of CO_2 over heterogeneous material can proceed *via* a reaction mechanism which involves initial formation of CO *via* rWGS and subsequent CO reduction.[166]

2.1.3 Selective CO_2 Reduction to Carbon Monoxide

Hydrogenation of CO_2 to methanol and methane is of high interest regarding the synthesis of hydrocarbons for application as energy carriers. In both reactions the initial formation of carbon monoxide *via* rWGS is relevant, making this a crucial reaction in CO_2 reduction chemistry (Scheme 26). This chapter will give a brief summary of important intermediates in different approaches of CO selective CO_2 reduction. Accordingly, catalytic systems which are not selective in CO formation, will not be discussed in detail.

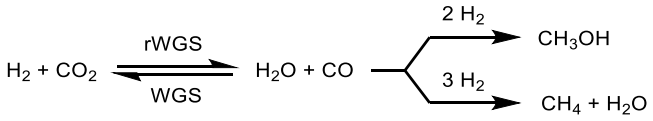

Scheme 26: Reduction of carbon dioxide to methanol and methane can proceed *via* carbon monoxide as intermediate.

2.1.3.1 Carbon Monoxide Dehydrogenases and Formate Dehydrogenases

Having a look at two electron interconversion of CO_2 and CO in nature reveals two carbon monoxide dehydrogenase (CODH) enzymes. The aerobic [MoCu] CODH is not discussed here, since it is only capable of irreversible CO oxidation. Anaerobic [NiFe] CODH in contrast is able to reversibly turn over CO_2 to CO by PCET at the active center consisting of Ni and Fe atoms attached to a Fe_3S_4 cluster.[167] The oxidized and reduced form of the cofactor are shown in Scheme 27.[168] In both forms, hydrogen bonding interactions to amino acids located in the second coordination sphere of the metal atoms are present and important in mediating proton transfer.[167] In the current mechanistic picture, reduction of Ni^{II} results in η^1-C coordination of CO_2 to Ni^{I} followed by a second electron transfer. Proton induced dehydration results in the formation of a hydroxycarbonyl which is coordinated to both metal centers. Addition of another proton facilitates C-O bond cleavage and carbon monoxide liberation regenerates the oxidized form of the enzyme. While this mechanistic picture for [NiFe] CODH does not include metal hydrides, the unusual T-shaped coordination mode of the Ni^{II} center in the oxidized form gave rise to the discussion if an additional metal-bridging hydride ligand is present in [NiFe] CODH.[168]

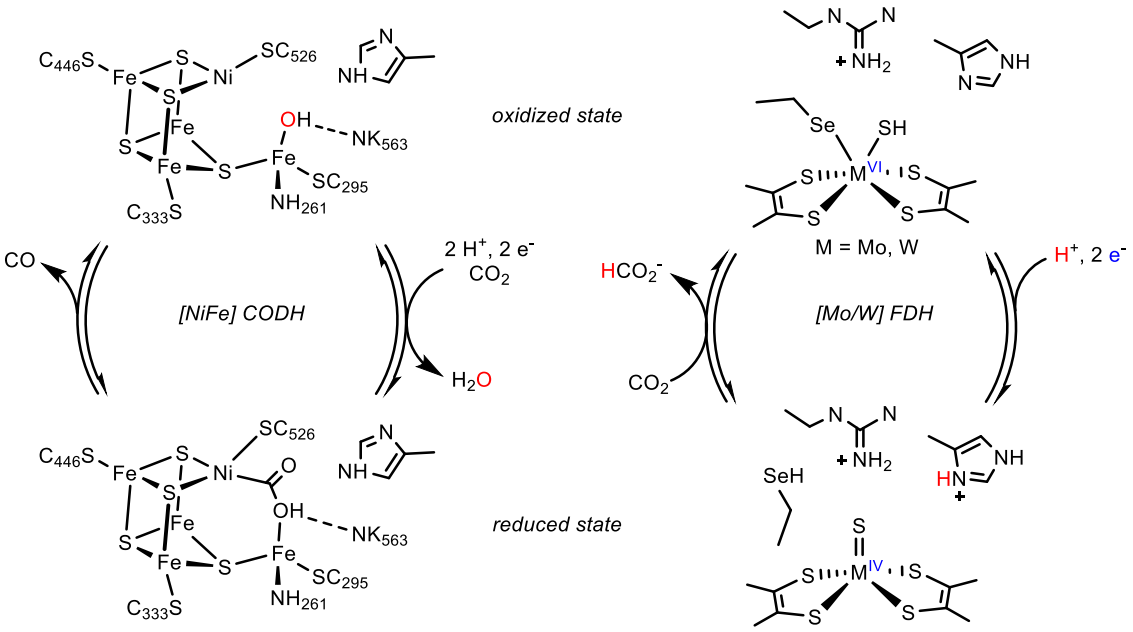

Scheme 27: Oxidized and reduced state of the active site of [NiFe] CODH and [Mo/W] FDH.

Formate dehydrogenases (FDH) can be separated into two classes. Metal-independent formate dehydrogenases make use of the ability of the NAD^+/NADH couple to mediate hydride transfer and irreversibly oxidize formate.[167] In contrast, anaerobic molybdenum and tungsten based FDH are capable of the reversible interconversion of CO_2 and formate.[169] In the reduced form, the active site consists of a single metal oxide or sulfide coordinated by two bidentate pyranopterin based ligands (Scheme 27).[170] Arginine, histidine and (seleno-)cysteine are present in the second coordination sphere of the metal center and crucial for proton transfer to the substrate. CO_2 activation proceeds by PCET from multiple sites resulting in a metal formate which forms the oxidized active site after formate dissociation.

2.1.3.2 Thermal Reverse Water-Gas Shift Catalysis

Heterogeneous catalyst systems are more popular than homogeneous complexes in thermal rWGS catalysis. Research on heterogeneous rWGS catalysis has shown activity of copper and platinum based materials.[151] Copper surfaces catalyze the rWGS reaction at low temperature with high selectivity. Unfavorable CO_2 dissociation on the copper surface results in the need for surface activation.[151] This can be achieved by increasing the H_2 content of the feed, which however results in formation of methane as byproduct.[171] Association of surface-bound hydrogen atoms and adsorbed CO_2 is postulated to give formates as intermediates in Cu catalyzed rWGS.[171] While pure platinum does not catalyze the rWGS reaction, the combination with a support like CeO_2 gives an active catalyst. The mechanistic understanding is that deoxygenation of CO_2 takes place on the support at a surface vacancy and that carbonates are formed as main intermediates.[172] Hydrogen is activated on Pt and regenerates the oxygen vacancies by formation of

water. Accordingly, in both Pt and Cu based systems, oxygen bound species are formed as carbon monoxide selective intermediates.

While several homogeneous catalysts, mainly based on transition metal carbonyls, are reported for the WGS reaction, the microscopic reverse is investigated less thoroughly.[173] Even though most WGS catalysts should in principle also catalyze the reverse reaction, reports are limited to trimetallic and monometallic ruthenium carbonyls by *Tominaga*.[174,175] In both cases harsh conditions ($p \geq 60$ atm, $T \geq 160$°C) are needed. While thermodynamic considerations of the rWGS discussed in the previous chapter suggest a thermodynamically uphill reaction under these conditions, the driving force is affected by solvation of the gases.[156] For the homogeneously catalyzed WGS equilibrium the general accepted mechanism involves formation of a carboxylate as key intermediate (Scheme 28).[155,156,173] This species is formed *via* the *Hieber* base reaction of a metal carbonyl in basic aqueous solution. Decarboxylation yields a metal hydride which regenerates the metal carbonyl upon hydrolysis, forming H_2 and closing the catalytic cycle.[176]

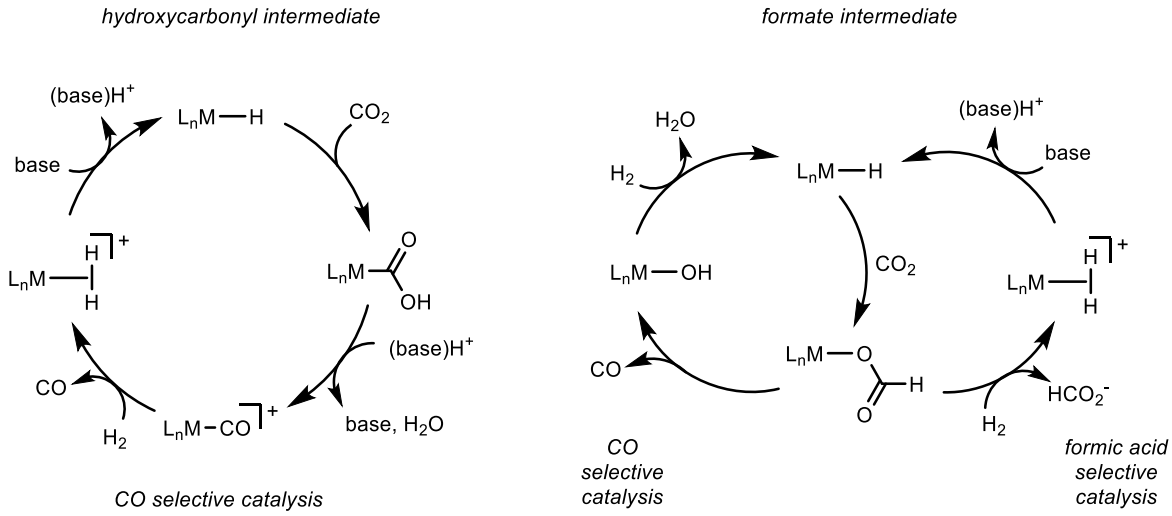

Scheme 28: Mechanisms for CO and formic acid selective hydrogenation of carbon dioxide.

Reversal of the reaction following the same mechanism requires formation of the hydroxycarbonyl by reaction of the metal hydride with CO_2. This so-called 'abnormal insertion' is unprecedented in the literature and *Tominaga* discusses CO_2 coordination instead of insertion in his proposed mechanism, giving a ruthenium hydrido carboxylate as alternative species.[156,175] The lack of reported catalysts for homogeneous rWGS catalysis can be understood as a consequence of 'normal' CO_2 insertion to formates which are in general considered intermediates in formic acid selective catalysis (Scheme 28).[156] While metal hydroxycarbonyl intermediates are generally seen as intermediates in CO selective reduction of CO_2 in homogeneous catalysis, hydrogenation of carbon dioxide to CO *via* metal formates is accepted in heterogeneous catalysis. A metal formate mediated mechanism is also discussed for homogeneous systems, however lacks unambiguous experimental evidence in rWGS catalysis.[155,173] Notably, the stoichiometric

dehydration of formic acid at transition metal complexes is reported and the hydration of carbon monoxide in aqueous solvent proceeds *via* formic acid as intermediate.[154,177,178]

2.1.3.3 (Photo-)Electrocatalytic CO_2 Reduction to CO

Since hydrogen gas is produced by steam reforming, hydrogen production by proton reduction from renewable energy sources at economic cost is required to use CO_2 as environmentally friendly carbon feedstock for hydrogenation. An alternate approach to carbon dioxide reduction features the use of photo- and electrochemical methods, providing the necessary driving force for the uphill reaction. Electrochemical reduction of CO_2 is catalyzed by several transition metal based heterogeneous materials. Electrodes based on Cu, Ag, Au or Zn show high selectivity in CO formation upon electrolysis in $KHCO_3^-$ aqueous solution. Further, adsorbed CO is often regarded as intermediate in reduction to lower oxidation states, including C2 products.[179,180] In a computational study, *Nørskov* considers surface bound hydroxycarbonyl species as possible intermediate of formation of both, formic acid and carbon monoxide.[181] A recent report by *Züttel* on Cu/In nanowires deposited on copper as electrode material rather suggests a surface-bound formate to yield formate as product.[182] Whether adsorption of the intermediate proceeds by initial adsorption of CO_2 or protons, or by a concerted reaction is not addressed in these studies.

Turning to heterogeneous photoelectrocatalytic carbon monoxide generation, the most relevant systems are semiconductor based photoelectrodes.[183] While the semiconductor generates an electric field upon illumination, an external potential is usually applied. Photocathodes based on boron-doped p-Si are reported to catalyze selective reduction to CO in a DMF/water mixture.[184] The system needs potentials close to $E^0(CO/CO^-)$ to operate, indicating reduction of carbon dioxide in solution and subsequent decomposition giving CO. Photocathodes based on III/V semiconductors are able to form CO as well. Research on p-GaP shows CO formation in the presence of water.[184] Computational and experimental analysis of the interaction of the semiconductor with water indicates formation of surface-bound hydrides which are discussed to be relevant for CO_2 activation.[185–187] Finally, n-type TiO_2 based photoelectrodes of different morphology reduce CO_2 to CO by substrate coordination at oxygen-vacant sites and subsequent electron transfer to the substrate which induces C-O bond dissociation.[188,189] Notably, for both p-Si and TiO_2 photoelectrodes, the mechanism of photoelectrocatalytic CO_2 reduction to CO is characterized by the one-electron reduction of CO_2 and subsequent dissociation of the carboxylate.

Cobalt and nickel complexes containing 1,4,8,11-tetraazacyclotetradecane (cyclam) based ligands are known to catalyze electrochemical CO_2 reduction in acidic media upon electron transfer from an electrode or a photosensitizer.[190,191] Importantly, in both platforms the formation of hydrides is not assumed to contribute to CO selective reduction of carbon dioxide.[192] After initial reduction of the Co^{II} precursor, Co^{I} complexes readily bind CO_2 *via* the carbon atom. Investigation of the electronic structure suggests one

electron transfer from the metal to the substrate upon binding and a more reducing metal center results in an increase in the CO_2 binding constant.[192] Coordination to the metal center greatly facilitates one electron reduction of CO_2 as the Co^{II}/Co^{I} couple is found at up to $E^0(Co^{II}/Co^{I})^{aq}$ = -0.1 V *vs.* NHE for certain derivatives ($E^0(CO_2)^{aq}$ = -1.90 V *vs.* NHE, pH = 7).[192] Upon axial coordination of a solvent molecule, the d_{xz} molecular orbital (MO) rises in energy, participating in π backbonding from the metal to the carboxylate. As consequence, an additional intramolecular electron transfer results in twofold CO_2 reduction. Slow conversion of $[Co(CO_2)L_4]^+$ to carbonyl $[Co(CO)L_4]^+$ and carbonate is observed, alternatively generation of $[Co(CO)L_4]^+$ can be accelerated by addition of acid. Metal centered protonation of Co^{I} complex $[CoL_4]^+$ is possible, resulting in production of H_2 and formic acid as side product by insertion of CO_2 into the Co-H bond (Scheme 29).

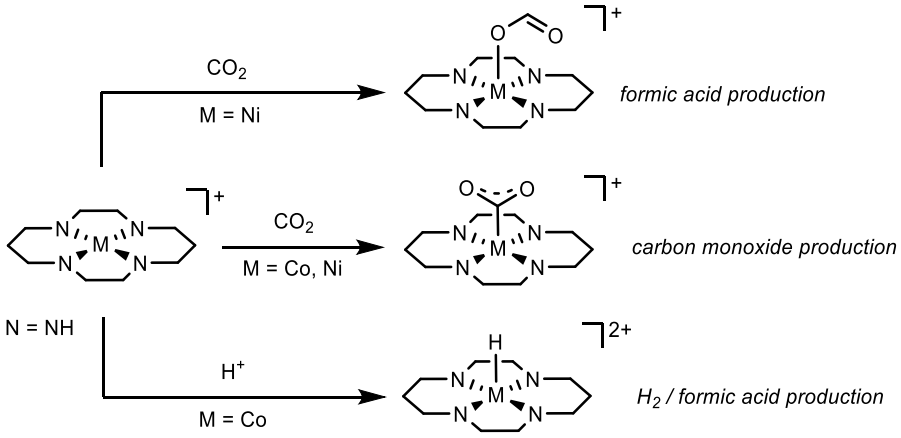

Scheme 29: Selectivity in substrate activation at reduced metal cyclam complexes relevant for the product distribution in (photo-)electrocatalytic CO_2 reduction.

Nickel cyclam complexes in contrast show high selectivity in CO_2 over proton reduction.[191] In general, CO is the favored product of CO_2 reduction by $[NiL_4]^{2+}$, however depending on the solvent, formate is produced in significant amounts.[193] As in case of cobalt as metal center, initial electron transfer gives a reduced metal center. However, Ni^{I} complex $[NiL_4]^+$ shows lower CO_2 binding constants compared to the cobalt complexes and less intramolecular electron transfer to the substrate.[192] Computational analysis shows η^1-CO_2 coordination as thermodynamic product of substrate activation at the Ni^{I} oxidation state.[194] Formate production is attributed to the unfavorable η^1-OCO coordination, therefore no hydride is involved here (Scheme 29). *Neese* proposes proton-coupled electron transfer as second reduction step for both isomers, giving a Ni^{II} hydroxycarbonyl $[Ni(CO_2H)L_4]^{2+}$ as intermediate for carbon monoxide selective reduction. Carbon bound carboxylate species are common intermediates in (photo-)electrochemical CO_2 reduction by metal cyclam complexes and related systems like iron porphyrins.[195,196]

The lack of H_2 formation by $[NiL_4]^{2+}$ is attributed to unfavorable hydride formation due to low basicity of the nickel center.[190] The outstanding selectivity compared to the related cobalt complexes is discussed by *Rodgers*.[197] In both cases, the one electron reduced precatalyst is active in substrate binding. While the initial reduction potential $E^0(M^{II}/M^{I})$ is nearly invariant for both metals, the relevant cobalt complexes are oxidized to Co^{III} much easier than analogous nickel complexes.[192,197,198] Accordingly, protonation of the active species in case of cobalt gives a highly reactive Co^{III} hydride, while protonation the Ni^{I} species is unlikely. Speaking more generally, one electron reduction of the M^{II} precatalyst gives a one-electron reductant in case of nickel, which is able to coordinate CO_2, however requires another reducing equivalent for turnover. In case of cobalt, a two-electron reductant results which efficiently reduces both carbon dioxide and protons. *Bullock* and *DuBois* have shown, that efficient nickel based electrocatalysts for proton reduction can be designed by including basic amines in the second coordination sphere, leading to ligand based protonation after reduction to Ni^{I}.[199,200] Turning to Fe^{II} porphyrins as precatalyst for electrochemical CO_2 reduction, the active formal Fe^0 species is formed by two electron reduction of the precursor. As a result, slightly more cathodic potentials are needed for catalysis compared to the Ni and Co complexes discussed previously. Since the active catalyst is a two electron reductant, proton reduction is a side reaction and in case of strong acids, protonation is observed even at the Fe^{II}/Fe^{I} potential.[195]

Photoelectrocatalytic systems are mostly based on a homogeneous catalyst immobilized on an (photo-)electrode surface. While immobilization is an active field of research in (photo-)electrocatalysis, these systems will not be discussed here, given the similarities in the CO_2 activation mechanism compared to the parent homogeneous catalysts.

2.1.3.4 Homogeneous Photocatalytic CO_2 Reduction to CO

In homogeneously catalyzed photochemical CO_2 reduction, a distinction between photosensitized, photoinduced and photoassisted catalysis has to be made.[201] In case of photosensitized catalysis, the catalytic system consists of a photosensitizer, which undergoes excited state reduction by a sacrificial electron/proton donor after light absorption. Electron transfer to a molecular catalyst then gives the species active in CO_2 reduction. Accordingly, homogeneous catalysts for electrochemical CO_2 reduction are in principle also suitable for photosensitized catalysis. In photoinduced carbon dioxide reduction by a catalyst, the CO_2 reduction is performed by a compound which is produced from a precursor in a photochemical reaction. Photoassisted catalysis means that the photochemical reaction is part of the actual catalytic circle. Accordingly, it is a prerequisite for performing thermodynamically uphill reactions. The mechanisms for electrochemical and photochemical CO_2 reduction can be closely related not only in photosensitized CO_2 reduction. Consequently, the photocatalysts discussed in the following are also active in electrochemical CO_2 reduction, which can proof valuable concerning mechanistic studies.[202]

Following seminal work by *Ziessel*, complexes of the general structure $[ReX(CO)_3(bpy)]$ (X = Cl, Br) are active in visible light photochemical reduction of CO_2 giving CO in high selectivity.[203] Triethanolamine (TEAO) or triethylamine (TEA) is commonly employed as sacrificial electron and proton donor. Photoexcitation results in population of a strongly oxidizing excited state which forms formal Re^0 $[Re(CO)_3(bpy)]$ by reduction of the complex and halide loss. Electronic structure investigation suggests intramolecular electron transfer from the metal to the diimine ligand rather than a Re^0 metalloradical.[204] In case of electrocatalytic CO_2 reduction by $[ReX(CO)_3(bpy)]$ type catalysts, initial two electron reduction opens up a second mechanism for substrate activation, which is not discussed here.[205]

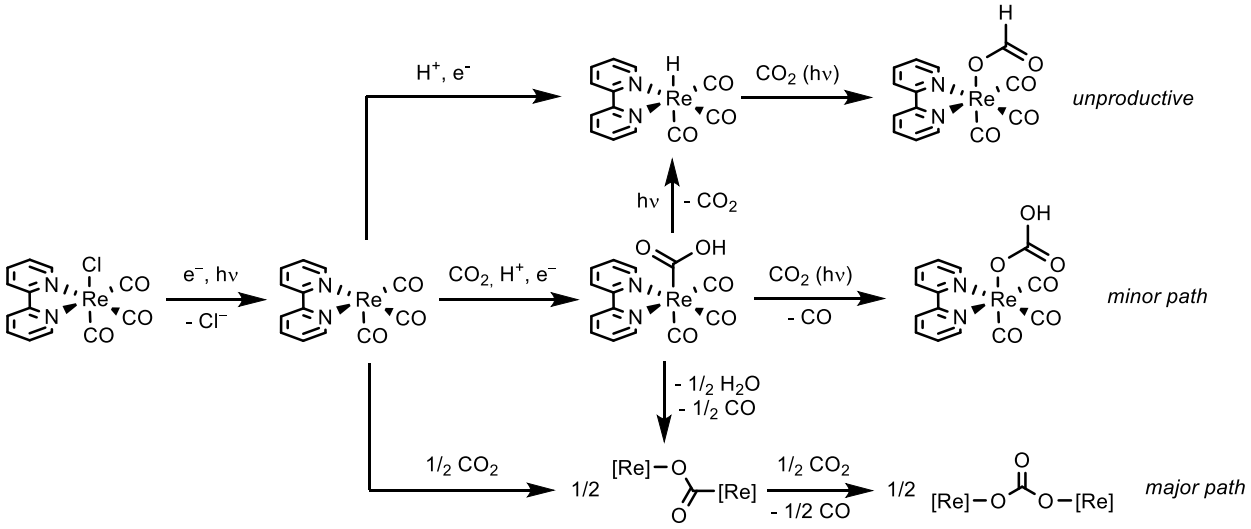

Scheme 30: Reactivity of $[ReCl(CO)_3(bpy)]$ upon photolysis in the presence of CO_2.

Productive carbon dioxide activation by $[Re(CO)_3(bpy)]$ can proceed *via* a dimeric or a monomeric pathway. As shown in Scheme 30, a carboxylate bridged Re^I-Re^I dimer or a Re^I hydroxycarbonyl is formed, respectively.[204] The dimeric complex has been shown to liberate CO upon reaction with an additional equivalent CO_2 giving a bridged carbonate. Based on computational analysis, *Fujita* proposes CO_2 insertion into the rhenium oxygen bond followed by decarbonylation rather than deoxygenation of coordinated CO_2.[206] The monomeric metallacarboxylic acid $[Re(CO_2H)(CO)_3(bpy)]$ forms hydrocarbonate $[Re(OCO_2H)(CO)_3(bpy)]$ under CO_2 atmosphere when irradiated. As in the dimeric pathway, CO is liberated and computational analysis suggests initial formation of tetracarbonyl $[Re(CO)_4(bpy)]^+$ by hydroxide abstraction.[207,208] *Fujita* proposes a minor role of the monomeric path based on the low concentration of $[Re(CO_2H)(CO)_3(bpy)]$ in stoichiometric CO_2 reduction by *in situ* generated $[Re(CO)_3(bpy)]$.[204] Re^I hydride complexes are not directly involved in CO formation, however photochemical decarboxylation of the hydroxycarbonyl is shown by *Gibson*.[209] Alternatively, net hydrogen atom transfer from TEA/TEAO to $[Re(CO)_3(bpy)]$ is a plausible route for hydride formation. While the

formed hydride can insert CO_2 thermally or photochemically to give a formate, the lack of catalytic formate production suggests this to be an unproductive reaction.[210,211]

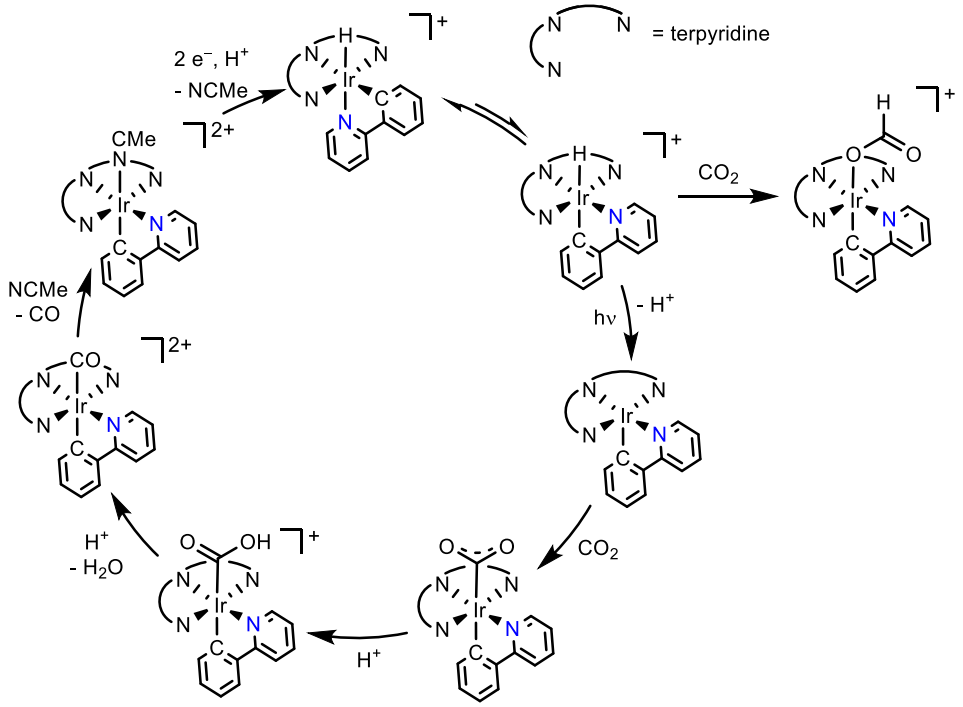

Scheme 31: Mechanistic picture of photochemical CO_2 reduction by $[IrCl(tpy)(ppy)]PF_6$.

In homogeneous thermal rWGS catalysis, metal hydrides play a role in CO formation. Photo- and electrocatalytic systems discussed so far coordinate CO_2 on a reduced metal center, instead. Hydrides are rather seen as intermediates in formation of side products like H_2 and formate. Turning to iridium based photocatalysts, the situation changes. In 2013, *Ishitani* reported selective photocatalytic CO_2 reduction to CO in the presence of TEAO by Ir^{III} precatalyst $[IrCl(tpy)(ppy)]PF_6$ (tpy: terpyridine, ppy: 2-phenylpyridinyl).[212] Hydride *N-trans*-$[IrH(tpy)(ppy)]^+$ was identified as active catalyst and photochemical reactivity of the Ir^{III} hydride was assumed due to the lack of thermal reactivity of *N-trans*-$[IrH(tpy)(ppy)]PF_6$ with CO_2. Mechanistic work by *Fujita* attributes this stability in the presence of CO_2 to the low hydricity of the complex.[213] Small quantities of formate produced in the catalytic experiment are formed by isomerization to the unfavorable isomer *C-trans*-$[IrH(tpy)(ppy)]PF_6$ which readily inserts CO_2 due to a more labile hydride ligand. Importantly, isomerization is relevant in photocatalytic CO_2 reduction as well. Once formed, *C-trans*-$[IrH(tpy)(ppy)]PF_6$ acts as a photoacid, forming low-valent *C-trans*-[Ir(tpy)(ppy)] upon irradiation.[16] Alternatively, Ir^I formation can take place from the thermodynamically favored isomer *N-trans*-$[IrH(tpy)(ppy)]PF_6$ by photoexcitation and subsequent reduction by TEAO. Notably, reduction of *N-trans*-$[IrH(tpy)(ppy)]PF_6$ results in formation of *C-trans*-[Ir(tpy)(ppy)] as well,

[16] *C-trans*-[Ir(tpy)(ppy)] shows a free coordination site *trans* to the carbon donor of the ppy ligand.

showing that this isomer is favored on the pentacoordinate species. Computational analysis reveals that *C-trans*-[Ir(tpy)(ppy)] binds CO_2 to yield a carboxylate and subsequent PCET steps result in formation of CO (Scheme 31).

Ishitani's [IrCl(tpy)(ppy)]PF_6 based system involves hydrides as intermediates in CO selective CO_2 reduction. While hydrides are generated by oxidation of H_2 in rWGS catalysis, the active Ir^{III} hydride is formed by oxidation of sacrificial TEAO, here. Photochemical rWGS catalysis, i.e. using H_2 as reductant instead of sacrificial donors, is a largely undeveloped field of research. Heterogeneous materials for photocatalytic CO_2 conversion to CO using H_2O as reductant suffer from proton reduction as side reaction, motivating the use of H_2 instead. Magnesium oxide was used by *Tanaka* as rWGS photocatalyst.[214] Interestingly, mechanistic work shows that a surface-bound formate is formed by CO_2 adsorption, photoinduced electron transfer and subsequent reaction with H_2. The formate is photochemically active and reduced another CO_2 molecule upon photoexcitation.[215] *Tahir* investigated rWGS catalysis in a TiO_2 based monolith photoreactor and could show higher activity compared to the use of H_2O as reductant.[216] The mechanism of CO_2 activation is assumed to be mostly identical to the photoelectrochemical approach discussed previously.

Homogeneous rWGS photocatalysis is limited to a notable example by *Neumann*.[217,218] Here, a three-component system is used consisting of Pt/C for H_2 activation and a tungsten based polyoxometallate $[PW_{12}O_{40}]^{3-}$ covalently bound to the already discussed rhenium tricarbonyl photocatalyst for CO_2 reduction. Activation of H_2 takes place heterogeneously on Pt/C and the activated hydrogen is transferred to the polyoxometallate giving separated protons and electrons. Photoinduced intramolecular electron transfer from the reduced polyoxometallate fragment to the rhenium catalyst results in formation of the crucial formal Re^0 active species. The following CO_2 reduction mechanism closely resembles the monomeric path discussed previously for [$ReX(CO)_3$(bpy)]. However, in this example, all protons and electrons necessary are provided by the reduced polyoxometallate fragment. Connecting the polyoxometallate and the rhenium catalyst is crucial, as combination of the unmodified species does not give a catalytically active mixture.

2.1.3.5 Key Intermediates in CO Selective Catalysis

The heterogeneous and homogeneous catalyst systems discussed show that CO selective CO_2 reduction can proceed by a variety of mechanisms. In general, attributing selectivity in solid state catalysis to a key intermediate is not easy since formates, carbonates, carboxylates and hydroxycarbonyls are relevant species for production of CO, depending on the catalyst system. Carbon monoxide selective catalysis in coordination compounds is mostly attributed to formation of metal carboxylates or metallacarboxylic acids which are formed by η^1-coordination of CO_2. A similar mechanism is assumed for [NiFe] CODH. The formation of hydrides often results in formation of H_2 or formate as byproducts which result in production

of formic acid. Notably, examples for heterogeneous catalysis propose hydroxycarbonyls as intermediates in formic acid production and formates for CO selective reduction. The iridium based photocatalyst reported by *Ishitani* proceeds by a unique mechanism which involves a hydride in CO selective catalysis. Mechanistic investigation reveals the formation of a low-valent Ir^{I} species by deprotonation and subsequent CO_2 activation *via* a carboxylate/hydroxycarbonyl.

2.1.4 CO_2 Activation on Molecular Nickel Complexes

Metallacarboxylates and metallacarboxylic acids are key intermediates in homogeneous CO selective CO_2 reduction. Nickel complexes show outstanding properties in electrochemical CO_2 reduction as discussed in Chapter 2.1.3.3, and CO_2 activation in [NiFe] CODH proceeds at the nickel cofactor.[192] The current mechanistic understanding of both reactions involves η^1-*C* coordination of CO_2 at the electrophilic carbon atom on the Ni^{I} oxidation state. In 1975, *Aresta* made an important contribution to the coordination chemistry of nickel complexes by isolation of the first example of a CO_2 ligated complex.[219] Complex $[Ni(CO_2)(PCy_3)_2]$ can be obtained by reacting the Ni^0 precursor $[Ni(N_2)(PCy_3)_2]$ with CO_2. Structural analysis shows η^2-*C,O* coordination and the asymmetric CO stretching vibration $\tilde{\upsilon}$ = 1736 cm^{-1} is significantly red shifted compared to free carbon dioxide due to π backbonding (Scheme 32). *Hillhouse* reported similar structural and spectroscopic features of a Ni^0 CO_2 complex featuring a bidentate phosphine ligand.[220]

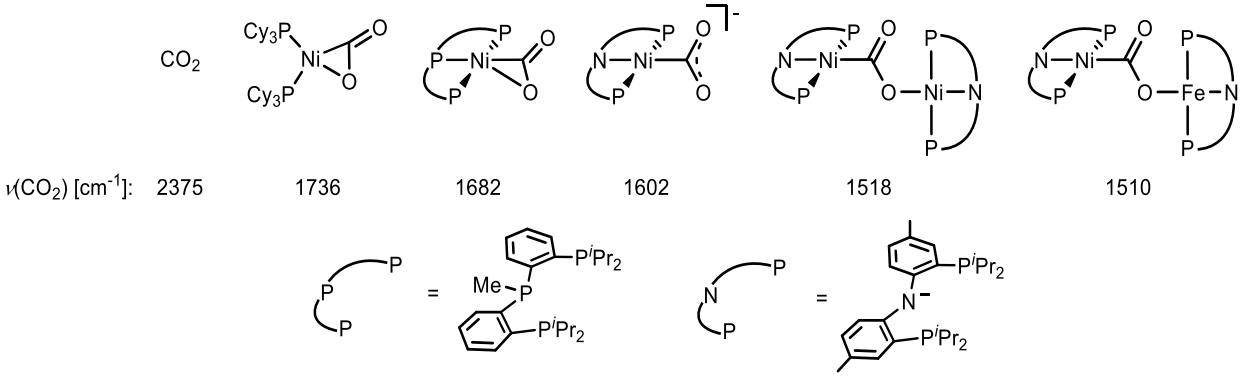

Scheme 32: Coordination of carbon dioxide by molecular nickel complexes.

In recent years, *Lee* contributed to CO_2 coordination chemistry of nickel complexes by investigating nickel pincer complexes (Scheme 32).[221] In case of a tris(phosphine) ligated complex, reacting a Ni^0 precursor with CO_2 gives a stable η^2-*C,O* pentacoordinate complex. Structural data and infrared spectroscopy shows stronger CO_2 activation compared to the four coordinate CO_2 adducts reported by *Aresta* and *Hillhouse*.[222] Turning to stronger donating amido diphosphine pincer ligands, the CO_2 adduct is best described as a Ni^{II} carboxylate and coordinating the carboxylate by a *Lewis* acid like Ni^{II} or Fe^{II} results in additional activation of the bridging carboxylate (Scheme 32).[223–225] Importantly, the Ni-Fe bridging carboxylate resembles the

binding motive present in [NiFe] CODH and shows the strongest activation of all complexes reported. Conversion of the metal bound CO_2 moiety to the carbonyl by C-O scission requires the addition of *Brønsted* acid and can be performed in most cases, regardless of the degree of CO_2 activation in the precursor.[223,224]

All complexes shown in Scheme 32 which can be obtained by reaction with CO_2 require the use of a Ni^0 precursor. Variation of the PNP pincer ligand allows for isolation of a T-shaped Ni^I precursor which gives a strongly activated Ni^{II}-Ni^{II}-bridging carboxylate upon bimetallic CO_2 reduction.[105] Similarly, intermolecular electron transfer is discussed to account for the second reduction equivalent in carbon dioxide reduction by Ni based electrocatalysts (Chapter 2.1.3.3).[194] Monomeric CO_2 activation by Ni^I complexes is limited to an example in the gas phase.[226,227] The observed asymmetric CO stretching frequency $\tilde{\upsilon}$ = 1923 cm^{-1} suggests weak CO_2 activation compared to the examples discussed in Scheme 32 and computational analysis predicts relatively weak bending of the CO_2 moiety. Bimetallic CO_2 reduction to oxalate has been shown by *Limberg*, representing a rare example of different selectivity in CO_2 reduction by Ni^I.[228] In another interesting contribution, *Limberg* showed the deprotonation of a Ni^{II} formate to the carboxylate and its follow-up chemistry yielding carbon monoxide.[229]

2.1.5 Hydricity of Transition Metal Hydrides and Insertion of CO_2 into Metal Hydrogen Bonds

Utilizing a single molecular complex for photochemical rWGS reactivity is unprecedented. This transformation is a demanding task since the complex has to fulfill multiple roles including light absorption as well as activation of H_2 and CO_2. In nature, activation of both substrates is performed on nickel and iron containing enzymes.[167] While *Neumann* shows that hydride formation can be avoided by choosing different sites for H_2 and CO_2 activation, using the same metal center most likely results in metal hydride species as intermediates. Accordingly, avoiding thermal CO_2 insertion giving the formate can be seen as a prerequisite to rWGS reactivity. *Ishitani's* iridium catalysts nicely show that matching the hydricity of the catalyst and formate is crucial to avoid CO_2 insertion and therefore side product formation. Similarly, *Tominaga* proposes a ruthenium hydrido carboxylate as intermediate in thermal rWGS catalysis instead of a possible insertion product.[175]

Comparison of the thermodynamic hydricities of a transition metal and formate ($\Delta G_{HT}(HCO_2^-)^{MeCN}$ = 44 kcal·mol^{-1}) can be used to estimate the feasibility of insertion of carbon dioxide into a metal hydride bond.[2,230,231] As discussed in Chapter 1.1.1, the free energy of concerted hydride transfer is identical to successive transfer of one proton and two electrons and can be expressed by a thermodynamic square scheme. The driving force for hydride transfer ΔG_{HT} is obtained by extending eq. (4) for ΔG_{HAT} by an additional redox process considering the redox potential of the H/H^- couple as shown in eq. (45). Since this redox potential is highly solvent dependent, the same goes for the hydricity.[2] Hydricities are commonly reported in acetonitrile and water as solvent. The following discussion will focus on acetonitrile as organic

solvent and the hydricity $\Delta G_{HT}(\text{M-H})^{MeCN}$ of a transition metal hydride M-H can be determined from redox potentials and acidity constants according to eq. (45). For hydride transfer, $C_G^{MeCN} = 80.9$ kcal·mol^{-1} accounts for the redox potential of the H/H$^-$ and H$^+$/H redox couple referenced to the Fc$^+$/Fc reference potential.[17][4]

$$\Delta G_{HT}(\text{M-H})^{MeCN} = 1.37\ \text{kcal·mol}^{-1}\cdot \text{p}K_a(\text{M-H}) + \text{kcal·mol}^{-1}\cdot\text{V}^{-1}\cdot(E^0(\text{M}^{I}/\text{M}^0) + E^0(\text{M}^{II}/\text{M}^{I}) + C_G^{MeCN} \quad (45)$$

Here, pK_a(M-H) accounts for the acidity of the hydride ligand and the redox potentials correspond to twofold oxidation of the deprotonated species. A *low* hydricity $\Delta G_{HT}(\text{M-H})^{MeCN}$ results in facile heterolytic M-H bond cleavage which is commonly expressed as *high* hydride donor strength. Since dissociation of a hydride ligand results in formation of a free coordination site of the metal complex and the solvent can act as ligand, experimentally determined hydricities are often contaminated by a contribution of solvent coordination. Interestingly, reported bond dissociation free energy of transition metal hydrides span a relatively small range around $\Delta G_{HAT}(\text{M-H})^{MeCN} = 60$ kcal·mol^{-1}.[15] Accordingly, the second redox potential $E^0(\text{M}^{II}/\text{M}^{I})$ can be used to estimate $\Delta G_{HT}(\text{M-H})^{MeCN}$ as reported by *Kubiak*.[232]

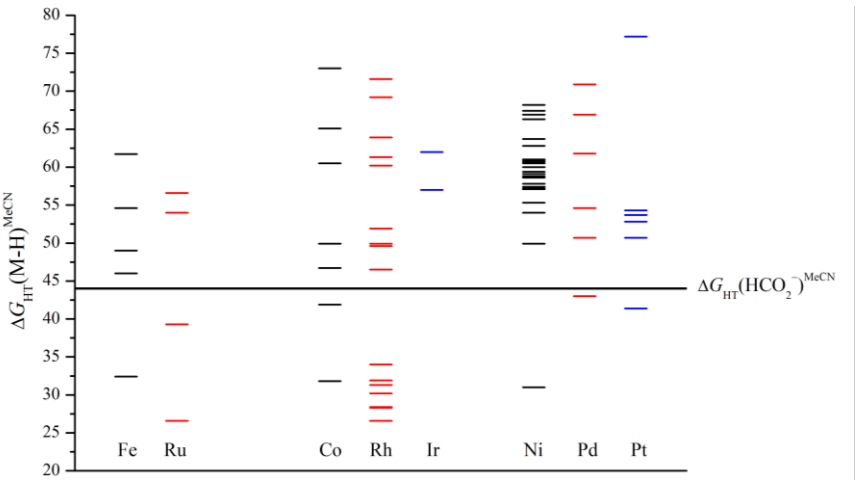

Figure 53: Hydricities $\Delta G_{HT}(\text{M-H})^{MeCN}$ of selected molecular transition metal hydrides (data taken from ref. [158] and references cited therein).

The necessity for thermodynamic data on one proton and two consecutive electron transfer steps greatly limits the scope of experimentally determinable hydricities. Alternatively, titration of a hydride donor with a hydride acceptor of known $\Delta G_{HT}(\text{M-H})$ can be performed for determination of a hydricity. An overview of available values for transition metal hydride complexes can be taken from *Appel* and *Miller*'s review

[17] *Appel* and *Miller* report $C_G^{MeCN} = 79.6$ kcal·mol^{-1} as alternative value for hydride transfer. For consistency, the value reported by *Mayer* is used here.

from 2016.[2] As shown in Figure 53, a rough trend can be observed upon variation of the metal. While 4d and 5d metal complexes are generally considered stronger hydride donors than their 3d analogues, late transition metal based complexes are poorer hydride donors compared to early transition metals. Notably, most data is available on nickel complexes with just a single reported hydricity below $\Delta G_{HT}(HCO_2^-)^{MeCN} = 44$ kcal·mol^{-1}. The low hydricity of this example reported by *Lu* can be easily understood based on the rare Ni^0 oxidation state of the hydride complex, compared to all other examples featuring Ni in the +2 oxidation state.[233] Since Figure 53 contains complexes of different coordination geometry and substitution pattern, several exceptions to the discussed trends are present. In general, detailed investigations of the individual contributions of these parameters is rare. Upon comparing nickel, palladium and platinum bis(diphosphine) complexes of different bidentate ligands, *DuBois* could show that the hydride affinity can be enhanced by increasing the bite angle and introducing less donating substituents on the ligand.[116,234] In both cases, a higher ΔG_{HT} results as a consequence of a lower LUMO of the hydride acceptor complex.

The thorough investigation of pentacoordinate bis(diphosphine) metal hydride complexes allows for a closer investigation of the effect of the metal center. Figure 54 compares the hydricity of complexes of this platform containing different transition metals in the d^8 electronic configuration. The Ni based complex clearly shows the highest hydricity within group 10, while moving to group 9 results in lability of the hydride ligand. A minor contribution of the different charge on the complexes of group 9 and 10 has to be considered.

[Co(dppe)H] 49.9[235]	$[Ni(dppe)H]^+$ 62.8[116]
[Rh(depe)H] 28.1[236]	$[Pd(depe)H]^+$ 43.2[234]
	$[Pt(dppe)H]^+$ 52.8[116]

Figure 54: Hydricities of selected d^8 transition metal hydrides derived from square-planar bis(diphosphine) complexes (values correspond to $\Delta G_{HT}(M\text{-}H)^{MeCN}$ in kcal·mol^{-1}, dppe = bis(diphenylphosphino)ethane, depe = bis(diethylphosphino)ethane).

Since hydride transfer can be regarded as proton-coupled electron transfer, the kinetic barrier for hydride transfer depends on hydride self-exchange rates (see Chapter 1.1.4. for detailed description). In contrast to $1e^-/1H^+$ transfer reaction, the literature on net hydride transfer does not contain a broad data basis for comparison of self-exchange rates. While *Bullock* investigated the rates of hydride transfer of molybdenum and tungsten complexes to organic hydride acceptors, the lack of thermodynamic data inhibits detailed

analysis of the kinetic barriers.[237] Determined hydride self-exchange rates on metal complexes are limited to a report by *Fujita* on Ru^{II} hydrides which shows a strong effect of ligand variation on the observed rate.[238]

Carbon dioxide hydrogenation to formic acid is a field of extensive research motivated by the importance of formic acid as industrially produced compound, its potential use as hydrogen storage material and its role as intermediate in homogeneously catalyzed methanol synthesis. Several highly active molecular catalysts have been developed in the past decades and consequently, kinetic data on CO_2 insertion by metal hydrides is reported. The lack of experimental thermodynamic data and self-exchange rates hinders application of the *Marcus* cross relation to quantitatively predict of the rate of CO_2 insertion. Nevertheless, trends can be observed in well examines systems. The following discussion will be limited to systems which are studied thoroughly with respect to their mechanism rather than giving an overview of state-of-the art catalysts concerning activity.

Catalytic formate production from CO_2 in aqueous KOH by iridium hydride complexes $[IrH_2X\{NC_6H_3\text{-}2,6\text{-}(CH_2P^iPr_2)_2]$ (X = Cl, H) was initially reported by *Nozaki*.[239] Investigation of the mechanism was performed by *Hazari*.[240] Computation predicts a strong impact of the *trans* ligand on the driving force of CO_2 insertion, following the trend expected for the *trans* influence. In agreement, experimental work shows most favorable CO_2 insertion for iridium trihydride $[IrH_3\{NC_6H_3\text{-}2,6\text{-}(CH_2P^iPr_2)_2]$ which, however, is not a result of the strong kinetic *trans* effect of the hydride ligand. Variation of the pincer ligand shows, that hydrogen bonding in the second coordination sphere can result in a lower energetic barrier and a thermodynamically more favorable insertion reaction.[239] In this case, the hydricity cannot be used to estimate the favorability of CO_2 insertion so easily, since H-bonding in the formate product results in additional stabilization of the product. Importantly, H-bonding interactions in the second coordination sphere can also result in lower catalytic activity due to resting state overstabilization as shown for formic acid hydrogenation by related iron based pincer complexes.[241,242]

In contrast to the square-pyramidal Ni^{II} hydride complexes discussed before, many square-planar Ni^{II} hydrides are reported to insert CO_2, showing the great influence of coordination geometry and electronic structure on hydricity. In most cases, fast CO_2 insertion is observed for *trans* carbon donors, whereas *trans* nitrogen donors result in slow insertion.[243] Studies on complexes based on PNP and PCP pincer ligands by *Hazari* confirm the impact of the *trans* influence on the thermodynamic hydricity and computations suggest, that the kinetic barrier follows the same trend.[244]

The mechanism of CO_2 insertion into metal hydride bonds often starts with nucleophilic attack of the hydride at the carbon atom followed by rearrangement to the η^1 bound formate.[245] The transition state of the first step does not include any CO_2 metal interaction. As a result, the mechanism is described as outersphere when this is the rate-determining step of the reaction, as in case of the discussed iridium hydride

complexes.[240] In contrast, if the second step is rate-determining or a concerted process is present, an innersphere mechanism results as observed for square-planar nickel pincer hydrides.[244]

2.1.6 Photochemical Reactivity of Transition Metal Hydrides

An overview of the photochemistry of transition metal hydrides is given by *Geoffrey*, *Perutz* and *Procacci*.[246,247] Among the most frequent photochemical reactions of metal hydride complexes is the reductive elimination of H_2 by polyhydrides. Since this reaction gives rise to a low-valent metal center, photoinduced H_2 liberation followed by substrate activation has found application in research on C-H activation. Following the initial report on photochemical benzene activation by $[WH_2Cp_2]$ (Cp = cyclopentadienyl), the quantum yield for H_2 loss was determined as $\Phi_{366} \geq 0.01 \pm 0.002$ and $[WCp_2]$ could be identified as intermediate by photolysis in Ar and N_2 matrices.[248–250] Homolytic metal hydrogen bond cleavage does not take place as labeling experiments suggest a concerted pathway for reductive elimination.[249] Similarly, the formation of square-planar $[Ru(dmpe)_2]$ from *cis*-$[RuH_2(dmpe)_2]$ (dmpe = bis(dimethylphosphino)ethane) by photolysis proceeds intramolecularly and subsequent substrate activation is reported.[251,252] In case of related *cis*-$[RuH_2(CO)(PPh_3)_3]$, transient IR and UV-vis spectroscopy show formation of the H_2 elimination product within t = 6 ps.[253,254] Time-dependent density functional theory (TD-DFT) was performed on model systems $[RuH_2(PH_3)_4]$ and $[RuH_2(CO)(PH_3)_3]$ showing that H_2 elimination results from population of the dissociative S_1 excited state.[255] In both cases, excitation results in transfer of electron density from metal centered *d* orbitals to a combination of metal centered $4d_{x^2-y^2}$, $4d_{z^2}$ as well as $1\sigma_g$ of the H_2 fragment, resulting in bonding H-H and antibonding metal-H_2 interactions.

Photochemical substitution reactions of adjacent ligands in metal hydride complexes are known, however in most cases do not directly involve the hydride ligand. *Jones* has shown that the phosphine ligand in $[ReH_2(PPh_3)_2Cp]$ can be substituted photochemically and in the presence of alkanes and deuterated benzene as solvent H/D scrambling of the alkane is observed.[256,257] Notably, the hydride ligands are not involved in the scrambling process, which contradicts the initially assigned mechanism based on phosphine dissociation and subsequent coordination of the low coordinate rhenium by the substrate. Kinetic investigation suggests photoinduced stepwise reductive transfer of both hydride ligands to the Cp ligand giving a η^3-allyl Re^{I} $14e^{-}$ intermediate which undergoes oxidative addition of the substrates.[258]

Turning to metal monohydride complexes, homolytic metal hydrogen bond dissociation is described repeatedly and is of synthetic use as $[ReCp^*_2]$ is prepared by irradiation of $[ReHCp^*_2]$ using a Hg arc lamp.[259] Photochemical reactivity of mixed metal carbonyl hydride complexes can result in competing CO and H loss by irradiation at the same wavelength as observed for $[CoH(CO)_4]$.[260] Experimental work on photolysis of $[MnH(CO)_5]$ in an Ar matrix allows for the IR spectroscopic detection of $[MnH(CO)_4]$ as product of decarbonylation and $[Mn(CO)_5]$ from H atom loss.[261,262] Analysis by EPR spectroscopy further

reveals the formation of H radicals and their carbonylation to formyl radicals.[263] While in the Ar matrix, decarbonylation is the major reaction, loss of CO is reversible in a CO matrix and results in selective formation of $[MnH(CO)_4]$.[246] The optical transitions of high oscillator strength are attributed to MLCT ($d_\pi \rightarrow \pi^*_{CO}$) transitions to the carbonyl ligand and ligand centered ($\sigma_{MnH} \rightarrow \sigma^*_{MnH}$) transitions which lead to CO loss and Mn-H bond homolysis, respectively.[264,265]

As in case of photochemical H_2 loss by metal dihydrides, photoinduced intramolecular reductive elimination on metal monohydrides is reported for C-H and O-H bond formation.[266][267] While photoinduced reductive elimination of alkanes from $[ZrH(R)(Cp^*)_2]$ (R = Et, Pr, ^{i}Bu) can also be performed thermally, $[IrH(OEt)PPh_3Cp^*]$ undergoes thermal β-H elimination and photochemical alcohol formation. Photoinduced reductive elimination of *trans*-$[PtH(R)(PPh_3)_2]$ (R = CH_2CN, $(CH_2)_2CN$, $(CH_2)_3CN$) is shown to proceed *via* initial photochemical isomerization to *cis*-$[PtH(R)(PPh_3)_2]$ followed by thermal concerted alkane elimination.[268]

Photoexcitation can have a strong effect on the redox properties and the acidity of a compound. Accordingly, population of an excited state influences the driving force for proton, hydrogen atom or hydride transfer of a hydride ligand. The excited state thermodynamics of PCET on a hydride complex are probably best examined for [IrH(L)Cp*]X (L = bpy, phen: 1,10-phenanthroline), initially reported by *Ziessel*.[269] Following early reports on photochemical WGS catalysis and formic acid dehydrogenation, photo(electro-)chemical proton reduction from different acids including water was investigated more recently by *Miller*.[270–275] Aside from photocatalytic application, [IrH(L)Cp*]X or its derivatives catalyze a great number of chemical reactions including electrochemical CO_2 reduction to formate, thermal (transfer-)hydrogenation of CO_2 to formic acid, formic acid disproportionation to methanol, water oxidation and hydrogenation of carboxylic acids among others.[276–281] Early mechanistic studies on the photochemical WGS catalysis suggest protonation of the hydride and subsequent H_2 liberation as photochemical step of the reaction since no formation of H_2 is observed in the dark.[282] Photochemical H_2 liberation can be rationalized based on enhanced hydricity of the triplet excited state (τ = 80 ns at 293 K) as predicted by an excited state cube scheme of [IrH(bpy)Cp*]X.[283,284] The low excited state hydricity is a result of photoacidic behavior and a low excited state reduction potential. Accordingly, [IrH(bpy)Cp*]X acts as both photochemical proton and hydride donor.[284,285] Detailed mechanistic work by *Miller* recently showed that H_2 formation proceeds *via* excited state self-quenching giving Ir^{II}/Ir^{IV} hydrides followed by thermal bimolecular H_2 formation rather than exited state hydride donation.[275] This mechanistic understanding reveals [IrH(bpy)Cp*]X as a rare example of a monohydride complex which liberates H_2 in a bimolecular reaction upon photoexcitation. Photochemical insertion of CO_2 into metal hydride bonds giving the formate

complex is reported for several compounds, however excited state thermodynamics or mechanistic investigations are not available in the literature.[211,286,287]

2.2 Outline

The reduction of carbon dioxide to carbon monoxide is of high relevance for liquid fuel generation since it is a common intermediate in production of hydrocarbons. While several approaches to this transformation exist, including thermal rWGS catalysis and (photo-)electrochemically driven reactions, photochemical rWGS catalysis on a single molecular catalyst is not reported in the literature. To perform such reactivity, the abnormal CO_2 insertion from a transition metal hydride to the hydroxycarbonyl can be regarded as the key step since this selectivity determining step results in carbon monoxide formation instead of formate production. Molecular nickel complexes play an outstanding role in CO selective CO_2 reduction chemistry as exemplified by [NiFe] CODH and Ni based electrocatalysts. Further, nickel hydride complexes show comparably high hydricity which results in low driving force for unwanted normal CO_2 insertion to the formate.

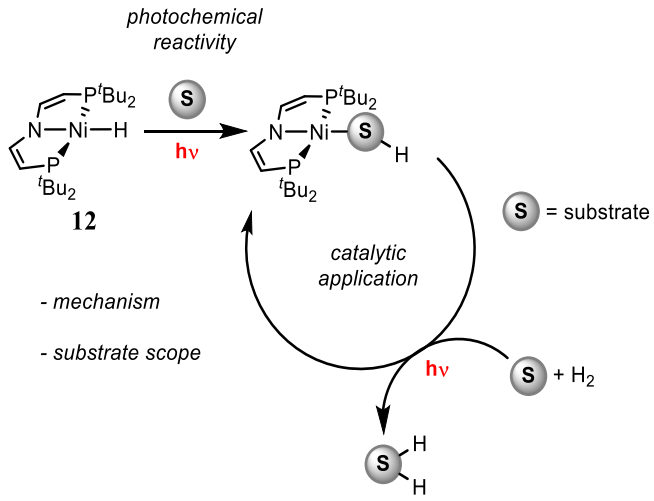

Scheme 33: Photochemical substrate activation by Ni^{II} hydride **12** and follow-up chemistry yielding hydrogenation products.

Starting from Ni^{II} hydride [NiH(^{tBu}P=N=P)] (**12**), the thermal and photochemical reactivity with CO_2 is to be investigated. While normal CO_2 insertion to the Ni^{II} formate is expected in the dark, photochemical excitation might result in a different selectivity for PCET of the hydride ligand. Mechanistic investigation by kinetic measurements and analysis of the photophysical processes by transient spectroscopy will be performed to examine the influence of photoexcitation. Monitoring the excited state metal hydride stretching vibration by UV-pump-IR-probe spectroscopy is of high interest and unprecedented in the literature. In case of successful photochemical activation of CO_2, the scope of photochemical reactivity will be broadened to other substrates. Based on the results of photochemical substrate activation, investigation of the follow-up reactivity will be performed to determine the suitability for catalytic application (Scheme 33). The

importance of the ^{tBu}P=N=P pincer ligand and the generality of the observed photochemical reactivity of **12** will be evaluated by comparison of the results to related pincer based Ni^{II} hydride complexes.

Metal azide complexes show a rich photochemistry including nitride/nitrene formation by N_2 loss and homo-/heterolytic metal nitrogen bond cleavage. Nickel nitrene complexes have been postulated based on photochemical reactivity of nickel azides, however experimental proof of these elusive intermediates has not been presented. The ^{tBu}P=N=P pincer ligand has repetitively shown outstanding properties in stabilization of highly reactive nitrido/nitrene complexes of late transition metal complexes.[288,289] Starting from Ni^{II} bromide **3** a Ni^{II} azide will be synthesized and its photochemical reactivity will be investigated. Transient spectroscopy will be performed to identify the photophysical and -chemical processes involved.

2.3 Nickel Pincer Complex Mediated Reverse Water-Gas Shift Reactivity

2.3.1 Thermal and Photochemical CO_2 Activation by [NiH(^{tBu}P=N=P)] (12)

The ability of the ^{tBu}P=N=P pincer scaffold to participate in electronic transitions is shown in Chapter 1.3.2 and motivates investigation of photochemical reactivity of ^{tBu}P=N=P nickel complexes. Hydrogen transfer from transition metal hydride complexes is pivotal as elementary reaction in many catalytic chemical and biochemical transformations. Therefore, photochemical excitation of Ni^{II} hydride **12** is an attractive approach to substrate activation.

Initially, the thermal reactivity of **12** with CO_2 was investigated. When a THF solution of **12** is exposed to 1 atm of CO_2, formation of a new species [Ni(O_2CH)(^{tBu}P=N=P)] (**15**) can be observed spectroscopically by NMR. $^{31}P\{^1H\}$ NMR spectra of complex **15** shows a resonance at δ = 56.1 ppm.

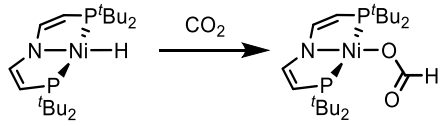

12 **15**

Scheme 34: Thermal reactivity of **12** with CO_2.

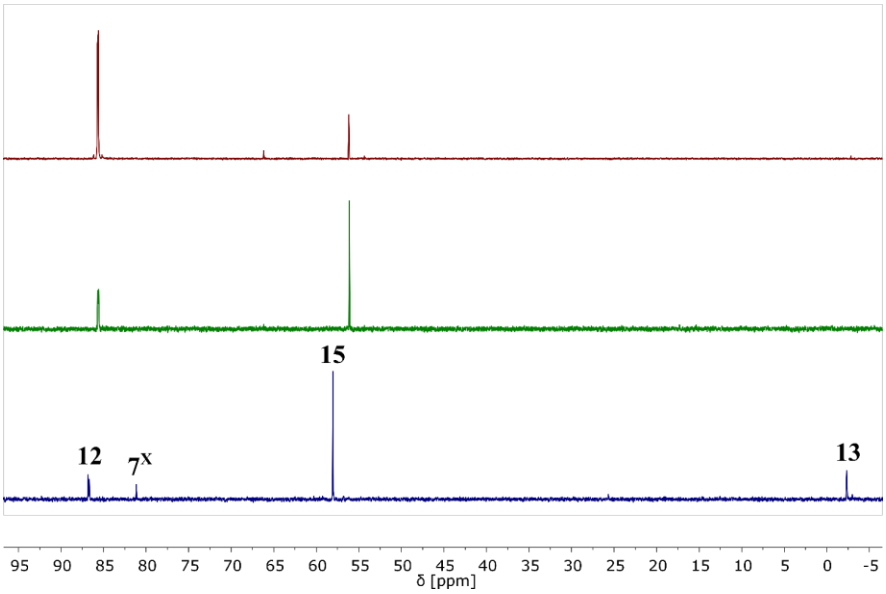

Figure 55: $^{31}P\{^1H\}$ NMR spectra of the reaction of **12** with CO_2 (top) at $p(CO_2)$ = 1 atm in THF, (middle) at $p(CO_2)$ = 10 atm in THF and (bottom) at $p(CO_2)$ = 1 atm in MeCN. All spectra are recorded after 1 day of reaction time.

The conversion of **12** to **15** is slow in THF but can be accelerated by working at higher CO_2 pressures as shown in Figure 55. Still, after two weeks under 10 atm CO_2 pressure, residual **12** can be detected. Continuous conversion of **12** to **15** was monitored NMR spectroscopically over this time, suggesting a slow

reaction rather than an equilibrium between both species. While compound **15** was not isolated, it can be readily assigned as a formate complex by its indicative NMR spectroscopic features including a downfield shifted triplet resonance in the ^{1}H NMR spectrum centered at δ = 7.25 ppm with a coupling constant of $^{4}J_{HP}$ = 3.4 Hz (Figure 56). Furthermore, by ^{1}H,^{13}C HSQC NMR spectroscopy the cross peak to a triplet resonance in the ^{13}C{^{1}H} NMR spectrum at δ = 168.3 ppm with $^{3}J_{CP}$ = 1.1 Hz can be detected. Both signals are in good agreement with reported pincer Ni^{II} formate complexes.[223]

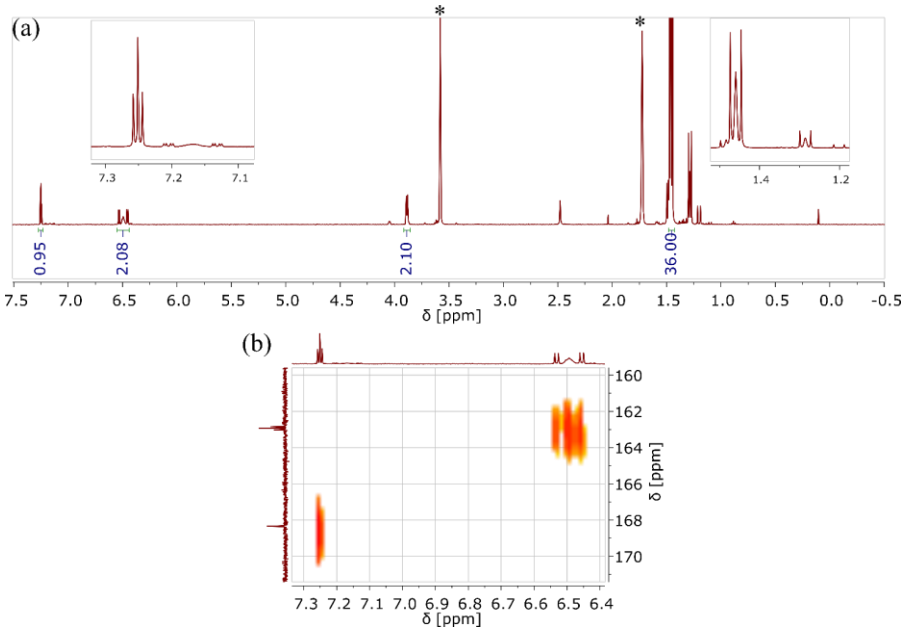

Figure 56: (a) ^{1}H and (b) ^{1}H,^{13}C HSQC NMR spectra of *in situ* formed **15** by stirring **12** at $p(CO_2)$ = 10 atm in THF for 14 days (*denotes THF-d_8).

Since both, the hydricity ΔG_{HT} of the formate anion and a transition metal hydride complex can be strongly depending on the solvent, the equilibrium constant of CO_2 insertion into a transition metal hydride complexes can be influenced by changing the solvent.[2] In addition, *Hazari* and *Bernskoetter* recently have shown that the rate of CO_2 insertion into transition metal hydrides giving formate complexes is solvent dependent for both inner- and outersphere processes. Here, a faster reaction is observed upon moving to solvents with a higher acceptor number.[245] In agreement with this, the reaction of **12** with CO_2 to **15** is accelerated upon changing the solvent from THF to MeCN as shown in Figure 55.

A change in selectivity can be observed if a solution of **12** in THF under CO_2 ($p(CO_2)$ = 1 atm) atmosphere is photolyzed with a 150 W Xe arc lamp using a white glass filter cutting off light of $\lambda_{exc.}$ < 305 nm. Formation of a mixture of hydroxycarbonyl [Ni(CO_2H)(^{tBu}P=N=P)] (**16**) and hydrocarbonate [Ni(OCO_2H)(^{tBu}P=N=P)] (**17**) is observed (Scheme 35). The formation of **17** is attributed to follow-up photochemical decarbonylation and subsequent CO_2 insertion of initial product **16** as will be discussed in detail in Chapter 2.4.1. In ^{1}H NMR spectroscopy a set of resonances corresponding to a C_{2v} symmetric

pincer ligand can be observed for both compounds. A single low field shifted broad resonance is observed, indicating chemical exchange of the protic hydrogen atoms of the bicarbonate and carboxylate moiety.

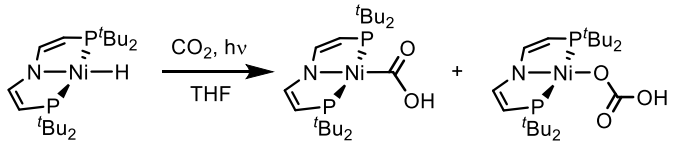

Scheme 35: Photochemical reactivity of **12** with CO_2.

The rate of the reaction drops significantly upon irradiation with $\lambda_{exc.} > 420$ nm, proving that UV light is crucial (Figure 57b). UV-vis measurement of **12** shows three transitions between $\lambda = 200$ nm and $\lambda = 400$ nm with the highest oszillator strength at $\lambda = 233$ nm ($\varepsilon = 4.1 \cdot 10^4$ $M^{-1}cm^{-1}$) (Figure 57c). The transitions with an absorption maxima at $\lambda = 305$ nm ($\varepsilon = 1.2 \cdot 10^4$ $M^{-1}cm^{-1}$) and $\lambda = 334$ nm ($\varepsilon = 2.1 \cdot 10^4$ $M^{-1}cm^{-1}$) are excited upon photolyzing with $\lambda_{exc.} > 305$ nm, but the conversion of **12** by photolysis with $\lambda_{exc} > 420$ nm indicates the red shifted transition which tails off to $\lambda > 400$ nm to be responsible for the observed reactivity. The magnitude of extinction of all three transitions suggests spin and symmetry allowed charge transfer or LC (ligand centered) transitions, excluding metal centered excitation.[152]

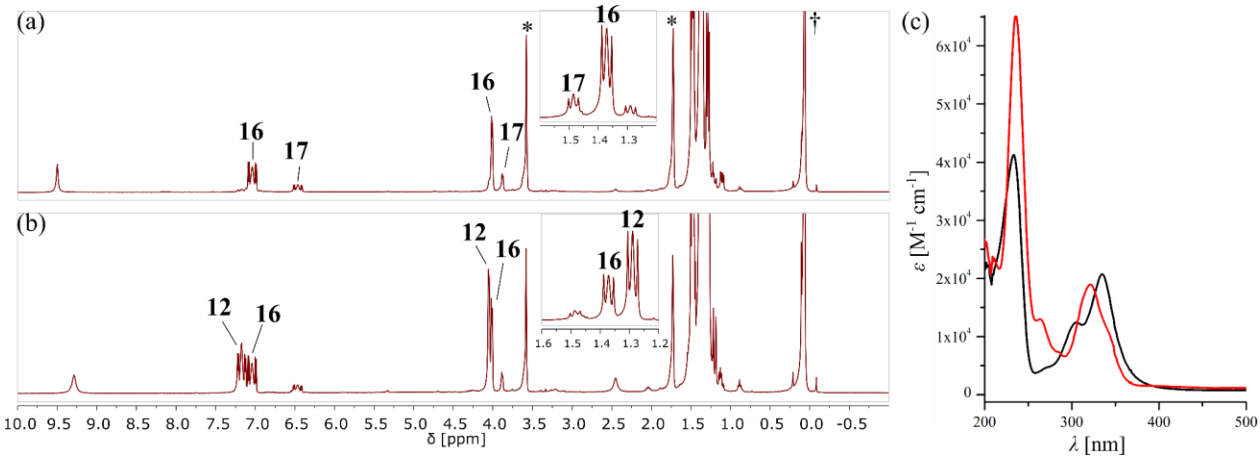

Figure 57: ^{1}H NMR spectra of a solution of **12** in THF-d_8 after 4 h of photolysis at $p(CO_2) = 1$ atm with (a) $\lambda_{exc} > 305$ nm and (b) $\lambda_{exc} > 420$ nm (*denotes THF-d_8; †denotes TMS_2O). (c) UV-vis spectra of hydride **12** (black) and hydroxycarbonyl **16** (red) in THF.

Since the photochemical conversion of **12** to **16** and **17** occurs within hours, only traces of formate **15** are formed over the course of the reaction. Compound **16** can be isolated from the obtained mixture by precipitation with unpolar solvents like benzene and *n*-pentane. Preparative synthesis of **16** is performed in benzene which results in precipitation of the desired product from the reaction mixture in an isolated yield of 73%.

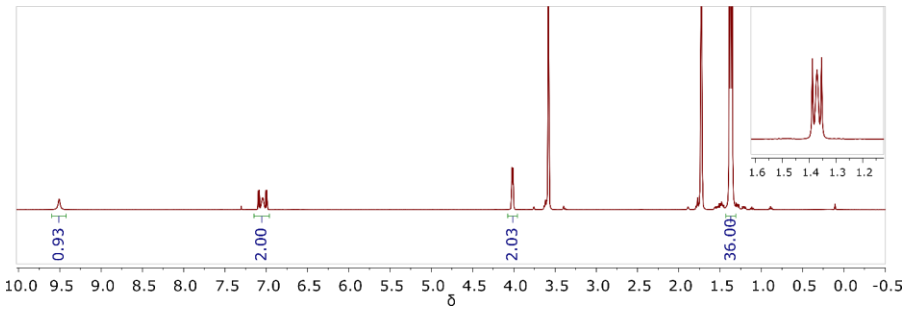

Figure 58: ^{1}H NMR spectrum of **16** in THF-d_8.

NMR spectroscopic analysis of isolated **16** shows a singlet in the $^{31}P\{^{1}H\}$ NMR spectrum at δ = 66.2 ppm. In the ^{1}H NMR spectrum the carboxylate gives rise to a broad downfield shifted resonance at δ = 9.51 ppm. A triplet at δ = 203.6 ppm can be observed in the $^{13}C\{^{1}H\}$ NMR spectrum. The coupling constant of $^{2}J_{CP}$ = 31.1 Hz is larger than in formate **15** as expected for a shorter distance between the coupling nuclei. The broad resonance of the carboxylic acid proton in **16** indicates chemical exchange which is commonly observed in carboxylic acids due to oligomerization in solution. [290]

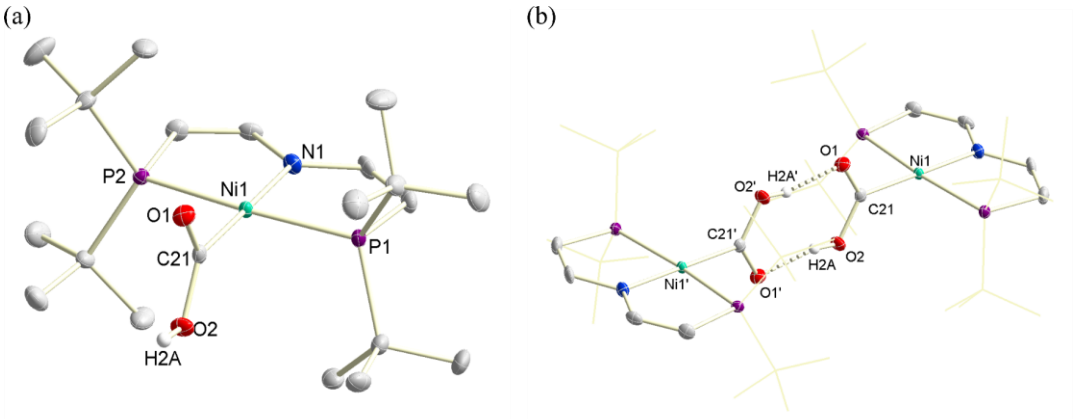

Figure 59: Solid state structure of **16** determined by X-ray diffraction. Thermal ellipsoids are drawn at the 50% probability level. Selected hydrogen atoms are omitted for clarity. (a) Asymmetric unit of the solid-state structure of **16** and (b) dimeric structure of **16** by hydrogen bonding.

Analysis of **16** by X-ray diffraction reveals a dimeric structure in the solid state which is formed due to hydrogen bonding between two carboxylic acid functions with *d*(O2-H2A) = 0.80 Å and *d*(O1'-H2A) = 1.85 Å (Figure 59). Further bond metrics of the carboxylic acid moiety in **16** agree well with reports of related structures in the literature (*d*(C21-O1) = 1.274(3) Å; *d*(C21-O2) = 1.299(3) Å; *d*(Ni1-C21) = 1.854(2) Å; α(O1-C21-O2) = 119.09(16)°).[223,225]

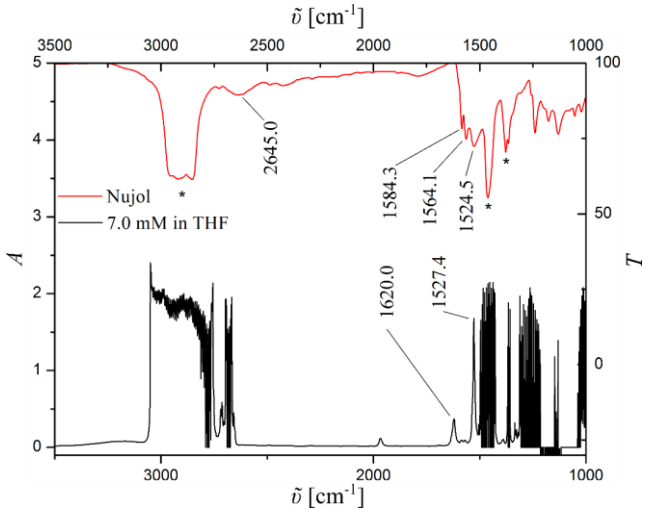

Figure 60: Infrared spectra of **16** in nujol (red) and THF solution (black) (*denotes absorption of nujol).

Infrared spectroscopy of **16** in nujol shows three strong bands in the range of $\tilde{\upsilon}$ = 1500–1600 cm^{-1} which is the typical observed region for carbonyl stretching vibrations of PNP ligated metallacarboxylates and the C-C double bond stretch of the pincer backbone in **16**. Further, the O-H stretch is visible as a broad absorption at $\tilde{\upsilon}$ = 2645 cm^{-1} which agrees with related PNP pincer Ni(II) hydroxycarbonyl compounds.[223,225] Upon measuring IR spectra of a THF solution of **16** the carbonyl region simplifies to two strong bands. Measuring the sample in nujol or THF solution is expected to have a strong effect on hydrogen bonding of the carboxylic acid moiety and accordingly a bigger influence on the carbonyl stretch is expected compared to the C-C double bond. The absorption at $\tilde{\upsilon}$ = 1620 cm^{-1} can be assigned as the carbonyl stretching vibration since it shifts strongly with respect to the spectrum in nujol. Accordingly, the absorption at $\tilde{\upsilon}$ = 1527.4 cm^{-1} resonates close to the absorption in nujol and can be identified as the C-C double bond stretching vibration.

Hydrocarbonate **17** cannot be isolated from the mixture of products obtained by photolysis of **12** under CO_2 since it forms hydroxide [Ni(OH)(^{tBu}P=N=P)] (**18**) by decarboxylation upon evaporation of the solvent. Accordingly, an alternative synthetic route to **17** was established starting from **18** which can be synthesized from Ni^{II} bromide **3** using potassium hydroxide. One equivalent 15-crown-5 is necessary to provide solubility of the KOH in THF and is separated from the reaction mixture by filtration over Celite®.

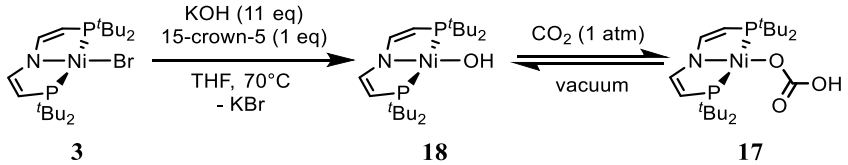

Scheme 36: Synthesis of hydroxide **18** and reversible CO_2 insertion to hydrocarbonate **17**.

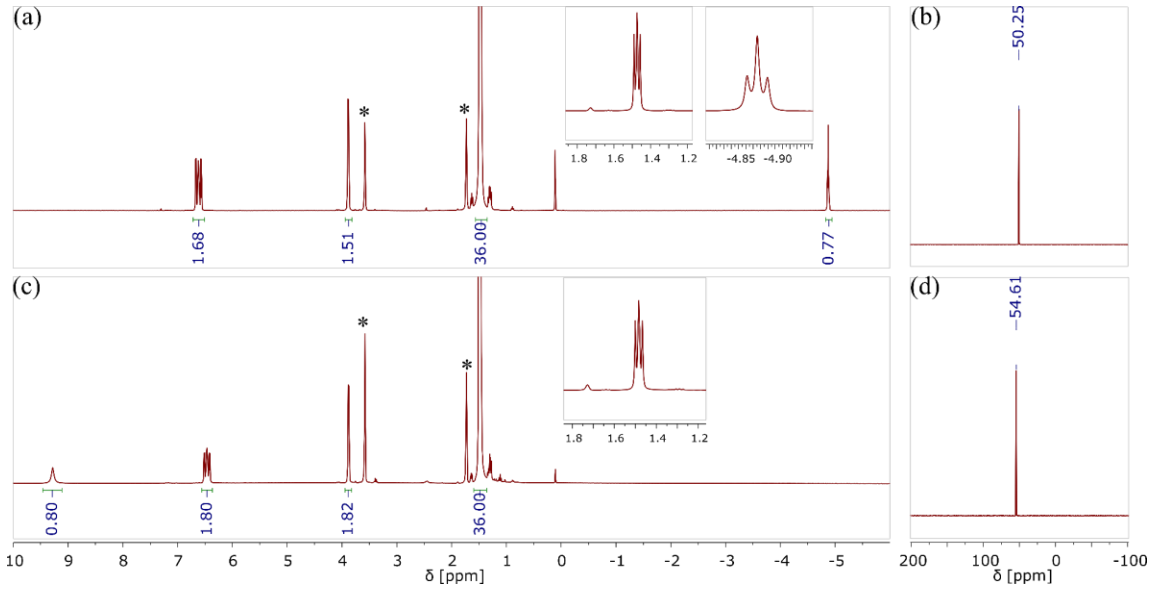

Figure 61: (a) ^{1}H and (b) ^{31}P{^{1}H} NMR spectra of **18** in THF-d_8 under Ar atmosphere and (a) ^{1}H and (b) ^{31}P{^{1}H} NMR spectra of **17** in THF-d_8 obtained by applying $p(CO_2)$ = 1 atm to a solution of **18** in THF-d_8.

In ^{1}H NMR spectroscopy, the hydroxide ligand in **18** gives rise to a triplet resonance at δ = -4.88 ppm with $^{3}J_{HP}$ = 5.6 Hz, similar to what is observed for *Mindiola*'s related pincer Ni^{II} system (Figure 61).[291] IR spectroscopy supports the presence of a hydroxide ligand by showing a vibration at $\tilde{\upsilon}$ = 3643.8 cm^{-1}.

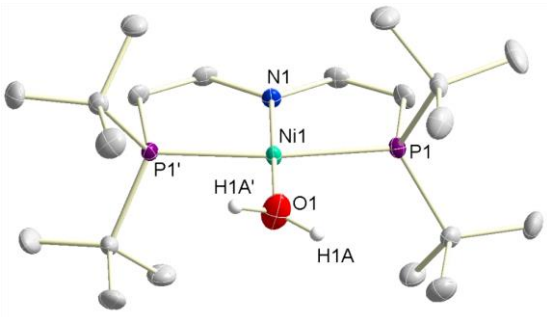

Figure 62: (a) Solid state structure of **18** determined by X-ray diffraction. Thermal ellipsoids are drawn at the 50% probability level. Selected hydrogen atoms are omitted for clarity. H1A and H1A' are populated with 50% probability, each.

X-ray diffraction of **18** confirms the structural assignment of a hydroxide complex with a nickel oxygen bond length of d(Ni1-O1) = 1.845(3) Å, marking the lower limit in reported Ni hydroxide complexes.[291–294]

Upon applying CO_2 to a THF solution of **18** the intense orange solution immediate brightens and ^{31}P{^{1}H} NMR spectroscopy shows clean conversion of **18** (δ = 50.3 ppm) to **17** (δ = 54.6 ppm) (Figure 61). The carbonate moiety is clearly identified by ^{31}C{^{1}H} NMR spectroscopy showing a singlet resonance at δ =

158.9 ppm. Hydrocarbonate **17** shows a broad singlet resonance at δ = 9.28 ppm in the ^{1}H NMR spectrum, indicating aggregation in solution as is observed for hydroxycarbonyl **16**. X-ray crystallographic analysis shows a dimeric structure of **17** in the solid state similar to **16**. While the hydrogen bond has similar bond metrics (*d*(O3-H3) = 0.98(4) Å, *d*(O2'-H3) = 1.61(4) Å) compared to **16**, the geometry of the carbonate ligand in **17** results in parallel orientation of the planes defined by the {Ni(^{tBu}P=N=P)} scaffold of the monomers in the dimeric structure, whereas the monomers in the dimeric structure of **16** are sharing the same plane.

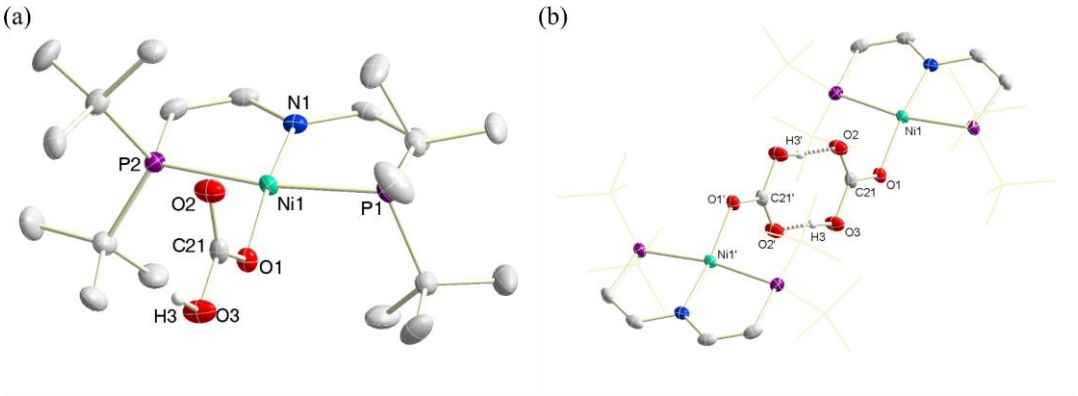

Figure 63: Solid state structure of **17** determined by X-ray diffraction. Thermal ellipsoids are drawn at the 50% probability level. Selected hydrogen atoms are omitted for clarity. (a) Asymmetric unit of the solid-state structure of **17** and (b) dimer structure of **17** by hydrogen bonding.

2.3.2 (De-)Protonation of [Ni(CO$_2$H)(^{tBu}P=N=P)] (16)

Hydroxycarbonyl complexes play an important role in transition metal mediated waster-gas shift (WGS) reactivity (Chapter 2.1.3). The WGS reaction is highly sensitive to pH and therefore the pK_a of metallacarboxylic acids is of great interest. While pK_a determination of these species is scarce, reports on [Co(CO$_2$H)(H$_2$O)(en)$_2$] (pK_a^{aq} = 2.5) and [Ru(CO$_2$H)(CO)(bpy)$_2$] (pK_a^{aq} = 9.6) show decent proton donating ability.[295–297]

The reaction of **16** with 1 eq NaHMDS (HMDS: hexamethyldisilazane) in THF gives clean conversion to a new species. In the ^{31}P{^{1}H} NMR spectrum a singlet resonance at δ = 57.5 ppm is visible. ^{1}H NMR spectroscopy only shows the spectroscopic signature of the pincer ligand, in agreement with deprotonation of the carboxylic acid to carboxylate Na[Ni(CO$_2$)(^{tBu}P=N=P)] (**19Na**). While carboxylate **19**$^{-}$ can also be regarded as a Ni^{0} CO$_2$ complex, detailed investigation by *Lee* and coworkers on related PNP nickel complexes suggests formulation as Ni^{II} carboxylates.[223,225] Titration of **16** with 1 eq of different bases results in a shift of the singlet resonance in ^{31}P{^{1}H} NMR spectroscopy towards **19Na** as can be seen in Figure 64. Addition of DBU (1,8-diazabycyclo[5.4.0]undec-7-ene) results in formation of a fast exchange equilibrium between **16** and **19**$^{-}$, while the stronger base TBD gives a resonance close to what is observed

for **19**^{Na} (Figure 64). The different in the chemical shift $\Delta\delta$ observed in $^{31}P\{^{1}H\}$ NMR spectroscopy of **16** in the presence of NaHMDS and TBD (1,5,7-triazabicyclo[4.4.0]dec-5-ene) is assumed to result from differences in aggregation due to variation of the cation.

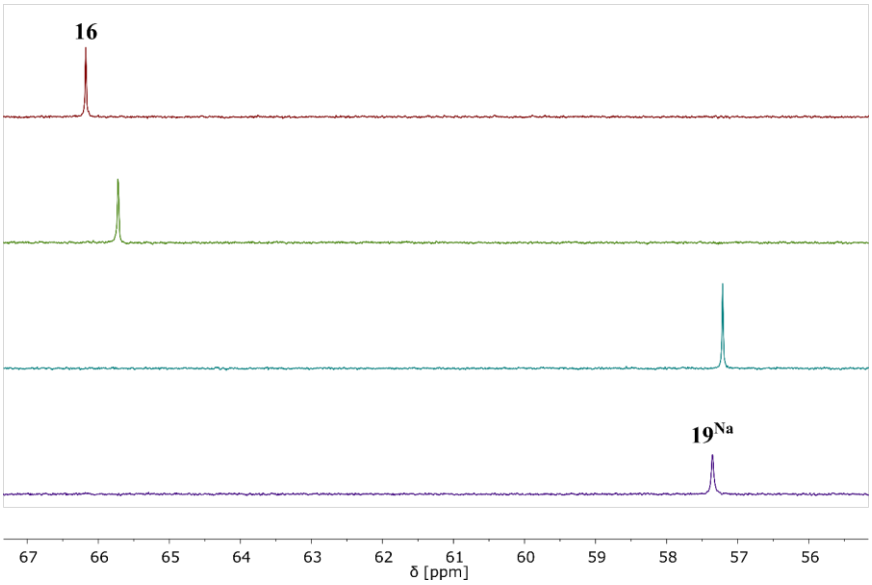

Figure 64: $^{31}P\{^{1}H\}$ NMR spectra of the reaction of **16** (top) without addition of base, (upper middle) with addition of 1 eq DBU, (lower middle) with addition of 1 eq TBD and (bottom) **19**^{Na} prepared by reaction of **16** with 1 eq NaHMDS in THF-d_8.

Determination of pK_α(**16**) can be performed assuming coupled equilibria in THF, as described for pK_α(**10**)^{BArF} (Chapter 1.4.2). Monomer-dimer equilibria of **16** are probably also involved as discussed earlier. These equilibria influence the experimental determined K_{eq}, are however neglected in the following discussion.

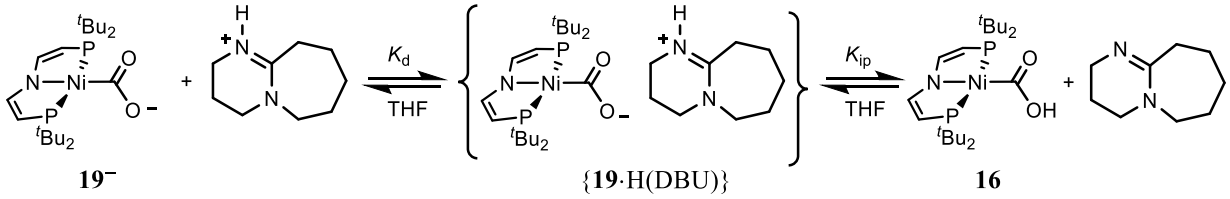

Scheme 37: Acid base equilibrium for deprotonation of **16**.

The molar fractions χ of **16** and **19**$^{-}$ are available from the observed chemical shift upon titration of **16** with 1 eq DBU (δ(**16**+DBU) = 65.7 ppm) and the chemical shift the conjugate acid and base measured at the identical concentration (δ(**16**) = 66.2 ppm, δ(**19**^{Na}) = 57.4 ppm). Following eq. (34), eq. (46) results, giving χ(**16**) = 0.949 and χ(**19**$^{-}$) = 0.051.

$$\delta(\mathbf{16}\text{+DBU}) = \chi(\mathbf{16})\delta(\mathbf{16}) + \chi(\mathbf{19}^{-})\delta(\mathbf{19}^{-}) \quad (46)$$

The equilibrium constant K_{ip} for proton transfer giving the acid-base ion pair is available as K_{eq} from the experiment following eq. (47).

$$K_{eq} = c(\mathbf{16})^2/c(\mathbf{19}^-)^2 = \chi(\mathbf{16})^2/\chi(\mathbf{19}^-)^2 = 357 \quad (47)$$

Deprotonation of **16** by DBU converts two neutral reactants to charged products. Accordingly, the influence of contact ion-pair formation is expected to be more severe as compared to the reaction of $\mathbf{10}^{\mathbf{BArF}}$ with NEt_3. The equilibrium constant K_d is calculated according to *Fuoss* equation eq. (32) using an ionic radius of $r = 4.0$ Å determined from the X-ray structure of **16** and an ionic radius of $r = 2.5$ Å for protonated DBU taken from literature.[298–300]

$$b = -e^2/(a\varepsilon kT) = -11.7 \quad (48)$$

Parameter $b = -11.7$ is obtained using the elementary charge $e = 4.80\cdot10^{-10}$ esu, the inter-ion distance $a = 6.5\cdot10^{-8}$ cm, the dielectric constant of THF $\varepsilon = 7.39$, the *Boltzmann* constant $k = 1.38\cdot10^{-16}$ erg/deg and the temperature T in Kelvin as explained by *Morris*.[108,298] Accordingly, the dissociation constant $K_d = 1.3\cdot10^{-5}$ M is obtained.

$$K_d = 3000e^b/(4\pi Na^3) = 1.25\cdot10^{-5}\ \text{M} \quad (49)$$

Taking literature known $pK_\alpha(\text{DBU})^{THF} = 16.8$, $pK_\alpha(\mathbf{16})^{THF} = 24.3$ results.

$$pK_\alpha(\mathbf{16})^{THF} = pK_\alpha(\text{DBU})^{THF} + \log(K_{eq}) + \Delta pK_d \quad (50)$$

$$pK_\alpha(\mathbf{16})^{THF} = 16.8 + 2.55 + 4.90 = 24.3 \quad (51)$$

Due to a net charge built-up, the influence of the dissociation of the contact ion-pair plays a much greater role in the determination of $pK_\alpha(\mathbf{16})^{THF}$ ($\Delta pK_d = 4.90$) than in the titration of $\mathbf{10}^{\mathbf{BArF}}$ with NEt_3 ($\Delta pK_d = 0.43$). Comparison of $pK_\alpha(\mathbf{16})^{THF}$ with reported acidities of metallacarboxylic acids shows, that **16** shows remarkably low acidity and is only deprotonated by strong bases like TBD.

Deprotonation of hydroxycarbonyl complexes results in formation of carboxylates which may undergo CO_2 liberation under formation of a reduced metal center. Accordingly, WGS catalysis is usually observed under basic conditions. Working under acidic conditions results in proton induced dehydration of the hydroxycarbonyl, a microscopic reverse of the *Hieber* base reaction, giving a metal carbonyl and *reverse* water-gas shift (rWGS) reactivity. Experimentally determined $pK_\alpha(\mathbf{16})^{THF}$ suggests that strongly basic conditions are necessary to drive WGS reactivity. Further, no signs for decarboxylation of $\mathbf{19}^-$ were observed rendering this {Ni(^{tBu}P=N=P)} platform unsuitable for performing WGS catalysis. Interested in performing rWGS reactivity, examination of dehydration of **16** in acidic media was investigated.

If **16** is reacted with strong acids like $[H(OEt_2)_2]BArF$ or $[H(OEt_2)]BF_4$, clean conversion to Ni^{II} carbonyl $[Ni(CO)(^{tBu}P{=}N{=}P)]X$ (**20^{X}**, X = BF_4, BArF) is observed. The reaction of **16** with 1 eq $[H(OEt_2)_2]BArF$ proceeds in 97% spectroscopic yield determined by integration against an internal standard in ^{1}H NMR spectroscopy (Figure 65). Trap-to-trap condensation of the volatiles confirms formation of water in 77% yield with respect to **20^{BArF}**.

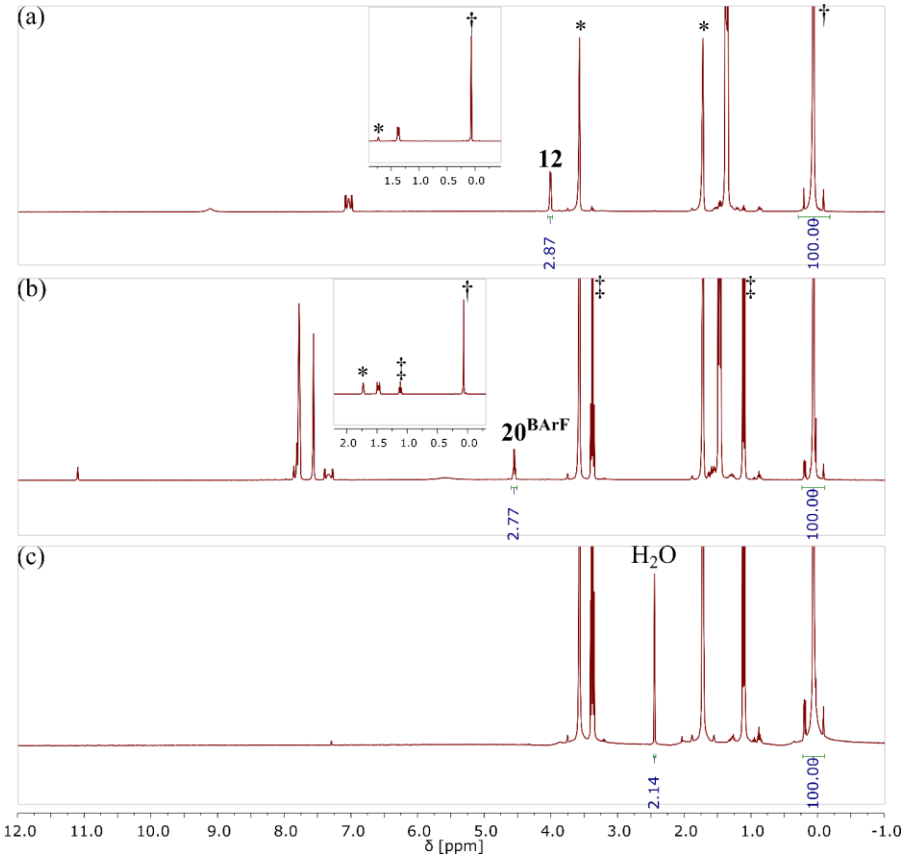

Figure 65: ^{1}H NMR spectra of the reaction of **16** with 1 eq of $[H(OEt_2)_2]BArF$ in THF-d_8, showing the recorded spectra (a) before and (b) after addition of $[H(OEt_2)_2]BArF$ and (c) after trap-to-trap condensation of the volatiles (*denotes THF-d_8, †denotes TMS_2O and ‡denotes Et_2O).

NMR spectra of compound **20^{X}** show the signature of diamagnetic C_{2v} symmetric $\{Ni(^{tBu}P{=}N{=}P)\}$ complexes in ^{1}H NMR spectroscopy with a downfield shifted resonance in $^{31}P\{^{1}H\}$ NMR spectroscopy at δ = 114.7 ppm. The carbonyl ligand can be clearly identified by a triplet resonance at δ = 191.3 ppm ($^{2}J_{CP}$ = 22.5 ppm) in the $^{31}C\{^{1}H\}$ NMR spectrum of **20^{BF4}** (Figure 71a). Accordingly, a strong signal at $\tilde{\upsilon}$ = 2062.4 cm^{-1} for the CO stretching vibration can be observed by ATR-IR spectroscopy.

Interested in the pK_a constrains of dehydration, **16** was titrated with different protonated nitrogen bases as can be seen in Figure 66. While $[H(NEt_3)]BArF$ and [H(piperidine)]BArF yield full conversion to **20^{BArF}**, addition of 1 eq [H(TMG)]BArF (TMG = 1,1,3,3-tetramethylguanidine) results in formation of an equilibrium between **16** and **20^{BArF}**. Determination of the pK_α for this reaction is complicated by coupling

of the acid base equilibrium to the dehydration reaction. Therefore, the titration experiments serve as determination of an upper limit of $pK_\alpha(H(TMG)^+)^{THF} = 15.3$ for the conversion of **16** to **20^X**.[300]

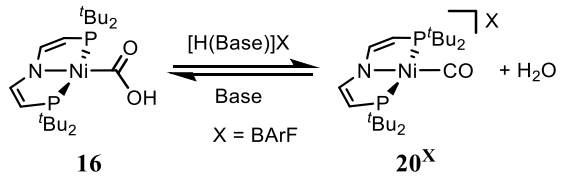

Scheme 38: Acid induced dehydration of hydroxycarbonyl **16**.

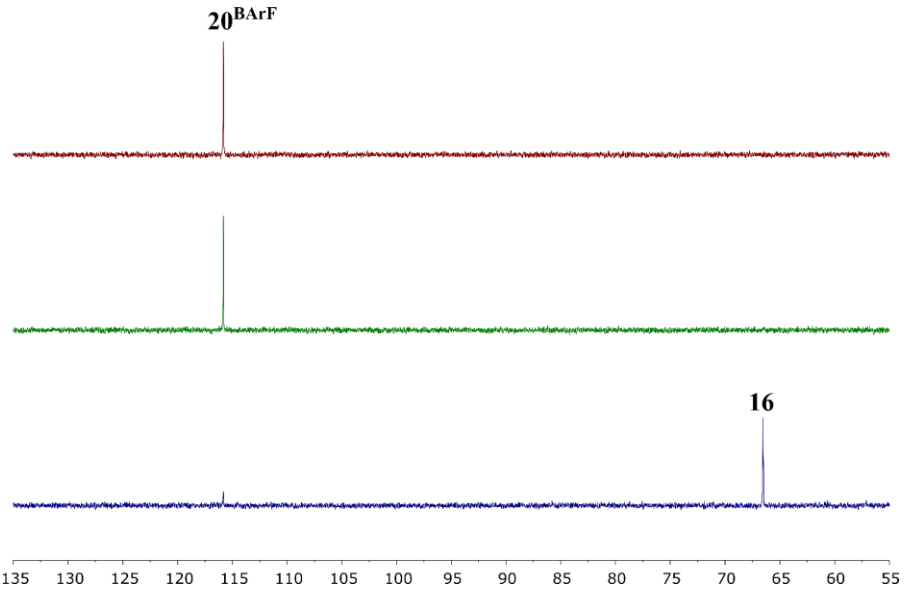

Figure 66: $^{31}P\{^1H\}$ NMR spectra of **16** in THF in the presence of (top) 1 eq [H(NEt$_3$)]BArF, (mid) 1 eq [H(piperidine)]BArF, and (bottom) 1 eq [H(TMG)]BArF.

Investigation of the deprotonation of hydroxycarbonyl **16** to **19^M** and the acid induced dehydration of **16** to **20^X** shows a difference in pK_α^{THF} of approximately 9 for the corresponding reactions. While **16** is a stable compound and not signs for dehydration to **19^M** and **20^X** are observed experimentally, formation of **19^M** and **20^X** is feasible in unpolar solvents like THF and Et_2O considering a significant gain in driving force by ion pair formation.

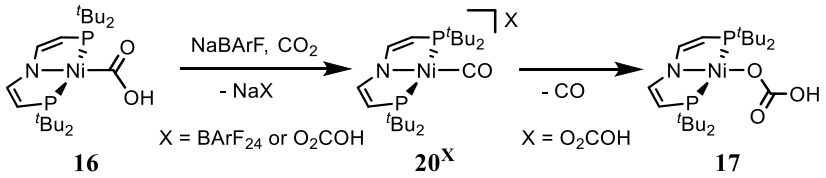

Scheme 39: Formation of hydrocarbonate **17** from carbonyl **20^X** in the presence of lewic acid and CO_2.

The ability of **16** to efficiently liberate water upon addition of weak *Brønsted* acids renders this an attractive platform to perform rWGS reactivity.Aside from *Brønsted* acids, *Lewis* acids can be used to convert hydroxycarbonyl **16** to Ni^{II} carbonyl $\mathbf{20^X}$ by hydroxide abstraction. Interestingly, dissolving a mixture of **16** and NaBArF in THF results in no apparent reaction overnight at room temperature. If the argon atmosphere is exchanged for carbon dioxide, within 30 minutes formation of $\mathbf{20^X}$ is observable by NMR spectroscopy, indicating formation of hydrocarbonate as anion rather than hydroxide. Accordingly, hydrocarbonate **17** can be observed in barely detectable amounts in the mixture, indicatingg substitution of the carbonyl ligand in $\mathbf{20^X}$ by bicarbonate (Figure 67).

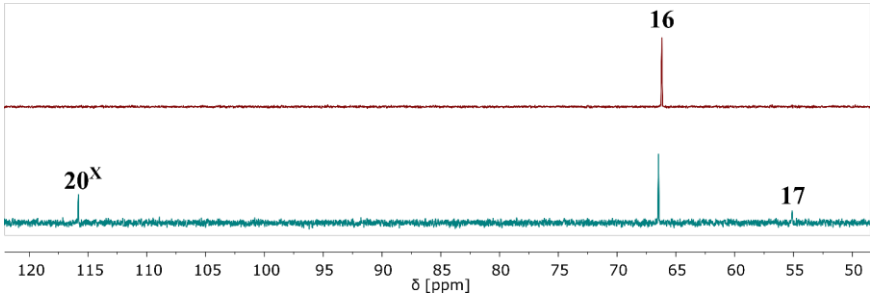

Figure 67: $^{31}P\{^1H\}$ NMR spectra of photolysis (λ > 305 nm) of a solution of **16** in THF-d_8 in the presence of 1 eq NaBArF (top) under argon atmosphere and (bottom) under carbon dioxide atmosphere.

2.3.3 Conversion of [Ni(CO)(^{tBu}P=N=P)]X (20^X) to [NiH(^{tBu}P=N=P)] (12) by addition of Li[HBEt$_3$]

Since hydroxycarbonyl complexes are key species in CO selective carbon dioxide reduction, converting hydroxycarbonyl **16** to parent hydride **12** by liberation of carbon monoxide is of interest (Scheme 40). Considering water as side product of this reaction, two equivalents of reductant and acid have to be provided. Using main group hydrides like silanes or boranes is a prominent approach for CO_2 reduction which is driven by formation of strong O-B/Si bonds. Using H_2 as electron source represents the reverse water-gas shift (rWGS) reaction which is thermodynamically uphill at standard conditions (Chapter 2.1.2). To provide the necessary potential, successive electron and proton transfer is investigated by (photo-)electrochemical approaches (Chapter 2.1.3).[167]

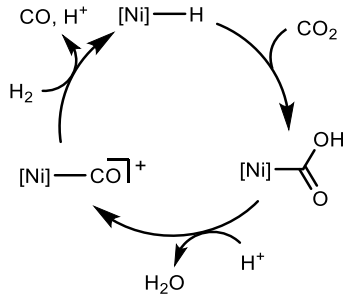

Scheme 40: Synthetic cycle for reverse water-gas shift reactivity.

As discussed previously, hydroxycarbonyl **16** can be converted to carbonyl **20^{X}** (X = BF_4, BArF) under acidic conditions with stoichiometric formation of water. While determination of pK_α(**16**)^{THF} is prohibited by a coupled equilibrium consisting of protonation and dehydration, titration with different *Brønsted* acids shows effective conversion to **20^{BArF}** upon addition of protonated amine bases.

Interested in the conversion of carbonyl **20^{X}** to hydride **12**, the synthetically most direct way was investigated: The substitution of the carbonyl for a hydride ligand by using a hydride donor. Reacting **20^{BF4}** with stoichiometric amounts of lithium triethylhydridoborate solution results in clean conversion of the starting material to hydride **12**. NMR spectroscopic monitoring of the reaction reveals the presence of an intermediate which can be stabilized at low temperature. NMR spectroscopic analysis at T = -25°C reveals formyl complex [Ni(CHO)(^{tBu}P=N=P)] (**21**) which can be identified by characteristic resonances shifted to low field in the ^{1}H and ^{13}C{^{1}H} NMR spectrum (Figure 68).

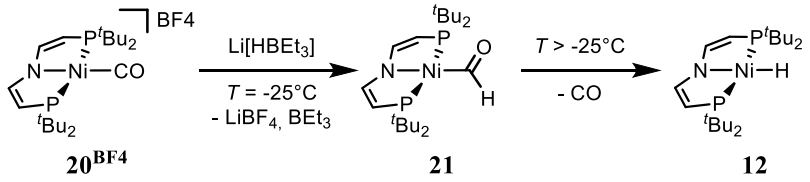

Scheme 41: Conversion of carbonyl **20^{BF4}** to formyl **21** and subsequent decarbonylation to hydride **12**.

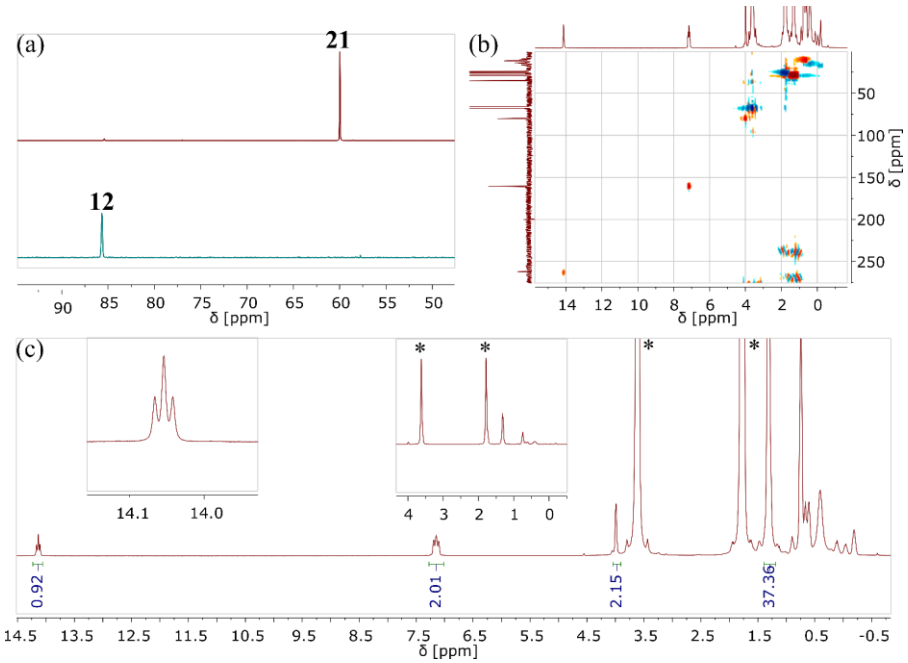

Figure 68: (a) ^{31}P{^{1}H} NMR spectra of the reaction of **20^{BF4}** with 1 eq Li[HBEt$_3$] in THF-d_8 (top) after 30 min at T = -30°C and (bottom) after 1 day at RT. (b) ^{1}H,^{13}C HSQC and (c) ^{1}H NMR spectrum of **21** (*denotes THF).

The ^{1}H NMR spectrum of **21** shows a triplet resonance at δ = 14.1 ppm corresponding to the formyl hydrogen atom with $^{3}J_{HP}$ = 12.2 ppm, while the corresponding carbon atom resonates at δ = 262.9 ppm in the ^{13}C{^{1}H} NMR spectrum. A cross peak of both signals in the ^{1}H,^{13}C HSQC spectrum further confirms the structural assignment of **21**. Notably, **21** represents the first nickel formyl with sufficient stability to allow for characterization by NMR spectroscopy. Stable pincer platinum formyl complexes have been reported by *Milstein*.[301,302] Conversion of formyl **21** to hydride **12** by CO extrusion can be monitored upon warming to T > 0°C.

2.3.4 Conversion of [Ni(CO)(^{tBu}P=N=P)]X (20^{X}) to [NiH(^{tBu}P=N=P)] (12) by Successive Reduction and Protonation

Conversion of carbonyl **20^{X}** to hydride **12** can be selectively performed using lithium triethylhydridoborate. However, successive electrochemical reduction and protonation represents a more economic approach to provide reducing equivalents. Synthesis of Ni^{II} carbonyl **20^{X}** (X = BF_4, BArF) by addition of acid to hydroxycarbonyl **16** was discussed earlier (Chapter 2.3.2). Alternative preparation of **20^{X}** can be accomplished by substitution of the acetonitrile ligand in **7^{X}** under carbon monoxide atmosphere. Cyclic voltammetry of **20^{BF4}** shows three redox events spanning a range of more than 3 V showing that {Ni(CO)(^{tBu}P=N=P)} provides an excellent platform for stabilization of different electronic situations (Figure 69).

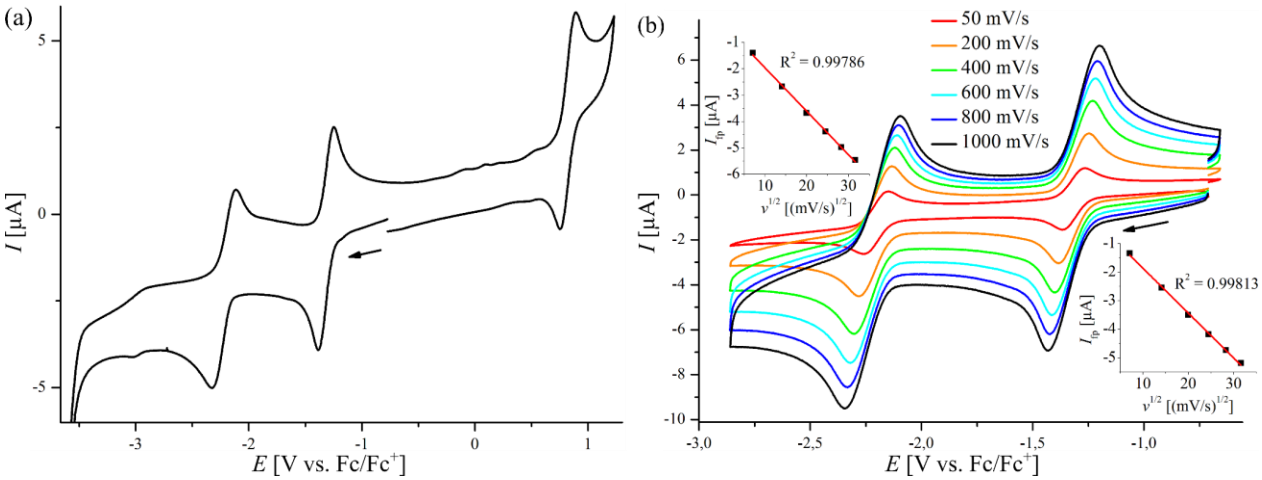

Figure 69: Cyclic voltammetry of a 1 mM solution of **20^{BF4}** in THF referenced to Fc^{+}/Fc (0.1 M [*n*-Bu_4N]PF_6, WE: GC, CE: Pt wire, RE: Ag wire). (a) Full range scan at v = 100 mV/s and (b) scan of the reduction events at different scan rates.

An Ni^{III}/Ni^{II} oxidation can be observed at $E^{1/2}$ = 0.82 V *vs*. Fc^{+}/Fc, shifted by 0.15 V anodically compared to acetonitrile coordinated **7^{BArF}** measured under the same conditions. The shift can be rationalized by the more electron withdrawing carbonyl ligand. Turning to reductive potentials, a first wave is located at $E^{1/2}$ = -1.31 V followed by a second reductive event at a lower potential of $E^{1/2}$ = -2.22 V. Since the peak

currents of all three redox processes are similar, a fully reversible $Ni^{III}/Ni^{II}/Ni^{I}/Ni^{0}$ interconversion is assumed. Investigation of the oxidation at different scan rates is not performed. Both reductive processes show nernstian electron transfer as shown by linear i_{fp} *vs.* $v^{1/2}$ plots. The peak separation exceeds the 59 mV expected for a one-electron process which is attributed to high solution resistance due to the use of low-polarity solvent THF (Table 18). Scan rate independent half wave potentials $E^{1/2}$and peak current ratios i_{rp} / i_{fp} close to 1 suggest chemically reversible redox processes for the Ni^{II}/Ni^{I} and Ni^{I}/Ni^{0} couple. Comparing the potential of the Ni^{II}/Ni^{I} redox couple with T-shaped Ni^{I} **9** ($E^{0} \geq$ -0.94 V) reveals a strong cathodic shift upon coordination of a carbonyl ligand (Chapter 1.4.2). This is surprising given the electron withdrawing nature of this ligand and can be understood as a result of unfavorable fourfold coordination at the Ni^{I} oxidation state.

Table 18: Peak analysis of the initial oxidative and reductive responses of $\mathbf{20^{BF4}}$ in cyclic voltammetry.

Ni^{II}/Ni^{I}	v [mV/s]	$E^{1/2}$ [V]	i_{rp} / i_{fp}	ΔE^{p} [mV]	Ni^{I}/Ni^{0}	v [mV/s]	$E^{1/2}$ [V]	i_{rp} / i_{fp}	ΔE^{p} [mV
	50	-1.316	0.97	98		50	-2.205	1.02	112
	200	-1.316	1.01	134		200	-2.207	0.98	149
	400	-1.317	1.06	168		400	-2.213	0.97	183
	600	-1.315	1.07	195		600	-2.214	0.97	210
	800	-1.316	1.07	215		800	-2.215	0.96	232
	1000	-1.314	1.08	230		1000	-2.219	0.96	247

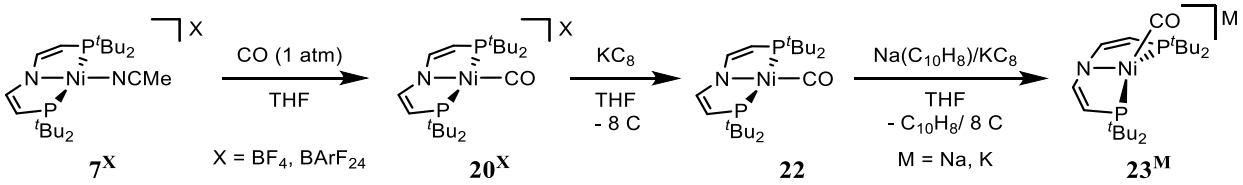

Scheme 42: Synthesis of Ni^{II} carbonyl $\mathbf{20^X}$ starting from acetonitrile coordinated $\mathbf{7^X}$ and preparation of Ni^{I} carbonyl **22** and Ni^{0} carbonyl $\mathbf{23^M}$ by reduction of $\mathbf{20^X}$.

Preparative reduction of $\mathbf{20^X}$ can be performed using a suspension of 1 eq KC_8 in THF, resulting in a color change from orange to intense green indicating formation of Ni^{I} carbonyl [Ni(CO)(^{tBu}P=N=P)] (**22**). In an alternative procedure, **22** can be prepared starting from T-shaped Ni^{I} **9** by addition of carbon monoxide. Paramagnetism of **22** results in the absence of any detectable signals in NMR spectroscopic analysis. EPR measurement of a THF solution of **22** at room temperature gives rise to an isotropic signal showing triplet multiplicity (Figure 70a).[18] The data can be simulated with an isotropic g value of g_{iso} = 2.046 and an intense

[18] EPR analysis was performed by Dr. A. Claudia Stueckl.

^{31}P hyperfine coupling of $A_{iso}(^{31}P)$ = 278 Hz. The *g* value is in good agreement with computational analysis by DFT calculations, while the hyperfine coupling is underestimated in theory.[19] An additional ^{14}N hyperfine coupling is not resolved in the experiment, which is attributed to the high line width. Further spin density analysis confirms a mainly metal centered radical with a contribution of the carbonyl and pincer ligand (Ni: 63%, CO: 17%, ^{tBu}P=N=P: 20%). If handled under strictly inert conditions, **22** is a stable compound at room temperature. Further reduction with sodium naphthalenide or potassium graphite results in formation of M[Ni(CO)(^{tBu}P=N=P)] (M = Na, K) (**23^{M}**) which decomposes to unidentified products within hours upon standing in solution at room temperature.[20] The increase of π backbonding due to reduction of the nickel center can be visualized by comparing the ATR-IR spectra of **20^{BArF}**, **22** and **23Na** which show a redshift of the carbonyl stretching vibration $\tilde{\upsilon}$(CO) upon reduction (Figure 70b). The carbonyl stretch $\tilde{\upsilon}$(CO) resonates at lower wavenumbers compared to *Lee*'s reported systems which is in good agreement with the more reductive Ni^{II}/Ni^{I} and Ni^{I}/Ni^{0} potentials presented here.[105,223,225,303]

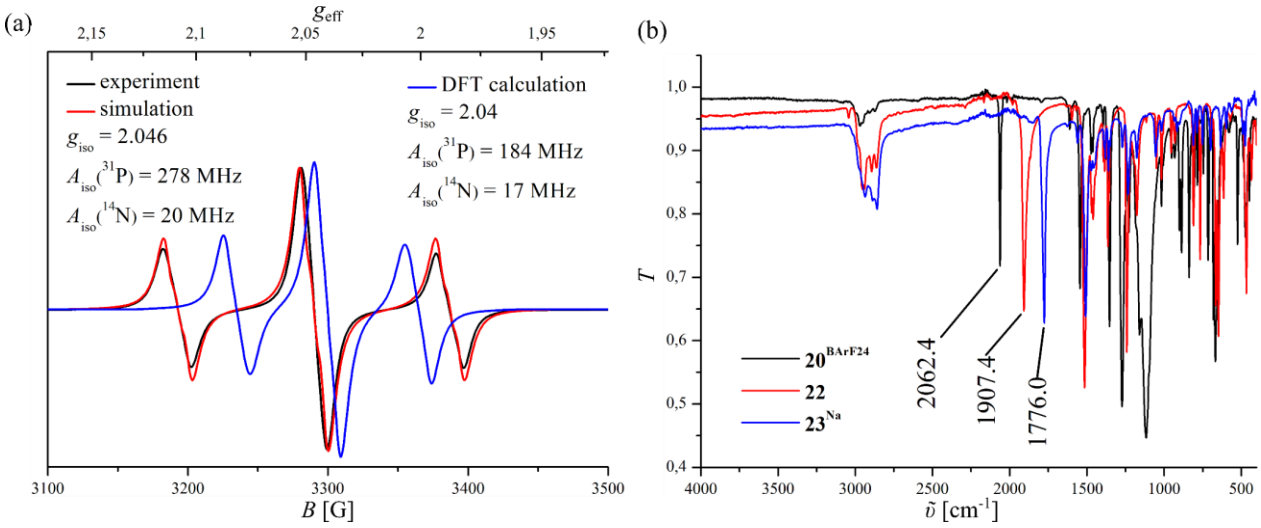

Figure 70: (a) EPR spectrum of **22** in THF (RT, *c*(**22**) = 17 mmol, *v* = 9.435505 GHz). (b) ATR-IR spectra of compounds **20^{BArF}**, **22** and **23Na**.

Reduction of reported PNP Ni compounds to Ni^{0} is commonly connected to a significant bending of the pincer ligand due to tetrahedral distortion.[225,303] ^{1}H NMR spectra of **23Na** shows C_{2v} symmetry on this timescale, giving one signal for all four ^{t}Bu groups, which is however broadened at room temperature (Figure 71a).

[19] Computational Analysis was performed by Dr. Markus Finger.
[20] NMR and IR spetroscopic characterization of **23Na** was performed by Florian Wätjen.

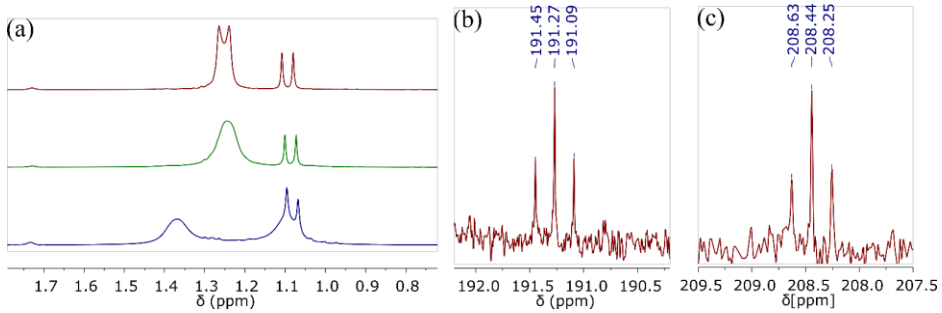

Figure 71: (a) ^{1}H NMR spectra of the ^{t}Bu region of **23Na** in THF-d_8 measured at (top) room temperature, (middle) -5°C and (bottom) -35°C. ^{13}C{^{1}H} NMR spectra of the carbonyl ligand of (b) **20^{BF4}** in CD_2Cl_2 and (c) **23Na** in THF-d_8.

Upon measuring at lower temperature, dynamic processes are indicated by additional broadening. While the coalescence temperature was not determined, two signals for chemically different ^{t}Bu groups can be detected at T = -35°C, indicating C_S symmetry. The carbonyl resonance in ^{13}C{^{1}H} NMR spectroscopy can again be observed in the expected region (Figure 71c).

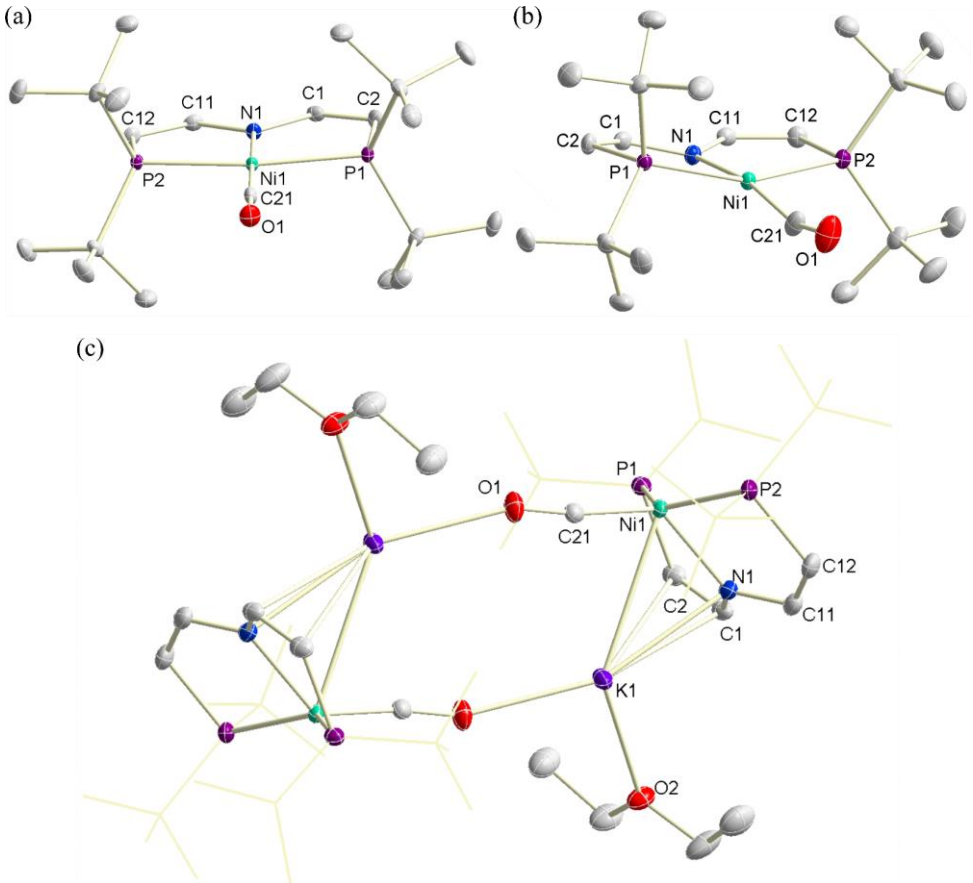

Figure 72: Solid state structure of (a) **20^{BF4}**, (b) **22** and (c) [**23^{K}**·OEt_2]$_2$ determined by X-ray diffraction. Thermal ellipsoids are drawn at the 50% probability level. The anion of **20^{BF4}** and hydrogen atoms are omitted for clarity. The ^{t}Bu groups in [**23^{K}**·OEt_2]$_2$ are shown as wireframes.

Crystals suitable for X-ray diffraction are obtained for **20**^{BF4}, **22** and [**23**^{K}·OEt_2]$_2$ as shown in Figure 72 with [**23**^{K}·OEt_2]$_2$ forming a dimeric structure. Comparison of the τ_4 values shows the change from square-planar geometry in **20**^{BF4} to a coordination which is closer to tetrahedral in [**23**^{K}·OEt_2]$_2$ (Table 19). The carbonyl C-O bond length follows the trend observed in ATR-IR, elongating upon reduction due to stronger π backbonding. Accordingly, the Ni-C bond in [**23**^{K}·OEt_2]$_2$ is the shortest, while a significant lengthening of the Ni-N bond to the amido donor can be observed in the series upon reduction. The bend CO coordination in **22** is attributed to lowering of the C-O bond order due to occupation of π* orbitals which is reflected by spin density localization on the carbon atom as confirmed by DFT analysis (C21: 12%).

Table 19: Crystallographic parameters of the solid state structure of **20**^{BF4}, **22** and [**23**^{K}·OEt_2]$_2$ determined by X-ray diffraction.

[Ni]	τ_4	d(Ni-C) [Å]	d(C-O) [Å]	d(Ni-N) [Å]	d(Ni-P) [Å]	α(Ni-C-O) [°]
20^{BF4}	0.065	1.7437(13)	1.1386(16)	1.8694(11)	2.2438(4)/ 2.2419(4)	179.38(13)
22	0.234	1.7849(19)	1.143(2)	1.9687(14)	2.2919(5)/ 2.2892(5)	162.8(2)
23^{K}	0.638	1.7076(12)	1.1863(15)	2.0202(10)	2.2645(4)/ 2.2748(4)	172.09(11)

The C-C double bond length is similar in all three compounds (Table 20). Deplanarization of the pincer ligand in [**23**^{K}·OEt_2]$_2$ is reflected by $\sum(\alpha(N))$ and φ(N-C-C-P). Potassium coordination of one pincer arm in [**23**^{K}·OEt_2]$_2$ apparently results in a roughly planar 5-ring, while more flexibility is observed in the remaining pincer arm (d(K1-N1) = 2.7792(11) Å; d(K1-C1) = 2.9921(12) Å; d(K1-C2) = 3.3883(13) Å). An additional nickel potassium interaction is observed with d(K1-Ni1) = 3.2316(3) Å.

Table 20: Crystallographic parameters of the solid state structure of **20**^{BF4}, **22** and [**23**^{K}·OEt_2]$_2$ determined by X-ray diffraction.

[Ni]	d(C=C) [Å]	$\sum(\alpha(N))$ [°]	φ(N-C-C-P) [°]
20^{BF4}	1.3432(19)/1.3423(18)	359.98	2.16(17)/2.36(17)
22	1.349(3)/1.351(2)	359.00	-2.6(2)/3.6(2)
23^{K}	1.3581(19)/1.351(2)	356.15	16.8(1)/-4.7(2)

As shown in Figure 69, Ni^{II} carbonyl **20**^{BF4} shows two reversible reduction events in cyclic voltammetry. Performing the same experiment in the presence of phenol results in chemical irreversibility of the Ni^{I}/Ni^{0} wave at v = 50 mV/s as shown in Figure 73.[304] Notably, the reductive peak potential shifts anodically,

indicating an *EC* mechanism upon reduction to Ni^0. Titration with more phenol further results in trace crossing and shifts the peak potential, indicating PCET. A report by *Dempsey* on concentration and scan rate dependent trace crossing of acids in cyclic voltammetry describes no trace crossing for phenol in acetonitrile.[304] Trace crossing is usually attributed formation of a species *via EC* which shows a redox event at slightly higher potential than the initial reduction event (in this case Ni^I/Ni^0).[305] Assuming protonation as chemical reaction might result in several products depending on the basic site in **23^M**. Reports by *Lee* on the reactivity of reduced Ni pincer carbonyl complexes with methyl iodide have shown that different reaction sites are favored depending on the oxidation state of the metal.[303] Protonation at the carbonyl carbon atom would result in formation of Ni^{II} formyl **21**, while metal centered protonation coupled to decarbonylation would give Ni^{II} hydride **12** and pincer ligand centered protonation would result in no change of the formal oxidation state. However, in case of pincer centered protonation, electrochemically formed anionic **23^M** would be converted to a neutral compound which would most likely result in an anodic shift of the Ni^I/Ni^0 oxidation potential and therefore might serve as explanation of the observed trace crossing. Increasing the scan rate shows that the trace crossing is observed up to v = 200 mV/s and that close to the Ni^{II}/Ni^I oxidation potential of the nickel carbonyl series an irreversible oxidation event can be observed which is not present in the absence of phenol (Figure 73b). Comparison of the peak potential $E^p \approx$ -0.8 V with electrochemical data on compounds reported within this thesis suggests a Ni^{II}/Ni^I process indicating pincer ligand centered protonation of **23^M**.

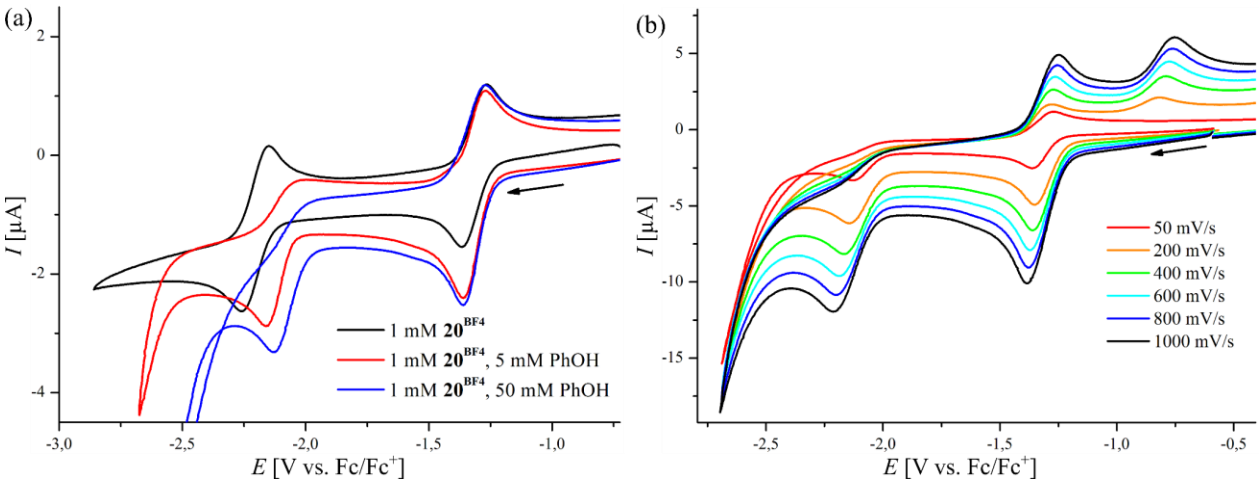

Figure 73: Cyclic voltammetry of a 1 mM solution of **20^{BF4}** in THF referenced to Fc^+/Fc (0.1 M [*n*-Bu_4N]PF_6, WE: GC, CE: Pt wire, RE: wire). (a) In the absence and presence of different concentration of phenol at v = 50 mV/s and (b) in the presence of 50 mM phenol at different scan rates v.

Reduction of Ni^{II} carbonyl **20^{BArF}** with an excess of KC_8 at subsequent addition of 2 equivalents of phenol at -36°C results in formation of a mixture of products as indicated by $^{31}P\{^1H\}$ and ^1H NMR spectroscopy (Figure 74). Hydride **12**, formyl **21** and free ligand **13** can be identified accompanied by several high field

shifted resonances in the $^{31}P\{^{1}H\}$ NMR spectrum, indicating at least partial decoordination of the pincer ligand upon protonation for additional unknown byproducts. In agreement, the ^{1}H NMR spectrum shows resonances which lack higher order coupling effects.

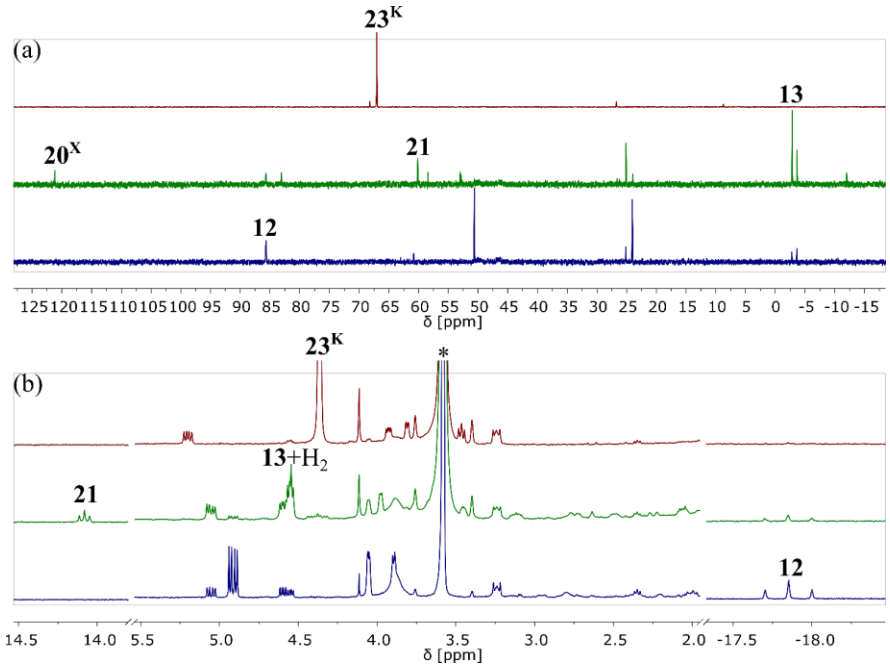

Figure 74: (a) $^{31}P\{^{1}H\}$ and (b) ^{1}H NMR spectra of (top) *in situ* prepared **23^{K}**, (middle) after addition 2 eq phenol and (bottom) after 16 h at RT (*denotes THF-d_8).

Reformation of parent Ni^{II} carbonyl **20^{X}** can be observed in small quantity and storing the reaction mixture at room temperature for 16 hours results in interconversion of several species. Notably, hydride **12** is built up in these processes and amino diphosphine **13** is nearly completely consumed. Optimizing the conditions for converting **23^{K}** to hydride **12** by addition of acid, gives a spectroscopic yield of 41–56% over three repeated experiments using 2.05 eq of [H(NEt$_3$)]BArF (Figure 75).

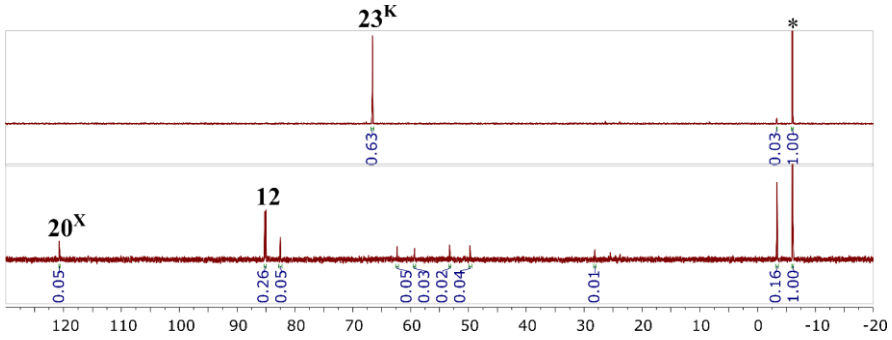

Figure 75: $^{31}P\{^{1}H\}$ NMR spectra of (top) *in situ* prepared **23^{K}** and (bottom) the reaction mixture obtained after addition of 2.05 eq [H(NEt$_3$)]BArF at -36°C and stirring at RT for 16 h (*denotes the internal standard).

Ni^0 carbonyl **23^{M}** can be converted to hydride **12** by addition of a proton source. Protonation of Ni^I carbonyl **22** was investigated to avoid the low potential of the Ni^{II}/Ni^I redox process (E^0 = -2.22 V). As discussed in Chapter 1.4.2, protonation at the Ni^I oxidation state results in formation of a weak methylene bond in four coordinate bromide and acetonitrile ligated nickel ^{tBu}P=N=P complexes.

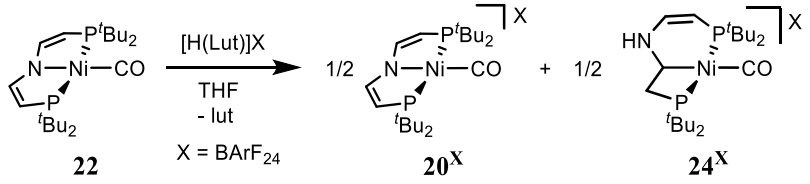

Scheme 43: Disproportionation of Ni^I carbonyl **22** upon protonation.

If **22** is reacted with [H(lut)]BArF, formation of two main species can be observed $^{31}P\{^1H\}$ NMR spectroscopically (Figure 76). The signal at δ = 115.5 ppm is readily assigned to the Ni^{II} carbonyl compound **20^{BArF}**, while the second species can be assigned as [Ni(CO)(κ^3*P,C,P*-^{t}Bu$_2$PCHCHNHCHCH$_2$P^{t}Bu$_2$)]BArF (**24^{BArF}**). Compound **24^{BArF}** is the product of net $1e^-/2H^+$ transfer to **22**. Both protons and the electron are stored in the pincer ligand and under formal metal oxidation a Ni^{II} complex with a twofold protonated and twofold reduced ligand is obtained. Therefore, the present anionic ligand κ^3*P,C,P*-^{t}Bu$_2$PCHCHNHCHCH$_2$P^{t}Bu$_2$)$^-$ can be seen as an isomer of the known amido diphosphine κ^3*P,N,P*-{N(CHCHP*t*Bu$_2$)(CH$_2$CH$_2$P*t*Bu$_2$)}$^-$.[65,69,306] Since initial protonation of **22** is likely, a formal disproportionation *via* PCET takes place, which might be driven by the low C-H bond strength at the Ni^I oxidation state (see Chapter 1.4.2).

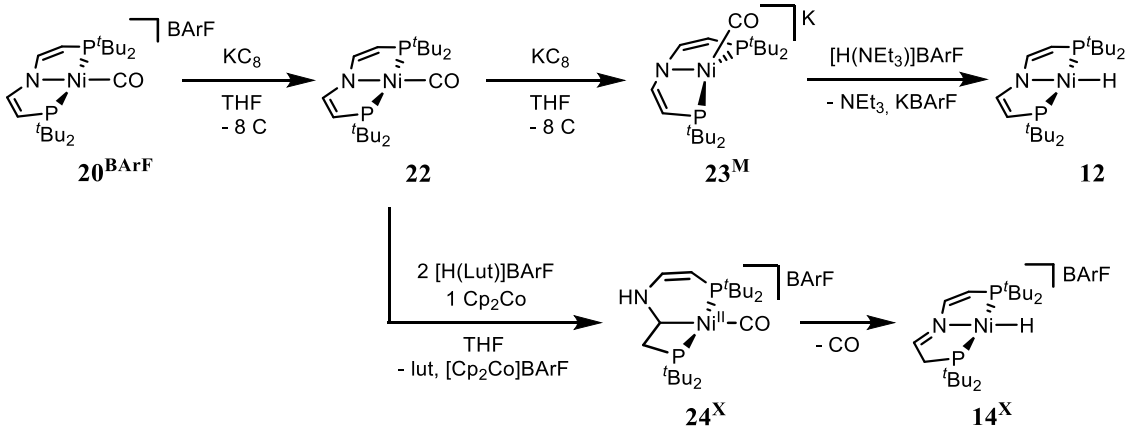

Scheme 44: Conversion of Ni^{II} carbonyl **20^{X}** to Ni^{II} hydrides **12** and **14^{X}** by subsequent reduction and protonation.

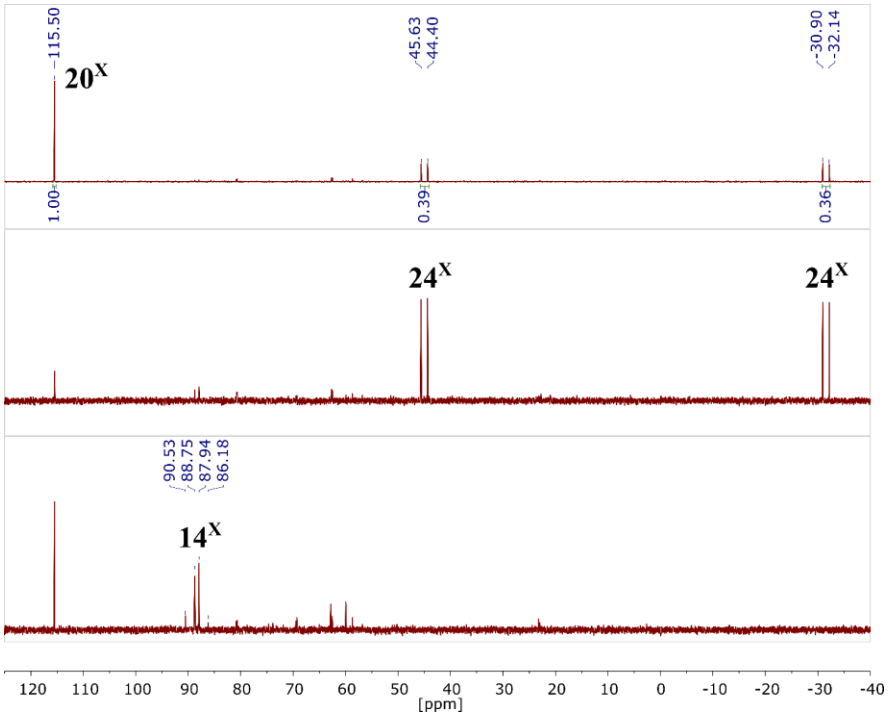

Figure 76: $^{31}P\{^{1}H\}$ NMR spectra of the reaction of **22** with 1 eq [H(lut)]X (top) and the reaction of **22** with 2 eq [H(lut)]X and 1 eq of Cp_2Co after 1 h (middle) and overnight (bottom)(X = BArF).

Accordingly, compound **24^{BArF}** is formed selectively upon reaction of **22** with 2 eq of [H(lut)]BArF and 1 additional equivalent of reductant, converting the half equivalent of formed **20^{BArF}** to **24^{BArF}** as well (Scheme 44). Compound **24^{BArF}** is not stable in solution at room temperature and converts to **14^{BArF}** with high selectivity by formal *β*-hydride shift and CO loss. Signs of formation of complexes containing a $\{(CHCHP\textit{t}Bu_2)(CH_2CH_2P\textit{t}Bu_2)\}^-$ ligand *via* proton shift from the amine to the nickel coordinated carbon atom cannot be detected. Disproportionation of Ni^I carbonyl **22** provides an elegant route for regeneration of hydride **12** by reduction of Ni^{II} carbonyl **20^{X}**. It makes use of the Ni^{II}/Ni^{I} potential for the overall two electron process instead of requiring the low Ni^{I}/Ni^{0} potential.

The limited stability of compound **24^{BArF}** inhibits full characterization. Structural assignment can be performed based on IR and NMR spectroscopy. An *in situ* generated solution of **24^{BArF}** in THF-d_8 shows an absorption at $\tilde{\upsilon}$ = 1886.1 cm^{-1} in IR spectroscopic measurement, confirming the presence of a carbonyl ligand. Comparison with the carbonyl stretching vibrations of the Ni carbonyl series discussed previously shows a strong redshift with respect to Ni^{II} carbonyl **20^{BArF}** ($\tilde{\upsilon}$ = 2062.4 cm^{-1}, ATR-IR), suggesting the presence of a more electron rich metal center in **24^{BArF}** as expected for a strongly donating alkyl ligand in *trans* position.

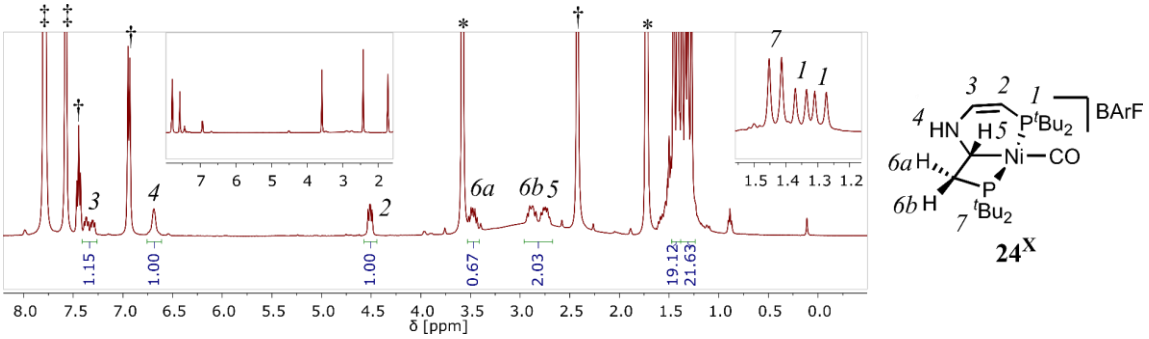

Figure 77: ^{1}H NMR spectra of the reaction of **22** with 2 eq [H(lut)]BArF and 1 eq of Cp_2Co in THF-d_8 (*denotes THF-d_8, †denotes 2,6-lutidine, ‡denotes BArF).

A coupling constant of $^{2}J_{PP}$ = 150.5 Hz in the $^{31}P\{^{1}H\}$ NMR spectrum indicates a *trans* coordination of both chemically inequivalent phosphorus donors in **24^{BArF}**. The different chemical shifts δ of both resonances in the $^{31}P\{^{1}H\}$ NMR spectrum suggest pincer ligand functionalization and the high field shifted δ = -31.52 ppm is interpreted as a four membered chelate.[120] Turning to ^{1}H NMR spectroscopy, twofold proton and reduction of the ^{tBu}P=N=P results in six chemically different hydrogen atoms (Figure 77). Importantly, the presence of a chiral carbon atom results in diastereotopic hydrogen atoms for the CH_2 group showing strong germinal coupling with $^{2}J_{HH}$ = 16.9 Hz. A high field shift is observed for the saturated pincer backbone resonances in ^{1}H NMR spectroscopy and the NH can be identified at δ = 6.68 ppm. Spectral assignment is based on ^{1}H,^{1}H COSY NMR. Detection of *m/z* = 444.2 in the LIFDI-MS experiment further confirms structural assignment of **24^{BArF}**.

2.3.5 Conversion of [Ni(CO)(^{tBu}P=N=P)]X (20^{X}) to [NiH(^{tBu}P=N=P^{H})]X (14^{X}) by Photochemical H_2 Addition

Interested in performing rWGS reactivity, the reactivity of Ni^{II} carbonyl **20^{X}** was examined in the presence of H_2 atmosphere. Up to $p(H_2)$ = 10 atm no conversion is observed. Since metal carbonyl complexes are well known to undergo photodissociation of the carbonyl ligand, **20^{BArF}** was illuminated ($\lambda_{exc.}$ > 305 nm) at $p(H_2)$ = 1 atm which results in clean formation of imine hydride **14^{BArF}** suggesting metal-ligand cooperative substrate activation (Scheme 45, Figure 78).[307]

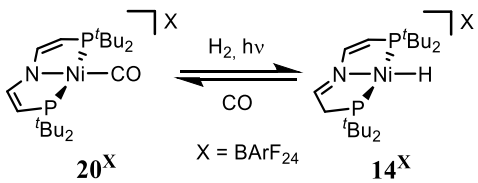

Scheme 45: Conversion of Ni^{II} carbonyl **20^{BArF}** to Ni^{II} hydrides **14^{BArF}** by photolysis under H_2 atmosphere.

This reaction proceeds in diethyl ether and fluorobenzene as solvent. Choosing a weakly coordinating solvent is crucial as the rate drops dramatically when the photolysis is performed in THF. Extrusion of carbon monoxide in the process of H_2 activation is confirmed by TCD-GC headspace analysis (Figure 79).

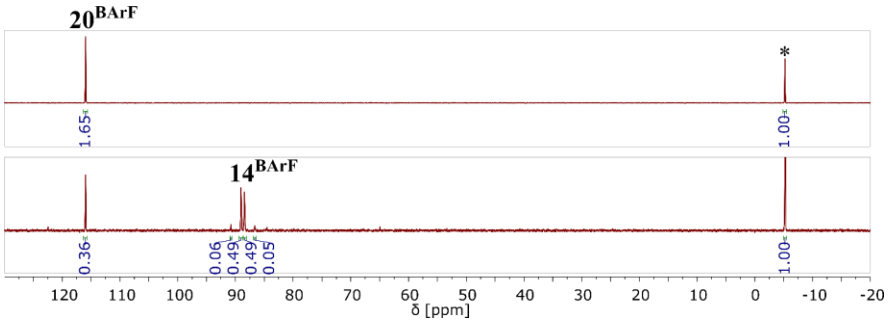

Figure 78: $^{31}P\{^1H\}$ NMR spectra of **20**$^{\mathbf{BArF}}$ in Et_2O at $p(H_2)$ = 1 atm (top) before and (bottom) after photolysis ($\lambda_{exc.}$ > 305 nm) for 4 h (*denotes the internal standard).

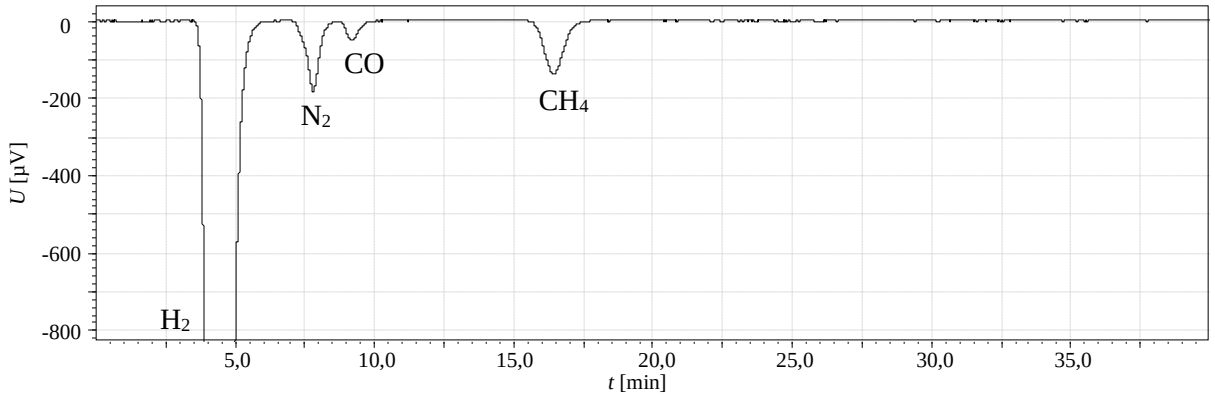

Figure 79: TCD-GC headspace analysis of the reaction mixture obtained by photolysis of **20**$^{\mathbf{BArF}}$ at $p(H_2)$ = 1 atm.

Performing the reaction in a closed vessel results in incomplete conversion of the starting material which indicates the presence of an equilibrium between **20**$^{\mathbf{BArF}}$ and **14**$^{\mathbf{BArF}}$. This is confirmed by production of carbonyl **20**$^{\mathbf{BArF}}$ upon applying carbon monoxide atmosphere to a solution of isolated hydride **14**$^{\mathbf{BArF}}$. Integration against an internal standard shows 78–83% conversion of starting material and formation of **20**$^{\mathbf{BArF}}$ in 67–73% yield over three repeated experiments giving an average selectivity of 87%.

To determine the quantum yield Φ_{337} of photolysis of **20**$^{\mathbf{BArF}}$ under H_2 atmosphere, a solution of **20**$^{\mathbf{BArF}}$ in Et_2O was photolyzed in a UV-vis cuvette at $\lambda_{exc.}$ = 337 nm under H_2 atmosphere ($p(H_2)$ = 1 atm) giving a quantum yield of Φ_{337} = 1.0% (see Chapter 2.12 for detailed description of the experimental procedure). The determined quantum yield has to be regarded as a lower limit, since the absorbance of the starting material and therefore the number of absorbed photons decreases with reaction progress. Photochemical decarbonylation of nickel tetracarbonyl in *n*-hexane solution shows a wavelength dependent quantum yield of 0.22–0.5%, close to Φ_{337}.[308]

2.3.6 Nickel Mediated rWGS Reactivity at Ambient Conditions

With both photochemical CO_2 reduction and H_2 activation in hand, nickel mediated reverse water-gas shift reactivity was investigated by combining the four individual steps discussed before: a) abnormal CO_2 insertion (Chapter 2.3.1); b) dehydration of hydroxycarbonyl **16** (Chapter 2.3.2); c) photochemical H_2 activation (Chapter 2.3.5) and d) deprotonation of imine hydride **14^{X}** to hydride **12** (Chapter 1.4.3). Formation of hydroxycarbonyl **16** is observed in several solvents like THF, Et_2O and benzene upon photolysis of hydride **12** under CO_2 atmosphere. In contrast, H_2 activation on carbonyl **20^{BArF}** is limited to weakly coordinating solvents. Furthermore, sufficient polarity is required to dissolve ionic **20^{BArF}**, excluding THF and benzene as solvent for an overall synthetic cycle. While the equilibrium between **16** and **20^{BArF}** was examined and discussed in THF previously (Chapter 2.3.2), moving to less polar Et_2O increases the impact of ion-pairing and therefore shifts the equilibrium. This can be visualized by comparing the results of photolysis of **12** under CO_2 atmosphere in the presence of by [H(TMG)]BArF (pK_a(H(TMG))^{THF} = 15.3) in THF and Et_2O (Figure 80). The products obtained in both reaction mixtures are mostly identical, however in THF hydroxycarbonyl **16** is not efficiently converted to carbonyl **20^{BArF}**. Unpolar Et_2O in contrast favors formation of **20^{BArF}** due to the higher driving force for ion-pair formation (eq. (33)).

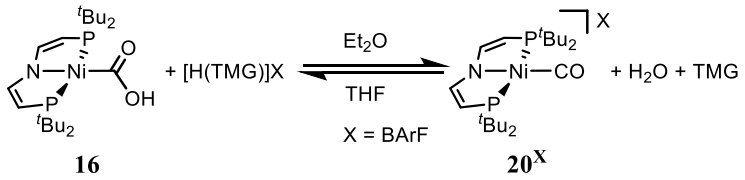

16 **20^{X}**

Scheme 46: Solvent dependent equilibrium between hydroxycarbonyl **16** and carbonyl **20^{BArF}**.

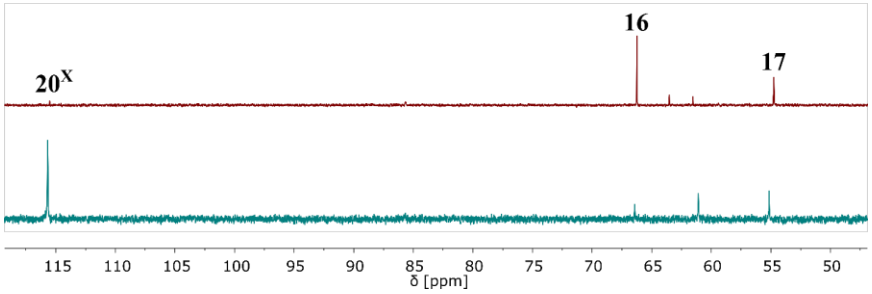

Figure 80: $^{31}P\{^{1}H\}$ NMR spectra of a solution of **12** in the presence of 1 eq [H(TMG)]BArF at $p(CO_2)$ = 1 atm after photolysis ($\lambda_{exc.}$ > 305 nm) (top) in THF and (bottom) in Et_2O.

Similarly, the equilibrium between hydride **12** and imine hydride **14^{X}** is affected by the solvent. [H(NEt$_3$)]BArF (pK_a(H(NEt$_3$)$^+$)^{THF} = 12.5) efficiently protonates **12** in Et_2O, while **12** is the main species in THF (Figure 81).[300] This directly affects the selectivity of formation of **20^{BArF}**, which is produced less efficiently if the equilibrium between **12** and added acid is shifted towards **14^{BArF}**. Consequently, photolysis of isolated imine hydride **14^{BArF}** under CO_2 atmosphere, does not produce carbonyl **20^{BArF}**. Therefore, aside

from the upper pK_a limit for formation of carbonyl **20**^{BArF} from hydride **12**, defined by dehydration of hydroxycarbonyl **16**, there is a lower pK_a limit defined by pK_α(**14**^{BArF})^{THF}. As discussed, the acid base equilibrium present in unpolar solution is influenced by the dissociation of ion-pairs. As result, the applicable acid/base of lowest/highest pK_a varies with solvent. However, changing the polarity of solvent is not beneficial or disadvantageous for the overall conversion of **12** to **20**^{BArF} in general. While working in more polar media *enables* the use of stronger acids without protonating **12** to **14**^{BArF}, dehydration of **16** to **20**^{BArF} *requires* a stronger acid under these conditions.

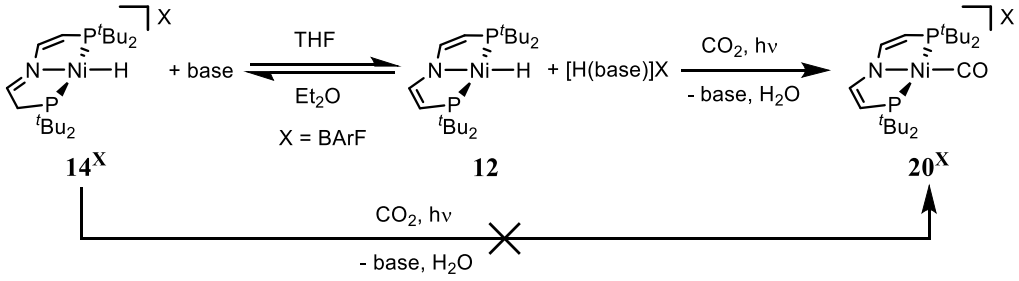

Scheme 47: Solvent dependent equilibrium between imine hydride **14**^{BArF} and hydride **12** and subsequent photochemical CO_2 activation.

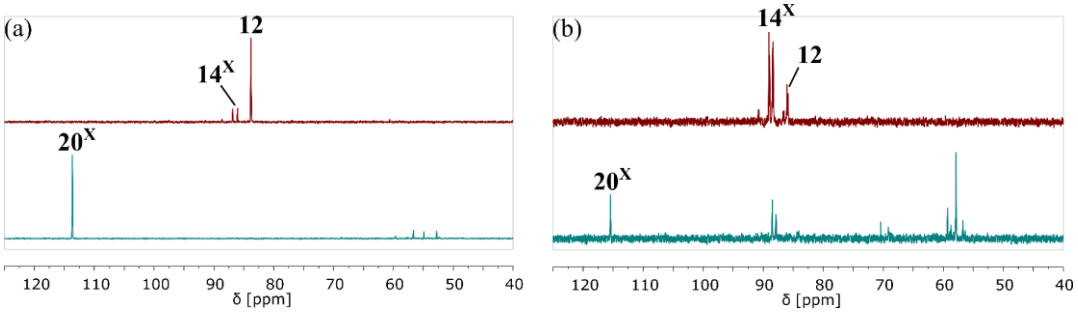

Figure 81: $^{31}P\{^1H\}$ NMR spectra of a solution of **12** in (a) THF and (b) Et_2O in the presence of 1 eq [H(NEt$_3$)]BArF at $p(CO_2)$ = 1 atm (top) before and (bottom) after photolysis ($\lambda_{exc.}$ > 305 nm).

Starting from imine hydride **14**^{BArF}, efficient conversion to carbonyl **20**^{BArF} in the presence of 1 eq of base in diethyl ether as solvent could not be achieved. In case of relatively strong bases like TMG, BTMG (2-*tert*-butyl-1,1,3,3-tetramethylguanidine) and NTMG (1,8-bis(tetramethylguanidino)naphthalene), hydrocarbonate **17** is the main product. The presence of residual hydroxycarbonyl **16** likely indicates slow conversion of **16** to **20**^{BArF} by protonation and therefore efficient photochemical conversion of **16** to **17** as side reaction. The most efficient conversion of **14**^{BArF} to **20**^{BArF} in Et_2O can be obtained using TMG, resulting in 14–18% yield over three repeated experiments. Changing to comparably weak bases like di-*iso*-propylethylamine or TMP (2,2,6,6-tetramethylpiperidine) hinders the built up of **17**, but results in large quantities of unconverted imine hydride **14**^{BArF}.

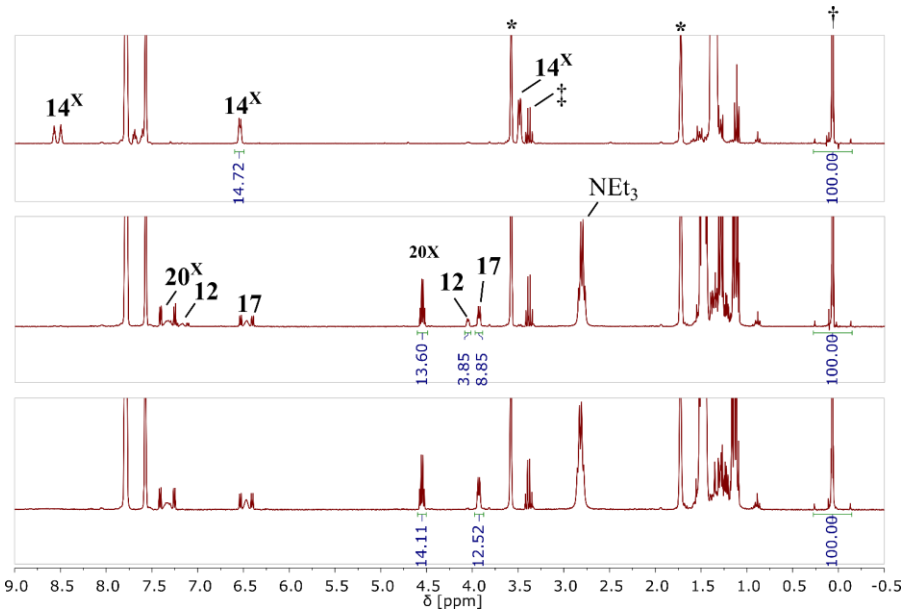

Figure 82: (top) ^{1}H NMR spectra of a solution of **14^{BArF}** in THF-d_8. (middle) After addition of 1 eq NEt_3 and photolysis ($\lambda_{exc.}$ > 305 nm) at $p(CO_2)$ = 1 atm for 4 h and (bottom) 6 h.

Moving to THF with triethylamine as base gives **20^{BArF}** in 47–50% yield over three repeated experiments with hydrocarbonate **17** as the only side product. While the stoichiometry indicates reductive disproportion of CO_2, NMR spectroscopic monitoring of the reaction progress shows initial formation of carbonyl **20^{BArF}** and increasing quantities of hydrocarbonate upon prolonged reaction time (Figure 80).

Formation of hydrocarbonate **17** can result from photochemical conversion of hydroxycarbonyl **16** in the presence of CO_2 (Chapter 2.3.1). Further, thermal formation of hydrocarbonate **17** from carbonyl **20^{X}** under basic conditions in the presence of CO_2 has been shown in Chapter 2.3.2 and is likely to be accelerated under photochemical conditions given the photochemical reacitivty of **20^{BArF}** (Chapter 2.3.5). While conversion of **14^{BArF}** to **20^{X}** in the presence of triethylamine results in the formation of water and no net consumption of triethylamine, $pK_a(H(NEt_3)^+)^{MeCN}$ = 18.8[103] and $pK_a(H_2O)^{MeCN} \approx 40$[309] suggest highly endergonic deprotonation of H_2O by NEt_3. However, *Lewis* acid induced increase of acidity is well known and *Heiden* and coworkers provide a computational study which correlates the hydricity of *Lewis* acid hydrides with the influence of the *Lewis* acid on pK_a upon coordination of a proton donor.[310] Since water represents one of the acids examined in this report and the hydricity of formate ($\Delta G_{HT}(HCO_2^-)^{MeCN}$ = 44 kcal·mol^{-1}) is reported in the literature, $pK_a(H_2O{\cdot}CO_2)^{MeCN}$ = 13.7±1.3 can be estimated for the acidity of water upon coordination to carbon dioxide as *Lewis* acid.[230,231] Conversion to THF according to *Morris* gives $pK_\alpha(H_2O{\cdot}CO_2)^{THF}$ = 14.1–16.0, and $pK_\alpha(H(NEt_3)^+)^{THF}$ = 12.5 suggests endothermic, but feasible triethylammonium bicarbonate formation, considering additional driving force due to ion-pair formation upon conversion of a neutral acid and base to an ionic acid base pair.[108] In agreement with this thermodynamic consideration, the methylene resonance of triethylamine in the ^{1}H NMR spectrum shown in

Figure 81 is shifted significantly from the expected shift ($\delta(NEt_3)$ = 2.44) towards triethylammonium ($\delta(H(NEt_3))$ = 3.25) with δ_{obs} = 2.81. Accordingly, formation of bicarbonate **17** can be attributed to photochemical decarbonylation of **20^{BArF}** in the presence of bicarbonate, which is produced from water and NEt_3 in the presence of CO_2 (Scheme 48). An influence of nickel hydroxycarbonyl **16** and hydrocarbonate **17** on the observed chemical shift of triethylamine is unlikely given the low acidity of hydroxycarbonyl **16** (pK_α(**16**)^{THF} = 24.4) and the similar acidity of formic acid ($pK_a(HCO_2H)^{aq}$ = 3.75) and carbonic acid ($pK_a(HCO_3H)^{aq}$ = 3.5).[311]

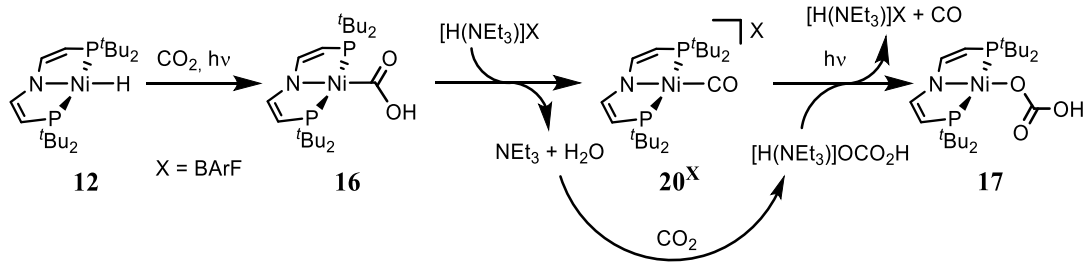

Scheme 48: Formation of hydrocarbonate **17** upon photolysis of hydride **12** in the presence of acid and CO_2.

Based on detailed examination of the individual equilibria involving **12**/**14^{BArF}** and **16**/**20^{BArF}** an acid with $pK_\alpha(HB^+)^{THF}$ = 12.5–15.3 is suitable for nickel pincer mediated rWGS reactivity. The experimental conditions however have shown to further narrow this range. Working at the upper limit ([H(TMG)]BArF) results in hydrocarbonate **17** formation by follow-up photochemistry of hydroxycarbonyl **16** due to inefficient conversion of hydroxycarbonyl **16** to carbonyl **20^{BArF}**. The lower limit ([H(NEt_3)]BArF) produces bicarbonate *via* reaction of the byproduct water with the conjugate base in the presence of CO_2. Moving to less polar Et_2O as solvent favors conversion of **16** to **20^{BArF}**. Integration against an internal standard shows, that formation of **20^{BArF}** does proceed in yields below 20% starting from imine hydride **14^{BArF}** and TMG as base. The highest yield in production of **20^{BArF}** can be achieved by using NEt_3 as base in THF, giving **20^{BArF}** in reproducible yields of approximately 50%.

While interconversion between hydride **12** and imine hydride **14^{BArF}** can be easily achieved by addition of acid/base, the photochemical H_2 activation at **20^{BArF}** in the presence of base is hampered significantly. Several bases like di-*iso*-propylethylamine, triethylamine, piperidine, 1,8-bis(dimethylamino)naphthalene, DABCO and *Verkade*'s base result in a decrease in selectivity and drop of the rate, up to no conversion at all. Since H_2 activation likely proceeds at a low coordinate Ni^{II} metal as the product of photodissociation of the carbonyl ligand, this retardation of the reaction can be explained by coordination of the base and subsequent ligand exchange with the liberated carbon monoxide which remains in the headspace of the closed reaction vessel, therefore reforming the starting compound.

Accordingly, photolysis of **20**$^{\mathbf{BArF}}$ in the presence of stoichiometric amounts of guanidine base TMG gives base adduct [Ni(k^1,*N*-TMG)($^{t\mathrm{Bu}}$P=N=P)]BArF (**25**$^{\mathbf{BArF}}$).[21] While this reaction is observed without irradiation, exposing the mixture to light greatly accelerates the reaction. If the released carbon monoxide is not removed, the back reaction to the starting material **20**$^{\mathbf{BArF}}$ is observed after photolysis (Figure 81).

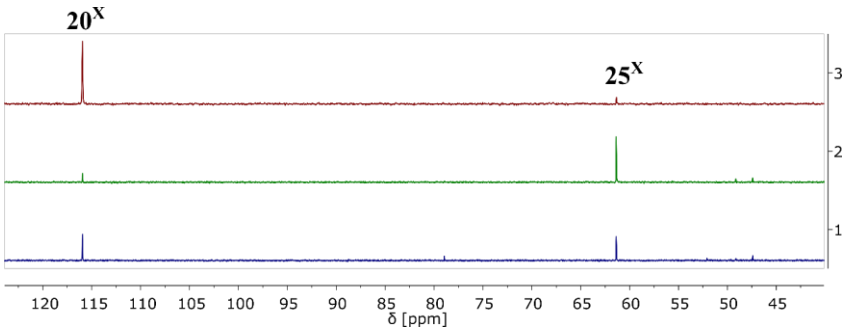

Figure 83: $^{31}P\{^1H\}$ NMR spectra of **20**$^{\mathbf{X}}$ (X = BArF) in Et_2O in the presence of 1 eq TMG (top) after stirring at RT for 1 day, (middle) after photolysis ($\lambda_{exc.}$ > 305 nm) for 15 min and (bottom) after again standing at RT for 1 day.

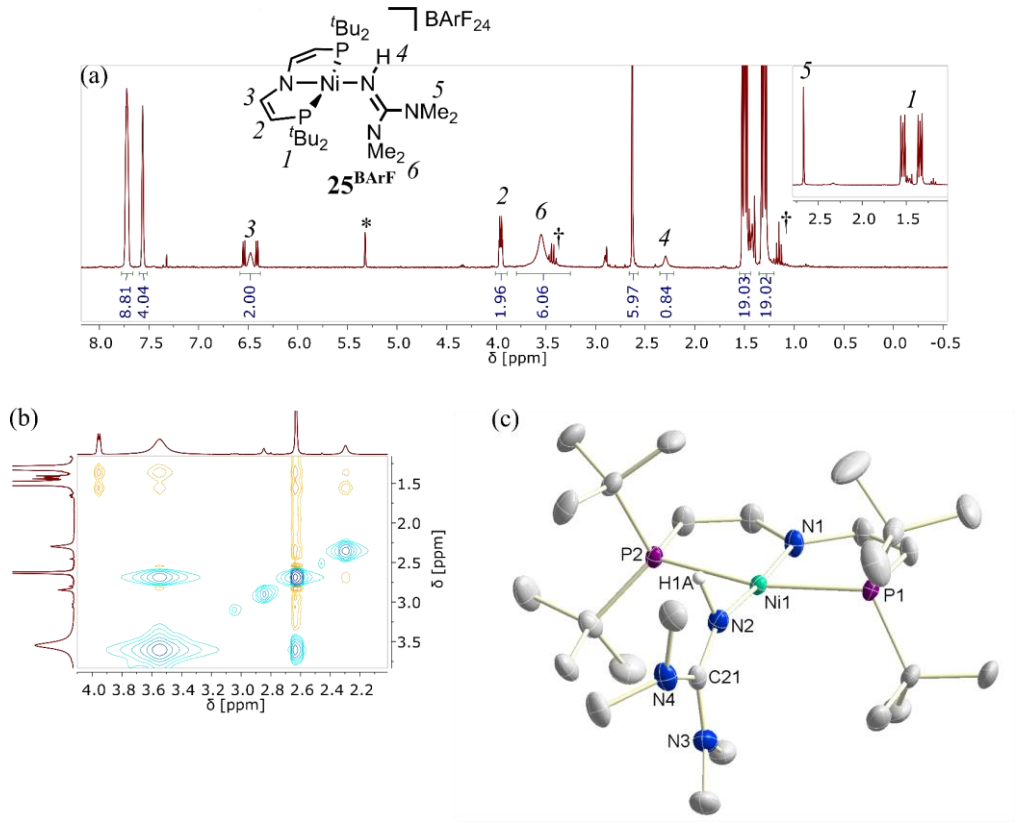

Figure 84: (a) ^1H and (b) $^1H,^1H$ NOESY NMR spectra of **25**$^{\mathbf{BArF}}$ in CD_2Cl_2 (*denotes CD_2Cl_2, †denotes Et_2O). (c) Solid state structure of **25**$^{\mathbf{BArF}}$ determined by X-ray diffraction. Thermal ellipsoids are drawn at the 50% probability level. Selected hydrogen atoms and anions are omitted for clarity.

[21] Synthesis and Characterization of **25**$^{\mathbf{BArF}}$ was performed by Florian Wätjen.

Irradiating a solution of **20**$^{\mathbf{BArF}}$ in Et_2O in an evacuated reaction vessel results in clean formation of **25**$^{\mathbf{ArF}}$ and allows for characterization. ^{1}H NMR spectroscopy of **25**$^{\mathbf{BArF}}$ reveals coordination of the metal center *via* the imine donor. Hindered rotation around the Ni-N bond results in C_S symmetry which gives rise to two ^{t}Bu and NMe_2 resonances (Figure 82). The ^{1}H NMR spectrum of **25**$^{\mathbf{BArF}}$ shows a sharp singlet at δ = 2.63 ppm for one of the NMe_2 resonances while the other NMe_2 group resonates as a broad signal shifted to lower field (δ = 3.55 ppm). Chemical exchange of both ^{t}Bu and NMe_2 signals is observable in the ^{1}H,^{1}H NOESY, indicating slow but present rotation of the TMG ligand. A cross peak to the NH at δ = 2.30 ppm due to spatial proximity further allows for assignment of the NMe_2 groups with regard to their orientation. Coordination of the TMG ligand in **25**$^{\mathbf{BArF}}$ is further corroborated by X-ray crystallographic analysis of single crystalline materiel (Figure 82c).

Similar reactivity as with TMG is observed in the case of DBU and DBN (1,5-diazabicyclo[4.3.0]non-5-en) as base. Conversion of **20**$^{\mathbf{X}}$ in the presence of DBU and DBN suggests formation of related base adducts [NiL($^{t\mathrm{Bu}}$P=N=P)]BArF (L = DBU, DBN) although no characterization or isolation of these compounds was performed. While at atmospheric pressure, no reactivity with hydrogen can be observed in case of all three bases, increasing $p(H_2)$ to 10 atm results in slow thermal conversion of the base adduct to hydride **12** in case of DBU as base (Figure 85).

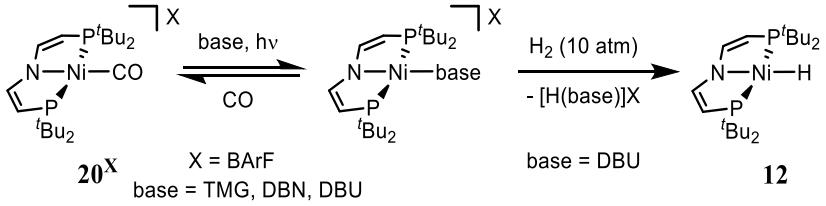

Scheme 49: Formation of base adducts from **20**$^{\mathbf{BArF}}$ and reactivity with H_2.

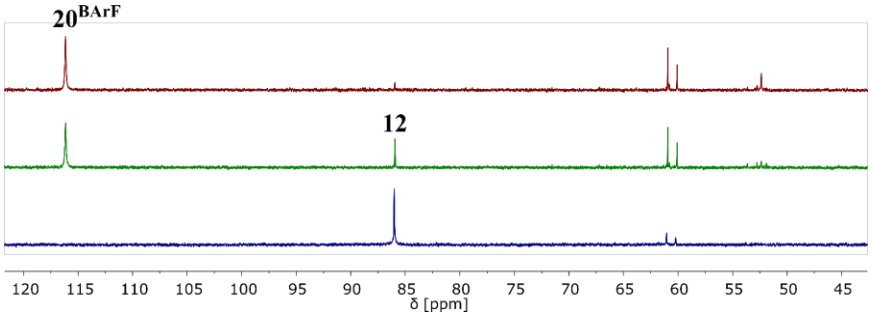

Figure 85: ^{31}P{^{1}H} NMR spectra of **20**$^{\mathbf{BArF}}$ in Et_2O at $p(H_2)$ = 10 atm in the presence of 1 eq DBU after stirring at RT for (top) 30 min, (middle) 1 h and (bottom) 1 day.

Summing up, based on photochemical abnormal CO_2 insertion and H_2 activation, a two-step synthetic cycle for nickel mediated rWGS reactivity can be performed. Conversion of carbonyl **20**$^{\mathbf{BArF}}$ to imine hydride **14**$^{\mathbf{BArF}}$ by photoinduced H_2 activation proceeds in high selectivity, can however not be performed in the

presence of base or coordinating solvents. Formation of TMG adduct **25**$^{\mathbf{BArF}}$ indicates formation of a low coordinate [Ni($^{t\mathrm{Bu}}$P=N=P)]BArF intermediate by dissociation of carbon monoxide. CO_2 reduction from **14**$^{\mathbf{BArF}}$ to **20**$^{\mathbf{BArF}}$ in the presence of base can be performed in the same solvent using TMG with yields of 14–18%. Moving to THF and NEt_3 as base gives higher yields of 47–50%. Both photochemical steps work at ambient pressures of $p(CO_2/H_2)$ = 1 atm and excitation wavelength of $\lambda_{exc.}$ > 305 nm, therefore giving overall mild conditions for rWGS reactivity. Computational analysis of the thermochemistry of the overall reaction shows, that CO_2 reduction is thermodynamically uphill, whereas H_2 activation is almost thermoneutral (Scheme 50).[22]

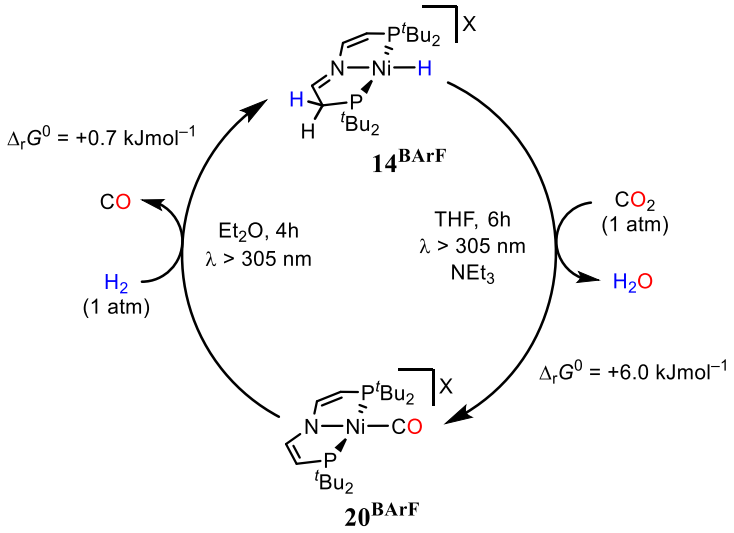

Scheme 50: Two-step synthetic cycle for Nickel pincer mediated rWGS reactivity and thermochemistry evaluated by DFT.

Detailed investigation of the conditions required for rWGS reactivity shows that CO_2 activation in general is hampered by bicarbonate production which can proceed *via* two pathways. Working at the lower pK_a limit, defined by the equilibrium of hydride **12** and imine hydride **14**$^{\mathbf{BArF}}$, results in efficient dehydration of **16** to **20**$^{\mathbf{BArF}}$. Deprotonation of the liberated water with base in the presence of CO_2 results in bicarbonate formation and accordingly decarbonylation of **20**$^{\mathbf{BArF}}$ to hydrocarbonate **17**. Working at the upper pK_a limit, defined by the equilibrium of hydroxycarbonyl **16** and carbonyl **20**$^{\mathbf{BArF}}$ results in slow dehydration of **16** and therefore competing photochemical conversion of **16** to hydrocarbonate **17**.

Based on the observed photochemical decarbonylation of hydroxycarbonyl **16**, a second approach to CO selective CO_2 reduction is possible (Scheme 51). While the performed synthetic cycle for the rWGS reaction proceeds *via* initial dehydration of the hydroxycarbonyl and subsequent decarbonylation, a reverse order of both reactions is in principle possible. Compound **16** shows photochemical decarbonylation giving

[22] Computational analysis was performed by Dr. Markus Finger.

hydrocarbonate **17** in the presence of CO_2 and hydroxide **18** under argon atmopshere. Following this reaction, H_2 activation on bicarbonate **17** or hydroxide **18** also closes a synthetic cycle for conversion of CO_2 to CO. However, up to $p(H_2)$ = 10 atm no conversion of **17** is observed and similarly, **16** does not convert to hydride **12** upon photolysis at $p(H_2)$ = 1 atm.

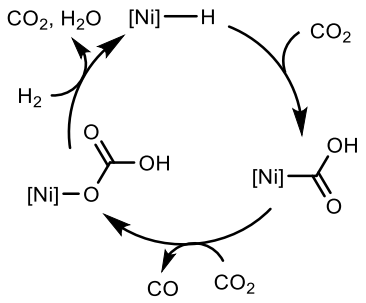

Scheme 51: Alternate synthetic cycle for the rWGS reaction *via* initial decarbonylation of the hydroxycarbonyl.

Catalytic hydrogenation of HCO_3^- to formate in strongly basic media is reported by *Himeda*.[312] As for hydrogenation of CO_2 to formate, the deprotonation of formic acid likely adds driving force to the reaction (Chapter 2.1.2). Formate synthesis from CO_2/HCO_3^- mixtures at low pH is reported by *Laurenczy*.[313] Bicarbonate could be identified as the actual substrate, suggesting that bicarbonate hydrogenation can be performed in acidic conditions as well. While no stabilization of the product is present under acidic conditions, destabilization of the starting material conceptually makes sense given the low stability of carbonic acid compared to bicarbonate. Accordingly, this effect might be transferable to formation of other hydrogenation products including CO. While bicarbonate **17** does not activate H_2 in the presence of base, the reactivity under acidic conditions was not investigated.

2.4 Mechanistic Investigation of Abnormal CO_2 Insertion

2.4.1 Evaluation of a Kinetic Model Based on NMR Spectroscopic Kinetic Measurements

Since the reaction of hydride **12** with CO_2 to hydroxycarbonyl **16** represents the first report of a so-called abnormal CO_2 insertion into a transition metal hydride bond, investigation of the mechanism of this transformation was performed.[156] Photochemical isomerization of formate **15** to **16** is ruled out based on photolysis experiments on *in situ* formed **15**. Heating a solution of **16** in THF shows formation of hydroxide **18** in small quantity, rendering thermal decarbonylation feasible. No formation of Ni^{II} hydride **12** can be observed, indicating that neither formation of **16** from **12** nor the reverse reaction, decarboxylation of **16**, proceeds thermally.

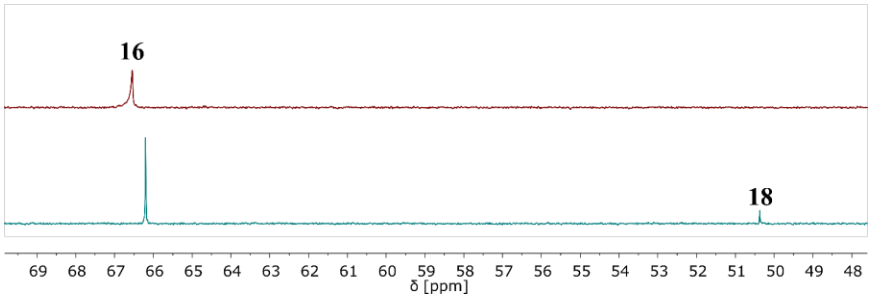

Figure 86: $^{31}P\{^{1}H\}$ NMR spectra of a THF-d_8 solution of **16** (top) before and (bottom) after heating to 70°C for 1 day.

Density functional theory was utilized to probe the thermodynamic data of CO_2 insertion into the nickel hydride bond of **12**, giving either formate **15** by normal or hydroxycarbonyl **16** by abnormal CO_2 insertion (Figure 87).[23] Solvent effects have been accounted for by the conductor-like screening model (COSMO, $\varepsilon = 7.25$ for THF) using the outlying charge corrected values. An initial benchmark study on truncated model compounds having methyl instead of *tert*-butyl substituents on the phosphorus atoms shows that the TPPS functional gives the least deviation from coupled cluster (DLPNO-CCSD(T)) single point ground state energy calculations.

Formation of formate **15** from hydride **12** and CO_2 is computed to be almost thermoneutral with $\Delta_R G^0(298\ K) = +1.7\ kcal{\cdot}mol^{-1}$. Since the experiment does show successive conversion of **12** to **15**, this value can be seen as the error of the DFT experiment (Chapter 2.3.1). The obtained barrier of $\Delta G^{\ddagger}_{eff}(298\ K) = +25.1\ kcal{\cdot}mol^{-1}$ is in good agreement with the slow reaction observed, since it is at the upper energetic limit of thermodynamically feasible barriers at room temperature according to the *Eyring-Polanyi* equation. The transition state structure TS_{15} shown in Figure 87 is typical for an innersphere CO_2

[23] Computational analysis was performed by Dr. Markus Finger.

insertion mechanism with an η^2-CO_2 coordination mode, showing an already present nickel carbon interaction.[245] The hydride ligand is best described as bridging μ-H, since it is positioned above the nickel carbon bond.

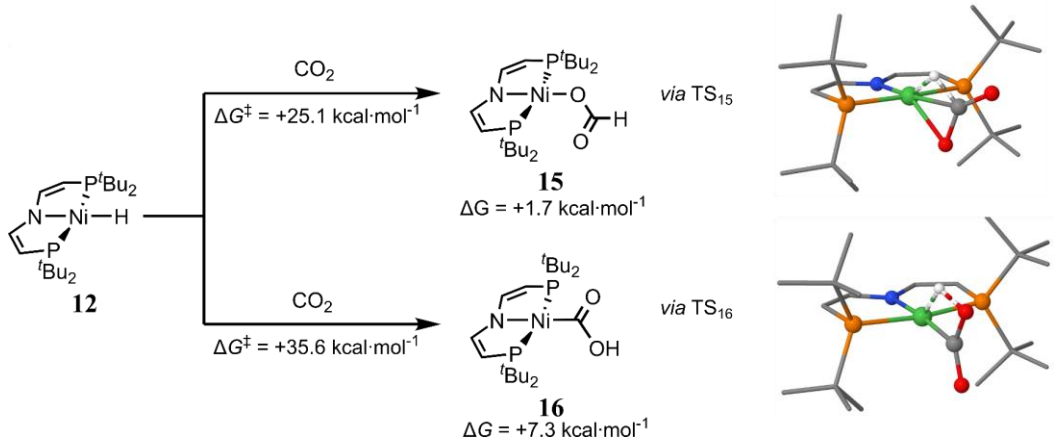

Figure 87: Thermodynamic data on thermal CO_2 insertion from hydride **12** to formate **15** *via* normal or to hydroxycarbonyl **16** *via* abnormal CO_2 insertion with the optimized transition state structure TS_{15} and TS_{16} (D3(BJ)-TPSS/def2-TZVP// D3(BJ)-RI-J-PBE/def2-SVP(Cosmo:THF)).

Thermal formation of hydroxycarbonyl **16** proceeds *via* an even higher transition state TS_{16} which is best described as a nickel carboxylate since no nickel oxygen interaction is present and the CO_2 fragment is clearly bend. While the CO_2 moiety resembles the structure of product **16**, the former hydride is located apical showing interaction to both oxygen and nickel. The high barrier of $\Delta G^{\ddagger}_{eff}$(298 K) = +35.6 kcal·mol^{-1} prevents formation of **16** on a thermal pathway at ambient conditions and the overall uphill reaction with $\Delta_R G^0$(298 K) = +7.3 kcal·mol^{-1} shows that **16** is only accessible *via* photochemical conditions.

To further explore the conversion of hydride **12** under photochemical conditions, the reaction progress was monitored NMR spectroscopically. To provide reproducibility of the obtained results, the experiments for kinetic investigation are performed under specific conditions (*e.g.* position of the reaction vessel with respect to the light source). This might result in differences in time scale of the performed reaction with respect to previously discussed experiments. The negligible underlying thermal reactivity of **12** with CO_2 allows for exact kinetic measurement since the progress of the reaction can essentially be stopped upon interrupting photolysis (Figure 88). The arrayed data show the reaction progress monitored by $^1H\{^{31}P\}$ NMR spectroscopy over two hours with the first spectrum representing measurement of the reaction mixture after 10 minutes of photolysis ($\lambda_{exc.}$ > 305 nm). Initially, clean conversion of **12** to **16** can be monitored, with increasing concentration of **17** at prolonged reaction times. While the OH resonances of hydroxycarbonyl **16** and hydrocarbonate **17** give rise to a single broad signal, unresolved fine structure is visible, suggesting conditions close to resonance of both signals due to chemical exchange. In agreement, the signal's chemical shift δ varies with the ratio of both compounds.

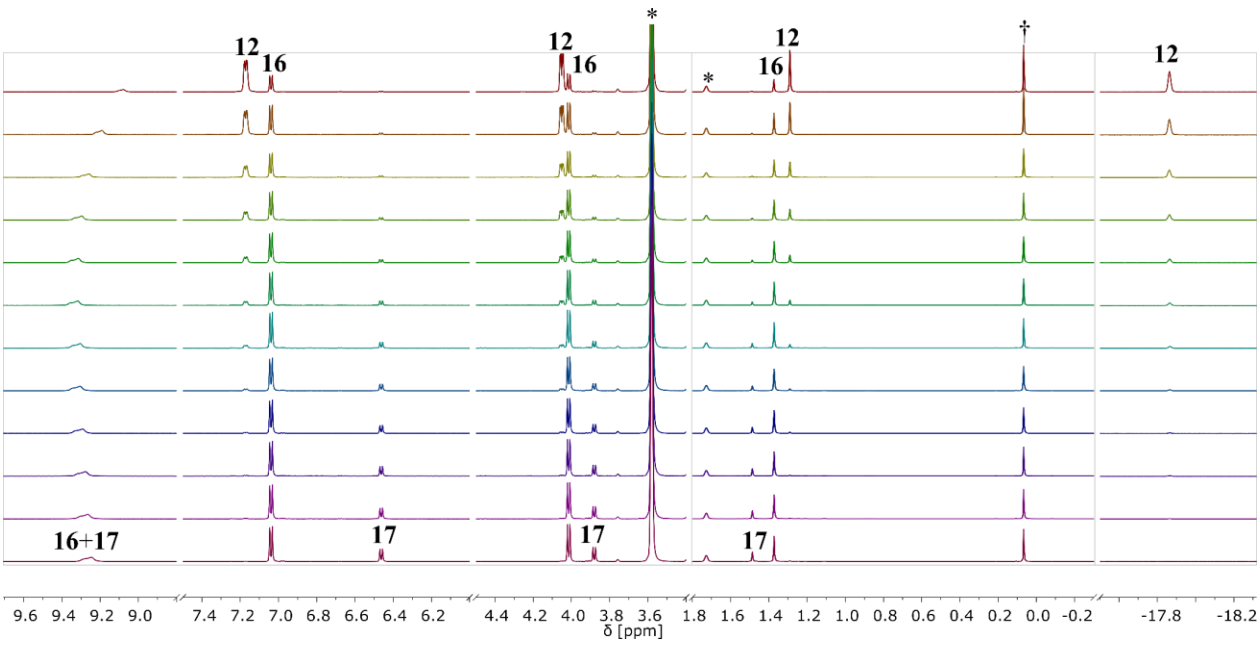

Figure 88: $^{1}H\{^{31}P\}$ NMR spectra of photolysis ($\lambda_{exc.}$ > 305 nm) of a solution of **12** in THF-d_8 at $p(CO_2)$ = 1 atm showing the reaction progress between (top) t = 10 min and (bottom) t = 120 min (*denotes THF-d_8; †denotes TMS_2O).

By integration against the internal standard TMS_2O, the concentrations of all involved compounds can be determined resulting in the plot shown in Figure 89a. Importantly, the concentration of **16** undergoes a maximum at t = 80 min, suggesting a follow-up reaction of photoproduct **16** to hydrocarbonate **17** and limiting the yield of **16** to 76% under these conditions. The obtained experimental data can be fitted as reactions which are first-order in starting material **12** and **16**, respectively. Assuming constant CO_2 concentration ($c(CO_2)$ = 0.34 M at 298.15 K and $p(CO_2)$ = 1 atm[314], c_0(**12**) = 9.7 mM) in solution and a constant photon flux, a satisfactory fit of the experimental data can be obtained over three half lifes $T_{1/2}$ with the first-order rate constants $k_{obs1} = (2.9\pm0.08)\cdot10^{-2}$ min^{-1} and $k_{obs2} = (4.4\pm0.1)\cdot10^{-3}$ min^{-1} (Figure 89a).[24] The plot of ln(c(**12**)) over t for 3×$T_{1/2}$ further shows decent agreement with a first-order reaction in **12** for the conversion of the starting material (Figure 89b).

[24] COPASI software is used for the simulation.[133]

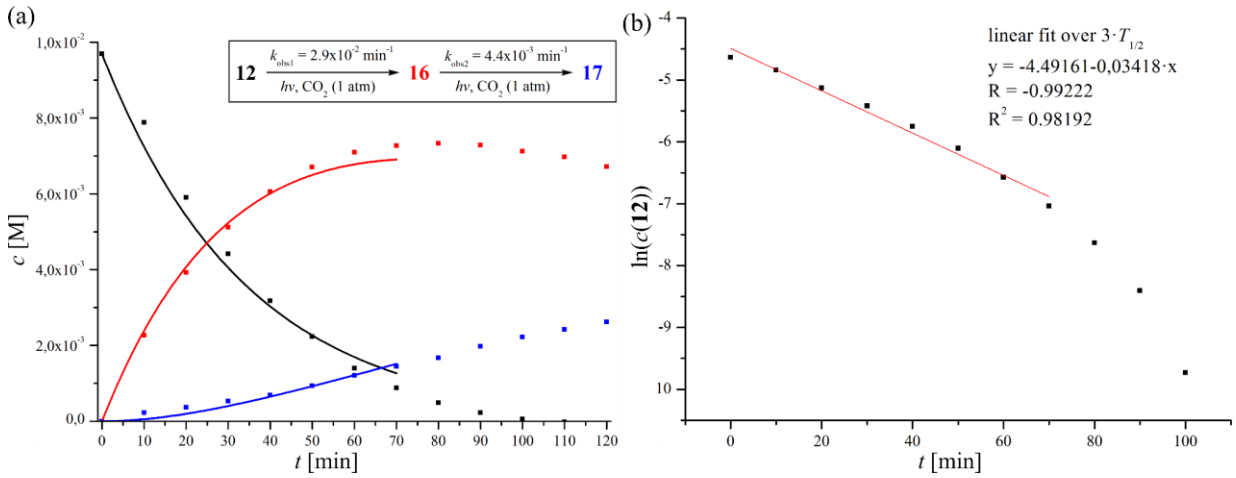

Figure 89: (a) Plot of *c vs. t* for the photolysis ($\lambda_{exc.}$ > 305 nm) of **12** in THF-d_8 determined by integration of $^1H\{^{31}P\}$ NMR spectra and fit of the experimental data by pseudo first-order model reactions. (b) Plot ln(*c*(**12**)) *vs t* and linear fit over 3·$T_{1/2}$.

The conversion of hydroxycarbonyl **16** to hydrocarbonate **17** was further explored by photolysis of a solution of isolated **16** under identical conditions as utilized in photolysis of **12** ($\lambda_{exc.}$ > 305 nm, $p(CO_2)$ = 1 atm). Hydroxycarbonyl **16** shows strong absorption above λ = 305 nm with an absorption maximum at λ = 320 ($\varepsilon = 1.9 \cdot 10^4$ M^{-1}cm^{-1}) (Figure 57c). Clean conversion of **16** to **17** is observed upon irradiation at $p(CO_2)$ = 1 atm, however minor reactivity is also monitored without irradiation by a light source (Figure 90a). While thermal decarbonylation of **16** to hydroxide **18** is observed upon prolonged heating to 70°C (Chapter 2.3.1), reversible decarbonylation might also be present at room temperature. This might serve as explanation for the underlying thermal conversion of **16** to **17**, considering the large excess of CO_2 under the given experimental conditions compared to liberated carbon monoxide by decarbonylation of **16**. As discussed in Chapter 2.3.6, formation of carbonyl **20^X** and carboxylate **19^M** from hydroxycarbonyl **16** by dehydration is feasible. In the presence of CO_2, formation of bicarbonate would result, which is shown to substitute the carbonyl ligand in **20^X** (Chapter 2.3.6). Photochemical acceleration of the reaction could be rationalized based on the photochemical CO loss of **20^X** (Chapter 2.3.5).

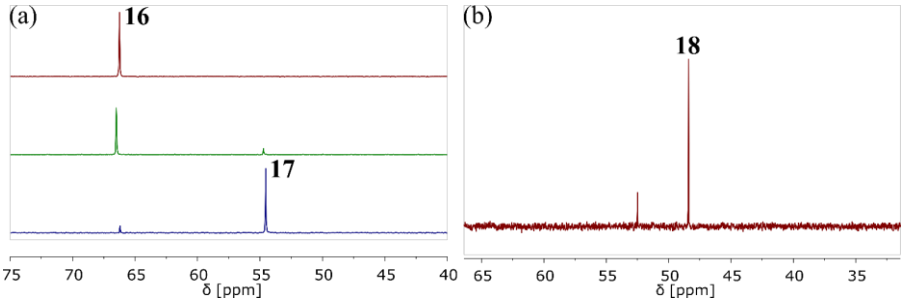

Figure 90: $^{31}P\{^1H\}$ NMR spectra of photolysis ($\lambda_{exc.}$ > 305 nm) of a solution of **16** in THF-d_8 at (a) $p(CO_2)$ = 1 atm (top: initial reaction mixture; middle: 18 h under CO_2 atmosphere; bottom: 18 h photolysis ($\lambda_{exc.}$ > 305 nm) under CO_2 atmosphere) and (b) p(Ar) = 1 atm.

Hydroxide **18** can be identified as initial product for both the thermal and photochemical decarbonylation of **16** by photolysis under argon atmosphere (Figure 90b). The absence of **18** in the photolysis of **12** under CO_2 atmosphere is therefore explained by the rapid CO_2 insertion to give hydrocarbonate **17** under the experimental conditions.

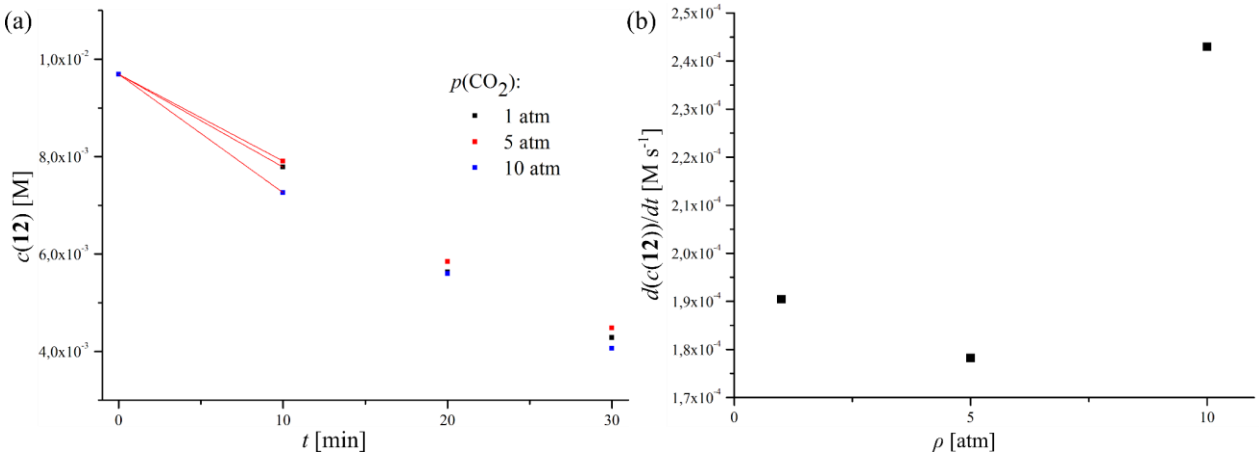

Figure 91: (a) Plot of c(**12**) *vs.* t for the photolysis ($\lambda_{exc.}$ > 305 nm) of **12** at different applied CO_2 pressures. (b) Plot of initial rates $d(c(\mathbf{12}))/dt$ *vs.* $p(CO_2)$.

To probe the order of the reaction of **12** to **16** in CO_2 pressure and photon flux, initial rate measurement at different CO_2 pressures and light source output currents were performed. The photon flux correlates linearly to the output current of the light source, as determined by actinometry (Chapter 2.3.6). Measurements at 1, 5 and 10 atm CO_2 pressure were performed using *Wilmad* medium wall precision pressure/vacuum valve NMR tubes. At the first measurement (t = 10 min) a minor difference between the three applied pressures can be observed (Figure 91). With increasing reaction progress, the experiments give nearly identical results. Comparison of the initial rates for consumption of starting material **12** over 10 minutes further shows no linear correlation between $p(CO_2)$ and the initial rate (Figure 91b). Accordingly, the reaction of **12** to **16** is derived to be zero-order in CO_2 under the investigated conditions.

Upon changing the output current of the Xe arc light source, an influence on the rate of the reaction is observed. As shown in Figure 92, lowering the output current results in a drop of the observed rate for consumption of the starting material. In contrast to the observation made upon variation of $p(CO_2)$, the difference between c(**12**) at t = 10 min for the individual experiments continues to grow with increasing reaction time. A plot of the initial rates derived at t = 10 min over the output current of the light source indicates a first-order reaction in photons (Figure 92b). While the data obtained with I = 3–6 A show minor variation from linearity, the results at I = 7 A and I = 7.5 A result in a significant error of the linear fit.

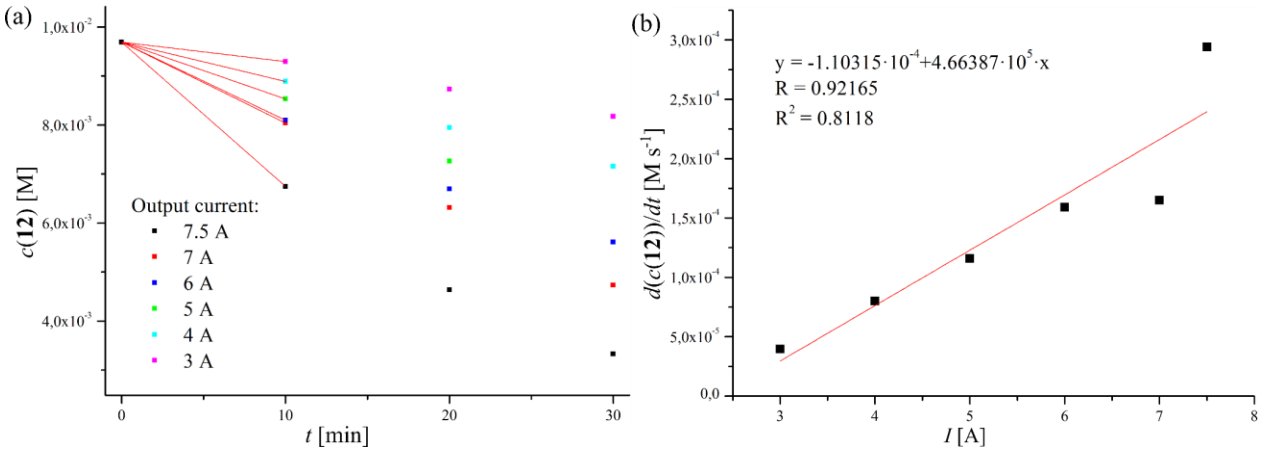

Figure 92: (a) Plot of c(**12**) *vs*. t for the photolysis ($\lambda_{exc.}$ > 305 nm) of **12** under CO_2 atmosphere ($p(CO_2)$ = 1 atm) at different output currents. (b) Plot of initial rates $d(c(\mathbf{12}))/dt$ *vs*. output current I.

The order of the photochemical reaction from **12** to **16** in starting material, CO_2 and photons give important information about the reaction's mechanism and allow for the formulation of a simplified mechanistic picture (Scheme 52). The reaction is first-order in starting material c(**12**) and photon flux while it is zero-order in $c(CO_2)$. Since the thermal reactivity of **12** with CO_2 is examined and does not suggest any reactivity aside from insertion to formate **15**, it is reasonable to assume the photochemical step to be located prior to CO_2 activation on the reaction coordinate. Since photoexcitation proceeds on the femtosecond timescale and is therefore faster than diffusion controlled processes by several orders of magnitude, the photoexcitation certainly is not the rate-determining step (RDS).[152] However, photoexcitation and relaxation to the ground state can be formulated as an equilibrium in the sense that excitation and relaxation represent conversion pathways between ground state **12** and excited state **12*** with, even though unknown, assignable rate constants.

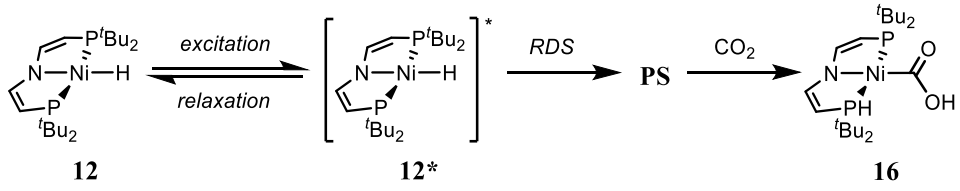

Scheme 52: Mechanistic picture for the conversion of **12** to **16**.

The RDS is assigned to the formation of a persistent species **PS** which is necessary to fulfill the requirement of zero-order in $c(CO_2)$. The classification *persistent* in this context means a lifetime in the nanosecond timescale, allowing bimolecular reactivity which is necessary for CO_2 activation.[315,316] Since **PS** forms from the excited state **12*** which is in equilibrium with starting material **12**, the overall reaction is first-order in c(**12**) and photon flux. Following the RDS, CO_2 activation takes place at **PS** and results in product formation. As pointed out, this mechanistic picture is a simplification. Vibrational cooling (VC) and internal

conversion (IC) are likely to occur after excitation and before formation of **PS**, however these processes occur on very fast timescales (ca. 10^{-12} s).[152] Further, they rather represent photophysical than -chemical processes since they do not change connectivity of atoms, even though they are crucial in influencing bond strength and therefore reactivity. Similarly, conversion of **PS** to **16** might involve several steps and is at this point reduced to a single transformation. Whether **PS** represents a long-lived excited state on the triplet hypersurface or a photoproduct cannot be differentiated based on the data available at this point, but will be addresses in the following. In photochemical proton reduction by [IrH(bpy)Cp*]PF_6, population of the long-lived excited state by intersystem crossing (ISC) actually represent the rate-determining step.[275]

To determine the quantum yield Φ for photochemical CO_2 activation by **12** in THF, a procedure similar to the one discussed previously for H_2 activation on $\mathbf{20}^{\mathbf{BArF}}$ was conducted. According to eq. (56)–(59), photolysis of a solution of **12** in a cuvette at $p(CO_2)$ = 1 atm resulting in a quantum yield of Φ_{410} = 9.0% (see Chapter 2.12 for detailed description of the experimental procedure). While this value for Φ shows that consumption of **12** does not proceed *via* a radical chain mechanism which would result in $\Phi > 1$, the overall photochemical process is rather efficient. Again, the determined quantum yield has to be regarded as a lower limit, since the absorbance of the starting material and therefore the number of absorbed photons decreases with reaction progress. While *Ishitani* reports a quantum yield of Φ_{480} = 13% for photocatalytic CO_2 reduction by $[IrH(tpy)(ppy)]^+$, a quantum yield for a stoichiometric experiment is not reported.[212] *Miller*'s report on photochemical proton reduction by $[IrH(bpy)Cp^*]^+$ states a quantum yield close to 1, which however strongly varies with the concentration of the photocatalyst due to the bimolecular mechanism.[275]

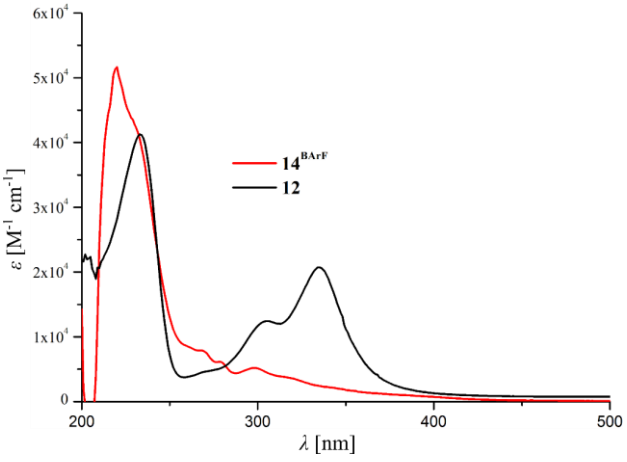

Figure 93: UV-vis spectra of **12** and $\mathbf{14}^{\mathbf{BArF}}$ in THF.

Similarly, the quantum yield Φ_{410} for the conversion of $\mathbf{14}^{\mathbf{BArF}}$ to $\mathbf{20}^{\mathbf{BArF}}$ in the presence of 1 eq NEt_3 at $p(CO_2)$ = 1 atm in THF is determined as Φ_{410} = 3.6%. Therefore, the photochemical conversion of $\mathbf{14}^{\mathbf{BArF}}$ to $\mathbf{20}^{\mathbf{BArF}}$ is approximately half as efficient as the conversion of **12** to **16**. Assuming that $\mathbf{14}^{\mathbf{BArF}}$ does not convert directly to the product but *via* the identical photochemical reaction, this result can be understood by

comparison of the absorption spectra of compounds **12** and **14^{BArF}** (Figure 93). Both **12** (ε_{410}(**12**) = $1.1 \cdot 10^3$ M^{-1} cm^{-1}) and **14^{BArF}** (ε_{410}(**14^{BArF}**) = $5.5 \cdot 10^2$ M^{-1} cm^{-1}) show absorption at λ = 410 nm, however only **12** undergoes productive photochemistry. Accordingly, the absorption of **14^{BArF}** contributed to the number of absorbed photons N_{Abs} but does not result in formation of **20^{BArF}**, resulting in a decrease of the overall quantum yield.

2.4.2 Photochemical Excitation, Transient Spectroscopy and Luminescence Spectroscopy of [NiH(^{tBu}P=N=P)] (12)

Based on the simplified mechanistic picture presented in Chapter 2.4.1, the excited state evolution of hydride **12** was investigated to extend the mechanistic understanding of the transformation of **12** to **16**. As shown in Figure 94, **12** shows strong absorption in the near UV spectrum, indicating ligand centered or charge transfer transitions. Interested in the nature of the electronic excitation responsible for the observed photochemical behavior of **12**, TD-DFT analysis of **12** was performed.[25] Figure 92a presents the overlap of the experimental and computational electronic spectra of **12**, showing a good agreement of the fine structure with a blue shift of approximately 0.4 eV which is commonly observed in TD-DFT.[317]

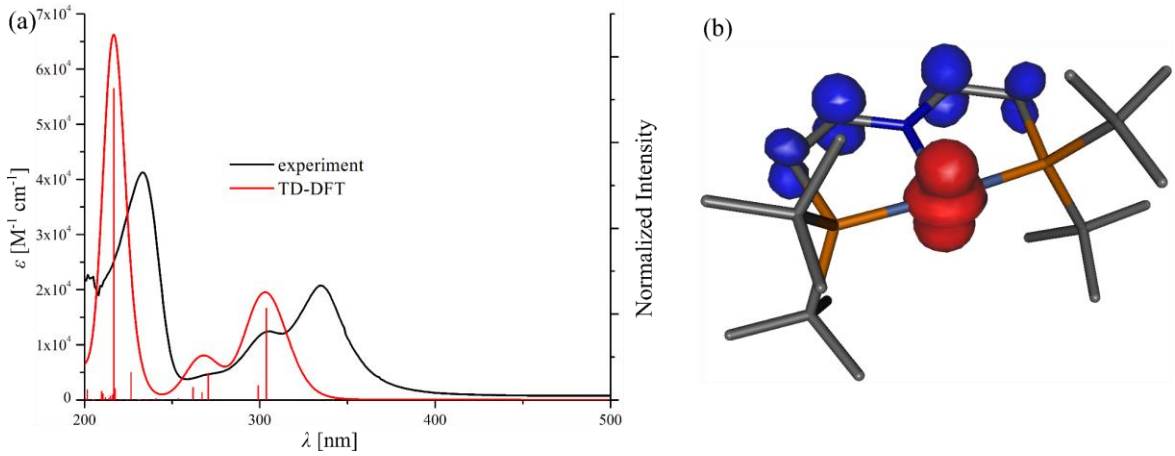

Figure 94: (a) Experimental UV-vis spectrum of **12** in THF and electronic transitions predicted by TD-DFT (ZORA-b3LYP/def2-TZVPP (Cosmo)). (b) Difference electron density of the transition at λ = 304 nm (blue color denotes increase and red color denotes a decrease in electron density; the hydride ligand is not shown).

The strongest absorption in the region responsible for the photochemical reactivity of **12** is present at λ = 334 nm in THF solvent. Theory predicts this transition to be a MLCT type transition which can be described as excitation from the metal centered d_{z^2} to a pincer ligand centered π^* orbital (Figure 94b). Formal dehydrogenation of the pincer ligand therefore is crucial for by introducing low lying ligand centered unpopulated orbitals.

[25] Computational analysis was performed by Dr. Markus Finger.

While optical excitation proceeds within $t = 10^{-15}$ s, the subsequent excited state evolution takes place on a picosecond timescale and can therefore be monitored using transient UV-pump spectroscopy which has a time resolution of 10^{-13} s. UV-pump-UV-vis- and IR-probe spectroscopy can be performed using a translation stage to adjust the time delay between the pump and probe pulse and is utilized to investigate **12** and isotopologue **12-D** in THF solution under argon atmosphere.[26]

Excitation of a THF solution of **12** at $\lambda_{exc.}$ = 385 nm results in immediate broad absorption in the whole visible spectrum (Figure 95a). Within 1 ps, the transient undergoes a decrease of the absorption above λ = 500 nm. The transient absorption further gets lower in intensity on the picosecond timescale and a persistent absorption centered at λ = 450 nm is obtained. The time trace of the spectral behavior at λ = 550 nm and λ = 480 nm is used to extract the time constants τ by a global biexponential fit giving τ_1 = 0.9±0.5 ps, τ_2 = 13±1 ps and τ_3 >> 1 ns. While the first time constant τ_1 is attributed to fast internal conversion and vibrational cooling from the initial populated *Frank-Condon*-state, the second time constant τ_2 is consistent with internal conversion and vibrational cooling into the electronic ground state of **12**. Time constant τ_3 describes the conversion of a persistent species which exceed the timescale of the experiment (1 ns).

Two possibilities arise for the assignment of the persistent absorption which is visible in the TR-UV-vis spectrum: staying on the singlet hypersurface, a lifetime in the nanosecond timescale of a metal complex most likely means formation of a photoproduct **PP** since fluorescence and thermal relaxation processes in most cases rule out long-lived excited state of the same multiplicity as the ground state.[316] Assuming intersystem crossing (ISC), population of a triplet state is possible as well, resulting in slow radiative (phosphorescence) and non-radiative (ISC) relaxation processes. While efficient ISC is rarely observed in 3d metal complexes due to a lack of spin-orbit coupling, *Scholes* and *Doyle* have recently shown that a series of [NiX(*o*-tolyl)(dtbbpy)] (X = Cl, Br, I, dtbbpy = 4,4'-di-*tert*-butyl-2,2'-bipyridyl) complexes undergoes formation of long-lived ^{3}MLCT states after ISC from ^{1}MLCT and ^{1}LLCT states on the picosecond timescale.[318] As an alternative to spin orbit coupling, close energetic proximity of excited singlet and triplet states giving rise to strong multiconfigurational interactions is discusses as the origin of the unusual fast ISC process.

[26] Transient spectroscopy was performed by Dr. Jennifer Ahrens from the group of Prof. Dirk Schwarzer, Max Planck Institute for biophysical chemistry.

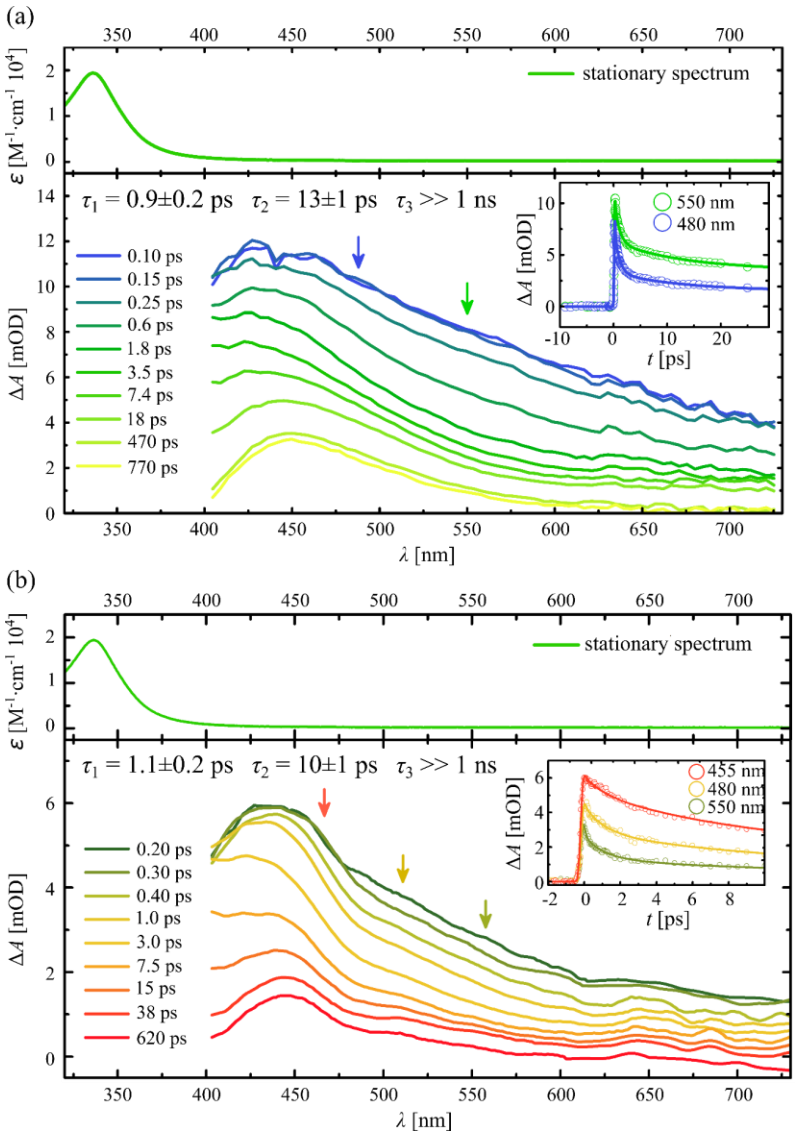

Figure 95: Transient UV-vis spectra generated by $\lambda_{exc.}$ = 385 nm excitation of a 6 mM solution of (a) **12** and (b) **12-D** in THF for selected pump-probe delays. The stationary UV-vis spectrum of **12** in THF solution is shown on top, while the time traces with global triexponential fits are shown as inlets.

Transient UV-vis-probe spectroscopy of isotopologues **12-D** gives similar results as **12** (Figure 95b). The time constants τ show minor variation with τ_1 = 1.1±0.2 ps, τ_2 = 10±1 ps and τ_3 >> 1 ns. The determined time constants allow for the calculation of rates with $\tau = 1/k$ and therefore kinetic isotope effects (KIEs) giving rise to KIE_{t1} = 0.8 and KIE_{t2} = 1.2 for the two processes, respectively (see Chapter 2.4.3). These values are best interpreted as negligible given the error of the experiment. In general, care has to be taken upon interpretation of the kinetic isotope effect determined from transient spectroscopy: Photochemical excitation proceeds vertically, as stated by the *Franck-Condon* principle, therefore resulting in population of vibrational excited states, resulting in a lower difference in activation energy between both isotopologues which accordingly results in a lower KIE, experimentally.[319] Additionally, the determined quantum yield

of Φ_{410} = 9% for conversion of **12** to **16** suggests that repopulation of the vibrational and electronic ground state after photoexcitation might contribute more strongly to the determined lifetime τ than the actual formation of the persistent species **PS**.

To obtain structural information on the species observed in the transient UV-vis spectrum, transient IR spectra of **12** and **12-D** were recorded. The spectral region containing the Ni-H stretch can be accessed using THF solvent. To observe the C-C double bond stretch and Ni-D stretch resonating at lower energy, measurement in THF-d_8 is required. The combination of these two solvents allows for the measurement in the region of $\tilde{\upsilon}$ =1250–3500 cm^{-1} in which no additional transient resonances can be observed aside from the signals shown in Figure 96.

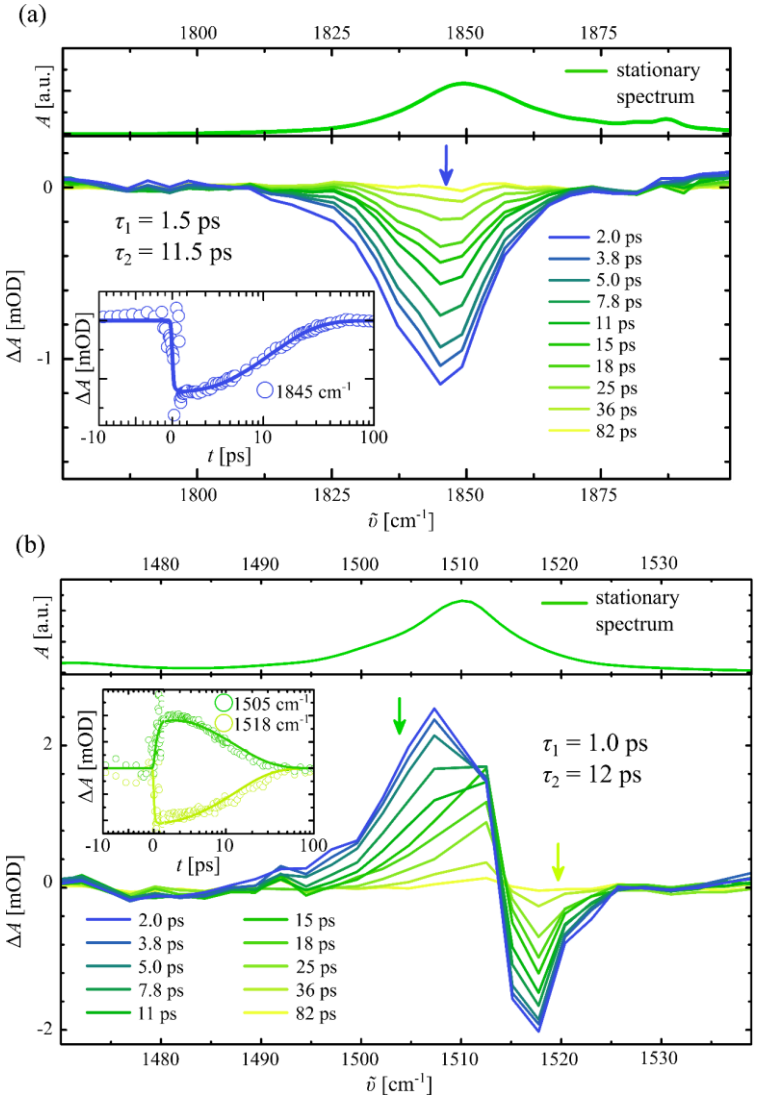

Figure 96: Transient IR spectra generated by $\lambda_{exc.}$ = 400 nm excitation of (a) a 11 mM solution of **12** in THF and (b) a 3 mM solution of **12** in THF-d_8 for selected pump-probe delays. The stationary IR spectrum of **12** in THF/ THF-d_8 solution are shown on top, while the time traces with biexponential fits are shown as inlets.

Starting with the Ni-H stretch shown in Figure 96a, an immediate bleach of the ground state vibration at $\tilde{\upsilon}$ = 1850 cm^{-1} is observed. The spectral evolution shows gradual relaxation to the ground state, which results in complete repopulation after ca. 80 ps. The absence of any positive signals in the region between 1775 cm^{-1} and 1900 cm^{-1} shows that photochemical excitation has a strong influence in the Ni-H stretching vibration. The repopulation of the ground state indicates that the persistent species monitored in the TR-UV-vis spectrum shows either the exact same IR signature in the Ni-H stretch region as parent **12** or, most likely, cannot be observed due to lower spectral resolution and a change in excitation wavelength from $\lambda_{exc.}$ = 385 nm in the TR-UV-vis (TR: time resolved) to $\lambda_{exc.}$ = 400 nm in the TR-IR. The biexponential fit of the time trace at the signal peak gives time constants which are in good agreement with the TR-UV-vis measurement. Monitoring the C-C double bond stretch also shows an immediate bleach at $\tilde{\upsilon}$ = 1518 cm^{-1} which repopulates within ca. 80 ps confirming the absence of the persistent species in TR-IR (Figure 96b). However, a positive red shifted signal can be observed, indicating population of π^* orbitals in the excited states, which is in agreement with a d_{z^2}-π^*-MLCT predicted by theory. Time traces at $\tilde{\upsilon}$ = 1518 cm^{-1} and $\tilde{\upsilon}$ = 1505 cm^{-1} show similar spectral evolution, giving biexponentially fitted time constants τ_1 = 1.0 ps and τ_2 = 12 ps, and globally fitted time constants τ_1 = 1.3±0.2 ps and τ_2 = 12±0.5 ps. While the Ni-H and C-C bond bleach show no underlying peak structure, the positive resonance at $\tilde{\upsilon}$ = 1507 cm^{-1} undergoes dynamic behavior which results in a shift of the maximum to $\tilde{\upsilon}$ = 1513 cm^{-1} after 7.8 ps. This can be interpreted as two overlapping resonances which decay with different time constants.

Similar to the bleach of the Ni-H stretch in TR-IR of **12**, transient spectra of deuterated **12-D** show a bleach of the Ni-D fermi doublet at $\tilde{\upsilon}$ = 1328 cm^{-1} and $\tilde{\upsilon}$ = 1340 cm^{-1} (Figure 97a, see Chapter 1.4.3 for detailed description of the IR spectrum of **12-D**). Repopulation with τ_1 = 10±2 ps fitted globally over both resonances is in good agreement with the value extracted from the Ni-H vibration (the initial very fast process is not considered in the global fit). Comparing the region at $\tilde{\upsilon}$ = 1470–1540 cm^{-1} however shows a difference between both isotopologues (Figure 97b). While the shape and temporal evolution of the bleach is mostly identical, it is shifted to $\tilde{\upsilon}$ = 1512 cm^{-1} for **12-D**. Since both spectra are measured in 3 mM solution, the magnitude of the bleach is nearly identical with approximately 2 mOD. Upon comparing the positive signals of **12** and **12-D** a huge difference in the intensity can be observed with **12*** showing approximately threefold signal strength. Importantly, two maxima at $\tilde{\upsilon}$ = 1505 cm^{-1} and $\tilde{\upsilon}$ = 1507 cm^{-1} are observed in the excited state **12-D***. In contrast to **12** an overall increase in intensity of the positive signal is observed until t = 4.8 ps. Over this time, the maximum shifts from $\tilde{\upsilon}$ = 1505 cm^{-1} to $\tilde{\upsilon}$ = 1507 cm^{-1}, therefore resembling the behavior observed for **12**. Additionally, measurement at short pump-probe delay (t < 1 ps) reveals vibrationally hot C-C stretching vibrations for **12-D***.

The difference in intensity between the resonance monitored for **12** and **12-D** is best interpreted as an overlap of the C-C double bond and Ni-H stretching vibration in the transient spectrum. The transient Ni-H stretch is therefore visible with $\tilde{\upsilon}$ = 1507 cm^{-1} in the initial spectral evolution of **12**, whereas **12-D** shows only the transient C-C double bond. Importantly, the huge difference in $\tilde{\upsilon}$(Ni-H) for the electronic ground state and the transient spectrum indicates population of an electronically excited state rather than a vibrationally excited molecule in the electronic ground state. The timescale of conversion of this electronically excited state τ_2 = 12±0.5 ps suggests population of the S_1 state. While transition metal hydride complexes have been examined by transient infrared spectroscopy, no excited state hydride stretching vibrations are reported in the literature.[247]

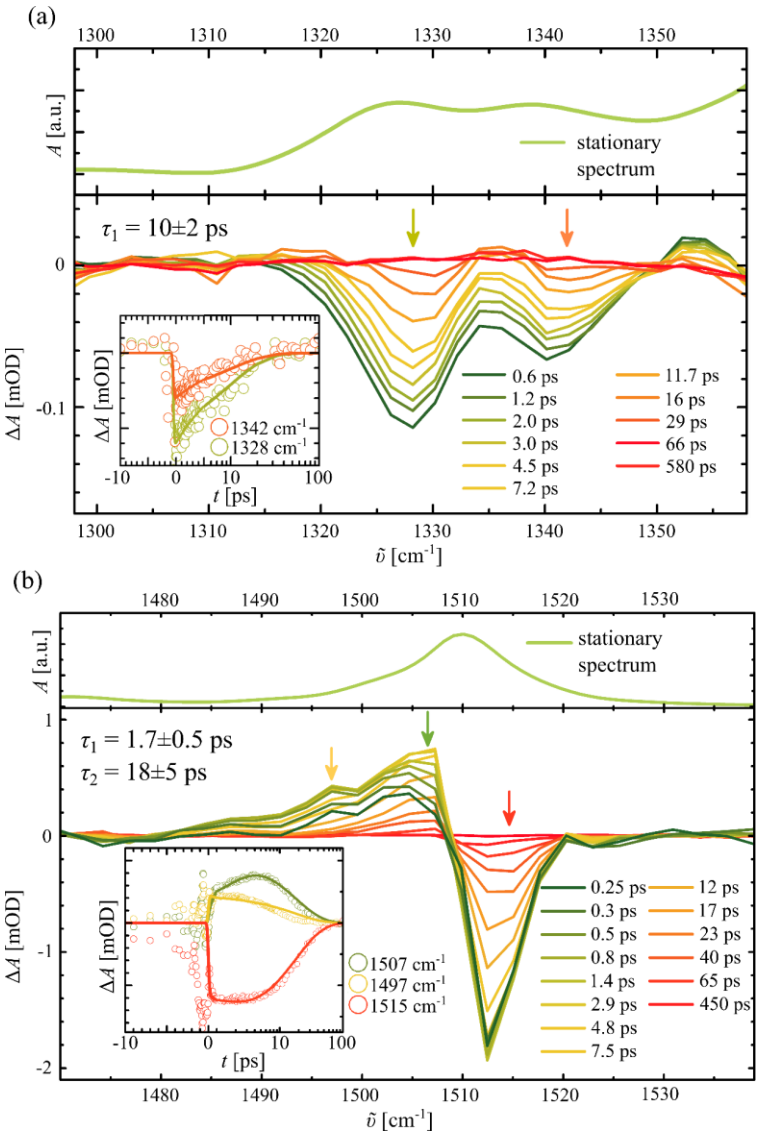

Figure 97: Transient IR spectra generated by $\lambda_{exc.}$ = 400 nm excitation of (a) a 11 mM solution of **12-D** in THF-d_8 and (b) a 3 mM solution of **12-D** in THF-d_8 for selected pump-probe delays. The stationary IR spectrum of **12-D** in THF-d_8 solution are shown on top, while the time traces with biexponential fits are shown as inlets.

UV-pump-UV-vis-pump spectroscopy reveals the formation of a persistent species **PS** with a life time allowing for bimolecular reactivity. Since this species is not observed in the UV-pump-IR-probe experiment, it is not possible to state if this species is produced from S_1 or higher electronically excited states S_n. However, TR-IR spectroscopy gives structural information on the excited state species populated after photoexcitation of **12**. Initially, weakening of the pincer C-C double bond is observed which is in agreement with population of π^* orbitals in the *Franck-Condon* state as predicted by theory. Internal conversion (IC) results in population of the S_1 state which shows severe lowering of the Ni-H bond based on a red shift of the Ni-H stretching vibration by $\Delta\tilde{\upsilon} = 343\ cm^{-1}$ compared to the ground state. Such a strong influence on the Ni-H bond order is in agreement with population of $\sigma^*_{Ni\text{-}H}$ orbitals, and therefore population of a metal centered excited state with occupation of $d_{x^2\text{-}y^2}$ (Figure 98). Summing up, the excited state evolution of **12*** results in population of state similar to the product obtained by excitation of a *d-d* transition. However, this state is obtained by a MLCT transition which shows a much greater extinction coefficient than symmetry forbidden metal centered transitions.

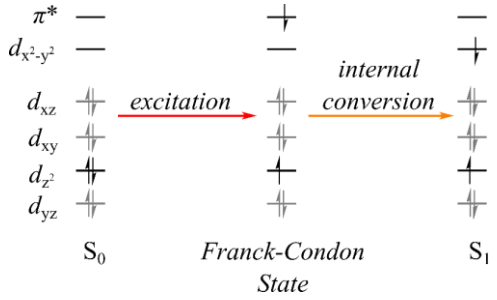

Figure 98: Simplified excited state evolution of **12**.

While kinetic analysis of the reaction of **12** to **16** allow for the formulation of a simple mechanistic model, transient spectroscopy and computational analysis give further insight in the initial photophysical events. In transient UV-vis spectroscopy a persistent absorption at $\lambda = 450$ nm is observed and assigned to the persistent species **PS** proposed based on kinetic analysis (Chapter 2.4.1), which is either a long-lived triplet state or a photoproduct.

To determine whether population of triplet excited states plays a role in the photochemistry of **12**, luminescence measurement of a benzene solution of **12** was performed. The long life time of triplet states usually results in efficient phosphorescence, even though *Scholes* and *Doyle* do not report luminescence for their nickel complexes.[318] Fluorescence on the contrary competes with fast internal conversion, therefore lowering the luminescence quantum yield.[152] While most data on the conversion **12** to **16** is obtained in THF solvent, polar solvents may result in excited state quenching due to exciplex formation, therefore rendering benzene more suitable for luminescence measurement.[320]

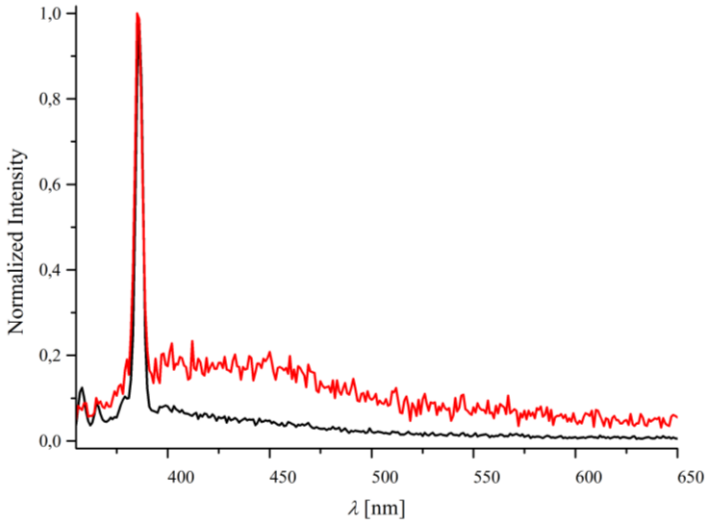

Figure 99: Fluorescence spectra of (black) benzene and (red) a $1 \cdot 10^{-4}$ M solution of **12** in benzene.

The emission spectrum of a $1 \cdot 10^{-4}$ M solution of **12** in benzene shows a sharp feature at λ = 386 nm close to the excitation wavelength of $\lambda_{exc.}$ = 345 nm (Figure 99). The energetic difference $\tilde{\upsilon}$ = 3079 cm^{-1} between excitation wavelength and observed emission suggests Raman scattering at the solvent C-H bond which is confirmed by blank measurement. Since no significant emission of an excited state can be observed by fluorescence spectroscopy, population of triplet states by photoexcitation of **12** is excluded. Accordingly, the long-lived species proposed by kinetic anlysis and observed in transient spectroscopy is assigned as a ground-state photoproduct **PP**.

2.4.3 Isotopic Labeling Studies and Ni-H/Ni-D Kinetic Isotope Effect

The simplified mechanistic picture for photochemical conversion of **12** to **16** (Scheme 52) emphasizes, that characterization of the persistent species **PP** is crucial to understand the change in selectivity in CO_2 activation with respect to ground state reactivity of hydride **12**. Several reactions are possible for the RDS which results in formation of **PP**. The influence of photoexcitation on the driving force of homo- and heterolytic metal-hydrogen bond scission is probably best examined for [IrH(bpy)(Cp*)], which is *both* a strong proton and hydride donor in the excited state (see Chapter 2.1.6).[284,285] Another possibility to affect ΔG for PCET by photochemistry is excited state redox chemistry which results in formation of oxidation states which are not accessible thermally.[275] While these examples require population of thermalized triplet states to provide sufficient excited state life time to allow bimolecular reactivity, metal hydrogen bond homolysis represents an intramolecular process which is often observed in transition metal hydride photochemistry.[247]

To probe if the Ni-H bond is kept intact upon conversion of **12** to **16**, the hydride position is deuterated and **12-D** is photolyzed under the conditions discussed previously. The efficiency of transfer of the label from **12-D** to **16-D** and **17-D** is investigated by integration in $^{1}H\{^{31}P\}$ NMR spectroscopy (Figure 100).

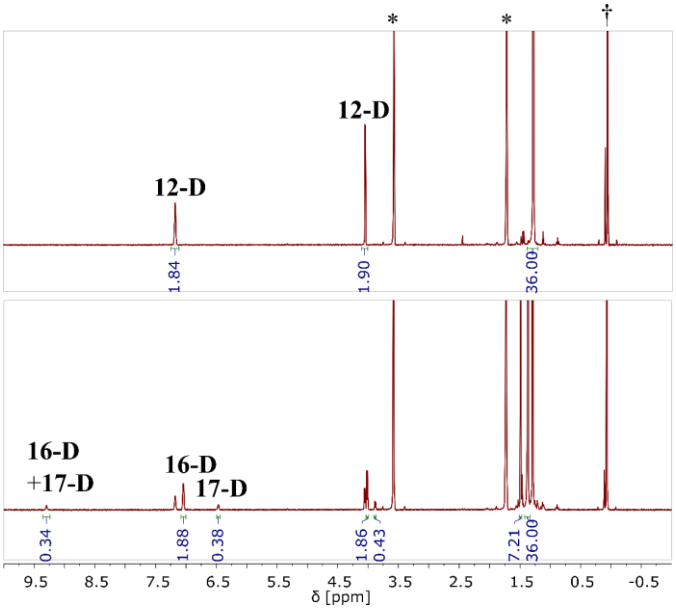

Figure 100: $^{1}H\{^{31}P\}$ NMR spectra of photolysis ($\lambda_{exc.}$ > 305 nm) of a solution of **12-D** in THF-d_8 at $p(CO_2)$ = 1 atm (top) initial reaction mixture, (bottom) 1 h photolysis. (*denotes THF-d_8, †denotes TMS_2O).

Based on comparison of the integration of the pincer *tert*-butyl resonances and the O-H/D resonance, an integral of 1.20 is expected for complete loss of the label, and therefore a transfer of 72% of the Ni-D label to the O-H/D position in **16-D** and **17-D** is observed. The accuracy of this value has to be taken with care, since the following errors have to be considered: As can be seen in the integration of the CH resonances in the spectra shown in Figure 100, an error of 10-20% is usually observed due to the huge difference in the integral of the *tert*-butyl groups and the remaining protons of the investigated complexes. A similar error can be observed for the O-H resonance in the spectra of isolated **16** and **17** (Figure 58 and Figure 61). Further, chemical exchange between the O-H position and the basic positions of the pincer backbone might occur (this effect is likely small due to low acidity of **16** as discussed in Chapter 2.3.2). Considering this uncertainty, the experiment suggests efficient, however not quantitative transfer of the label from **12-D** to **16-D** and **17-D**. While complete metal hydrogen bond scission under extrusion of a proton/hydrogen atom/hydride can be ruled out based on this study, initial bond cleavage followed by efficient geminate recombination in the solvent cage might serve as explanation of the partial loss of the deuterium label. Additionally, chemical exchange or reversible deprotonation of the photoproduct **PP** might result in loss of the deuterium label.

Since the formation of the photoproduct **PP** from the excited state **12*** represents the RDS of the formation of hydroxycarbonyl **16**, the role of the hydride ligand in this step is examined by measuring the kinetic isotope effect (KIE). The upper limit of a KIE for a reaction in the vibrational ground state without consideration of tunneling effects can be estimated based on eq. (52). Here, $\tilde{\upsilon}_H$ and $\tilde{\upsilon}_D$ represents the wavenumber of the respective bond which is effected by deuteration.

$$k_H/k_D = \exp\{hc/2k_BT\,(\tilde{\upsilon}_H - \tilde{\upsilon}_D)\} \quad (52)$$

Based on the experimental $\tilde{\upsilon}_H$ = 1834 cm^{-1} and $\tilde{\upsilon}_D$ = 1318 cm^{-1} a maximal KIE of 3.47 is expected. While this value is an upper limit in the sense of assuming vibrational ground states of identical energy in the transition state for both isotopologues, is also is an upper limit in the following sense: the rate-determining step takes place from excited state **12***. As discussed previously, the population of vibrationally excited states can result in a lower experimental KIE. Further, $\tilde{\upsilon}_{S1}$ = 1507 cm^{-1} can be assigned to the Ni-H stretch in the excited state S_1 which might be involved in formation of **PP**. The time constant $\tau_2 \approx 10$ ps for conversion of S_1 suggests population of the vibrational ground state in S_1. Therefore a refined upper limit of 2.90 for the KIE can be calculated using eq. (40) for formation of **PP** from S_1, based on the excited state stretching vibration $\tilde{\upsilon}_{S1}$. Kinetic measurements for CO_2 activation by **12-D** were performed and are compared to the data obtained for hydride **12**.

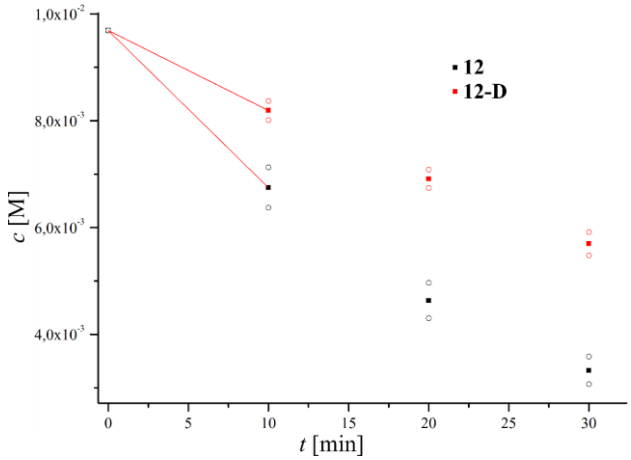

Figure 101: Plot of *c vs. t* for the photolysis ($\lambda_{exc.}$ > 305 nm) of **12** and **12-D** under CO_2 atmosphere ($p(CO_2)$ = 1 atm, empty sphere show individual data points and solid spheres show average values).

Deuteration of the hydride position results in a retardation of the reaction as shown in Figure 101. Comparison of the initial rates for the conversion of starting material over 10 minutes results in KIE = 1.96. This value can be interpreted as a *primary normal* kinetic isotope effect, giving important structural information on the photoproduct **PP**. The effect of deuteration on the rate indicates that the vibrational ground state of the transition state is less effected by deuteration than the vibrational ground state of the starting material, suggesting that Ni-H bond elongation makes a significant contribution to the reaction

coordinate. Work by *Norton* and coworkers on KIE in proton self-exchange in $CpM(CO)_3H/CpM(CO)_3^-$ (M = Cr, Mo, W) shows good agreement between experimental and expected values according to eq. 56. This is attributed to a linear motion of the proton along the M–H–M axis in the transition state, resulting in a complete conversion of the vibrational to a translational degree of freedom.[237] Values for KIE similar to the measured KIE for conversion of **12** are reported by *Bullock* and coworkers on the hydride transfer of $CpM(CO)_3H$ to the trityl cation and interpreted as an indication of a nonlinear transition state since '*…hydride abstracting reagents would attack the electron density in the bond (…) rather than the hydrogen atom itself.*'.[237] Therefore, the Ni-H bond is directly involved in the formation of **PP** and the magnitude of the measured KIE suggests a nonlinear transition state with a still intact Ni-H bond.

2.4.4 Mechanistic Picture of Photophysical Evolution of Excited State [NiH(^{tBu}P=N=P)] (12)

The mechanistic picture shown in Scheme 52 simplifies the photoexcitation and relaxation of ground state hydride **12** and the excited state **12*** as an equilibrium. Transient spectroscopic measurement, luminescence spectroscopy and labeling studies supported by DT-DFT allow for the formulation of a *Jablonski* diagram to describe the excited state photophysical events (Figure 102).

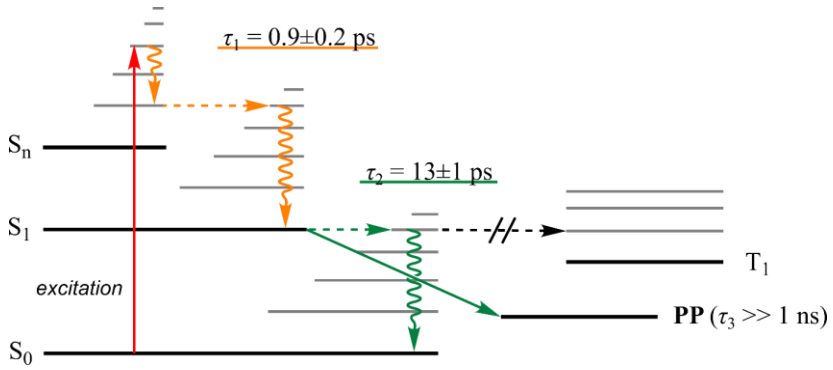

Figure 102: Jablonski diagram describing the excited state photophysical processes of **12***.

Initial photoexcitation from the vibrational and electronic ground state of **12** results in population of the vibrationally excited *Franck-Condon* state *via* MLCT on the singlet hypersurface as indicated by the high extinction coefficient, transient UV-pump-IR-probe spectroscopy and computational analysis. Internal conversion results in population of the excited state S_1 with a time constant of τ_1 = 0.9±0.2 ps. Structural information at this state taken from transient infrared spectroscopy shows significant lowering of the Ni-H bond strength. This state is best described as dissociative with respect to the Ni-H bond due to population of the $d_{x^2-y^2}$ orbital, therefore resembling an excited state obtained by metal centered excitation. Both UV-vis- and IR-probe spectroscopy indicates repopulation of the electronic and vibrational ground state of **12** with τ_2 = 13±1 ps. Transient UV-vis spectroscopy further reveals formation of a persistent species which does not show conversion within the time restrains of the measurement, giving rise to τ_3 >> 1 ns. Evidence

for intersystem crossing to the triplet energy hypersurface cannot be obtained by luminescence spectroscopy, therefore this persistent species is assigned as photoproduct **PP**. In agreement, a persistent species is also predicted based on kinetic analysis of the reaction of **12** to **16**. While the transient spectroscopic data does not show which electronically excited-state converts to **PP**, the low excited-state Ni-H stretching vibration in S_1 and the major contribution of Ni-H bond activation to the RDS suggested by KIE measurement suggest formation of **PP** from S_1. Significant non-radiative relaxation of S_1 to the ground state is suggested based on a low-intensity spectroscopic signature of **PP** in the transient experiments and is in agreement with the determined quantum yield of Φ_{410} = 9%.

2.4.5 Photochemical Reactivity of [NiH(^{tBu}P=N=P)] (12) in the Absence of Substrate

Kinetic investigation of the abnormal CO_2 insertion by Ni^{II} hydride **12** to hydroxycarbonyl **16** suggests the formation of a persistent species **PS**, which is identified as photoproduct **PP** by transient spectroscopy and luminescence spectroscopy. To obtain structural information on this compound, trapping experiments were performed on this persistent, but on a preparative timescale short lived, species.

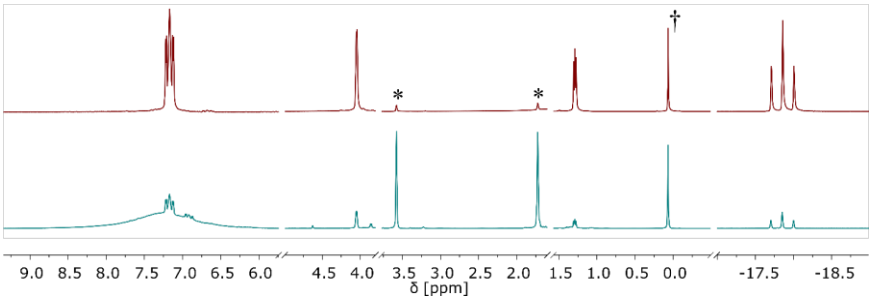

Figure 103: ^{1}H NMR spectra of photolysis ($\lambda_{exc.}$ > 305 nm) of a solution of **12** in THF-d_8 under Ar (1 atm) atmosphere. (top) Initial reaction mixture, (bottom) 15 h photolysis. (*denotes THF-d_8, †denotes TMS_2O).

Initially, **12** was photolyzed under argon atmosphere and the reaction progress was monitored by NMR spectroscopy. Photolysis of a THF-d_8 solution of **12** under argon atmosphere results in a significant slower rate as compared with conversion of **12** to **16** under CO_2 atmosphere. While a diamagnetic product at δ = 53.9 ppm can be observed in the $^{31}P\{^1H\}$ NMR spectrum, integration against an internal standard in the ^{1}H NMR spectrum shows, that the quantity of this product does not contribute significantly to the conversion of **12**. Due to a lack of NMR resonances aside from the pincer ligand in the ^{1}H NMR spectrum, identification of this compound by NMR spectroscopy is not possible from the data at hand. Aside from this diamagnetic species, a broad resonance can be observed at δ = 6–8 ppm in the ^{1}H NMR spectrum, as is observed for Ni^I complexes **9** and **10^{BArF}**. EPR spectroscopy indicates the formation of **9** as main product of photolysis of **12** which proceeds *via* loss of H_2 as confirmed by TCD-GC measurement of the headspace (Figure 104, see Chapter 1.4.2 for EPR spectroscopic analysis). LIFDI-MS measurement of the mixture obtained by photolysis of **12** in THF-d_8 shows signals for starting material **12** and main product **9**. Additionally, a signal

at *m/z* = 492.3 is present which is in agreement with formation of a tetrahydrofuranyl-d_7 coordinated Ni(^{tBu}P=N=P) fragment corresponding to the diamagnetic species observed in NMR spectroscopy. Given the low Ni-H stretching vibration in the excited state **12***, Ni-H bond homolysis might be a valid pathway resulting in formation of **9**. Reactivity of the liberated hydrogen atom with the solvent is a possible source of H_2/HD which in agreement with the formation of a tetrahydrofuranyl-d_7 substituted complex.[27] However, C-H bond homolysis of THF does not contribute significantly to H_2/HD liberation as the concentration of this diamagnetic byproduct is low compared to the conversion of the starting material.

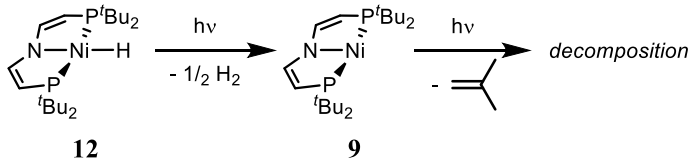

Scheme 53: Photochemical reactivity of **12** in the absence of substrate.

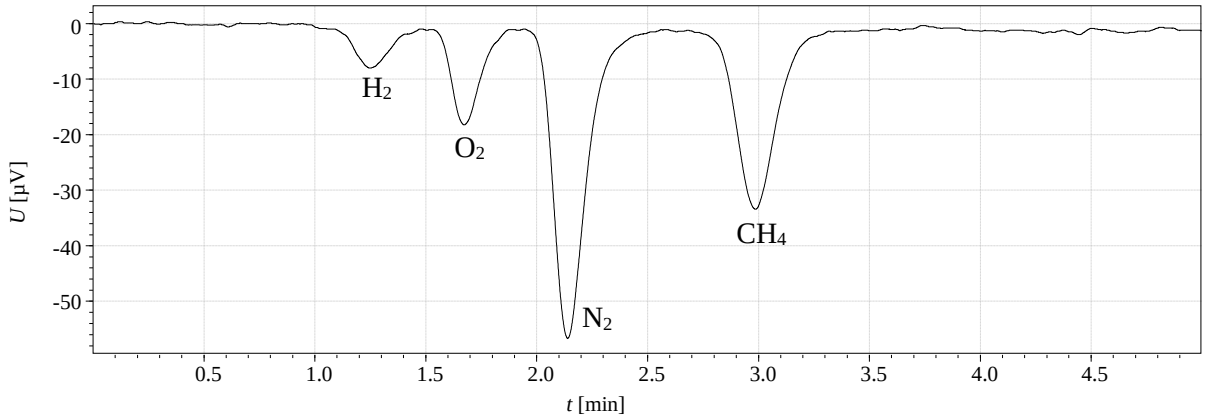

Figure 104: TCD-GC chromatogram of the headspace of photolysis ($\lambda_{exc.}$ > 305 nm) of a solution of **12** in THF-d_8 under Ar (1 atm) atmosphere.

To further investigate if Ni-H bond dissociation is the origin of **9** upon excitation of **12**, the fate of the hydride ligand was monitored by photolysis of deuteride **12-D** in THF in the presence of stoichiometric amounts of C_6D_6 as internal standard. While prior to irradiation, the deuteride ligand in **12-D** can be readily observed by ^{2}H NMR spectroscopy, neither the nickel deuteride nor an enrichment of the naturally occurring THF-d_1 resonances is detected after photolysis (Figure 105). Since hydrogen formation from photolysis of **12** is confirmed by TCD-GC even though no corresponding ^{1}H NMR resonance is present, a similar fate of the deuterium is likely in this case and can be explained by loss of H_2/D_2/HD to the headspace as reported in the literature.[275] If C-H bond homolysis of THF would contribute significantly to H_2/HD liberation, the

[27] The absence of a ^{1}H NMR spectroscopic resonance for H_2/HD hinders analysis of the isotopic composition.

formation of THF-d_1 is expected as a result of the reaction of the initially formed tetrahydrofuranyl radical with **12-D**. Accordingly, formation of **9** and H_2 is mainly attributed to a different process.

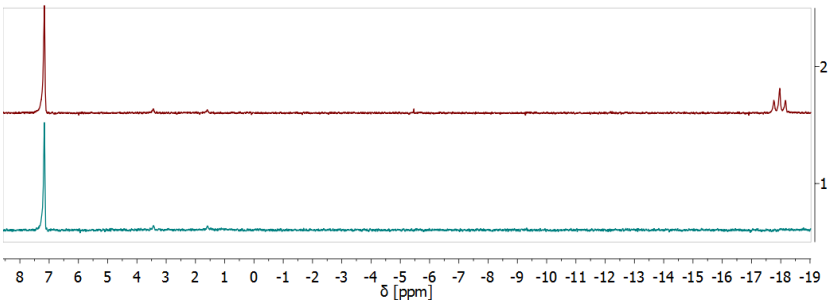

Figure 105: ^{2}H NMR spectra of photolysis ($\lambda_{exc.}$ > 305 nm) of a solution of **12-D** in THF under Ar (1 atm) atmosphere (top: before photolysis; bottom: after 14 h photolysis).

Photochemical metal bond homolysis is reported on a number of transition metal hydrides (Chapter 2.1.6): Photolysis of $[MH(CO)_3Cp]$ (M = Mo, W) and *trans*-$[RhH(OH_2)(NH_3)_5]$ gives rise to radical chain processes and formation of decamethylrhenocene by photolysis of $[RhH(Cp^*)_2]$ proceeds *via* unknown fate of the hydrogen atom.[259,321,322] Photochemical conversion of related $[RhH(Cp)_2]$ to rhenocene in low temperature CO matrices shows formyl formation as in $[CoH(CO)_4]$ and $[MnH(CO)_5]$ which show concurring metal carbonyl and metal hydride homolysis in low temperature argon matrices upon irradiation.[260,262,263,323,324] Notably, photochemical H_2 formation is a common product of reductive elimination from polyhydride complexes, but is limited to monohydride $[IrH(bpy)(Cp^*)]^+$ and derivatives thereof which liberated H_2 *via* excited state redox self-quenching.[247,275]

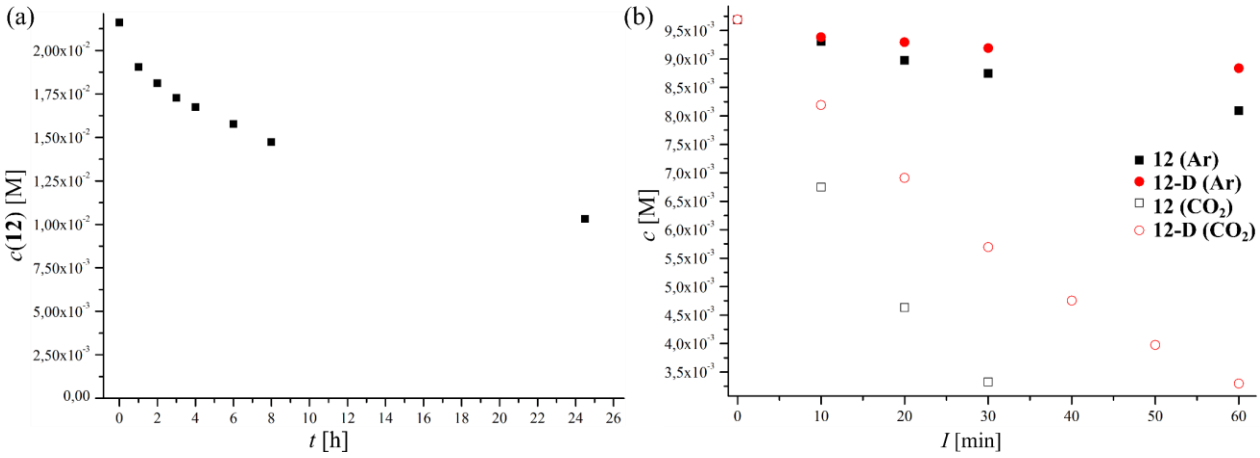

Figure 106: Plot of *c vs. t* for the photolysis ($\lambda_{exc.}$ > 305 nm) under Ar atmosphere (p(Ar) = 1 atm) of (a) a solution of **12** in C_6D_6 and (b) solutions of **12** and **12-D** in THF-d_8 (data at $p(CO_2)$ = 1 atm is given as average of two measurements).

Performing the photolysis of **12** under argon atmosphere in C_6D_6 results in similar reactivity giving **9** as main product. The diamagnetic side product observed upon irradiation of **12** in THF-d_8 is not observed in

deuterated benzene. However, free amino diphosphine **13** can be identified in ^{1}H NMR spectroscopy by the characteristic coupling pattern of the pincer backbone resonances. Additionally, low quantities of *iso*-butene can be observed, indicating ligand decomposition as underlying reactivity.

Monitoring the reaction progress of the photolysis of **12** under argon atmosphere in C_6D_6 shows that conversion of approximately 50% of the starting material takes one day (Figure 106a). While the reaction proceeds reasonably fast at the beginning, the last measurement shows low conversion over 16 hours, indicating a significantly faster initial rate. To provide better comparability with the kinetic data on CO_2 activation by photolysis of **12**, photolysis of **12** and **12-D** under argon atmosphere was performed at identical conditions as for CO_2 activation and monitored over 1 hours. The plot of *c vs. t* for the experiments under CO_2 and Ar are shown in Figure 106b and the low rate of conversion under Ar is confirmed. While a KIE is not determined given the limited number of experiments, both reactions under CO_2 and Ar show a decrease in rate upon deuteration and therefore a normal KIE. While the slow conversion of **12** in the absence of substrate is in agreement with reversible formation of **PP** in the absence of substrate, the retardation of the reaction with increasing reaction progress indicates reformation of the starting material **12** by reaction of **PP** with Ni^I **9**.

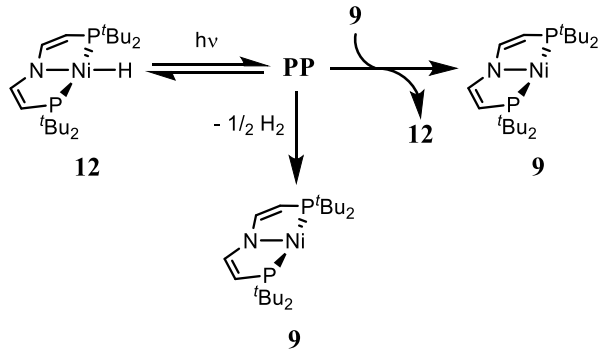

Scheme 54: Photochemical reactivity of **12** in the absence of substrate and in the presence of **9**.

As discussed, the products of photolysis of **12** under argon can be observed NMR spectroscopically. However, what is probably most intriguing about the NMR spectra shown in Figure 103 is the remarkable increase in the intensity of the solvent resonance upon photolysis. Neither can a significant change in the ratio of the ^{1}H NMR resonances of **12** or **12-D** be monitored over the course of the measurements, nor is this effect observable upon photolysis of **12** or **12-D** under CO_2 atmosphere. A possible H/D exchange between **12** and the deuterated solvent is not present, as the deuterium label of **12-D** is completely lost to the headspace upon photolysis.

While NMR and EPR spectroscopy as well as headspace analysis of the reaction by TCD-GC suggest H_2 loss from **12** to **9** as the main photochemical event under argon, UV-vis spectra of **9** do not show absorption

at λ = 450 nm as observed for **PP** in the transient spectroscopy of **12** (Figure 95 and Figure 107b). Accordingly, Ni^I **9** is not the transient species observed in pump-probe spectroscopy and is most likely a product of H_2 loss from the photoproduct **PP** in the absence of CO_2. While formation of $H_2/D_2/HD$ is partially formed by Ni-H bond homolysis in the excited state **12*** and subsequent reaction of the liberated hydrogen atom with the solvent, the high selectivity of the reaction rather suggests a bimetallic mechanism for H_2 liberation from **12**.

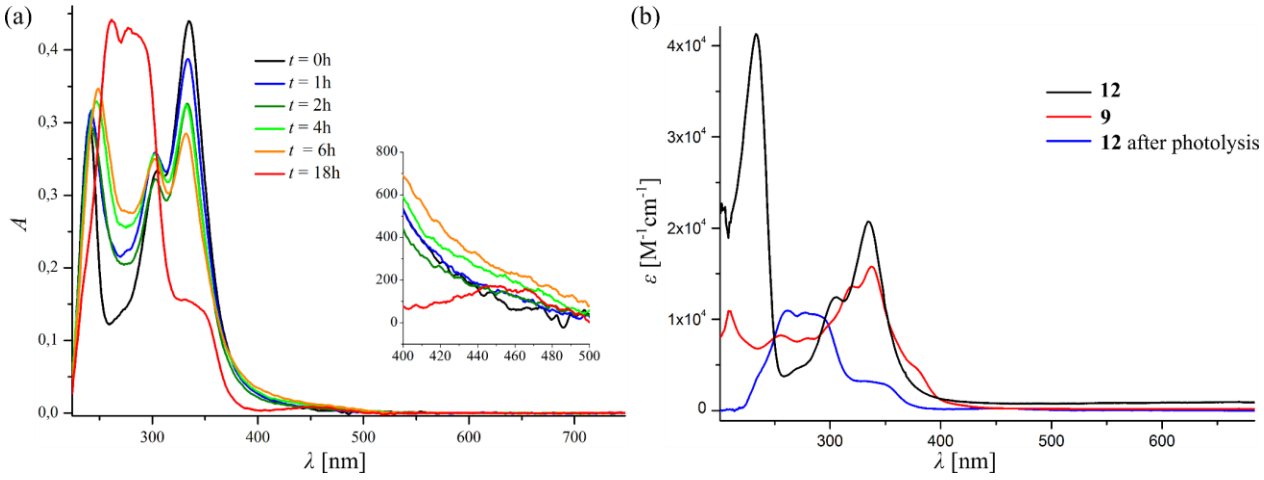

Figure 107: (a) UV-vis spectra for the photolysis (λ > 305 nm) of a solution of **12** in THF under Ar atmosphere and (b) UV-vis spectra of **12**, **9** and the spectrum obtained after 18 h of photolysis of **12** under Ar atmosphere in THF.[28]

Monitoring the photolysis of **12** under argon by UV-vis spectroscopy shows slow conversion of **12** over 6 hours resulting in a decrease of the absorption maxima located at λ = 334 nm. This is accompanied by an increase in the absorption at λ = 276 nm which is in agreement with conversion of **12** to **9** as indicated by spectra of authentic samples of both substances (Figure 107). After prolonged photolysis for 18 h, minor absorption at λ = 450 cm can be observed, however the spectral region below λ = 400 nm shows no sign of **12** or **9** anymore, suggesting complete degradation of the sample which is in agreement with the detection of *iso*-butene in NMR spectroscopy.

2.4.6 The Role of [Ni(^{tBu}P=N=P)] (9) in the Conversion of [NiH(^{tBu}P=N=P)] (12) to [Ni(CO_2H)(^{tBu}P=N=P)] (16)

Since **9** is the main product of photolysis of **12** under argon the role of **9** as intermediate in formation of hydroxycarbonyl **16** was examined. EPR spectroscopic analysis of the reaction mixture obtained by photolysis of **12** under CO_2 atmosphere, confirms the formation of Ni^I species by observation of carbonyl **22** (Figure 108). While the absence of an internal standard does prohibit determination of the concentration of **22**, the resolved ^{14}N hyperfine coupling due to a lower line width as compared to the authentic sample

[28] The extinction coefficient ε for the photolyzed sample is calculated based on assuming a constant concentration.

(Figure 70) indicates formation of **22** in low concentration which is in agreement with no apparent observation of paramagnetic species in kinetic analysis of the reaction (Chapter 2.4.1). This result shows, that there is no significant built up of Ni^I species upon photolysis of **12** under CO_2 atmosphere.

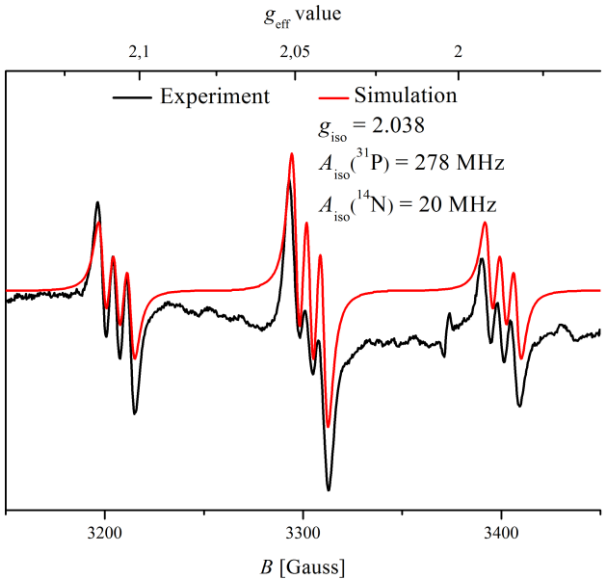

Figure 108: X-Band EPR spectra of a solution of **12** photolyzed at $p(CO_2)$ = 1 atm in THF-d_8 showing formation of **22** (RT, ν = 9.456767 GHz).

To investigate if **9** nevertheless plays a role as intermediate in formation of hydroxycarbonyl **16**, CO_2 activation by **9** was examined. Placing a solution of **9** in THF-d_8 under CO_2 atmosphere results in bimetallic CO_2 reduction as was reported by *Lee* and coworkers for a related Ni^I pincer complex.[105] Initially, formation of an unsymmetrical species [(^{tBu}P=N=P)Ni(*1κC,2κ²O,O'*-CO_2)Ni{*κ²P,N*-N(CHCHP*t*Bu$_2$)$_2$}] (**26**) is observed ^{31}P{^{1}H} NMR spectroscopically, while bridging carbonate [(^{tBu}P=N=P)Ni(OC(O)O)Ni(^{tBu}P=N=P)] (**27**) is formed over the course of several days (Figure 109). Compound **26** shows a complex NMR signature in ^{31}P{^{1}H} NMR spectroscopy due to its low symmetry, resulting in three resonances with 1:2:1 intensity (Figure 109). While two resonances are observed in the expected region ($\delta \approx$ 120–50 ppm), δ = 4.77 suggest dissociation of one phosphorus donor upon formation of **26** from **9** and therefore hemilability of the ^{tBu}P=N=P pincer ligand. The integral ratio is therefore attributed to one pincer ligand showing threefold coordination and one pincer ligand with a non-coordinating phosphine. Since the κ^3 pincer shows just one singlet resonance, a mirror plane is present. Surprisingly, ^{31}P{^{1}H} NMR spectra of **26** show a P-P coupling constant of $^5J_{PP}$ = 8.7 Hz for both phosphorus atoms of the partially dissociated pincer ligand despite the distance of both atoms.

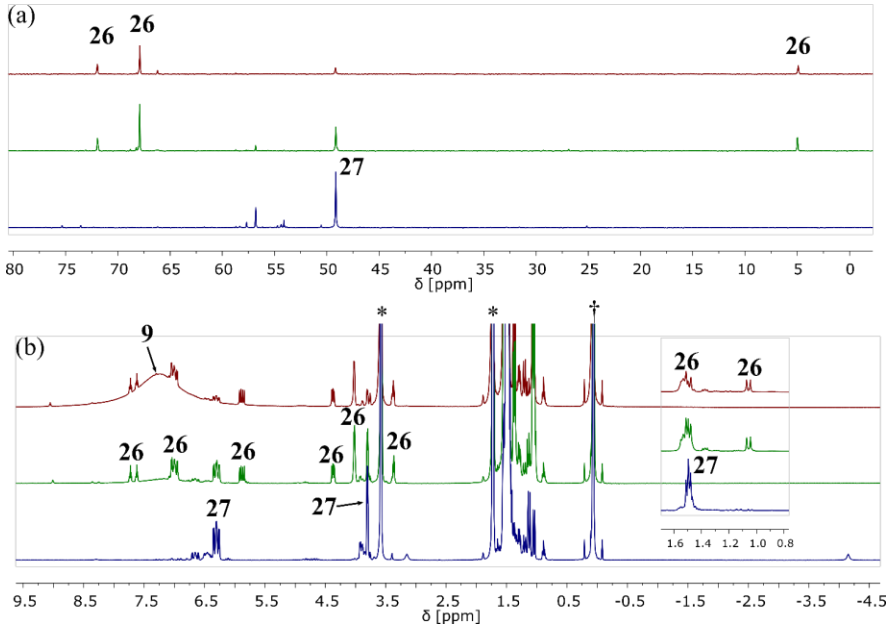

Figure 109: (a) $^{31}P\{^{1}H\}$ and (b) ^{1}H NMR spectra of the reaction of a solution of **9** in THF-d_8 with CO_2 ($p(CO_2)$ = 1 atm) after (top) 1 h, (middle) 1 day and (bottom) 11 days (*denotes THF-d_8, †denotes TMS_2O).

^{1}H NMR spectroscopy shows that formation of dimeric **26** is slow, since after 1 day under CO_2 atmosphere a broad resonance attributed to a paramagnetic species can still be observed (Figure 109). The chemical shift δ and shape of this signal resembles the spectroscopic signature **9**, however, formation of another paramagnetic species as intermediate, *e.g.* a Ni^{I} CO_2 adduct, cannot be ruled out based on the data at hand. Built-up of **27** and consumption of **9** is observed over 24 hours. Upon prolonged reaction time, **9** and **26** are completely converted, suggesting **26** as an intermediate in formation of carbonate **27**. Complex **27** can be clearly identified by a $^{13}C\{^{1}H\}$ NMR singlet resonance at δ = 162.5 ppm and a LIFDI-MS measurement showing a signal at *m/z* = 889.3, both obtained for the ^{13}C isotopologue.

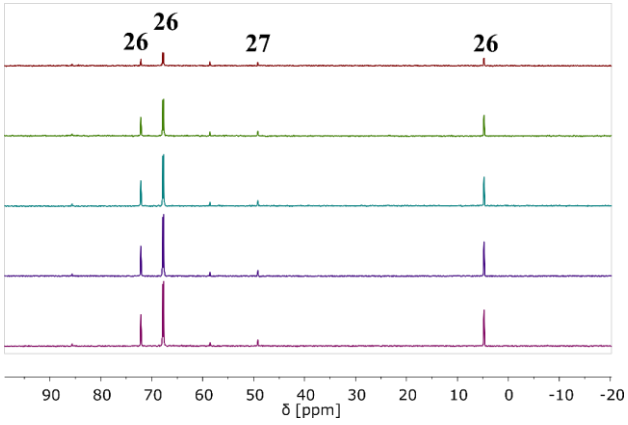

Figure 110: $^{31}P\{^{1}H\}$ spectra of the reaction of a solution of **9** in C_6D_6 with 1 eq $^{13}CO_2$ monitored over 15 hours in 3 h intervals.

Conversion of **26** to carbonate **27** can be prevented by lowering $c(CO_2)$ and the structure of **26** is assigned based on NMR spectroscopy upon treatment of **9** with stoichiometric amounts of $^{13}CO_2$. Figure 110 shows that addition of 1 eq of $^{13}CO_2$ to a THF-d_8 solution of **9** results in successive conversion of starting material over 24 hours to **26** without significant built-up of carbonate **27**.

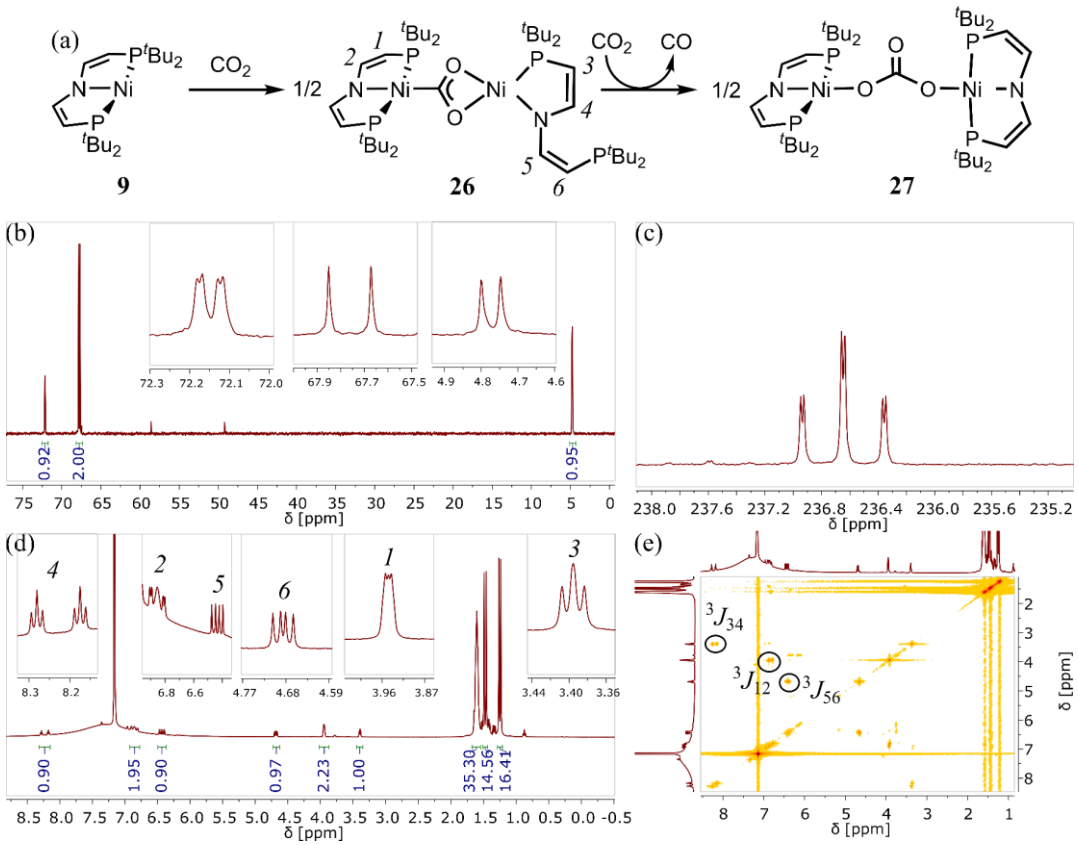

Figure 111: (a) Reaction of **9** with CO_2 giving CO_2 bridged **26** and carbonate **27**. (b) $^{31}P\{^1H\}$, (c) $^{13}C\{^1H\}$, ^1H and $^1H,^1H$ COSY NMR spectra of **26-^{13}C** obtained from the reaction of **9** with 1 eq $^{13}CO_2$ in C_6D_6.

$^{31}P\{^1H\}$ NMR spectroscopy of **26-^{13}C** reveals P-C coupling of both chemically different metal coordinated phosphorus atoms (Figure 111b). The coupling constant $^2J_{PC}$ = 29.1 Hz for the three-coordinate pincer suggests a carbon-bound CO_2 ligand attached to this nickel center, while significant lower $^3J_{PC}$ = 2.4 Hz is observed for the phosphorus bound to the second metal center. Accordingly, $^{13}C\{^1H\}$ NMR spectroscopy of **26-^{13}C** shows a doublet of triplets at δ = 236.7 ppm with fitting coupling constants. The structure of **26** can therefore be assigned as CO_2 bridged dimer given the indicative shift of the $^{13}C\{^1H\}$ NMR resonance and the coupling of the carbon atom to phosphorus atoms on both metal centers. The structural assignment is supported by a signal at m/z = 872.3 in LIFDI-MS analysis. The C_S symmetry of **26** on the NMR timescale suggests perpendicular orientation of the pincer ligand planes. ^1H NMR spectroscopy of **26-^{13}C** shows eight resonances for the pincer backbone hydrogen atoms and three *tert*-butyl resonances (Figure 111d). Broadening of the ^{t}Bu resonances of the threefold coordinating pincer suggests dynamic behavior. The ^{t}Bu

resonances of the hemilabile pincer can be readily assigned due to the lack of higher order coupling patterns with a high field shifted resonance of the non-coordinating P^{t}Bu$_2$ moiety. ^{1}H,^{1}H COSY NMR spectroscopy allows for identification of the neighboring hydrogen atoms in **26-^{13}C** as shown in Figure 111e. By selective decoupling, hydrogen atom *3* and *4* can be identified with a strong high and low field shift, respectively. Notably, the NCH hydrogen atom *4* has an unusual strong H-P coupling with $^3J_{HP}$ = 42.4 Hz, and $^3J_{HH}$ = 10.5 of the uncoordinated pincer arm is increased with respect to the coordinated pincer arm ($^3J_{HH}$ = 5.5 Hz), showing an intact *trans* geometry of the C-C double bond. While distortion of the pincer ligand in **26** due to twofold coordination might serve as explanation of the unusual shift and coupling constants, attempts to crystallize **26** did not succeed. A η^2-P,π coordination is also possible in **26**, would however most likely result in a high field shift of both hydrogen atoms of the donating olefin. Therefore formulation of **26** as shown in Figure 111 is preferred.[325]

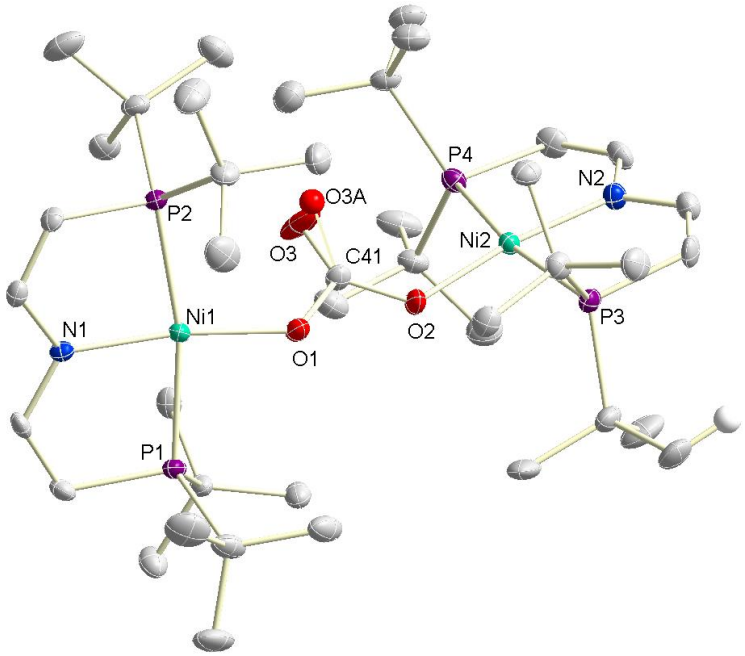

Figure 112: Solid state structure of **27** determined by X-ray diffraction. Thermal ellipsoids are drawn at the 50% probability level. Selected hydrogen atoms are omitted for clarity. Minor occupation of disordered atoms is shown as spheres.

Structural assignment of **27** as bridged carbonate dimer is confirmed by X-ray crystallographic analysis (Figure 112). The pincer ligands are arranged perpendicular which is attributed to the steric bulk of the ^{t}Bu fragments. An effect of the dimerization on τ_4 cannot be observed compared to monomeric hydrocarbonate **17** (τ_4(**17**) = 0.14; (τ_4(**27**) = 0.14/0.15). The nickel oxygen distances in monomeric and dimeric carbonate complexes **17** and **27** are nearly identical, while the carbon oxygen bond distances show less variation in **27**

due to the more symmetric structural environment (**17**: *d*(O1-C21) = 1.271(3) Å, *d*(O2-C21) = 1.246(3) Å, *d*(O3-C21) = 1.327(3) Å; **27**: *d*(O1-C41) = 1.313(4) Å, *d*(O3-C41) = 1.23(2) Å, *d*(O2-C41) = 1.298(4) Å).

Monitoring the reaction progress of the reaction of **9** with CO_2 suggests bridged carboxylate **26** as intermediate in formation of carbonate **27**. Furthermore, performing the reaction at different CO_2 pressures, shows that conversion of **26** to **27** involves CO_2, therefore suggesting reductive disproportionation of CO_2 to carbonate and carbon monoxide, which however could not be confirmed NMR spectroscopically nor by TCD-GC measurement of the headspace. Reductive disproportionation of CO_2 can proceed *via* multiple pathways. The formation of oxo complexes by decarbonylation of carboxylates is commonly observed for early transition metal complexes, while *Milstein* reported the dimerization of CO_2 on a single iridium center, resulting in extrusion of carbonate and formation of an iridium carbonyl.[326] Computational analysis of the popular CO_2 reduction photocatalyst [$ReCl(CO)_3$(bpy)] by *Fujita* and coworkers indicates a mechanism which resembles the observed reactivity of **9**: CO_2 activation at reduced rhenium carbonyl [$Re(CO)_3$(bpy)] results in formation of a bridged carboxylate dimer as thermodynamic product. Insertion of a second CO_2 molecule is slightly uphill and results in formation of a bridged carbonate dimer by CO extrusion (Chapter 2.1.3.4).[206]

As discussed, Ni^I complex **9** shows a different selectivity in CO_2 reduction compared to **12**. While photolysis of **12** under CO_2 results in 2 electron reduction of CO_2 to carbon monoxide, bimolecular CO_2 reduction by **9** results in reductive disproportionation to carbon monoxide and carbonate instead, limiting the maximum yield in CO to 50% with respect to **9**. Kinetic analysis of photochemical reduction of carbon dioxide by **12** shows that **16** is produced in yields beyond 50%, indicating that the 2 electrons of the nickel hydrogen bond of **12** are used efficiently for CO_2 reduction. Initial H_2 production from photolysis of **12** and successive CO_2 reduction by Ni^I **9** *via* dimeric **26** and **27** can therefore be excluded.

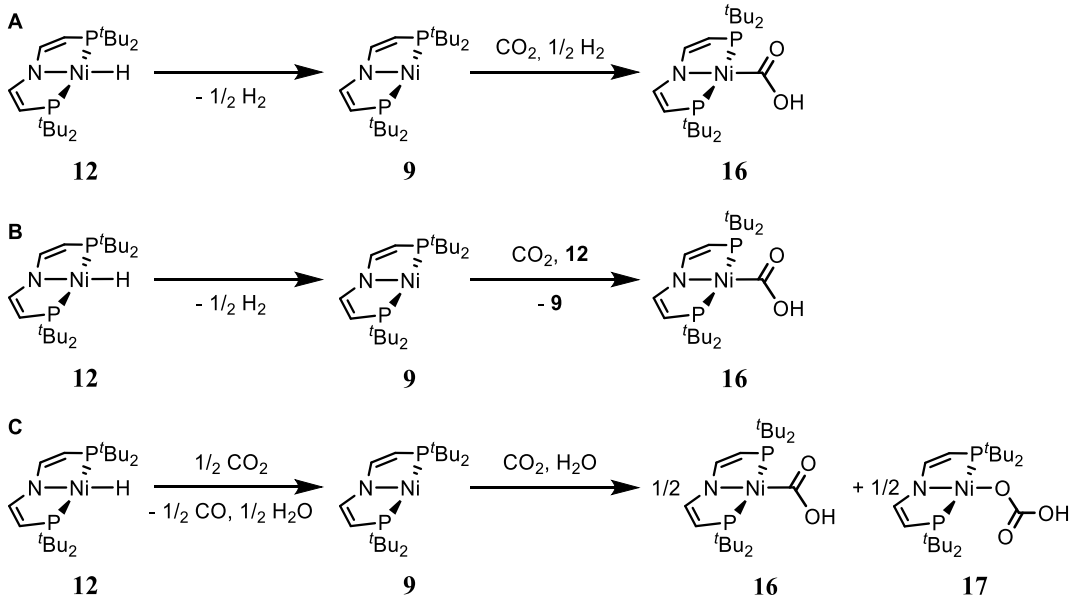

Scheme 55: Possible reactions for efficient two-electron reduction of carbon dioxide starting from hydride **12** *via* intermediate formation of Ni^I **9**.

Including Ni^I in the mechanism would require for formation of **9** without loss of the reduction equivalents of the Ni-H bond in **12**. A possible pathway for this reaction would be formation of **9** *via* H_2 loss, followed by CO_2 coordination and H_2 activation at a Ni^I carboxylate to yield hydroxycarbonyl **16** (Scheme 55A). A second mechanism would include a radical chain mechanism with formal HAT from nickel hydride **12** to a Ni^I carboxylate (Scheme 55B). This mechanism is in principle ruled out by the determined quantum yield of Φ_{410} = 9% for conversion of **12** to **16**, nevertheless will be considered in the following discussion. A third possible pathway is formal CO_2 reduction to CO by 2 eq of hydride **12** under formation of **9** and water, followed by subsequent CO_2 reduction by **9** (Scheme 55C). To probe these reactions, **9** was first reacted with H_2 and H_2O to check for reactivity in the absence of CO_2.

If H_2 pressure is applied to a solution of **9** in C_6D_6, formation of hydride **12** is observed NMR spectroscopically (Figure 113). Low quantities of hydroxide **18** are attributed to traces of water in the H_2 gas. After 3 hours, starting material **9** can still be observed. While no quantification of **12** was performed, integration against an internal standard suggests no further production of **12** after 2 days with no residual starting material observable by NMR spectroscopy. Homolytic H_2 activation on Ni^I was reported previously by *Lee* on a related T-shaped PNP Ni^I complex and by *Walter* on a mercury bridged dinuclear complex as Ni^I synthon.[105,327] Work by *Gade* presents the reverse reaction, H_2 loss from Ni^{II} hydride complexes.[328]

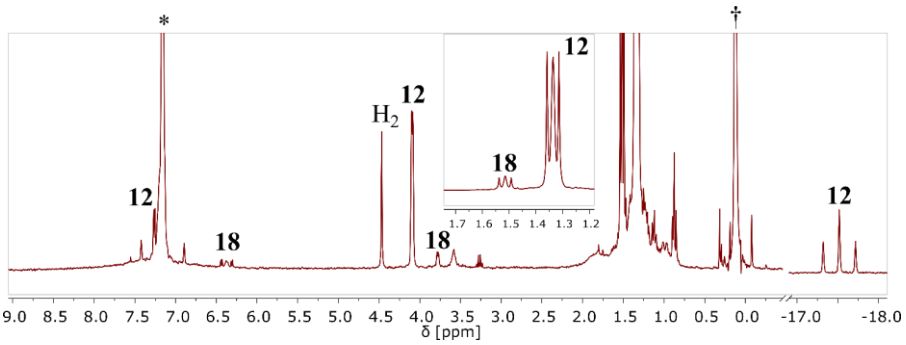

Figure 113: ^{1}H NMR spectrum of the reaction of **9** with H_2 ($\rho(H_2)$ = 1 atm) after 3 h in C_6D_6 (*denotes C_6D_6, †denotes TMS_2O).

When **9** is reacted with a six-fold excess of water in THF-d_8, barely detectable amounts of hydride **12** and hydroxide **18** are observable as product of homolytic O-H bond activation. The reverse reaction, so dissolving equivalent amounts of **12** and **18** in THF-d_8 results in formation of **9** and H_2O, suggesting the presence of an equilibrium in this reaction.

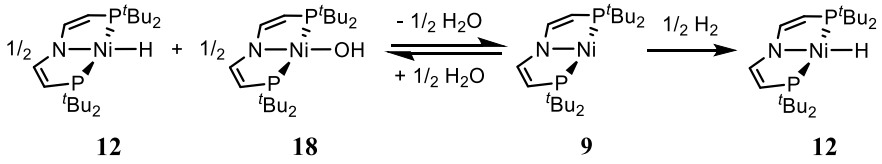

Scheme 56: Homolytic activation of substrates by Ni^I **9**.

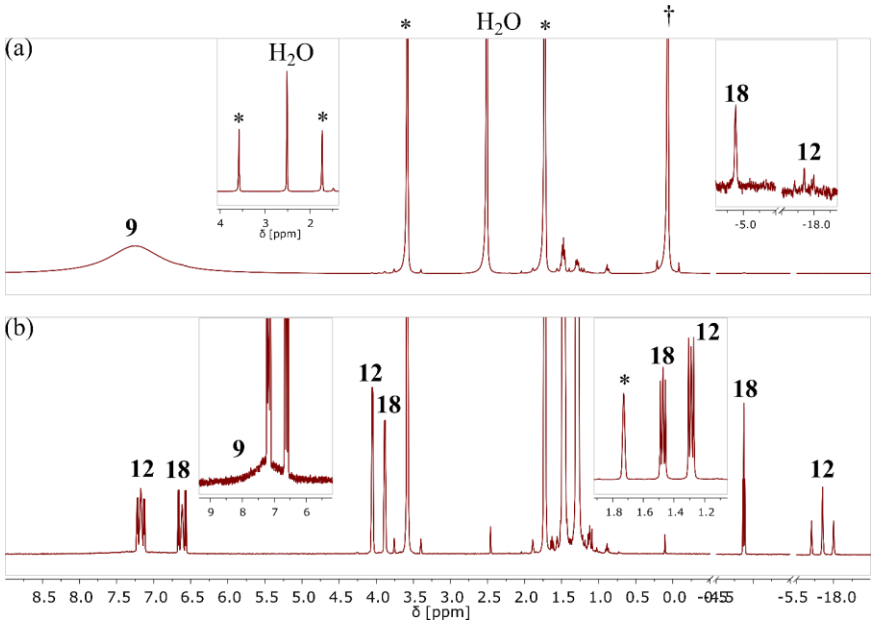

Figure 114: ^{1}H NMR spectrum of the reaction of (a) **9** with 6 eq of H_2O after 1 h and (b) **12** with 1 eq of **18** after 1 day in THF-d_8. (*denotes THF-d_8, †denotes TMS_2O).

While *Lee*'s paper on reactivity of a T-shaped PNP Ni^I complex reports on several bond activation reactions, homolytic activation of water is not included.[105] *Anderson* recently reported bimolecular water activation by a T-shaped Ni^{II} complex featuring an ligand centered radical.[329]

Since **9** shows homolytic H_2 activation at $p(H_2)$ = 1 atm, **9** was reacted with stoichiometric quantities of CO_2 and H_2 to prevent formation of dimeric carbonate **26** and hydride **12**. To be relevant for this mechanistic study, H_2 activation by a Ni^I carboxylate would have to be efficient at these H_2 concentrations, since it is the highest possible concentration accessible by H_2 production from photolysis of **12**. The low concentrations of CO_2 however might result in low concentration of a possible Ni^I carboxylate which is postulated as the reactive species. Since bridged carboxylate **26** is formed in the presence of stoichiometric amounts of CO_2 and most likely forms *via* such a Ni^I species, the lack of reaction products aside from **26** in this experiment indicates no H_2 activation after CO_2 coordination by **9**. A similar result is obtained by reacting a 1:1 mixture of **9** and **12** with 1 eq of CO_2, showing formation of **26** and no conversion of hydride, ruling out a radical chain mechanism (Figure 115).

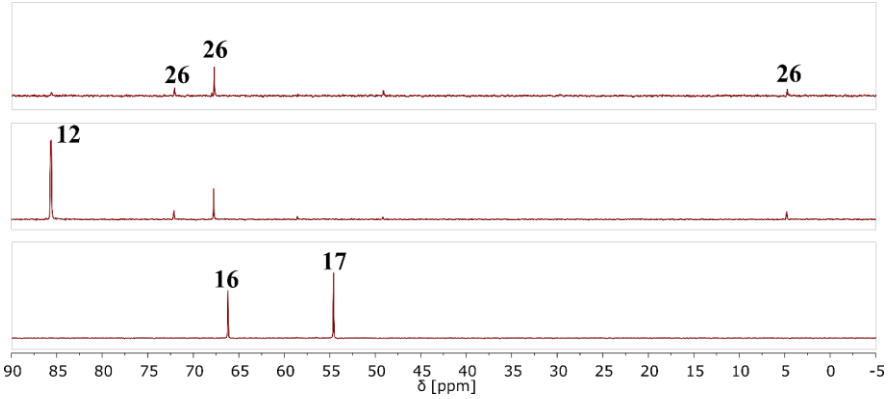

Figure 115: $^{31}P\{^1H\}$ NMR spectrum of the reaction of (top) **9** with 1 eq of CO_2 and 1 eq of H_2 after 1 day in C_6D_6, (middle) **9** with 1 eq of CO_2 and 1 eq of **12** after 1 day in C_6D_6 and (bottom) **9** with 1 eq of H_2O and CO_2 ($p(CO_2)$ = 1 atm) after 30 min in THF-d_8.

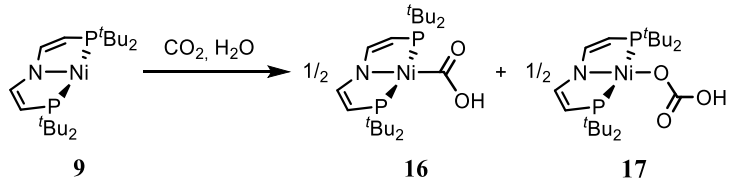

9 16 17

Scheme 57: Formation of hydroxycarbonyl **16** and hydrocarbonate **17** from **9**, CO_2 and H_2O.

If CO_2 pressure is applied to a solution of **9** in THF-d_8 in the presence of 10 eq of water, a rapid reaction to hydroxycarbonyl **16** and hydrocarbonate **17** in approximately 1:1 ratio is observed. The formation of **16** and **17** from **9**, CO_2 and H_2O would explain efficient two electron reduction of CO_2 in the photolysis of **12**, if **12** would reduce CO_2 under formation of **9**, CO and H_2O. The varying ratio of **16** and **17** in kinetic analysis

of photolysis of **12** under CO_2 (Chapter 2.4.1) indicates a different mechanism with initial formation of **16** and subsequent conversion of initial product **16** to **17** due to follow-up photochemistry.

Since photochemical reactivity of **9** is not considered in these control experiments, kinetic measurement on photochemical carbon dioxide reduction by **12** in the presence of **9** was performed to ultimately rule out **9** as intermediate in the formation of hydroxycarbonyl **16** (Figure 116). NMR spectroscopic monitoring of the photolysis of **12** under CO_2 atmosphere in the presence of 0.75 eq **9**, essentially shows concurrent photochemical conversion of **12** to **16** and **17** as well as bimolecular CO_2 reduction by **9** to **26** and **27**. As shown in Figure 116, all species involved building up in significant concentration can be clearly identified by comparison with authentic samples and are plotted as *c vs. t* in Figure 117. Determination of the initial rate of conversion of **12** shows that a significant drop of the reaction rate results from addition of **9**. The retardation of the rate further relates to the amount of added **9** as determined from experiments with varying c_0(**9**), therefore ruling out **9** as intermediate in the formation of **16** (Figure 118).

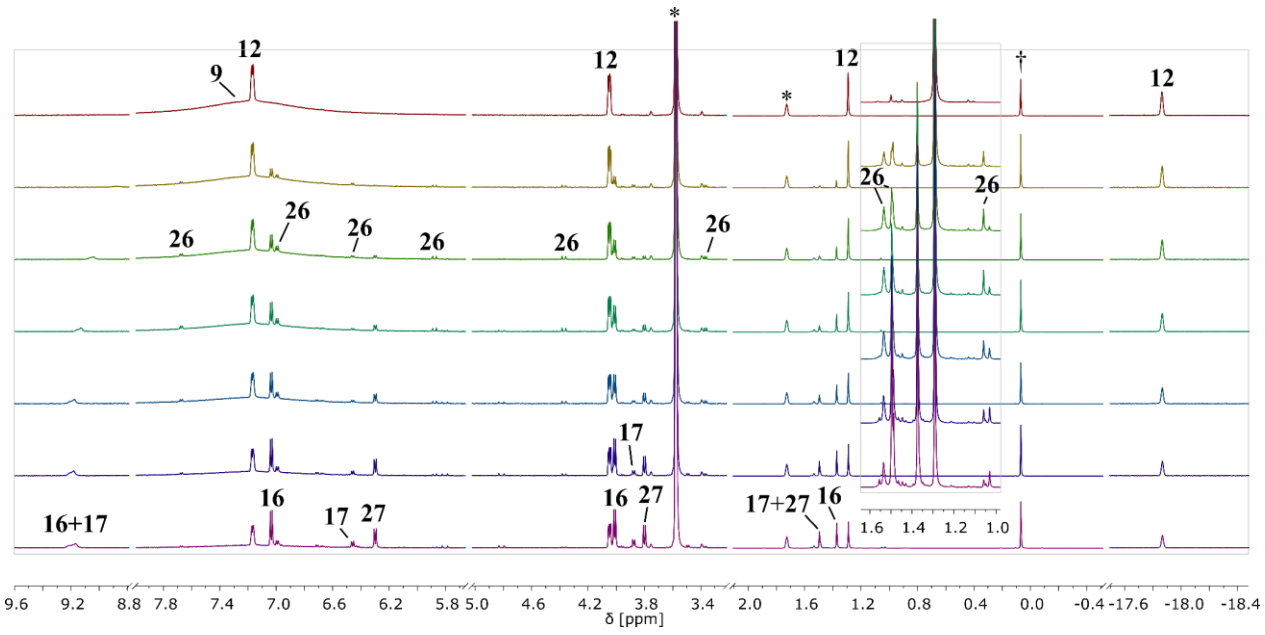

Figure 116: $^1H\{^{31}P\}$ NMR spectra of photolysis ($\lambda_{exc.}$ > 305 nm) of a solution of **12** in THF-d_8 at $p(CO_2)$ = 1 atm in the presence of 0.75 eq of **9** showing the reaction progress between (top) t = 0 min and (bottom) t = 60 min (*denotes THF-d_8; †denotes TMS_2O).

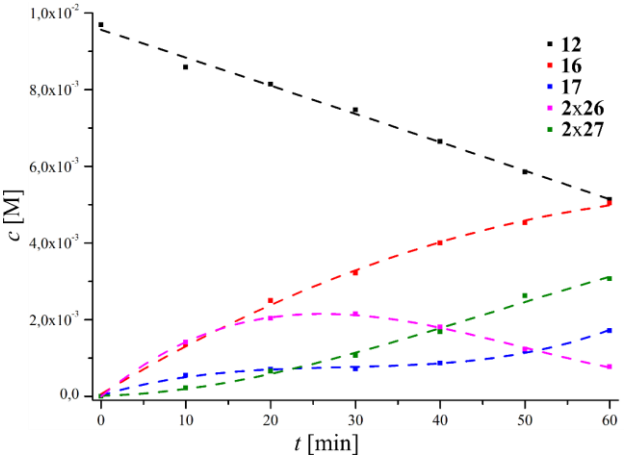

Figure 117: Plot of *c vs. t* for the photolysis (λ > 305 nm) of **12** at $p(CO_2)$ = 1 atm in the presence of 0.75 eq of **9** (lines are exponential fits as guide for the eye).

The rate of formation of **16** follows this trend and the selectivity in CO_2 reduction by **9** is unaffected by photolysis, as increasing formation of dimeric species **26** and **27** are observable upon increasing c_0(**9**). Conversion of **26** to **27** can be accurately followed in these measurements, confirming the mechanism of **27** formation proposed earlier (Figure 118). The formation of Ni^I carbonyl **22** in the photolysis of **12** under CO_2 is attributed to underlying conversion of **12** to **9** and subsequent coordination of CO which is released upon formation of hydrocarbonate **17** from initial photoproduct **16**, rather than **22** playing a role in formation of **16**.

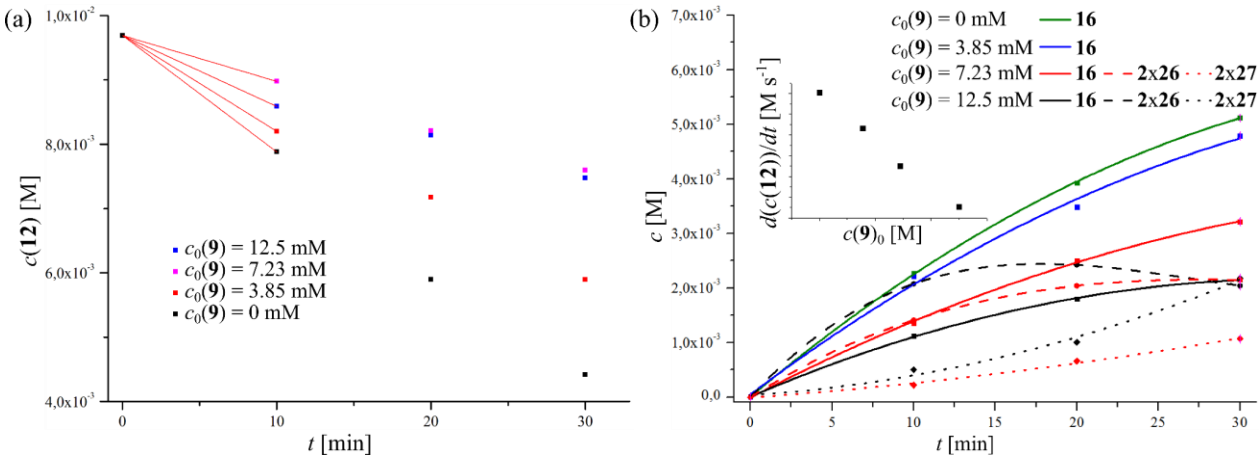

Figure 118: (a) Plot of *c*(**12**) *vs. t* for the photolysis ($\lambda_{exc.}$ > 305 nm) of **12** at pCO_2) = 1 atm in the presence of different c_0(**9**). (b) Plot of *c vs t* for **16**, **26** and **27** and initial rate $d(c(\mathbf{12}))/dt$ *vs.* *c*(**12**). Rates determined at c_0(**9**) = 0 show deviation from the results discussed in Chapter 2.4.1 due to exchange of the Xe arc lamp.

2.4.7 H/D Exchange of [NiH(^{tBu}P=N=P)] (12) with Substrates upon Photolysis

Photoacidic behavior is a well-known phenomenon upon excitation of a molecule and the *Förster cycle* represents an early model to predict the thermodynamics of such a process.[330] Here, a square-scheme

assumption predicts the influence of photoexcitation on the driving force for proton transfer based on the excitation energy $\tilde{\upsilon}$ of the conjugate acid and base (eq. (53)).

$$\mathrm{p}K_\mathrm{a}^* - \mathrm{p}K_\mathrm{a} = (\tilde{\upsilon}_\mathrm{base} - \tilde{\upsilon}_\mathrm{acid}) \frac{hc}{k_\mathrm{B}T} \tag{53}$$

While numerous organic photoacids like phenol derivatives are reported, detailed investigations of excited state proton transfer in coordination compounds are rare. H/D exchange of Ir^{III} hydride $[IrH(bpy)(Cp^*)]^+$ upon photolysis in the presence of methanol-d_1 was observed by *Guldi* and *Fukuzumi* and can be rationalized based on photoacidic behavior.[284,285] Further, a strong influence of photoexcitation on homo-and heterolytic Ir-H bond scission is reported by *Miller* based on a cube scheme consideration (Chapter 2.1.6).

Formation of photoproduct **PP** upon excitation of Ni^{II} hydride **12** prohibits reactivity prediction based on the *Förster cycle*. Examining of the excited state exchange of **12** nevertheless is of great interest to get further insight into the reactivity of **PP**, which might be formed reversibly as discussed in Chapter 2.4.5. Initially, photolysis of **12** was performed in the presence of approximately 10 eq ^{t}BuOD to probe for acidic behavior of **PP**. While small quantities of products including Ni^I **9** can be observed in this reaction, **12** remains largely unaffected with no detectible deuterium incorporation at the hydride position derived by ^{2}H NMR spectroscopy. Starting from **12-D** and ^{t}BuOH, a small hydride resonance can be detected in ^{1}H NMR spectroscopy upon irradiation as shown in Figure 119. While these two experiments seem contradictory at first, the extend of H/D exchange is low as evident from the ^{1}H NMR spectrum and might result in a resonance which is too weak to allow for detection in ^{2}H NMR spectroscopy. The low H/D exchange upon photolyzing **12**/**12-D** in the presence of ^{t}BuOH/D as acid proceeds on a slower timescale than reactivity of **12** with CO_2. Nevertheless, the presence of H/D exchange can be regarded as indication for protic reactivity of **PP**.

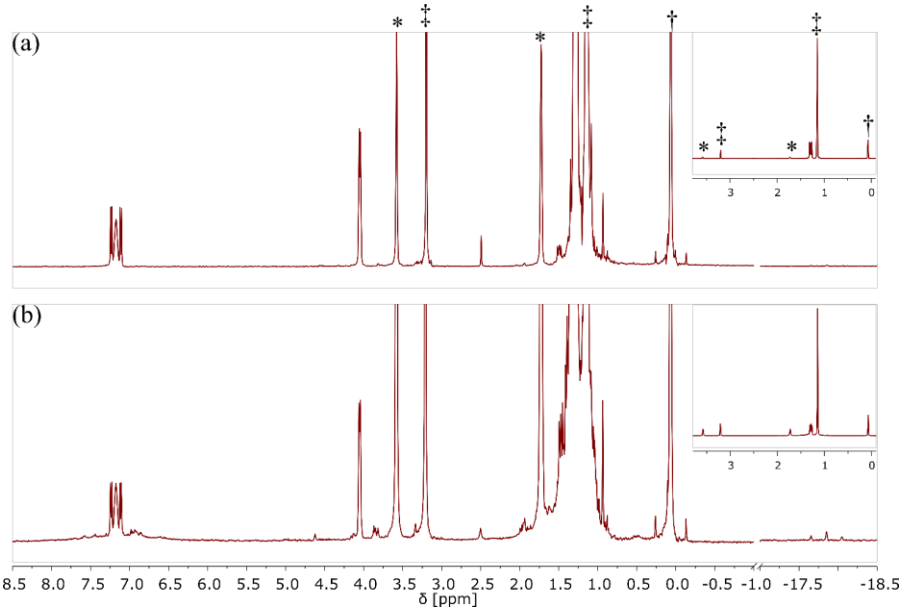

Figure 119: ^{1}H NMR spectra of a solution of **12-D** in THF-d_8 in the presence of ^{t}BuOH (a) before and (b) after 2 h photolysis ($\lambda_{exc.}$ > 305 nm).

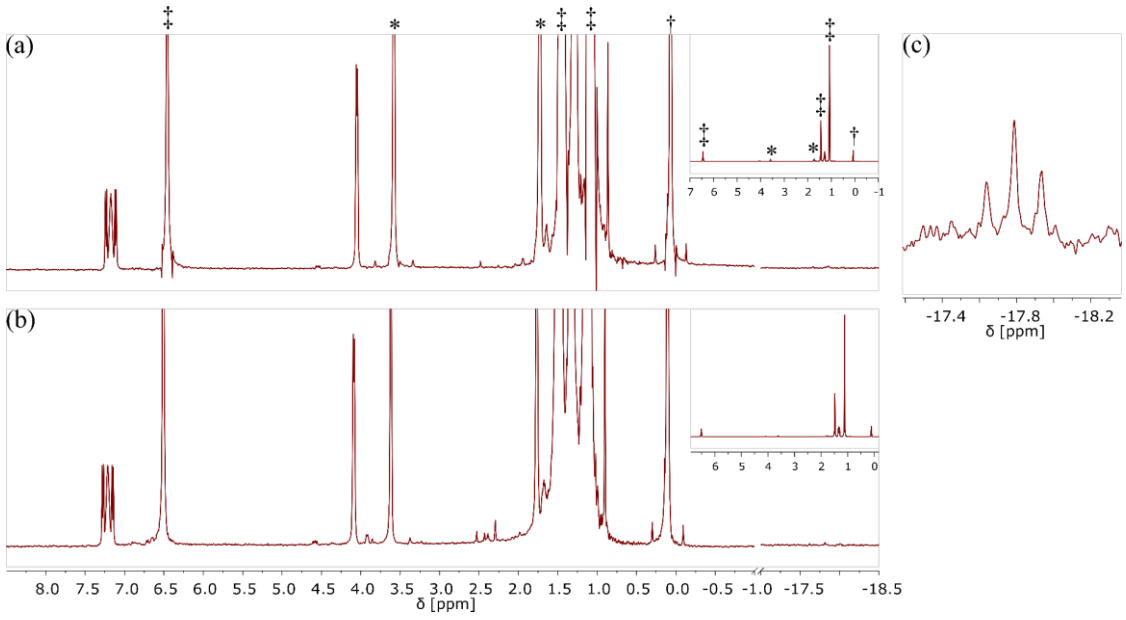

Figure 120: ^{1}H NMR spectra of a solution of **12-D** in THF-d_8 in the presence of TEMPO-H (a) before and (b) after 2 h photolysis ($\lambda_{exc.}$ > 305 nm). (c) ^{2}H NMR spectrum of a solution of **12** in THF-d_8 in the presence of TEMPO-D after 3.5 h photolysis ($\lambda_{exc.}$ > 305 nm)

Turning to TEMPO-H as substrate for exchange experiments, barely detectable hydrogen incorporation into **12-D** is observed ^{1}H NMR spectroscopically upon photolysis (Figure 120). ^{2}H NMR spectroscopy of the experiment starting from **12** and TEMPO-D however clearly shows the presence of a deuteride ligand. In contrast to illumination in the presence of ^{t}BuOH, no formation of Ni^I **9** can be observed which indicates formation of **12**/**12-D** from **9** and TEMPO-H/D. Therefore, the observed H/D exchange in the presence of

TEMPO-H is best interpreted as ground state reactivity of photochemically generated **9** with the substrate. The reactivity of isolated **9** with TEMPO-H/D was not investigated, however $\Delta G_{HAT,MeCN}$(TEMPO-H) = 66.5 kcal·mol^{-1} is comparable to reported metal hydrogen BDFEs.[4,122]

2.4.8 Photochemical Reactivity of [NiH(^{tBu}P=N=P)] (12) with Carbon Monoxide

While detailed studies of the role of Ni^I in abnormal CO_2 insertion to **16** suggest **9** as product of thermal reactivity of the photoproduct **PP** in the absence of CO_2, formation of a reduced metal center conceptually makes sense given the prominent role of low-valent Ni in CO_2 reduction, including [NiFe] CODH (Chapter 2.1.3).[167]

Aiming for trapping of such a low-valent intermediate, photolysis of **12** under carbon monoxide atmosphere was performed. While no detectable conversion of **12** at *p*(CO) = 1 atm takes place over night without irradiation, upon photolysis ($\lambda_{exc.}$ > 305 nm) formation of Ni^0 tricarbonyl [Ni(CO)$_3${κ*P*-(^{tBu}P=N=P)] (**28**) is observed as main species among several side products. NMR spectroscopic monitoring of the reaction progress, initially reveals selective formation of **28** as shown in Figure 121. Importantly, the reaction is finished after 1.5 h and therefore proceeds on the same timescale as CO_2 activation to **16**, unlike formation of **9** under argon. Free ligand **13** can be identified by $^{31}P\{^1H\}$ NMR spectroscopy in the reaction mixture finally obtained. The presence of an additional high field shifted resonance in the $^{31}P\{^1H\}$ NMR spectrum and several broad resonances in the NH region (δ = 8–9 ppm) of the ^1H NMR spectrum suggest, that other products form *via* N-H bond formation and partial decoordination of the pincer.

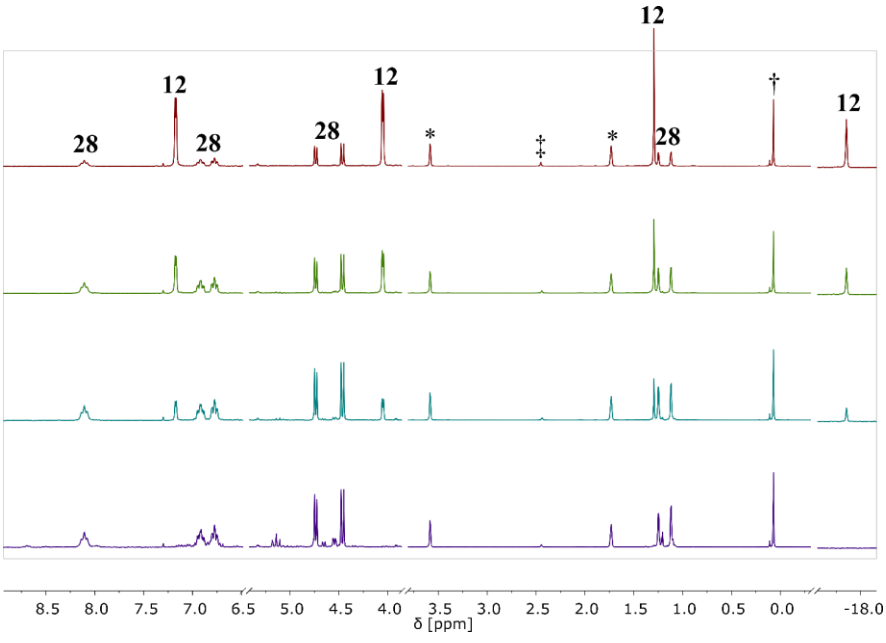

Figure 121: $^1H\{^{31}P\}$ NMR spectra of photolysis ($\lambda_{exc.}$ > 305 nm) of a solution of **12** in THF-d_8 at *p*(CO) = 1 atm after (top) 10 min, (upper middle) 20 min, (lower middle) 30 min and (bottom) 90 min (*denotes THF-d_8; †denotes TMS_2O; ‡denotes water).

Interestingly, upon evaporation of the solvent and redissolving the residue, starting material **12** is reformed, indicating oxidative addition of the N-H bond at the metal center upon displacement of carbonyl ligands (Scheme 58). Lability of the carbonyl ligand is further corroborated by LIFDI-MS analysis which shows *m/z* = 443.4, corresponding to [**28**-2(CO)]$^+$.

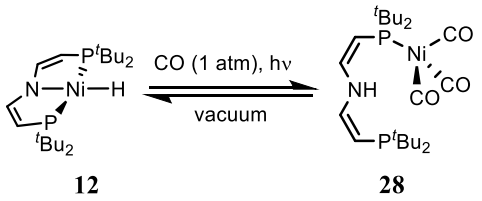

12 **28**

Scheme 58: Photochemical reactivity of Ni^{II} hydride **12** with carbon monoxide.

As in bridged carboxylate **26**, the dangling phosphine in **28** gives rise to a high shifted $^{31}P\{^1H\}$ NMR resonance at δ = -5.2 ppm, however no P-P coupling to the metal coordinate phosphorous donor at δ = -39.3 ppm is observed. The absence of higher order coupling effects in the ^1H NMR spectra (Figure 122a), combined with the additional H-H coupling between the backbone protons and the N-H, results in a spectrum close to what is observed for free ligand **13** (Figure 42).

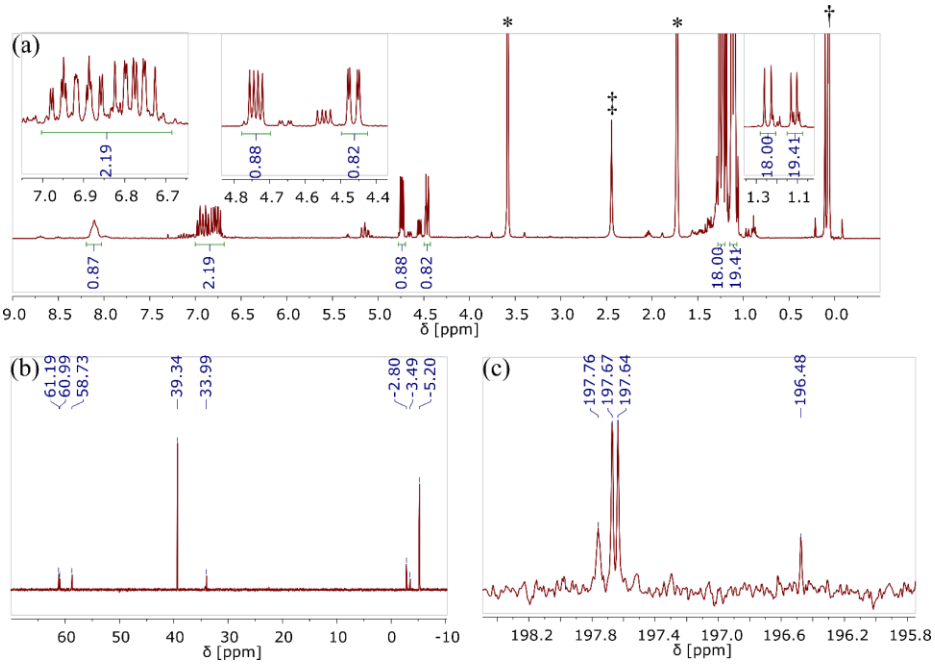

Figure 122: (a) ^1H, (b) $^{31}P\{^1H\}$ and (c) $^{31}C\{^1H\}$ NMR spectra of photolysis (λ_{exc} > 305 nm) of a solution of **12** in THF-d_8 at p(CO) = 1 atm after 90 min (*denotes THF-d_8; †denotes TMS_2O; ‡denotes water).

In both cases the N-H proton gives rise to a broad resonance in the low field of the ^1H NMR spectrum. Selective decoupling of the ^1H NMR spectroscopic resonances allows for assignment of the observed signals to both pincer arms. $^{13}C\{^1H\}$ NMR spectroscopy of **28** reveals a strong doublet at δ = 198.5 ppm for all

three carbonyl ligands with $^2J_{CP}$ = 3.8 Hz, indicating rotation around the Ni-P axis on the NMR timescale. While the coupling constant is significantly smaller than in both reported carbonyl complexes **20**$^{\mathbf{BArF}}$ and **23**$^{\mathbf{Na}}$, the chemical shift of the carbonyl ligand is closer what is observed for Ni^{II} carbonyl **20**$^{\mathbf{BArF}}$ which can be attributed to the strongly electron withdrawing ligands in tricarbonyl **28**.

Infrared spectroscopic analysis of *in* situ generated **28** confirms the presence of a N-H bond resonating at $\tilde{\upsilon}$ = 3316.5 cm^{-1} (Figure 123a). The carbonyl ligands give rise to a medium $\tilde{\upsilon}(A_1)$ = 2062.7 cm^{-1} and a strong $\tilde{\upsilon}$(E) = 1987.9 cm^{-1} band, as is observed for C_3 symmetric [Ni(CO)$_3$L] complexes in solution.[331] $\tilde{\upsilon}(A_1)$ is close to reports on [Ni(CO)$_3$P^{t}Bu$_3$], however for comparison of the donating properties of free ligand **13** with the *Tolman* electronic parameter of other ligands, an IR measurement in dichloromethane would have to be performed. The presence of two additional absorptions between $\tilde{\upsilon}$ = 1900 and $\tilde{\upsilon}$ = 2000 cm^{-1} suggests the presence of additional carbonyl complexes, as indicated by NMR spectroscopy. Notably, the C-C double bond stretch in IR spectroscopic analysis of **28** is shifted to higher energy by more than $\Delta\tilde{\upsilon}$ = 100 cm^{-1} compared to Ni^0 complexes showing tridentate coordination of the pincer. Comparison with the presented nickel carbonyl redox series further shows that this effect is due to protonation of the nitrogen and change in hapticity, rather than reduction of the metal center (Figure 70b). This effect can be explained by delocalization of the formal negative charge in the deprotonated pincer ^{tBu}P=N=P and therefore population of π* orbitals.

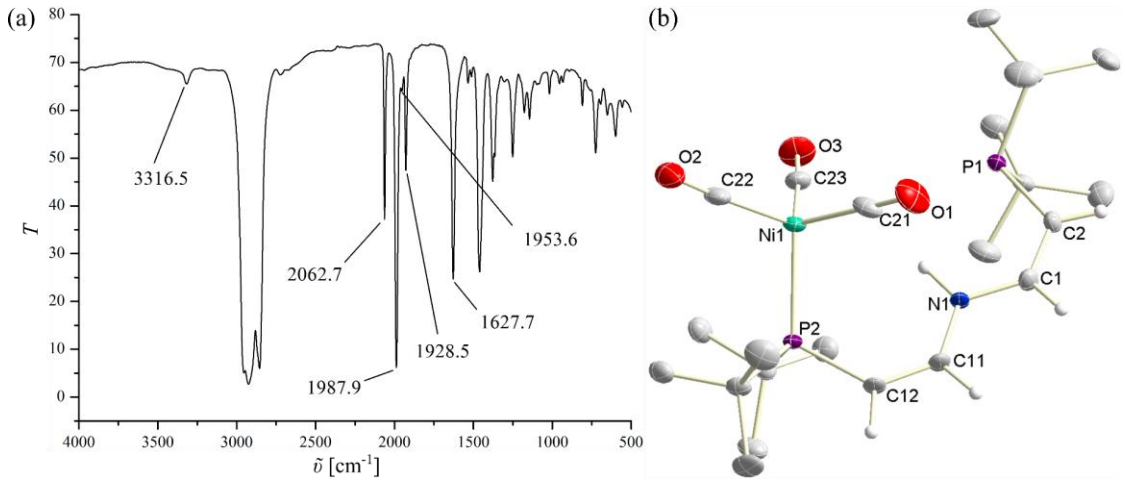

Figure 123: (a) Solid state structure of **28** determined by X-ray diffraction. Thermal ellipsoids are drawn at the 50% probability level. Selected hydrogen atoms are omitted for clarity. (b) Infrared Spectrum of **28** in nujol emulsion obtained from the reaction mixture of photolysis (λ_{exc} > 305 nm) of **12** at p(CO) = 1 atm.

In agreement with reduction to Ni^0, X-ray diffraction reveals near-perfect tetrahedral coordination of **28** with τ_4 = 0.960, which contrasts with Ni^0 carbonyl **23**$^{\mathbf{K}}$ (τ_4 = 0.638) showing significant planarization due to rigidity of the pincer ligand (Figure 123b). The C-O bond length averages to d(C-O) = 1.140 Å confirming the low π-backbonding in **28** due to the presence of three carbonyl ligands (**23**$^{\mathbf{K}}$: d(C-O) = 1.1863(15) Å).

As indicated by NMR spectroscopy, both vinyl moieties in **28** show *trans*-configuration, confirming the configurational retention upon decoordination of the phosphine observed in bridging carboxylate **26** and free amino diphosphine **13**. Nevertheless, steric pressure from {Ni(CO)$_3$} coordination results in mild out-of-plane bending of the pincer ligand apparent from φ(P2-C12-C2-P1) = -15.852°. While IR spectroscopy indicates significant strengthening of the C-C double bond in **28** compared to complexes containing tridentate pincer ligands presented in this thesis, no such effect is visible in the C-C bond length (d(C1-C2) = 1.337(4) Å; d(C11-C12) = 1.341(4) Å).

2.4.9 Photochemical Reactivity of [NiH($^{t\text{Bu}}$P=N=P)] (12) at Low Carbon Dioxide Concentration

In Chapter 2.4.1 is shown, that variation of $p(CO_2)$ can be utilized to study the mechanism of formation of **16**. Considering the solubility of CO_2 in THF at these conditions and c_0(**12**) shows that pseudo first-order requirements are fulfilled and comparison of the initial rate at different $p(CO_2)$ shows no effect. Photolyzing **12** in the presence of stoichiometric amounts of CO_2 however greatly affects the outcome of the experiments as will be discussed in the following.

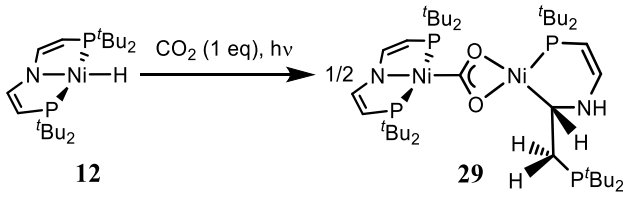

Scheme 59: Photochemical reactivity of Ni^{II} hydride **12** at low CO_2 concentration.

Performing irradiation of **12** in the presence of 1 eq of CO_2 in THF-d_8 results in retardation of both, formation of **16** and **17**. However, upon reaching complete conversion of starting material, formation of Ni^{I} **9** makes a significant contribution accompanied by formation of an asymmetric species [($^{t\text{Bu}}$P=N=P)Ni(*1 κC,2 κ^{2}O,O'*-CO_2)Ni(*κ^{2}P,C*-^{t}Bu$_2$PCHCHNHCHCH$_2$P^{t}Bu$_2$)] (**29**) showing four ^{31}P{^{1}H} NMR resonances indicating a dimeric structure. Changing the solvent to C_6D_6 results in more efficient formation of **29** which allows for isolation of the substance. Based on available data at atmospheric pressure ($c(CO_2)^{THF}$ = 0.34 mol/L; $c(CO_2)^{benzene}$ = 0.11 mol/L), the solubility of CO_2 in THF is expected to be higher than in benzene at these conditions.[314] Since the formation of **29** is highly dependent on $c(CO_2)$, this serves as explanation of the solvent dependent selectivity in formation of **29**.

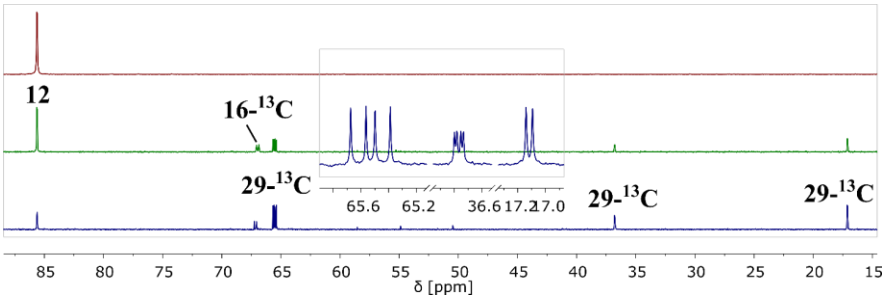

Figure 124: $^{31}P\{^{1}H\}$ NMR spectra of photolysis ($\lambda_{exc.}$ > 305 nm) of a solution of **12** in THF-d_8 in the presence of 1 eq of $^{13}CO_2$ at (top) t = 0, (middle) t = 1 h and (bottom) t = 2 h.

$^{31}P\{^{1}H\}$ NMR spectroscopic analysis of **29-^{13}C** allows for several key features on the species' structure to be assigned: Two resonances at $\delta \approx 65$ ppm show strong C-P coupling with $^{2}J_{PC}$ = 18.0 Hz and $^{2}J_{PC}$ = 17.8 Hz suggesting a κC bound carboxylate as in related **26** and hydroxycarbonyl **16** (Figure 124). The high field shift of the signal at δ = 36.8 ppm suggests a non-chelating pincer as in Ni^0 tricarbonyl **28** (δ = 39.3 ppm) or a 4/6 membered ring involving a chelating pincer, resulting in the absence of the low field shift commonly observed in 5-membered coordination. The resonance at δ = 17.1 ppm lies close to the reported value for parent amino diphosphine $^{tBu}PN^{H}P$ and indicates a CH_2 group attached to a dangling phosphine, not coordinated to the metal center. In line with this assignment, the resonance at δ = 36.8 ppm shows weak carbon coupling with $^{3}J_{PC}$ = 3.0 Hz to the bridging carboxylate while the dangling phosphine lacks carbon coupling. As in **26**, long range P-P coupling with $^{4}J_{P}$ = 7.6 Hz is present indicating bidentate, rather than monodentate coordination.

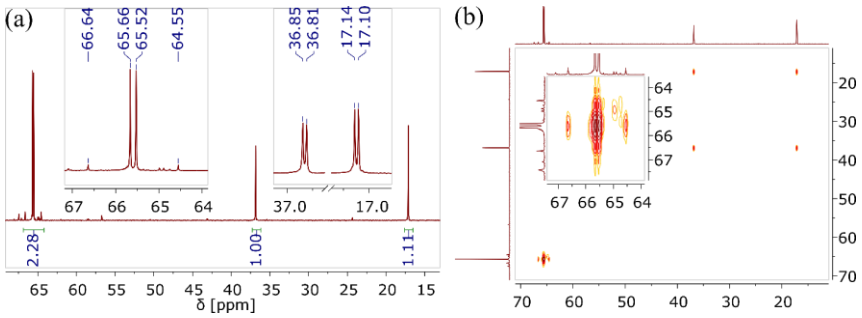

Figure 125: (a) $^{31}P\{^{1}H\}$ and (b) $^{31}P,^{31}P$ COSY NMR spectra of **29** in C_6D_6.

Complete NMR spectroscopic analysis of isolated **29** reveals a bimetallic complex containing a carboxylate bridge and one intact {Ni(^{tBu}P=N=P)} fragment as well as a twofold reduced and protonated, κ^2P,C bound ligand on the second nickel atom. The ligand motive is closely related to carbonyl **24^{BArF}**, showing bi- instead of tridentate coordination (Chapter 2.3.4). The $^{31}P\{^{1}H\}$ NMR spectrum of **29** shows a tremendous roofing effect in the coupling of the phosphorus donors of the intact pincer, which is not resolved in $^{31}P\{^{1}H\}$ NMR spectroscopy of **29-^{13}C** and confirmed by $^{31}P,^{31}P$ COSY (Figure 125). $^{13}C\{^{1}H\}$ NMR spectra of **29** reproduces the P-C coupling for the carboxylate moiety determined by $^{31}P\{^{1}H\}$ NMR spectroscopy of

29-^{13}C and shows a doublet of triplets at δ = 228.3 ppm, close to the carboxylate observed in **26** (Figure 127a).

The nickel coordinating CH group in **29** results in a chiral carbon center, and therefore the neighboring CH_2 group has diastereotopic hydrogen substituents. Since **29** has C_1 symmetry, this results in a total of 18 resonances in the ^{1}H NMR spectrum (Figure 126). While the threefold coordinating pincer ligand shows two ^{31}P{^{1}H} NMR spectroscopic resonances and each ^{t}Bu group gives an individual signal in the ^{1}H NMR spectrum, the signals of both pincer vinylene moieties cannot be distinguished in the ^{1}H NMR spectrum and give two overlapping signals. Selective decoupling at δ = 65.5 ppm in the ^{1}H{^{31}P} NMR spectrum reveal the corresponding signals and the assignment is supported by integration. Accordingly, the hydrogen atoms coupling to the remaining phosphorous atoms can be identified on the same way. While the NH is readily identified by ^{1}H,^{13}C HSQC and the vinylene moiety shows chemical shifts close to the intact pincer ^{tBu}P=N=P, assignment of the α-CH and the diastereotopic CH_2 resonances is not trivial since one signal overlaps with the ^{t}Bu resonances.

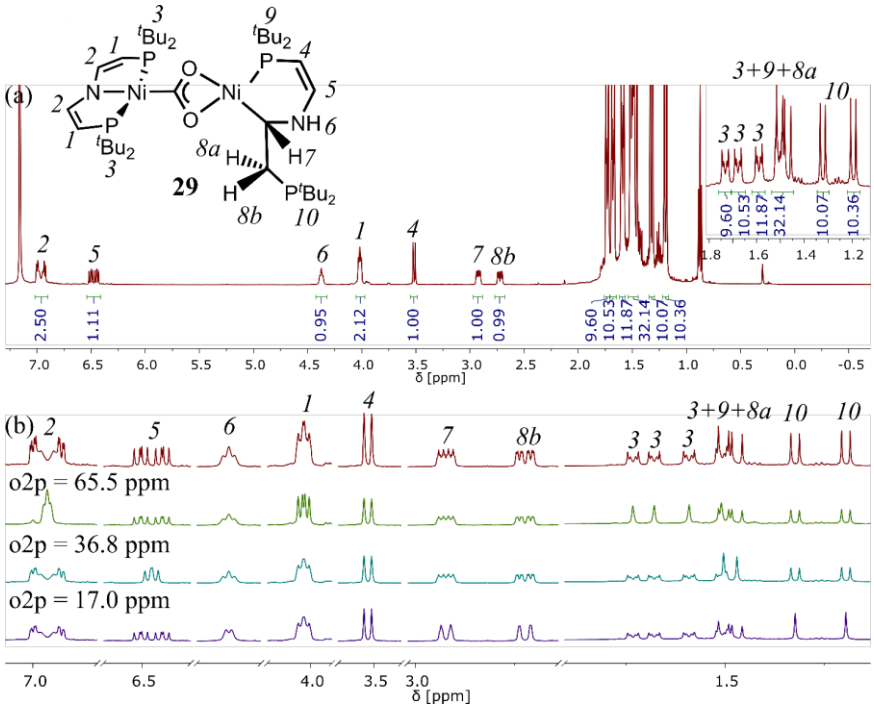

Figure 126: (a) ^{1}H and (b) ^{1}H{^{31}P} NMR spectra of **29** in C_6D_6.

Based on the chemical shift, the resonances at δ = 2.92 ppm and δ = 2.72 ppm in the ^{1}H NMR spectrum can be assigned to this aliphatic moiety of **29**. The ^{1}H,^{13}C HSQC NMR spectrum shows that signal *7* corresponds to the α-CH and *8b* is diastereotopic since they differ in phase (Figure 127b, see Figure 127a for the ^{13}C{^{1}H} NMR resonances). The ^{1}H,^{1}H COSY NMR spectrum shows a strong cross peak at δ = 1.47 ppm to the second diastereotopic proton *8a* for both signals *7* and *8b*. Additionally, a ^{1}H,^{1}H-NOESY contact is observed

at the same position (Figure 127d). Given the distance to the ^{t}Bu group *9* overlapping with *8a*, such a cross peak would not be observed to *9*. Selective decoupling in the $^{1}H\{^{31}P\}$ NMR spectrum further allows for determination of the coupling constant $^{3}J_{HH}$ = 12.4 Hz for the coupling between *7* and *8a*, suggesting an *anti*-conformation of these protons. In line with this assignment, $^{3}J_{HH}$ = 1.9–2.1 Hz for the coupling between *7* and *8b* is much smaller.

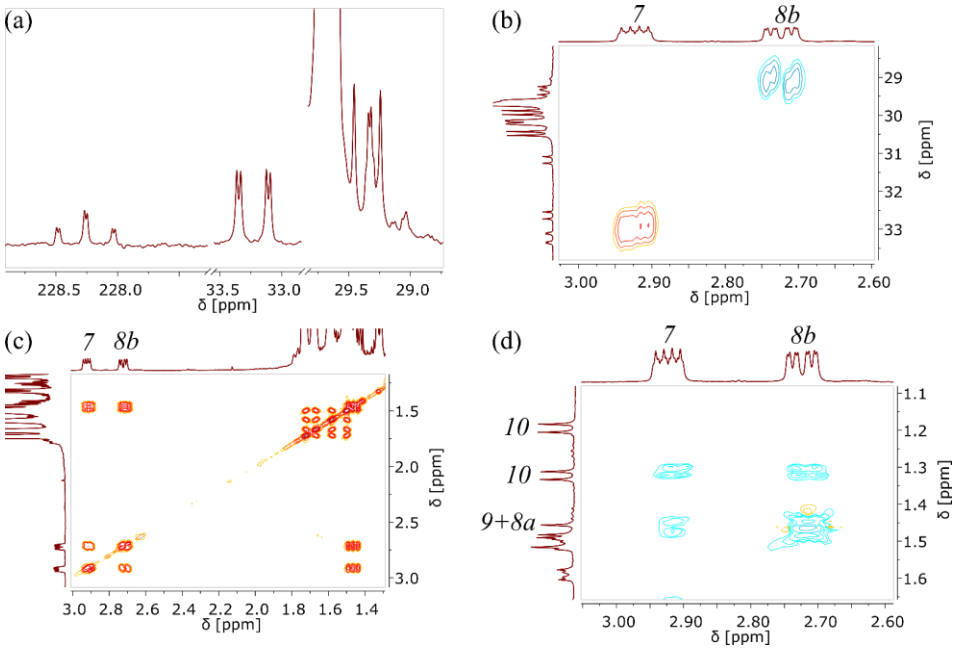

Figure 127: (a) $^{31}C\{^{1}H\}$ (b) $^{1}H,^{13}C$ HSQC, (c) $^{1}H,^{1}H$ COSY and (d) $^{1}H,^{1}H$ NOESY NMR spectra of **29** in C_6D_6.

X-ray diffraction of crystalline **29** confirms the structural assignment with the solid state structure shown in Figure 128. The different coordination sphere of both metal centers is apparent, however has just a minor effect on the geometry as comparison of τ_4 shows (Table 21). The bond metrics of the {Ni(CO_2)(^{tBu}P=N=P)} fragment closely resembles the structural data on hydroxycarbonyl **16**. In comparison, Ni2 has a shortened Ni-P bond distance. Further a rather long Ni-C distance to the alkyl is present and *d*(C41-Ni2) = 2.356(3) Å suggests major interaction with the carboxylate carbon, even though the coordination mode is best described as *κ2-O,O'*. The six membered chelate results in a widened C-C-N bond angle compared to the five membered chelate (Table 22). The C-C and C-N bond distances lie close to what is observed for a tridentate pincer, therefore suggesting delocalization of the amine lone pair which is further supported by a flat coordination geometry of N2. Both *d*(N2-C31) = 1.448(3) Å and *d*(C31-C32) = 1.543(3) Å clearly indicated single bond character. Since the *π* system does not extend over the complete six membered ring, a torsion angle of *φ*(P3-C22-N2-C31) = 22.208(2)° is present.

Table 21: Crystallographic parameters of the solid state structure of **29** determined by X-ray diffraction.

[Ni]	τ_4	*d*(Ni-C) [Å]	*d*(Ni-O) [Å]	*d*(C-O) [Å]	*d*(Ni-P) [Å]	(*α*(Ni-C-O)) [°]
Ni1	0.141	1.875(3)		O1: 1.292(3)	P1: 2.2112(8)	O1: 116.70(18)
				O2: 1.280(3)	P2: 2.2120(7)	O2: 129.29(19)
Ni2	0.208	C41: 2.356(3)	O1: 1.9500(18)		P3: 2.1305(8)	
		C31: 1.919(2)	O2: 2.0056(18)			

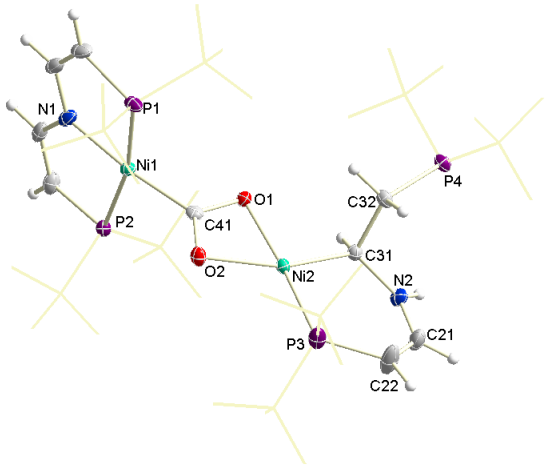

Figure 128: Solid state structure of **29** determined by X-ray diffraction. Thermal ellipsoids are drawn at the 50% probability level. Selected hydrogen atoms and solvent molecules are omitted for clarity.

Table 22: Crystallographic parameters of the solid state structure of **29** determined by X-ray diffraction.

[Ni]	*d*(C-C) [Å]	*d*(C-N) [Å]	*α*(C-C-N))	∑(*α*(N)) [°]
Ni1	1.344(4)	1.366(4)	112.2(3)	359.92
	1.346(4)	1.363(4)	112.1(2)	
Ni2	1.347(4)	1.336(4)	128.1(3)	360.0
	1.543(4)	1.448(3)	109.5(2)	

Monitoring of the reaction of **9** with equimolar amounts of CO_2 by NMR spectroscopy shows that prior to formation of **29**, hydroxycarbonyl **16** is produced. Accordingly, formation of **29** by trapping of the photoproduct **PP** with **16** was investigated. Photolysis of a mixture of isolated **12** and **16** under argon atmosphere confirms this hypothesis: Aside from Ni^I **9** and hydroxide **18**, which are the products of the individual photochemistry of **12** and **16** as shown earlier (Chapter 2.4.1 and 2.4.5), **29** is clearly identified by $^{31}P\{^1H\}$ NMR spectroscopy aside from small quantities of free ligand **13** as shown in Figure 129.

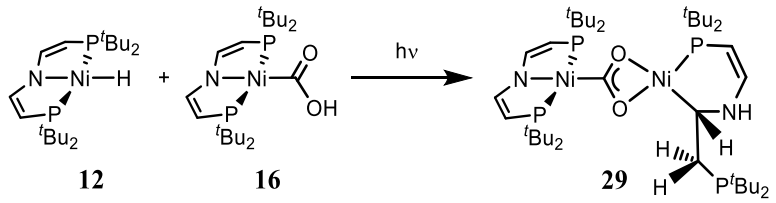

Scheme 60: Formation of bimetallic **29** by photolysis of **12** in the presence of **16**.

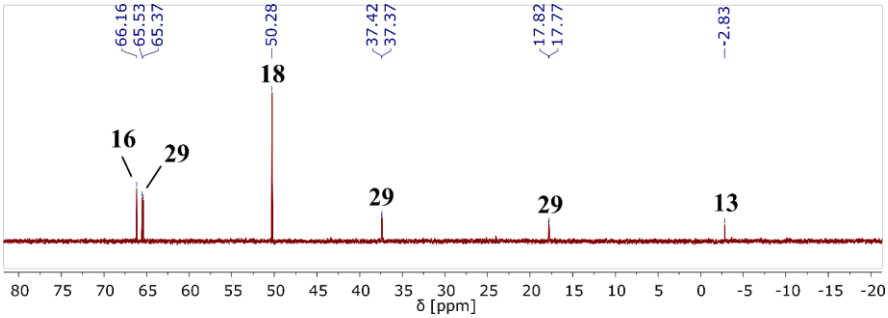

Figure 129: $^{31}P\{^{1}H\}$ NMR spectra of photolysis ($\lambda_{exc.}$ > 305 nm) of a solution of **12** in THF-d_8 in the presence of 1 eq of **16** after 7 h.

2.4.10 Structural Assignment of Photoproduct PP and CO_2 Activation Mechanism

Based on kinetic analysis of the conversion of hydride **12** to hydroxycarbonyl **16**, formation of a persistent species **PS** is postulated as the rate-determining step, which then undergoes CO_2 activation (Chapter 2.4.1). A combination of transient UV-vis- and IR-probe as well as luminescence spectroscopy allows for assignment of this persistent species **PS** as a ground state photoproduct **PP** (Chapter 2.4.2). Isotopic labeling of the hydride position further shows, that the Ni-H bond does not undergo complete homolysis over the course of the reaction (Chapter 2.4.3). A primary normal KIE suggests that Ni-H bond elongation is the main trajectory of the reaction coordinate in the RDS.

Trapping with carbon monoxide and hydroxycarbonyl **16** suggests N-H bond formation as RDS allowing for structural assignment of **PP** as a low-coordinate Ni^0 amino diphosphine (Chapter 2.4.8 and 2.4.9). While formation of Ni^0 tricarbonyl **28** can be rationalized by reaction of **PP** with carbon monoxide, bimetallic **29** can be explained by formal oxidative addition of the carboxylic acid **16** on the low-valent Ni^0 followed by migratory insertion giving the alkyl ligand in **29**. The retardation in conversion of **12** to **16** upon addition of Ni^I **9** accordingly is a result of N-H homolysis of the photoproduct **PP** by reaction with **9**, 'quenching' the photochemistry of **12** (Scheme 61).

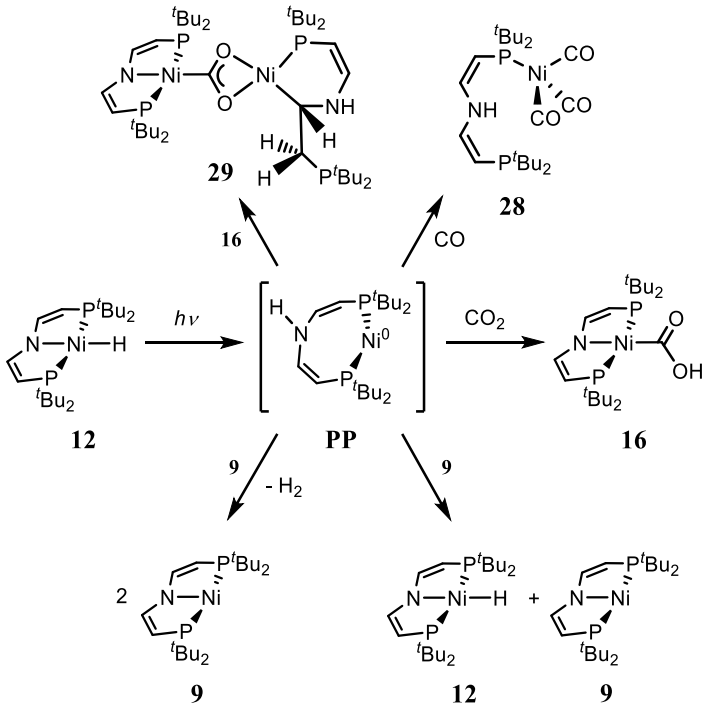

Scheme 61: Structural assignment of photoproduct **PP** based on observed reactivity.

Notably, formation of a Ni^0 amino diphosphine is the product of formal *trans*-reductive elimination, whereas thermal reductive elimination usually required *cis* arrangement of the substituents involved in bond formation.[332] Exchange studies using ^{t}BuOH hint acidic reactivity of **PP** motivating proton shift from the hydride position to the pincer nitrogen as alternative description of the process. While *Chen* and coworkers report a comparable reaction showing thermal formation of a Ni^0 dicarbonyl amino diphosphine upon reacting [NiH{N(2-C_6H_3-5-CH_3-$PR_2)_2$}] complexes with excess carbon monoxide, a mechanistic investigation is not reported.[333] Further, oxidative addition of the free amino diphosphine pincer ligand to a zero valent nickel precursor represents a common synthetic pathway for complexation.[130] Again, the report by *Ozerov* lacks a mechanistic investigation, however initial phosphine coordination followed by N-H oxidative addition of the prearranged complex seems intuitive, being the reverse of *trans*-reductive elimination. Finally, recent work by *Milstein* on dearomatized Nickel hydride [NiH{NC_6H_3-2,6-(CH_2PR_2)($CHPR_2$)] shows ligand induced metal reduction by formal proton transfer to the ligand backbone.[334]

Well-defined thermal N-H reductive elimination on transition metal hydride complexes is scarce and examples for iridium pincer complexes are reported by *Hartwig* and coworkers.[335,336] Further, *Takemoto* and *Matsuka* report on the conversion of [(Cp*Ru)$_2$(μ-NAr)(μ-H)$_2$] to [(Cp*Ru)$_2$(μ-NHAr)(μ-H)(μ-η^2:η^2-C_6H_6)] (Ar = Ph, *p*-$MeOC_6H_4$, *p*-ClC_6H_4) upon addition of benzene.[337] Kinetic investigation suggests N-H reductive elimination as RDS with an kinetic isotope effects of 1.7 and

2.1 for the methoxy and chloro substituted derivative, respectively, upon deuterium labeling of the bridging hydride ligands. Given the maximum KIE of 3.2 and 3.1 expected according to eq. (52) for these examples, a remarkable agreement with the KIE = 1.96 determined for conversion of **12** to **16** is present.

The mechanistic picture of the photophysical processes of **12** upon excitation does not include excited states on the triplet hypersurface. To investigate whether N-H reductive elimination on the singlet hypersurface is reasonable, a relaxed surface scan of the N-Ni-H angle α in **12** was performed by DFT as shown in Figure 130.[29] Initially, a steadily increasing destabilization of the singlet state results from bending the N-Ni-H angle which reaches a maximum at $\alpha \approx 50°$. N-H interaction at $\alpha < 50°$ however results in subsequent stabilization. The energetic minimum on the triplet hypersurface possesses a bend N-Ni-H geometry with $\alpha \approx 100°$. While both multiplicities show similar energies at this geometry, all remaining geometries (α = 10–170°) predict a favored singlet state rendering *trans*-reductive elimination feasible on the singlet hyper surface.

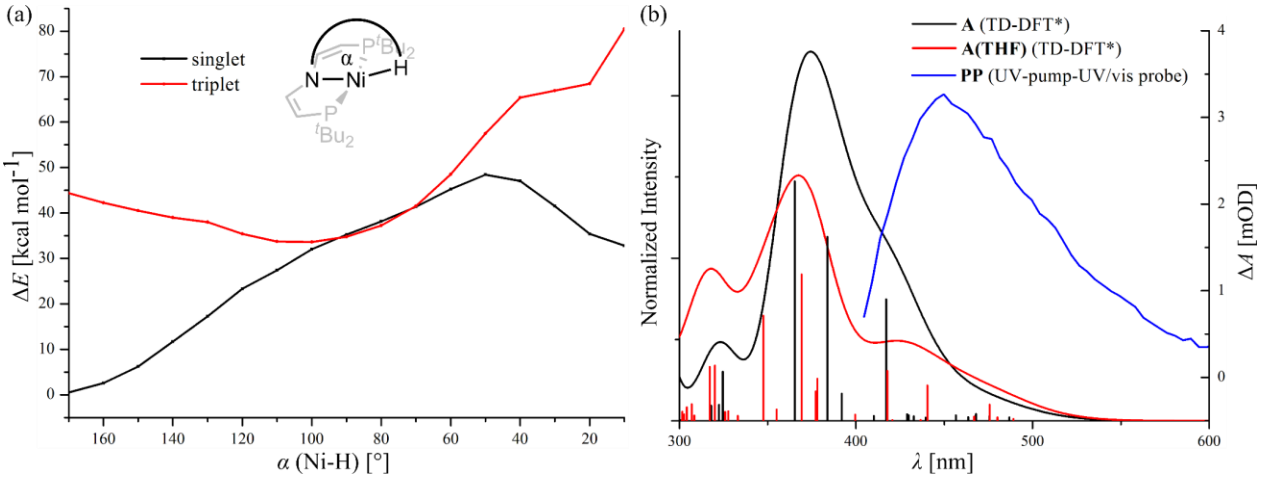

Figure 130: (a) Relaxed surface scan of *a*(N-Ni-H) on the singlet and triplet hyper surface of **12**. Geometry optimization is performed on D3(BJ)RI-*J*PBE/def2-SVP, followed by D3(BJ)-TPSS/def2-TZVP (Cosmo: THF) single point calculations. (b) Electronic spectra for **A** and **A(THF)** on ZORA-B3LYP/def2-TZVPP (Cosmo:THF) and transient absorption at t = 770 ps from UV-pump-UV-vis-probe measurement of **12** in THF.

DFT predicts a κ^2P,P coordination for Ni^0 amino diphosphine [Ni{κ^2P,P-HN(CHCHP^{t}Bu$_2$)$_2$}] **A** showing an additional N-H anagostic interaction as a result of the reducing metal center (Figure 131). The optimized geometry is located well above the ground state with ΔG = +33.2 kcal·mol^{-1} and THF solvent adduct **A(THF)** is accessible at ΔG = +35.9 kcal·mol^{-1}. In agreement with the relaxed-surface scan, reformation of **12** from **A** *via* oxidative addition shows a sizable barrier of $\Delta G^{\ddagger}$ = +13.8 kcal·mol^{-1} which is reflected by the stability of **PP** on the nanosecond time scale observed in transient spectroscopy. Notably, TD-DFT of **A** and **A(THF)** shows absorption at λ = 400–450 nm (Figure 130b) in contrast to Ni^I **9**. Considering the blue shift

[29] Computational analysis was performed by Dr. Markus Finger.

of ca. 0.4 eV observed upon comparison of the experimental absorption spectra of **12** and DFT computation (Chapter 2.4.2), the experimentally observed absorption at λ = 450 nm in the transient experiment is in good agreement with the calculated spectra of Ni^0 amino diphosphine complexes **A** and **A(THF)**.

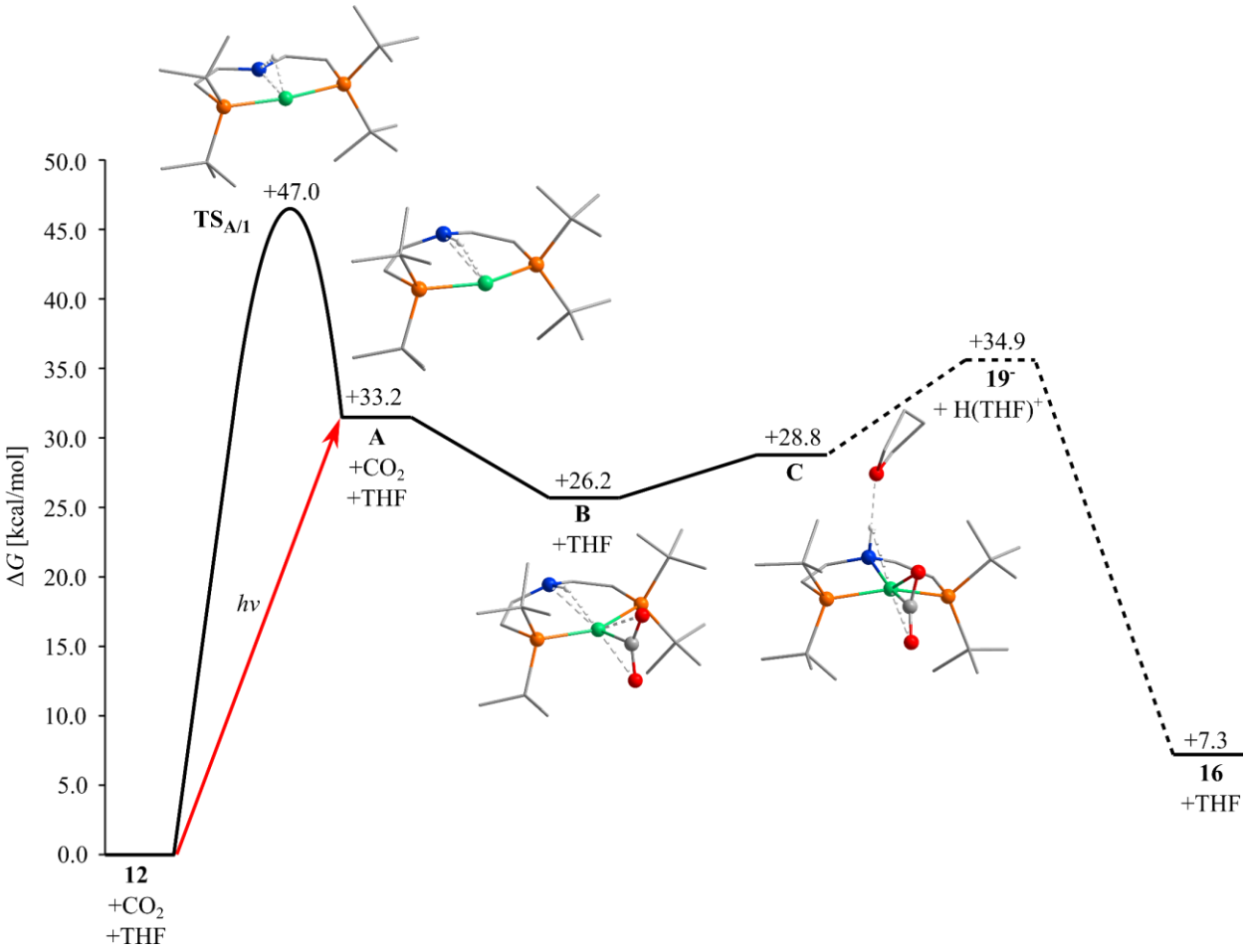

Figure 131: Computational analysis of the proposed mechanism for CO_2 activation by Ni^0 amino diphosphine **A** (D3(NJ)-RI-*J*-PBE/def2-SVP//D3(BJ)-TPSS/def2-TZVP (Cosmo:THF)) and estimation of the barrier for proton transfer from Ni^{II} carboxylate **C** to hydroxycarbonyl **16** based on experimental $pK_{ip}(\mathbf{16})^{THF}$.

While formation of **A** *via* reductive elimination is highly endergonic, incoming light of the wavelength corresponding to the absorption maximum λ = 335 nm of **12** in THF means E > 85 kcal·mol^{-1}, therefore providing sufficient energy. Once highly energetic **A** is formed, CO_2 coordination is downhill giving Ni^0 carbon dioxide adduct **B** in which the bidentate coordination of the former pincer ligand is retained and the N-H metal interaction is still present. Formation of a hydrogen bond results in in electronic and geometric rearrangement to Ni^{II} carboxylate **C** upon incorporating a solvent molecule in the system, which suggests high flexibility of the pincer ligand. Without π acceptor CO_2, no such rearrangement of the pincer ligand is observed upon solvent coordination, hinting lower metal basicity in **B** due to CO_2 coordination. Even though CO_2 coordination on **A** is exergonic, formal proton shift from the N-H position to the carboxylate makes up

for most of the driving force for formation of hydroxycarbonyl **16** from Ni^0 **A** and CO_2. This last step most likely involves significant charge-separation which DFT has difficulties to describe and therefore determination of an upper energetic limit for proton shift was performed based on $pK_\alpha(\mathbf{16})^{THF}$, assuming complete proton dissociation, *e.g.* solvent protonation giving an {$[H(THF)_X]\cdot$**19**} ion-pair.[338]

As shown in eq. (31), the equilibrium constant K_{eq} for an acid base equilibrium can be determined based on pK_a or pK_α in unpolar solvents, further requiring for a correction term which considers ion-pairing. While $pK_\alpha([H(THF)_x])^{THF} = 0$ defines the lower end of the acidity scale in that particular solvent, $pK_\alpha(\mathbf{16})^{THF} = 24.3$ was determined earlier (Chapter 2.3.2) The ion-pairing contribution is calculated using *Fuoss* equation eq. (32) based on X-ray crystallographic data for **16** ($r = 4.0$ Å) and $[H(THF)_2][CHB_{11}H_5Br_6]$ ($r = 4.3$ Å) giving the theoretical equilibrium constant $K_{eq} = 10^{-20.2}$ and therefore the free energy $\Delta G = 27.6$ kcal·mol^{-1} according to eq. (54).[339]

$$\Delta G = -\ln(K_{eq})\cdot RT \tag{54}$$

This value places the upper energetic limit for the barrier of proton transfer from THF coordinated Ni^{II} carboxylate **C** to hydroxycarbonyl **16** at $\Delta G = +34.9$ kcal·mol^{-1} with respect to the starting material and at $\Delta G = +6.1$ kcal·mol^{-1} with respect to **C**, well below the barrier of $\Delta G^{\ddagger} = 13.8$ kcal·mol^{-1} for oxidative addition of **A** to parent **12**. While detailed mechanistic investigation by kinetics and computation was performed in THF, photochemical conversion of **12** to **16** in benzene shows that THF coordination is not crucial in stabilization of intermediate**s** and that proton transfer from the pincer to the carboxylate moiety most likely does not proceed *via* solvent protonation.

2.5 Transfer of Photochemical CO_2 Activation to other Complexes and Substrates

2.5.1 Photochemical CO_2 Activation by Related Nickel Pincer Hydride Complexes

Mechanistic investigation of photochemical CO_2 activation by **12** suggests a crucial role of the pincer ligand given the MLCT type character of the electronic transition and the N-H reductive elimination upon formation of the photoproduct **PP**. Saturated Ni^{II} hydrides [NiH($^{tBu}PN^{H}P$)}]OTf (**30^{OTf}**) and [NiH(^{tBu}PNP)] (**31)** were prepared and investigation of the thermal and photochemical reactivity with carbon dioxide allows for judgement of the impact of pincer backbone oxidation on the photochemical properties of the compounds.

Complexes **30^{OTf}** and **31** can be prepared according to a procedure related to published work by the *Hanson* group for cyclohexyl substituted derivatives of **30^{OTf}** and **31**.[340] Starting from Ni^{II} bromide **2**, *in situ* protonation with triflic acid and subsequent addition of sodium tetrahydridoborate in THF solvent yields amino hydride complex **30^{OTf}**. Neutral amido hydride **31** is accessible by deprotonation with potassium *tert*-butoxide in high yield.

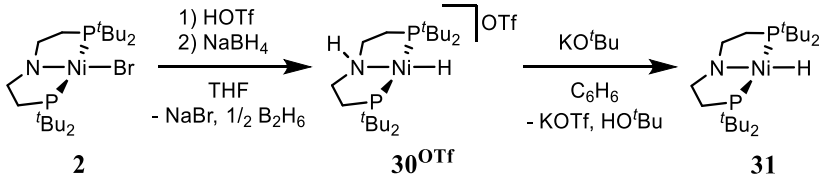

Scheme 62: Synthesis of Ni^{II} hydrides **30^{OTf}** and **31**.

Protonation of the pincer ligand in **30^{OTf}** results in a C_S symmetric compound with a mirror plane perpendicular to the pincer ligand plane, resulting in chemically different pincer backbone hydrogen atoms attached to the same carbon center. The NH proton is readily assigned by the low field shift to δ = 5.64 ppm in the ^{1}H NMR spectrum and the hydride ligand resonates at δ = -19.35 ppm with $^2J_{HP}$ = 60.1 Hz, close to what is observed for compound **12** (Figure 132). Compared to parent bromide **2**, the backbone signals of amido hydride **31** shows a low field shifted backbone resonances in the ^{1}H NMR spectrum. Again, the hydride ligand's spectroscopic signature is comparable to **12** and **30^{OTf}** with δ = -17.36 ppm and $^2J_{HP}$ = 60.5 Hz.

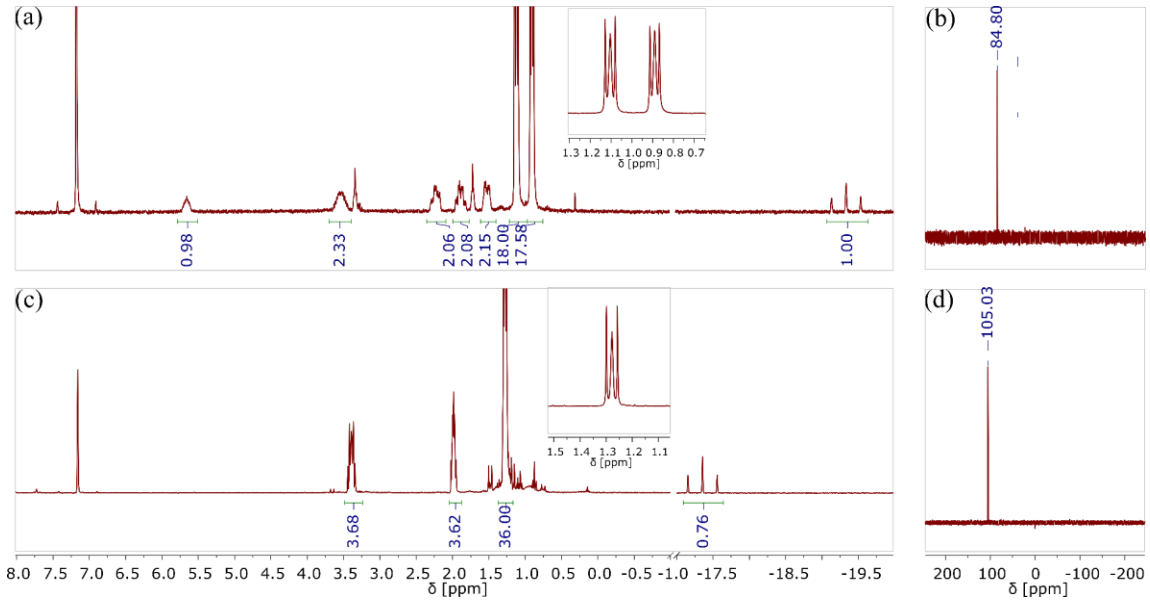

Figure 132: (a) ^{1}H and (b) $^{31}P\{^{1}H\}$ NMR spectra of **30^{OTf}** in C_6D_6 and (c) ^{1}H and (d) $^{31}P\{^{1}H\}$ NMR spectra of **31** in C_6D_6.

Comparison of the Ni-H stretch at $\tilde{\upsilon}$ = 1832 cm^{-1} (KBr) in the infrared spectrum of **31** shows a small effect of the more donating *trans* ligand compared to **12** ($\tilde{\upsilon}$ = 1850 cm^{-1}, KBr) and is close to the related compound reported by *Hanson et al.* ($\tilde{\upsilon}$ = 1811 cm^{-1}). While protonation of **12** to **14^{BArF}** results in a shift of the Ni-H stretch to $\tilde{\upsilon}$ = 1884 cm^{-1}, the effect of protonation is more severe in case of **30^{OTf}** ($\tilde{\upsilon}$ = 1900 cm^{-1}). *Hanson* reports the Ni-H stretch of the amino hydride at $\tilde{\upsilon}$ = 1886 cm^{-1}. Additionally, protonation in **30^{OTf}** gives rise to a N-H stretch at $\tilde{\upsilon}$ = 3194 cm^{-1} in the IR spectrum.

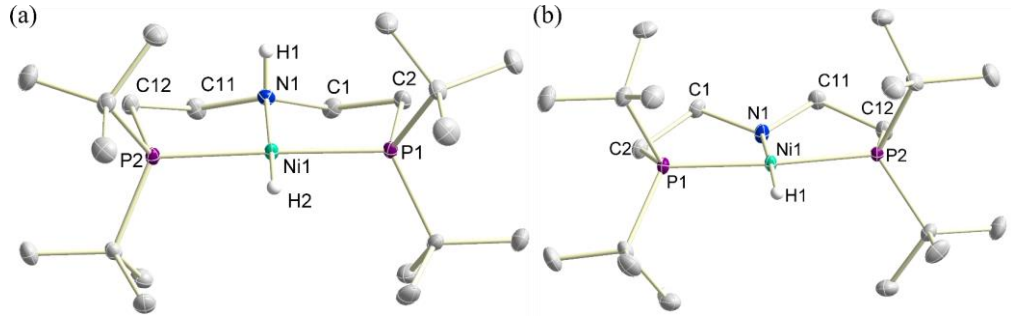

Figure 133: Solid state structure of (a) **30^{OTf}** and (b) **12** determined by X-ray diffraction. Thermal ellipsoids are drawn at the 50% probability level. Selected hydrogen atoms, solvent molecules and anions are omitted for clarity.

Table 23: Crystallographic parameters of the solid state structure of **30^{OTf}** and **12** determined by x-ray diffraction.

[Ni]	τ_4	d(Ni-H) [Å]	d(Ni-N) [Å]	$\sum(\alpha(N))$ [°]	φ(N-C-C-P) [°]
30^{OTf}	0.04	1.43(2)	1.9710(13)	339.29	43.85(15)/-43.04(16)
31	0.07	1.44(2)	1.8781(11)	352.03	37.93(13)/-35.14(13)

X-ray crystallographic analysis of **30^{OTf}** and **31** shows square-planar coordination for both compounds which is confirmed by low τ_4 values (Figure 133, Table 23). As in parent bromide **2**, the ethylene bridged pincer ligand in **31** results in a deplanarization of the amido nitrogen atom. This effect is even more pronounced in protonated **30^{OTf}** which further shows an elongated Ni-N distance due to the less donating nitrogen atom.

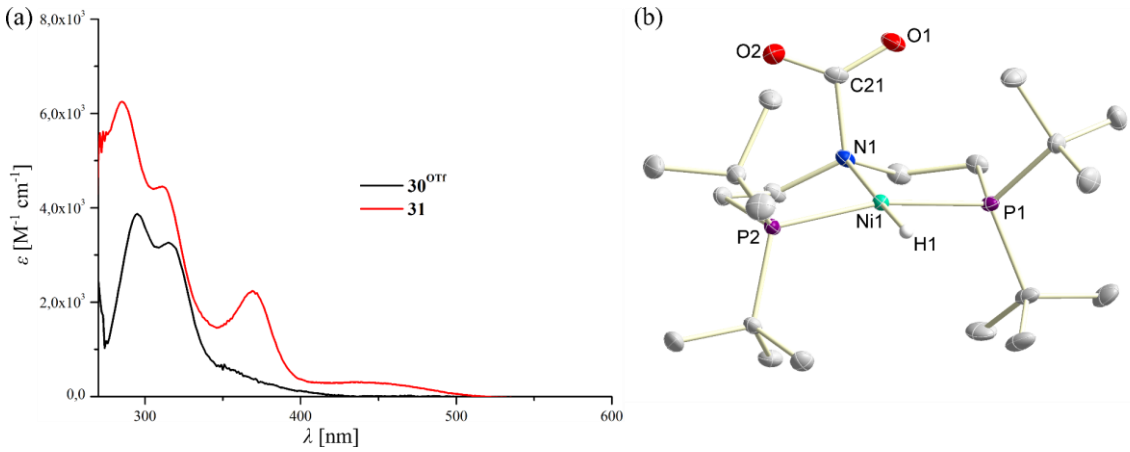

Figure 134: (a) UV-vis spectra of **30^{OTf}** and **31** in benzene. (b) Solid state structure of **32** determined by X-ray diffraction. Thermal ellipsoids are drawn at the 50% probability level. Selected hydrogen atoms are omitted for clarity.

UV-vis spectroscopic investigation of amino hydride **30^{OTf}** and amido hydride **31** reveals absorption at λ > 305 nm (Figure 134a). Comparison with hydride **12** and **14^{BArF}** containing the unsaturated pincer ligand reveals a difference in ε of approximately one order of magnitude (Figure 93). Compound **30^{OTf}** neither undergoes thermal nor photochemical reactivity with carbon dioxide. Reacting **31** with CO_2 results in immediate formation of carbon dioxide adduct [NiH{N(CO_2)($CH_2CH_2P^tBu_2$)$_2$}] (**32**) in a reversible reaction (Scheme 63). Photolysis of *in situ* generated **32** results in conversion of the starting material with no apparent NMR spectroscopic signature of the product, indicating formation of paramagnetic species.

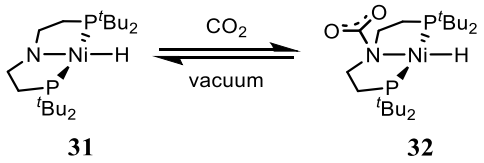

31 **32**

Scheme 63: Reversible coordination of carbon dioxide by hydride **31**.

NMR spectroscopic analysis of *in situ* generated **^{13}C-32** reveals C_{2v} symmetry, which is attributed to fast reversible binding of carbon dioxide (Scheme 63). The hydride position resonates at δ = -21.11 ppm in the ^{1}H NMR spectrum, close to parent **31**. In the ^{13}C{^{1}H} NMR spectrum, the carboxylate can be observed at δ = 168.6 ppm.

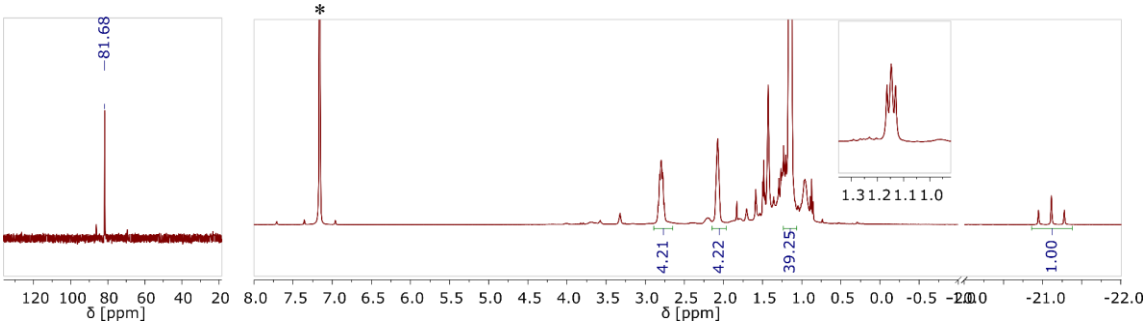

Figure 135: (a) ^{31}P{^{1}H} and (b) ^{1}H NMR spectra of *in situ* generated **^{13}C-32** in C_6D_6 (*denotes C_6D_6).

The structural identity of **32** is confirmed by X-ray diffraction (Figure 134b). Coordination of CO_2 results in a significant elongation of the Ni-N distance (*d*(Ni1-N1) = 2.0171(11) Å) and a deplanarization of the nitrogen coordination geometry as is expected for coordination of the amido fragment by a *Lewis* acid.

Ligand centered CO_2 activation is reported for several pincer metal complexes and related compounds.[341–346] While most work is limited to pyridine based ligands, *Berke* showed formation of a CO_2 adduct on an aliphatic PNP pincer complex. Using tungsten as metal center results in 1,2-addition of CO_2 along the N-W bond in contrast to exclusively ligand centered reactivity in **32**. Accordingly, the literature example shows varying C-O bond distances (*d*(C-O) = 1.283(3) Å, *d*(C-O) = 1.208(3) Å) whereas *d*(O1-C21) = 1.2262(17) Å and *d*(O2-C21) = 1.2267(18) Å are much closer in **32**. The N-C distance (*d*(N1-C21) = 1.5589(17) Å) and carboxylate bond angle (α(O1-C21-O2) = 130.78(14)°) is comparable in both cases.

Lee investigated CO_2 reduction on a related PNP nickel platform (see Chapter 2.1.4).[221,223] Initial experiments using the Ni^{II} hydride [NiH{N(2-C_6H_3-5-CH_3-P*i*Pr$_2$)$_2$}] **L$_1$** indicate similar reactivity as observed for hydride **12** (Figure 136). Strong absorption above λ = 400 nm enables efficient formation of literature-known hydroxycarbonyl [Ni(CO_2H){N(2-C_6H_3-5-CH_3-P*i*Pr$_2$)$_2$}] **L$_2$** by photolysis with visible light. While the reaction is less selective as in the conversion of **12** to **16**, the product **L$_2$** is reported to show limited stability in THF which might contribute to side product formation.[223]

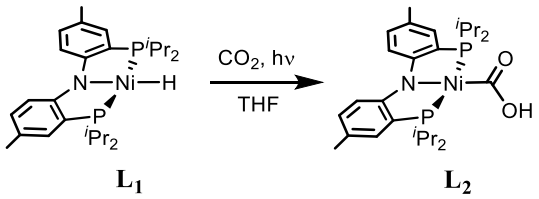

L$_1$ **L$_2$**

Scheme 64: Photochemical CO_2 activation by [NiH{N(2-C_6H_3-5-CH_3-P*i*Pr_2)$_2$}] **L$_1$**.

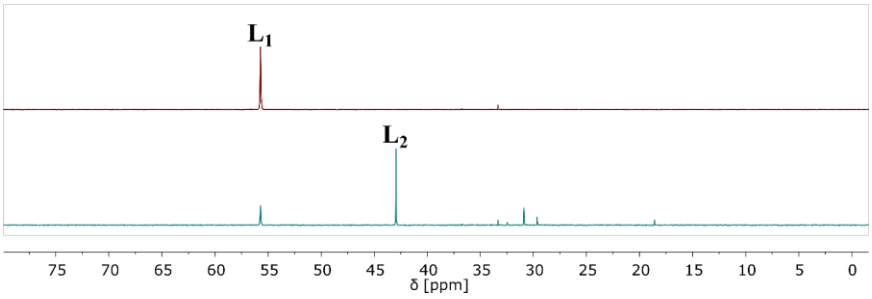

Figure 136: $^{31}P\{^1H\}$ NMR spectra of a THF solution of **L$_1$** under 1 atm CO_2 (top) before and (bottom) after 2 h photolysis ($\lambda_{exc.}$ > 420 nm).

2.5.2 Photochemical and Thermal Nickel Pincer Catalyzed Olefin Hydrogenation

Based on the results on photochemical CO_2 reduction by hydride **12**, broadening the scope of substrates was investigated. Since olefins offer a rich coordination chemistry in Ni^0 complexes, photocatalytic olefin hydrogenation is an attractive reaction. Interested in the efficiency of different nickel complexes in the hydrogenation of alkenes, screening of several potential precatalysts in the hydrogenation of model substrate styrene using 5 mol-% nickel complex was performed.

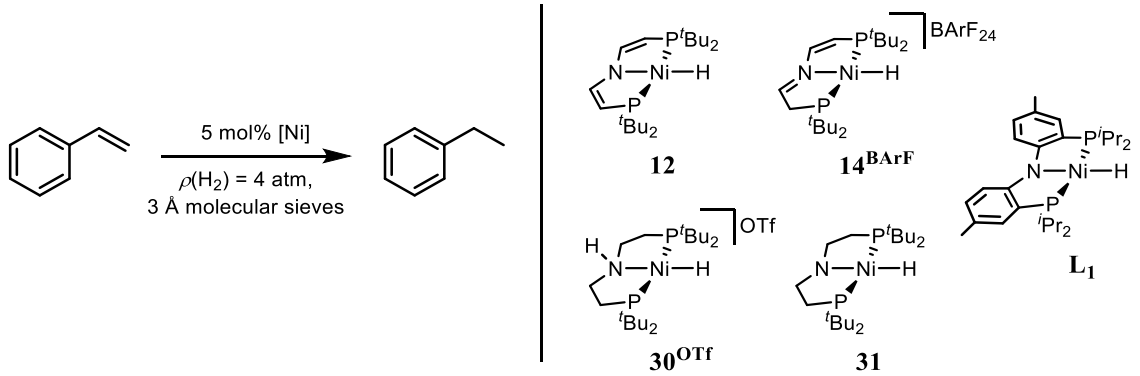

Scheme 65: Ni^{II} hydride catalyzed hydrogenation of styrene.

Table 24: Performance of different Ni^{II} hydrides in styrene hydrogenation under thermal and photochemical conditions.

Entry	Cat.	Solvent	conditions	t [h]	conversion [%]	Yield [%]
1	**12**	C_6D_6	80°C	15	1	1
2	**31**	C_6D_6	80°C	80	94	86
3	**14^{BF4}**	C_6D_6	80°C	16	100	100
4	**30^{OTf}**	C_6D_6	80°C	80	9	5
5	**L_1**	C_6D_6	80°C	16	50	48
6	**12**	C_6D_6	λ > 305 nm	16	74	69
7	**31**	C_6D_6	λ > 305 nm	15	22	13
8	**14^{BF4}**	C_6D_6	λ > 305 nm	16	6	6
9	**30^{OTf}**	C_6D_6	λ > 305 nm	15	1	1
10	**L_1**	C_6D_6	λ > 305 nm	16	-	-
11[a]	$[NiH(^{Cy}PN^{H}P)]BPh_4$	THF-d_8	80°C	24	100	100
12[a]	$[NiH(^{Cy}PNP)\}]$	THF-d_8	80°C	24	-	30
13[b]	[NiH(PBP)]	C_6D_6	*RT*	2	100	100

[a]10 mol-% catalyst as reported by *Hanson*. [340] [b]2 mol-% catalyst, $p(H_2)$ = 1 atm as reported by *Peters*.[348]

Photocatalytic olefin hydrogenation of olefins using $[MoH_4(dppe)_2]$ is reported by *Geoffrey*.[347] The Ni^{II} hydride complexes **12**, $\mathbf{14^{BF4}}$, $\mathbf{30^{OTf}}$ and **31**, as well as literature known $\mathbf{L_1}$ were investigated for catalytic activity at both, 80°C, and RT with photolysis at $\lambda_{exc.} > 305$ nm. The experiments were performed in C_6D_6 solvent giving homogeneous solutions even for the cationic hydride complexes $\mathbf{14^{BF4}}$ and $\mathbf{30^{OTf}}$. The reaction progress was determined NMR spectroscopically by integration against an internal standard (Table 24).

Complex **12** shows no conversion of styrene under thermal conditions, whereas **31** gives nearly complete conversion of the substrate with high selectivity (Table 24, entry 1 & 2). Surprisingly, amino hydride $\mathbf{30^{OTf}}$ does show significantly less activity than **31** (entry 4), contradicting the report by *Hanson*, which shows higher efficiency for the protonated cyclohexyl derivative, working in THF-d_8 solvent (entry 11 & 12).[340] Imine hydride $\mathbf{14^{BF4}}$ shows the highest activity in styrene hydrogenation at high temperature giving ethylbenzene selectively (entry 3) while $\mathbf{L_1}$ shows moderate activity (entry 5). Turning to photochemical conditions, saturated hydrides $\mathbf{30^{OTf}}$ and **31** as well as imine hydride $\mathbf{14^{BF4}}$ and $\mathbf{L_1}$ convert the substrate less efficient compared to thermal conditions (entry 7–10). In contrast, thermally inactive compound **12** is a decent photocatalyst for hydrogenation of styrene under these conditions (entry 6).

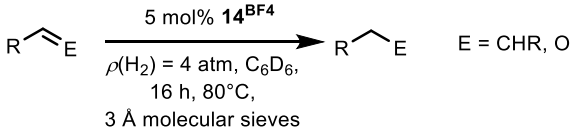

Scheme 66: Ni^{II} hydride $\mathbf{14^{BF4}}$ catalyzed thermal hydrogenation.

Table 25: Performance of $\mathbf{14^{BF4}}$ in thermal hydrogenation of alkenes and aldehydes.

Entry	Substrate.	Product	conversion [%]	Yield [%]
1			100	100
2			7	0
3	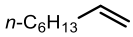	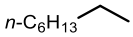	0	0
4			3	0
5		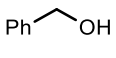	6	0

Based on this initial evaluation of the catalytic activity of different PNP Ni^{II} hydrides in styrene hydrogenation, closer investigation of imine hydride $\mathbf{14^{BF4}}$ in thermal hydrogenation and hydride **12** in photochemical hydrogenation catalysis was performed by expanding the scope of substrates. While $\mathbf{14^{BF4}}$ cleanly converts styrene at the conditions utilized, no activity in hydrogenation of 2,2-dimethylbut-3-ene,

1-octene and cyclooctadiene is observed (Table 25, entry 1–4). Turning to benzaldehyde, no product could be detected NMR spectroscopically, while stoichiometric conversion of starting material can be observed (entry 5).

Evaluation of the substrate scope for photochemical hydrogenation using **12** was performed using a 150 W LED with a peak wavelength of λ = 390 nm, therefore performing photocatalysis with visible light. As shown in Table 26, styrene is efficiently hydrogenation under these conditions (entry 1). Turning to sterically more demanding 2,2-dimethylbut-3-ene a decrease in activity is observed which is even more pronounced in case of cyclooctene (entry 2 and 4). Accordingly, in case of 1-octene internal olefins are the main product since the products of isomerization are not efficiently hydrogenated (entry 3). Finally, **12** shows moderate activity in hydrogenation of benzaldehyde forming benzyl alcohol in high selectivity (entry 5).

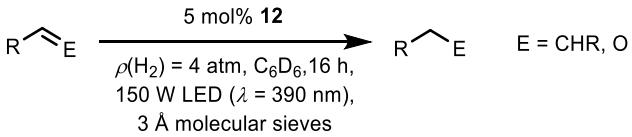

Scheme 67: Ni^{II} hydride **12** catalyzed photochemical hydrogenation.

Table 26: Performance of **12** in photochemical hydrogenation of alkenes and aldehydes.

Entry	Substrate.	Product	conversion [%]	Yield [%]
1	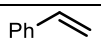		99	97
2			77	70
3[a,b]	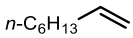	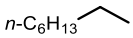	100	-
4[b]			9	-
5			30	28

[a]Internal olefins are formed in 62% yield. [b]No determination of the yield possible, due to strong overlap with the starting material in ^{1}H NMR spectroscopy.

Compound **12** represents a rare example of a homogeneous nickel based catalyst which is able to hydrogenate aldehydes. The low activity of nickel hydrides in carbonyl reduction is attributed to the lack of carbonyl insertion into the Ni-H bond.[340] While no mechanistic examination of the hydrogenation catalysis is performed, based on the mechanistic understanding of photochemical reactivity of **12** with CO_2, photochemical excitation of **12** might offer an alternate pathway for substrate activation based on N-H

reductive elimination followed by substrate coordination and subsequent intramolecular proton and electron transfer.

2.5.3 Photochemical and Reactivity of a Nickel Pincer Methyl Complex

Interested in the photochemical properties of other {Ni(^{tBu}P=N=P)} compounds, methyl complex [NiMe{N($CH_2CH_2P^tBu_2$)$_2$}] (**33**) was synthesized according to Scheme 68. NMR spectroscopic analysis of isolated **33** reveals a triplet resonance in the ^{1}H NMR spectrum at δ = -0.03 ppm with $^3J_{HP}$ = 8.2 Hz according to the methyl ligand (Figure 137). Accordingly, the carbon atom resonates at δ = -28.63 ppm with $^2J_{CP}$ = 25.5 Hz in the ^{13}C{^{1}H} NMR spectrum. X-ray crystallographic analysis reveals a Ni-C distance of *d*(Ni-C) = 1.9610(12) Å, close to reports on similar complexes by *Milstein* (Figure 138a).[342]

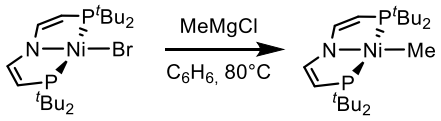

Scheme 68: Synthesis of Ni^{II} methyl complex **33**.

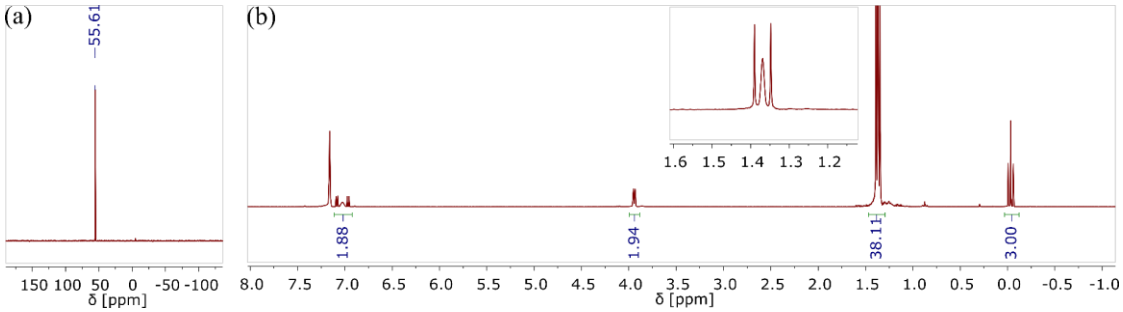

Figure 137: (a) ^{31}P{^{1}H} and (b) ^{1}H NMR spectra of **33** in C_6D_6.

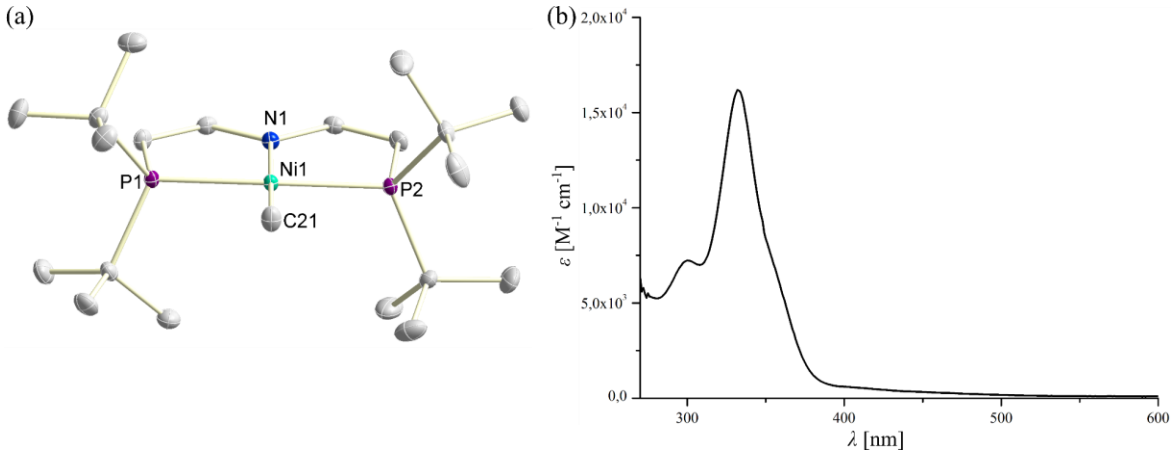

Figure 138: (a) Solid state structure of **33** determined by X-ray diffraction. Thermal ellipsoids are drawn at the 50% probability level. Hydrogen atoms are omitted for clarity. (b) UV-vis spectrum of **33** in benzene.

Compound **33** shows absorption at λ = 333 nm with an extinction coefficient comparable to hydride **12** (Figure 138b). A shoulder is present at lower energy, tailing off into the visible region and giving rise to the more intense orange color of isolated **33**.

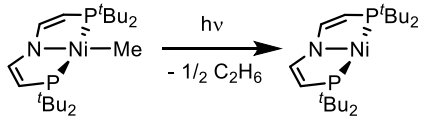

33 **9**

Scheme 69: Photochemical reactivity of Ni^{II} methyl complex **33**.

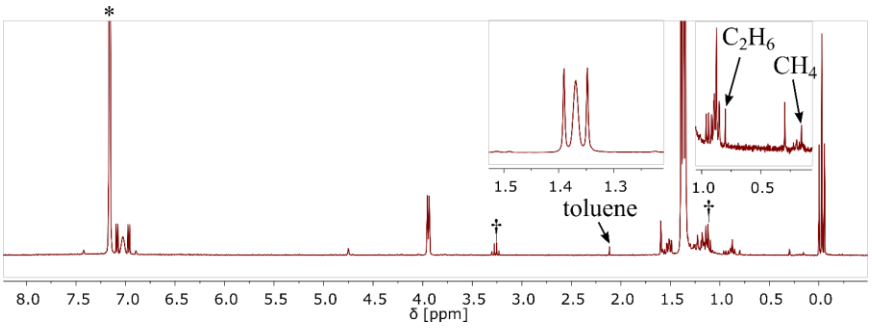

Figure 139: ^{1}H NMR spectra of a C_6D_6 solution of **33** after photolysis overnight ($\lambda_{exc.}$ = 390 nm).

Photochemical excitation of a C_6D_6 solution of **33** with a 150 W LED (λ_{exc} = 390 nm) results in low conversion of the starting material. ^{1}H NMR spectroscopy reveals the appearance of a broad resonance centered at δ = 7 ppm as is observed for Ni^I **9**, indicating the formation of a paramagnetic product (Figure 139). Examination of the aliphatic region of the spectrum shows formation of toluene, ethane and methane, which could be further corroborated by TCD-GC analysis of the headspace (Figure 140).

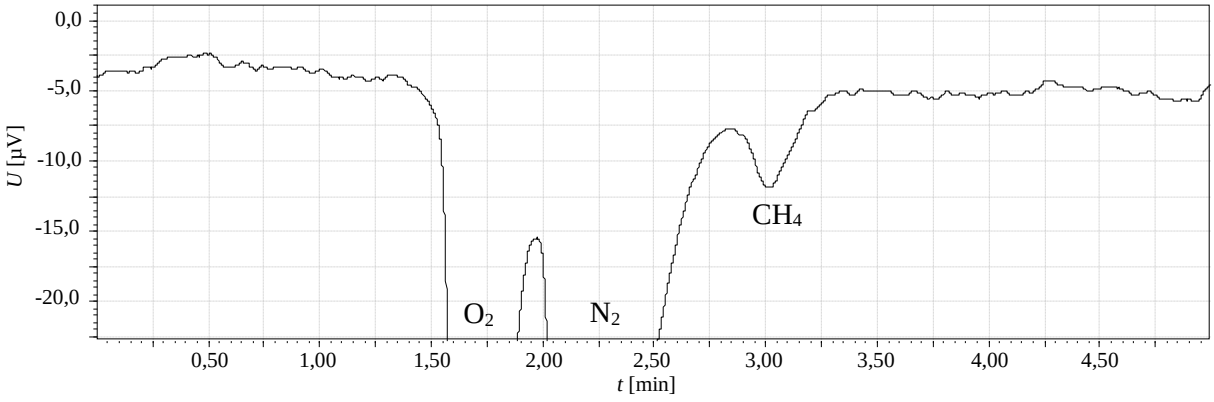

Figure 140: TCD-GC headspace analysis of a C_6D_6 solution of **33** after photolysis overnight ($\lambda_{exc.}$ = 390 nm).

Both, the formation of Ni^I **9** and methane suggest Ni-C bond homolysis as photochemical reactivity of Ni^{II} methyl **33** as is reported by *Miller* for [IrMe(bipy)Cp*].[349] However, such reactivity and subsequent

hydrogen atom abstraction from the solvent giving methane is expected to give CH_3D, which is not observed. Considering the low driving force for this reaction based on $\Delta H(CH_4)^{gas}$ = 96.8 kcal·mol^{-1} and $\Delta H(C_6H_6)^{gas}$ = 104.7 kcal·mol^{-1} representing C_6D_6, methane formation might result from reactivity of the initially formed methyl radical with a different hydrogen atom source.[4] While no other hydrogen atom source can be identified based on the experimental results, the formation of toluene hints at the intermediate formation of phenyl radicals. Finally, ethane production is in agreement with a sufficient lifetime of the methyl radical to allow for diffusion out of the solvent cage and subsequent reaction with **33** or another methyl radical. Alternatively, ethane production could result from bimolecular reactivity of **33** after photoexcitation.

Since the formation of alkyl radicals is crucial in nickel catalyzed alkyl-alkyl cross coupling, the photochemical reactivity of **33** in the presence of benzyl bromide was investigated (Scheme 70).[350] While small amounts of Ni^{II} bromide **3** are observed upon stirring the reaction mixture overnight, **33** converts to **3** within 1 h upon photolysis (Figure 141a). ^{1}H NMR spectroscopy reveals the formation of small quantities of toluene, ethane and methane as in the absence of substrate. Additionally, the formation of ethylbenzene can be observed as the product of stoichiometric C-C cross coupling. Further, large amounts of bibenzyl and unidentified byproducts are present, suggesting the intermediate formation of benzyl radicals.

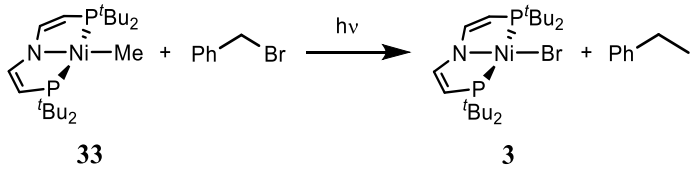

33 **3**

Scheme 70: Photochemical reactivity of Ni^{II} methyl complex **33** in the presence of benzyl bromide.

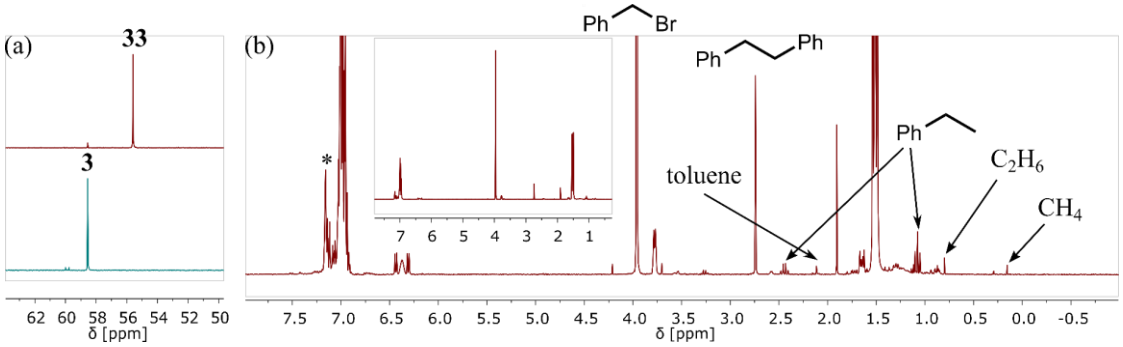

Figure 141: (a) ^{31}P{^{1}H} NMR spectra of a C_6D_6 solution of **33** in the presence of 10 eq benzyl bromide after (top) stirring overnight and (bottom) photolysis for 1 h ($\lambda_{exc.}$ = 390 nm). (b) ^{1}H NMR spectra of a C_6D_6 solution of **33** in the presence of 10 eq benzyl bromide after photolysis for 1 h ($\lambda_{exc.}$ = 390 nm).

2.5.4 Photochemical and Reactivity of a Nickel Pincer Azide

Starting from bromide **3**, substitution of the bromide with an azide ligand can be achieved upon stirring in the presence of an excess sodium azide und stoichiometric amounts of $[PPN]N_3$ (PPN: μ-nitrido-bis(triphenylphosphan)). The product $[NiN_3\{N(CH_2CH_2P^tBu_2)_2\}]$ (**34**) shows a strong azide asymmetric stretch in the infrared spectrum at $\tilde{\upsilon}$ = 2058.6 cm^{-1} in KBr matrix close to related $[NiN_3\{N(2\text{-}C_6H_3\text{-}5\text{-}CH_3\text{-}PiPr_2)_2\}]$ ($\tilde{\upsilon}$ = 2051 cm^{-1}) and X-ray diffraction confirms the structural assignment of **34** as azido complex (Figure 142, Figure 144).

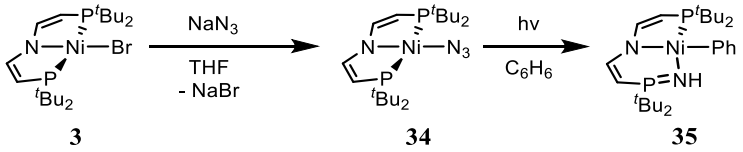

Scheme 71: Synthesis and photochemical reactivity of Ni^{II} azide **34**.

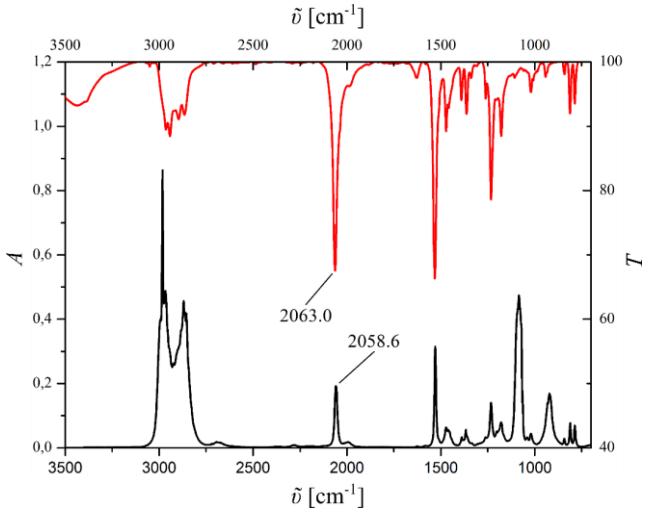

Figure 142: Infrared spectra of **34** in THF solution (black) and KBr matrix (red).

Compound $[NiN_3\{N(2\text{-}C_6H_3\text{-}5\text{-}CH_3\text{-}PiPr_2)_2\}]$ is reported to undergo rapid photochemical reactivity upon photolysis at λ_{exc} > 305 nm giving a phosphorimidate by N_2 loss and oxidation insertion of the transient nitride into the Ni-P bond, followed by benzene activation. Compound **34** shows similar, but significantly slower reactivity. The photochemical conversion of **34** giving phosphorimidate $[NiPh\{\kappa^3P,N,N\text{-}N(CHCHP^tBu_2)(CHCHP(NH)^tBu_2)\}]$ (**35**) can be accelerated by irradiating with the full spectrum of the Xe arc light source, indicating the position of the relevant electronic transition to be in the middle ultraviolet region. Even under these conditions, 5 hours of illumination are needed to reach full conversion of the starting material giving **35** as product of benzene activation.

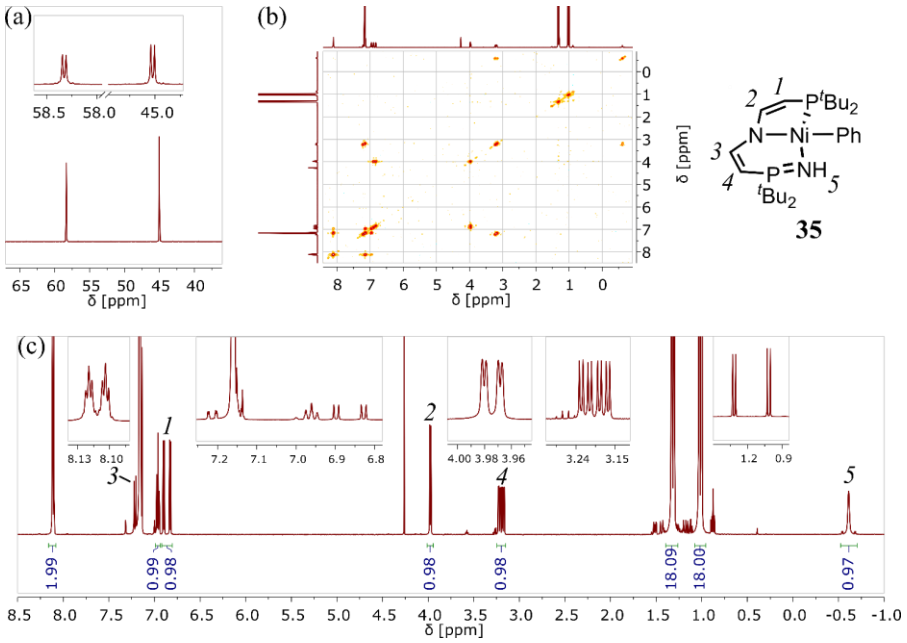

Figure 143: (a) $^{31}P\{^1H\}$ (b) $^1H,^1H$ COSY and (c) ^1H NMR spectra of **35** in C_6D_6.

Due to nitrogen insertion into the former P-Ni bond, **35** possesses C_S symmetry resulting in two chemically inequivalent phosphorus atoms in $^{31}P\{^1H\}$ NMR spectroscopic analysis with a relatively small coupling constant of $^3J_{PP}$ = 7.4 Hz (Figure 143). Accordingly, all four vinylene hydrogen atoms can be observed in ^1H NMR spectroscopy. Coupling to the N-H allows for facile assignment of the ^1H NMR spectroscopic resonances.

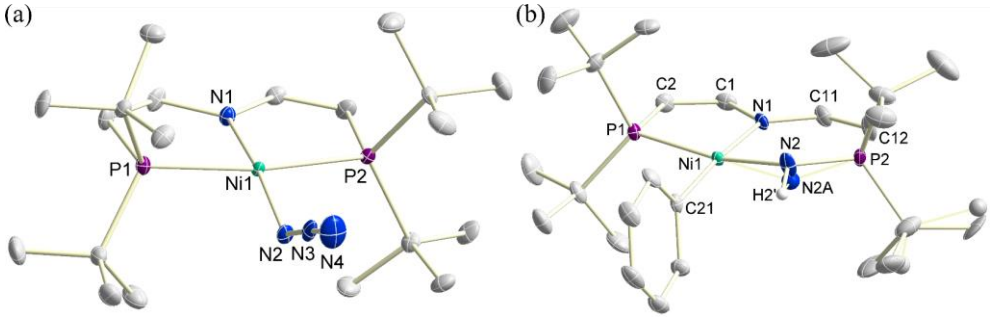

Figure 144: Solid state structure of (a) **34** and (b) **35** determined by X-ray diffraction. Thermal ellipsoids are drawn at the 50% probability level. Selected hydrogen atoms are omitted for clarity.

Both compounds **34** and **35** show a similar coordination geometry as taken from τ_4 (Table 27). While the pincer ligand C-C double bond length is nearly unaffected by nitrogen insertion in **35**, the nickel amide bond elongates due to the strongly donating phenyl *trans* ligand. The N-P bond *d*(N-P) = 1.616(18) Å length taken from the main domain of the disordered structure of **35** is close to the report of *van der Vlugt* (*d*(N-P) = 1.597(2) Å).[351]

Table 27: Crystallographic parameters of the solid state structure of **34** and **35** determined by X-ray diffraction.

[Ni]	τ_4	*d*(Ni-N) [Å]	*d*(C=C) [Å]
34	0.135	N1: 1.887(3)	1.340(5)/ 1.335(5)
		N2: 1.883(3)	
35	0.150	N1: 1.962(3)	1.335(5)/1.346(6)
		N2: 1.94(3)	

Interestingly, ^{1}H NMR spectroscopic monitoring of the reaction reveals the formation of an intermediate in the conversion of azide **34** to phosphorimidate **35** (Figure 145). While one hour of photolysis results in significant conversion of starting material, diamagnetic **35** does not built up to a large extend. However, four relatively sharp singlet resonances in the aliphatic region of the spectrum indicate formation of a different product. Measurement over a larger sweep reveals additional resonances of less intensity, indicating a paramagnetic species due to chemical shifts up to δ = 46.54 ppm. With increasing reaction progress, the concentration of this paramagnetic species decreases while **35** is produced as main product, indicating intermediacy of this species.

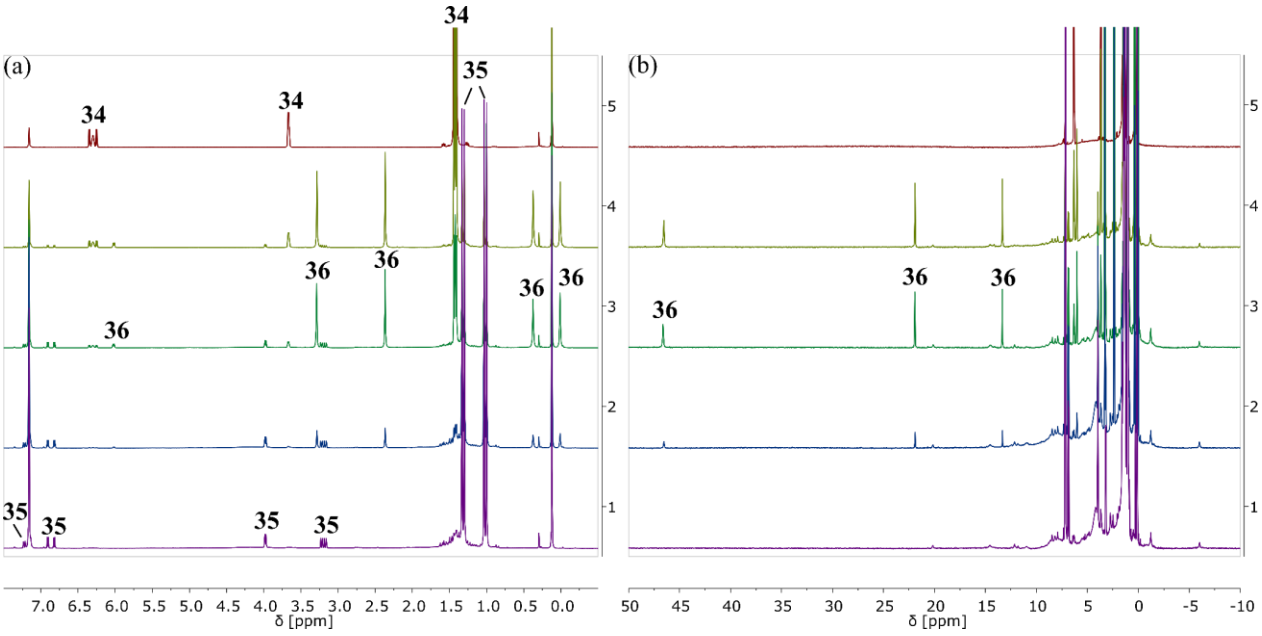

Figure 145: ^{1}H NMR spectra of photolysis ($\lambda_{exc.}$ > 305 nm) of **34** in C_6D_6.

Selective formation of paramagnetic intermediate [Ni{κ^3*P*,*N*,*N*-N($CH_2CH_2P^tBu_2N$)($CH_2CH_2P^tBu_2$)}]$_2$ (**36**) can be performed by irradiation of azide **34** at low temperature in toluene-d_8, showing that **36** is produced prior to benzene activation (Figure 146). The number and integration ratio of the ^{1}H NMR spectroscopic resonances of **36** suggests the absence of a mirror planes and therefore chemically inequivalent ^{t}Bu and

pincer backbone hydrogen atoms. While the range of the chemical shift δ in ^{1}H NMR spectroscopy suggests **36** to be a paramagnetic compound, the sharp resonances rather indicate a triplet than a singlet ground state, with well-resolved *J*-coupling for individual signals. Strongly shifted, however sharp ^{1}H NMR signals in osmium pincer complexes are attributed to a thermally isolated ground state showing large temperature independent paramagnetism (TIP) due to spin-orbit coupling.[86] While significant spin-orbit coupling is usually observed only for 4 and 5d metals, no further investigation of the magnetic properties of **36** was performed.

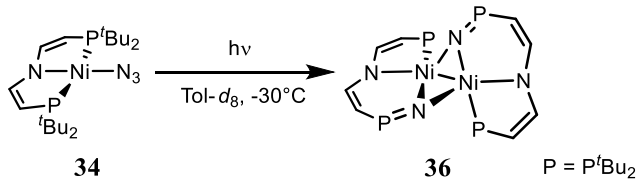

Scheme 72: Photochemical reactivity of Ni^{II} azide **34** at low temperature.

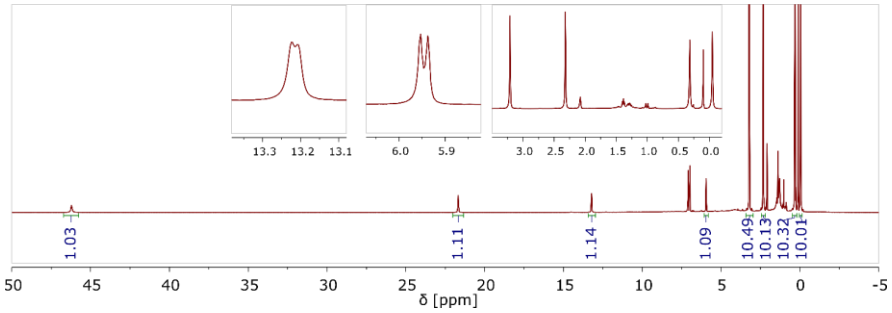

Figure 146: ^{1}H NMR spectra of photolysis of **34** in toluene-d_8 at -30°C.

UV-vis spectroscopic measurement of *in situ* generated **36** shows overlap of several transitions in the near UV region, resulting in a broad absorption which tails into the visible (Figure 147). UV-vis spectroscopic monitoring of the photolysis of parent azide **34** in *n*-pentane shows consumption of starting material as evident from the decreasing absorption at λ = 500 nm. An isosbestic point at λ = 390 nm shows selective conversion over 5 minutes and the spectroscopic features of the product indicate formation of paramagnetic **36** based on the disappearance of the features around λ = 300 nm and the increasing absorption at λ > 330 nm.

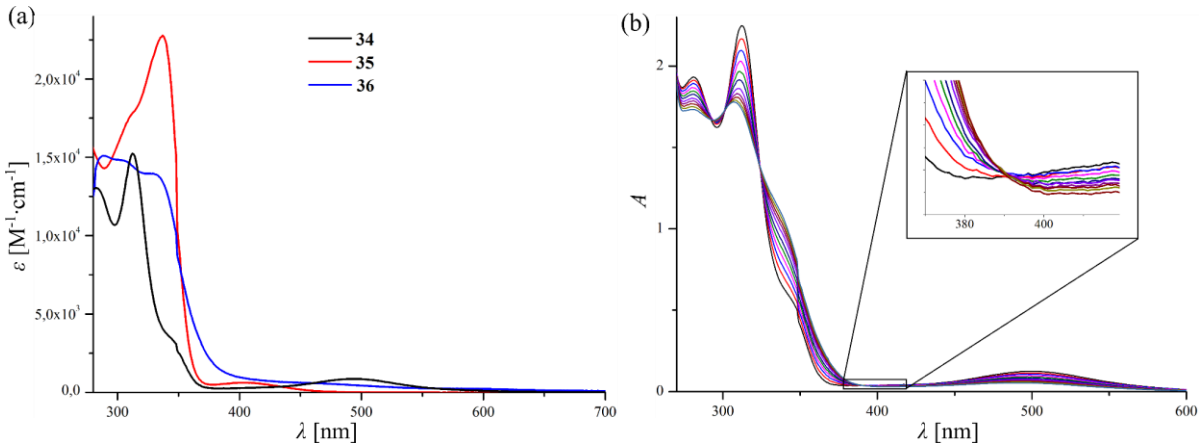

Figure 147: UV-vis absorption spectra of (a) **34**, **35** and **36** in benzene and (b) the photolysis of a solution of **34** in *n*-pentane monitored over 5 minutes.

Photolysis of azide **34** in pentane, followed by cooling to -36°C results in crystallization of **36** which enables structural assignment as dimeric nickel phosphorimidate (Figure 148). Compound **36** features the dimeric product of nitrogen insertion into the Ni-P bond prior to benzene activation. A metal-metal bond is present in **36**, and similar products are obtained upon photolysis of $[MN_3\{N(2\text{-}C_6H_3\text{-}5\text{-}CH_3\text{-}P\textit{i}Pr_2)_2\}]$ (M = Fe,Co) as reported by *Mindiola* and *van der Vlugt*, whereas fast benzene activation in the analogous Ni complex does not allow for observation of the intermediate.[351–353] With *d*(Ni-Ni) = 2.3868(3) Å, the Ni-Ni distance in **36** is close to reports on interactions of five-coordinate Ni^{II} metals in $[Ni(dpt)_2]_2$ (*d*(Ni-Ni) = 2.38 Å, dpt = 1,3-diphenyltriazenid) and *Agapie*'s work on bimetallic Ni^{I} complex $[Ni_2Cl_2\{\kappa^4\textit{P,C,C,P}\text{-}1,4\text{-}C_6H_4\text{-}(2\text{-}C_6H_4\text{-}P\textit{i}Pr_2)_2\}]$ (*d*(Ni-Ni) = 2.36580(16) Å).[354,355] Four-coordinate Ni^{I} dimer $[Ni\{N(2\text{-}C_6H_3\text{-}5\text{-}CH_3\text{-}P\textit{i}Pr_2)_2\}]_2$ (*d*(Ni-Ni) = 2.3288(7) Å) as well as *Hillhouse*'s report on four coordinate Ni^{II} dimer [{(IPr)Ni}$_2$(*μ*-Cl)(*μ*-NMes)]BArF (*d*(Ni-Ni) = 2.2911(8) Å, IPr = 1,3-di(2,6-di-*iso*-propylphenyl)imidazolin-2-ylidene) show stronger metal-metal interaction.[291,356]

Based on τ_5, the coordination geometry of the Ni metal in **36** is best described as square pyramidal with basal coordination by the three donor atoms of the phosphorimidate and the second Ni atom (Table 28).[357] The Ni-N bond distances in **36** do not deviate strongly and are close to crystallographic data in **35**. The same goes for the P-N bond length, suggesting a strong interaction between the monomer fragments. In contrast, a stronger deplanarization of the phosphorimidate nitrogen atom is observed compared to **35** (α(N) = 346.0°). While **36** crystallizes as one dimer molecule per asymmetric unit, a possible C_2 axis serves as explanation for the NMR spectroscopic signature of **36** which shows identical phosphorimidate ligands (Figure 148b). The presence of a monomer-dimer equilibrium in solution is possible as well.

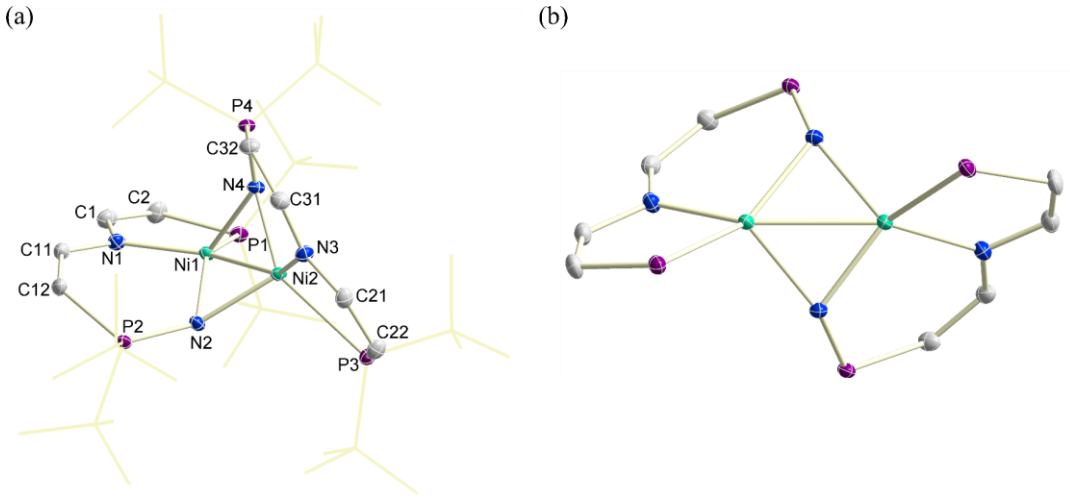

Figure 148: (a) Solid state structure of **36** determined by X-ray diffraction. Thermal ellipsoids are drawn at the 50% probability level. Hydrogen atoms and solvent molecules are omitted for clarity. (b) View along the pseudo C_2 axis in a reduced structural model of **36**.

Table 28: Crystallographic parameters of the solid state structure of **36** determined by X-ray diffraction.

[Ni]	τ_5	*d*(Ni-N) [Å]	*d*(P=N) [Å]	∑(α(N)) [°]
Ni1	0.098	N1: 1.9505(17)	1.5953(17)	335.8
		N2: 1.9407(17)		
		N4: 1.9922(17)		
Ni2	0.089	N2: 1.9865(17)	1.5945(17)	337.38
		N3: 1.9460(17)		
		N4: 1.9473(17)		

Van der Vlugt attributes the observed photochemical reactivity of $[NiN_3\{N(2\text{-}C_6H_3\text{-}5\text{-}CH_3\text{-}PiPr_2)_2\}]$ to formation of a transient Ni nitrene species.[351] Aside from N_2 loss, liberation of an azidyl radical or azide anion upon photochemical excitation of a metal azide complex is possible.[358] Early examples for photochemical formation of metal nitrenes include reports on $[MN_3(NH_3)_5]^{2+}$ (M = Rh, Ir) by *Basolo*.[359,360] Here, the mechanistic understanding is based on follow-up reactivity rather than characterization of the nitrene intermediate. In constrast, work on $[Fe(N_3)_2(cyclam)]^+$ by *Wieghardt* shows detection of oxidized $[FeN(N_3)(cyclam)]^+$ and reduced $[FeN_3(cyclam)]^+$ by EPR analysis and Mössbauer measurement as products of photochemical N_2 loss and Fe-N homolysis, respectively.[361] Transient spectroscopy on $[Fe(N_3)_2(cyclam)]^+$ and related complexes was performed by *Vöhringer*.[362,363] Similarly, photolysis of $[MN_3(salen)]$ (M = Cr, Mn; salen: *N,N'*-bis(salicyliden)ethylendiamine) results in either formation of a nitrene intermediate or loss of an azidyl radical as shown by laser flash photolysis.[364] Turning to the photochemistry of nickel azide complexes, *Hennig* proposes the formation of Ni nitrene intermediates upon

photolysis of *cis*-[Ni(N$_3$)$_2$(P$_2$)] (P$_2$ = diphosphine) based on trapping reactions like the formation of cyclohexylamine in the presence of cyclohexane.[365] Ni-N bond heterolysis is described for solid-state photolysis of *trans*-[Ni(N$_3$)$_2$(PEt$_3$)$_2$].[366]

Interested in the effect of photoexcitation on the asymmetric stretching vibration of the azide bond upon photolysis of azide **34**, transient UV-pump-IR-probe spectroscopy was performed (Figure 149).[30] Following photochemical excitation, a bleach of the ground-state asymmetric N$_3$ stretching vibration at $\tilde{\upsilon}$ = 2066 cm^{-1} can be observed which gradually refills over the course of the measurement. Partial photochemical conversion of the starting material due to photolysis is reflected by an incomplete repopulation of the ground state and the conversion of starting material proceeds with an approximate quantum yield of $\Phi_{260} \approx 15\%$. A positive, red shifted resonance is visible at $\tilde{\upsilon}$ = 2051 cm^{-1} and the increase in absorption is slightly delayed with respect to the ground state bleach. Importantly, Ni-N bond homo-/heterolysis is excluded based on reported $\tilde{\upsilon}$(N$_3$) = 1659 cm^{-1} and $\tilde{\upsilon}$(N$_3^-$) = 2006 cm^{-1}.[31][362,363] Both time constants τ_1 = 3.1±1.7 ps and τ_2 = 16.2±6.8 ps are attributed to vibrational cooling in the electronic ground state, since the positive signal rather resembles an vibrationally hot state than an electronically excited state. Accordingly, internal conversion from the *Frank-Condon* state to the electronic ground state proceeds with $\tau < 1$ ps. Overall, the excited state evolution of **34** closely resembles the photophysical processes attributed to N$_2$ loss in an iron azide reported by *Vöhringer*.[363]

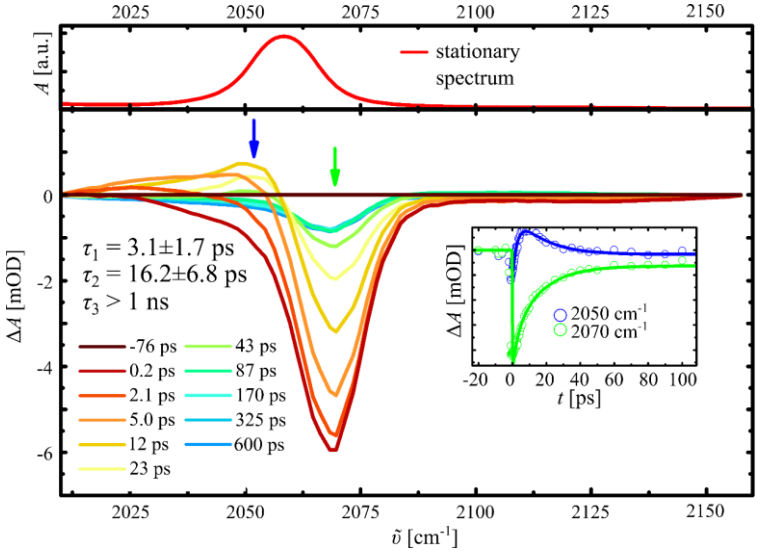

Figure 149: Transient IR spectra generated by $\lambda_{exc.}$ = 260 nm excitation of a 5.5 mM solution of **34** in THF for selected pump-probe delays. The stationary IR spectrum of **34** in THF solution are shown on top, while the time traces with biexponential fits are shown as inlets.

[30] Transient spectroscopy was performed by Jan-Hendrik Borter from the group of Prof. Dirk Schwarzer, Max Planck Institute for biophysical chemistry.
[31] reported in acetonitrile.

UV-pump-UV-vis-probe spectroscopy was performed to investigate the formation of a photoproduct upon photoexcitation of **34** (Figure 150). As in the transient IR spectrum, the ground-state absorption of **34** bleaches at $\lambda \approx 500$ nm. A strong absorption at $\lambda = 365$ nm and weaker absorption in the whole visible spectrum is observed. Fitting the spectral behavior with a global tri-exponential fit allows for determination of the time constants $\tau_1 = 2.7 \pm 0.4$ ps, $\tau_2 = 11.6 \pm 1.0$ ps and $\tau_3 > 1$ ns, which is in good agreement with the results of UV-vis-pump-IR-probe experiments. In agreement with the transient IR measurement, the initial fast processes τ_1 and τ_2 are attributed to vibrational cooling in the electronic ground state. At long pump-probe delay, the conversion of the starting material **34** is reflected by a constant bleach at $\lambda = 550$ nm. Additionally, a constant absorption at $\lambda < 450$ nm indicates formation of a photoproduct with $\tau_3 > 1$ ns.

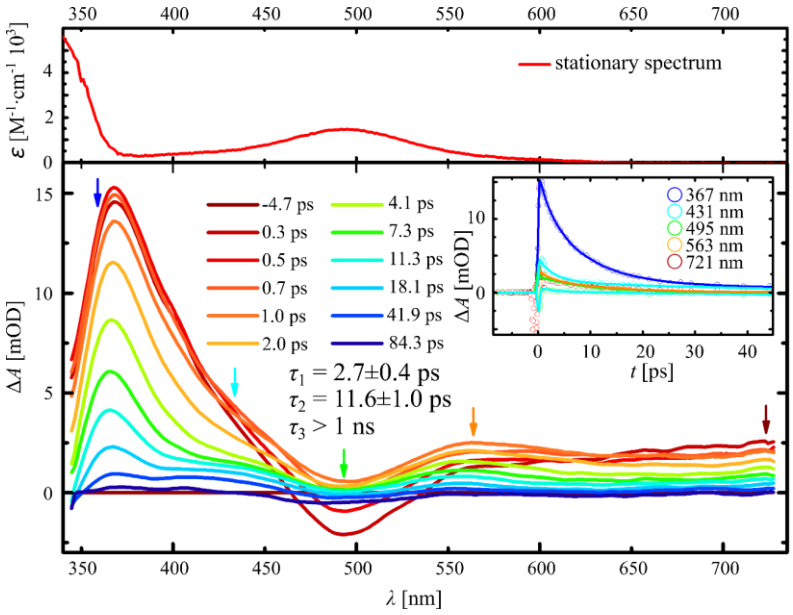

Figure 150: Transient UV-vis spectra generated by $\lambda_{exc.} = 260$ nm excitation of a 6 mM solution of **34** in THF for selected pump-probe delays. The stationary UV-vis spectrum of **34** in THF solution is shown on top, while the time traces with global triexponential fits are shown as inlets.

The transient UV-vis spectrum at $t = 84.3$ ps and the ground-state UV-vis spectrum of **34** allows for determination of the spectrum of the photoproduct (Figure 151a). Comparison of the obtained spectroscopic signature of the photoproduct and the spectrum of [NiN(^{tBu}P=N=P)] based on TD-DFT computation shows similarities in key features like the presence of transitions at $\lambda \approx 420$ nm and $\lambda \approx 520$ nm. The optimized geometry of [NiN(^{tBu}P=N=P)] in the electronic triplet ground state is shown in Figure 151b. The photoproduct is therefore tentatively assigned as [NiN(^{tBu}P=N=P)] which shows lifetime on the nanosecond timescale in solution, potentially allowing for bimolecular reactivity before insertion of the nitrogen into the Ni-P bond.

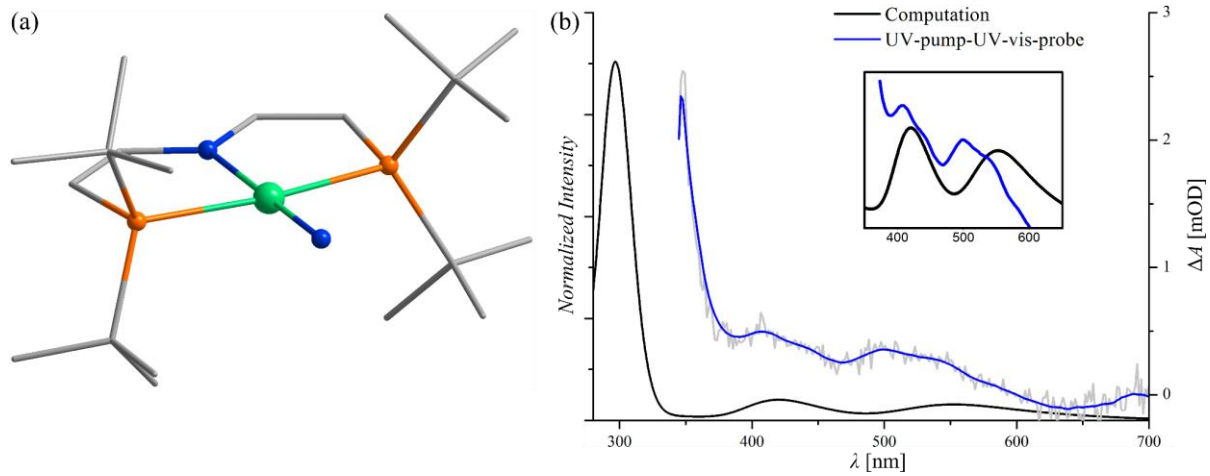

Figure 151: (a) Optimized geometry of [NiN(^{tBu}P=N=P)] (ZORA-B3LYP/def2-TZVPP). (b) (blue) Product spectrum based on the ground-state UV-vis spectrum of **34** and the transient measurement at t = 84.3 ps. (black) Computational absorption spectrum of [NiN(^{tBu}P=N=P].[32]

[32] Computational analysis was performed by Dr. Markus Finger.

2.6 Conclusion

Carbon dioxide activation by Ni^{II} hydride [NiH(^{tBu}P=N=P)] **12** proceeds with different selectivity when performed thermally or photochemically. While the ground-state reactivity gives Ni^{II} formate [Ni(O_2CH)(^{tBu}P=N=P)] **15**, photochemical CO_2 activation gives the hydroxycarbonyl **16** [Ni(CO_2H)(^{tBu}P=N=P)] as primary product *via* the first example of the so-called abnormal CO_2 insertion. Based on this reactivity, synthetic models for photochemical CO_2 reduction were constructed based on subsequent electron and proton transfer or initial hydride transfer, allowing for the characterization of a rare Ni^{II} formyl [Ni(CHO)(^{tBu}P=N=P)] **21**. Metal-ligand cooperative H_2 activation in a second photochemical step could be utilized to enable the use of H_2 as electron and proton source. Actinometry was performed to determine the efficiency of both photochemical reactions giving Φ_{410} = 9.0% and Φ_{337} = 1.0% for photochemical CO_2 and H_2 activation, respectively. Detailed investigation of all involved reactions and their pK_a constrains results in a two-step synthetic cycle for photochemical reverse water-gas shift reactivity on a single nickel center at mild conditions.

Kinetic analysis of the photochemical conversion of **12** to **16** by NMR spectroscopy shows a first-order dependence of the reaction rate in starting material **12** and photons. The rate is independent of $p(CO_2)$ at 1–10 atm, suggesting the formation of a photoproduct in the rate-determining step prior to CO_2 coordination. Labeling of the hydride position shows efficient retention of the label upon photochemical CO_2 activation, excluding intermolecular PCET as RDS. Detailed investigation of the photophysical processes was performed by transient and luminescence spectroscopy as well as TD-DFT computations. Optical excitation *via* a MLCT type process results in population of the *Frank-Condon* state which undergoes rapid internal conversion to S_1. This state is characterized by a weak Ni-H bond which is red shifted by $\Delta\tilde{\upsilon}$ = 343 cm^{-1} with respect to the ground-state and can therefore be assigned as a metal centered excited state. Importantly, this represents the first IR spectroscopic characterization of an excited state metal hydrogen bond. Formation of a photoproduct is confirmed by observation of a persistent absorption in the UV-pump-UV-vis-probe experiment and the population of long-lived excited states is excluded based on the lack of emission of **12**.

Measurement of the kinetic isotope effect of photochemical CO_2 activation suggests that Ni-H bond elongation contributed significantly to the reaction coordinate of the rate-determining step. Photolysis of **12** in the absence of substrate results in formation of T-shaped Ni^{I} complex [Ni(^{tBu}P=N=P)] **9** by a rare example of bimolecular photochemical H_2 loss. Extensive reactivity studies on substrate activation by **9** and its influence on the rate of photochemical CO_2 activation by **12** suggest **9** to be a product of follow-up reactivity of the photoproduct, rather than the photoproduct itself. Trapping experiments by photolysis of **12** the

presence of carbon monoxide and hydroxycarbonyl **16** result in N-H bond formation, indicating N-H reductive elimination as rate-determining step, conceptually introducing metal-ligand cooperativity in photochemistry. Computational analysis presents a mechanism for CO_2 activation by Ni^0 amino diphosphine complex [Ni{κ^2*P,P*-HN(CHCHP^{t}Bu$_2$)$_2$}] **A** which is supported by the transient absorption spectrum of the photoproduct and the experimentally determined acidity of **16**.

Interested in CO_2 activation by similar Ni^{II} pincer hydride complexes, amino hydride [NiH(^{tBu}PN^{H}P)]OTf **30^{OTf}** and amido hydride [NiH(^{tBu}PNP)] **31** are prepared. While **30^{OTf}** does not undergo thermal or photochemical CO_2 activation, **31** reversibly binds CO_2 at the amido position. Moving to literature reported [NiH{N(2-C$_6$H$_3$-5-CH$_3$-P*i*Pr$_2$)$_2$}] **L$_1$**, formation of hydroxycarbonyl [Ni(CO$_2$H){N(2-C$_6$H$_3$-5-CH$_3$-P*i*Pr$_2$)$_2$}] **L$_2$** is observed upon photolysis in the presence of CO_2, showing that the observed reactivity of **12** can be transferred to other complexes. The photochemical substrate activation by **12** can be extended to olefins and aldehydes as substrates. Using a visible light LED, photocatalytic olefin and aldehyde hydrogenation is performed. The activity of **12** rivals reported Ni based homogeneous catalysts for thermal olefin hydrogenation and exceeds reports on thermal hydrogenation of benzaldehyde. Investigation of thermal and photochemical hydrogenation of styrene by several Ni^{II} pincer hydrides further reveals efficient thermal styrene hydrogenation by imine hydride [NiH(^{tBu}P=N=P^H)]BArF **14^{BArF}** and reveals an outstanding role of ^{tBu}P=N=P in photocatalytic hydrogenation. Initial experiments on the reactivity of [NiMe(^{tBu}P=N=P)] **33** show liberation of ethane upon photolysis in the absence of substrate which is attributed to Ni-C bond homolysis and subsequent free radical chemistry.

Starting from bromide **3**, azide complex [NiN$_3$(^{tBu}P=N=P)] **34** is obtained and photolysis in benzene results in formation of [NiPh{κ^3*P,N,N*- N(CH$_2$CH$_2$P^{t}Bu$_2$NH)(CH$_2$CH$_2$P^{t}Bu$_2$)}] **35** as product of nitrogen insertion into a Ni-P bond and subsequent benzene activation. Irradiation in *n*-pentane allows for isolation of paramagnetic dimer [Ni{κ^3*P,N,N*-N(CH$_2$CH$_2$P^{t}Bu$_2$N)(CH$_2$CH$_2$P^{t}Bu$_2$)}]$_2$ **36**, representing the product prior to C-H activation. Transient spectroscopy of **34** shows rapid internal conversion and vibrational cooling in the electronic ground-state. The formation of a photoproduct proceeds with $\Phi_{260} \approx 15\%$ and comparison of the UV-vis spectroscopic signature of the transient with TD-DFT suggests the formation of a nickel nitrene intermediate. Accordingly, the first spectroscopic characterization of such a species is presented herein.

Part II: Experimental Data

2.7 Material and Methods

See Chapter 1.6.

2.8 Isolated Substances

2.8.1 [Ni(CO$_2$H)(^{tBu}P=N=P)] (16)

[NiH(^{tBu}P=N=P)] (**12**) (20 mg, 0.048 mmol, 1.0 eq) is dissolved in 6 mL of benzene, degassed by three freeze-pump-thaw cycles and CO_2 atmosphere ($p(CO_2)$ = 1 atm, ≥99.5%, no further purification) is applied. The reaction mixture is photolyzed ($\lambda_{exc.}$ > 305 nm) for 8 hours, followed by washing with 5×2 mL of benzene and 5×2 mL of *n*-pentane. The product is dissolved in THF and dried *in vacuo* to give a yellow solid. Yield: 15 mg (73%).

Crystals suitable for X-ray diffraction are obtained by diffusion of *n*-pentane into a solution of **16** in THF.

Anal. Calcd. for $C_{21}H_{41}NO_2NiP_2$ (460.20): C, 54.81; H, 8.98; N, 3.04%. Found: C, 54.92 H, 8.98; N, 2.91%.

^{31}P{^{1}H} NMR (162 MHz, THF-d_8) δ = 66.2 ppm.

^{1}H NMR (400 MHz, THF-d_8) δ = 9.51 (br, 1H, CO_2H), 6.49 ($A_{18}BCXX'C'B'A'_{18}$, $N = \left|{}^3J_{CX} + {}^4J_{CX'}\right|$ = 36.8 Hz, $^3J_{CB}$ = 5.3 Hz, 2H, NC*H*), 4.02 ($A_{18}BCXX'C'B'A'_{18}$, $N = \left|{}^2J_{BX} + {}^4J_{BX'}\right|$ = 2.0 Hz, $^3J_{BC}$ = 5.2 Hz, 2H, PC*H*), 1.37 ($A_{18}BCXX'C'B'A'_{18}$, $N = \left|{}^3J_{AX} + {}^5J_{AX'}\right|$ = 13.4 Hz, 36H, P^{t}Bu) ppm.

^{13}C{^{1}H} NMR (126 MHz, THF-d_8) δ = 203.6 (t, $^2J_{CP}$ = 31.1 Hz, *C*O$_2$H), 161.1 (vt, $^2J_{CP}$ = 10.7 Hz, N*C*H), 82.4 (vt, $^1J_{CP}$ = 18.6 Hz, P*C*H), 35.9 (vt, $^1J_{CP}$ = 10.2 Hz, P*C*Me$_3$), 29.3 (vt, $^2J_{CP}$ = 2.7 Hz, PC*Me*$_3$) ppm.

IR (Nujol): $\tilde{\upsilon}$ = 2645.0, 1584.3, 1564.1 cm^{-1}.

MS (LIFDI, toluene): *m/z* = 459.0 (100%, $[C_{21}H_{41}NO_2NiP_2]^+$).

2.8.2 [Ni(OCO$_2$H)(^{tBu}P=N=P)] (17)

A solution of [Ni(OH)(^{tBu}P=N=P)] (**18**) in THF-d_8 is filled into a J Young NMR tube. The solution is degassed by three freeze-pump-thaw cycles and CO_2 atmosphere ($p(CO_2)$ = 1 atm, ≥99.9993%, purification by passing through P_4O_{10}, Drierite^{TM} and cooling to -40°C) is applied. Upon removing the solvent, reformation of **18** is observed.

Crystals suitable for X-ray diffraction are obtained by diffusion of *n*-pentane onto a solution of **17** in THF.

$^{31}P\{^{1}H\}$ NMR (162 MHz, THF-d_8) δ = 54.6 ppm.

^{1}H NMR (400 MHz, THF-d_8) δ = 9.28 (br, 1H, OCO_2H), 6.47 ($A_{18}BCXX'C'B'A'_{18}$, $N = |{}^{3}J_{CX} + {}^{4}J_{CX'}|$ = 38.2 Hz, ${}^{3}J_{CB}$ = 5.5 Hz, 2H, NC*H*), 3.88 ($A_{18}BCXX'C'B'A'_{18}$, $N = |{}^{2}J_{BX} + {}^{4}J_{BX'}|$ = 2.0 Hz, ${}^{3}J_{BC}$ = 5.4 Hz, 2H, PC*H*), 1.48 ($A_{18}BCXX'C'B'A'_{18}$, $N = |{}^{3}J_{AX} + {}^{5}J_{AX'}|$ = 13.6 Hz, 36H, P^{t}Bu) ppm.

$^{13}C\{^{1}H\}$ NMR (126 MHz, THF-d_8) δ = 163.0 (vt, ${}^{2}J_{CP}$ = 11.1 Hz, N*C*H), 158.9 (s, O*C*O_2H), 82.2 (vt, ${}^{1}J_{CP}$ = 18.8 Hz, P*C*H), 35.7 (vt, ${}^{1}J_{CP}$ = 8.6 Hz, P*C*Me_3), 29.0 (vt, ${}^{2}J_{CP}$ = 2.9 Hz, PC*Me*$_3$) ppm.

2.8.3 [Ni(OH)(^{tBu}P=N=P)] (18)

[NiBr(^{tBu}P=N=P)] (**3**) (24 mg, 0.048 mmol, 1.0 eq), KOH (30 mg, 0.54 mmol, 11 eq) and 15-crown-5 (10 µL, 0.051 mmol, 1.1 eq) is filled into a J Young NMR tube and dissolved in 1 mL of THF. The solution is warmed to 70°C for 2 days. After evaporation of the solvent, the orange solid is extracted with *n*-pentane and filtered over Celite®. The solvent is evaporated and the orange powder is dissolved in *n*-pentane and recrystallized at -36°C. Removal of the solvent and drying *in vacuo* yields the product as red crystals. Yield: 14 mg (69%).

Crystals suitable for X-ray diffraction are obtained from a solution of **18** in *n*-pentane by crystallization at -36°C.

Anal. Calcd. for $C_{20}H_{41}NONiP_2$ (432.19): C, 55.58; H, 9.56; N, 3.24%. Found: C, 55.50 H, 9.46; N, 3.12%.

$^{31}P\{^{1}H\}$ NMR (162 MHz, THF-d_8) δ = 50.3 ppm.

^{1}H NMR (400 MHz, THF-d_8) δ = 6.62 ($A_{18}BCXX'C'B'A'_{18}$, $N = |{}^{3}J_{CX} + {}^{4}J_{CX'}|$ = 37.6 Hz, ${}^{3}J_{CB}$ = 5.4 Hz, 2H, NC*H*), 3.88 ($A_{18}BCXX'C'B'A'_{18}$, $N = |{}^{2}J_{BX} + {}^{4}J_{BX'}|$ = 1.9 Hz, ${}^{3}J_{BC}$ = 5.3 Hz, 2H, PC*H*), 1.37 ($A_{18}BCXX'C'B'A'_{18}$, $N = |{}^{3}J_{AX} + {}^{5}J_{AX'}|$ = 13.2 Hz, 36H, P^{t}Bu), -4.88 (t, ${}^{3}J_{HP}$ = 5.6 Hz, O*H*) ppm.

$^{13}C\{^{1}H\}$ NMR (126 MHz, THF-d_8) δ = 162.8 (vt, ${}^{2}J_{CP}$ = 11.8 Hz, N*C*H), 81.2 (vt, ${}^{1}J_{CP}$ = 18.3 Hz, P*C*H), 35.2 (vt, ${}^{1}J_{CP}$ = 8.6 Hz, P*C*Me_3), 29.3 (vt, ${}^{2}J_{CP}$ = 2.9 Hz, PC*Me*$_3$) ppm.

IR (Nujol): $\tilde{\upsilon}$ = 3643.8 cm^{-1}.

MS (LIFDI, toluene): *m/z* = 431.2 (100%, $[C_{20}H_{41}NONiP_2]^{+}$).

2.8.4 [Ni(CO)(^{tBu}P=N=P)]BF_4 (20^{BF4})

Route A: [Ni(NCMe)(^{tBu}P=N=P)]BF_4 (**7^{BF4}**) (167 mg, 0.308 mmol, 1.00 eq) is dissolved in 10 mL of THF, degassed three times by freeze-pump-thaw and CO atmosphere (p(CO) = 1 atm) is applied. The solution is stirred for 2 days at room temperature. The solvent is evaporated and the red residue is suspended in benzene

and filtered, washed with 10×5 mL of benzene and 10×5 mL of *n*-pentane. The red powder is dried *in vacuo*. Yield: 132 mg (87%).

Route B: [Ni(CO_2H)(^{tBu}P=N=P)] (**16**) (30 mg, 0.060 mmol, 1.0 eq) is dissolved in 1 mL Et_2O and $HBF_4{\cdot}OEt_2$ (11 mg, 0.068 mmol, 1.1 eq) is added which results in precipitation of a red solid. After removal of the solvent, the product is washed with 2 mL of *n*-pentane and dried *in vacuo*. Yield: 29 mg (83%).

Crystals suitable for X-ray diffraction are obtained by layering a solution of **20^{BF4}** in THF with *n*-pentane.

Anal. Calcd. for $C_{21}H_{40}BF_4N_2ONiP_2$ (530.00): C, 47.59; H, 7.61; N, 2.64%. Found: C, 47.40 H, 7.65; N, 2.62%.

^{31}P{^{1}H} NMR (203 MHz, CD_2Cl_2) δ = 114.7 ppm.

^{1}H NMR (500 MHz, CD_2Cl_2) δ = 7.22 (A_{18}BCXX'C'B'A'$_{18}$, N = $|{}^3J_{CX} + {}^4J_{CX'}|$ = 48.0 Hz, $^3J_{CB}$ = 5.1 Hz, 2H, NC*H*), 4.39 (A_{18}BCXX'C'B'A'$_{18}$, N = $|{}^2J_{BX} + {}^4J_{BX'}|$ = 2.5 Hz, $^2J_{BC}$ = 4.9 Hz, 2H, PC*H*), 1.45 (A_{18}BCXX'C'B'A'$_{18}$, N = $|{}^3J_{AX} + {}^5J_{AX'}|$ = 15.8 Hz, 36H, P^{t}Bu) ppm.

^{13}C{^{1}H} NMR (126 MHz, CD_2Cl_2) δ = 191.3 (t, $^2J_{CP}$ = 22.5 Hz, *C*O), 164.4 (vt, $^2J_{CP}$ = 7.5 Hz, NC*H*), 82.6 (vt, $^1J_{CP}$ = 21.5 Hz, P*C*H), 37.0 (vt, $^1J_{CP}$ = 10.7 Hz, P*C*Me$_3$), 29.1 (vt, $^2J_{CP}$ = 2.0 Hz, PC*Me*$_3$), ppm.

IR (KBr): $\tilde{\upsilon}$ = 2039.9 cm^{-1}.

MS (LIFDI, CH_2Cl_2): *m/z* = 442.0 (100%, $[C_{21}H_{40}N_2ONiP_2]^+$).

2.8.5 [Ni(CO)(^{tBu}P=N=P)]BArF (20^{BArF})

Route A: [Ni(NCMe)(^{tBu}P=N=P)]BArF (**7^{BArF}**) (200 mg, 0.151 mmol, 1.00 eq) is dissolved in 10 mL of THF. The solution is degassed by three freeze-pump-thaw cycles and CO atmosphere (p(CO) = 1 atm) is applied. After stirring at room temperature for 2 days the solvent is evaporated. The red residue is washed with 4 mL of benzene *n*-pentane 1:1 and 2×4 mL of *n*-pentane. The solid is dissolved in Et_2O and *n*-pentane is added to yield a red precipitate. After drying *in vacuo* the product is obtained as a red powder. Yield: 160 mg (81%).

Route B: [Ni(^{tBu}P=N=P)] (**9**) (80.0 mg, 0.193 mmol, 1.05 eq) is dissolved in 3 mL of THF. The solution is degassed by three freeze-pump-thaw cycles and CO atmosphere (p(CO) = 1 atm) is applied. After stirring at RT for 3 minutes the solvent is evaporated *in vacuo*. A solution of [Fc]BArF (192 mg, 0.183 mmol, 1.00 eq) in 3 mL of THF is added. After stirring at RT for 1.5 h the solvent is evaporated, the residue is extracted with Et_2O and the solvent is removed evaporated. After washing with *n*-pentane and drying *in vacuo*, the product is obtained as a red powder. Yield: 226 mg (95%).

Anal. Calcd. for $C_{53}H_{52}BF_{24}NONiP_2$ (1306.42): C, 48.73; H, 4.01; N, 1.07%. Found: C, 48.60 H, 3.80; N, 1.13%.

IR (ATR): $\tilde{\upsilon}$ = 2062.4 cm^{-1}.

2.8.6 [Ni(CO)(^{tBu}P=N=P)] (22)

Method A: [Ni(CO)(^{tBu}P=N=P)]BArF (**20^{BArF}**) (50 mg, 0.038 mmol, 1.0 eq) and KC_8 (5.0 mg, 0.037 mmol, 1.0 eq) is suspended in THF and stirred for 1 h at room temperature. After evaporation of the solvent, the blackish residue is dissolved in *n*-pentane, filtered and dried *in vacuo*. Yield: 14 mg (86%).

Method B: [Ni(^{tBu}P=N=P)] (**9**) (10 mg, 0.024 mmol, 1.0 eq) is filled into a J Young NMR tube and dissolved in 0.5 mL of THF. The solution is degassed by three freeze-pump-thaw cycles and CO atmosphere (p(CO) = 1 atm) is applied. The solution is stirred at RT for 30 minutes and the solvent is evaporated. The black residue is dissolved in *n*-pentane and filtered. Evaporation of the solvent and drying *in vacuo* gives the product as a black solid. Yield: 9 mg (83%).

Crystals suitable for x-ray diffraction are obtained from a solution of **22** in Et_2O by crystallization at -36°C.

IR (KBr): $\tilde{\upsilon}$ = 1910.1 cm^{-1}.

MS (LIFDI, toluene): *m/z* = 414.1 (55%, $[C_{20}H_{40}NP_2Ni]^+$), 442.1 (45%, $[C_{21}H_{40}NOP_2Ni]^+$).

2.8.7 K[Ni(CO)(^{tBu}P=N=P)] (23^{K})

[Ni(CO)(^{tBu}P=N=P)]BF_4 (**20^{BF4}**) (20 mg, 0.015 mmol, 1.0 eq) and KC_8 (8.0 mg, 0.059 mmol, 3.9 eq) is suspended in 2 mL of Et_2O, filtered and cooled to -36°C, yielding crystals suitable for X-ray diffraction.

2.8.8 [Ni{κN-HNC(NMe$_2$)$_2$}(^{tBu}P=N=P)] (25^{BArF})

[Ni(CO)(^{tBu}P=N=P)]BArF (**20^{BArF}**) (15 mg, 12 µmol, 1.0 eq) and 1,1,3,3-tetramethylguanidine (1.4 µL, 12 µmol, 1.0 eq) is dissolved in 0.5 mL of Et_2O and filled into an J Young NMR tube and the tube is degassed. Under static vacuum the sample is photolyzed for 2 h ($\lambda_{exc.}$ >305 nm). The solvent is immediately removed *in vacuo* and the product is washed with benzene 2×0.5 mL and dried *in vacuo*. Yield: 11.5 mg (72%).

Crystals suitable for X-ray diffraction are obtained by diffusion of *n*-pentane onto a solution of **25^{BArF}** in THF.

Anal. Calcd. for $C_{57}H_{65}BF_{24}N_4NiP_2$ (1393.59): C, 49.13; H, 4.70; N, 4.21%. Found: C, 48.89 H, 4.33; N, 3.98%.

$^{31}P\{^{1}H\}$ NMR (162 MHz, CD_2Cl_2) δ = 60.5 ppm.

^{1}H NMR (400 MHz, CD_2Cl_2) δ = 7.72 (m, 8H, BArF), 7.56 (br, 4H, BArF), 6.48 ($A_9B_9CDXX'D'C'B'_9A'_9$, $N = |^3J_{DX} + {}^5J_{DX'}|$ = 39.6 Hz, $^3J_{DC}$ = 5.6 Hz, 2H, NC*H*CH), 3.96 ($A_9B_9CDXX'D'C'B'_9A'_9$, $N = |^2J_{CX} + {}^4J_{CX'}|$ = 2.2 Hz, $^3J_{CD}$ = 5.6 Hz, 2H, PC*H*), 3.54 (br, 6H, N(CH_3)$_2$), 2.63 (s, 6H, N(CH_3)$_2$), 2.30 (br, 1H, N*H*), 1.50 ($A_9B_9CDXX'D'C'B'_9A'_9$, $N = |^3J_{AX} + {}^5J_{AX'}|$ = 13.8 Hz, 18H, P^{t}Bu), 1.31 ($A_9B_9CDXX'D'C'B'_9A'_9$, $N = |^3J_{BX} + {}^5J_{BX'}|$ = 13.8 Hz, 18H, P^{t}Bu) ppm.

$^{13}C\{^{1}H\}$ NMR (101 MHz, CD_2Cl_2) δ = 168.9 (s, *C*(NMe_2)$_2$), 163.2 (vt, $^2J_{CP}$ = 9.8 Hz, N*C*H), 161.7 (q, $^1J_{BC}$ = 49.9 Hz, BArF), 134.7 (s, BArF), 128.8 (qq, $^2J_{CF}$ = 31.1 Hz, $^3J_{BC}$ = 2.9 Hz, BArF), 124.5 (q, $^1J_{CF}$ = 272.4 Hz, BArF), 117.4 (m, BArF), 82.0 (vt, $^1J_{CP}$ =20.0 Hz, P*C*H), 40.8 (br, N(CH_3)$_2$), 39.6 (s, N(CH_3)$_2$), 36.5 (vt, $^1J_{CP}$ = 8.4 Hz, P*C*Me$_3$), 35.6 (vt, $^1J_{CP}$ = 8.4 Hz, P*C*Me$_3$), 30.0 (vt, $^2J_{CP}$ = 2.4 Hz, PC*Me*$_3$), 28.5 (vt, $^2J_{CP}$ = 2.3 Hz, PC*Me*$_3$) ppm.

MS (LIFDI, CH_2Cl_2): *m/z* = 529.3 (100%, $[C_{25}H_{53}N_4NiP_2]^+$).

2.8.9 [(^{tBu}P=N=P)Ni(OC(O)O)Ni(^{tBu}P=N=P)] (27)

[Ni(^{tBu}P=N=P)] (**9**) (3.2 mg, 7.7 µmol, 1.0 eq) and 3 µL of TMS_2O is dissolved in 0.5 mL of THF-d_8. The solution is degassed by three freeze-pump-thaw-cycles and CO_2 atmosphere ($p(CO_2)$ = 1 atm, ≥99.9993%, purification by passing through P_4O_{10}, Drierite™ and cooling to -40°C) is applied. The solution is stirred at room temperature for 11 days.

Crystals suitable for X-ray diffraction are obtained from a solution of **27** in *n*-pentane by crystallization at -36°C.

$^{31}P\{^{1}H\}$ NMR (162 MHz, THF-d_8) δ = 49.2 ppm.

^{1}H NMR (400 MHz, THF-d_8) δ = 6.31 ($A_{18}BCXX'C'B'A'_{18}$, $N = |^3J_{CX} + {}^4J_{CX'}|$ = 35.8 Hz, $^3J_{CB}$ = 5.6 Hz, 4H, NC*H*), 3.80 (d, $^3J_{BC}$ = 5.6 Hz, 4H, PC*H*), 1.50 ($A_{18}BCXX'C'B'A'_{18}$, $N = |^3J_{AX} + {}^5J_{AX'}|$ = 13.4 Hz, 72H, P^{t}Bu) ppm.

$^{13}C\{^{1}H\}$ NMR (126 MHz, C_6D_6) δ = 162.5 (s, O*C*(O)O) ppm.

MS (LIFDI, toluene): *m/z* = 889.3 (100%, $[C_{41}H_{80}N_2Ni_2O_3P_4]^+$, $^{13}CO_3^{2-}$-isotopologue).

2.8.10 [Ni(CO)$_3${κ*P*-(^{tBu}P=N=P)] (28)

A solution of [NiH(^{tBu}P=N=P)] (**12**) (9.69 mM in THF-d_8, 0.50 mL, 4.8 µmol, 1.0 eq) containing TMS_2O as internal standard is filled into a J Young NMR tube and degassed by three freeze-pump-thaw cycles and CO

atmosphere ($p(CO_2)$ = 1 atm) is applied. The sample is photolyzed ($\lambda_{exc.}$ > 305 nm) for 90 minutes. After removal of the CO atmosphere and work-up reformation of **12** can be observed.

Crystals suitable for X-ray diffraction are obtained from a solution of **28** in acetonitrile by crystallization at -36°C.

^{31}P{^{1}H} NMR (162 MHz, THF-d_8) δ = 39.3 (PNi(CO)$_3$), -5.2 ppm.

^{1}H NMR (400 MHz, THF-d_8) δ = 8.10 (dd, $^3J_{HH}$ = 12.3 Hz, $^3J_{HH}$ = 12.3 Hz, 1H, N*H*), 6.92 (dddd, $^3J_{HP}$ = 24.8 Hz, $^3J_{HH}$ = 13.0 Hz, $^3J_{HH}$ = 10.8 Hz, $^4J_{HH}$ = 2.4 Hz, 1H, NC*H*CHPNi(CO)$_3$), 6.88 (ddd, $^3J_{HP}$ = 18.1 Hz, $^3J_{HH}$ = 11.6 Hz, $^3J_{HH}$ = 9.5 Hz, 1H, NC*H*), 4.74 (dd, $^3J_{HH}$ = 9.5 Hz, $^2J_{HP}$ = 4.8 Hz, 1H, PC*H*), 4.46 (dd, $^3J_{HH}$ = 10.7 Hz, $^2J_{HP}$ = 2.4 Hz, 1H, *H*CPNi(CO)$_3$), 1.24 (d, $^3J_{HP}$ = 13.3 Hz, 18H, ^{t}Bu$_2$PNi(CO)$_3$), 1.23 (d, $^3J_{HP}$ = 12.3 Hz, 18H, P^{t}Bu$_2$) ppm.

^{13}C{^{1}H} NMR (101 MHz, THF-d_8) δ = 198.5 (d, $^2J_{CP}$ = 3.8 Hz, Ni(*C*O)$_3$), 145.5 (d, $^2J_{CP}$ = 5.8 Hz, N*C*H), 145.0 (d, $^2J_{CP}$ = 20.4 Hz, N*C*H), 95.3 (d, $^1J_{CP}$ = 17.1 Hz, P*C*H), 84.9 (d, $^1J_{CP}$ = 30.7 Hz, P*C*H), 35.9 (d, $^1J_{CP}$ = 35.9 Hz, P*C*Me$_3$), 31.9 (d, $^1J_{CP}$ = 16.3 Hz, P*C*Me$_3$), 29.7 (d, $^2J_{CP}$ = 13.8 Hz, P*CMe*$_3$), 29.2 (d, $^2J_{CP}$ = 7.1 Hz, P*CMe*$_3$) ppm.

IR (Nujol): $\tilde{\upsilon}$ = 3316.5, 2062.7, 1987.9 cm^{-1}.

MS (LIFDI, toluene): *m/z* = 443.4 (100%, [$C_{21}H_{41}NOP_2Ni$]$^+$).

2.8.11 [(^{tBu}P=N=P)Ni(*1 κC,2 κ^{2}O,O'*-CO$_2$)Ni(*κ^{2}P,C*-^{t}Bu$_2$PCHCHNHCHCH$_2$P^{t}Bu$_2$)] (29)

Route A: [NiH(^{tBu}P=N=P)] (**12**) (30 mg, 0.072 mmol, 1.0 eq) is dissolved in 3 mL of benzene and CO_2 (1.8 mL, 0.074 mmol, 1.0 eq, ≥99.9993%, purification by passing through P_4O_{10}, Drierite™ and cooling to -40°C) is added. The solution is photolyzed ($\lambda_{exc.}$ > 305 nm) overnight and the solvent is evaporated. The residue is dissolved in *n*-pentane, filtered and the solvent is evaporated. The residue is suspended in 1 mL of acetonitrile and diethyl ether is added dropwise until the solid is dissolved completely. The solution is stored at -36°C overnight for crystallization and the mother liquor is removed. The procedure is repeated followed by drying *in vacuo*. Yield: 7 mg (22%).

Route B: [Ni(CO$_2$H)(^{tBu}P=N=P)] (**16**) (1.5 mg, 3.3 µmol, 1.0 eq) and [NiH(^{tBu}P=N=P)] (**12**) (1.4 mg, 3.4 µmol, 1.0 eq) is dissolved in 0.5 mL of THF and filled into a J Young NMR tube and the sample is photolyzed ($\lambda_{exc.}$ > 305 nm).

Crystals suitable for X-ray diffraction are obtained from a solution of **29** in *n*-pentane by crystallization at -36°C.

$^{31}P\{^{1}H\}$ NMR (203 MHz, C_6D_6) δ = 66.2 (d. $^{2}J_{PP}$ = 197.3 Hz, 1P, (*PNP*)$NiCO_2Ni$(PC)), 65.0 (d. $^{2}J_{PP}$ = 197.1 Hz, 1P, (*PNP*)$NiCO_2Ni$(PC)), 36.8 (d, $^{4}J_{PP}$ = 7.4 Hz, 1P, (PNP)$NiCO_2Ni$(*PC*)), 17.1 (d, $^{4}J_{PP}$ = 7.2 Hz, 1P, non-coordinating pincer arm) ppm.

^{1}H NMR (500 MHz, C_6D_6) δ = 6.96 (m, 2H, NC*H*), 6.48 (ddd, $^{2}J_{HP}$ = 27.2 Hz, $^{3}J_{HH}$ = 9.6 Hz, $^{3}J_{HH}$ = 7.5 Hz, 1H, NC*H*), 4.37 (dd, $^{4}J_{HP}$ = 7.4 Hz, $^{3}J_{HH}$ = 7.4 Hz, 1H, N*H*), 4.02 (m, 2H, PC*H*), 3.52 (d, $^{3}J_{HH}$ = 9.6 Hz, 1H, PC*H*), 2.92 (dddd, $^{3}J_{HH}$ = 12.4 Hz, $^{3}J_{HP}$ = 6.1 Hz, $^{3}J_{HH}$ = 1.9 Hz, $^{3}J_{HH}$ = 1.9 Hz, 1H, NC*H*CH_2), 2.72 (ddd, $^{2}J_{HH}$ = 14.3 Hz, $^{2}J_{HP}$ = 5.9 Hz, $^{3}J_{HH}$ = 2.1 Hz, 1H, NCHC*H*H), 1.73 (m, 9H, P^{t}Bu), 1.68 (m, 9H, P^{t}Bu), 1.59 (m, 9H, P^{t}Bu), 1.51 (m, 9H, P^{t}Bu), 1.50 (d, $^{3}J_{HP}$ = 12.9 Hz, 9H, P^{t}Bu), 1.47 (d, $^{3}J_{HP}$ = 13.1 Hz, 9H, P^{t}Bu), 1.47 (*detected by $^{1}H,^{1}H$ COSY*, NCHCH*H*), 1.32 (d, $^{3}J_{HP}$ = 10.7 Hz, 9H, P^{t}Bu), 1.19 (d, $^{3}J_{HP}$ = 10.9 Hz, 9H, P^{t}Bu) ppm.

$^{13}C\{^{1}H\}$ NMR (126 MHz, C_6D_6) δ = 228.3 (dt, $^{2}J_{CP}$ = 28.5 Hz, $^{3}J_{CP}$ = 3.0 Hz, Ni*C*O_2Ni), 160.7 (dd, $^{3}J_{CP}$ = 13.9 Hz, $^{2}J_{CP}$ = 7.3 Hz, N*C*H), 160.7 (dd, $^{3}J_{CP}$ = 14.0 Hz, $^{2}J_{CP}$ = 7.1 Hz, N*C*H), 149.0 (d, $^{2}J_{CP}$ = 7.3 Hz, N*C*H), 82.6 (dd, $^{1}J_{CP}$ = 33.3 Hz, $^{3}J_{CP}$ = 9.4 Hz, P*C*H), 82.4 (dd, $^{1}J_{CP}$ = 32.5 Hz, $^{3}J_{CP}$ = 9.5 Hz, P*C*H), 68.0 (dd, $^{1}J_{CP}$ = 50.7 Hz, P*C*H), 36.2 (dd, $^{1}J_{CP}$ = 13.8, $^{3}J_{CP}$ = 6.0 Hz, P*C*Me_3), 35.9 (dd, $^{1}J_{CP}$ = 14.0, $^{3}J_{CP}$ = 5.8 Hz, P*C*Me_3), 35.8 (dd, $^{1}J_{CP}$ = 14.2, $^{3}J_{CP}$ = 6.0 Hz, P*C*Me_3), 35.4 (dd, $^{1}J_{CP}$ = 14.2, $^{3}J_{CP}$ = 6.4 Hz, P*C*Me_3), 35.0 (d, $^{1}J_{CP}$ = 21.4, P*C*Me_3), 34.6 (d, $^{1}J_{CP}$ = 24.4, P*C*Me_3), 33.2 (dd, $^{2}J_{CP}$ = 30.4 Hz, $^{2}J_{CP}$ = 4.1 Hz, N*C*HNi), 32.6 (d, $^{1}J_{CP}$ = 22.9 Hz, P*C*Me_3), 31.2 (d, $^{1}J_{CP}$ = 21.6 Hz, P*C*Me_3), 30.5 (d, $^{2}J_{CP}$ = 12.7 Hz, PC*Me*$_3$), 30.2 (dd, $^{2}J_{CP}$ = 3.9 Hz, $^{4}J_{CP}$ = 1.8 Hz, PC*Me*$_3$), 30.1 (dd, $^{2}J_{CP}$ = 3.8 Hz, $^{4}J_{CP}$ = 1.8 Hz, PC*Me*$_3$), 39.9 (d, $^{1}J_{CP}$ = 13.3 Hz, P*C*Me_3), 29.7 (d, $^{2}J_{CP}$ = 5.0 Hz, P*CMe*$_3$), 29.7 (dd, $^{2}J_{CP}$ = 3.7 Hz, $^{4}J_{CP}$ = 1.8 Hz, PC*Me*$_3$), 29.6 (dd, $^{2}J_{CP}$ = 3.7 Hz, $^{4}J_{CP}$ = 1.6 Hz, PC*Me*$_3$), 29.4 (d, $^{1}J_{CP}$ = 26.9 Hz, *C*H_2) ppm.

IR (THF-d_8): $\tilde{\upsilon}$ = 1526.4, 1611.3, 3333.5 cm^{-1}.

MS (LIFDI): *m/z* = 873.4 (50%, $[C_{41}H_{81}N_2Ni_2O_2P_4]^+$), 1392.5 (50%).

2.8.12 [NiH(^{tBu}PN^{H}P)]OTf (**30^{OTf}**)

[NiBr(^{tBu}PNP)] (**3**) (100 mg, 0.200 mmol, 1.00 eq) is dissolved in 10 mL of THF and triflic acid (19.5 µL, 0.220 mmol, 1.10 eq) is added. After stirring for 1 h, $NaBH_4$ (15.6 mg, 0.412 mmol, 2.06 eq) is dissolved in 4 mL ethanol and added to the reaction mixture. The solution is stirred for 30 min until no further gas evolution is observed. After evaporation of the solvent, the residue is dissolved in benzene. Filtration at 70°C followed by evaporation of the solvent gives the product as an off-white powder. Yield: 93 mg (81%).

Isolated **30^{OTf}** can be recrystallized quantitatively from toluene at -36°C yielding crystals suitable for X-ray diffraction. Elemental analysis performed on recrystallized material shows good agreement with calculated values for **30^{OTf}**·(C_7H_8), confirming incorporation of an additional solvent molecule in the crystal lattice observed in X-ray diffraction (Chapter 4.3.22).

Anal. Calcd. for $C_{28}H_{54}F_3NNiO_3P_2S$ (662.44): C, 50.77; H, 8.22; N, 2.11%. Found: C, 51.34 H, 8.73; N, 1.76%.

$^{31}P\{^1H\}$ NMR (203 MHz, THF-d_8) δ = 85.2 pm.

^1H NMR (500 MHz, C_6D_6) δ = 5.33 (br, 1H, N*H*), 3.46 (m, 2H, NCH_2), 2.43 (m, 2H, NCH_2), 2.28 (m, 4H, PCH_2), 1.37 ($A_9B_9XX'B'_9A'_9$, N = $|{}^3J_{AX} + {}^5J_{AX'}|$ = 14.6 Hz, 18H, P^{t}Bu), 1.36 ($A_9B_9XX'B'_9A'_9$, N = $|{}^3J_{BX} + {}^5J_{BX'}|$ = 16.4 Hz, 18H, P^{t}Bu) ppm.

$^{13}C\{^1H\}$ NMR (126 MHz, C_6D_6) δ = 53.2 (vt, $^2J_{CP}$ = 4.3 Hz, N*C*H$_2$), 34.8 (vt, $^1J_{CP}$ = 9.5 Hz, P*C*Me$_3$), 34.3 (vt, $^1J_{CP}$ = 10.9 Hz, P*C*Me$_3$), 29.6 (vt, $^2J_{CP}$ = 2.7 Hz, PC*Me*$_3$), 29.3 (vt, $^2J_{CP}$ = 2.9 Hz, PC*Me*$_3$), 24.9 (vt, $^2J_{CP}$ = 7.3 Hz, P*C*H$_2$) ppm.

IR (ATR): $\tilde{\upsilon}$ = 3159.4, 1900.0 cm^{-1}.

MS (LIFDI, toluene): *m/z* = 420.2 (100%, $[C_{20}H_{46}NNiP_2]^+$).

2.8.13 [NiH(tBuPNP)] (31)

[NiH(^{tBu}PN^{H}P)]OTf (**30^{OTf}**) (50 mg, 88 µmol, 1.0 eq) and KO^{t}Bu (11 mg, 98 µmol, 1.1 eq) is dissolved in 5 mL of benzene and stirred for 1 h. After evaporation of the solvent, the yellow residue is extracted with *n*-pentane and the solution is filtered over Celite®. Evaporation of the solvent gives the product as yellow powder. Yield: 32.7 mg (89%).

Crystals suitable for X-ray diffraction are obtained from a solution of **31** in *n*-pentane by crystallization at -36°C.

Anal. Calcd. for $C_{20}H_{45}NP_2Ni$ (420.23): C, 57.16; H, 10.79; N, 3.33%. Found: C, 56.79 H, 10.76; N, 3.30%.

$^{31}P\{^1H\}$ NMR (121 MHz, C_6D_6): δ = 105.1 ppm.

^1H NMR (300 MHz, C_6D_6): δ = 3.46–3.32 (m, 4H, NCH_2), 2.03–1.94 (m, 4H, PCH_2), 1.28 ($A_{18}B_2C_2XX'C_2'B_2'A'_{18}$, N = $|{}^3J_{AX} + {}^5J_{AX'}|$ = 12.6 Hz, 36H, ^{t}Bu), -17.36 (t, $^2J_{HP}$ = 60.5, 1H, Ni*H*) ppm.

$^{13}C\{^1H\}$ NMR (75 MHz, C_6D_6): δ = 60.4 (vt, $^2J_{CP}$ = 7.0 Hz, N*C*H$_2$), 33.9 (vt, $^1J_{CP}$ = 8.8 Hz, P*C*Me$_3$), 29.5 (vt, $^2J_{CP}$ = 3.1 Hz, PC*Me*$_3$), 26.9 (vt, $^1J_{CP}$ = 7.2 Hz, P*C*H$_2$) ppm.

IR (KBr): $\tilde{\upsilon}$ = 1831.6 cm^{-1}.

MS (LIFDI, toluene): *m/z* = 419.2 (100%, $[C_{20}H_{45}NP_2Ni]^+$).

2.8.14 [NiMe(^{tBu}P=N=P)] (33)

[NiBr(^{tBu}P=N=P)] (**3**) (54 mg, 0.11 mmol, 1.0 eq) is dissolved in 4 mL benzene and MeMgCl (3 M in THF, 0.040 mL, 0.12 mmol, 1.1 eq) is added. After stirred at 80°C for 1 h, the solvent is evaporated. The residue is extracted with *n*-pentane and the solution is filtered over Celite®. Evaporation of the solvent gives the product as orange powder. Yield: 41 mg (87%).

Crystals suitable for X-ray diffraction are obtained from a solution of **33** in Et_2O by crystallization at -36°C.

^{31}P{^{1}H} NMR (121 MHz, C_6D_6): δ = 55.6 ppm.

^{1}H NMR (300 MHz, C_6D_6): δ = 7.02 ($A_{18}BCXX'C'B'A'_{18}$, $N = |{}^{3}J_{CX} + {}^{4}J_{CX'}| = 35.5$ Hz, $^{3}J_{CB}$ = 5.3 Hz, 2H, NC*H*), 3.94 ($A_{18}BCXX'C'B'A'_{18}$, $N = |{}^{2}J_{BX} + {}^{4}J_{BX'}| = 1.5$ Hz, $^{2}J_{BC}$ = 5.3 Hz, 2H, PC*H*), 1.37 ($A_{18}BCXX'C'B'A'_{18}$, $N = |{}^{3}J_{AX} + {}^{5}J_{AX'}| = 12.7$ Hz, 36H, P^{t}Bu), -0.03 (t, $^{3}J_{HP}$ = 8.2 Hz, 3H, NiCH_3) ppm.

^{13}C{^{1}H} NMR (75 MHz, C_6D_6): δ = 161.2 (vt, $^{2}J_{CP}$ = 11.4 Hz, N*C*H), 82.1 (vt, $^{1}J_{CP}$ = 17.7 Hz, P*C*H), 35.1 (vt, $^{1}J_{CP}$ = 8.7 Hz, P*C*Me$_3$), 29.7 (vt, $^{2}J_{CP}$ = 2.8 Hz, PC*Me*$_3$), -28.6 (t, $^{2}J_{CP}$ = 25.5 Hz, Ni*C*H$_3$) ppm.

MS (LIFDI, toluene): *m/z* = 429.2 (100%, $[C_{21}H_{43}NP_2Ni]^+$).

2.8.15 [NiN$_3${N(CHCHP^{t}Bu$_2$)$_2$}] (34)

[NiBr(^{tBu}P=N=P)] (**3**) (317 mg, 0.640 mmol, 1.00 eq), [PPN]N_3 (372 mg, 0.641 mmol, 1.00 eq) and NaN_3 (416 mg, 6.40 mmol, 10.0 eq) is dissolved in 15 mL of THF and the suspension is stirred overnight. After evaporation of the solvent, the residue is extracted with *n*-pentane and filtered. Evaporation of the solvent followed by crystallization from a minimum amount of *n*-pentane at -36°C gives the product as red crystalline material. The mother liquor is decanted and the crystallization process is repeated two times. Yield: 263 mg, 90%).

Crystals suitable for X-ray diffraction are obtained from a solution of **34** in Et_2O by crystallization at -36°C.

Anal. Calcd. for $C_{40}H_{40}N_4NiP_2$ (457.21): C, 52.54; H, 8.82; N, 12.25%. Found: C, 24.19 H, 8.93; N, 12.24%.

^{31}P{^{1}H} NMR (121 MHz, C_6D_6) δ = 62.2 ppm.

^{1}H NMR (300 MHz, C_6D_6) δ = 6.30 ($A_{18}BCXX'C'B'A'_{18}$, $N = |{}^{3}J_{CX} + {}^{4}J_{CX'}| = 38.6$ Hz, $^{3}J_{CB}$ = 5.4 Hz, 2H, NC*H*), 3.67 ($A_{18}BCXX'C'B'A'_{18}$, $N = |{}^{2}J_{BX} + {}^{4}J_{BX'}| = 2.2$ Hz, $^{3}J_{BC}$ = 5.4 Hz, $^{4}J_{HH}$ = 1.8 Hz, 2H, PC*H*), ($A_{18}BCXX'C'B'A'_{18}$, $N = |{}^{3}J_{AX} + {}^{5}J_{AX'}| = 13.8$ Hz, 36H, P^{t}Bu) ppm.

^{13}C{^{1}H} NMR (75 MHz, C_6D_6) δ = 162.5 (vt, $^{2}J_{CP}$ = 11.2 Hz, N*C*H), 81.9 (vt, $^{1}J_{CP}$ = 18.4 Hz, P*C*H), 35.3 (vt, $^{1}J_{CP}$ = 9.2 Hz, P*C*Me$_3$), 29.1 (vt, $^{2}J_{CP}$ = 2.8 Hz, PC*Me*$_3$) ppm.

IR (ATR): $\tilde{\upsilon}$ = 2058.6 cm^{-1}.

MS (LIFDI, toluene): *m/z* = 456.2 (100%, $[C_{40}H_{40}N_4NiP_2]^+$).

2.8.16 [NiPh{κ^3*P,N,N*-N(CHCHP^{t}Bu$_2$)(CHCHP(NH)^{t}Bu$_2$)}] (35)

[NiN$_3$(^{tBu}P=N=P)] (**34**) (9.3 mg, 0.020 mmol, 1.0 eq) is dissolved in 1 mL of benzene and filled into a J Young NMR tube. The solution is photolyzed ($\lambda_{exc.}$ > 305 nm) for 22 h and the solvent is evaporated. The residue is extracted with *n*-pentane and filtered over silanized silica. After evaporation of the solvent, the yellow residue is dissolved in a minimum amount of *n*-pentane and recrystallized at -36°C. Crystals suitable for X-ray diffraction are obtained from *n*-pentane at -36°C. Yield: 6.2 mg (60%).

Crystals suitable for X-ray diffraction are obtained from a solution of **35** in *n*-pentane by crystallization at -36°C.

^{31}P{^{1}H} NMR (203 MHz, C_6D_6) δ = 58.3 (d, $^3J_{PP}$ = 7.4 Hz, Ni*P*), 45.0 (d, $^3J_{PP}$ = 7.4 Hz, NiN*P*) ppm.

^{1}H NMR (500 MHz, C_6D_6) δ = 8.11 (dt, $^3J_{HH}$ = 7.8 Hz, $^4J_{HH}$ = 1.5 Hz, 2H, *o-H*), 7.23–7.13 (m, 3H, C*H*CHPNH and *m-H*), 6.96 (m, 1H, *p-H*), 6.86 (ddd, $^3J_{HP}$ = 35.1 Hz, $^3J_{HH}$ = 6.0 Hz, $^4J_{HH}$ = 0.6 Hz, 1H, C*H*CHP), 3.97 (dd, $^3J_{HH}$ = 6.0 Hz, $^2J_{HP}$ = 1.5 Hz, 1H, C*H*P), 3.20 (ddd, $^2J_{HP}$ = 21.0 Hz, $^3J_{HH}$ = 9.8 Hz, $^3J_{HP}$ = 4.2 Hz, 1H, C*H*PNH), 1.32 (d, $^3J_{HP}$ =13.0 Hz, 18H, P^{t}Bu$_2$), 1.02 (d, $^3J_{HP}$ = 13.5 Hz, 18H, P^{t}Bu$_2$NH), -0.61 (br, 1H, N*H*) ppm.

^{13}C{^{1}H} NMR (126 MHz, C_6D_6) δ = 165.2 (d, $^2J_{CP}$ = 17.3 Hz, *C*HCHP), 160.1 (d, $^2J_{CP}$ = 4.0 Hz, *i-C*), 158.9 (d, $^2J_{CP}$ = 42.2 Hz, *C*HCHPNH), 139.5 (d, $^3J_{CP}$ = 1.5 Hz, *o-C*), 125.7 (d, $^4J_{CP}$ = 2.9 Hz, *m-C*), 122.0 (d, $^5J_{CP}$ = 1.5 Hz, *p-C*), 85.6 (d, $^1J_{CP}$ = 33.2 Hz, *C*HP), 64.0 (d, $^1J_{CP}$ = 108.9 Hz, *C*HPNH), 36.1 (d, $^1J_{CP}$ = 51.7 Hz, HNP*C*Me$_3$), 34.9 (d, $^1J_{CP}$ = 20.6 Hz, P*C*Me$_3$), 29.7 (d, $^2J_{CP}$ = 4.2 Hz, PC*Me*$_3$), 26.8 (d, $^2J_{CP}$ = 1.0 Hz, HNPC*Me*$_3$) ppm.

IR (ATR): $\tilde{\upsilon}$ = 3363.0 cm^{-1}.

MS (LIFDI, toluene): *m/z* = 506.4 (100%, $[C_{46}H_{46}NNiP_2]^+$).

2.8.17 [Ni{κ^3*P,N,N*-N(CH$_2$CH$_2$P^{t}Bu$_2$N)(CH$_2$CH$_2$P^{t}Bu$_2$)}]$_2$ (36)

[NiN$_3$(^{tBu}P=N=P)] (**34**) (30 mg, 0.066 mmol, 1.0 eq) is dissolved in 8 mL of *n*-pentane and filled into a quartz tube. The solution is photolyzed for 3 h and filtered. After evaporation of the solvent, the red residue is dissolved in a minimum amount of *n*-pentane and recrystallized at -36°C.

Crystals suitable for X-ray diffraction are obtained from a solution of **36** in *n*-pentane by crystallization at -36°C.

2.9 Nickel Pincer Complex mediated Reverse Water-Gas Shift Reactivity

2.9.1 Thermal Reactivity of [NiH(^{tBu}P=N=P)] (12) with CO_2

[NiH(^{tBu}P=N=P)] (**12**) (2.0 mg, 4.8 µmol, 1.0 eq) is dissolved in 0.3 mL of THF-d_8 and filled into a Medium Wall Precision Pressure/Vacuum Valve NMR tube. The Sample is degassed by three freeze-pump-thaw cycles. CO_2 pressure ($p(CO_2)$ = 10 atm, ≥99.5%, no further purification) is applied. After 14 days, nearly complete conversion can be detected.

*Spectroscopic signature of [Ni(O$_2$CH)(^{tBu}P=N=P)] (**15**):*

^{31}P{^{1}H} NMR (203 MHz, THF-d_8) δ = 56.1 ppm.

^{1}H NMR (500 MHz, THF-d_8) δ = 7.25 (t, $^4J_{HP}$ = 3.4 Hz, 1H, OCO*H*), 6.49 (A_{18}BCXX'C'B'A'$_{18}$, $N = |{}^3J_{CX} + {}^4J_{CX'}|$ = 38.2 Hz, $^3J_{CB}$ = 5.5 Hz, 2H, NC*H*), 4.09 (A_{18}BCXX'C'B'A'$_{18}$, $N = |{}^2J_{BX} + {}^4J_{BX'}|$ = 2.0 Hz, $^3J_{BC}$ = 5.5 Hz, 2H, PC*H*), 1.51 (A_{18}BCXX'C'B'A'$_{18}$, $N = |{}^3J_{AX} + {}^5J_{AX'}|$ = 13.6 Hz, 36H, P^{t}Bu) ppm.

^{13}C{^{1}H} NMR (126 MHz, THF-d_8) δ = 168.3 (t, $^3J_{CP}$ = 1.1 Hz, O*C*OH), 162.9 (vt, $^2J_{CP}$ = 11.0 Hz, N*C*H), 83.0 (dd, $^1J_{CP}$ = 19.6 Hz, $^3J_{CP}$ = 18.7 Hz, P*C*H), 35.8 (vt, $^1J_{CP}$ = 8.5 Hz, P*C*Me$_3$), 29.0 (vt, $^2J_{CP}$ = 2.8 Hz, PC*Me*$_3$) ppm.

2.9.2 Reaction of [Ni(CO$_2$H)(^{tBu}P=N=P)] (16) with NaBArF

[Ni(CO$_2$H)(^{tBu}P=N=P)] (**16**) (1.0 mg, 2.2 µmol, 1.0 eq) and NaBArF (2.0 mg, 2.3 µmol, 1.0 eq) is filled into a J Young NMR tube and 0.5 mL of THF-d_8 is added. The solution is degassed by three freeze-pump-thaw cycles and CO_2 atmosphere ($p(CO_2)$ = 1 atm, ≥99.9993%, purification by passing through P_4O_{10}, Drierite^{TM} and cooling to -40°C) is applied.

2.9.3 Reaction of [Ni(CO)(^{tBu}P=N=P)]BF$_4$ (20^{BF4}) with LiHBEt$_3$

[Ni(CO)(^{tBu}P=N=P)]BF$_4$ (**20^{BF4}**) (20 mg, 0.038 mmol, 1.0 eq) is dissolved in 0.7 mL of THF-d_8 and cooled to -30°C. A solution of LiHBEt$_3$ (1M in THF, 50 µL, 0.050 mmol, 1.3 eq) is added dropwise and the solution is stirred for 30 minutes at -30°C. The solution is cooled to -45°C, filled into an J Young NMR tube and frozen using liquid nitrogen. The solution is thawed at the NMR spectrometer which is cooled to -25°C, at which temperature NMR characterization is performed. Upon warming above 0°C, conversion of **21** to **12** is observed.

*Spectroscopic signature of [Ni(COH)(^{tBu}P=N=P)] (**21**):*

^{31}P{^{1}H} NMR (162 MHz, THF-d_8) δ = 60.0 ppm.

^{1}H NMR (400 MHz, THF-d_8) δ = 14.1 (t, $^{3}J_{HP}$ = 12.2 Hz, NiCO*H*), 7.15 ($A_{18}BCXX'C'B'A'_{18}$, N = $|^{3}J_{CX} + {}^{4}J_{CX'}|$ = 35.2 Hz, $^{3}J_{CB}$ = 5.2 Hz, 2H, NC*H*), 3.99 (br, PCH_2), 1.32 ($A_{18}BCXX'C'B'A'_{18}$, N = $|^{3}J_{AX} + {}^{5}J_{AX'}|$ = 12.4 Hz, 36H, P^{t}Bu) ppm.

^{13}C{^{1}H} NMR (101 MHz, THF-d_8) δ = 262.9 (t, $^{2}J_{CP}$ = 21.3 Hz, Ni*C*OH), 161.2 (vt, $^{2}J_{CP}$ = 10.4 Hz, N*C*H), 80.8 (vt, $^{1}J_{CP}$ = 19.6 Hz, P*C*H), 35.7 (vt, $^{1}J_{CP}$ = 10.5 Hz, P*C*Me$_3$), 29.1 (vt, $^{2}J_{CP}$ = 2.6 Hz, PC*Me*$_3$) ppm.

2.9.4 Reduction of [Ni(CO)(^{tBu}P=N=P)]BArF (**20^{BArF}**) to Na[Ni(CO)(^{tBu}P=N=P)] (**23Na**)

A solution of [Ni(^{tBu}P=N=P)] (**9**) (6.0 mg, 0.014 mmol, 1.0 eq) in Et_2O is filled into a J Young NMR tube, degassed by three freeze-pump-thaw cycles and CO atmosphere (p(CO) = 1 atm) is applied. After shaking the tube, the solvent is evaporated. Sodium (1.0 mg, 0.043, 3.1 eq) and naphthalene (2.0 mg, 0.016 mmol, 1.1 eq) is stirred in THF-d_8 for 1.5 h and the green solution is filtered into the J Young NMR tube and the mixture is characterized in solution by NMR spectroscopy. Attempts to isolate **23Na** by solvent evaporation result in decomposition into unidentified products.

*Spectroscopic signature of Na[Ni(CO)(^{tBu}P=N=P)] (**23Na**):*

^{31}P{^{1}H} NMR (162 MHz, THF-d_8) δ = 67.6 ppm.

^{1}H NMR (400 MHz, THF-d_8) δ = 7.25 (m, $^{3}J_{HH}$ = 5.4 Hz, 2H, NC*H*), 4.40 (d, $^{3}J_{HH}$ = 5.7 Hz, 2H, PCH_2), 1.25 ($A_{18}BCXX'C'B'A'_{18}$, N = $|^{3}J_{AX} + {}^{5}J_{AX'}|$ = 15.8 Hz, 36H, P^{t}Bu) ppm.

^{13}C{^{1}H} NMR (101 MHz, THF-d_8) δ = 208.4 (t, $^{2}J_{CP}$ = 18.9 Hz, *C*O), 157.6 (vt, $^{2}J_{CP}$ = 11.7 Hz, N*C*H), 90.6 (dd, $^{1}J_{CP}$ = 14.6 Hz, $^{3}J_{CP}$ = 10.7 Hz, P*C*H), 34.5 (br, P*C*Me$_3$), 31.4 (vt, $^{2}J_{CP}$ = 4.9 Hz, PC*Me*$_3$) ppm.

IR (ATR): $\tilde{\upsilon}$ = 1776.0 cm^{-1}.

2.9.5 Reduction of [Ni(CO)(^{tBu}P=N=P)]BArF (**20^{BArF}**) to K[Ni(CO)(^{tBu}P=N=P)] (**23^{K}**) and Subsequent Addition of Acid

[Ni(CO)(^{tBu}P=N=P)]BArF (**20^{BArF}**) (10 mg, 7.7 µmol, 1.0 eq) and KC_8 (4.0 mg, 30 µmol, 3.8 eq) is filled into a J Young NMR tube and a solution of TMS_2O in 0.5 mL of THF-d_8 is added. The ratio between the internal standard and K[Ni(CO)(^{tBu}P=N=P)] **(23^{K})** is determined NMR spectroscopically. The sample is cooled to -36°C and phenol (1.5 mg, 16 µmol, 2.1 eq) is added.

[Ni(CO)(^{tBu}P=N=P)]BArF (**20^{BArF}**) (10 mg, 7.7 µmol, 1.0 eq) and KC_8 (4.0 mg, 30 µmol, 3.8 eq) is filled into a J Young NMR tube and a capillary containing a solution of PPh_3 in toluene is added. After 0.5 mL of

THF is added, the ratio between the internal standard and K[Ni(CO)(^{tBu}P=N=P)] (**23^{K}**) is determined NMR spectroscopically. The sample is cooled to -36°C and [HNEt$_3$]BArF (15 mg, 16 µmol, 2.2 eq) is added. ^{31}P{^{1}H} NMR spectroscopy shows formation of [NiH(^{tBu}P=N=P)] (**12**) in 41-56% yield over three repeated experiments.

2.9.6 Reaction of [Ni(CO)(^{tBu}P=N=P)] (22) with [(Lut)H]BArF

[Ni(CO)(^{tBu}P=N=P)] (**22**) (5.0 mg, 0.011 mmol, 1.0 eq) and [H(lut)]BArF (11 mg, 0.011 mmol, 1.0 eq) is filled into a J Young NMR tube and 0.5 mL of THF-d_8 is added.

2.9.7 Reaction of [Ni(CO)(^{tBu}P=N=P)] (22) with [(Lut)H]BArF and Cp$_2$Co

[Ni(CO)(^{tBu}P=N=P)] (**22**) (6.0 mg, 0.014 mmol, 1.0 eq), cobaltocene (2.6 mg, 0.014 mmol, 1.0 eq) and [H(lut)]BArF (26 mg, 0.027 mmol, 1.9 eq) is filled into a J Young NMR tube and 0.5 mL of THF-d_8 is added.

*Spectroscopic signature of [Ni(CO)(κ^3P,C,P-^{t}Bu$_2$PCHCHNHCHCH$_2$P^{t}Bu$_2$)]BArF (**24^{BArF}**):*

^{31}P{^{1}H} NMR (162 MHz, THF-d_8) δ = 45.02 ($^3J_{PP}$ = 150.1 Hz), -31.51 ($^3J_{PP}$ = 150.4 Hz) ppm.

^{1}H NMR (400 MHz, THF-d_8) δ = 7.79 (br, 8H, BArF), 7.58 (br, 4H, BArF), 7.34 (ddd, $^3J_{HP}$ = 26.2 Hz, $^3J_{HH}$ = 10.0 Hz, $^3J_{HH}$ = 6.4 Hz, 1H, NC*H*CH), 6.69 (br, N*H*), 4.51 (dd, $^2J_{HP}$ = 6.4 Hz, $^3J_{HH}$ = 10.1 Hz, 1H, PC*H*), 3.48 (ddd. $^2J_{HP}$ = 8.9 Hz, $^2J_{HH}$ = 16.9 Hz, $^3J_{HH}$ = 8.9 Hz, 1H, PC*H*H), 2.88 (m, 1H, PCH*H*), 2.75 (m, 1H, NiC*H)* ppm.

IR (ATR, THF-d_8): $\tilde{\upsilon}$ = 1886.1 cm^{-1}.

MS (LIFDI, THF-d_8): *m/z* = 416.2 (100%, [C$_{20}$H$_{42}$NNiP$_2$]$^+$), 444.2 (60%, [C$_{21}$H$_{42}$NNiOP$_2$]$^+$).

2.9.8 Photochemical H$_2$ Activation by [Ni(CO)(^{tBu}P=N=P)]BArF (20^{BArF})

A solution of [Ni(CO)(^{tBu}P=N=P)]BArF (**20^{BArF}**) (10 mg, 7.7 µmol, 1.0 eq) in 0.5 mL of Et$_2$O is filled into a J Young NMR tube and a capillary containing a solution of PPh$_3$ in toluene is added. The solution is cooled to -78°C and the headspace of the tube is evacuated. After warming to room temperature H$_2$ atmosphere (p(H$_2$) = 1 atm) is applied. The ratio between [NiH(^{tBu}P=N=P^H)]BArF (**14^{BArF}**) and the internal standard is determined by ^{31}P{^{1}H} NMR spectroscopy. The sample is photolyzed for 4 h ($\lambda_{exc.}$ >305 nm) with an output current of I = 3 A. ^{31}P{^{1}H} NMR spectroscopy shows 78-83% conversion of **20^{BArF}** and formation of [NiH(^{tBu}P=N=P^H)]BArF (**14^{BArF}**) in 67-73% yield over three repeated experiments. 100 µL CH$_4$ is added *via* a septum and 1 mL of the headspace is analyzed by TCD-GC showing formation of carbon monoxide.

2.9.9 Photolysis of [NiH(^{tBu}P=N=P^{H})]BArF (**14**^{BArF}) under CO_2 Atmosphere

[NiH(^{tBu}P=N=P^{H})]BArF (**14**^{BArF}) (3.0 mg, 2.3 µmol, 1.0 eq) is filled into a J Young NMR tube and 0.5 mL of THF-d_8 is added. The solution is degassed by three freeze-pump-thaw cycles, CO_2 atmosphere ($p(CO_2)$ = 1 atm, ≥99.9993%, purification by passing through P_4O_{10}, Drierite^{TM} and cooling to -40°C) is applied and the sample is photolyzed ($\lambda_{exc.}$ > 305 nm).

2.9.10 Photochemical CO_2 Activation by [NiH(^{tBu}P=N=P^{H})]BArF (**14**^{BArF}) in the Presence of Base

A solution of [NiH(^{tBu}P=N=P^{H})]BArF (**14**^{BArF}) (10 mg, 7.8 µmol, 1.0 eq) in 0.5 mL of THF-d_8 is filled into a J Young NMR tube. One pellet of 3 Å molecular sieve and 1 µL of TMS_2O is added. After determining the ratio between internal standard and **14**^{BArF} NMR spectroscopically, NEt_3 (1.1 µL, 7.9 µmol, 1.0 eq) is added. The solution is degassed by three subsequent freeze-pump-thaw cycles and CO_2 atmosphere ($p(CO_2)$ = 1 atm) is applied. The sample is photolyzed for 6 h ($\lambda_{exc.}$ >305 nm) with an output current of I = 3 A. ^{1}H NMR spectroscopy shows formation of [Ni(CO)(^{tBu}P=N=P)]BArF (**20**^{BArF}) in 47-50% yield over three repeated experiments.

2.9.11 Photolysis of [Ni(CO)(^{tBu}P=N=P)]BArF (**20**^{BArF}) in the Presence of TMG

[Ni(CO)(^{tBu}P=N=P)]BArF (**20**^{BArF}) (5.0 mg, 3.8 µmol, 1.0 eq) and TMG (0.5 µL, 4.0 µmol, 1.1 eq) is filled into a J Young NMR tube and 0.5 mL Et_2O is added. The sample is photolyzed ($\lambda_{exc.}$ > 305 nm) for 15 minutes and stored at room temperature afterwards.

2.9.12 Reaction of [Ni(CO)(^{tBu}P=N=P)]BArF (**20**^{BArF}) with H_2 in the Presence of DBU

[Ni(CO)(^{tBu}P=N=P)]BArF (**20**^{BArF}) (10 mg, 7.7 µmol, 1.0 eq) and DBU (11 µL, 74 µmol, 9.6 eq) is filled into a Medium Wall Precision Pressure/Vacuum Valve NMR tube and 0.5 mL of THF-d_8 is added. The solution is degassed by three freeze-pump-thaw cycles and H_2 pressure ($p(H_2)$ = 10 atm) is applied.

2.9.13 Reaction of [Ni(OCO$_2$H)(^{tBu}P=N=P)] (17) with H_2

[Ni(OH)(^{tBu}P=N=P)] (**18**) (4.0 mg, 9.3 µmol, 1.0 eq) is filled into a Medium Wall Precision Pressure/Vacuum Valve NMR tube and 0.5 mL of THF-d_8 is added. The solution is degassed by three freeze-pump-thaw cycles and CO_2 atmosphere ($p(CO_2)$ = 1 atm) is applied. Afterwards, the sample is pressurized to p = 10 atm using H_2. Since no conversion can be detected NMR spectroscopically, TMG (1.2 µL, 9.3 µmol, 1.0 eq) is added. The solution is degassed by three freeze-pump-thaw cycles and H_2 pressure ($p(H_2)$ = 10 atm) is applied.

2.10 Mechanistic Investigation of Abnormal CO_2 Insertion of [NiH(^{tBu}P=N=P)] (12) to [Ni(CO_2H)(^{tBu}P=N=P)] (16)

2.10.1 UV-pump-UV-vis-probe

UV-vis pump-probe experiments were performed with a 1 kHz Ti:sapphire regenerative amplifier system (Clark-MXR, CPA-1000) producing 150 fs pulses at λ = 775 nm. Pump pulses were generated by second harmonic generation resulting in 387 nm pulses, which were focused to a diameter of about 200 μm at the sample. To exclude multi-photon processes the pump pulse energies were set below 1 μJ. For probing a white-light continuum was generated by focusing a small portion of the 775 nm pulse in a CaF_2 crystal of 4 mm thickness. The white-light was split into a reference and a probe beam, with the probe being superimposed with the pump pulse in the sample cell. The spectra of reference and probe continua were each recorded at wavelengths of λ = 350–730 nm with a 256-element linear diode array attached to a spectrograph. A translation stage was used to adjust the time delay between pump and probe pulses covering a time range of up to 1 ns. The relative plane of polarization between pump and probe was set to the magic angle of 54.7°. The measured time-dependent transient spectra were corrected for a wavelength dependent temporal shift introduced by group delay dispersion within the white-light-probe continuum. Experiments were performed with a hermetically sealed quartz glass cell of 2 mm optical path length filled under argon atmosphere. A magnetic stirrer was included to avoid accumulation of photoproducts in the laser focus.

2.10.2 UV-pump-IR-probe

UV-pump-mid-IR-probe experiments were performed with a 1 kHz Ti:sapphire oscillator/regenerative amplifier system (Coherent, Libra) producing 100 fs pulses at λ = 800 nm. Part of the output energy was used to generate pump pulses at λ = 400 nm by second harmonic generation. Pulse energies of about 0.4 μJ focused to a diameter of about 200 μm were used to excite the sample. Tuneable mid-IR probe pulses were generated by difference frequency mixing of idler and signal pulses from a home-build two stage optical parametric amplifier (OPA)*(11)* pumped by 0.5 mJ of the regenerative amplifier output. The mid-IR beam was split into a reference and a probe beam. The probe pulse passed a translation stage and was superimposed with the pump pulse in the sample cell. To eliminate over-all molecular rotational effects to the signal the relative plane of polarization between pump and probe was set to the magic angle of 54.7°. Probe and reference pulses were directed to a polychromator and separately detected by a liquid-nitrogen cooled HgCdTe-detector of 2 x 32 pixels. To minimize CO_2 and water absorptions the mid-IR beam path was purged with dry nitrogen. The hermetically sealed stainless steel sample cell equipped with two CaF_2 windows of 1 mm thickness and a magnetic stirrer had an optical path length of 0.6 mm.

2.10.3 Wavelength Dependence of Photochemical CO_2 Activation by [NiH(^{tBu}P=N=P)] (12)

[NiH(^{tBu}P=N=P)] (**12**) (3.3 mg, 7.9 µmol, 1.0 eq) and 2 µL of TMS_2O is dissolved in 0.5 mL of THF-d_8 and filled into a J Young NMR tube. The solution is degassed by three freeze-pump-thaw cycles, CO_2 atmosphere ($p(CO_2)$ = 1 atm, ≥99.5%, no further purification) is applied and the sample is photolyzed using a white-glass ($\lambda_{exc.}$ > 305 nm) or green-glass filter ($\lambda_{exc.}$ > 420 nm).

2.10.4 Deprotonation of [Ni(CO_2H)(^{tBu}P=N=P)] (16) to Na[Ni(CO_2)(^{tBu}P=N=P)] (19Na)

[Ni(CO_2H)(^{tBu}P=N=P)] (**16**) (3.0 mg, 6.5 µmol, 1.0 eq) and NaHMDS (1.3 mg, 7.1 µmol, 1.1 eq) is dissolved in 0.5 mL of THF-d_8 and filled into a J Young NMR tube.

*Spectroscopic signature of Na[Ni(CO_2)(^{tBu}P=N=P)] (**19Na**):*

^{31}P{^{1}H} NMR (162 MHz, THF-d_8) δ = 57.5 ppm.

^{1}H NMR (400 MHz, THF-d_8) δ = 7.03 (A_{18}BCXX'C'B'A'$_{18}$, $N = |{}^3J_{CX} + {}^4J_{CX'}|$ = 37.2 Hz, $^3J_{CB}$ = 5.3 Hz, 2H, NC*H*), 3.80 (d, $^3J_{BC}$ = 5.2 Hz, 2H, PC*H*), 1.50 (A_{18}BCXX'C'B'A'$_{18}$, $N = |{}^3J_{AX} + {}^5J_{AX'}|$ = 13.0 Hz, 36H, P^{t}Bu) ppm.

2.10.5 Determination of pK_{ip}(16)^{THF} and pK_{α}(16)^{THF} by reaction of [Ni(CO_2H)(^{tBu}P=N=P)] (16) with Base

[Ni(CO_2H)(^{tBu}P=N=P)] (**16**) (3.0 mg, 6.5 µmol, 1.0 eq) is dissolved in 2 mL of THF-d_8 and samples of the solution are measured by ^{31}P{^{1}H} NMR spectroscopy in the presence of 1.0 eq of DBU, TBD, NaHMDS and in the absence of base.

2.10.6 Quantification of Water for the Conversion of [Ni(CO_2H)(^{tBu}P=N=P)] (16) to [Ni(CO)(^{tBu}P=N=P)]BArF (20^{BArF})

[Ni(CO_2H)(^{tBu}P=N=P)] (**16**) (1.0 mg, 2.2 µmol, 1.0 eq) is dissolved in 0.5 mL of THF-d_8 containing TMS_2O as internal standard. After determining the ratio between **16** and internal standard by ^{1}H NMR spectroscopy, a solution of [H(OEt_2)$_2$]BArF (2.3 mg, 2.3 µmol, 1.1 eq) in 0.1 mL of THF-d_8 is added. After recording a ^{1}H NMR spectrum, the volatiles are collected by trap-to-trap condensation in a new J Young NMR tube and the water is quantified by ^{1}H NMR spectroscopy.

2.10.7 Dehydration of [Ni(CO_2H)(^{tBu}P=N=P)] (16) by Addition of Acid

A solution of [Ni(CO_2H){N(CHCHP^{t}Bu$_2$)$_2$}] (**16**) (4.34 mM in THF-d_8, 0.50 mL, 2.2 µmol, 1.0 eq) is filled into a J Young NMR tube. Acid (2.2 µmol, 1.0 eq) is added and the sample is characterized by NMR spectroscopy.

2.10.8 Thermal Stability of [Ni(CO$_2$H)(^{tBu}P=N=P)] (16)

[Ni(CO$_2$H)(^{tBu}P=N=P)] (**16**) (3.0 mg, 6.5 µmol, 1.0 eq) is dissolved in 0.5 mL of THF-d_8, filled into a J Young NMR tube and heated to 70°C overnight.

2.10.9 Photolysis of [Ni(CO$_2$H)(^{tBu}P=N=P)] (16) under Ar Atmosphere

[Ni(CO$_2$H)(^{tBu}P=N=P)] (**16**) (1.0 mg, 2.2 µmol, 1.0 eq) is dissolved in 0.5 mL of THF-d_8, filled into a J Young NMR tube and photolyzed ($\lambda_{exc.}$ > 305 nm).

2.10.10 Photolysis of [Ni(CO$_2$H)(^{tBu}P=N=P)] (16) under CO$_2$ Atmosphere

[Ni(CO$_2$H)(^{tBu}P=N=P)] (**16**) (2.5 mg, 5.4 µmol, 1.0 eq) is dissolved in 0.5 mL of THF-d_8 and filled into a J Young NMR tube. CO$_2$ atmosphere (p(CO$_2$) = 1 atm, ≥99.9993%, purification by passing through P$_4$O$_{10}$, Drierite™ and cooling to -40°C) is applied and the sample is photolyzed ($\lambda_{exc.}$ > 305 nm).

2.10.11 Rate Dependence of Photochemical CO$_2$ Activation on Photon Flux

A solution of [NiH(^{tBu}P=N=P)] (**12**) (9.69 mM in THF-d_8, 0.50 mL, 4.8 µmol, 1.0 eq) containing TMS$_2$O as internal standard is filled into a J Young NMR tube. The solution is degassed by three freeze-pump-thaw cycles, CO$_2$ atmosphere (p(CO$_2$) = 1 atm, ≥99.9993%, purification by passing through P$_4$O$_{10}$, Drierite™ and cooling to -40°C) is applied and the sample is photolyzed ($\lambda_{exc.}$ > 305 nm) with different lamp intensity.

2.10.12 Rate Dependence of Photochemical CO$_2$ Activation on CO$_2$ Pressure

A solution of [NiH(^{tBu}P=N=P)] (**12**) (9.69 mM in THF-d_8, 0.50 mL, 4.8 µmol, 1.0 eq) containing TMS$_2$O as internal standard is filled into a Medium Wall Precision Pressure/Vacuum Valve NMR tube. The solution is degassed by three freeze-pump-thaw cycles, CO$_2$ pressure (p(CO$_2$) = 1 atm, ≥99.9993%, purification by passing through P$_4$O$_{10}$, Drierite™ and cooling to -40°C) is applied and the sample is photolyzed ($\lambda_{exc.}$ > 305 nm).

2.10.13 Isotopic Labeling Studies on Photochemical CO$_2$ Activation

A solution of [NiD(^{tBu}P=N=P)] (**12-D**) (9.69 mM in THF-d_8, 0.50 mL, 4.8 µmol, 1.0 eq) containing TMS$_2$O as internal standard is filled into a J Young NMR tube. The solution is degassed by three freeze-pump-thaw cycles, CO$_2$ atmosphere (p(CO$_2$) = 1 atm,≥99.9993%, purification by passing through P$_4$O$_{10}$, Drierite™ and cooling to -40°C) is applied and the sample is photolyzed ($\lambda_{exc.}$ > 305 nm).

2.10.14 Photolysis of [NiH(^{tBu}P=N=P)] (12) in the Presence of ^{t}BuOD

[NiH(^{tBu}P=N=P)] (**12**) (3.0 mg, 7.2 µmol, 1.0 eq) and ^{t}BuOD (10 µL, 0.10 mmol, 14 eq) is dissolved in 0.5 mL of THF-d_8 and 2 µL of TMS_2O is added as internal standard. The sample is filled into a J Young NMR tube, stirred overnight at RT and analyzed by NMR spectroscopy before photolysis ($\lambda_{exc.}$ > 305 nm).

2.10.15 Photolysis of [NiD(^{tBu}P=N=P)] (12-D) in the Presence of ^{t}BuOH

[NiD(^{tBu}P=N=P)] (**12-D**) (3.0 mg, 7.2 µmol, 1.0 eq) and ^{t}BuOH (7.0 µL, 0.075 mmol, 10 eq) is dissolved in 0.5 mL of THF-d_8 and 2 µL of TMS_2O is added as internal standard. The sample is filled into a J Young NMR tube, stirred overnight at RT and analyzed by NMR spectroscopy before photolysis ($\lambda_{exc.}$ > 305 nm).

2.10.16 Photolysis of [NiH(^{tBu}P=N=P)] (12) in the Presence of TEMPO-D

[NiH(^{tBu}P=N=P)] (**12**) (3.3 mg, 7.9 µmol, 1.0 eq) and TEMPO-D (13 mg, 0.082 mmol, 10 eq) is dissolved in 0.5 mL of THF-d_8 and 2 µL of TMS_2O is added as internal standard. The sample is filled into a J Young NMR tube, stirred for 1.5 h at RT and analyzed by NMR spectroscopy before photolysis ($\lambda_{exc.}$ > 305 nm).

2.10.17 Photolysis of [NiD(^{tBu}P=N=P)] (12-D) in the Presence of TEMPO-H

[NiD(^{tBu}P=N=P)] (**12-D**) (3.0 mg, 7.2 µmol, 1.0 eq) and TEMPO-H (11 mg, 0.070 mmol, 10 eq) is dissolved in 0.5 mL of THF-d_8 and 2 µL of TMS_2O is added as internal standard. The sample is filled into a J Young NMR tube, stirred overnight at RT and analyzed by NMR spectroscopy before photolysis ($\lambda_{exc.}$ > 305 nm).

2.10.18 Photolysis of [NiH{N(CHCHP^{t}Bu$_2$)$_2$}] (12) under Ar Atmosphere

[NiH{N(CHCHP^{t}Bu$_2$)$_2$}] (**12**) (4.5 mg, 0.011 mmol, 1.0 eq) is dissolved in 0.5 mL of C_6D_6 and 3 µL of TMS_2O is added as internal standard. The sample is filled into a J Young NMR tube and the sample is photolyzed ($\lambda_{exc.}$ > 305 nm). ^{1}H NMR spectroscopy is measured repetitively to determine the conversion of [NiH{N(CHCHP^{t}Bu$_2$)$_2$}] (**12**).

2.10.19 Photolysis of [NiD(^{tBu}P=N=P)] (12-D) under Ar Atmosphere

[NiD(^{tBu}P=N=P)] (**12-D**) (10 mg, 24 µmol, 1.0 eq) is dissolved in 0.5 mL of benzene and 1 µL of C_6D_6 is added as internal standard. The sample is filled into a J Young NMR tube and the sample is photolyzed ($\lambda_{exc.}$ > 305 nm).

2.10.20 Detection of [Ni(tBuP=N=P)] (9) by EPR Analysis from Photolysis of [NiH(tBuP=N=P)] (12) under Ar Atmosphere

[NiH(tBuP=N=P)] (**12**) (4.4 mg, 11 µmol, 1.0 eq) is dissolved in 0.5 mL of THF-d_8 and 3 µL of TMS_2O is added as internal standard. The sample is filled into a J Young NMR tube and the sample is photolyzed (λ_{exc} > 305 nm). 57% conversion of **1** is observed by ^{1}H NMR spectroscopy. 0.2 mL of the sample is filled into a quartz tube and analyzed by EPR measurement

2.10.21 Detection of [Ni(CO)(tBuP=N=P)] (22) by EPR Analysis from Photolysis of [NiH(tBuP=N=P)] (12) under CO_2 Atmosphere

A solution of [NiH(tBuP=N=P)] (**12**) (9.69 mM in THF-d_8, 0.50 mL, 4.8 µmol, 1.0 eq) containing TMS_2O as internal standard is filled into a J Young NMR tube. The solution is degassed by three freeze-pump-thaw cycles and CO_2 atmosphere ($p(CO_2)$ = 1 atm, ≥99.9993%, purification by passing through P_4O_{10}, Drierite™ and cooling to -40°C) is applied and the sample is photolyzed ($\lambda_{exc.}$ > 305 nm) for 2 h. 0.2 mL of the sample is filled into a quartz tube and analyzed by EPR measurement.

2.10.22 Reaction of [Ni(tBuP=N=P)] (9) with stoichiometric amounts of $^{13}CO_2$

[Ni(tBuP=N=P)] (**9**) (5.0 mg, 12 µmol, 1.0 eq) is dissolved in 0.5 mL of C_6D_6, filled into a J Young NMR tube and $^{13}CO_2$ (300 µL, 12 µmol, 1.0 eq) is added with a syringe. The solution is kept at room temperature for 24h.

*Spectroscopic signature of [(tBuP=N=P)Ni(1κC,2κ^{2}O,O'-$^{13}CO_2$)Ni{κ^{2}P,N-N(CHCHPtBu$_2$)$_2$}] (**^{13}C-26**):*

^{31}P{^{1}H} NMR (162 MHz, C_6D_6) δ = 72.2 (dd, $^5J_{PP}$ =8.7 Hz, $^3J_{PC}$ = 2.4 Hz, 1P, (PNP)NiCO$_2$Ni(*P*N)), 67.8 (d, $^2J_{PC}$ = 29.1 Hz, 2P, (*PNP*)NiCO$_2$Ni(PN)), 4.77 (d, $^5J_{PP}$ = 8.6 Hz, 1P, non-coordinating pincer arm) ppm.

^{1}H NMR (400 MHz, C_6D_6) δ = 8.23 (ddd, $^3J_{HP}$ = 42.4 Hz, $^4J_{HP}$ = 5.5 Hz, $^3J_{HH}$ = 5.5 Hz, 1H, NCH of coordinating pincer arm), 6.86 ($A_{18}BCXX'C'B'A'_{18}$, N = $|^3J_{CX} + {}^4J_{CX'}|$ = 36.8 Hz, $^3J_{CB}$ = 5.2 Hz, 2H, NC*H*), 6.43 (dd, $^3J_{HP}$ = 20.8 Hz, $^2J_{HH}$ = 10.5 Hz, 1H, NCH of non-coordinating pincer arm), 4.69 (dd, $^2J_{HH}$ = 10.5 Hz, $^2J_{HP}$ = 6.4 Hz, 1H, PCH of non-coordinating pincer arm), 3.95 (m, 2H, PC*H*), 3.40 (dd, $^2J_{HP}$ = 4.8 Hz, $^2J_{HH}$ = 4.8 Hz, 1H, PCH of coordinating pincer arm), 1.60 (m, 36H, ^{t}Bu), 1.47 (d, $^3J_{HP}$ = 13.6 Hz, 18H, P^{t}Bu of non-coordinating pincer arm), 1.25 (d, $^3J_{HP}$ = 10.9 Hz, 18H, P^{t}Bu of coordinating pincer arm) ppm.

^{13}C{^{1}H} NMR (101 MHz, C_6D_6) δ = 236.7 (dt, $^2J_{CP}$ = 29.1 Hz, $^3J_{CP}$ = 2.4 Hz, *C*O$_2$), 165.8 (dd, $^2J_{CP}$ = 23.0 Hz, $^3J_{CP}$ = 13.7 Hz, NCH of coordinating pincer arm), 160.9 (vt, $^2J_{CP}$ = 10.4 Hz, N*C*H), 149.8 (d, $^2J_{CP}$ = 14.1 Hz, N*C*H of non-coordinating pincer arm), 96.4 (d, $^1J_{CP}$ = 18.8 Hz, P*C*H of non-coordinating pincer arm), 82.3

(vt, $^{1}J_{CP}$ = 18.6 Hz, P*C*H), 74.9 (d, $^{1}J_{PC}$ = 47.5 Hz, PCH of coordinating pincer arm), 36.0 (vt, $^{1}J_{CP}$ = 10.3 Hz, P*C*Me$_3$), 35.0 (d, $^{1}J_{CP}$ = 20.9 Hz, P*C*Me$_3$), 32.4 (d, $^{1}J_{CP}$ = 19.5 Hz, P*C*Me$_3$), 30.0 (d, $^{2}J_{CP}$ = 14.3 Hz, PC*Me*$_3$), 29.7 (br, PC*Me*$_3$), 28.9 (d, $^{1}J_{CP}$ = 4.1 Hz, P*C*Me$_3$), 30.0 (d, $^{2}J_{CP}$ = 14.3 Hz, PC*Me*$_3$) ppm.

MS (LIFDI, toluene): *m/z* = 872.3 (100%, $[C_{41}H_{80}N_2Ni_2O_2P_4]^+$, $^{12}CO_2$-isotopologue).

2.10.23 Reaction of [Ni(tBuP=N=P)] (9) with H_2

[Ni(tBuP=N=P)] (**9**) (3.0 mg, 7.2 µmol) is dissolved in 0.5 mL of C_6D_6 and 2 µL of TMS_2O is added as internal standard. The sample is filled into a J Young NMR tube and H_2 atmosphere ($p(H_2)$ = 1 atm) is applied.

2.10.24 Reaction of [Ni(tBuP=N=P)] (9) with H_2O

[Ni(tBuP=N=P)] (**9**) (3.8 mg, 9.2 µmol, 1.0 eq) is filled into a J Young NMR tube and 2 mL of TMS_2O is added as internal standard. H_2O (1.0 µL, 56 µmol, 6.1 eq) and 0.5 mL of THF-d_8 is condensed into the tube.

2.10.25 Reaction of [NiH(tBuP=N=P)] (12) with [Ni(OH)(tBuP=N=P)] (18)

[NiH(tBuP=N=P)] (**12**) (1.0 mg, 2.4 µmol, 1.0 eq) and [Ni(OH)(tBuP=N=P)] (**18**) (1.0 mg, 2.3 µmol, 1.0 eq) is filled into a J Young NMR tube and dissolved in 0.5 mL of THF-d_8.

2.10.26 Reaction of [Ni(tBuP=N=P)] (9) with H_2O under CO_2 Atmosphere

[Ni(tBuP=N=P)] (**9**) (2.7 mg, 6.5 µmol, 1.0 eq) is filled into a J Young NMR tube and 2 mL of TMS_2O is added as internal standard. H_2O (2.0 µL, 0.11 mmol, 17 eq) and 0.5 mL of THF-d_8 is condensed into the NMR tube and CO_2 atmopshere ($p(CO_2)$ = 1 atm, ≥99.9993%, purification by passing through P_4O_{10}, Drierite™ and cooling to -40°C) is applied.

2.10.27 Rate Dependence of Photochemical CO_2 Activation on Addition of [Ni(tBuP=N=P)] (9)

[Ni(tBuP=N=P)] (**9**) is filled into a J Young NMR tube and a solution of [NiH(tBuP=N=P)] (**12**) (9.69 mM in THF-d_8, 0.50 mL, 4.8 µmol, 1.0 eq) containing TMS_2O as internal standard is added. The solution is degassed by three freeze-pump-thaw cycles, CO_2 atmosphere ($p(CO_2)$ = 1 atm, ≥99.9993%, purification by passing through P_4O_{10}, Drierite™ and cooling to -40°C) is applied and the sample is photolyzed ($\lambda_{exc.}$ > 305 nm).

2.10.28 Investigation of a radical chain mechanism

[NiH(tBuP=N=P)] (**12**) (3.0 mg, 7.2 µmol, 1.0 eq) and [Ni(tBuP=N=P)] (**9**) (3.0 mg, 7.2 µmol, 1.0 eq) is filled into a J Young NMR tube and dissolved in 0.5 mL of THF-d_8. CO_2 (0.19 mL, 8.5 µmol, 1.2 eq) is added to the tube with a Hamilton® syringe.

2.11 Transfer of Photochemical CO_2 Activation to other Substrates and Complexes

2.11.1 Photolysis of [NiH(^{tBu}PN^{H}P)}]OTf (**30^{OTf}**) under CO_2 atmosphere

[NiH(^{tBu}PN^{H}P)}]OTf (**30^{OTf}**) (9.5 mg, 17 µmol, 1.0 eq) is dissolved in 0.5 mL of C_6D_6 and filled into a J Young NMR tube. The solution is degassed by three freeze-pump-thaw cycles, CO_2 atmosphere ($p(CO_2)$ = 1 atm, ≥99.9993%, purification by passing through P_4O_{10}, Drierite™ and cooling to -40°C) is applied and the sample is photolyzed ($\lambda_{exc.}$ > 305 nm).

2.11.2 Reaction of [NiH(^{tBu}PNP)] (31) with CO_2

[NiH(^{tBu}PNP)] (**31)** (4.0 mg, 9.5 µmol, 1.0 eq) is dissolved in 0.5 mL of C_6D_6 and filled into a J Young NMR tube containing 3 Å molecular sieves. The solution is degassed by three freeze-pump-thaw cycles and $^{13}CO_2$ atmosphere ($p(^{13}CO_2)$ = 1 atm) is applied. After NMR spectroscopic characterization of [NiH{N(CO_2)($CH_2CH_2P^tBu_2$)$_2$}] (**32**), the sample is photolyzed using a 150 W LED ($\lambda_{exc.}$ = 390 nm).

*Spectroscopic signature of [NiH{N(CO_2)($CH_2CH_2P^tBu_2$)$_2$}] (**32**):*

^{31}P{^{1}H} NMR (162 MHz, C_6D_6) δ: 81.68 ppm.

^{1}H NMR (400 MHz, C_6D_6) δ = 2.89–2.70 (m, 4H, NCH_2), 2.15–2.00 (m, 4h, PCH_2), 1.28 ($A_{18}B_2C_2XX'C_2'B_2'A'_{18}$, $N = |{}^3J_{AX} + {}^5J_{AX'}|$ = 13.1 Hz, 36H, ^{t}Bu), -21.11 (t, $^2J_{HP}$ = 65.8, 1H, NiH) ppm.

^{13}C{^{1}H} NMR (101 MHz, C_6D_6): δ = 168.6 (s, NCO_2), 58.1 (vt, $^2J_{CP}$ = 4.8 Hz, NCH_2), 33.7 (vt, $^1J_{CP}$ = 9.8 Hz, PC(CH_3)$_3$), 29.8 (vt, $^2J_{CP}$ = 2.7 Hz, PC(CH$_3$)$_3$), 26.3 (vt, $^1J_{CP}$ = 5.6 Hz, PCH$_2$) ppm.

Crystals suitable for X-ray diffraction are obtained by applying CO_2atmosphere ($p(CO_2)$ = 1 atm) to a degassed solution of **31** in Et_2O and storing the solution at -32°C.

2.11.3 Photolysis of [NiH{N(2-C_6H_3-5-CH_3-P^{i}Pr$_2$)$_2$}] (L1) under CO_2 atmosphere

[NiH{N(2-C_6H_3-5-CH_3-PiPr$_2$)$_2$}] (**L$_1$**) (4.4 mg, 9.0 µmol, 1.0 eq) is dissolved in 0.5 mL of THF-d_8 and filled into a J Young NMR tube. The solution is degassed by three freeze-pump-thaw cycles, CO_2 atmosphere ($p(CO_2)$ = 1 atm, ≥99.5%, no further purification) is applied and the sample is photolyzed using a green-glass filter ($\lambda_{exc.}$ > 420 nm).

2.11.4 General Procedure for Nickel catalyzed photochemical alkene hydrogenation

Catalyst (2.4 µmol, 1.0 eq), substrate (48 µmol, 20 eq), TMS_2O (1 µL) is filled into a J Young NMR tube, 0.5 mL of C_6D_6 is added and the ratio between internal standard and substrate is determined by ^{1}H NMR

spectroscopy. The sample is degassed by three freeze-pump-thaw cycles and hydrogen atmosphere is applied at -196°C, giving $p(H_2)$ = 4 atm upon warming to room temperature.[340] The sample is heated to 80°C or photolyzed ($\lambda_{exc.}$ > 305 nm) and the conversion of starting material and yield of product is determined ^{1}H NMR spectroscopically.

2.11.5 Photolysis of [NiMe(^{tBu}P=N=P)] (33)

[NiMe(^{tBu}P=N=P)] (**33)** (4.0 mg, 9.3 µmol, 1.0 eq) is dissolved in 0.5 mL of C_6D_6 and filled into a J Young NMR tube and the sample is photolyzed using a 150 W LED ($\lambda_{exc.}$ = 390 nm).

2.11.6 Photolysis of [NiMe(^{tBu}P=N=P)] (33) in the presence of benzyl bromide

[NiMe(^{tBu}P=N=P)] (**33)** (4.0 mg, 9.3 µmol, 1.0 eq) and benzyl bromide (11 µL, 0.093 mmol, 10 eq) is dissolved in 0.5 mL of C_6D_6 and filled into a J Young NMR tube. After stirring overnight at room temperature, the sample is photolyzed using a 150 W LED ($\lambda_{exc.}$ = 390 nm).

2.11.7 UV-pump-UV-vis-probe and UV-pump-IR-probe

See Chapter 2.10.1 and 2.10.2.

2.12 Actinometry and Quantum Yield Determination

2.12.1 Actinometry

To investigate the efficiency of the photochemical process the quantum yield Φ is determined as the ratio between converted molecules as the moles of product n and absorbed photons N_{Abs}.

$$\Phi = n / N_{Abs} \tag{55}$$

$$N_{Abs} = N(1\text{-}10^{-A}) \tag{56}$$

While the conversion can be monitored by numerus spectroscopic methods, the determination of N_{Abs} requires measurement of the number of photons N emitted by the light source (eq. (56)). Chemical actinometry describes the characterization of a light source by using it to perform a well-examined photochemical reaction involving a chemical actinometer. The conversion of the actinometer upon photolysis and the known quantum yield Φ of the actinometer is used to determine N_{Abs} and therefore N. The number of photons N emitted by a light source are commonly expressed as a photon flux I which is the rate of emitted photons per surface area of irradiation a:

$$I = \frac{N}{a \cdot t} \tag{57}$$

A popular chemical actinometer is potassium ferrioxalate $K_3[Fe(C_2O_4)_3]$ which undergoes reduction to Fe^{II} by CO_2 loss upon irradiation at $\lambda_{exc.}$ = 200–550 nm.[367] The conversion of $K_3[Fe(C_2O_4)_3]$ can be monitored UV-vis spectroscopically by complexation to $K_2[Fe(phen)_3]$ (phen = 1,10-phenanthroline) which shows characteristic absorption at λ = 510 nm.

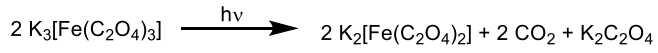

Scheme 73: Photochemical decomposition of $K_3[Fe(C_2O_4)_3]$.

To determine the photon flux of the Xe arc light source utilized in this study, solutions of $K_3[Fe(C_2O_4)_3]$ are photolyzed with a λ = 337 nm or λ = 410 nm bandpass filter (FWHM = 10±2 nm) at different light intensities as follows:

Actinometry experiments are performed under strictly dark conditions using a red light source to avoid photochemical decomposition of the chemical actinometer by light contamination. Photolyzed samples are positioned in 22 cm distance of the Xe arc light source and mounted on a scissor jack in 14 cm height. A solution of $K_3[Fe(C_2O_4)_3]$ (6 mM in H_2O, 2 mL) is filled into a UV-vis cuvette and photolyzed using a

bandpass filter for a certain time ($\lambda_{exc.}$ = 410 nm: t = 15 s; $\lambda_{exc.}$ = 337 nm: t = 60 s) by the light source at a certain output current. A 1 mL aliquot is taken, 1,10-phenathroline solution (5.5 mM in H_2O, 1 mL) and 1 mL of sodium acetate buffer at pH = 3.5 is added before diluting to an overall volume of 10 mL. After equilibration in the dark for 1 hour, the concentration of $[Fe(phen)_3]^{2+}$ is determined UV-vis spectroscopically. After subtraction of a blank measurement, the photon flux I of the light source is determined from the measured absorbance A_{510} at λ = 510 nm using eq(55)–(57), considering the dilution factor k prior to UV-vis measurement:

$$I = \frac{k \cdot V \cdot A_{510}}{\phi \cdot \varepsilon_{510} \cdot d \cdot a \cdot t \cdot (1\text{-}10^{-A})} \tag{58}$$

ε = 1.11·104 $M^{-1}cm^{-1}$ denotes the extinction coefficient of $[Fe(phen)_3]^{2+}$ at λ = 510 nm.[367] Φ is the quantum yield of the chemical actinometer at the excitation wavelength and A is the absorbance of the actinometer solution prior to photolysis at the same wavelength. a is the surface area of irradiation in cm^2, d is the cuvette path length in cm and t is the time of photolysis in min. V is the total volume of actinometer solution photolyzed in liters.

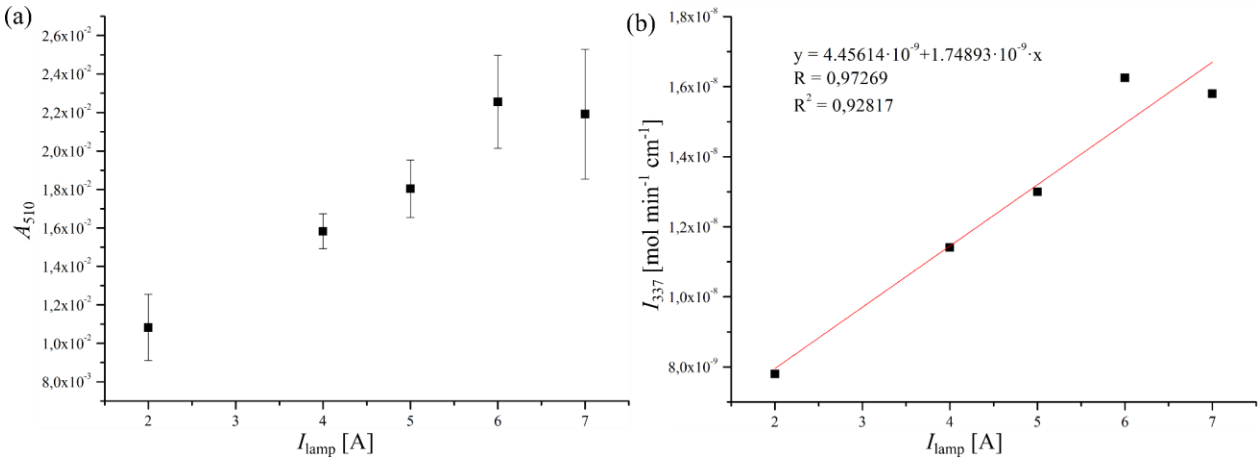

Figure 152: Plot of (a) A_{510} *vs.* I_{lamp} and (b) I_{337} *vs.* I_{lamp} for the photolysis ($\lambda_{exc.}$ = 337 nm) of $K_3[Fe(C_2O_4)_3]$.

The obtained data over three repeated experiments show that the absorbance measured at λ = 510 nm linearly increases with the output current I_{lamp} for $\lambda_{exc.}$ = 337 nm, indicating higher conversion of the actinometer $K_3[Fe(C_2O_4)_3]$ (Figure 152a). According to eq. (55), N_{Abs} can now be determined with the literature reported quantum yield $\Phi_{406.7}$ = 1.188 at λ = 406.7 nm, using *Labert-Beer* to calculate the concentration c and therefore n from the measured absorbance A_{510} with ε_{510} = 1.11·10^4 $M^{-1}cm^{-1}$.[367]

$$N_{abs} = \frac{n}{\Phi} = \frac{V \cdot A_{510}}{\Phi_{406.7} \cdot \varepsilon_{510} \cdot d} \tag{59}$$

Finally, the absorbed photons N_{Abs} have to be converted to the total number of emitted photons N considering the absorbance A of the actinometer solution. While no UV-vis spectra of the solution prior to photolysis were recorded, strong absorption of potassium ferrioxalate in the UV spectral region results in high absorbance and therefore $N \approx N_{Abs}$.[368] Finally, the photon flux I_{337} is calculated from the time of photolysis t = 0.25 min and the irradiated surface area a = 2 cm^2 giving the correlation between I_{lamp} and I_{337} shown in Figure 152b.

In contrast to actinometry at $\lambda_{exc.}$ = 337 nm potassium ferrioxalate shows significantly weaker absorption at λ = 410 m.[368] The absorbed photons N_{Abs} have to be converted to the total emitted photons N considering the extinction coefficient ε of the actinometer. While no UV-vis spectra of the solution prior to photolysis were recorded, ε_{400} = 1.4·10^2 M cm^{-1} close to the irradiation wavelength is taken from the literature giving $N = N_{Abs}$ / 0.86 at the concentrations used following eq. (56).[95] Actinometry on potassium ferrioxalate at $\lambda_{exc.}$ = 410 nm gives the plot for the photon flux I_{410} at different lamp output currents I_{lamp} shown in Figure 153.

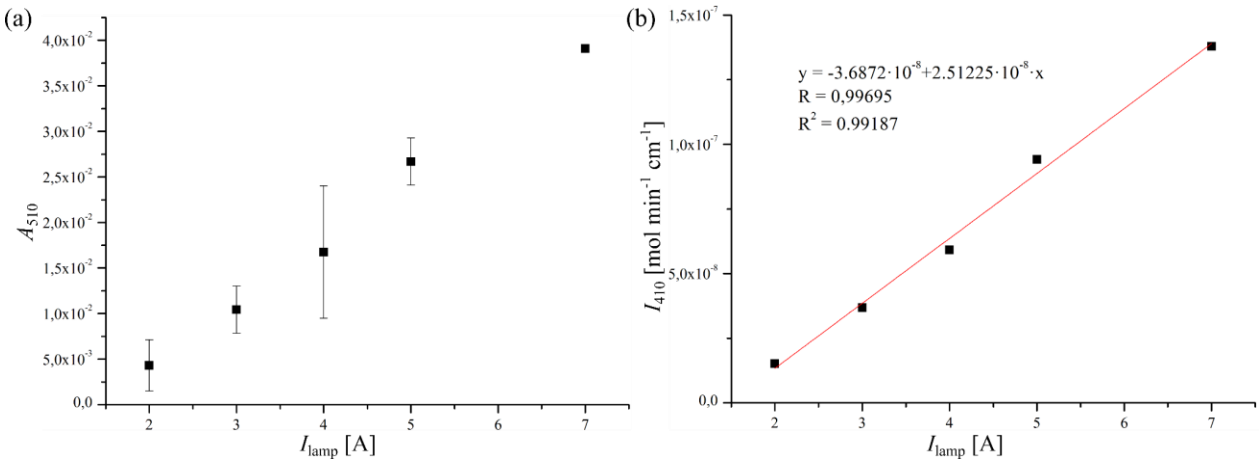

Figure 153: Plot of (a) A_{510} *vs.* I_{lamp} and (b) I_{410} *vs.* I_{lamp} for the photolysis ($\lambda_{exc.}$ = 410 nm) of $K_3[Fe(C_2O_4)_3]$.

2.12.2 Quantum Yield for the Conversion of [Ni(CO)(tBuP=N=P)}]BArF (20BArF) to [NiH(tBuP=N=PH)]BArF (14BArF)

[Ni(CO)(^{tBu}P=N=P)]BArF (**20^{BArF}**) (5.0 mg, 3.8 µmol, 1.0 eq) is dissolved in 4 mL of Et_2O and 0.5 mL of the solution is filled into a J Young NMR tube. A capillary containing a solution of PPh_3 in toluene is added as internal standard. The ratio between **20^{BArF}** and the internal standard is determined by $^{31}P\{^1H\}$ NMR spectroscopy. The remaining solution is degassed by three subsequent freeze-pump-thaw cycles and H_2 atmosphere($p(H_2)$ = 1 atm) is applied. 2 mL of the H_2 saturated solution is filled into a UV-vis cuvette which was previously purged with H_2 for 5 minutes. A UV-vis spectrum is recorded to determine the absorption at λ = 337 nm (A = 1.703). The cuvette is photolyzed at the identical position used for actinometry with

$\lambda_{exc.}$ = 337 nm using a bandpass filter (FWHM = 10±2 nm) for 7 hours with an output current of I = 7 A giving the number of emitted photons $N = 1.4 \cdot 10^{-5}$ mol according to Figure 152 and therefore the number of absorbed photons $N_{abs} = 1.4 \cdot 10^{-5}$ mol. An aliquot of the photolyzed solution is taken and a $^{31}P\{^{1}H\}$ NMR spectrum containing the internal standard is measured. A conversion of 7% ($1.34 \cdot 10^{-7}$ mol) can be observed by comparison with the spectrum recorded before photolysis giving a quantum yield of 1.0% according to eq. (55).

2.12.3 Quantum Yield Determination for the Conversion of [NiH(^{tBu}P=N=P)] (12) to [Ni(CO$_2$H)(^{tBu}P=N=P)] (16)

[NiH(^{tBu}P=N=P)] (**12**) (10 mg, 24 µmol, 1.0 eq) is dissolved in 5 mL of THF. An aliquot of the solution is filled into a J Young NMR tube and a capillary containing a solution of PPh_3 in toluene is added as internal standard. A $^{31}P\{^{1}H\}$ NMR is recorded. The remaining solution of **12** is degassed by three freeze-pump-thaw cycles and CO_2 atmosphere ($p(CO_2)$ = 1 atm, ≥99.9993%, purification by passing through P_4O_{10}, Drierite and cooling to -40°C) is applied. An Argon filled UV-vis cuvette is purged with CO_2 for 5 minutes and 2 mL of the CO_2 saturated solution of **12** is added giving 2 cm² surface area of photolysis. A UV-vis spectrum is recorded to determine the absorption at λ = 410 nm (A = 1.617). The cuvette is photolysed ($\lambda_{exc.}$ = 410 nm) at the identical position used for actinometry using a bandpass (FWHM = 10±2 nm) filter for 3 h with an output current of I = 7 A giving the number of emitted photons $N = 5.0 \cdot 10^{-5}$ mol according to Figure 153 and therefore the number of absorbed photons $N_{abs} = 4.9 \cdot 10^{-5}$ mol. Afterwards an aliquot of the photolyzed solution is taken and a $^{31}P\{^{1}H\}$ NMR spectrum containing the PPh_3 solution as internal standard is measured to determine the conversion of **12** by comparison with the spectrum recorded before photolysis. 46% conversion ($n = 4.4 \cdot 10^{-6}$ mol) could be observed giving a quantum yield of Φ = 9.0% according to eq. (55).

2.12.4 Quantum Yield for the Conversion of [NiH(^{tBu}P=N=P^{H})]BArF ($\mathbf{14^{BArF}}$) to [Ni(CO)(^{tBu}P=N=P)}]BArF ($\mathbf{20^{BArF}}$)

[NiH(^{tBu}P=N=P^{H})]BArF (**14^{BArF}**) (30 mg, 23 µmol, 1.0 eq) and NEt_3 (3.3 µL, 24 µmol, 1.0 eq) is dissolved in 4 mL of THF and 0.5 mL of the solution is filled into a J Young NMR tube. A capillary containing a solution of PPh_3 in toluene is added as internal standard. The ratio between **14^{BArF}**, [NiH(^{tBu}P=N=P] (**12**) and the internal standard is determined by $^{31}P\{^{1}H\}$ NMR spectroscopy. The remaining solution is degassed by three subsequent freeze-pump-thaw cycles and CO_2 atmosphere ($p(CO_2)$ = 1 atm, ≥99.9993%, purification by passing through P_4O_{10}, Drierite and cooling to -40°C) is applied. 2 mL of the CO_2 saturated solution is filled into an UV-vis cuvette which was previously purged with CO_2 for 5 minutes. A UV-vis spectrum is recorded to determine the absorption at 410 nm (A = 2.261). The cuvette is photolyzed at the identical position used for actinometry with $\lambda_{exc.}$ = 410 nm using a bandpass (FWHM = 10±2 nm) filter for

6.5 h with an output current of I = 7 A giving the number of emitted photons $N = 1.1 \cdot 10^{-4}$ mol according to Figure 153 and therefore the number of absorbed photons $N_{abs} = 1.1 \cdot 10^{-4}$ mol. An aliquot of the photolyzed solution is taken and a $^{31}P\{^{1}H\}$ NMR spectrum containing the internal standard is measured. A conversion of 33% ($3.87 \cdot 10^{-6}$ mol) can be observed by comparison with the spectrum recorded before photolysis, giving a quantum yield of 3.6% according to eq. (55).

Literature

[1] R. A. Binstead, B. A. Moyer, G. J. Samuels, T. J. Meyer, *J. Am. Chem. Soc.* **1981**, *103*, 2897–2899.

[2] E. S. Wiedner, M. B. Chambers, C. L. Pitman, R. M. Bullock, A. J. M. Miller, A. M. Appel, *Chem. Rev.* **2016**, *116*, 8655–8692.

[3] C. Costentin, D. H. Evans, M. Robert, J.-M. Savéant, P. S. Singh, *J. Am. Chem. Soc.* **2005**, *127*, 12490–12491.

[4] J. J. Warren, T. A. Tronic, J. M. Mayer, *Chem. Rev.* **2010**, *110*, 6961–7001.

[5] M. H. V. Huynh, T. J. Meyer, *Chem. Rev.* **2007**, *107*, 5004–5064.

[6] D. R. Weinberg, C. J. Gagliardi, J. F. Hull, C. F. Murphy, C. A. Kent, B. C. Westlake, A. Paul, D. H. Ess, D. G. McCafferty, T. J. Meyer, *Chem. Rev.* **2012**, *112*, 4016–4093.

[7] J. M. Mayer, *Annu. Rev. Phys. Chem.* **2004**, *55*, 363–390.

[8] C. Costentin, *Chem. Rev.* **2008**, *108*, 2145–2179.

[9] J. P. McEvoy, G. W. Brudvig, *Chem. Rev.* **2006**, *106*, 4455–4483.

[10] T. J. Meyer, M. H. V. Huynh, H. H. Thorp, *Angew. Chem. Int. Ed.* **2007**, *46*, 5284–5304.

[11] K. N. Ferreira, T. M. Iverson, K. Maghlaoui, J. Barber, S. Iwata, *Science* **2004**, *303*, 1831–1838.

[12] J. W. Whittaker, *Chem. Rev.* **2003**, *103*, 2347–2364.

[13] F. Rappaport, M. Guergova-Kuras, P. J. Nixon, B. A. Diner, J. Lavergne, *Biochemistry* **2002**, *41*, 8518–8527.

[14] W. T. Dixon, D. Murphy, *J. Chem. Soc., Faraday Trans. 2* **1976**, *72*, 1221–1230.

[15] M. Tilset, V. D. Parker, *J. Am. Chem. Soc.* **1989**, *111*, 6711–6717.

[16] E. A. Mader, E. R. Davidson, J. M. Mayer, *J. Am. Chem. Soc.* **2007**, *129*, 5153–5166.

[17] E. A. Mader, V. W. Manner, T. F. Markle, A. Wu, J. A. Franz, J. M. Mayer, *J. Am. Chem. Soc.* **2009**, *131*, 4335–4345.

[18] J. P. Roth, J. M. Mayer, *Inorg. Chem.* **1999**, *38*, 2760–2761.

[19] J. M. Mayer, *Acc. Chem. Res.* **1998**, *31*, 441–450.

[20] J. P. Roth, S. Lovell, J. M. Mayer, *J. Am. Chem. Soc.* **2000**, *122*, 5486–5498.

[21] J. M. Mayer, I. J. Rhile, *Biochim. Biophys. Acta* **2004**, *1655*, 51–58.

[22] M. Kilpatrick, M. L. Kilpatrick, *Chem. Rev.* **1932**, *10*, 213–227.

[23] L. P. Hammett, *J. Am. Chem. Soc.* **1937**, *59*, 96–103.

[24] J. A. Kerr, *Chem. Rev.* **1966**, *66*, 465–500.

[25] J. M. Tedder, *Angew. Chem. Int. Ed.* **1982**, *21*, 401–410.

[26] H. Eyring, *J. Chem. Phys.* **1935**, *3*, 107–115.

[27] R. A. Marcus, N. Sutin, *Biochim. Biophys. Acta* **1985**, *811*, 265–322.

[28] R. A. Marcus, *Angew. Chem. Int. Ed.* **1993**, *32*, 1111–1121.

[29] S. S. Kristjánsdóttir, J. R. Norton, *J. Am. Chem. Soc.* **1991**, *113*, 4366–4367.

[30] K. Gardner, J. M. Mayer, *Science* **1995**, *269*, 1849–1851.

[31] I. S. H. Lee, K. H. Chow, M. M. Kreevoy, *J. Am. Chem. Soc.* **2002**, *124*, 7755–7761.

[32] E. U. Würthwein, G. Lang, L. H. Schappele, H. Mayr, *J. Am. Chem. Soc.* **2002**, *124*, 4084–4092.

[33] S. Hammes-Schiffer, *Acc. Chem. Res.* **2001**, *34*, 273–281.

[34] E. A. Mader, J. M. Mayer, *Inorg. Chem.* **2010**, *49*, 3685–3687.

[35] B. P. Roberts, *Chem. Soc. Rev.* **1999**, *28*, 25–35.

[36] J. R. Bryant, J. M. Mayer, *J. Am. Chem. Soc.* **2003**, *125*, 10351–10361.

[37] K. A. Gardner, L. L. Kuehnert, J. M. Mayer, *Inorg. Chem.* **1997**, *36*, 2069–2078.

[38] I. W. C. E. Arends, P. Mulder, K. B. Clark, D. D. M. Wayner, *J. Phys. Chem.* **1995**, *99*, 8182–8189.

[39] J. A. Howard, K. U. Ingold, *Can. J. Chem.* **1968**, *46*, 2661–2666.

[40] A. S. Larsen, K. Wang, M. A. Lockwood, G. L. Rice, T.-J. Won, S. Lovell, M. Sadílek, F. Tureček, J. M. Mayer, *J. Am. Chem. Soc.* **2002**, *124*, 10112–10123.

[41] C. R. Waidmann, X. Zhou, E. A. Tsai, W. Kaminsky, D. A. Hrovat, W. T. Borden, J. M. Mayer, *J. Am. Chem. Soc.* **2009**, *131*, 4729–4743.

[42] J. M. Mayer, *Acc. Chem. Res.* **2011**, *44*, 36–46.

[43] J. J. Warren, J. M. Mayer, *Proc. Natl. Acad. Sci. U. S. A.* **2010**, *107*, 5282–5287.

[44] J. P. Roth, J. C. Yoder, T. J. Won, J. M. Mayer, *Science* **2001**, *294*, 2524–2526.

[45] M. H. Abraham, P. L. Grellier, D. V. Prior, R. W. Taft, J. J. Morris, P. J. Taylor, C. Laurence, M. Berthelot, R. M. Doherty, M. J. Kamlet, et al., *J. Am. Chem. Soc.* **1988**, *110*, 8534–8536.

[46] G. Litwinienko, K. U. Ingold, *Acc. Chem. Res.* **2007**, *40*, 222–230.

[47] B. A. Moyer, T. J. Meyer, *J. Am. Chem. Soc.* **1978**, *100*, 3601–3603.

[48] B. A. Moyer, T. J. Meyer, *Inorg. Chem.* **1981**, *20*, 436–444.

[49] J. R. Bryant, T. Matsuo, J. M. Mayer, *Inorg. Chem.* **2004**, *43*, 1587–1592.

[50] L. Duan, F. Bozoglian, S. Mandal, B. Stewart, T. Privalov, A. Llobet, L. Sun, *Nat. Chem.* **2012**, *4*, 418–423.

[51] B. M. Lindley, A. M. Appel, K. Krogh-Jespersen, J. M. Mayer, A. J. M. Miller, *ACS Energy Lett.* **2016**, *1*, 698–704.

[52] M. G. Scheibel, J. Abbenseth, M. Kinauer, F. W. Heinemann, C. Würtele, B. de Bruin, S. Schneider, *Inorg. Chem.* **2015**, *54*, 9290–9302.

[53] I. Pappas, P. J. Chirik, *J. Am. Chem. Soc.* **2016**, *138*, 13379–13389.

[54] I. Pappas, P. J. Chirik, *J. Am. Chem. Soc.* **2015**, *137*, 3498–3501.

[55] B. D. Matson, J. C. Peters, *ACS Catal.* **2018**, *8*, 1448–1455.

[56] J. D. Soper, J. M. Mayer, *J. Am. Chem. Soc.* **2003**, *125*, 12217–12229.

[57] M. A. Lockwood, K. Wang, J. M. Mayer, *J. Am. Chem. Soc.* **1999**, *121*, 11894–11895.

[58] J. R. Bryant, J. E. Taves, J. M. Mayer, *Inorg. Chem.* **2002**, *41*, 2769–2776.

[59] E. Khaskin, Y. Diskin-Posner, L. Weiner, G. Leitus, D. Milstein, *Chem. Commun.* **2013**, *49*, 2771–2773.

[60] S. P. Semproni, C. Milsmann, P. J. Chirik, *J. Am. Chem. Soc.* **2014**, *136*, 9211–9224.

[61] M. J. Chalkley, T. J. Del Castillo, B. D. Matson, J. P. Roddy, J. C. Peters, *ACS Cent. Sci.* **2017**, *3*, 217–223.

[62] H. A. Trujillo, C. M. Casado, D. Astruc, *J. Chem. Soc., Chem. Commun.* **1995**, 7–8.

[63] M. E. Kerr, X. M. Zhang, J. W. Bruno, *Organometallics* **1997**, *16*, 3249–3251.

[64] M. J. Bezdek, P. J. Chirik, *J. Am. Chem. Soc.* **2018**, *140*, 13817–13826.

[65] P. O. Lagaditis, B. Schluschaß, S. Demeshko, C. Würtele, S. Schneider, *Inorg. Chem.* **2016**, *55*, 4529–4536.

[66] D. Adhikari, S. Mossin, F. Basuli, J. C. Huffman, R. K. Szilagyi, K. Meyer, D. J. Mindiola, *J. Am. Chem. Soc.* **2008**, *130*, 3676–3682.

[67] S. S. Rozenel, J. B. Kerr, J. Arnold, *Dalton Trans.* **2011**, *40*, 10397–10405.

[68] W. E. Truce, M. L. Gorbaty, *J. Org. Chem.* **1970**, *35*, 2113–2117.

[69] A. Friedrich, M. Drees, M. Käss, E. Herdtweck, S. Schneider, *Inorg. Chem.* **2010**, *49*, 5482–5494.

[70] D. F. Evans, *J. Chem. Soc.* **1959**, 2003–2005.

[71] L. Yang, D. R. Powell, R. P. Houser, *Dalton Trans.* **2007**, 955–964.

[72] K. E. Rosenkoetter, M. K. Wojnar, B. J. Charette, J. W. Ziller, A. F. Heyduk, *Inorg. Chem.* **2018**, *57*, 9728–9737.

[73] P. Mondal, P. Pirovano, A. Das, E. R. Farquhar, A. R. Mcdonald, *J. Am. Chem. Soc.* **2018**, *140*, 1834–1841.

[74] P. Pirovano, E. R. Farquhar, M. Swart, A. R. McDonald, *J. Am. Chem. Soc.* **2016**, *138*, 14362–14370.

[75] K. Ray, T. Petrenko, K. Wieghardt, F. Neese, *Dalton Trans.* **2007**, 1552–1566.

[76] G. J. Colpas, M. J. Maroney, C. Bagyinka, M. Kumar, W. S. Willis, S. L. Suib, N. Baidya, P. K. Mascharak, *Inorg. Chem.* **1991**, *30*, 920–928.

[77] A. N. Marziale, E. Herdtweck, J. Eppinger, S. Schneider, *Inorg. Chem.* **2009**, *48*, 3699–3709.

[78] T. Büttner, F. Breher, H. Grützmacher, *Chem. Commun.* **2004**, 2820–2821.

[79] B. Askevold, A. Friedrich, M. R. Buchner, B. Lewall, A. C. Filippou, E. Herdtweck, S. Schneider, *J. Organomet. Chem.* **2013**, *744*, 35–40.

[80] L. Alig, M. Fritz, S. Schneider, *Chem. Rev.* **2018**, *119*, 2681–2751.

[81] F. G. Bordwell, G. E. Drucker, H. E. Fried, *J. Org. Chem.* **1981**, *46*, 632–635.

[82] B. G. Cox, *Acids and Bases: Solvent Effects on Acid-Base Strength.*, Oxford University Press, Oxford, **2013**.

[83] F. G. Bordwell, *Acc. Chem. Res* **1988**, *21*, 456–463.

[84] B. Askevold, M. M. Khusniyarov, W. Kroener, K. Gieb, P. Müller, E. Herdtweck, F. W. Heinemann, M. Diefenbach, M. C. Holthausen, V. Vieru, et al., *Chem. Eur. J.* **2015**, *21*, 579–589.

[85] J. Meiners, M. G. Scheibel, M.-H. Lemée-Cailleau, S. A. Mason, M. B. Boeddinghaus, T. F. Fässler, E. Herdtweck, M. M. Khusniyarov, S. Schneider, *Angew. Chem. Int. Ed.* **2011**, *50*, 8184–8187.

[86] J. Abbenseth, M. Diefenbach, S. C. Bete, C. Würtele, C. Volkmann, S. Demeshko, M. C. Holthausen, S. Schneider, *Chem. Commun.* **2017**, *53*, 5511–5514.

[87] F. G. Bordwell, J.-P. Cheng, J. A. Harrelson, *J. Am. Chem. Soc.* **1988**, *110*, 1229–1231.

[88] E. Cadenas, L. Packer, Eds. , *Handbook of Antioxidants*, Marcel Dekker, New York, **2002**.

[89] K. L. Handoo, J.-P. Cheng, V. D. Parker, *J. Am. Chem. Soc.* **1993**, *115*, 5067–5072.

[90] J.-P. Cheng, K. L. Handoo, V. D. Parker, *J. Am. Chem. Soc.* **1993**, *115*, 2655–2660.

[91] X.-M. Zhang, J. W. Bruno, E. Enyinnaya, *J. Org. Chem.* **1998**, *63*, 4671–4678.

[92] T. Fox, P. A. Kollman, *J. Phys. Chem.* **1996**, *100*, 2950–2956.

[93] K. M. Biswas, L. E. Houghton, A. H. Jackson, *Tetrahedron* **1966**, *22*, 261–270.

[94] M. Salmón, R. Miranda, I. Nicolás-Vázquez, Y. M. Vargas-Rodriguez, J. Cruz-Borbolla, M. I. Medrano, J. A. Morales-Serna, *Molecules* **2011**, *16*, 1761–1775.

[95] H.-X. Zou, Y. Li, Y. Yang, J.-H. Li, J. Xiang, *Adv. Synth. Catal.* **2018**, *360*, 1439–1443.

[96] D. D. M. Wayner, V. D. Parker, *Acc. Chem. Res.* **1993**, *26*, 287–294.

[97] J. Ferguson, L. W. Reeves, W. G. Schneider, *Can. J. Chem.* **1957**, *35*, 1117–1136.

[98] A. Fernández-Ramos, B. A. Ellingson, R. Meana-Pañeda, J. M. C. Marques, D. G. Truhlar, *Theor. Chem. Acc.* **2007**, *118*, 813–826.

[99] J. C. Yoder, J. P. Roth, E. M. Gussenhoven, A. S. Larsen, J. M. Mayer, *J. Am. Chem. Soc.* **2003**, *125*, 2629–2640.

[100] J. W. Williams, I. J. Krchma, *J. Am. Chem. Soc.* **1926**, *48*, 1888–1896.

[101] A. Clerici, F. Minisci, O. Porta, *Tetrahedron* **1973**, *29*, 2775–2779.

[102] A. Wu, J. M. Mayer, *J. Am. Chem. Soc.* **2008**, *130*, 14745–14754.

[103] I. Kaljurand, A. Kütt, L. Sooväli, T. Rodima, V. Mäemets, I. Leito, I. A. Koppel, *J. Org. Chem.* **2005**, *70*, 1019–1028.

[104] P. Zanello, *Inorganic Electrochemistry: Theory, Practive and Application*, Royal Society Of Chemistry, Cambridge, **2003**.

[105] C. Yoo, Y. Lee, *Angew. Chem. Int. Ed.* **2017**, *56*, 9502–9506.

[106] J.-P. Cloutier, L. Rechignat, Y. Canac, D. H. Ess, D. Zargarian, *Inorg. Chem.* **2019**, *2*, DOI 10.1021/acs.inorgchem.8b03489.

[107] C. A. Rettenmeier, H. Wadepohl, L. H. Gade, *Chem. Sci.* **2016**, *7*, 3533–3542.

[108] K. Abdur-Rashid, T. P. Fong, B. Greaves, D. G. Gusev, J. G. Hinman, S. E. Landau, A. J. Lough, R. H. Morris, *J. Am. Chem. Soc.* **2000**, *122*, 9155–9171.

[109] M. J. Kaufman, S. Gronert, A. Streitwieser, *J. Am. Chem. Soc.* **1988**, *110*, 2829–2835.

[110] I. S. Antipin, R. F. Gareyev, A. N. Vedernikov, A. I. Konovalov, *J. Phys. Org. Chem.* **1994**, *7*, 181–191.

[111] R. M. Fuoss, *J. Am. Chem. Soc.* **1958**, *80*, 5059–5061.

[112] B. C. Fullmer, H. Fan, M. Pink, J. C. Huffman, N. P. Tsvetkov, K. G. Caulton, *J. Am. Chem. Soc.* **2011**, *133*, 2571–2582.

[113] E. A. LaPierre, M. L. Clapson, W. E. Piers, L. Maron, D. M. Spasyuk, C. Gendy, *Inorg. Chem.* **2018**, *57*, 495–506.

[114] E. P. Cappellani, S. D. Drouin, G. Jia, P. A. Maltby, R. H. Morris, C. T. Schweitzer, *J. Am. Chem. Soc.* **1994**, *116*, 3375–3388.

[115] E. Brunner, *J. Chem. Eng. Data* **1985**, *30*, 269–273.

[116] D. E. Berning, B. C. Noll, D. L. DuBois, *J. Am. Chem. Soc.* **1999**, *121*, 11432–11447.

[117] D. E. Berning, A. Miedaner, C. J. Curtis, B. C. Noll, M. C. Rakowski DuBois, D. L. DuBois, *Organometallics* **2001**, *20*, 1832–1839.

[118] C. J. Curtis, A. Miedaner, W. W. Ellis, D. L. DuBois, *J. Am. Chem. Soc.* **2002**, *124*, 1918–1925.

[119] N. A. Eberhardt, H. Guan, *Chem. Rev.* **2016**, *116*, 8373–8426.

[120] O. Kühl, *Phosphorus-31 NMR Spectroscopy*, Springer, Berlin, **2008**.

[121] L.-C. Liang, P.-S. Chien, P.-Y. Lee, *Organometallics* **2008**, *27*, 3082–3093.

[122] Y. Hu, A. P. Shaw, D. P. Estes, J. R. Norton, *Chem. Rev.* **2016**, *116*, 8427–8462.

[123] D. R. Lide, Ed. , *CRC Handbook of Chemistry and Physics, Internet Version 2005*, CRC Press, Boca Raton, **2005**.

[124] V. W. Manner, T. F. Markle, J. H. Freudenthal, J. P. Roth, J. M. Mayer, *Chem. Commun.* **2008**, *246*, 256–258.

[125] A. K. Hijazi, Z. A. Taha, A. Ajlouni, N. Radhakrishnan, B. Voit, F. E. Kühn, *J. Organomet. Chem.* **2014**, *763*, 65–68.

[126] I. Chávez, A. Alvarez-Carena, E. Molins, A. Roig, W. Maniukiewicz, A. Arancibia, V. Arancibia, H. Brand, J. Manuel Manríquez, *J. Organomet. Chem.* **2000**, *601*, 126–132.

[127] N. A. Yakelis, R. G. Bergman, *Organometallics* **2005**, *24*, 3579–3581.

[128] J.-M. Lalancette, G. Rollin, P. Dumas, *Can. J. Chem.* **1972**, *50*, 3058–3062.

[129] A. Martinsen, J. Songstad, *Acta Chem. Scand.* **1977**, *31A*, 645–650.

[130] O. V. Ozerov, C. Guo, L. Fan, B. M. Foxman, *Organometallics* **2004**, *23*, 5573–5580.

[131] J. Meiners, A. Friedrich, E. Herdtweck, S. Schneider, *Organometallics* **2009**, *28*, 6331–6338.

[132] A. J. Ozinskas, A. M. Bobst, *Helv. Chim. Acta* **1980**, *63*, 1407–1411.

[133] S. Hoops, S. Sahle, R. Gauges, C. Lee, J. Pahle, N. Simus, M. Singhal, L. Xu, P. Mendes, U. Kummer, *Bioinformatics* **2006**, *22*, 3067–3074.

[134] M. W. Chase Jr., *NIST-JANAF Themochemical Tables, Fourth Edition*, American Institute Of Physics, College City, **1998**.

[135] S. Daniele, P. Ugo, G. Mazzocchin, G. Bontempelli, *Anal. Chim. Acta* **1985**, *173*, 141–148.

[136] I. Noviandri, K. N. Brown, D. S. Fleming, P. T. Gulyas, P. A. Lay, A. F. Masters, L. Phillips, *J. Phys. Chem. B* **1999**, *103*, 6713–6722.

[137] V. D. Parker, *J. Am. Chem. Soc.* **1992**, *114*, 7458–7462.

[138] M. M. Elsemongy, A. A. Abdel-Khalek, **1991**, *181*, 79–94.

[139] J. Datta, K. K. Kundu, *Can. J. Chem.* **1981**, *59*, 3149–3156.

[140] I. M. Sidahmed, C. F. Wells, *J. Chem. Soc., Faraday Trans. 1* **1987**, *83*, 439–449.

[141] C. Kalidas, G. Hefter, Y. Marcus, *Chem. Rev.* **2000**, *100*, 819–852.

[142] D. Dhar, W. B. Tolman, *J. Am. Chem. Soc.* **2015**, *137*, 1322–1329.

[143] G. Jia, A. J. Lough, R. H. Morris, *Organometallics* **1992**, *11*, 161–171.

[144] P. Tans, R. Keeling, "Trends in Atmospheric Carbon Dioxide," https://www.esrl.noaa.gov/gmd/ccgg/trends/data.html, date of accession: 02/05/2019.

[145] BP Statistical Review of World Energy BP p.l.c., "BP Statistical Review of World Energy," https://www.bp.com/content/dam/bp/business-sites/en/global/corporate/pdfs/energy-economics/statistical-review/bp-stats-review-2018-full-report.pdf, **2018**, date of accession: 02/05/2019.

[146] J. G. Canadell, C. Le Quere, M. R. Raupach, C. B. Field, E. T. Buitenhuis, P. Ciais, T. J. Conway, N. P. Gillett, R. A. Houghton, G. Marland, *Proc. Natl. Acad. Sci. U. S. A.* **2007**, *104*, 18866–18870.

[147] U. S. Department of Energy, "Carbon Cycling and Biosequestration: Report from the March 2008 Workshop," https://genomicscience.energy.gov/carboncycle/report/, **2008**, date of accession: 02/06/2019.

[148] Global CCS Institute, *The Global Status of CCS*, **2018**.

[149] C. P. Consoli, N. Wildgust, *Energy Procedia* **2017**, *114*, 4623–4628.

[150] P. Kaiser, R. B. Unde, C. Kern, A. Jess, *Chem. Ing. Tech.* **2013**, *85*, 489–499.

[151] Y. A. Daza, J. N. Kuhn, *RSC Adv.* **2016**, *6*, 49675–49691.

[152] D. Wöhrle, M. W. Tausch, W.-D. Stohrer, *Photochemie: Konzepte, Methoden, Experimente*, Wiley-VCH, Weinheim, **1998**.

[153] P. Moriarty, D. Honnery, *Renew. Sustain. Energy Rev.* **2012**, *16*, 244–252.

[154] K. Yoshida, C. Wakai, N. Matubayasi, M. Nakahara, *J. Phys. Chem. A* **2004**, *108*, 7479–7482.

[155] J. Klankermayer, S. Wesselbaum, K. Beydoun, W. Leitner, *Angew. Chemie* **2016**, *128*, 7416–7467.

[156] P. G. Jessop, T. Ikariya, R. Noyori, *Chem. Rev.* **1995**, *95*, 259–272.

[157] D. Mellmann, P. Sponholz, H. Junge, M. Beller, *Chem. Soc. Rev.* **2016**, *45*, 3954–3988.

[158] D. S. Newsome, *Catal. Rev. Sci. Eng.* **1980**, *21*, 275–318.

[159] S. Wesselbaum, V. Moha, M. Meuresch, S. Brosinski, K. M. Thenert, J. Kothe, T. Vom Stein, U. Englert, M. Hölscher, J. Klankermayer, et al., *Chem. Sci.* **2015**, *6*, 693–704.

[160] Methanol Institute, "The Methanol Industry," https://www.methanol.org/the-methanol-industry/, date of accession: 02/05/2019.

[161] G. A. Olah, *Angew. Chem. Int. Ed.* **2005**, *44*, 2636–2639.

[162] M. Behrens, *Angew. Chem. Int. Ed.* **2014**, *53*, 12022–12024.

[163] F. Studt, M. Behrens, E. L. Kunkes, N. Thomas, S. Zander, A. Tarasov, J. Schumann, E. Frei, J. B. Varley, F. Abild-Pedersen, et al., *ChemCatChem* **2015**, *7*, 1105–1111.

[164] O.-S. Joo, K.-D. Jung, I. Moon, A. Y. Rozovskii, G. I. Lin, S.-H. Han, S.-J. Uhm, *Ind. Eng. Chem. Res.* **1999**, *38*, 1808–1812.

[165] Deutsche Energie-Agentur, "The Power to Gas Strategy Platform," http://www.powertogas.info/, date of accession: 02/05/2019.

[166] W. Wang, S. Wang, X. Ma, J. Gong, *Chem. Soc. Rev.* **2011**, *40*, 3703–3727.

[167] A. M. Appel, J. E. Bercaw, A. B. Bocarsly, H. Dobbek, D. L. DuBois, M. Dupuis, J. G. Ferry, E. Fujita, R. Hille, P. J. A. A. Kenis, et al., *Chem. Rev.* **2013**, *113*, 6621–6658.

[168] J. H. Jeoung, H. Dobbek, *Science* **2007**, *318*, 1461–1464.

[169] T. Reda, C. M. Plugge, N. J. Abram, J. Hirst, *Proc. Natl. Acad. Sci. U. S. A.* **2008**, *105*, 10654–10658.

[170] H. Dobbek, *Coord. Chem. Rev.* **2011**, *255*, 1104–1116.

[171] C.-S. Chen, W.-H. Cheng, S.-S. Lin, *Catal. Letters* **2000**, *68*, 45–48.

[172] A. Goguet, F. C. Meunier, D. Tibiletti, J. P. Breen, R. Burch, *J. Phys. Chem. B* **2004**, *108*, 20240–20246.

[173] P. C. Ford, *Acc. Chem. Res.* **1981**, *14*, 31–37.

[174] K.-I. Tominaga, Y. Sasaki, M. Kawai, T. Watanabe, M. Saito, *J. Chem. Soc., Chem. Commun.* **1993**, 629–631.

[175] K. Tsuchiya, J.-D. Huang, K.-I. Tominaga, *ACS Catal.* **2013**, *3*, 2865–2868.

[176] N. Liu, L. Guo, Z. Cao, W. Li, X. Zheng, Y. Shi, J. Guo, Y. Xi, *J. Phys. Chem. A* **2016**, *120*, 2408–2419.

[177] J. Halpern, A. L. W. Kemp, *J. Am. Chem. Soc.* **1966**, *88*, 5147–5150.

[178] M. A. Mcloughlin, N. L. Keder, W. T. A. Harrison, R. J. Flesher, H. A. Mayer, W. C. Kaska, *Inorg. Chem.* **1999**, *38*, 3223–3227.

[179] J. Qiao, Y. Liu, F. Hong, J. Zhang, *Chem. Soc. Rev.* **2014**, *43*, 631–675.

[180] Y. Hori, H. Wakebe, T. Tsukamoto, O. Koga, *Electrochim. Acta* **1994**, *39*, 1833–1839.

[181] A. A. Peterson, F. Abild-Pedersen, F. Studt, J. Rossmeisl, J. K. Nørskov, *Energy Environ. Sci.* **2010**, *3*, 1311–1315.

[182] W. Luo, W. Xie, R. Mutschler, E. Oveisi, G. L. De Gregorio, R. Buonsanti, A. Züttel, *ACS Catal.* **2018**, *8*, 6571–6581.

[183] J. L. White, M. F. Baruch, J. E. Pander, Y. Hu, I. C. Fortmeyer, J. E. Park, T. Zhang, K. Liao, J. Gu, Y. Yan, et al., *Chem. Rev.* **2015**, *115*, 12888–12935.

[184] I. Taniguchi, B. Aurian-Blajeni, J. O. Bockris, *Electrochim. Acta* **1984**, *29*, 923–932.

[185] A. B. Muñoz-García, E. A. Carter, *J. Am. Chem. Soc.* **2012**, *134*, 13600–13603.

[186] C. X. Kronawitter, M. Lessio, P. Zhao, C. Riplinger, A. Boscoboinik, D. E. Starr, P. Sutter, E. A. Carter, B. E. Koel, *J. Phys. Chem. C* **2015**, *119*, 17762–17772.

[187] M. Lessio, J. M. Dieterich, E. A. Carter, *J. Phys. Chem. C* **2017**, *121*, 17321–17331.

[188] L. Liu, Y. Li, *Aerosol Air Qual. Res.* **2014**, *14*, 453–469.

[189] L.-C. Liang, C.-W. Li, P.-Y. Lee, C.-H. Chang, H. M. Lee, *Dalton Trans.* **2011**, *40*, 9004–9011.

[190] A. H. A. Tinnemans, T. P. M. Koster, D. H. M. W. Thewissen, A. Mackor, *Recl. Trav. Chim. Pays-Bas* **1984**, *103*, 288–295.

[191] M. Beley, J.-P. Collin, R. Ruppert, J.-P. Sauvage, *J. Chem. Soc., Chem. Commun.* **1984**, 1315–1316.

[192] J. Schneider, H. Jia, J. T. Muckerman, E. Fujita, *Chem. Soc. Rev.* **2012**, *41*, 2036–2051.

[193] J. P. Collin, A. Jouaiti, J.-P. Sauvage, *Inorg. Chem.* **1988**, *27*, 1986–1990.

[194] J. Song, E. L. Klein, F. Neese, S. Ye, *Inorg. Chem.* **2014**, *53*, 7500–7507.

[195] I. Bhugun, D. Lexa, J.-M. Savéant, *J. Am. Chem. Soc.* **1996**, *118*, 1769–1776.

[196] M. Hammouche, D. Lexa, J.-M. Savéant, M. Momenteau, *J. Electroanal. Chem.* **1988**, *249*, 347–351.

[197] C. A. Kelly, Q. G. Mulazzani, M. Venturi, E. L. Blinn, M. A. J. Rodgers, *J. Am. Chem. Soc.* **1995**, *117*, 4911–4919.

[198] C. Creutz, H. A. Schwarz, J. F. Wishart, E. Fujita, N. Sutin, *J. Am. Chem. Soc.* **1991**, *113*, 3361–3371.

[199] M. Rakowski DuBois, D. L. DuBois, *Acc. Chem. Res.* **2009**, *42*, 1974–1982.

[200] R. M. Bullock, A. M. Appel, M. L. Helm, *Chem. Commun.* **2014**, *50*, 3125–3143.

[201] A. J. Morris, G. J. Meyer, E. Fujita, *Acc. Chem. Res.* **2009**, *42*, 1983–1994.

[202] B. P. Sullivan, C. M. Bolinger, D. Conrad, W. J. Vining, T. J. Meyer, *J. Chem. Soc., Chem. Commun.* **1985**, *985*, 1414–1416.

[203] J. Hawecker, J.-M. Lehn, R. Ziessel, *J. Chem. Soc., Chem. Commun.* **1983**, 536–538.

[204] Y. Hayashi, S. Kita, B. S. Brunschwig, E. Fujita, *J. Am. Chem. Soc.* **2003**, *125*, 11976–11987.

[205] F. P. A. Johnson, M. W. George, F. Hartl, J. J. Turner, *Organometallics* **1996**, *15*, 3374–3387.

[206] J. Agarwal, E. Fujita, H. F. Schaefer, J. T. Muckerman, *J. Am. Chem. Soc.* **2012**, *134*, 5180–5186.

[207] D. H. Gibson, X. Yin, *Chem. Commun.* **1999**, 1411–1412.

[208] J. Agarwal, B. C. Sanders, E. Fujita, H. F. Schaefer, T. C. Harrop, J. T. Muckerman, *Chem. Commun.* **2012**, *48*, 6797–6799.

[209] D. H. Gibson, X. Yin, *J. Am. Chem. Soc.* **1998**, *120*, 11200–11201.

[210] B. P. Sullivan, T. J. Meyer, *Organometallics* **1986**, *5*, 1500–1502.

[211] B. P. Sullivan, T. J. Meyer, *J. Chem. Soc., Chem. Commun.* **1984**, 1244–1245.

[212] S. Sato, T. Morikawa, T. Kajino, O. Ishitani, *Angew. Chem. Int. Ed.* **2013**, *52*, 988–992.

[213] K. Garg, Y. Matsubara, M. Z. Ertem, A. Lewandowska-Andralojc, S. Sato, D. J. Szalda, J. T. Muckerman, E. Fujita, *Angew. Chem. Int. Ed.* **2015**, *54*, 14128–14132.

[214] Y. Kohno, H. Ishikawa, T. Tanaka, T. Funabiki, S. Yoshida, *Phys. Chem. Chem. Phys.* **2001**, *3*, 1108–1113.

[215] K. Teramura, T. Tanaka, H. Ishikawa, Y. Kohno, T. Funabiki, *J. Phys. Chem. B* **2004**, *108*, 346–354.

[216] M. Tahir, N. S. Amin, *Chem. Eng. J.* **2016**, *285*, 635–649.

[217] J. Ettedgui, Y. Diskin-Posner, L. Weiner, R. Neumann, *J. Am. Chem. Soc.* **2011**, *133*, 188–190.

[218] C. Ci, J. J. Carbó, R. Neumann, C. de Graaf, J. M. Poblet, *ACS Catal.* **2016**, *6*, 6422–6428.

[219] M. Aresta, C. F. Nobile, V. G. Albano, E. Forni, M. Manassero, *J. Chem. Soc., Chem. Commun.* **1975**, 636–637.

[220] J. S. Anderson, V. M. Iluc, G. L. Hillhouse, *Inorg. Chem.* **2010**, *49*, 10203–10207.

[221] C. Yoo, Y.-E. Kim, Y. Lee, *Acc. Chem. Res.* **2018**, *51*, 1144–1152.

[222] Y.-E. Kim, J. Kim, Y. Lee, *Chem. Commun.* **2014**, *50*, 11458–11461.

[223] C. Yoo, J. Kim, Y. Lee, *Organometallics* **2013**, *32*, 7195–7203.

[224] C. Yoo, Y. Lee, *Chem. Sci.* **2017**, *8*, 600–605.

[225] D. Sahoo, C. Yoo, Y. Lee, *J. Am. Chem. Soc.* **2018**, *140*, 2179–2185.

[226] F. S. Menges, S. M. Craig, N. Tötsch, A. Bloomfield, S. Ghosh, H.-J. Krüger, M. A. Johnson, *Angew. Chem. Int. Ed.* **2016**, *128*, 1304–1307.

[227] P. Zimmermann, C. Limberg, *J. Am. Chem. Soc.* **2017**, *139*, 4233–4242.

[228] B. Horn, C. Limberg, C. Herwig, B. Braun, *Chem. Commun.* **2013**, *49*, 10923–10925.

[229] P. Zimmermann, S. Hoof, B. Braun-Cula, C. Herwig, C. Limberg, *Angew. Chem. Int. Ed.* **2018**, *57*, 7230–7233.

[230] A. J. M. Miller, J. A. Labinger, J. E. Bercaw, *Organometallics* **2011**, *30*, 4308–4314.

[231] D. L. DuBois, D. E. Berning, *Appl. Organomet. Chem.* **2000**, *14*, 860–862.

[232] K. M. Waldie, A. L. Ostericher, M. H. Reineke, A. F. Sasayama, C. P. Kubiak, *ACS Catal.* **2018**, *8*, 1313–1324.

[233] R. C. Cammarota, M. V Vollmer, J. Xie, J. Ye, J. C. Linehan, S. A. Burgess, A. M. Appel, L. Gagliardi, C. C. Lu, *J. Am. Chem. Soc.* **2017**, *139*, 14244–14250.

[234] J. W. Raebiger, A. Miedaner, C. J. Curtis, S. M. Miller, O. P. Anderson, D. L. DuBois, *J. Am. Chem. Soc.* **2004**, *126*, 5502–5514.

[235] R. Ciancanelli, B. C. Noll, D. L. DuBois, M. Rakowski DuBois, *J. Am. Chem. Soc.* **2002**, *124*, 2984–2992.

[236] M. T. Mock, R. G. Potter, D. M. Camaioni, J. Li, W. G. Dougherty, W. S. Kassel, B. Twamley, D. L. DuBois, *J. Am. Chem. Soc.* **2009**, *131*, 14454–14465.

[237] T.-Y. Cheng, R. M. Bullock, *J. Am. Chem. Soc.* **1999**, *121*, 3150–3155.

[238] Y. Matsubara, E. Fujita, M. D. Doherty, J. T. Muckerman, C. Creutz, *J. Am. Chem. Soc.* **2012**, *134*, 15743–15757.

[239] R. Tanaka, M. Yamashita, K. Nozaki, *J. Am. Chem. Soc. Commun.* **2009**, *131*, 14168–14169.

[240] T. J. Schmeier, G. E. Dobereiner, R. H. Crabtree, N. Hazari, *J. Am. Chem. Soc.* **2011**, *133*, 9274–9277.

[241] E. A. Bielinski, P. O. Lagaditis, Y. Zhang, B. Q. Mercado, C. Würtele, W. H. Bernskoetter, N. Hazari, S. Schneider, *J. Am. Chem. Soc.* **2014**, *136*, 10234–10237.

[242] Y. Zhang, A. D. MacIntosh, J. L. Wong, E. A. Bielinski, P. G. Williard, B. Q. Mercado, N. Hazari, W. H. Bernskoetter, *Chem. Sci.* **2015**, *6*, 4291–4299.

[243] S. Chakraborty, P. Bhattacharya, H. Dai, H. Guan, *Acc. Chem. Res.* **2015**, *48*, 1995–2003.

[244] H.-W. Suh, T. J. Schmeier, N. Hazari, R. A. Kemp, M. K. Takase, *Organometallics* **2012**, *31*, 8225–8236.

[245] J. E. Heimann, W. H. Bernskoetter, N. Hazari, J. M. Mayer, *Chem. Sci.* **2018**, *9*, 6629–6638.

[246] G. L. Geoffroy, in *Prog. Inorg. Chem.* (Ed.: S.J. Lippard), John Wiley & Sons, Inc., New York, **1980**, pp. 123–152.

[247] R. N. Perutz, B. Procacci, *Chem. Rev.* **2016**, *116*, 8506–8544.

[248] J. N. Hill, R. N. Perutz, A. D. Rooney, *J. Phys. Chem.* **1995**, *99*, 538–543.

[249] G. L. Geoffroy, M. G. Bradley, *Inorg. Chem.* **1978**, *17*, 2410–2414.

[250] C. Giannotti, M. L. H. Green, *J. Chem. Soc., Chem. Commun.* **1972**, 1114–1115.

[251] P. Bergamani, S. Sostero, O. Traverso, *J. Organomet. Chem.* **1986**, *299*, C11–C14.

[252] C. Hall, W. D. Jones, R. J. Mawby, R. Osman, R. N. Perutz, M. K. Whittlesey, *J. Am. Chem. Soc.* **1992**, *114*, 7425–7435.

[253] M. Colombo, M. W. George, J. N. Moore, D. I. Pattison, R. N. Perutz, I. G. Virrels, T.-Q. Ye, *J. Chem. Soc., Dalton Trans.* **1997**, 2857–2860.

[254] M. G. Colombo, M. W. George, J. N. Moore, D. I. Pattison, R. N. Perutz, I. G. Virrels, T.-Q. Ye, *Laser Chem.* **1999**, *19*, 283–285.

[255] L. Torres, R. Gelabert, M. Moreno, J. M. Lluch, *Chem. Phys.* **2003**, *286*, 149–163.

[256] W. D. Jones, J. A. Maguire, *Organometallics* **1986**, *5*, 590–591.

[257] W. D. Jones, J. A. Maguire, G. P. Rosini, *Inorganica Chim. Acta* **1998**, *270*, 77–86.

[258] W. D. Jones, G. P. Rosini, J. A. Maguire, *Organometallics* **1999**, *18*, 1754–1760.

[259] J. A. Bandy, F. G. N. Cloke, G. Copper, J. P. Day, R. B. Girling, R. G. Graham, J. C. Green, R. Grinter, R. N. Perutz, *J. Am. Chem. Soc.* **1988**, *110*, 5039–5050.

[260] R. L. Sweany, *Inorg. Chem.* **1980**, *19*, 3512–3516.

[261] A. J. Rest, J. J. Turner, *Chem. Commun.* **1969**, 375–376.

[262] S. P. Church, M. Poliakoff, J. A. Timney, J. J. Turner, *Inorg. Chem.* **1983**, *22*, 3259–3266.

[263] M. C. R. Symons, R. L. Sweany, *Organometallics* **1982**, *1*, 834–836.

[264] C. Daniel, *J. Am. Chem. Soc.* **1992**, *114*, 1625–1631.

[265] M. R. J. Hachey, C. Daniel, *Inorg. Chem.* **1998**, *37*, 1387–1391.

[266] F. D. Miller, R. D. Sanner, *Organometallics* **1988**, *7*, 818–825.

[267] D. S. Glueck, L. J. N. Winslow, R. G. Bergman, *Organometallics* **1991**, *10*, 1462–1479.

[268] S. Sostero, O. Traverso, R. Ros, R. A. Michelin, *J. Organomet. Chem.* **1983**, *246*, 325–329.

[269] M.-T. Youinou, R. Ziessel, *J. Organomet. Chem.* **1989**, *363*, 197–208.

[270] R. Ziessel, *J. Chem. Soc., Chem. Commun.* **1988**, 16–17.

[271] R. Ziessel, *Angew. Chemie* **1991**, *103*, 863–866.

[272] K. J. Watson, R. Ziessel, *Inorganica Chim. Acta* **1992**, *197*, 125–127.

[273] C. L. Pitman, A. J. M. Miller, *ACS Catal.* **2014**, *4*, 2727–2733.

[274] S. M. Barrett, S. A. Slattery, A. J. M. Miller, *ACS Catal.* **2015**, *5*, 6320–6327.

[275] M. B. Chambers, D. A. Kurtz, C. L. Pitman, M. K. Brennaman, A. J. M. Miller, *J. Am. Chem. Soc.* **2016**, *138*, 13509–13512.

[276] C. Caix, S. Chardon-Noblat, A. Deronzier, *J. Electroanal. Chem.* **1997**, *434*, 163–170.

[277] Y. Himeda, N. Onozawa-Komatsuzaki, H. Sugihara, K. Kasuga, *J. Photochem. Photobiol. A* **2006**, *182*, 306–309.

[278] S. Sanz, M. Benítez, E. Peris, *Organometallics* **2010**, *29*, 275–277.

[279] A. J. M. Miller, D. M. Heinekey, J. M. Mayer, K. I. Goldberg, *Angew. Chem. Int. Ed.* **2013**, *125*, 4073–4076.

[280] J. D. Blakemore, N. D. Schley, D. Balcells, J. F. Hull, G. W. Olack, C. D. Incarvito, O. Eisenstein, G. W. Brudvig, R. H. Crabtree, *J. Am. Chem. Soc.* **2010**, *132*, 16017–16029.

[281] T. P. Brewster, A. J. M. Miller, D. M. Heinekey, K. I. Goldberg, *J. Am. Chem. Soc.* **2013**, *135*, 16022–16025.

[282] R. Ziessel, *J. Am. Chem. Soc.* **1993**, *115*, 118–127.

[283] D. Sandrini, M. Maestri, R. Ziessel, *Inorganica Chim. Acta* **1989**, *163*, 177–180.

[284] S. M. Barrett, C. L. Pitman, A. G. Walden, A. J. M. Miller, *J. Am. Chem. Soc.* **2014**, *136*, 14718–14721.

[285] T. Suenobu, D. M. Guldi, S. Ogo, S. Fukuzumi, *Angew. Chem. Int. Ed.* **2003**, *42*, 5492–5495.

[286] T. Ito, T. Matsubara, *J. Chem. Soc., Dalton Trans.* **1988**, 2241–2242.

[287] R. Shimogawa, T. Takao, G.-I. Konishi, H. Suzuki, *Organometallics* **2014**, *33*, 5066–5069.

[288] M. G. Scheibel, B. Askevold, F. W. Heinemann, E. J. Reijerse, B. de Bruin, S. Schneider, *Nat. Chem.* **2012**, *4*, 552–558.

[289] M. G. Scheibel, Y. Wu, A. C. Stückl, L. Krause, E. Carl, D. Stalke, B. de Bruin, S. Schneider, *J. Am. Chem. Soc.* **2013**, 17719–17722.

[290] N. Muller, O. R. Hughes, *J. Phys. Chem.* **1966**, *70*, 3975–3982.

[291] D. Adhikari, S. Mossin, F. Basuli, B. R. Dible, M. Chipara, H. Fan, J. C. Huffman, K. Meyer, D. J. Mindiola, *Inorg. Chem.* **2008**, *47*, 10479–10490.

[292] J. Cámpora, I. Matas, P. Palma, C. Graiff, A. Tiripicchio, *Organometallics* **2005**, *24*, 2827–2830.

[293] M. T. Kieber-Emmons, R. Schenker, G. P. A. Yap, T. C. Brunold, C. G. Riordan, *Angew. Chem. Int. Ed.* **2004**, *116*, 6884–6886.

[294] J. Cámpora, P. Palma, D. del Río, E. Álvarez, *Organometallics* **2004**, *23*, 1652–1655.

[295] H. Ishida, K. Tanaka, M. Morimoto, T. Tanaka, *Organometallics* **1986**, *5*, 724–730.

[296] H. Nakajima, K. Tsuge, K. Toyohara, K. Tanaka, *J. Organomet. Chem.* **1998**, *569*, 61–69.

[297] N. E. Katz, D. J. Szalda, M. H. Chou, C. Creutz, N. Sutin, *J. Am. Chem. Soc.* **1989**, *111*, 6591–6601.

[298] D. J. Metz, A. Glines, *J. Phys. Chem.* **1967**, *71*, 1158.

[299] G. Smith, D. E. Lynch, *Acta Crystallogr.* **2016**, *E72*, 382–386.

[300] T. Rodima, I. Kaljurand, A. Pihl, V. Mäemets, I. Leito, I. A. Koppel, *J. Org. Chem.* **2002**, *67*, 1873–1881.

[301] D. Vuzman, E. Poverenov, Y. Diskin-Posner, G. Leitus, L. J. W. Shimon, D. Milstein, *Dalton Trans.* **2007**, 5692–5700.

[302] L. Schwartsburd, E. Poverenov, L. J. W. Shimon, D. Milstein, *Organometallics* **2007**, *26*, 2931–2936.

[303] C. Yoo, S. Oh, J. Kim, Y. Lee, *Chem. Sci.* **2014**, *5*, 3853–3858.

[304] B. D. McCarthy, D. J. Martin, E. S. Rountree, A. C. Ullman, J. L. Dempsey, *Inorg. Chem.* **2014**, *53*, 8350–8361.

[305] C. Amatore, J. Pinson, J.-M. Savéant, A. Thiebault, *J. Electroanal. Chem.* **1980**, *107*, 59–74.

[306] M. Käß, A. Friedrich, M. Drees, S. Schneider, *Angew. Chem. Int. Ed.* **2009**, *48*, 905–907.

[307] M. Wrighton, *Chem. Rev.* **1974**, *74*, 401–430.

[308] A. P. Garratt, H. W. Thompson, *J. Chem. Soc.* **2004**, 1817–1822.

[309] F. Jiang, K. Biradha, W. K. Leong, R. K. Pomeroy, M. J. Zaworotko, *Can. J. Chem* **1999**, *77*, 1327–1335.

[310] A. P. Lathem, Z. M. Heiden, *Dalton Trans.* **2017**, *46*, 5976–5985.

[311] D. Pines, J. Ditkovich, T. Mukra, Y. Miller, P. M. Kiefer, S. Daschakraborty, J. T. Hynes, E. Pines, *J. Phys. Chem. B* **2016**, *120*, 2440–2451.

[312] Y. Himeda, N. Onozawa-Komatsuzaki, H. Sugihara, H. Arakawa, K. Kasuga, *Organometallics* **2004**, *23*, 1480–1483.

[313] G. Laurenczy, F. Joó, L. Nádasdi, *Inorg. Chem.* **2000**, *39*, 5083–5088.

[314] P. G. T. Fogg, Ed. , *Carbon Dioxide in Non-Aqueous Solvents at Pressures Less than 200 KPa*, Pergamon Press, Oxford, **1992**.

[315] M. Eigen, *Pure Appl. Chem.* **1963**, *6*, 97–115.

[316] R. A. Kirgan, B. P. Sullivan, D. P. Rillema, in *Photochemistry and Photophysics of Coordination Compounds II: Topics in Current Chemistry* (Eds.: V. Balzani, S. Campagna), Springer, Berlin, Heidelberg, **2007**, pp. 45–100.

[317] F. Neese, *Coord. Chem. Rev.* **2009**, *253*, 526–563.

[318] B. J. Shields, B. Kudisch, G. D. Scholes, A. G. Doyle, *J. Am. Chem. Soc.* **2018**, *140*, 3035–3039.

[319] J. Bigeleisen, *J. Chem. Phys.* **1949**, *17*, 675–678.

[320] L. X. Chen, G. Jennings, T. Liu, D. J. Gosztola, J. P. Hessler, D. V. Scaltrito, G. J. Meyer, *J. Am. Chem. Soc.* **2002**, *124*, 10861–10867.

[321] N. W. Hoffman, T. L. Brown, *Inorg. Chem.* **1978**, *17*, 613–617.

[322] J. F. Endicott, C.-L. Wong, T. Inoue, P. Natarajan, *Inorg. Chem.* **1979**, *18*, 450–454.

[323] P. Wermer, B. S. Ault, M. Orchin, *J. Organomet. Chem.* **1978**, *162*, 189–194.

[324] J. Chetwynd-Talbot, P. Grebenik, R. N. Perutz, *J. Chem. Soc., Chem. Commun.* **1981**, 452–454.

[325] D. Gareau, C. Sui-Seng, L. F. Groux, F. Brisse, D. Zargarian, *Organometallics* **2005**, *24*, 4003–4013.

[326] M. Feller, U. Gellrich, A. Anaby, Y. Diskin-Posner, D. Milstein, *J. Am. Chem. Soc.* **2016**, *138*, 6445–6454.

[327] M. Kreye, M. Freytag, P. G. Jones, P. G. Williard, W. H. Bernskoetter, M. D. Walter, *Chem. Commun.* **2015**, *51*, 2946–2949.

[328] N. Grüger, H. Wadepohl, L. H. Gade, *Dalton Trans.* **2012**, *41*, 14028–14030.

[329] M.-C. Chang, K. A. Jesse, A. S. Filatov, J. S. Anderson, *Chem. Sci.* **2019**, *10*, 1360–1367.

[330] Z. R. Grabowski, W. Rubaszewska, *J. Chem. Soc., Faraday Trans. 1* **1977**, *73*, 11–28.

[331] C. A. Tolman, *Chem. Rev.* **1977**, *77*, 313–348.

[332] R. H. Crabtree, *The Organometallic Chemistry of the Transition Metals: Sixth Edition*, John Wiley & Sons, Inc., Hoboken, **2014**.

[333] L.-C. Liang, Y.-T. Hung, Y.-L. Huang, P.-S. Chien, P.-Y. Lee, W.-C. Chen, *Organometallics* **2012**, *31*, 700–708.

[334] D. Oren, Y. Diskin-Posner, L. Avram, M. Feller, D. Milstein, *Organometallics* **2018**, *37*, 2217–2221.

[335] J. Zhao, A. S. Goldman, J. F. Hartwig, *Science* **2005**, *307*, 1080–1082.

[336] M. Kanzelberger, X. Zhang, T. J. Emge, A. S. Goldman, J. Zhao, C. Incarvito, J. F. Hartwig, *J. Am. Chem. Soc.* **2003**, *125*, 13644–13645.

[337] S. Takemoto, Y. Yamazaki, T. Yamano, D. Mashima, H. Matsuzaka, *J. Am. Chem. Soc.* **2012**, *134*, 17027–17035.

[338] J. Ho, M. L. Coote, *Theor. Chem. Acc.* **2010**, *125*, 3–21.

[339] D. Stasko, S. P. Hoffmann, K.-C. Kim, N. L. P. Fackler, A. S. Larsen, T. Drovetskaya, F. S. Tham, C. A. Reed, C. E. F. Rickard, P. D. W. Boyd, et al., *J. Am. Chem. Soc.* **2002**, *124*, 13869–13876.

[340] K. V. Vasudevan, B. L. Scott, S. K. Hanson, *Eur. J. Inorg. Chem.* **2012**, 4898–4906.

[341] R. Stichauer, A. Helmers, J. Bremer, M. Rohdenburg, A. Wark, E. Lork, M. Vogt, *Organometallics* **2017**, *36*, 839–848.

[342] M. Vogt, M. Gargir, M. A. Iron, Y. Diskin-Posner, Y. Ben-David, D. Milstein, *Chem. Eur. J.* **2012**, *18*, 9194–9197.

[343] S. Chakraborty, O. Blacque, H. Berke, *Dalton Trans.* **2015**, *44*, 6560–6570.

[344] M. Vogt, A. Nerush, Y. Diskin-Posner, Y. Ben-David, D. Milstein, *Chem. Sci.* **2014**, *5*, 2043–2051.

[345] C. A. Huff, J. W. Kampf, M. S. Sanford, *Organometallics* **2012**, *31*, 4643–4645.

[346] M. Vogt, O. Rivada-Wheelaghan, M. A. Iron, G. Leitus, Y. Diskin-Posner, L. J. W. Shimon, Y. Ben-David, D. Milstein, *Organometallics* **2013**, *32*, 300–308.

[347] J. L. Graff, T. J. Sobieralski, M. S. Wrighton, G. L. Geoffroy, *J. Am. Chem. Soc.* **1982**, *104*, 7526–7533.

[348] T.-P. Lin, J. C. Peters, *J. Am. Chem. Soc.* **2014**, *136*, 13672–13683.

[349] C. L. Pitman, A. J. M. Miller, *Organometallics* **2017**, *36*, 1906–1914.

[350] X. Hu, *Chem. Sci.* **2011**, *2*, 1867–1886.

[351] V. Vreeken, M. A. Siegler, B. de Bruin, J. N. H. Reek, M. Lutz, J. I. van der Vlugt, *Angew. Chem. Int. Ed.* **2015**, *54*, 7055–7059.

[352] D. Adhikari, F. Basuli, H. Fan, J. C. Huffman, M. Pink, D. J. Mindiola, *Inorg. Chem.* **2008**, *47*, 4439–4441.

[353] V. Vreeken, L. Baij, B. de Bruin, M. A. Siegler, J. I. van der Vlugt, *Dalton Trans.* **2017**, *46*, 7145–7149.

[354] A. Velian, S. Lin, A. J. M. Miller, M. W. Day, T. Agapie, *J. Am. Chem. Soc.* **2010**, *132*, 6296–6297.

[355] M. Corbett, B. F. Hoskins, *Chem. Commun.* **1968**, 1602–1604.

[356] C. A. Laskowski, G. L. Hillhouse, *Organometallics* **2009**, *28*, 6114–6120.

[357] A. W. Addison, T. N. Rao, J. Reedijk, J. van Rijn, G. C. Verschoor, *J. Chem. Soc., Dalton Trans.* **1984**, 1349–1356.

[358] J. Šima, *Coord. Chem. Rev.* **2006**, *250*, 2325–2334.

[359] J. L. Reed, F. Wang, F. Basolo, *J. Am. Chem. Soc.* **1972**, *94*, 7173–7174.

[360] H. D. Gafney, J. L. Reed, F. Basolo, *J. Am. Chem. Soc.* **1973**, *95*, 7998–8005.

[361] K. Meyer, E. Bill, B. Mienert, T. Weyhermüller, K. Wieghardt, *J. Am. Chem. Soc.* **1999**, *121*, 4859–4876.

[362] J. Torres-Alacan, U. Das, A. C. Filippou, P. Vöhringer, *Angew. Chem. Int. Ed.* **2013**, *52*, 12833–12837.

[363] H. Vennekate, D. Schwarzer, J. Torres-Alacan, O. Krahe, A. C. Filippou, F. Neese, P. Vöhringer, *Phys. Chem. Chem. Phys.* **2012**, *14*, 6165–6172.

[364] P. Formentín, M. Álvaro, H. García, E. Palomares, M. J. Sabater, *New J. Chem.* **2002**, *26*, 1646–1650.

[365] H. Hennig, K. Hofbauer, K. Handke, R. Stich, *Angew. Chemie* **1997**, *109*, 373–375.

[366] A. Becalska, R. J. Batchelor, F. W. B. Einstein, R. H. Hill, B. J. Palmer, *Inorg. Chem.* **1992**, *31*, 3118–3123.

[367] J. N. Demas, W. D. Bowman, E. F. Zalewskl, R. A. Velapoldl, *J. Phys. Chem* **1981**, *85*, 2766–2771.

[368] I. P. Pozdnyakov, O. V. Kel, V. F. Plyusnin, V. P. Grivin, N. M. Bazhin, *J. Phys. Chem. A* **2008**, *112*, 8316–8322.

[369] J. R. Bryant, Mechanistic Studies of the Oxidations of Hydrocarbons by Manganese and Ruthenium Transition Metal Complexes, University of Washington, **2002**.

[370] M. H. Abraham, P. L. Grellier, D. V. Prior, P. P. Duce, J. J. Morris, P. J. Taylor, *J. Chem. Soc., Perkin Trans. 2* **1989**, 699–711.

[371] J. Cioslowski, G. Liu, D. Moncrieff, *J. Phys. Chem. A* **1997**, *101*, 957–960.

Appendix

4.1 Abbreviations

BArF	tetrakis{3,5-bis(trifluoromethyl)phenyl}borate
BDE	bond dissociation enthalpy
BDFE	bond dissociation free energy
bpy	2,2'-bipyridine
BTMG	2-*tert*-butyl-1,1,3,3-tetramethylguanidine
CCS	carbon capture and storage
CE	counter electrode
CODH	carbon monoxide dehydrogenase
COSMO	conductor like screening model
COSY	correlation spectroscopy
Cp	cyclopentadienyl
Cp*	pentamethylcyclopentadienyl
CPET	concerted proton-electron transfer
CT	charge transfer
CV	cyclic voltammetry
cyclam	1,4,8,11-tetraazacyclotetradecane
DABCO	1,4-diazabicyclo[*2.2.2*]octan
DBU	1,8-diazabycyclo[*5.4.0*]undec-7-ene
DCM	dichloromethane
depe	bis(diethylphosphino)ethane
DFT	density functional theory
DHA	9,10-dihydroanthracene
dme	1,2-dimethoxyethane
dmpe	bis(dimethylphosphino)ethane
DMSO	dimethylsulfoxide
dppe	bis(diphenylphosphino)ethane

dpt	1,3-diphenyltriazenid
dtbbpy	4,4’-di-*tert*-butyl-2,2’-bipyridyl
e.g.	exempli gratia
EC	electrochemical-chemical
ECE	electrochemical-chemical-electrochemical
EI	electron ionization
EPR	electron paramagnetic resonance
eq	equivalents
eq.	equation
ET	electron transfer
et al	et alii, et aliae
EXAFS	extended X-ray absorption fine structure
facac	hexafluoroacetylacetonate
Fc	ferrocene
FDH	formate dehydrogenase
FWHM	full width at half maximum
GC	glassy carbon
GC-MS	gas chromatography-mass spectrometry
HAA	hydrogen atom abstraction
HAT	hydrogen atom transfer
HOMO	highest occupied molecular orbital
HMBC	heteronuclear multiple bond correlation
HMDS	hexamethyldisilazane
HSQC	heteronuclear single quantum coherence
HT	hydride transfer
H_2bim	2,2’-biimidazolin
i.e.	id est
IPr	1,3-di(2,6-di-*iso*-propylphenyl)imidazolin-2-ylidene
IR	infrared
KIE	kinetic isotope effect

LIFDI	liquid injection field desorption ionization
LFER	linear free energy relationship
LLCT	ligand-to-ligand charge transfer
LUMO	lowest unoccupied molecular orbital
lut	2,6-lutidine
MCR	*Marcus* cross relation
MLCT	metal-to-ligand charge-transfer
MO	molecular orbital
MS	mass spectrometry
MS-CPET	multiple-site concerted proton-electron transfer
NHE	normal hydrogen electrode
NIR	near infrared
NOESY	nuclear *Overhauser* enhancement and exchange spectroscopy
NMR	nuclear magnetic resonance
NNN	*N*,*N*'-(2,6-dimethylphenyl)-2,6-pyridinedicarboxamidate
NTMG	1,8-bis(tetramethylguanidino)naphthalene
OEC	oxygen evolving complex
PCET	proton-coupled electron transfer
phen	1,10-phenanthroline
PPN	bis(triphenylphosphino)iminium
ppy	2-phenylpyridinyl
PS I/II	photosystem I/II
PT	proton transfer
RDS	rate-determining step
RE	reference electrode
salen	*N,N'*-bis(salicyliden)ethylendiamine
SOMO	singly occupied molecular orbital
SNS	bis(2-mercapto-4-methylphenylamine
TATB	tetraphenylarsonium tetraphenylborate
TBD	1,5,7-triazabicyclo[4.4.0]dec-5-ene

TBP	tris(2,4,6-*tert*-butyl)phenoxyl
$^{tBu}PN^{H}P$	$NH(CH_2CH_2{}^tBu_2P)_2$
^{tBu}PNP	$N(CH_2CH_2{}^tBu_2P)_2$
$^{tBu}P{=}N{=}P$	$N(CHCH{}^tBu_2P)_2$
$^{tBu}P{=}N{=}P^{H}$	$N(CHCH{}^tBu_2P)(CHCH_2{}^tBu_2P)$
TEA	triethylamine
TEAO	triethanolamine
THF	tetrahydrofuran
TIP	temperature independent paramagnetism
TMP	2,2,6,6-tetramethylpiperidine
TCD-GC	thermal conductivity detector gas chromatography
TD-DFT	time-dependent density functional theory
TEMPO	2,2,6,6-tetramethylpiperidinyloxyl
TEMPO-H	2,2,6,6-tetramethylpiperidin-1-ol
THF	tetrahydrofuran
TMG	1,1,3,3-tetramethylguanidine
Tp	tris(pyrazolyl)borate
tpy	terpyridine
TST	transition state theory
UV	ultraviolet
vis	visible
vs.	versus
Verkade's base	2,8,9-tri-*iso*-propyl-2,5,8,9-tetraaza-1-phosphabicyclo[*3,3,3*]undecane
WE	working electrode
XANES	X-ray absorption near-edge structure

4.2 List of Chemical Compounds

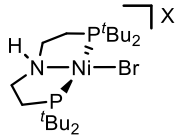
1^{X}

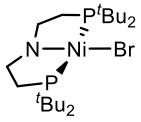
2

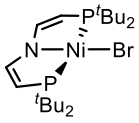
3

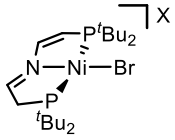
4^{X}

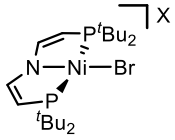
5^{X}

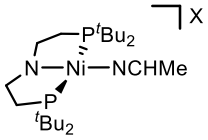
6^{X}

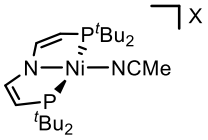
7^{X}

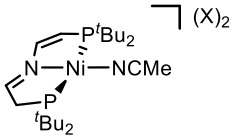
8$^{(X)2}$

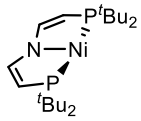
9

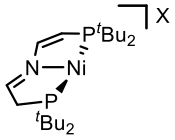
10^{X}

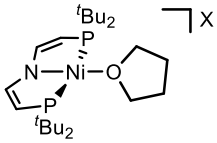
11^{X}

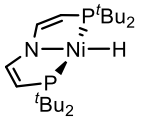
12

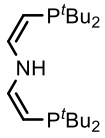
13

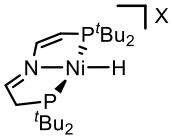
14^{X}

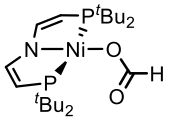
15

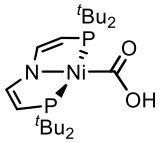
16

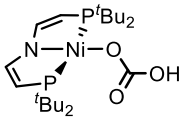
17

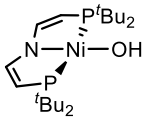
18

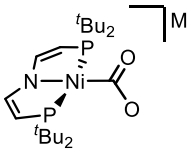
19^{M}

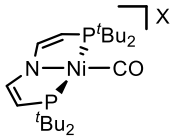
20^{X}

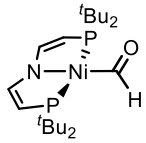
21

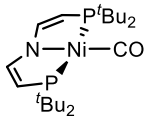
22

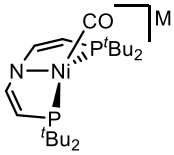
23^{M}

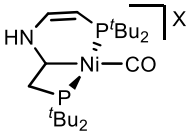
24^{X}

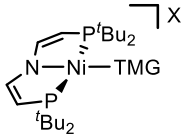
25^{X}

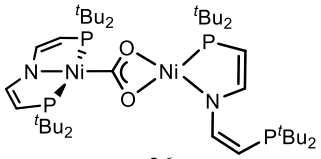

26

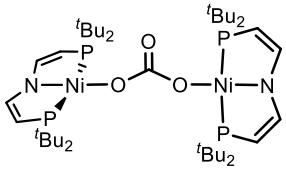

27

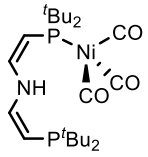

28

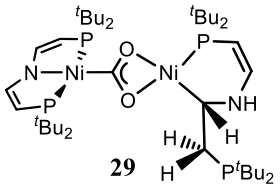

29

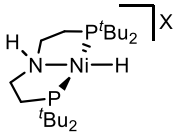

30^{X}

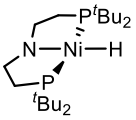

31

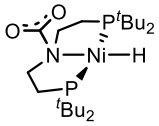

32

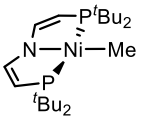

33

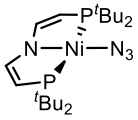

34

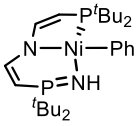

35

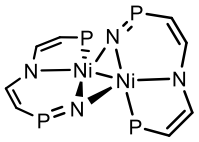

36 P = P^{t}Bu$_2$

4.3 Crystallographic Data

4.3.1. [NiBr(^{tBu}PNP)] (2)

Identification code	mo_SF_SF_180615_0m_a	
Empirical formula	$C_{20}H_{44}BrNNiP_2$	
Formula weight	499.12	
Temperature	100(2) K	
Wavelength	0.71073 Å	
Crystal system	Monoclinic	
Space group	$P2_1/c$	
Unit cell dimensions	a = 12.1365(4) Å	α= 90°
	b = 14.2113(5) Å	β= 104.268(2)°
	c = 14.4743(5) Å	γ = 90°
Volume	2419.45(14) $Å^3$	
Z	4	
Density (calculated)	1.370 Mg/m^3	
Absorption coefficient	2.590 mm^{-1}	
F(000)	1056	
Crystal size	0.154×0.093×0.048 mm^3	
Crystal shape and color	Plate,	green
Theta range for data collection	2.248 to 28.350°	
Index ranges	-16<=h<=16, -18<=k<=18, -19<=l<=19	
Reflections collected	39230	
Independent reflections	6018 [R(int) = 0.0677]	
Completeness to theta = 25.242°	99.9 %	
Max. and min. transmission	0.7457 and 0.6263	
Refinement method	Full-matrix least-squares on F^2	
Data / restraints / parameters	6018 / 0 / 238	
Goodness-of-fit on F^2	1.060	
Final R indices [I>2sigma(I)]	R1 = 0.0304	wR2 = 0.0548
R indices (all data)	R1 = 0.0479	wR2 = 0.0597
Largest diff. peak and hole	0.393 and -0.574 e·$Å^3$	

4.3.2. [NiBr(^{tBu}P=N=P)] (3)

Identification code	mo_SF_SF_240615_0m_a	
Empirical formula	$C_{20}H_{40}BrNNiP_2$	
Formula weight	495.09	
Temperature	100(2) K	
Wavelength	0.71073 Å	
Crystal system	Monoclinic	
Space group	*P*2/c	
Unit cell dimensions	a = 11.4598(5) Å	α= 90°
	b = 8.5648(4) Å	β= 114.624(2)°
	c = 13.4024(6) Å	γ= 90°
Volume	1195.83(9) Å^3	
Z	2	
Density (calculated)	1.375 Mg/m^3	
Absorption coefficient	2.620 mm^{-1}	
F(000)	520	
Crystal size	0.320×0.311×0.108 mm^3	
Crystal shape and color:	Block,	green
Theta range for data collection	2.378 to 32.146°	
Index ranges	-15<=h<=17, -12<=k<=12, -20<=l<=20	
Reflections collected	44757	
Independent reflections	4204 [R(int) = 0.0614]	
Completeness to theta = 25.242°	100.0 %	
Max. and min. transmission	0.7463 and 0.5951	
Refinement method	Full-matrix least-squares on F^2	
Data / restraints / parameters	4204 / 0 / 121	
Goodness-of-fit on F^2	1.060	
Final R indices [I>2sigma(I)]	R1 = 0.0284	wR2 = 0.0555
R indices (all data)	R1 = 0.0442	wR2 = 0.0604
Largest diff. peak and hole	0.425 and -0.675 e·Å^3	

4.3.3. [NiBr(^{tBu}P=N=P^{H})]OTf (4^{OTf})

Identification code	SF_SF_120416	
Empirical formula	$C_{21}H_{41}BrF_3NNiO_3P_2S$	
Formula weight	645.17	
Temperature	100(2) K	
Wavelength	0.71073 Å	
Crystal system	Orthorhombic	
Space group	*P*bca	
Unit cell dimensions	a = 13.4735(6) Å	α = 90°
	b = 14.8989(7) Å	β = 90°
	c = 27.7644(13) Å	γ = 90°
Volume	5573.4(4) Å^3	
Z	8	
Density (calculated)	1.538 Mg/m^3	
Absorption coefficient	2.363 mm^{-1}	
F(000)	2672	
Crystal size	0.166×0.184×0.230 mm^3	
Crystal shape and color:	Block,	orange-red
Theta range for data collection	2.166 to 33.271°	
Index ranges	-20<=h<=20, -22<=k<=22, -42<=l<=42	
Reflections collected	274389	
Independent reflections	10712 [R(int) = 0.1420]	
Completeness to theta = 25.242°	100.0 %	
Max. and min. transmission	0. 0.7465 and 0.7024	
Refinement method	Full-matrix least-squares on F^2	
Data / restraints / parameters	10712 / 0 / 310	
Goodness-of-fit on F^2	1.034	
Final R indices [I>2sigma(I)]	R1 = 0.0469	wR2 = 0.0670
R indices (all data)	R1 = 0.0923	wR2 = 0.0760
Largest diff. peak and hole	0.553 and -0.611 e·Å^3	

4.3.4. [NiBr(^{tBu}P=N=P)]PF_6 (5^{PF6})

Identification code	mo_SF_SF_050815_0m_a	
Empirical formula	$C_{46}H_{85}Br_2ClF_{12}N_2Ni_2P_6$	
Formula weight	1392.67	
Temperature	100(2) K	
Wavelength	0.71073 Å	
Crystal system	Triclinic	
Space group	$P\bar{1}$	
Unit cell dimensions	a = 14.1913(5) Å	α = 77.162(2)°
	b = 15.3383(6) Å	β = 66.414(2)°
	c = 15.6567(6) Å	γ = 77.204(2)°
Volume	3011.5(2) $Å^3$	
Z	2	
Density (calculated)	1.536 Mg/m^3	
Absorption coefficient	2.226 mm^{-1}	
F(000)	1432	
Crystal size	0.262×0.206×0.073 mm^3	
Crystal shape and color:	Block,	dark red
Theta range for data collection	1.884 to 27.169°	
Index ranges	-18<=h<=18, -19<=k<=19, -20<=l<=20	
Reflections collected	216769	
Independent reflections	13347 [R(int) = 0.0664]	
Completeness to theta = 25.242°	100.0 %	
Max. and min. transmission	0.7452 and 0.6365	
Refinement method	Full-matrix least-squares on F^2	
Data / restraints / parameters	13347 / 60 / 835	
Goodness-of-fit on F^2	1.112	
Final R indices [I>2sigma(I)]	R1 = 0.0326	wR2 = 0.0662
R indices (all data)	R1 = 0.0497	wR2 = 0.0768
Largest diff. peak and hole	1.181 and -1.367 e·$Å^{-3}$	

4.3.5. [Ni(NCMe)(^{tBu}PNP)]BArF (6^{BArF})

Identification code	SF_SF_240116	
Empirical formula	$C_{54}H_{59}BF_{24}N_2NiP_2$	
Formula weight	1323.49	
Temperature	102(2) K	
Wavelength	0.71073 Å	
Crystal system	Monoclinic	
Space group	*P*1c1	
Unit cell dimensions	a = 22.5849(11) Å	α = 90°
	b = 12.8398(6) Å	β = 110.137(2)°
	c = 21.8552(11) Å	γ = 90°
Volume	5950.3(5) Å^3	
Z	4	
Density (calculated)	1.477 Mg/m^3	
Absorption coefficient	0.493 mm^{-1}	
F(000)	2704	
Crystal shape and color	Block,	clear intense violet red
Crystal size	0.538×0.215×0.094 mm^3	
Theta range for data collection	2.24 to 28.32°	
Index ranges	-30<=h<=30, -17<=k<=17, -29<=l<=29	
Reflections collected	184776	
Independent reflections	29508 [R(int) = 0.0424]	
Completeness to theta = 28.32°	99.9 %	
Absorption correction	Semi-empirical from equivalents	
Max. and min. transmission	0.7457 and 0.7037	
Refinement method	Full-matrix least-squares on F^2	
Data / restraints / parameters	29508 / 163 / 1574	
Goodness-of-fit on F^2	1.032	
Final R indices [I>2sigma(I)]	R1 = 0.0317	wR2 = 0.0709
R indices (all data)	R1 = 0.0375	wR2 = 0.0740
Absolute structure parameter	0.499(6)	
Largest diff. peak and hole	0.581 and -0.468 e·Å^{-3}	

4.3.6. [Ni(NCMe)(^{tBu}P=N=P)]BF_4 (7^{BF4})

Identification code	SF_SF_260416_2	
Empirical formula	$C_{22}H_{47}BF_4N_2NiP_2$	
Formula weight	547.07	
Temperature	100(2) K	
Wavelength	0.71073 Å	
Crystal system	Monoclinic	
Space group	$P12_1/c1$	
Unit cell dimensions	a = 8.0801(7) Å	α = 90°
	b = 28.848(2) Å	β = 97.288(3)°
	c = 11.9209(10) Å	γ = 90°
Volume	2756.2(4) $Å^3$	
Z	4	
Density (calculated)	1.318 Mg/m^3	
Absorption coefficient	0.860 mm^{-1}	
F(000)	1168	
Crystal size	0.382×0.214×0.054 mm^3	
Crystal shape and color	Plate,	clear violet
Theta range for data collection	2.23 to 30.58°	
Index ranges	-11<=h<=11, -41<=k<=41, -17<=l<=16	
Reflections collected	92065	
Independent reflections	8475 [R(int) = 0.0672]	
Completeness to theta = 30.58°	99.9 %	
Absorption correction	Semi-empirical from equivalents	
Max. and min. transmission	0.75 and 0.69	
Refinement method	Full-matrix least-squares on F^2	
Data / restraints / parameters	8475 / 0 / 339	
Goodness-of-fit on F^2	1.109	
Final R indices [I>2sigma(I)]	R1 = 0.0402	wR2 = 0.0721
R indices (all data)	R1 = 0.0587	wR2 = 0.0767
Largest diff. peak and hole	0.375 and -0.512 e·$Å^3$	

4.3.7. [Ni(^{tBu}P=N=P)] (9)

Identification code	mo_SF_SF_030417_0m_a	
Empirical formula	$C_{20}H_{40}NNiP_2$	
Formula weight	415.18	
Temperature	100(2) K	
Wavelength	0.71073 Å	
Crystal system	Monoclinic	
Space group	*C*2/c	
Unit cell dimensions	a = 21.5733(10) Å	α = 90°
	b = 7.6788(3) Å	β = 102.388(2)°
	c = 14.0606(7) Å	γ = 90°
Volume	2275.01(18) Å^3	
Z	4	
Density (calculated)	1.212 Mg/m^3	
Absorption coefficient	0.996 mm^{-1}	
F(000)	900	
Crystal size	0.192×0.137×0.099 mm^3	
Crystal shape and color:	Block,	clear, dark orange
Theta range for data collection	2.823 to 34.851°	
Index ranges	-34<=h<=34, -12<=k<=12, -22<=l<=21	
Reflections collected	54032	
Independent reflections	4966 [R(int) = 0.0677]	
Completeness to theta = 25.242°	100.0 %	
Max. and min. transmission	0.7468 and 0.6942	
Refinement method	Full-matrix least-squares on F^2	
Data / restraints / parameters	4966 / 0 / 116	
Goodness-of-fit on F^2	1.043	
Final R indices [I>2sigma(I)]	R1 = 0.0339,	wR2 = 0.0648
R indices (all data)	R1 = 0.0579,	wR2 = 0.0710
Largest diff. peak and hole	0.476 and -0.295 e·Å^{-3}	

4.3.8. [Ni(^{tBu}P=N=P^{H})]BArF (10^{BArF})

Identification code	SF_SF_050418_02	
Empirical formula	$C_{52}H_{53}BF_{24}NNiP_2$	
Formula weight	1279.41	
Temperature	101(2) K	
Wavelength	0.71073 Å	
Crystal system	Triclinic	
Space group	$P\bar{1}$	
Unit cell dimensions	a = 12.1761(8) Å	α = 85.299(2)°
	b = 15.2233(10) Å	β = 85.867(2)°
	c = 15.4728(8) Å	γ = 85.573(2)°
Volume	2843.6(3) Å^3	
Z	2	
Density (calculated)	-	
Absorption coefficient	0.512 mm^{-1}	
F(000)	1302	
Crystal size	0.351×0.259×0.207 mm^3	
Crystal shape and color:	Block,	clear intense red-yellow
Theta range for data collection	2.21 to 28.36°	
Index ranges	-16<=h<=16, -20<=k<=20, -19<=l<=20	
Reflections collected	177751	
Independent reflections	14207 [R(int) = 0.1032]	
Completeness to theta = 28.36°	99.9 %	
Absorption correction	Semi-empirical from equivalents	
Max. and min. transmission	0.7454 and 0.7219	
Refinement method	Full-matrix least-squares on F^2	
Data / restraints / parameters	14207 / 627 / 882	
Goodness-of-fit on F^2	1.064	
Final R indices [I>2sigma(I)]	R1 = 0.0507	wR2 = 0.0942
R indices (all data)	R1 = 0.0862	wR2 = 0.1084
Largest diff. peak and hole	0.440 and -0.423 e·Å^{-3}	

4.3.9. [Ni(κ*O*-THF)(^{tBu}P=N=P)]PF_6 (11^{PF6})

Identification code	SF_SF_110716	
Empirical formula	$C_{24}H_{48}F_6NNiOP_3$	
Formula weight	632.25	
Temperature	102(2) K	
Wavelength	0.71073 Å	
Crystal system	Monoclinic	
Space group	$P12_1/c1$	
Unit cell dimensions	a = 10.8174(8) Å	α = 90°
	b = 16.3076(13) Å	β = 106.843(2)°
	c = 17.7915(14) Å	γ = 90°
Volume	3003.9(4) Å^3	
Z	4	
Density (calculated)	1.398 Mg/m^3	
Absorption coefficient	0.861 mm^{-1}	
F(000)	1336	
Crystal size	0.423×0.329×0.092 mm^3	
Crystal shape and color	Plate,	clear red orange
Theta range for data collection	2.33 to 30.16°	
Index ranges	-15<=h<=15, -23<=k<=23, -25<=l<=25	
Reflections collected	138443	
Independent reflections	8880 [R(int) = 0.1398]	
Completeness to theta = 30.16°	99.8 %	
Absorption correction	Semi-empirical from equivalents	
Max. and min. transmission	0.7460 and 0.6259	
Refinement method	Full-matrix least-squares on F^2	
Data / restraints / parameters	8880 / 0 / 337	
Goodness-of-fit on F^2	1.056	
Final R indices [I>2sigma(I)]	R1 = 0.0459	wR2 = 0.0730
R indices (all data)	R1 = 0.0828	wR2 = 0.0824
Largest diff. peak and hole	0.504 and -0.424 e·Å^3	

4.3.10. [NiH(^{tBu}P=N=P)] (12)

Identification code	SF_SF_010216	
Empirical formula	$C_{20}H_{41}NNiP_2$	
Formula weight	416.19	
Temperature	104(2) K	
Wavelength	0.71073 Å	
Crystal system	Monoclinic	
Space group	*C*2/c	
Unit cell dimensions	a = 21.4284(12) Å	α = 90°
	b = 7.7159(4) Å	β = 101.926(2)°
	c = 14.0489(8) Å	γ = 90°
Volume	2272.7(2) Å^3	
Z	4	
Density (calculated)	1.216 Mg/m^3	
Absorption coefficient	0.997 mm^{-1}	
F(000)	904	
Crystal size	0.202×0.126×0.103 mm^3	
Crystal shape and color:	Block,	clear light yellow
Theta range for data collection	2.813 to 33.217°	
Index ranges	-31<=h<=32, -11<=k<=11, -21<=l<=21	
Reflections collected	61848	
Independent reflections	4349 [R(int) = 0.0355]	
Completeness to theta = 25.242°	99.9 %	
Max. and min. transmission	0.7465 and 0.7109	
Refinement method	Full-matrix least-squares on F^2	
Data / restraints / parameters	4349 / 0 / 118	
Goodness-of-fit on F^2	1.050	
Final R indices [I>2sigma(I)]	R1 = 0.0239,	wR2 = 0.0535
R indices (all data)	R1 = 0.0340,	wR2 = 0.0574
Largest diff. peak and hole	0.379 and -0.484 e·Å^{-3}	

4.3.11. [NiH(^{tBu}P=N=P^{H})]O_2CCF_3 (14^{O2CCF3})

Identification code	mo_SF_SF_220917_0m_a	
Empirical formula	$C_{24}H_{43}F_6NNiO_4P_2$	
Formula weight	644.24	
Temperature	101(2) K	
Wavelength	0.71073 Å	
Crystal system	Monoclinic	
Space group	$P2_1/c$	
Unit cell dimensions	a = 12.1453(6) Å	α = 90°
	b = 11.0920(5) Å	β = 99.656(2)°
	c = 23.4279(10) Å	γ = 90°
Volume	3111.4(2) Å^3	
Z	4	
Density (calculated)	1.375 Mg/m^3	
Absorption coefficient	0.791 mm^{-1}	
F(000)	1352	
Crystal size	0.303×0.163×0.079 mm^3	
Crystal shape and color:	Block,	clear yellow
Theta range for data collection	2.235 to 30.576°	
Index ranges	-17<=h<=17, -15<=k<=15, -33<=l<=31	
Reflections collected	109712	
Independent reflections	9547 [R(int) = 0.0528]	
Completeness to theta = 25.242°	99.9 %	
Max. and min. transmission	0.7461 and 0.6908	
Refinement method	Full-matrix least-squares on F^2	
Data / restraints / parameters	9547 / 30 / 450	
Goodness-of-fit on F^2	1.045	
Final R indices [I>2sigma(I)]	R1 = 0.0374,	wR2 = 0.0803
R indices (all data)	R1 = 0.0526,	wR2 = 0.0863
Largest diff. peak and hole	1.222 and -0.605 e·Å^{-3}	

4.3.12. [Ni(CO$_2$H)(^{tBu}P=N=P)] (16)

Identification code	mo_SF_SF_290816_0m_a	
Empirical formula	$C_{21}H_{41}NNiO_2P_2$	
Formula weight	460.20	
Temperature	100(2) K	
Wavelength	0.71073 Å	
Crystal system	Triclinic	
Space group	$P\bar{1}$	
Unit cell dimensions	a = 8.4481(5) Å	α = 103.507(2)°
	b = 11.4423(6) Å	β = 92.683(2)°
	c = 13.6806(7) Å	γ = 110.468(2)°
Volume	1192.64(11) Å^3	
Z	2	
Density (calculated)	1.281 Mg/m^3	
Absorption coefficient	0.963 mm^{-1}	
F(000)	496	
Crystal size	0.136×0.117×0.111 mm^3	
Crystal shape and color:	Block,	clear light yellow
Theta range for data collection	2.156 to 28.396°	
Index ranges	-11<=h<=11, -15<=k<=15, -18<=l<=17	
Reflections collected	46494	
Independent reflections	5980 [R(int) = 0.1041]	
Completeness to theta = 25.242°	100.0 %	
Max. and min. transmission	0.7457 and 0.6905	
Refinement method	Full-matrix least-squares on F^2	
Data / restraints / parameters	5980 / 0 / 258	
Goodness-of-fit on F^2	1.015	
Final R indices [I>2sigma(I)]	R1 = 0.0425,	wR2 = 0.0684
R indices (all data)	R1 = 0.0787,	wR2 = 0.0773
Largest diff. peak and hole	0.467 and -0.415 e·Å^{-3}	

4.3.13. [Ni(OCO$_2$H)(^{tBu}P=N=P)] (17)

Identification code	mo_SF_SF_130417_2_0ma_a	
Empirical formula	$C_{21}H_{41}NNiO_3P_2$	
Formula weight	476.20	
Temperature	100(2) K	
Wavelength	0.71073 Å	
Crystal system	Monoclinic	
Space group	$P2_1/n$	
Unit cell dimensions	a = 14.9312(6) Å	α = 90°
	b = 11.4998(5) Å	β = 116.777(2)°
	c = 16.4761(7) Å	γ = 90°
Volume	2525.67(19) Å^3	
Z	4	
Density (calculated)	1.252 Mg/m^3	
Absorption coefficient	0.914 mm^{-1}	
F(000)	1024	
Crystal size	0.174×0.088×0.034 mm^3	
Crystal shape and color:	Plate,	clear orange
Theta range for data collection	2.248 to 28.398°	
Index ranges	-19<=h<=19, -15<=k<=15, -22<=l<=21	
Reflections collected	122428	
Independent reflections	6296 [R(int) = 0.1642]	
Completeness to theta = 25.242°	100.0 %	
Max. and min. transmission	0.7457 and 0.6896	
Refinement method	Full-matrix least-squares on F^2	
Data / restraints / parameters	6296 / 0 / 269	
Goodness-of-fit on F^2	1.081	
Final R indices [I>2sigma(I)]	R1 = 0.0492,	wR2 = 0.0873
R indices (all data)	R1 = 0.0799,	wR2 = 0.0968
Largest diff. peak and hole	0.572 and -0.508 e·Å^{-3}	

4.3.14. [Ni(OH)(^{tBu}P=N=P)] (18)

Identification code	mo_SF_SF_250517_2_0m_a	
Empirical formula	$C_{20}H_{41}NNiOP_2$	
Formula weight	432.19	
Temperature	100(2) K	
Wavelength	0.71073 Å	
Crystal system	Monoclinic	
Space group	*C*2/c	
Unit cell dimensions	a = 21.4757(14) Å	α = 90°
	b = 7.8122(6) Å	β = 102.380(3)°
	c = 13.9003(10) Å	γ = 90°
Volume	2277.9(3) Å^3	
Z	4	
Density (calculated)	1.260 Mg/m^3	
Absorption coefficient	1.001 mm^{-1}	
F(000)	936	
Crystal size	0.245×0.188×0.086 mm^3	
Crystal shape and color:	Block	clear, intense red
Theta range for data collection	2.782 to 26.480°	
Index ranges	-26<=h<=26, -9<=k<=9, -17<=l<=17	
Reflections collected	21536	
Independent reflections	2362 [R(int) = 0.1001]	
Completeness to theta = 25.242°	100.0 %	
Max. and min. transmission	0.7454 and 0.6365	
Refinement method	Full-matrix least-squares on F^2	
Data / restraints / parameters	2362 / 0 / 121	
Goodness-of-fit on F^2	1.012	
Final R indices [I>2sigma(I)]	R1 = 0.0381,	wR2 = 0.0723
R indices (all data)	R1 = 0.0640,	wR2 = 0.0795
Largest diff. peak and hole	0.648 and -0.284 e·Å^{-3}	

4.3.15. [Ni(CO)(^{tBu}P=N=P)]BF_4 (20^{BF4})

Identification code	mo_SF_SF_281116_0m_a	
Empirical formula	$C_{21}H_{40}BF_4NNiOP_2$	
Formula weight	530.00	
Temperature	100(2) K	
Wavelength	0.71073 Å	
Crystal system	Monoclinic	
Space group	$P2_1/c$	
Unit cell dimensions	a = 7.8970(4) Å	α = 90°
	b = 25.4605(11) Å	β = 91.616(2)°
	c = 12.7114(6) Å	γ = 90°
Volume	2554.8(2) $Å^3$	
Z	4	
Density (calculated)	1.378 Mg/m^3	
Absorption coefficient	0.927 mm^{-1}	
F(000)	1120	
Crystal size	0.190×0.120×0.093 mm^3	
Crystal shape and color:	Block,	clear intense red
Theta range for data collection	2.265 to 30.560°	
Index ranges	-11<=h<=11, -36<=k<=36, -18<=l<=18	
Reflections collected	100564	
Independent reflections	7805 [R(int) = 0.0588]	
Completeness to theta = 25.242°	99.9 %	
Max. and min. transmission	0.7461 and 0.7149	
Refinement method	Full-matrix least-squares on F^2	
Data / restraints / parameters	7805 / 0 / 311	
Goodness-of-fit on F^2	1.069	
Final R indices [I>2sigma(I)]	R1 = 0.0320,	wR2 = 0.0592
R indices (all data)	R1 = 0.0480,	wR2 = 0.0631
Largest diff. peak and hole	0.395 and -0.390 e·$Å^{-3}$	

4.3.16. [Ni(CO)(^{tBu}P=N=P)] (22)

Identification code	mo_SF_SF_240517_0m_a	
Empirical formula	$C_{21}H_{40}NNiOP_2$	
Formula weight	443.19	
Temperature	100(2) K	
Wavelength	0.71073 Å	
Crystal system	Monoclinic	
Space group	$P2_1/c$	
Unit cell dimensions	a = 7.8351(5) Å	α = 90°
	b = 26.8613(15) Å	β = 107.270(2)°
	c = 11.7832(6) Å	γ = 90°
Volume	2368.1(2) Å^3	
Z	4	
Density (calculated)	1.243 Mg/m^3	
Absorption coefficient	0.964 mm^{-1}	
F(000)	956	
Crystal size	0.289×0.192×0.041 mm^3	
Crystal shape and color:	Plate,	clear dark green-red
Theta range for data collection	2.361 to 30.571°	
Index ranges	-11<=h<=11, -38<=k<=38, -16<=l<=16	
Reflections collected	76684	
Independent reflections	7257 [R(int) = 0.0579]	
Completeness to theta = 25.242°	100.0 %	
Max. and min. transmission	0.7465 and 0.7109	
Refinement method	Full-matrix least-squares on F^2	
Data / restraints / parameters	7257 / 0 / 247	
Goodness-of-fit on F^2	1.137	
Final R indices [I>2sigma(I)]	R1 = 0.0403,	wR2 = 0.0743
R indices (all data)	R1 = 0.0537,	wR2 = 0.0774
Largest diff. peak and hole	0.555 and -0.518 e·Å^{-3}	

4.3.17. [K(OEt$_2$)][Ni(CO)(^{tBu}P=N=P)] (23^K)

Identification code	mo_SF_SF_270318_0m_a	
Empirical formula	$C_{25}H_{50}KNNiO_2P_2$	
Formula weight	556.41	
Temperature	101(2) K	
Wavelength	0.71073 Å	
Crystal system	Triclinic	
Space group	$P\bar{1}$	
Unit cell dimensions	a = 10.6617(3) Å	α = 79.880(2)°
	b = 10.7204(3) Å	β = 85.536(2)°
	c = 15.4175(5) Å	γ = 61.873(2)°
Volume	1529.88(8) Å^3	
Z	2	
Density (calculated)	1.208 Mg/m^3	
Absorption coefficient	0.895 mm^{-1}	
F(000)	600	
Crystal size	0.273×0.203×0.142 mm^3	
Crystal shape and color:	Block,	clear intense red-orange
Theta range for data collection	2.246 to 30.686°	
Index ranges	-11<=h<=11, -38<=k<=38, -16<=l<=16	
Reflections collected	108221	
Independent reflections	9413 [R(int) = 0.0469]	
Completeness to theta = 25.242°	99.9 %	
Max. and min. transmission	0.7461 and 0.7066	
Refinement method	Full-matrix least-squares on F^2	
Data / restraints / parameters	9413 / 0 / 303	
Goodness-of-fit on F^2	1.050	
Final R indices [I>2sigma(I)]	R1 = 0.0277,	wR2 = 0.0581
R indices (all data)	R1 = 0.0406,	wR2 = 0.0637
Largest diff. peak and hole	0.447 and -0.460 e·Å^{-3}	

4.3.18. [Ni{κN-HNC(NMe$_2$)$_2$}(^{tBu}P=N=P)]BArF (25^{BArF})

Identification code	mo_CW_FS_230218_0m_a	
Empirical formula	C57H65BF24N4NiP2	
Formula weight	1393.59	
Temperature	100(2) K	
Wavelength	0.71073 Å	
Crystal system	Monoclinic	
Space group	$P2_1/n$	
Unit cell dimensions	a = 13.3114(7) Å	α = 90°
	b = 13.2023(7) Å	β = 97.672(2)°
	c = 35.6488(19) Å	γ = 90°
Volume	6208.9(6) Å^3	
Z	4	
Density (calculated)	1.491 Mg/m^3	
Absorption coefficient	0.477 mm^{-1}	
F(000)	2856	
Crystal size	0.240×0.138×0.103 mm^3	
Crystal shape and color:	Block,	intense yellow-green
Theta range for data collection	2.159 to 30.594°	
Index ranges	-18<=h<=19, -18<=k<=18, -50<=l<=50	
Reflections collected	144076	
Independent reflections	19054 [R(int) = 0.0391]	
Completeness to theta = 25.242°	99.9 %	
Max. and min. transmission	0.7461 and 0.6955	
Refinement method	Full-matrix least-squares on F^2	
Data / restraints / parameters	9054 / 282 / 999	
Goodness-of-fit on F^2	1.074	
Final R indices [I>2sigma(I)]	R1 = 0.0464,	wR2 = 0.1062
R indices (all data)	R1 = 0.0587,	wR2 = 0.1114
Largest diff. peak and hole	0.610 and -0.563 e·Å^{-3}	

4.3.19. [(^{tBu}P=N=P)Ni(OC(O)O)Ni(^{tBu}P=N=P)] (27)

Identification code	mo_SF_SF_090617_0m_a	
Empirical formula	$C_{41}H_{80}N_2Ni_2O_3P_4$	
Formula weight	890.37	
Temperature	100(2) K	
Wavelength	0.71073 Å	
Crystal system	Triclinic	
Space group	$P\bar{1}$	
Unit cell dimensions	a = 12.0918(7) Å	α = 77.041(4)°
	b = 13.3064(8) Å	β = 87.050(4)°
	c = 16.5140(9) Å	γ = 66.641(4)°
Volume	2375.1(2) Å^3	
Z	2	
Density (calculated)	1.245 Mg/m^3	
Absorption coefficient	0.963 mm^{-1}	
F(000)	960	
Crystal size	0.152×0.081×0.039 mm^3	
Crystal shape and color:	Plate	clear, orange
Theta range for data collection	2.274 to 26.461°	
Index ranges	-15<=h<=15, -16<=k<=16, -20<=l<=20	
Reflections collected	47157	
Independent reflections	9744 [R(int) = 0.1590]	
Completeness to theta = 25.242°	99.9 %	
Max. and min. transmission	0.7454 and 0.6329	
Refinement method	Full-matrix least-squares on F^2	
Data / restraints / parameters	9744 / 0 / 496	
Goodness-of-fit on F^2	1.003	
Final R indices [I>2sigma(I)]	R1 = 0.0514,	wR2 = 0.0850
R indices (all data)	R1 = 0.1181,	wR2 = 0.1029
Largest diff. peak and hole	0.567 and -0.584 e·Å^{-3}	

4.3.20. [Ni(CO)$_3${*κP*-(^{tBu}P=N=P)] (28)

Identification code	SF_SF_300817	
Empirical formula	$C_{23}H_{41}NNiO_3P_2$	
Formula weight	500.22	
Temperature	100(2) K	
Wavelength	0.71073 Å	
Crystal system	Monoclinic	
Space group	$P2_1/c$	
Unit cell dimensions	a = 8.7840(11) Å	α = 90°
	b = 16.0680(19) Å	β = 91.080(4)°
	c = 19.419(2) Å	γ = 90°
Volume	2740.3(6) Å^3	
Z	4	
Density (calculated)	1.212 Mg/m^3	
Absorption coefficient	0.846 mm^{-1}	
F(000)	1072	
Crystal size	0.302×0.121×0.067 mm^3	
Crystal shape and color:	Block,	clear light yellow
Theta range for data collection	2.319 to 26.442°	
Index ranges	-10<=h<=10, -20<=k<=20, -23<=l<=24	
Reflections collected	62264	
Independent reflections	5624 [R(int) = 0.1224]	
Completeness to theta = 25.242°	100.0 %	
Max. and min. transmission	0.7454 and 0.6236	
Refinement method	Full-matrix least-squares on F^2	
Data / restraints / parameters	5624 / 0 / 287	
Goodness-of-fit on F^2	1.128	
Final R indices [I>2sigma(I)]	R1 = 0.0499,	wR2 = 0.0925
R indices (all data)	R1 = 0.0712,	wR2 = 0.0992
Largest diff. peak and hole	0.481 and -0.524 e·Å^{-3}	

4.3.21. [(^{tBu}P=N=P)Ni(*1 κC,2 κ^{2}O,O'*-CO_2)Ni{*κ^{2}P,C*-*t*Bu_2PCHCHNHCHCH_2P*t*Bu_2)}] (29)

Identification code	SF_SF_120617	
Empirical formula	$C_{41}H_{82}N_2Ni_2O_2P_4 \cdot C_5H_{12}$	
Formula weight	948.53	
Temperature	100(2) K	
Wavelength	0.71073 Å	
Crystal system	Triclinic	
Space group	$P\bar{1}$	
Unit cell dimensions	a = 11.5412(5) Å	α = 93.693(2)°
	b = 19.3558(8) Å	β = 97.673(2)°
	c = 24.1966(10) Å	γ = 96.435(2)°
Volume	5305.8(4) Å^3	
Z	4	
Density (calculated)	1.187 Mg/m^3	
Absorption coefficient	0.865 mm^{-1}	
F(000)	2064	
Crystal size	0.276×0.144×0.087 mm^3	
Crystal shape and color:	Block,	clear orange
Theta range for data collection	2.194 to 28.368°	
Index ranges	-15<=h<=14, -25<=k<=25, -32<=l<=32	
Reflections collected	183629	
Independent reflections	26493 [R(int) = 0.0898]	
Completeness to theta = 25.242°	99.9 %	
Max. and min. transmission	0.7457 and 0.6886	
Refinement method	Full-matrix least-squares on F^2	
Data / restraints / parameters	26493 / 70 / 1083	
Goodness-of-fit on F^2	1.048	
Final R indices [I>2sigma(I)]	R1 = 0.0481,	wR2 = 0.0975
R indices (all data)	R1 = 0.0776,	wR2 = 0.1082
Largest diff. peak and hole	1.222 and -1.068 e·Å^{-3}	

4.3.22. [NiH(^{tBu}PN^{H}P)]OTf (30^{OTf})

Identification code	mo_SF_SF_130417_0m_a	
Empirical formula	$C_{28}H_{54}F_3NNiO_3P_2S$	
Formula weight	662.43	
Temperature	100(2) K	
Wavelength	0.71073 Å	
Crystal system	Triclinic	
Space group	$P\bar{1}$	
Unit cell dimensions	a = 12.0446(6) Å	α = 101.407(2)°.
	b = 12.2179(6) Å	β = 91.855(2)°.
	c = 12.2993(6) Å	γ = 106.940(2)°.
Volume	1689.39(15) Å^3	
Z	2	
Density (calculated)	1.302 Mg/m^3	
Absorption coefficient	0.775 mm^{-1}	
F(000)	708	
Crystal size	0.273×0.090×0.089 mm^3	
Crystal shape and color	Block,	clear colourless
Theta range for data collection	2.180 to 32.694°	
Index ranges	-18<=h<=18, -18<=k<=18, -18<=l<=18	
Reflections collected	87860	
Independent reflections	12396 [R(int) = 0.0881]	
Completeness to theta = 25.242°	99.9 %	
Refinement method	Full-matrix least-squares on F^2	
Data / restraints / parameters	12396 / 0 / 373	
Goodness-of-fit on F^2	1.047	
Final R indices [I>2sigma(I)]	R1 = 0.0478	wR2 = 0.0748
R indices (all data)	R1 = 0.0901	wR2 = 0.0851
Largest diff. peak and hole	0.481 and -0.455 e·Å^{-3}	

4.3.23. [NiH(^{tBu}PNP)] (31)

Identification code	mo_SF_SF_310317_0m_a	
Empirical formula	$C_{20}H_{45}NNiP_2$	
Formula weight	420.22	
Temperature	100(2) K	
Wavelength	0.71073 Å	
Crystal system	Triclinic	
Space group	$P\bar{1}$	
Unit cell dimensions	a = 8.5336(7) Å	α = 64.433(3)°
	b = 11.9913(10) Å	β = 72.373(3)°
	c = 13.6451(11) Å	γ = 71.824(3)°
Volume	1173.45(17) Å^3	
Z	2	
Density (calculated)	1.189 Mg/m^3	
Absorption coefficient	0.966 mm^{-1}	
F(000)	460	
Crystal size	0.179×0.155×0.092 mm^3	
Crystal shape and color	PÜlate,	clear light yellow orange
Theta range for data collection	2.562 to 30.665°	
Index ranges	-11<=h<=12, -17<=k<=17, -19<=l<=19	
Reflections collected	74027	
Independent reflections	7212 [R(int) = 0.0460]	
Completeness to theta = 25.242°	99.9 %	
Refinement method	Full-matrix least-squares on F^2	
Data / restraints / parameters	7212 / 0 / 233	
Goodness-of-fit on F^2	1.068	
Final R indices [I>2sigma(I)]	R1 = 0.0296	wR2 = 0.0597
R indices (all data)	R1 = 0.0444	wR2 = 0.0648
Largest diff. peak and hole	0.367 and -0.476 e·Å^{-3}	

4.3.24. [NiH{N(CO$_2$)(CH$_2$CH$_2$P^{t}Bu$_2$)$_2$}] (32)

Identification code	mo_SF_SF_230417_0ma_a	
Empirical formula	$C_{21}H_{45}NNiO_2P_2$	
Formula weight	464.23	
Temperature	100(2) K	
Wavelength	0.71073 Å	
Crystal system	Monoclinic	
Space group	$P2_1/c$	
Unit cell dimensions	a = 16.2269(6) Å	α = 90°
	b = 23.8622(10) Å	β = 109.739(2)°
	c = 13.5992(5) Å	γ = 90°
Volume	4956.3(3) Å^3	
Z	8	
Density (calculated)	1.244 Mg/m^3	
Absorption coefficient	0.927 mm^{-1}	
F(000)	2016	
Crystal size	0.312×0.248×0.125 mm^3	
Crystal shape and color	Plate,	clear yellow
Theta range for data collection	2.166 to 33.221°	
Index ranges	-25<=h<=25, -36<=k<=36, -20<=l<=20	
Reflections collected	227055	
Independent reflections	18991 [R(int) = 0.0812]	
Completeness to theta = 25.242°	99.9 %	
Refinement method	Full-matrix least-squares on F^2	
Data / restraints / parameters	18991 / 0 / 538	
Goodness-of-fit on F2	1.042	
Final R indices [I>2sigma(I)]	R1 = 0.0420,	wR2 = 0.0709
R indices (all data)	R1 = 0.0719,	wR2 = 0.0785
Largest diff. peak and hole	0.548 and -0.477 e·Å^{-3}	

4.3.25. [NiMe(^{tBu}P=N=P)] (33)

Identification code	SF_SF_110716	
Empirical formula	$C_{21}H_{43}NNiP_2$	
Formula weight	430.21	
Temperature	100(2) K	
Wavelength	0.71073 Å	
Crystal system	Monoclinic	
Space group	$P12_1/c1$	
Unit cell dimensions	a = 7.8078(3) Å	α = 90°
	b = 26.9707(10) Å	β = 107.9130(10)°
	c = 11.6822(5) Å	γ = 90°
Volume	2340.81(16) Å^3	
Z	4	
Density (calculated)	1.221 Mg/m^3	
Absorption coefficient	0.970 mm^{-1}	
F(000)	936	
Crystal size	0.174×0.148×0.092 mm^3	
Crystal shape and color	Block,	clear intense yellow
Theta range for data collection	1.98 to 33.26°	
Index ranges	-12<=h<=12, -41<=k<=41, -17<=l<=17	
Reflections collected	105934	
Independent reflections	8958 [R(int) = 0.0556]	
Completeness to theta = 33.26°	99.5 %	
Absorption correction	Semi-empirical from equivalents	
Max. and min. transmission	0.75 and 0.71	
Refinement method	Full-matrix least-squares on F^2	
Data / restraints / parameters	8958 / 0 / 239	
Goodness-of-fit on F^2	1.075	
Final R indices [I>2sigma(I)]	R1 = 0.0334	wR2 = 0.0665
R indices (all data)	R1 = 0.0482	wR2 = 0.0704
Largest diff. peak and hole	0.596 and -0.377 e·Å^{-3}	

4.3.26. [$NiN_3(^{tBu}P{=}N{=}P)$] (34)

Identification code	SF_MH_180618	
Empirical formula	$C_{20}H_{40}N_4NiP_2$	
Formula weight	457.21	
Temperature	100(2) K	
Wavelength	0.71073 Å	
Crystal system	Monoclinic	
Space group	$P12_1/n1$	
Unit cell dimensions	a = 12.5189(6) Å	α = 90°
	b = 26.3134(16) Å	β = 91.026(2)°
	c = 14.5733(8) Å	γ = 90°
Volume	4799.9(5) $Å^3$	
Z	8	
Density (calculated)	1.265 Mg/m^3	
Absorption coefficient	0.954 mm^{-1}	
F(000)	1968	
Crystal size	0.209×0.143×0.125 mm^3	
Crystal shape and color	Block,	clear dark orange
Theta range for data collection	2.16 to 28.36°	
Index ranges	-16<=h<=16, -35<=k<=35, -19<=l<=19	
Reflections collected	97273	
Independent reflections	11982 [R(int) = 0.1612]	
Completeness to theta = 28.36°	99.8 %	
Absorption correction	Semi-empirical from equivalents	
Max. and min. transmission	0.7457 and 0.7075	
Refinement method	Full-matrix least-squares on F^2	
Data / restraints / parameters	11982 / 0 / 511	
Goodness-of-fit on F^2	1.041	
Final R indices [I>2sigma(I)]	R1 = 0.0675	wR2 = 0.1038
R indices (all data)	R1 = 0.1284	wR2 = 0.1200
Largest diff. peak and hole	0.846 and -0.521 $e·Å^{-3}$	

4.3.27. [NiPh{κ^3*P,N,N*-{N(CHCHP^{t}Bu$_2$)(CHCHP(NH)^{t}Bu$_2$)}] (35)

Identification code	SF_MH_200418	
Empirical formula	$C_{26}H_{46}N_2NiP_2$	
Formula weight	507.30	
Temperature	102(2) K	
Wavelength	0.71073 Å	
Crystal system	Orthorhombic	
Space group	*P*na2$_1$	
Unit cell dimensions	a = 23.0304(10) Å	α = 90°
	b = 8.3149(3) Å	β = 90°
	c = 28.7420(12) Å	γ = 90°
Volume	5504.0(4) Å^3	
Z	8	
Density (calculated)	1.224 Mg/m^3	
Absorption coefficient	0.837 mm^{-1}	
F(000)	2192	
Crystal size	0.202×0.124×0.109 mm^3	
Crystal shape and color	Block,	clear yellow brown
Theta range for data collection	2.27 to 30.57°	
Index ranges	-32<=h<=32, -11<=k<=11, -41<=l<=41	
Reflections collected	248369	
Independent reflections	16839 [R(int) = 0.1280]	
Completeness to theta = 30.57°	99.8 %	
Absorption correction	Semi-empirical from equivalents	
Max. and min. transmission	0.913 and 0.883	
Refinement method	Full-matrix least-squares on F^2	
Data / restraints / parameters	16839 / 42 / 604	
Goodness-of-fit on F^2	1.041	
Final R indices [I>2sigma(I)]	R1 = 0.0474	wR2 = 0.0752
R indices (all data)	R1 = 0.0719	wR2 = 0.0811
Absolute structure parameter	0.126(11)	
Largest diff. peak and hole	0.492 and -0.439 e·Å^{-3}	

4.3.28. [Ni{κ^3*P,N,N*-N($CH_2CH_2P^tBu_2N$)($CH_2CH_2P^tBu_2$)}]$_2$ (36)

Identification code	SF_MH_180618_2	
Empirical formula	$C_{45}H_{92}N_4Ni_2P_4$	
Formula weight	930.52	
Temperature	100(2) K	
Wavelength	0.71073 Å	
Crystal system	Monoclinic	
Space group	$P12_1/n1$	
Unit cell dimensions	a = 13.9648(5) Å	α = 90°
	b = 20.4638(7) Å	β = 96.702(2)°
	c = 17.9171(7) Å	γ = 90°
Volume	5085.2(3) Å^3	
Z	4	
Density (calculated)	1.215 Mg/m^3	
Absorption coefficient	0.899 mm^{-1}	
F(000)	2024	
Crystal size	0.412×0.202×0.174 mm^3	
Crystal shape and color	Plate,	clear dark brown
Theta range for data collection	2.29 to 28.38°	
Index ranges	-18<=h<=18, -27<=k<=27, -23<=l<=23	
Reflections collected	166469	
Independent reflections	12685 [R(int) = 0.0882]	
Completeness to theta = 28.38°	99.6 %	
Absorption correction	Semi-empirical from equivalents	
Max. and min. transmission	0.86 and 0.75	
Refinement method	Full-matrix least-squares on F^2	
Data / restraints / parameters	12685 / 0 / 522	
Goodness-of-fit on F^2	1.038	
Final R indices [I>2sigma(I)]	R1 = 0.0367	wR2 = 0.0776
R indices (all data)	R1 = 0.0620	wR2 = 0.0892
Largest diff. peak and hole	0.518 and -0.538 e·Å^{-3}	

4.4 Scientific Contributions

4.4.1. Publications in Peer-reviewed Scientific Journals

1. **F. Schneck**, F. Schendzielorz, N. Hatami, M. Finger, C. Würtele, S. Schneider*,
Photochemically Driven Reverse Water-Gas Shift at Ambient Conditions mediated by a Nickel Pincer-Complex,
Angew. Chem. Int. Ed. **2018**, *57*, 14482−14487.

2. **F. Schneck**, J. Ahrens, M. Finger, A.C. Stückl, C. Würtele, D. Schwarzer, S. Schneider*,
The elusive abnormal CO_2 insertion enabled by metal-ligand cooperative photochemical selectivity inversion,
Nat. Commun. **2018**, *9*, 1161−1169.

3. **F. Schneck**, M. Finger, M. Tromp, S. Schneider*,
Chemical Non-Innocence of an Aliphatic PNP Pincer Ligand,
Chem. Eur. J. **2017**, 23, 33–37.

4. **F. Schneck,** M. Assmann, M. Balmer, K. Harms, R. Langer*,
Selective Hydrogenation of Amides to Amines and Alcohols Catalyzed by Improved Iron Pincer Complexes,
Organometallics **2016**, 35 (11), 1934–1943.

5. E. Leusmann, **F. Schneck**, S. Dehnen*,
Functionalization of Sn/S Clusters with Hetero- and Polyaromatics,
Organometallics **2015**, 34 (13), 3264–3271.

6. R. Langer*, A. Gese, D. Gesevicius, M. Jost, B. R. Langer, **F. Schneck**, A. Venker, W. Xu,
Formation of Different Isomers of Phosphine–Imidazolyl and –Pyridyl Ruthenium(II) Complexes Affecting the Catalyst Activity in the Acceptorless Dehydrogenation of Alcohols,
Eur. J. Inorg. Chem. **2015**, 4, 696–705.

4.4.2. Oral Contributions to Scientific Conferences

1 03/19 Noordwijkerhout, The Netherlands
The Netherlands' Catalysis and Chemistry Conference.

2 07/18 Florence, Italy
28th International Conference on Organometallic Chemistry.

3 03/18 Cancun, Mexico
3rd Molecules and Materials for Artificial Photosynthesis Conference (Short Talk Award).

4 03/17 Potsdam, Germany
Koordinationschemie-Treffen 2017.

4.4.3. Poster Presentations at Scientific Conferences

1 08/17 Göttingen, Germany
Anglo-German Inorganic Chemistry Conference 2017.

2 07/17 Copenhagen, Denmark
4th EuCheMS Inorganic Chemistry Conference.

3 09/16 Berlin, Germany
Woehler-Tagung 2016.

4 03/16 Kiel, Germany
Koordinationschemie-Treffen 2016.

5 09/14 Saarbrücken, Germany
Woehler-Tagung 2014.